



HAL
open science

Material and mechanical emulation of the human hand

Nick Hockings

► **To cite this version:**

Nick Hockings. Material and mechanical emulation of the human hand. Computer science. University of Bath, 2017. English. NNT: . tel-02424937

HAL Id: tel-02424937

<https://hal.science/tel-02424937>

Submitted on 29 Dec 2019

HAL is a multi-disciplinary open access archive for the deposit and dissemination of scientific research documents, whether they are published or not. The documents may come from teaching and research institutions in France or abroad, or from public or private research centers.

L'archive ouverte pluridisciplinaire **HAL**, est destinée au dépôt et à la diffusion de documents scientifiques de niveau recherche, publiés ou non, émanant des établissements d'enseignement et de recherche français ou étrangers, des laboratoires publics ou privés.

Material and Mechanical Emulation of the Human Hand

submitted by

Nick Hockings

for the degree of Doctor of Philosophy

of the

University of Bath

Department of Mechanical Engineering

August 2016

COPYRIGHT

Attention is drawn to the fact that copyright of this thesis rests with the author. A copy of this thesis has been supplied on condition that anyone who consults it is understood to recognise that its copyright rests with the author and that they must not copy it or use material from it except as permitted by law or with the consent of the author.

This thesis may be made available for consultation within the University Library and may be photocopied

or lent to other libraries for the purposes of consultation with effect from.....

.....

Signed on behalf of the Faculty of Engineering

Part I

Front matter

Acknowledgements

Firstly I am grateful to my supervisors Dr. Pejman Iravani and Professor Chris R. Bowen for allowing me to pursue so unusual a thesis. Thanks to my fellow PhD students in the mechatronics lab, and anybody else in the corridor who had to put up with the odour of various polymers occasionally undergoing partial thermal degradation.

Thank you to Professor Tony Miles who lent me his copy of Daniel Sirkett's PhD thesis on carpal bone motion, and allowed me to borrow part of the Orthopaedic Biomechanics group's demonstration skeleton. Thank you to Bristol anatomy labs who allowed me to take casts from a canine skeleton. Thanks also to the University of Sussex Clinical Imaging Research Unit who provided the MRI scan of the author's hand used in this work. Thank you to the libraries of the Royal United Hospital, Bath and of the Royal Society of Medicine, London which provided access to many anatomical and surgical journals.

A special thank you to Professor Noel Fitzpatrick of Fitzpatrick's Referrals and of the University of Surrey Veterinary School, who provided the CT scan of the dogs paw, and provided the funding for PhD studentship to implement soft tissue modelling based on the SPMP algorithm in Chapter 13 of this thesis.

Thank you to Professor Andrew Davison of Imperial College London who gave the author a tutorial in the DTAM algorithm, and to Dr. Walterio Mayol-Cuevas who co-hosted the British Machine Vision Association technical meeting on "Vision for language and manipulation" with the author. Thank you also to Dr. Paul Siebert of the University of Glasgow for having twice sent the author to the EU Robotics Forum, and for being the academic lead for the InnovateUK and EU Horizon 2020 funding bids.

Thank you to Prof. Dr. Jan Peters and Prof. Dr. Gerhard Neuman of T.U Darmstadt, to Prof. Dr. Marco Hutter of ETH Zurich, Dr. Thomas Voegtlin of INRIA Lorraine, and to Professor Giorgio Metta of IIT Genova whose labs I visited, for discussions, feedback and encouragement.

Summary

The hands and feet account for half of the complexity of the musculoskeletal system, while the skin of the hand is specialised with many important structures. Much of the subtlety of the mechanism of the hand lies in the soft tissues, and the tactile and proprioceptive sensitivity depends on the large number of mechanoreceptors embedded in specific structures of the soft tissues.

This thesis investigates synthetic materials and manufacturing techniques to enable building robots that reproduce the biomechanics and tactile sensitivity of vertebrates – histomimetic robotics.

The material and mechanical anatomy of the hand is reviewed, highlighting difficulty of numerical measurement in soft-tissue anatomy, and the predictive nature of descriptive anatomical knowledge. The biomechanical mechanisms of the hand and their support of sensorimotor control are presented.

A palette of materials and layup techniques are identified for emulating ligaments, joint surfaces, tendon networks, sheaths, soft matrices, and dermal structures. A method for thermoplastically drawing fine elastic fibres, with liquid metal amalgam cores, for connecting embedded sensors is demonstrated.

The performance requirements of skeletal muscles are identified. Two classes of muscle-like bulk MEMS electrostatic actuators are shown theoretically to be capable of meeting these requirements. Means to manufacture them, and their additional application as mechanoreceptors are described.

A novel machine perception algorithm is outlined as a solution to the problem of measuring soft tissue anatomy, CAD/CAE/CNC for layup of histomimetic robots, and sensory perception by such robots.

The results of the work support the view that histomimetic robotics is a viable approach, and identify a number of areas for further investigation including: polymer modification by graft-polymerisation, automated layup tools, and machine perception.

List of Figures

Owing to the large number of figures used to illustrate anatomical structures, the list of figures is in the appendix 16.1.4.

List of Tables

1.1	Table caption text	23
1.2	Table caption text	24
7.1	Physical properties of Poly-Optic polyurethane casting resins [1]	139
7.2	Approximate ranges of properties of rigid thermoplastics. Note (1) ABS has no simple phase change. (2) All values are altered by chain length, monomer ratios, and compounding additives.	141
7.3	Physical properties of thermoset elastomer resins	142
7.4	Physical properties of thermoplastic elastomers and elastomer-gels.	146
7.5	Table caption text	149
7.6	Table caption text	151
7.7	Composition, thermal and electrical properties of some low melting point metals, and comparison to common metals, [2]	157
12.1	Maximum power per unit body mass for a single jump, for sedentary adults, children and athletes[3].	269
12.2	Maximum instantaneous pedalling leg power, calculated by regression of fatigue curve. (Data read from graphs in figure 1 of [4] .)	269
12.3	Anaerobic leg power over 5 and 30 seconds, measured by pedalling. The data demonstrate the range of performance due to maturation, fitness level and focus of training.	271
12.4	Aerobic maximum pedalling power of adult long distance cyclists, from [5]. Subjects remained seated and cycled at a rate of 80-90 rpm (1.33-1.5Hz).	272
12.5	Whole body skeletal muscle mass, measured by anthropometry [6]	272
12.6	Muscle mass, proportion and distribution for different age groups of adults. Data from table 1 of [7]	272
12.7	Estimates of specific power of muscle tissue for different durations and subjects, based on tables listed and muscle mass data from table 12.6.	273
12.8	The decline in power to weight ratio of the body with age. Data on whole body muscle power and body weight from Table 1 of [8]. Note that the power here is for knee extension only on an isokinetic dynamometer for single repetition maximum force.	277

12.9 Increasing dielectric strength with decreasing film thickness for DuPont Kapton-HRTM (poly-oxydiphenylene-pyromellitimide), from [9]. Test condition 60 Hz, 1/4 in electrodes, 500 V/sec rise. 288

Contents

I Front matter	1
List of Tables	5
II Introduction	15
1 Introduction	16
1.1 Starting from anatomy	16
1.1.1 This thesis relative to other work in bio-inspired robotics.	17
1.2 The nature of anatomical knowledge	18
1.2.1 Why anatomy is non-numerical	19
1.2.2 What is learnt from dissection	19
1.2.3 The importance of pathology and surgery	21
1.3 How to emulate anatomy	21
1.3.1 Functional components required	22
1.3.2 To emulate passive mechanical anatomical tissues - joints, tendons, dermis	23
1.3.3 To emulate muscle	25
1.3.4 To emulate the somatosensory system	25
1.4 Contributions of this thesis	25
1.4.1 Conceptual contributions	26
1.4.2 Technical contributions	27
1.5 Organisation of this thesis	28
III Review	30
2 Robot hands	31
2.1 The difficulty of hands	31
2.2 Humanoid hands	32
2.2.1 Under actuated tendons	32
2.2.2 Flexural joints	33
2.2.3 Soft Robotic hands	33

2.3	Quasi-ligamentous joints in robots, machines and orthopaedics	33
2.4	Anatomical robotic hands	34
3	Anatomy	41
3.1	General anatomy	41
3.1.1	Types of tissue	41
3.1.2	Connective tissue types	41
3.1.3	Types of ligament	43
3.1.4	Anatomical joints	44
3.1.5	Stabilisation of synovial joints	45
3.1.6	Structure of synovial joints	45
3.1.7	Muscles	48
3.1.8	Tendons	55
3.1.9	General dermal structures	56
3.1.10	Sensing	57
3.1.11	Structure and scale of somatosensory dendrites and nerve fibres	59
3.2	Anatomical directions and terminology	62
3.2.1	Directions:	62
3.2.2	Motions:	62
3.2.3	Locations:	63
3.3	Human hands: bones and joints	66
3.3.1	Fingers	69
3.3.2	Bones and joints of the thumb	73
3.3.3	Wrist	76
3.3.4	Motions of the carpal bones	77
3.3.5	Forearm	80
3.4	Human hands: muscle-tendon networks	83
3.4.1	The digital flexor apparatus	83
3.4.2	Palmar fascia	87
3.4.3	Digital extensor apparatus	93
3.4.4	Carpal flexors	103
3.4.5	Carpal extensors	103
3.4.6	Muscles and tendons of the thumb	104
3.4.7	Little finger	105
3.4.8	Rotators of the forearm	106
3.5	Human hands: dermal structures	107
3.5.1	Digital pads	107
3.5.2	Finger nail	112
3.5.3	Crease ligaments	112
3.5.4	Palmar pads	113
3.6	Human hands: nerves and vessels	114

3.7	Comparative anatomy: canine lower forelimb	116
4	Biomechanics	118
4.1	Biomechanics as the basis of sensorimotor ability	118
4.2	The role of dermal structures	119
4.2.1	Soft pads	119
4.2.2	Grip/slip	120
4.2.3	Vibration finger ridges	120
4.2.4	Structure of finger tip - spectrum of compliance	120
4.3	Hand movements	121
4.3.1	Kinematic support of movements	121
4.3.2	Thumb web	126
4.3.3	Precision Grips	126
5	Review of Materials	128
5.1	Flexible Materials	128
5.1.1	Flexible composites	128
5.1.2	Elastic wires	128
IV	Histomimetic Robot Construction - Experimental Section	129
6	Equipment and Software	130
6.1	Anatomical Imaging	130
6.1.1	MRI scan of human hand	130
6.1.2	CT scan of dog's paw	131
6.2	Software	132
6.2.1	Clinical image segmentation	132
6.2.2	3D printing software	132
6.2.3	CAD software	133
6.2.4	Finite element software	134
6.3	3D printers & materials	135
6.3.1	Up! Plus 2 3D-printer	135
6.3.2	RepRap Mendel 3D-printer	135
7	Materials used in this thesis	136
7.1	Notes on state transitions in polymers and amalgams	136
7.1.1	Polymers	136
7.1.2	Metal amalgams	138
7.2	Rigid matrix	139
7.2.1	Thermoset polyurethane resin	139
7.2.2	Rigid thermoplastics	139
7.3	Flexible matrix	142

7.3.1	Thermoset elastomer resins	142
7.3.2	ACC silicones	142
7.3.3	Thermoplastic elastomers	143
7.4	Blending, laminating, plasticizing and cross-linking	147
7.4.1	PCL-SEBS blends and laminates	147
7.4.2	Polyacrylic acid polyacrylate plasticized with oil	147
7.4.3	PCL plasticized with glycerol	147
7.4.4	EVA cross linked with Sodium Borate	147
7.5	Fibres	148
7.5.1	Polyamides	148
7.5.2	Polyamide-6,6 (Nylon)	148
7.5.3	Polyaramide (Kevlar)	148
7.6	Thermoplastic composites	150
7.6.1	Compatible thermoplastics	150
7.6.2	Anchoring Polyamide and Polyaramide fibres in PCL	151
7.6.3	Hyper-elastic composites	152
7.6.4	Controlled non-adhesion	154
7.6.5	Key concepts	155
7.7	Sensor fibre materials	156
7.7.1	Gallium-Indium amalgams	156
7.7.2	Thermoplastic elastomers	158
7.7.3	Modifying additives	160
7.7.4	Piezoresistive composite sensor materials	160
8	Synthetic ligamentous Joints	163
8.1	Nature of fibrous mechanisms	163
8.2	Layup iterations	164
8.2.1	First prototype ligamentous joint	164
8.2.2	First multi-jointed finger	165
8.2.3	Polyurethane bones moulded from anatomy skeleton	167
8.2.4	Ultra soft silicone joint capsule and ligament matrix	170
8.2.5	Moulded polycaprolactone bones	172
8.2.6	Thermoplastically welded ligaments	174
8.2.7	Polylactic Acid (PLA) Printed bones	177
8.2.8	Dog's paw - complete carpus and digits	180
8.2.9	First finger with PCL-SEBS matrix soft tissues	184
8.2.10	Second finger with SEBS matrix soft tissues	185
8.2.11	Final iteration	189
8.3	Discussion	191
8.3.1	Key features of technique	191
8.3.2	Comparison to other joint types	192

8.3.3	Conclusions	192
9	Tendon Networks	193
9.1	Layup iterations	193
9.1.1	First flexor sheath	193
9.1.2	First tendon actuated finger	194
9.1.3	Second tendon actuated finger - polyurethane rubber matrix retinacular ligaments	198
9.1.4	PCL matrix tendons, silicone gel lubrication pad and EVA flexor sheath	199
9.1.5	Dry PCL finger - individual extensor tendons	200
9.1.6	Second dry PCL finger	202
9.1.7	Canine paw and carpus - flexor and extensor tendon networks	205
9.1.8	First SEBS-PCL flexor sheath	212
9.1.9	Structured flexor sheath	214
9.1.10	First SEBS-gel film lubricated extensor hood	216
9.1.11	Final finger	218
9.2	Discussion	224
9.2.1	Control of fusion	224
9.2.2	Control of friction	224
9.2.3	SEBS matrix wetting and adhesion of fibres	226
9.2.4	Precision of manufacture	227
9.2.5	The problem of measurement & possibility of automation	227
9.2.6	Conclusion	227
10	Dermal Structures	228
10.1	Importance of dermal structures	228
10.2	Canine paw pad and epidermis	228
10.2.1	Canine paw dermal pads	229
10.2.2	Canine paw epidermis	229
10.2.3	Assessment of canine paw pads	230
10.3	First finger prototype - subcutis-epidermis	230
10.4	Fingernail prototype	231
10.5	Final finger prototype - subcutis-epidermis	231
10.6	Conclusions	233
11	Sensor signal fibres	234
11.1	Concept & structure	234
11.2	Drawing from preform	235
11.2.1	Background - optical fibres	235
11.2.2	Preform	235
11.2.3	Fibre drawing tower	238
11.2.4	Furnace	241
11.2.5	EVA	242

11.2.6	SEBS	246
11.2.7	Ionomer fibres	249
11.3	Drawing from nozzle	252
11.3.1	Background - melt spinning	252
11.3.2	Nozzles	252
11.3.3	Setup	260
11.3.4	Operation	260
11.3.5	Fibre quality	260
11.3.6	The fibre conducts	261
11.4	Discussion	263
11.4.1	Conclusions on preform drawing	263
11.4.2	Preform drawing is preferred over nozzle drawing	266

V Histomimetic Robot Construction - Theoretical Section 267

12 Actuators 268

12.1	Requirements	268
12.1.1	Specific power & work per stroke	268
12.1.2	Required muscle performance for safe operation	274
12.1.3	Performance trade-offs in muscles	278
12.1.4	Minimum specifications for a muscle-like actuator	278
12.2	Rolled dielectric elastomer actuator	281
12.2.1	Concept	281
12.2.2	Optimising performance of the actuator	283
12.2.3	Fibrous rolled dielectric elastomer sensor (FR-DES)	286
12.3	Dual excitation multiphase electrostatic drive	287
12.3.1	Proposed quasi-fibrous DEMED	288

13 Perception 292

13.1	Visual tactile fusion challenges	292
13.1.1	Representation and modelling	292
13.1.2	Inference from sensor data	292
13.2	Terminology in machine perception	293
13.3	Recent publications that are close to SPMP	294
13.4	Smoothed Particle Machine Perception (SPMP)	295
13.4.1	Smoothed particle hydrodynamics (SPH) as the basis of a physical perception system	295
13.4.2	How SPMP works	295
13.4.3	Interpretations of smoothed particle models for higher perception	297
13.5	Applications of SPMP for histomimetic robotics	298
13.5.1	Digital Anatomy	298

13.5.2	CADEM for histomimetic robots	298
13.5.3	Closed loop control of CNC lay up	298
13.5.4	Visual-tactile perception and motion planning by histomimetic robots	298
VI	Conclusions	299
14	Conclusions	300
14.1	Synergies, reflexes and biomechanics	301
14.2	Complex composites	301
14.3	Bulk MEMS	302
14.3.1	Fibre drawing	302
14.3.2	Muscle-like actuators	302
15	Future Work	303
15.1	Soft matter perception	303
15.1.1	Smoothed particle modelling of anatomical soft tissues	303
15.1.2	Capture of anatomical models from dissection	303
15.1.3	Application of SPMP to robotic manipulation	303
15.1.4	Commercial applications of Smoothed Particle Machine Perception	303
15.2	Complex composites	304
15.2.1	Automatic laying heads, path planning	304
15.2.2	CADEM	304
15.2.3	Materials	304
15.3	Bulk MEMS	305
15.3.1	Elastic electrical wires	305
15.3.2	Somatosensory arrays	305
15.3.3	Muscle-like actuators	306
VII	Appendices	308
16	Supplementary material	309
16.1	Publications	309
16.1.1	IEEE Humanoids paper : Artificial ligamentous joints	309
16.1.2	Technical report: tendon networks for artificial ligamentous joints	317
16.1.3	Visual Image Interpretation in Humans and Machines (ViiHM) 2014 poster: Smoothed-Particle-Machine-Perception	325
16.1.4	Building Bridges to Building Brains (BBtBB) 2013 poster: Simulation of so- matosensory input	328
	List of Figures	330

Part II

Introduction

Chapter 1

Introduction

It is not necessary to build robots. It is also not necessary to build aircraft. However, there is no shortage of demand or potential applications for both, but the robots built so far do not meet expectations in things that humans and animals are good at. This is particularly true in manipulation, where robotic hands do not approach the sensory motor ability of human hands.

This thesis is exploratory. It seeks to find the approximate location of the envelope of viable solutions within the design space, by locating one point in or near that envelope. To this end information is collated from diverse fields including anatomy, histology, biomechanics, polymer chemistry, soft matter physics and composite materials. Much of this information is basic within its field of origin, but in combination lays the foundation for a new technology for building robots with the potential to match the useful aspects of human and animal performance.

1.1 Starting from anatomy

It is conventional in robotics to take mechanical engineering as the starting point of robot design. This thesis takes the anatomical sciences as its starting point. The author is a veterinary surgeon of ten years clinical experience, and a key aim of this thesis is to make the insight of the anatomical ¹ sciences accessible to those robotics engineers who seek to replicate the sensory motor abilities of vertebrate bodies. It introduces a set of manufacturing technologies to enable the practical application of anatomy to building robots.

The anatomical sciences are amongst the oldest and most exhaustively studied of natural sciences. The dissection of cadavers for the study of anatomy has been routine since at least 1505 when provision of cadavers for dissection was explicitly included in the first charter of the Royal College of Surgeons of Edinburgh [10]. The mechanical structure and material composition of humans and domestic animals are known in detail at every scale from the molecular upwards. This knowledge is not limited to mapping what exists, but includes the effects of alterations through the study of comparative and functional

¹Standard anatomical terms are used, labelled diagrams are provided in the review of relevant anatomy, Chapter3. Definitions of terms and concepts are provided in the introduction to the review Chapter3.1 .

anatomy, histology, pathology and surgery. The successful practice of surgery depends upon this causal understanding of tissue mechanics.

Social conventions and separation of professions make the detail of anatomical knowledge hard to access, but more important is the conceptual barrier due to the very strangeness of hyper-elastic, fibrous anatomical tissues relative to familiar engineering materials. Roboticians and engineers tend to focus on the bones as something solid, but vertebrate anatomy is fully functional in children and young animals while the bones are still cartilaginous. These difficulties may have contributed to the rejection of reverse engineering as a means of acquiring technology in robotics [11], a view which is at odds with the reputation for efficacy of reverse engineering across engineering as a whole.

1.1.1 This thesis relative to other work in bio-inspired robotics.

Robots as models of biological behaviour

Some biologists have used robots to replicate and investigate specific aspects of animal behaviour. Webb [12] seeks to address the question "*How should biological behaviour be modelled?*" in the context of neuroethology, writing in the journal Behavioral and Brain Sciences. To this end Webb sets out her case for "*building physical robot models of biological sensorimotor systems ... within a framework for describing and comparing models in the behavioural and biological sciences.*" To this end Webb prescribes a seven dimension framework for comparing such models in that context Webb's paper is accompanied by commentaries from readers of that journal [13] published alongside it. Counter arguments are provided there and this author will not add further to that debate.

Bio-inspired engineering

In the field of engineering research termed 'bio-inspired engineering' the aim is to generate novel engineering designs by abstracting a mechanism of interest from a biological system.

A canonical paper in bio inspired engineering is Full and Koditschek's paper "*Templates and Anchors*" [14], on the design and control of legged locomotion machines inspired by legged animals. Full and Koditschek prescribe a combination of high and lower level abstractions as their preferred way to model the limbs and locomotion of legged animals. They name these abstractions '*templates*' (high level) and '*anchors*' (lower level) and propose that low level controllers be designed for any given legged robot that coordinate the parts to produce action that approximates that prescribed by the simpler high level abstraction. This might be termed a 'walk-by-wire' system that allows the direction, speed and gait of the robot to be controlled in the smaller parameter space of the high level abstraction.

The difference between approaches

The aim in this thesis is orthogonal to that of both the biological research of Webb and the bio-inspired engineering of Full and Koditschek, and consequently brings with it different value judgements. The problems of bio-inspired robotics are dependent on the end sought and different for each case. Webb is concerned with the validity of inference from experiments applying robots and insight into biology

from those experiments. Full and Koditschek are concerned with abstracting a single mechanism from a biological system for reapplication in diverse non-biological systems.

The histomimetic (tissue emulation) approach of this thesis

This author is concerned with applying the conventional reverse engineering paradigm to the knowledge held in the anatomical sciences, in order to produce robots that reproduce the useful functions of human or animal, dermal and musculoskeletal systems. The principle application of this kind of robot is the service robotics that science fiction writers and their public have been declaring their demand for over the last hundred plus years.

This reverse engineering of anatomy is precisely what is commonly explicitly prohibited in robotics and predicted to be impossible. The results of this thesis are not finally conclusive, but suggest that the hypothesis of the impossibility of such a task, is likely to be false.

1.2 The nature of anatomical knowledge

Perhaps the greatest difficulty in presenting anatomy to an engineering audience is the non-numerical nature of the anatomical sciences. While anatomists do take numerical measurements in studies of particular properties, the anatomical knowledge which enables the practice of surgery is overwhelmingly non-numerical. By contrast, in engineering the default expectation is three significant figures of precision in measurements, and all relevant factors quantified objectively from instrument measurements.

The emphasis on numerical understanding is perhaps best expressed by the following well known quotation:

In physical science the first essential step in the direction of learning any subject is to find principles of numerical reckoning and practicable methods for measuring some quality connected with it. I often say that when you can measure what you are speaking about, and express it in numbers, you know something about it; but when you cannot measure it, when you cannot express it in numbers, your knowledge is of a meagre and unsatisfactory kind; it may be the beginning of knowledge, but you have scarcely in your thoughts advanced to the state of Science, whatever the matter may be.

William Thomson (Lord Kelvin), Lecture on 'Electrical Units of Measurement' at the Institution of Civil Engineers 1883 [15]

However, despite the utility of numerical methods when they are feasible, they are not the essence of science. The philosophically minded might dispute the reality of non-numerical knowledge, but very few would submit to being operated on by a surgeon not trained in anatomy. The best evidence of the reality of surgeons' knowledge of anatomy, is their ability to predict the consequences of cutting and suturing on the functioning of the body; that is,

- **the descriptive account of body structure, composition and function provided by anatomy amounts to a predictive model.**

This model is not tested by any single crucial experiment, but iteratively in relating every sensory motor interaction involving the patient's body. Notably the training of surgeons in anatomy depends critically on extensive tangible interaction to relate anatomical descriptions to sensory motor experience².

1.2.1 Why anatomy is non-numerical

A general solution for Thomson's 'numerical reckoning' in anatomy would be very useful. As yet none exists³. Numerical models are widely used for real-time surgical simulation (e.g. SOFA [17]), and non-real-time modelling for biomechanics research using conventional engineering finite element software. However a common problem of objective measurement and consequent dependence on expert opinion, underlies all existing tissue models.

The fundamental issue is that anatomical structures are free-form, hyper-elastic, and continuous such that they

1. lack precisely defined corners from which to take geometric measurements,
 2. deform under their own weight, such that there is no clear rest shape,
 3. lack distinct boundaries between structures.
- **Soft fibro-elastic connection between structures is essential to how the body works mechanically.**

Many tendons insert into indistinct regions of fibrous 'fascia', while ligaments are local densities of orientated tension bearing fibres within the surrounding tissue.

- **It is wrong however to think that anatomical descriptions are not quantitative.**

Shear and tensile moduli of individual tissues vary by orders of magnitude, e.g fat vs bone vs tendon vs dermis. The significant information is the relative order of magnitude. This does not require an instrument to measure. These are 'quantified' by the descriptive terms used, and in reference to general expectations for each class of tissue, learnt from experience of dissection.

1.2.2 What is learnt from dissection

When a student surgeon performs dissection they are taught to use blunt dissection to separate structures. This constitutes prising the tissues apart along planes of least resistance. This process reveals structures by their relative tensile modulus and yield stress. It is important to understand that cavities are exceptional, and the body is a continuous solid elastic composite structure. Different tissues differ in tensile and shear modulus by many orders of magnitude. Blunt dissection occurs through the loose

²In June 2014, the shortage of dissection based training of medical undergraduates in the UK lead to the Royal College of Surgeons of England to warn "For the past two years, Britain has failed to fill all of its training places for new surgeons, not for want of applicants, but because many candidates did not meet minimum standards." [16]

³A potential solution is presented in chapter-13.

areolar connective tissue that is topologically continuous throughout the body and exists between all other structures.

Dissection involves a continuous process of exploratory manipulation. For example, a student will manipulate a joint to learn its range of motion, which tissues are slack and which bear tension under which loadings of the joint, and what motions are actuated by which combinations of tendons. The articular ligaments of a joint are discovered within the fascia of the joint capsule by a combination of manipulation and blunt dissection, until the fibres of the ligament are separated from the surrounding tissue, and a probe can be passed under the ligament. The ligament is then sharply transected with a scalpel, and 'reflected' (folded back on itself) to reveal its 'origin' and 'insertion' (proximal and distal attachments), so demonstrating that it is a fibrous structure that principally bears tension between two regions. The change in the range of motion after transection of a ligament reveals the role of the ligament in stabilising the joint.

From anatomical dissection, relative geometric proportions, the topology of body structures, the density and orientation of fibres are learnt. In parallel, the microscopic structure and composition of tissues are learnt from tissue sections in which histologic dyes indicate the material composition of fibres and matrices, and the arrangement of the living cells. This reveals that,

- **there are just two fundamental classes of tissue - epithelia and connective tissues** and,
- **a small palette of basic materials from which all tissues are composed**, (table-1.1).

Epithelia are topologically two dimensional tissues that form the boundary and regulate chemical exchange between two compartments. They are composed of at least one densely packed layer of living cells arranged on an extra-cellular 'basement membrane'.

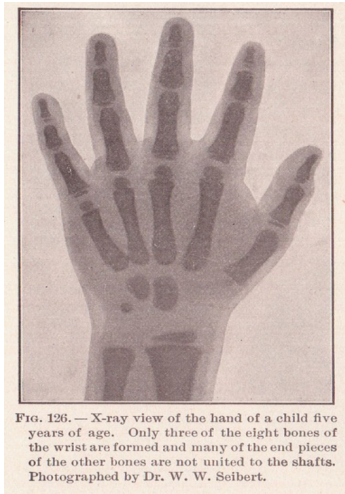
Connective tissues are topologically three dimensional tissues, composed of a matrix with cells and fibres dispersed through the matrix. With the exception of muscle, the metabolically active tissues are epithelia, and with the exception of the epidermis the load bearing tissues are connective tissues.

The training of surgeons in functional anatomy causally relates the observed structure of the body to its physiological and behavioural functions as an integrated network of systems. Crucial to this is, the transmission of forces through the body as a whole, and the interaction of those forces with each tissue structure and body system.

The variation in anatomy of healthy individuals shows that the material properties may vary by an order of magnitude without altering the function, e.g. hands are fully functional before calcification of the bones of the wrist in late childhood, figure-1-1 . The study of developmental anatomy reveals how the variation in geometric and compositional proportions of the tissues over the life of an individual affects their function and adaptation. Developmental anatomy shows that musculoskeletal structures such as ligamentous joints are formed by progressive differentiation of tissues, and are fully functional whilst entirely soft prior to calcification of the bones. What is critical is sufficient strain tolerance and the ratio of stiffness between the different materials. In the case of veterinary surgeons, interspecies comparative anatomy reveals that:

- **there is just one vertebrate body plan, in which topology is highly conserved across species**, while

- **differences of adaptation and function result from variation of geometric and compositional proportion.**



(a) Cartilaginous carpus of children. Repeated from figure-1-1a .



(b) Variation in conformation of adult male hands

Figure 1-1

1.2.3 The importance of pathology and surgery

Training in normal anatomy is followed by pathology - the study of how changes in the body lead to dysfunction and disease. This is also the point at which students dissect unpreserved tissues, and so learn the their true material properties in life and how they are altered in disease.

A central concept in pathology is the continuous remodelling of living tissues in response to mechanical loads and biochemical conditions. Under loaded tissues tend to atrophy, as is seen in 'de-conditioning' of athletes out of training or astronauts in space, and the wasting of the residual limb stumps of amputees. Where tissues are loaded beyond their adaptation various modes of mechanical failure and pathology occur. Hence,

- **the adaptation of the tissues indicates the mechanical forces in life.**

Finally this material and mechanical knowledge of the body is completed by learning the techniques of surgery, that allow major changes in the mechanical structure of the body to be made that restore or modify function. Taken together the anatomical sciences provide a detailed guide to the boundaries of and variation within the viable envelope of design parameters for body-like machines.

1.3 How to emulate anatomy

It has been believed that the materials are not available to allow direct emulation of musculoskeletal fibrous soft tissue structures [18]. This thesis sets out to demonstrate that :

The material and mechanical structure of the bodies of vertebrates have been extensively studied in the anatomical sciences. Developing equivalent synthetic materials allows this knowledge to be exploited for robotics.

It is important to appreciate the dominant role of fibre topology and elastic matrices in musculoskeletal tissues. The critical material factors of joint and tendon mechanisms are strain tolerance and relative stiffness differing by several orders of magnitude between different tissues or directions within fibrous structures.

The purpose of material emulation is to reproduce the macro scale function of human/animal bodies. Once a scale is found at which a synthetic material can match the behaviour of an anatomical tissue, this allows structures and mechanisms to be reproduced from this scale upwards.

What mechanical emulation does NOT require:

Autopoiesis - it is not necessary for a robot to build itself.

Biochemistry - robots are not restricted to being built from materials that are synthesized enzymatically in aqueous solution.

Downward emulation - it is not the purpose of emulation to reproduce structures down towards the molecular scale.

1.3.1 Functional components required

Deciding what to emulate is a value judgement which depends on the purpose in mind, for example in making humanoid hands:

1. in developmental robotics used to study human cognitive development it may be desirable to capture a close approximation to the sensorimotor interaction of a particular stage of development,
2. in robotic semantic grounding of natural language it would be useful to have a sensorimotor interaction that enabled the same percepts as a human,
3. in service robotics it would be useful to match human manipulation abilities across a diverse range of daily tasks,
4. in regenerative medicine it would be critical that the tissue scaffold hand support the growth and correct physiological organisation of cells into functional tissues.

The methods developed in this thesis are transferable to tissue scaffold materials, and so applicable to regenerative medicine. However the focus is robotics, so synthetic materials are used to avoid the problem of unwanted biodegradation. The needs of 1-3 above can be met by the same techniques. The functional components required would be:

Ligamentous joints - compact, robust articulations with large useful range of motion

Tendon networks - compact, robust, transmission of actuation, and 'preflexes' i.e. kinematics favourable for control.

Skin - (epidermis, dermis, subcutis) tactile perception, soft (pads) and hard (finger nails) contact interface for grip, and protection from environment (abrasion, infiltration)

Muscles/actuators - compact, soft actuators that integrate with the soft composite structure of the body, provide sufficient tendon excursion, work-per-stroke and speed of actuation, with adequate force-extension profile for normal human(oid) activities - not necessarily peak athletic performance.

Somatosensors - sensory nerve endings are $\approx 0.1mm$ in external diameter, and provide sensation of temperature, pressure, vibration, stretch, and damage. These are arranged at a density of $1permm^2$ in the finger pads, and lower densities elsewhere. Similar stretch and pressure sensory endings are present in the deep tissues, especially the joint capsules, ligaments and tendons where they provide proprioception.

Elastic nerves - connecting a large sensory array implanted in soft structures requires a way of connecting the sensors that will tolerate the deformation without adversely affecting the material properties, and fits into the available space. A sensor fibre that approximates the dimensions and elasticity of somatosensory nerve fibres would fit into the protected anatomical paths where the sensory nerves run.

Material	Description	Mechanical properties
Water	60 % of body by mass	liquid
Actin-Myosin	contractile fibre	50% contraction
Collagen	high modulus fibre	tensile modulus 5 GPa to 11.5 GPa, yield strain 10-18%
Elastin	low modulus fibre	tensile modulus 0.0011 GPa, yield strain 150-1,000 %
Proteoglycan	hygroscopic gel matrix	osmotic draw
Lipid	cell membranes and fat vesicles	hydrophobic liquid
Apatite	polycrystalline solid matrix	brittle, Mohs hardness 5
Keratin	high modulus epidermal material	Modulus 1 to 5 GPa, yield strain 5-40%

Table 1.1: The major families of base materials responsible for the mechanical properties of anatomical tissues

1.3.2 To emulate passive mechanical anatomical tissues - joints, tendons, dermis

When considering anatomy we must distinguish how it is made from how it works. Biological materials are necessarily made autopoietically by enzymatic catalysis in aqueous solution. When building artificial structures we are not so restricted. Synthetic materials can be used that are not enzymatically synthesized, and cannot be enzymatically degraded, hence do not require an immune system to protect

Tissue	Function	Composition
Areolar loose connective tissue (loose fascia)	allows motion of adjacent structures	sparse disordered collagen & elastin in proteoglycan matrix
Dense fascia	transmits force in multiple directions	dense multi directional collagen and elastin in proteoglycan matrix
Muscle	mechanical work	dense, parallel actin-myosin
Tendon	transmit muscle actuation forces	dense, parallel collagen
Bone	support compressive forces	apatite matrix with collagen fibres
Cartilage	support compressive force and low sliding friction	collagen fibres with turgid proteoglycan matrix
Synovial fluid	lubrication of sliding friction	shear thinning aqueous proteoglycan solution
Joint capsule	stabilise joint, retain synovial fluid	dense random collagen and elastic matrix
Ligament	stabilise joint	dense orientated collagen in elastic matrix
Dermis	mechanical covering of body	dense random collagen and elastin in soft matrix (typically more elastic than dense fascia)
Epidermis	impermeable outer surface	thin layer of keratin
Horn/h hoof/nail	impact and abrasion resistant outer surface	thick dense keratin
Hair	insulation and abrasion resistant covering	fibres of keratin

Table 1.2: Major tissue types of musculoskeletal system and skin

them. Likewise an individual robot may not need to grow through a continuous range of body sizes. What is needed is to reproduce the structures of the anatomy responsible for the functions we wish to reproduce.

To reproduce the mechanical functions of the body it is the connective tissues and epidermis that need to be emulated. The behaviour of a complex structure can be predicted by discretizing it into parts that are simple in shape and composition. It follows that,

- **the properties of composite materials, such as anatomical tissues, can be predicted from the interaction of its parts,**
- **and therefore emulated by another composite whose parts have the same behaviour.**

The families of base materials and the major tissue types of the musculoskeletal system and skin are provided in tables (1.1 & 1.2).

1.3.3 To emulate muscle

Muscle is composed of densely packed, parallel actin-myosin contractile fibres, enclosed within muscle cells which provide the chemical energy supply, and nervous control of contraction. (Note, the cells are named 'muscle fibres'.) The mechanism of actuation is the adhesion of myosin fibril heads to binding sites on the actin fibril, followed by flexion of the neck of the myosin fibril, coupled to the enzymatic hydrolysis of adenosine triphosphate(ATP), then release of the binding site and return to the original shape of the myosin. The action occurs cyclically, leading to the myosin moving along the actin. Myosin is arranged in bundles which are interleaved with actin fibres to form 'sarcomeres' - the basic contractile unit of muscles.

The physical force responsible for the adhesion of myosin to actin, and the flexion of the myosin neck, driving muscle actuation, is electrostatic force [19]. This exists in a saline solution between single electron charges in the form of hydrogen bonds between actin binding sites and myosin heads. In an artificial electrostatic actuator, higher dielectric strength and dielectric constant materials could be used, so allowing sufficient electric fields at larger scales, more practical for manufacturing. Muscle is also an iterative actuator, hence the work done per stroke can be many times higher than the maximum energy in the electric field.

To be used in the anatomical role of skeletal muscle, an actuator would need to be a fibro-gel at macroscopic scale, with 'floppy' low modulus in the relaxed state. It would also need to integrate with tendons and be affordable to produce in adequate quantity. These constraints point to a bulk micro-electromechanical system that can be produced in a continuous process. There is likely to be an optimal scale range for ease of manufacturing and performance.

1.3.4 To emulate the somatosensory system

The tactile and proprioceptive somatosensory systems of the skin and musculoskeletal system are essential to the control of movement [20]. It would be necessary to sample the deformation of dermal and musculoskeletal tissues with approximately the same resolution as the somatosensory nerve endings, and to connect those sensors without disrupting the mechanical properties of the tissues in which they are embedded. MEMS sensors exist, but fine elastic signal fibres of some form would be needed to connect them. These signal fibres would need to be robust, reliable and low cost. There would also need to be the hardware to read and connect such a sensory array to a computer, and the software to make perceptual inference from the raw sensor data.

1.4 Contributions of this thesis

This thesis flags the fact that robotics is peculiar in engineering for its rejection of reverse engineering, and that rejection is not justifiable. It further flags the large body of knowledge about the mechanical material properties, structure, mechanism and function of the body that is already well established in the anatomical sciences and in extensive daily use in the practice of surgery. The refusal of the robotics community to properly acknowledge a body of knowledge very much larger than their own is inexcusable.

1.4.1 Conceptual contributions

The basic conceptual contribution of this thesis is a direct falsification of vitalism. The general method of the thesis is simply reverse engineering as it is practised in any other branch of engineering. The peculiarity is that the vitalist presumption 'reverse engineering could not be done for anatomy', somehow took hold in the field of robotics.

The structure, composition and mechanism of the body are stock-in-trade for practising surgeons and exquisitely well documented in the anatomical sciences. For example the lubrication of unsheathed tendons by the hyper-elastic peritendon tissue, section 7.6.3 – was commended as 'amazing' by a reviewer of the paper on tendons – yet this structure and its mechanism are just one point on the syllabus taught to first year veterinary and medical students.

It is imperative that anyone wishing to reproduce the function of the body, should thoroughly familiarize themselves with what is known in the anatomical sciences about how that function is implemented in the body. This applies first and foremost to material properties and composition, which underlie structure and mechanism. Most importantly when an engineer proposes to reproduce the function of an anatomical mechanism, using dissimilar materials or structures to the original, then the engineer must explain why the different design should be expected to work. Most existing robots are substantially disabled due to derogations from the anatomical structure that leave them fragile and unnecessarily difficult to control.

Terminology

The term histomimetic, used by the author to name the class of robotics described in this thesis, is constructed in the conventional lexicon of biomedical terminology: histo = tissue, mimetic = emulating. This author is firmly opposed to the invention of any terminology or other presentational complexities that are not strictly necessary to describe a system in the clearest possible way.

Nature of fibrous mechanisms

The mechanisms of fibrous and elastic structures, such as dermal and musculoskeletal anatomy, are the straightforward consequences of geometry and elasticity. What is important to appreciate is that structures of deformable materials cannot be robustly emulated by rigid materials. Rigidity causes excess stress concentrations, shock loading and material failure.

Bridge to anatomy for robotics engineers

Chapters 1, 3 & 4 provide for robotics engineers an introduction to the anatomical sciences and detailed review of the mechanisms of the human hand.

Relevance of this thesis to medicine and surgery

It was asked in the viva what roboticists would be able to teach to surgeons. As a veterinary surgeon of ten years clinical practice, this author answers that, there is nothing that roboticists could teach about the body that is not already known to the most attentive and conscientious surgeons. This should not

be surprising, because it is the dissection, manipulation and alteration of anatomy that is the source of knowledge about the mechanical mechanisms of the body.

The major contribution to medicine and surgery stemming from this thesis will be the soft matter perception system outlined in Chapter 13. This will enable first the objective capture of anatomical tissue mechanics models from dissection. Such models can be used to generate patient specific surgical simulations from clinical imaging, and eventually the automation of surgery.

The field of regenerative medicine, (i.e. in vitro tissue culture of replacement body parts), is already well established. The techniques in this thesis are directly transferable to tissue culture materials, and to the modelling, design and automated manufacture of tissue scaffolds.

1.4.2 Technical contributions

This thesis:

- Identifies a palette of base materials and layup techniques by which enable direct emulation of anatomical ligamentous joints, tendon networks and dermal structures for application in robotics.

These include:

- Viscoelastic behaviour in the melt state creates smooth surfaces
 - Low temp thermoplastic welding allows precise fibre placement & adjustment
 - Intermolecular forces allow controlled adhesion non-adhesion
 - Hyper-elasticity can take the place of lubrication
 - Composite hyper-elastic structure creates mechanisms
- Develops a technique of drawing ultra fine elastic electrical wires for application in connecting arrays of sensors embedded in soft materials, such as somatosensory arrays in soft tissues of robots.
 - Identifies two classes of muscle-like fibrous electrostatic actuator with the potential to emulate the performance of skeletal muscle
 - Outlines a visual-tactile machine perception algorithm for solving the problem of numerical measurement of ultra-soft and fibrous materials such as anatomical soft tissues.

1.5 Organisation of this thesis

This thesis aims to demonstrate the feasibility of the histomimetic approach to building robots. It is recommended to

Part 1 - Introduction The nature of anatomical knowledge and the approach to emulation of anatomical tissues for robotics.

Part 2 - Review of the literature relevant to this thesis:

Chapter 2 Robots The need for robot hands and the short comings of existing methods are discussed. Robots based on vertebrate anatomy, and related structures are reviewed.

Chapter 3 Anatomy General anatomical concepts and terminology are introduced. The mechanical anatomy of the human hand is reviewed in detail with reference to the primary anatomical literature.

Chapter 4 Biomechanics The biomechanical mechanisms arising from the anatomical structure and tissues of the hand are described.

Chapter 5 Soft Composites Examples of soft fibrous composites in the wider engineering literature.

Part 3 - Experimental work development of a palette of materials, and manufacturing techniques:

Chapter 6 Equipment and Software

Chapter 7 Materials The base materials used in this thesis, their properties and behaviour.

Chapter 8 Synthetic Ligamentous Joints The development of the technique for making ligamentous joints.

Chapter 9 Artificial Tendon Networks The development of the techniques for making sheathed and unsheathed tendon networks.

Chapter 10 Dermal Structures An initial test of composites and layup for dermal structures.

Chapter 11 Sensor Signal Fibres The development thermoplastic drawing of fine elastic fibres with conductive metal amalgam cores. These fibres provide a potential functional analogue of sensory nerve fibres for connecting large arrays of mechanosensors embedded in soft structures.

Part 4 - Theoretical work exploration of potential solutions:

Chapter 12 Actuators The required performance of skeletal-muscle is analysed on the basis of human performance and the threshold of frailty. Two classes of bulk micro-electro-mechanical electrostatic actuators are shown theoretically to surpass the requirements. Methods for cost effective manufacture of these actuators and their additional application as mechanosensors are discussed.

Chapter 13 Perception The Smoothed Particle Machine Perception (SPMP) algorithm is presented in overview. Its application as a solution to the problems of numerical measurement in soft tissue anatomy, CAD/CAE/CNC manufacture of histomimetic robots, and the sensory integration of histomimetic robots is discussed.

Part 5 - Conclusions .

Chapter 14 Conclusions .

Chapter 15 Further work The funding that has been secured to further develop the ideas of this thesis, and the various branches of the thesis where collaborations are being pursued are presented.

Part 6 - Appendices .

Chapter 16 Supplementary Material Information on the collaborations formed, funding bids submitted, and publications.

Chapter 17 References

Part III

Review

Chapter 2

Robot hands

Robot hands are reviewed here for comparison in the context of robots based on vertebrate anatomy. Exhaustive coverage of other types robot hands would be out of scope for this review. Conventional robotic hands have been reviewed in greater detail by [21, 22] .

2.1 The difficulty of hands

Locomotion and manipulation require interaction with an uncertain physical world. Consequently robotic limbs and hands need robust joints, with good range of motion. Vertebrate anatomy provides evidence of one physical solution - ligamentous synovial joints - that remains superior to other methods. This is highlighted by the work of Melchiorri et al (2013) [23] who stated,

“The replication of the human hand’s functionality and appearance is one of the main reasons for the development of robot hands. Despite 40 years of research in the field, the reproduction of human capabilities, in terms of dexterous manipulation, still seems unachievable by the state-of-the-art technologies.”

and of Grebenstein (2014) [24],

“The gap between the basic principles and solutions of bio-mechanical systems and the capabilities of technical systems is too wide to develop a proper hand design by simply copying the human hand using methods and solutions of the current robotics state of the art. It is currently still not possible to construct an exact copy of the human hand.”

The challenge is how to reproduce the material properties of the soft tissues involved, and how to layup those materials to reproduce the mechanism of anatomical joints. This is commonly considered a difficult task, e.g.

“many joints are held together ... by ligaments or tough soft tissues which are almost impossible to duplicate” [18]

2.2 Humanoid hands

A robotic 'hand', as opposed to a 'gripper' is implicitly biomimetic to some extent in its role and outward form. In materials, structure and mechanism robotic hands may be much less related to biology. Non-anatomical robot hands are not the subject of this thesis, only a few examples are reviewed here.

Robotic hands which approximate the external envelope and degrees of freedom of the joints are too numerous to list here. The field of robotic hands has been active for more than forty years, but also has a precursor in eighteenth century clockwork automata [25, 26] . As stated by (Melchiorri 2013) [23] current methods, derived from conventional engineering methodology using rigid parts and pin hinges, have reached a plateau. There has been a trend over the last decade from miniature electric motors in the fingers to tendon actuation. This is largely due to the lower cost and greater power of external actuators, and a change from steel rope to polymer string for the tendons. Previously steel tendons were limited in bending radius and prone to fatigue failure, [23] . Tendon actuation has also facilitated the use of underactuated fingers [27] .

More recently there is a drive to make cheaper hands made by 3D-printing [23, 28, 29] . The use of flexural joints is also gaining popularity [29, 30] . As alluded to by Melchiorri et al (2013) [23] the story of humanoid robotics has been one of exhaustively proving the unsuitability of rigid mechanisms for replicating the function of a compliant structure. There has been a gradual adoption of compliant mechanisms such as under-actuated tendons, force controlled actuators, and soft tactile sensors.

2.2.1 Under actuated tendons

Various projects have demonstrated underactuated hands and grippers that form stable grasps around objects of unknown shape, controlled by regulating the force of a single actuator e.g. [31, 29] . Twenty three robotic hand joints from current projects were reviewed in appendix A of Catalano (2013) [28] . None of these projects use fibrous soft composites to emulate the structure of anatomical ligamentous joints.

DLR-IV AWIWI Robot Hand

This is most sophisticated tendon actuated metal hand to date. It fully reproduces the degrees of freedom of the human wrist and digits, though through a rather different tendon mechanism. It also was a early example of a hand made robust by the use of elastic ligaments, famously surviving the "Gebenstein impact test" - i.e. being hit across the fingers with a hammer [32] . This resilience to collisions is important because previously robot hands were typically brittle structures prone to breaking under the kind of accidental contacts that occur when interacting with the uncontrolled external environment. The use of under-actuation however is minimized with tendons passing through the centre of rotation of joints that they do not actuate.

IIT-Pisa

The IIT-Pisa Softhand [28] is a maximally under actuated hand with a single tendon passing through pulleys on every finger. It also uses elastic ligaments to make it extremely resilient to collisions. It

uses rolling contact hinges to minimize friction, and is built from 3D printed polymer parts. When operated by a human holding the hand, a remarkable diversity of grasps and manipulations are possible by interaction with the object to shape the grasp.

Shadow dexterous hand

The Shadow Robot Ltd dexterous hand [33] uses under-actuated tendons within each finger, but unlike the anatomical wrist the digital tendons pass close to the centre of rotation of the wrist. As with the other hands above, this arrangement therefore omits the reflexes that act between the wrist and digits in the anatomical hand, see section-4.1 .

2.2.2 Flexural joints

iRobot-Harvard-Yale iHY hand

Flexural joints have been used since prehistory, and are widely used in commercial thermoplastics where they are termed 'living hinges'. They have become of interest in robotic hands through the work of Dollar and co-workers [29] , who developed new manufacturing techniques including "shape deposition manufacturing". This is a variant of what in industry is termed "overmoulding", except that instead of ,e.g. adding a soft grip surface to a handle, softer material is added to form the flexural joint between rigid segments. The alternation of materials allows the hinge to be thicker and so less prone to buckling and fatigue in compression. This makes flexural hinges useful and cost effective for robotic grippers.

The iHY hand is a non-anthropomorphic, underactuated three finger gripper with flexural joints and tendon guide channels made by shape deposition manufacturing [34] . It is capable of a variety of grasps and manipulations through interaction between the object and environment with the kinematics of the hand.

2.2.3 Soft Robotic hands

There are many soft pneumatic actuators and grippers. The most capable humanoid hand built this way is the 3D printed pneumatic hand produced by Scharff and co-workers [35] presented at the Soft Robotics week in Livorno, Italy in 2016. This hand is 3D printed as a single piece in elastomeric material. It includes torsional bellows chambers in the forearm that rotate the hand about the long axis of the forearm, as well as bellows actuators to flex each finger and the thumb. Being entirely composed of elastomer of rubber medium modulus (i.e. not as soft as gel elastomers) it is capable of shaking hands with a human and forming compliant grasps on a wide range of different shaped objects.

2.3 Quasi-ligamentous joints in robots, machines and orthopaedics

In robotics flexural joints have been used in 3D printed structures, notably the iRobot-Harvard-Yale hand [34]. These allow buckling and axial twisting of the joint, and can be built into a shape deposition

cast skeleton. The flexible mechanism is robust to collisions, but this flexibility limits the ability to stably transmit force along the column of bones.

Another example of fibrous joints are the ribbon joints of the “Kilck-Klack” or “Jacobs Ladder” falling blocks illusion toy, [36] [37]. The mechanism is close to that of a four bar linkage, and to the cruciate ligaments of knees. The fibrous constraint is very stable, but the contact area between the blocks is minimal for all but one point in the range of motion. Consequently the motion is well constrained, but any compressive force would produce high pressure loadings at the contact surfaces.

Etoundi et al [38] [39] produced a condylar knee mechanism that used nylon cord ligaments in a four bar linkage, emulating the cruciate ligament mechanism of knees. Cords were also used as ligaments in ECCE Robot [40] to prevent dislocation of the shoulder joint. These were composed of stiff cords of ultra high molecular weight polyethylene (UHMWPE), or series combination of elastic and stiff cords. While these cord-ligaments reproduce some of the topology of anatomical ligaments, they lack the broad attachment and integration with the bones that make anatomical joints robust.

Van den Broek et al [41] [42] developed a prototype artificial inter-vertebral disk (AID) emulating the structure of anatomical inter-vertebral disks. The AID was composed of an ionized hydrogel core, wrapped in a hydrophobic membrane, enveloped by five layers of UHMWPE fibre, reproducing the nucleus pulposus constrained by the annulus fibrosus. Loading and fatigue testing showed that the prototype could withstand the maximum biological loading and fatigue, while providing stiffness and hysteresis close to that of healthy anatomical inter-vertebral disks.

The closest approximation of a ligamentous joint in a robot may be the silicone rubber joint capsule tested on the Anatomically Correct Testbed (ACT) hand [43]. This lacks the stiff fibrous constraint of articular ligaments, but does preserve the large radius, compression bearing articular faces.

2.4 Anatomical robotic hands

Those not familiar with the anatomy of the hand may benefit from browsing the review of human hand anatomy (Ch-3), before reading this section.

Budapest biomimetic hand testbed

[44] Produced a 3D anthropomorphic biomimetic hand testbed, which has 3D printed condylar joints and is actuated by opposing flexor and extensor tendons. The 'bones' of the joint were tied to each other with thread ligaments as shown in the lefthand image in figure-2-1 .

Anatomically Correct Test-bed' ACT Hand

For more than a decade the best known explicitly biomimetic robot hand was the 'Anatomically Correct Testbed' ACT Hand of Matsuoka and co-workers, [45, 46, 47, 48] , figure-2-2a . This attempted to reproduce the tendon network of the fingers to study the control of human hands for application to robotics, and succeeded in replicating motor synergies in precision grasps[49, 50, 43].

The original version used plastic mouldings of human phalanges and metacarpi, with metal ball joints set at the centre of rotation of the anatomic joints, string tendons, and a crocheted extensor hood

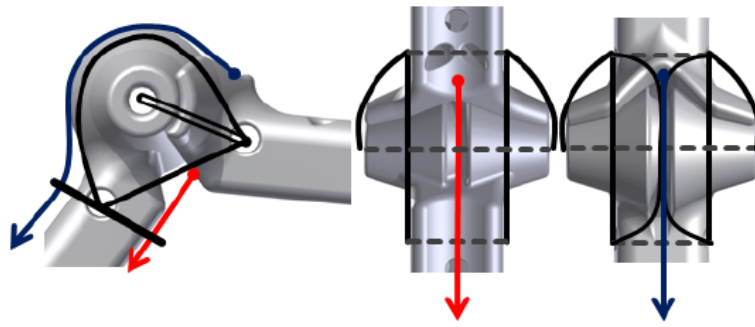
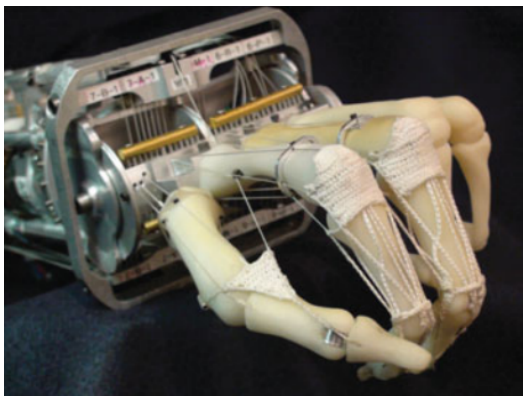


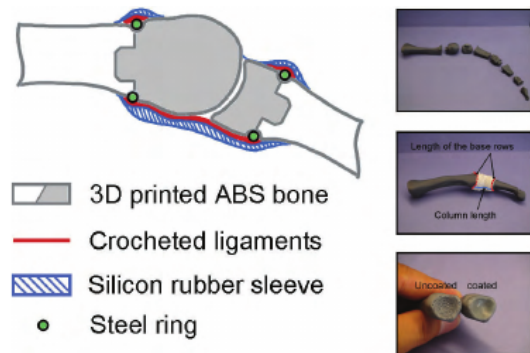
Figure 2-1: The articulation of the biomimetic joint. Fig.7 from [44] .

(see section on human hand anatomy). Later versions [51] used a hemi-tubular flexible rubber joint capsule to emulate ligamentous joints, figures-2-2b .

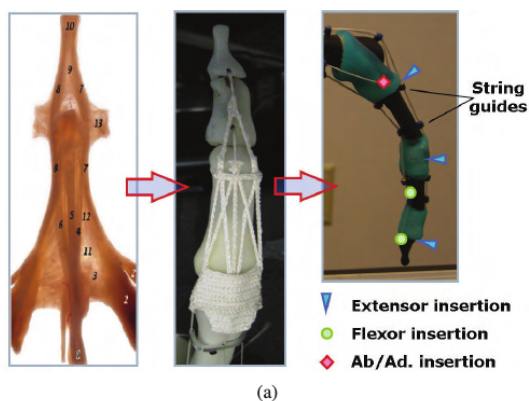
Owing to difficulties modelling the dynamics of the tendon network, the later version of the ACT hand had a simplified 2D tendon network 2-3a . However this simplified network could only move the finger tip within one plane 2-3b [51] .



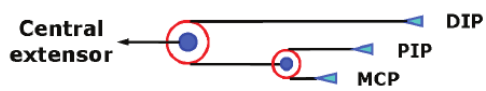
(a) The Anatomically correct testbed (ACT) hand. Fig 1 from [48] .



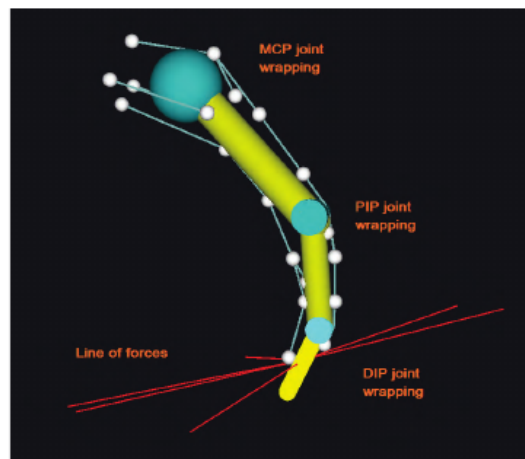
(b) ACT hand: biomimetic artificial joint design from [20]. Fig. 3 from [51] .



(a)



(a) Comparison of the extensor mechanism between the human hand [52], the ACT Hand and the robotic finger (a) Design evolution of the tendon hood. (b) Schematic drawing of the pulley system used for the robotic finger. Fig-4 from [51].



(b) ACT hand : 3D Visualization of the kinematic model of the robotic finger in OpenGL. Fig. 8 in [51].

Washington Hand

The successor to the ACT hand is the "Highly Biomimetic Anthropomorphic Robotic Hand" [53, 54], figure-2-4.

"reinterpreted the important biomechanical advantages of the human hand from roboticists perspective and design a biomimetic robotic hand that closely mimics its human counterpart with artificial joint capsules, crocheted ligaments and tendons, laser-cut extensor hood, and elastic pulley mechanism ... to identify the important biomechanical information of the human hand and then biomimetically replicate it. This allows a close replica that shares the same kinematic and even dynamic properties of its human counterpart."

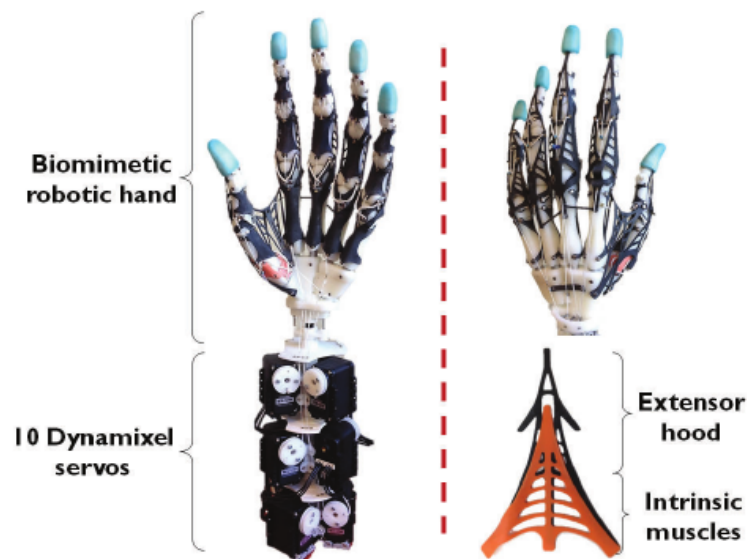


Figure 2-4: The fully assembled biomimetic robotic hand. Left: The palmar aspect of the biomimetic robotic hand system. Top right: The dorsal view of the robotic hand. Bottom right: The laser-cut extensor hood integrated with intrinsic muscles. Note: The total weight of our biomimetic robotic hand is less than 1 kg (942 grams) including the actuation system. Fig.1 from [54].

This robot hand uses laser cut rubber as elastic joint tissue and 'crocheted' string as the ligaments, "anchored by 1 mm screws at their biological insertion sites" into 3D printed bones figure2-5. Extensor hood and flexor tendon pulleys are also made with laser cut rubber sheet. The inter-osseous muscles are emulated by passive elastic rubber. The mechanism of the flexor tendons differs from the anatomical tendon in that the string passes through eyelets in the rubber sheets, which stretch at their attachments, rather than a tendon sliding inside stationary annular ligaments, figure-2-6. Importantly this hand appears to be the first example of a thumb web in a robotic hand.

This hand was demonstrated performing grasps and in-hand manipulation controlled via a master glove. It was able to lift and manipulate objects as light as 1 gram and as heavy as 500 grams. Notably the thumb web was exploited in power grasps to pick up heavy objects. This hand is a substantial advance over the ACT hand tendon network implementation, but inevitably much less forceful

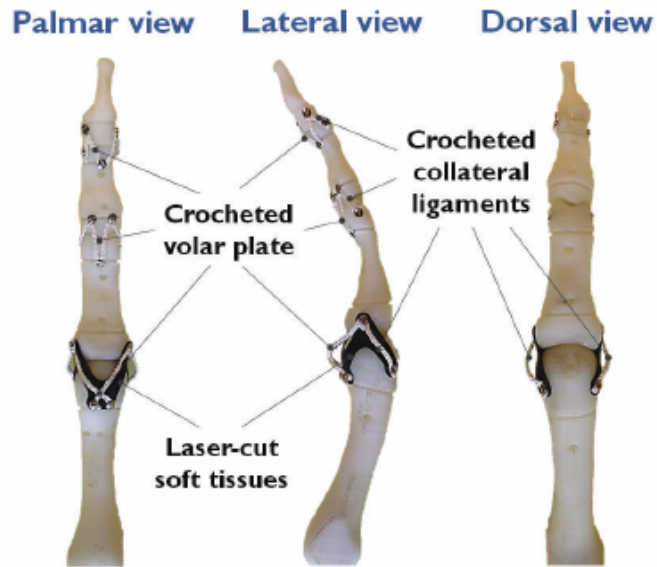


Figure 2-5: The skeleton of the 3D-printed finger connected by crocheted ligaments and laser-cut joint soft tissues. Note: All the crocheted ligaments are anchored by 1 mm screws at their biological insertion sites. Fig.5 from [54] .

and powerful than a human hand. The ligament and tendon attachments are not likely to tolerate the same magnitude of forces and impacts that anatomical ligaments and tendons do. The altered tendon mechanism will have some significant differences in behaviour. There will also be significant friction in the extensor mechanism where rubber sheet slides over 3D printed polymer. Whether these differences matter depend on the value judgements appropriate for a particular end use.

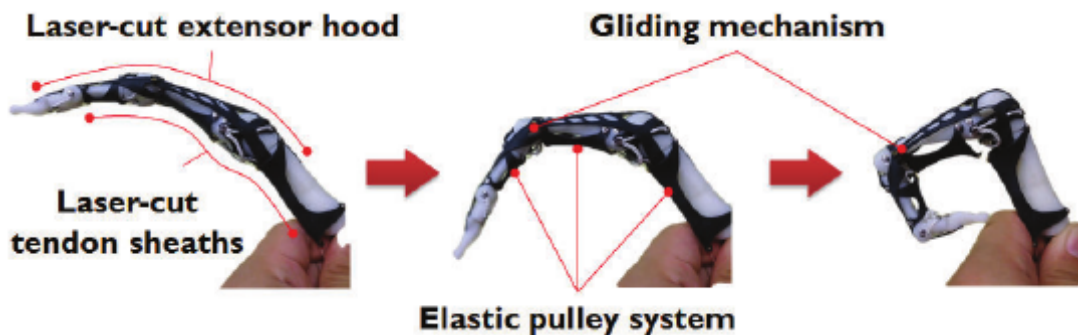


Figure 2-6: Snapshots of an assembled finger showing both the gliding mechanism of the extensor hood and the bulging effect of the tendon sheaths during finger flexion. Fig.7 from [54] .

Cambridge finger and thumb

Culha [55] created an

”anatomically correct finger bones, elastic ligaments and antagonistic tendons to build anthropomorphic joints with multi-directional passive compliance and strong force exertion capabilities”

This had elastic joint capsules incorporating rubber collateral ligaments. The trapezio-metacarpal and index finger carpo-metacarpal joints shared one elastic joint capsule. The tendons ran in rigid thin tube tendon guides at the joints. The extensor tendons differ from anatomy in that there is no hood, but separate proximal and distal extensor tendons. This appears to be the first example of an actuated thumb web in a robotic hand. (The ACT hand had a thumb adductor tendon, but it inserted close to the base of the metacarpals so did not form a web. The Washington hand has a well developed thumb web, but it is a passive structure.) A later version has no thumb web, and the metacarpals are set in a block palm, figure-2-8. This version has been used for chopstick manipulation demonstrating compliant underactuated antagonism between the digits, (and possibly surpassing the modal performance local human population in manipulation of this class of cutlery).

The central concept of this design is the combination of rigid bones and joint faces with elastic joint capsules and tendon actuation. It is demonstrated that this produces a very robust structure that can survive severe deflections, yet also forms strong truss with tendon actuation. It shares this property with the DLR IV [32] and IIT-Pisa Softhand [28].

Difference between robot and anatomical tendons

Stabilization and control of friction are critical in tendon networks. All of the robot tendons described above use rigid constraints and minimise sliding contact to avoid friction. These tendons are made of spun, braided cord or webbing. This differs markedly from anatomical tendons, which are composed of parallel fibres held together in a hierarchy of bundles by endotendon matrix and epitendon fibrous membrane. Anatomical tendons are in continuous contact with surrounding tissues along their length. They are enveloped in soft tissue either hyperelastic peritendon loose connective tissue, or fluid lubricated synovial tendon sheaths and bursas formed by extension of the capsule of synovial joints. Unlike Bowden cables, tendon sheaths do not bear compression along their length.

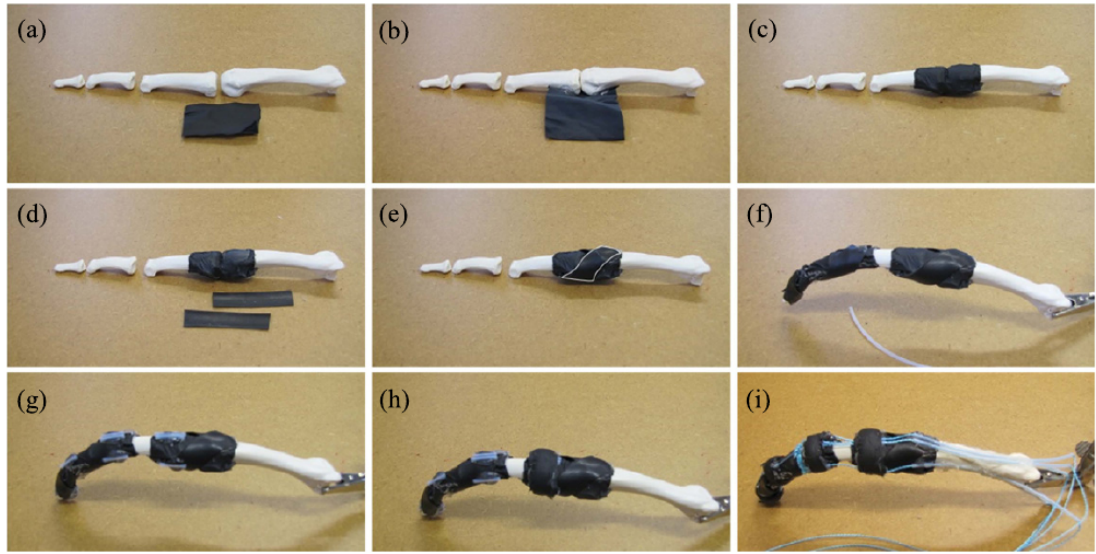


Figure 2-7: Fabrication stages of the index finger. The capsule ligament covers the joint cavity by attaching to end parts of bones with hot melt adhesives (a)(c). Collateral ligaments whose geometry is highlighted in (e) are placed on the side for torsional stability of joints (d)(e). Remaining joints are covered with ligaments with the same method (f). Low friction short tube pieces are placed on anatomically inspired pulley positions (g). Pulleys are fixed with additional hot melt adhesives and nitrile rubber to withstand torques (h). Tendon cables are routed through pulleys and longer tubes on non-moving bones (i). Fig.3 from [55].

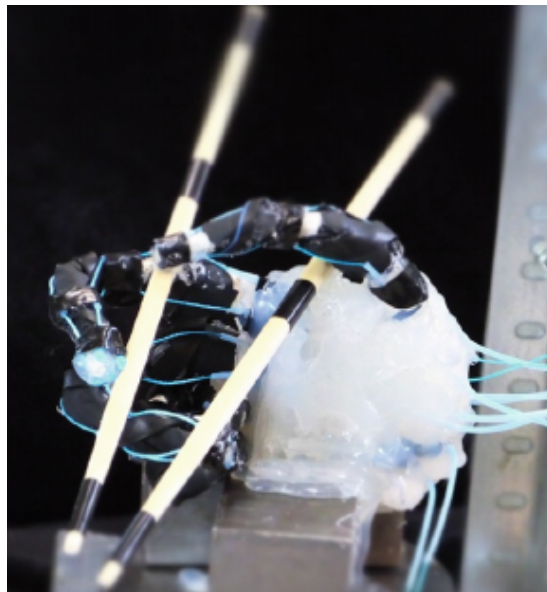


Figure 2-8: A picture of the built soft robotic hand. Fig.1 from [56].

Chapter 3

Anatomy

This review is intended to introduce the reader to the mechanical structures and mechanisms of anatomy demonstrated in the human hand. It cannot provide exhaustive coverage of all that is known about the anatomy of human hands. The topics covered have individually been the subjects of many theses. Those looking for further detail are recommended to read Landsmeer's Anatomy of the Human Hand [57], and the primary anatomical research literature.

Sections 3.1 provides an overview of anatomical concepts. Section 3.2 provides a guide to anatomical directions. Sections 3.3 to 3.6 cover the anatomy of human hands. Sections 3.7 and 3.8 provide a comparison to animal anatomy.

3.1 General anatomy

3.1.1 Types of tissue

As described in Ch.1.2.2, there are just two basic types of tissue to which all others belong: (i)connective tissues and (ii)epithelia. For mechanical emulation of the body we are concerned with the connective tissues, and the epidermis of the skin.

3.1.2 Connective tissue types

Areolar loose connective tissue

This is the base form of connective tissue from which others are specialized. It is a hyper-elastic tissue, typically resilient to tensile and shear strains around 1,000%. It is composed of randomly arranged sparse fibres of hyper-elastic 'elastin' and stiff 'collagen' with a predominantly water matrix retained by hygroscopic proteo-glycan molecules (proteins polymers with hydrophilic sugar based side chains). As mentioned in Ch.1.2.2 the areolar loose connective tissue "is topologically continuous throughout the body and exists between all other structures."

Fascia

Fascia is the collective term for dense connective tissues, including all tendons, ligaments and capsules. These contain a high density of fibres, usually collagen. These tissues are covered in further detail in sections Ch.3.1.3 to Ch.3.1.8.

Adipose

Adipose tissue commonly known as 'fat' may serve either metabolic (energy store, thermal insulation, heat generation) or mechanical (padding) functions. The extracellular matrix of adipose may vary from that of loose connective tissue to that of fascia. The characteristic feature of adipose tissue is a high percentage of its volume is composed of adipose cells. These are the fat storage cells containing large vacuoles filled with tri-glyceride fats (glycerol with three fatty acid chains ester-linked to the alcohol groups of the glycerol).

Cartilage

Cartilage is characterised by increased shear modulus due to increased cross-linked proteo-glycan content forming a turgid gel.

Hyaline cartilage has the highest shear modulus of cartilage, but the lowest proportion of tension bearing collagen or elastin fibres. It is found in the cartilage precursors of bones, on the compression bearing surfaces of synovial joints, and at sites requiring sliding between two surfaces while under compression, including parts of some tendons and ligaments. The collagen fibres of hyaline cartilage have stratified orientation, with the those near the surface oriented with the direction of sliding contact, while deeper layers have collagen orientated perpendicular to the surface.

Elastic cartilage sometimes called 'yellow cartilage' is dominated by hyper-elastic elastin fibres and is most notably found in the lobes of human ears, parts of the vocal tract and other highly flexible structures.

Fibrocartilage is dominated by dense collagen fibres and is found where fascia has to bear some degree of compression, often as a transitional zone between hyaline cartilage and ligament or tendon.

Bone

Bone is the principle compression bearing tissue in the adult body. The extracellular matrix of bone is dominated by mineral 'bone apatite', a form of Calcium Phosphate apatite, which confers its high compression modulus. Bone also contains collagen fibres without which it would be brittle. Together apatite and collagen form a composite with high compressive strength and elastic modulus. Bone tissue is classified by structure and developmental origin. Bones have detailed geometric form and structure that transmits physiological forces with the minimum of dense mineral material. As mentioned in Ch.1.2.2 bone is continuously remodelled in response to the forces on it, hence the forces on a bone can be inferred from its structure.

Types of bone tissue:

Lamellar bone is the dense 'compact' bone that forms the outer surface of bones away from the joint faces (which are covered by hyaline cartilage instead).

Spongy bone also called 'cancellous' or 'trabecular' bone, is porous network of mineral bone tissue. It usually exhibits an orientated lattice work aligned to the dominant forces in the bone. It is found filling the interior of bones except in the mid shaft of some mature long bones which may be hollow.

Types of bone formation:

Endochondral ossification starts with a hyaline cartilage 'model' of the bone which is progressively calcified then ossified starting at one or more 'centres of ossification'.

Intra-membranous ossification starts in a fibrous connective tissue membrane without a cartilage precursor. This form of ossification is responsible for the formation of 'flat' bones (e.g the pelvis, mandible and skull), and the 'subperiosteal' formation of lamellar bone on the outer surface of other bones.

Parts of bones:

Periosteum is the fibrous connective tissue membrane that covers the surface of bone, commonly known as 'sinew'. It is the site of new lamellar bone deposition.

Physis is the 'growth plate', a layer of hyaline cartilage that transects a bone orthogonal to its long axis. This is the primary site of elongation of bones during growth. There is one centre of ossification either side of a physis.

Diaphysis is the tubular shaft that forms the middle section of a 'long' bone.

Metaphysis is the flared end of a 'long' bone before the physis.

Epiphysis is the part of a bone beyond the physis.

'Head' of a bone is proximal end of a long bone, associated with the articulation with the next proximal bone

'Condyles' of a bone are the paired medial and lateral cylindrical structures at the distal end of a long bone forming the articulation with the next most distal bone.

3.1.3 Types of ligament

The term 'ligament' is used to describe a tension bearing fascia structure with dense orientated fibres that is not part of a muscle-tendon unit.

Elastin ligaments are typically yellow in colour due to being composed of hyper-elastic elastin fibres, rather than collagen. They provide parallel elastic actuation alongside muscles. They are typically found where constant force at variable lengths is needed to support posture, e.g the nuchal ligament of neck, and the yellow ligaments (ligamenta flava) of the spine.

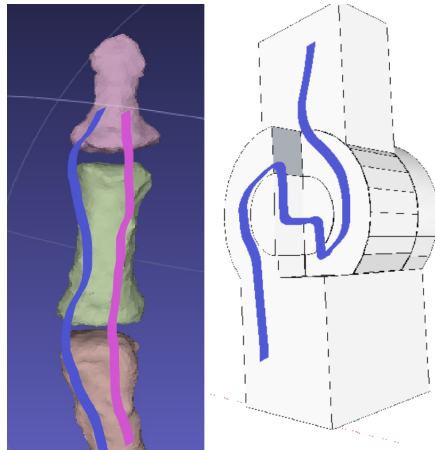


Figure 3-1: Force paths through ligamentous versus pin-hinge joints. (Blue) tensile force, (Pink) compressive force. Note how the force has to be transmitted as compression across the discontinuity of rigid materials, and consequently the has to double back on itself making the pin-hinge joint much bulkier than the ligamentous joint for the same strength. This also causes a lateral dog-leg in the compressive force path and, reduced radius and increased pressure at the contact surfaces.

Articular ligaments connect two or more bones at a joint, prevent misalignment of the joint surfaces and restrict its range of movement, see Ch.3.1.6 in synovial joints generally, and for each joint of the hand Ch.3.3.

Retinacular ligaments hold tendons in their correct paths. The flexor and extensor retinacular systems of the digits, palm and wrist are critical to the the kinematics of the hand, Ch.3.1.8, Ch.3.4.1 and Ch.3.4.3.

Dermal ligaments connect the skin to the underlying musculoskeletal system. These are of particular importance to the structure of the skin of the hands and feet, Ch3.1.9 and Ch3.5.

3.1.4 Anatomical joints

Anatomical joints are unlike most engineering joints between rigid materials in that tension across joints is borne by continuous fibres. Unlike flexural joints and 'living hinges' found in some robots and thermoplastic consumer products, anatomical joints also provide substantial transmission of compressive force.

Fibrous transmission of tension is very important because it saves weight and bulk, while making the joints tougher and more robust, in the same way that a cable is thinner and lighter than a chain of the same strength made of the same material, figure-3-1 . This is because in a joint between rigid materials there has to be a discontinuity in the structure to allow flexion of the joint. Only compression can be transmitted across the discontinuity, hence the force and the structure has to double back on itself to achieve this, requiring three times the cross section area of a continuous tension bearing structure. Fibrous tension transmission also allows larger cross section area for transmission of compression, and larger radius of curvature where compressive force transmission occurs across a discontinuity.

Types of anatomical joints:

Fibrous joints are the least flexible, these include the 'suture' joints between the plates of the skull, the attachment of the teeth to their sockets, and the attachments of the left and right sides of the pelvis to each other and to the sacrum.

Cartilaginous joints are of intermediate flexibility and include the connections of the ends of the ribs, the joints of the sternum, and the intervertebral disks of the spine.

Synovial joints are the most mobile joints and form the articulations of the limbs and jaw.

3.1.5 Stabilisation of synovial joints

The stability of ligamentous joints is dependent the action of the tendons/muscles around the joint, and curvature of the articular surfaces. The articular ligaments of synovial joints do not generally provide the stiffness of constraint provided by engineering joints in rigid materials. For example for any given ligament it is generally possible to manipulate the joint to a position where the ligament is slack enough to pass a probe under it. By itself the joint capsule, including ligaments, prevents dislocation (luxation) of the articular surfaces, but commonly does allow some separation of the joint surfaces (subluxation). The action of the tendons causes pressure between the joint faces. Under the action of this pressure, the curvature of the joint faces drives the joint into congruence.

The series arrangement and under-actuation of joints is such that a load not supported by a tendon will commonly cause rotation of other joints that either transfers the load onto a tendon, or releases the load altogether. The exception to this being the function of suspensory and check ligaments which act on tendons in parallel with muscles in “passive stay” mechanisms.

3.1.6 Structure of synovial joints

Joint capsule

The joint cavity of the synovial joints is enclosed by a fibrous joint capsule lined with a synovial membrane which secretes synovial fluid. The joint capsule is continuous with the articular cartilage of the concave side of the joint. The capsule is reinforced with dense orientated collagen fibres. The matrix allows the capsule to stretch orthogonal to the collagen, and lubricates relative movement of the fibres in shear motions.

Bursa

A 'bursa' is a pocket of synovial membrane connected to a joint capsule and surrounding one or more tendons and providing fluid lubrication in a manner similar to a tendon sheath.

Joint surfaces

The joint surfaces have to convey compressive force across the joint. In a juveniles some bones (e.g. the carpal bones of the wrist) remain entirely hyaline cartilage until late childhood, but are fully functional, (figure-1-1a). In adults the cartilage is restricted to a thin layer supported by spongy bone. While the bone is stiffer than cartilage both have a degree of compliance. Consequently are to some extent deformed into congruence under load, which helps to distribute force over a wide area and avoid excessive pressure. This is important to prevent gouging and wear of the sliding surfaces.

Articular cartilage

Articular cartilage is a thin layer of hyaline cartilage. This is a turgid proteo-glycan hydrogel composed of the glucose amino-glycan chondroitin sulphate, and type II collagen. As mentioned in Ch.3.1.2 the collagen fibres are orientated with the direction of sliding near the surface, and perpendicular to the surface in the deeper layers. This arrangement helps to resist the shear forces due to movement of the joint under load.

When subject to pressure the hydrogel of hyaline cartilage exudes aqueous fluid. This has a lubricating effect similar to the melting of ice under the pressure of skate blades, and accounts for the slipperiness of fresh hyaline cartilage. By contrast partially dehydrated hyaline cartilage becomes tacky.

Synovial fluid

Synovial joints are named for the thick proteinaceous synovial fluid that fills the cavity of the joint. This fluid is an aqueous colloid of the glucose amino-glycans 'hyaluronic acid' and 'lubricin'. Hyaluronic acid has very similar structure to the chondroitin sulphate of the cartilage, except that it is not sulphated and therefore does not form ionomer cross-links. This difference accounts for hyaluronic acid being soluble, while chondroitin sulphate is hygroscopic but insoluble.

Synovial fluid is a viscous, shear thinning fluid that acts as a boundary lubricant between the articular surfaces, and between the joint capsule and articular convex surface [58]. This contrasts with typical engineering hypoid gear oils for example which are designed to avoid shear thinning. However the shear thinning behaviour of synovial fluid contributes to very low sliding friction, while the exuding behaviour of hyaline cartilage helps to prevent dry contact and wear between opposing joint surfaces.

Articular ligaments

The articular ligaments are dense bundles of collagen fibres in the joint capsule. They are the strongest part of the joint capsule, but they are not distinct from it. Their areas of attachment to the proximal and distal bones of the joint with respect to the shape of the joint surfaces are critical, because these determine the range of motion that the ligaments permit, and the motions that they restrict. The fibres of the ligaments extend into the bones at their origin and insertion and connect the collagen fibres within the bones.

Check ligaments

Check ligaments prevent over extension of joints. They are typically large thick articular ligaments that lie under the flexor tendons, e.g. the volar beak ligament of trapezio-metacarpal joint (Ch.3.3.2), the check ligaments of the metacarpo-phalangeal, and inter-phalangeal joints Ch.3.3.1).

Plates and sesamoid bones

Where tendons or ligaments are subject to pressure, due to bearing tension around a corner, or being pressed on by another tendon, they become modified to support that compression. These modifications are progressive and variable depending on the degree of pressure. Moderate pressure results in hyaline

cartilage deposition, providing a smooth sliding surface. This cartilage deposition can form thickened plates such as the dorsal plates of the extensor tendon slips of the interphalangeal joints, and the volar plate of the check ligaments of the interphalangeal joints and metacarpophalangeal joints. Where the pressure is greater ossification occurs, providing increased resistance to compression. The bones formed in this way are called sesamoid bones, and are found variably in the metacarpophalangeal volar plates. The largest sesamoid bone is the patella of the knee, which is in the quadriceps tendon.

Meniscus

Some joints have a motion does not have a fixed centre of rotation and therefore cannot be described by the movement of two surfaces sliding over each other. In these joints an additional fibrocartilaginous structure called a 'meniscus' fits between the two bones. The faces of the meniscus approximate the those of the different bone surfaces. The fibres in the meniscus run circumferentially, preventing the outward displacement of the cartilage. The net effect is to maintain a large area for the transmission of compressive force, while allowing complex motion of the bones relative to each other. Menisci are found in the temporo-mandibular joint of the jaw, the paired femoro-tibial joints of the knee, and the ulnar-carpal joint of the wrist.

3.1.7 Muscles

Muscle fibres

Muscle are composed of cells called 'muscle fibres' or 'myocytes', which contain contractile bundles of molecular linear motors called 'myofibrils' composed of the active biopolymers actin and myosin. The molecules within a fibril are arranged in repeating units of overlapping actin and myosin called 'sarcomeres'. These are typically about 2 – 3.4 microns long, and give skeletal muscle its striated (stripey) appearance.

The myosin heads bind to sites on the actin fibrils. The 'necks' of the myosin molecules flex, iteratively 'walking' the myosin bundles along the actin chains. The energy source powering this action is the de-phosphorylation of adenosine triphosphate (ATP) to adenosine diphosphate (ADP) by the ATP-ase enzymic site on the heads of the myosin molecules.

The physical force responsible for the mechanical action is the electrostatic force, in the form of hydrogen bonds between the actin and myosin at the binding site. Hence, at the mechanical level actin-myosin can be considered a a form of iterative molecular linear electrostatic motor, integrated with a fuel cell. For each walking step one ATP is consumed and the myosin head moves between 5 – 25nm along the actin fibril, depending on the length of the lever arm of the myosin 'neck' region. [59]

The tensile stress produced by a muscle fibre depends on both the density of actin and myosin fibres, and the number of myosin heads engaged on each actin fibre - which depends on the length of overlap between the actin and myosin. This produces a non-linear force extension curve with a peak in at the optimal overlap, (fig.3-3d). Speed of contraction is dependent on the number of sarcomeres in series per unit length, and hence inversely on the length of sarcomere. The work done per stroke depends on the number of walking iterations, and hence the length of the sarcomere. The power depends on the type of myosin head, which determines the speed of reaction of de-phosphorylation. Different types of muscle fibre have different types of myosin, and densities of actin-myosin depending on what else takes up volume in the cell, including mitochondria fro aerobic respiration, myoglobin oxygen stores, glycogen stores for glucose, glycolytic enzymes for anaerobic respiration, and sarcoplasmic reticulum to pump and release calcium ions to control contraction.

In humans there are three classes of skeletal muscle fibre optimised for different modes of metabolism and speeds of contraction:

Type I slow twitch aerobic have approximately 6% mitochondria [61] by volume, slow contraction speed and smaller sarcoplasmic reticulum. .

Type II-A mixed aerobic-anaerobic have 4.5% mitochondria by volume, fast twitch contraction speed, medium force, and slow fatigue.

Type II-X anaerobic previously identified as II-B in humans, have 2.3% mitochondria by volume, fast twitch, high force and rapid fatigue.

Type II-B pure anaerobic found in other species, not in humans, have the fastest twitch speed and highest contraction stress.

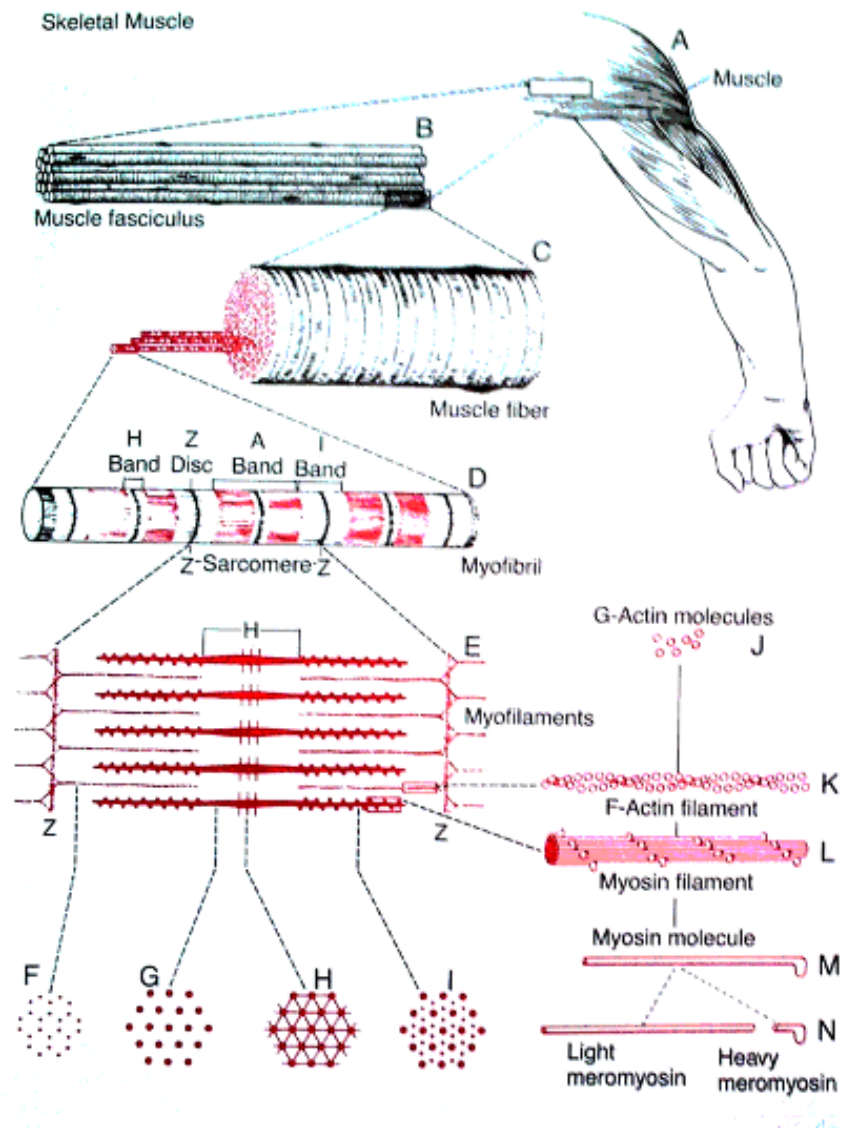
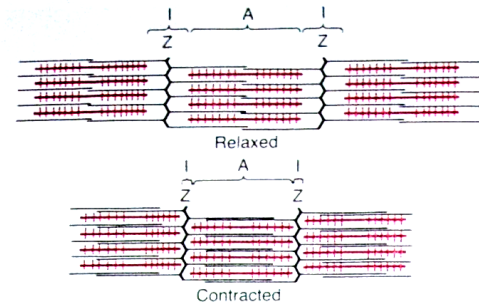
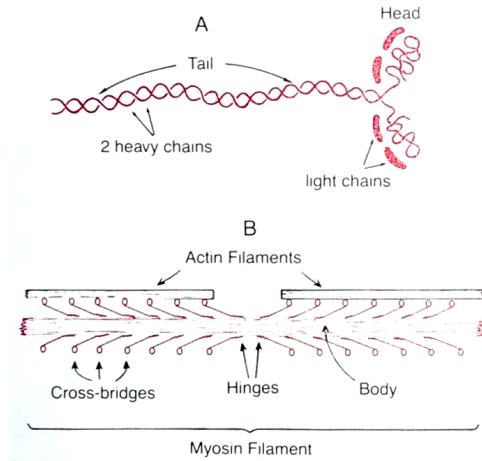


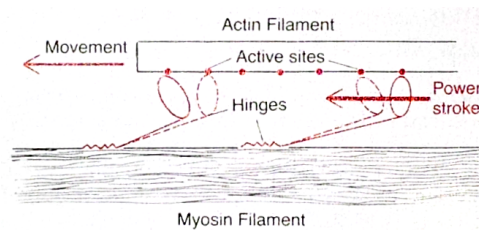
Figure 3-2: Organisation of Skeletal muscle, from the gross to the molecular level. F,G,H, and I are cross sections at the levels indicated.(Drawing by Sylvia Colard Keene. Modified from Fawcett: Bloom and Fawcett: A Textbook of Histology. Philadelphia, W.B.Sunders Company, 1986.) Adapted from fig.6-1 [60]



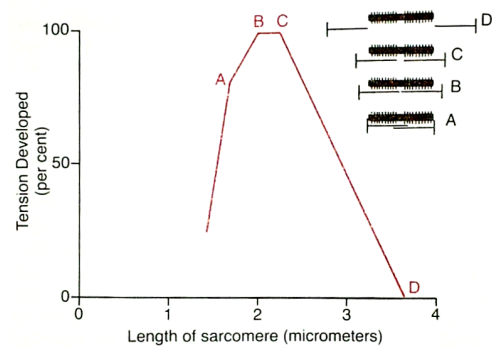
(a) The relaxed and contracted states of a myofibril, showing sliding of the actin filaments (black) into the spaces between the myosin filaments (red). Adapted from fig.6-4 [60]



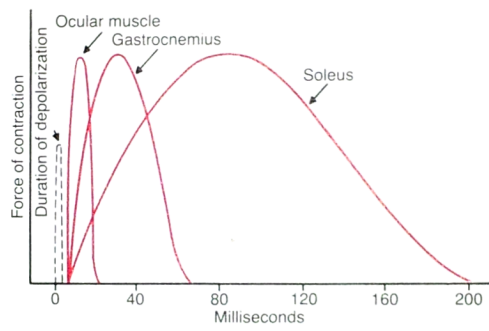
(b) A, The myosin molecule. B, Combination of many myosin molecules to form a myosin filament. Also shown are the cross-bridges and the interaction between the heads of the cross-bridges and adjacent actin filaments. Adapted from fig.6-5 [60]



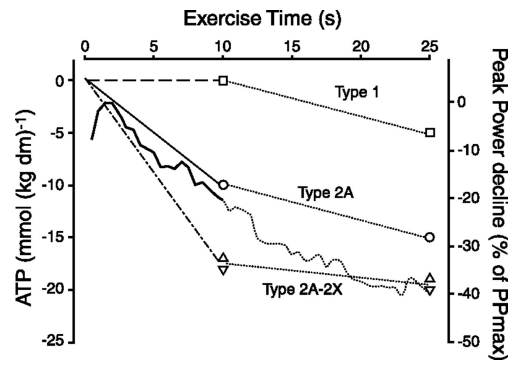
(c) The "walk-along" mechanism for contraction of the muscle. Adapted from fig.6-7 [60]



(d) Length-tension diagram for a single sarcomere, illustrating maximum strength of contraction when the sarcomere is 2.0 to 2.2 micrometres in length. At the upper right are shown the relative positions of the actin and myosin filaments at different sarcomere lengths from point A to point D. (Modified from Gordon, Huxley, and Julian: The length-tension diagram of single vertebrate striated muscle fibres. *J.Pysiol.*, 171:28P, 1964.) Adapted from fig.6-8 [60]



(a) Duration of isometric contractions of different types of mammalian muscles, showing also a latent period between the action potential and muscle contraction. Adapted from fig.6-11 [60]



(b) ATP concentration declines in different human muscle fibres during during a brief maximal exercise. Mean ATP concentration values are shown at 10 and 25 s for type 1 (squares), 2A (circles), and 2A/2X (triangles) fibres. The continuous noisy line represents the decline of the muscle power in one subject. [Modified from Karatzaferi et al. (397).] Adapted from fig.13 [61]

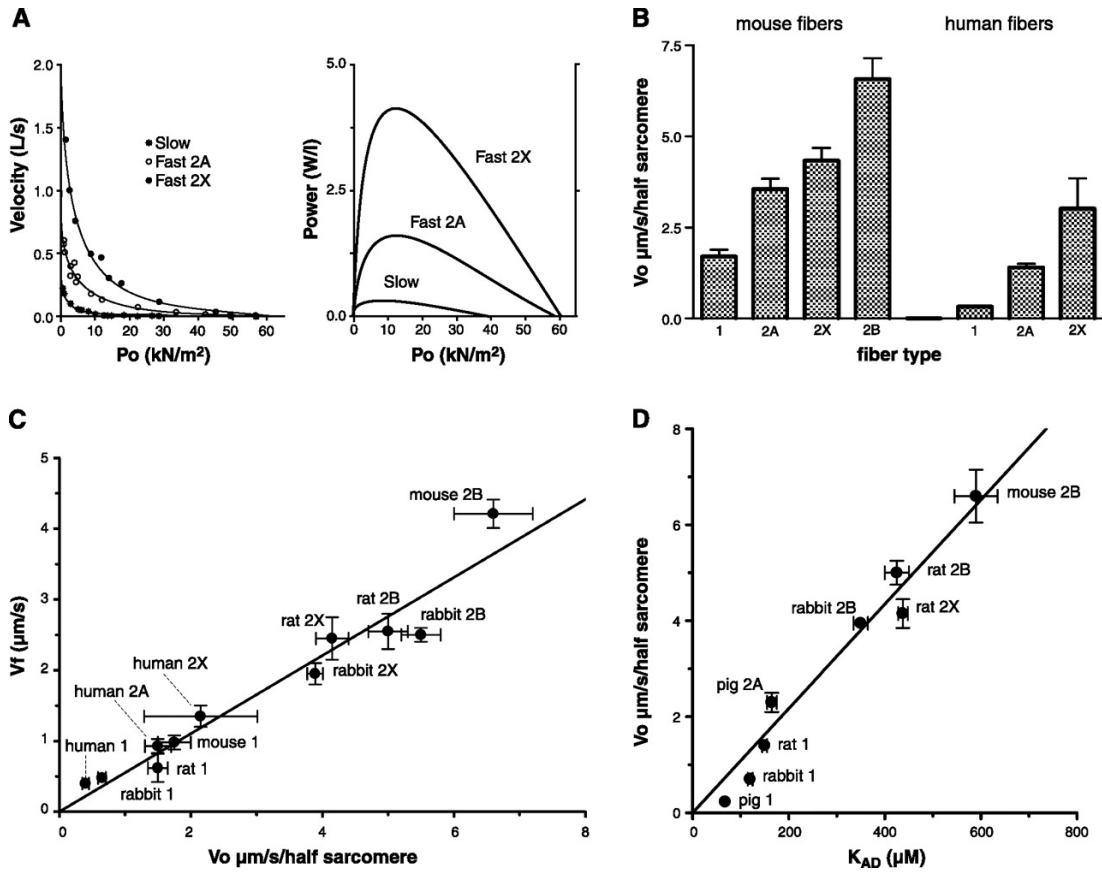


Figure 3-5: Contraction kinetics of slow and fast fibres. A: representative force-velocity (left panel) and force-power (right panel) curves of three single human muscle fibres (slow, fast 2A, and fast 2X) permeabilized and maximally activated at 12C. B: comparison of unloaded shortening velocity values (V_o) of mouse and human muscle fibres classified according to myosin heavy chain composition. Each column represents the average of V_o values obtained with the slack test protocol on 6-25 single fibres, permeabilized and maximally activated at 12C. C: correlation between sliding filament velocity of purified myosins (V_f) determined by in vitro motility assay at 25C and unloaded shortening velocity of corresponding isolated single fibres (V_o) permeabilized and maximally activated at 12C. Fibres were obtained from four different species. [Modified from Pellegrino et al. (594).] D: correlation between unloaded shortening velocity of isolated single muscle fibres (V_o) and ADP affinity (K_{AD}) of corresponding myosins from different muscles and different species. [Modified from Nyitrai et al. (570), with permission from Elsevier. Adapted from fig.10 [61]

Functional anatomy of muscles

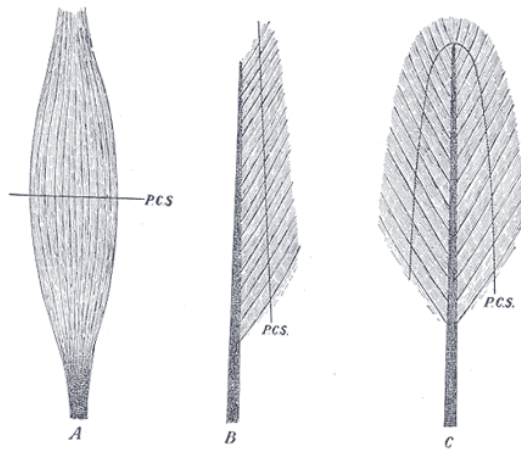


Figure 3-6: A, fusiform; B, unipennate; C, bipennate; P.C.S., physiological cross-section, from fig.365 of [62].

Tendon of origin - the proximal attachment of muscle.

Tendon of insertion - the distal attachment of muscle.

Muscle belly - the contractile region of the muscle-tendon unit.

Digastric - a muscle having two bellies in series.

Biceps/triceps/quadriceps - a muscle having two/three/four sites of origin and associated bellies.

Fusiform - 'spindle shaped', a muscle where the contractile muscle fibres are orientated in parallel to the tendon fibres.

Pennation - 'feather like' oblique orientation of muscle fibres relative to the tendon fibres, providing an increase in the PCS, at the cost of reduction in stroke length - the effect is equivalent to gearing.

Unipennate/bipennate/multipennate - having one/two/many muscle fibre orientations between interdigitated tendons of origin and insertion, providing higher levels of 'gearing'.

Physiological cross section (PCS) - the cross section area of a hypothetical rearrangement of a pennate muscle as a short, wide fusiform muscle. Together with the fibre type, PCS predicts the contractile force a muscle is capable of producing.

Muscle spindle - the specialised stretch receptor of muscle tissue, part of the alpha-motor neurone reflex which provides low level control of muscle contraction.

Motor unit - a group of muscle fibres which are supplied by the same motor neurone and contract together as a unit.

Performance of muscle

The output of muscle contraction can be described in terms of the work done per stroke per unit mass ($J.kg^{-1}$), and the power per unit mass ($W.kg^{-1}$). Muscle performance varies markedly depending on the number of repetitions required, due to the energy reserve being drawn upon.

There are six metabolic limits to muscle performance:

Single contraction is limited only by the performance of the actin-myosin bundles, this can be as high as 800watts/kg and 80J/kg as found for Gibbons leaping, [63].

Phosphate reserve is limited by the store of creatinine phosphate (CrP) available to regenerate adenosine-triphosphate (ATP) to release myosin heads from actin binding sites.

Anaerobic metabolism is limited by the store of glycogen in the muscle fibre available for lactic anaerobic respiration to regenerate the ATP. For sprint cyclists [4] reported 560J per cycle from 14kg of muscle. Assuming 2.5Hz pedalling frequency, this would give $200W.kg^{-1}$ at 50% duty cycle and $40J.kg^{-1}$.

Myoglobin oxygen reserve is limited by the store of oxygen bound to myoglobin in the muscle to support aerobic respiration, which makes much more efficient use of glucose to regenerate ATP.

Cardiovascular aerobic metabolism is limited by the ability of the heart, lungs, and blood vessels to deliver oxygen to the muscles and remove waste products [64] .

Lipid metabolism known colloquially as 'the wall' in endurance sports. This limit applies in a whole body fatigue or starvation state when the body's carbohydrate supply is finished, triglyceride in adipose cells is broken down to release fat is the last remaining energy source for aerobic metabolism in the respiring tissues. Available muscular power is substantially lower, and absence of carbohydrate prevents bursts of anaerobic metabolism when needed e.g. to prevent a marathon runner from stumbling.

Type-I fibre performance contributes to steady locomotion and posture, while Type-II fibres confer intermittent bursts of power and speed for agility and heavy manipulation. Frailty - muscular weakness causing disability - indicates the minimum power and strength required for everyday tasks, as opposed to peak athletic ability. In ageing Type-II muscle fibres are lost more rapidly than Type-I. Type-I muscles have slower contraction speed, making them ineffective when fast movement is required e.g. to recover balance. Thus loss of peak muscle power rather than static strength is the critical cause of frailty, [65]

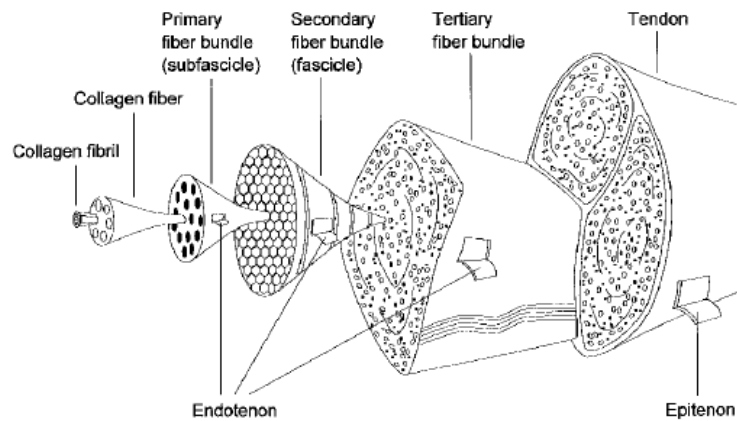


Figure 3-7: The organization of tendon structure from collagen fibrils to the entire tendon. From Fig.1 [66]

3.1.8 Tendons

The specific details of the tendon networks of the hand are covered in Section 3.4. The following terms and concepts are used to describe the structure of tendons:

Round Tendons - Fibrous non-contractile connection between muscle and other tissues, composed of densely packed bundles of parallel collagen fibres. Tendons are typically 60-85% collagen by dry mass.

Sheet tendons - Aponeuroses - Broad flattened tendons that may extend over a wide area, but have the same histological structure as round tendons.

Retinacular system - the system of retinacular ligaments and tendon sheaths that retain a tendon network in its correct path.

Retinacular ligaments - ligaments orthogonal to the path of a tendon that stabilize the tendon relative to a bone or fascia. These may connect to the tendon directly, or may wrap around the sheath of a tendon.

Tendon sheath fluid filled membranous structure that surrounds a tendon and is not continuous with a joint capsule.

Endotendon - the connective tissue inside the tendon, dividing it into fibre bundles.

Epitenon - the 'skin' of the tendon - a fine fibrous covering that forms the outer surface of the tendon.

Peritendon or paratenon loose areolar connective tissue surrounding the tendon, allowing it to move relative to adjacent tissues.

Tendon synechiae secondary connections between branches of a tendon that transfer load depending on the relative extension of the branches, most notably seen in the common digital extensor tendon.

3.1.9 General dermal structures

Specific anatomy of the dermal structures of human hands is given in section-3.5. The following terms and concepts are used to describe dermal tissues and structures:

Skin / integument The 'organ' that forms the protective exterior of an animal. It is composed of epithelial tissue 'epidermis', and the underlying connective tissue 'dermis'.

Epidermis The epithelial tissue that forms the watertight, and waterproof outer boundary and exterior contact surface of an animal. It is composed of the following layers in sequence:

Stratum basale - attached to the basement membrane and each other. The cells here divide supplying a flow of new cells to the other layers.

Stratum spinosum - living cells synthesize keratin, hyaline and lipid.

Stratum granulosum - cells die here and release lipid into the inter cellular space.

Stratum lucidum - dead cells containing keratohyaline.

Stratum corneum - final water proof, layer formed of the dehydrated remains of dead cells, hardened with the protein keratin.

Dermis The connective tissue layer supporting the epidermis. It

Hypodermis / subcutis Areolar and adipose beneath the dermis that allow the dermis to move freely over the underlying musculoskeletal structures, and may also provide thermal insulation or mechanical padding.

Dermal ligaments - Ligaments passing through the hypodermis, connecting between the dermis and the underlying musculoskeletal system. These ligaments stabilize the skin and help to shape its surface creases. Dermal ligaments are especially important in the glabrous skin, where large forces may be transmitted.

Glabrous skin - Specialized skin found on the soles of the feet and palms of the hands. It is hairless, with greatly thickened stratum corneum of the epidermis to withstand abrasion. The surface of glabrous skin has a 'print' pattern of ridges that facilitates both control of friction and vibrotactile sensation.

Haired skin - the 'default' form of skin, covering the backs of the hands and the body generally.

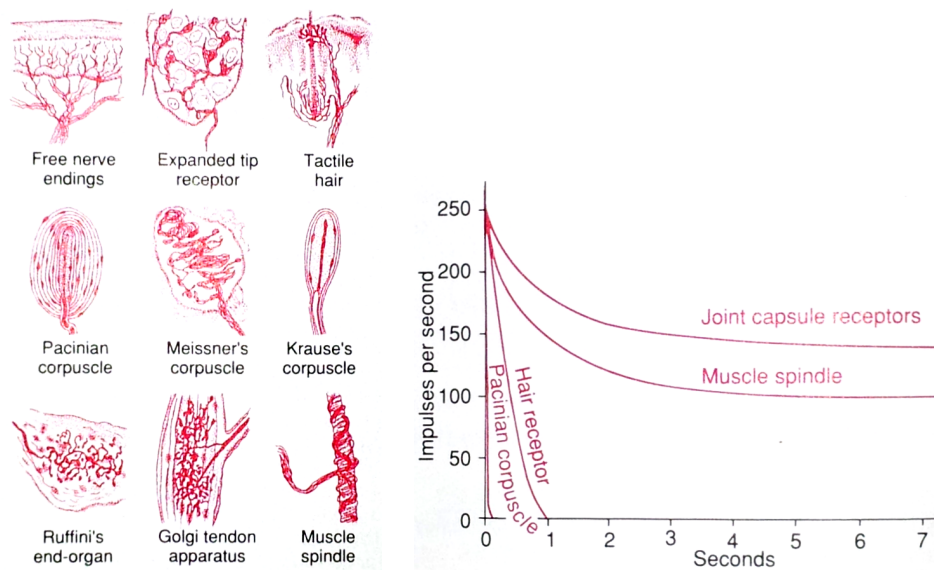
Nails, hooves and claws - variations of the same basic structure - a specialized stratum corneum tightly adhered to the dorsal surface of the distal phalangeal bone of the digit, enabling high stiffness force transmission from the bone to the exterior of the body without intervening soft tissues.

3.1.10 Sensing

The somatosensory nerve endings have been reviewed in the context of robot tactile sensor design by [67], [68] and [69]. Discussions of the histology and function of the peripheral somatosensory nervous system are available in most introductory physiology [60], anatomy [70] and neuroscience [71] texts. In recent years the classical histological categorisation of somatosensory receptors has given way to immuno-histochemical typing [26], and investigation into the subcellular anatomy and biochemistry by which the receptors function is currently an active field of research.

However, for the purpose of creating a functionally equivalent machine at the gross anatomical scale, the model has remained stable. Mechanosensory nerve endings sample either the mechanical strain or the rate of change of strain of the tissue into which they are embedded. Functionally tactile mechanoreceptors in the skin are referred to as "fast adapting" FA (change/vibration receptors) or "slow adapting" SA (stretch receptors), each divided into "type I" (epidermal), and "type II" (deep dermal). In addition to mechano-sensation there are thermoreceptors that are important for both thermoregulation and cutaneous perception.

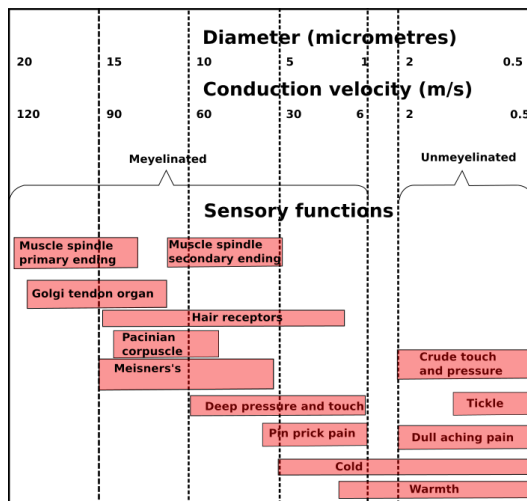
The material properties and mechanical topology of the tissue into which the receptors are embedded is crucial to determining the information which they sample, and its relation to the body and the external world. These include the sensory structures around hairs (figure-3-10) and the specialized Golgi tendon organs and muscle spindles, as well as more general slow and fast adapting receptors in joint capsules, articular ligaments, and fibrous fascia generally. The details of dermal-epidermal structure including fingernails and dermal ligaments are covered in section 3.5. The innervation of joints is covered in 3.3.



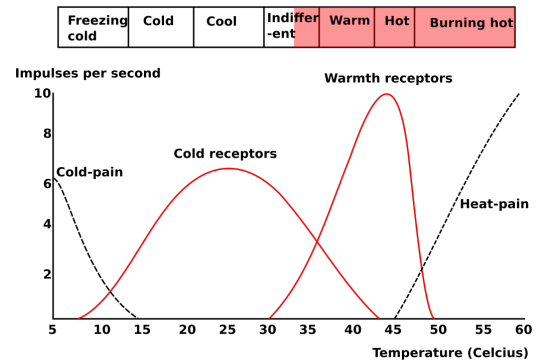
(a) Several types of somatic sensory nerve endings. Adapted from fig.32-1 [60]

(b) Adaptation of different types of receptors, showing rapid adaptation of some receptors and slow adaptation of others. Adapted from fig.32-5 [60]

Figure 3-8



(a) The diameter, conduction speed and function of somatosensory nerve axons. Adapted from fig.32-6 [60]



(b) Frequencies of discharge of (1) a cold-pain fibre, (2) a cold fibre, (3) a warmth fibre, and (4) a heat-pain fibre. (The responses of these fibres are drawn from original data collected in separate experiments by Zottermant, Hensel, and Kenshalo.) Adapted from fig.33-8 [60]

Figure 3-9

Dermal sensory nerve endings

See figure-3-10 and table-3-11 [72].

FA-I Meissner's corpuscles are found in the tips of the dermal papillae, under the ridges of the epidermis of glabrous skin.

SA-I Merkel cells are found in contact with the basal layer of the epidermis of glabrous skin, and arranged in 'touch domes' around the follicles of guard hairs on hairy skin. They are slow adapting and respond to indentations of the skin as small as $15\mu\text{m}$ in humans. They convey fine spatial information and are especially sensitive to corners and edges.

FA-II Pacinian corpuscles are found in the deeper layers of the epidermis

SA-II Ruffini nerve endings are found in the dermis, and fibrous connective tissues generally. These are stretch receptors which adapt very little, so signal the state of deformation of the tissues.

Temperature receptors The type of nerve endings responsible for cold and warmth sensation is the subject of on going research [73]. Extremes of cold ($< 15^\circ\text{C}$) or heat ($> 45^\circ\text{C}$) likely to cause injury cause pain neurones to fire. Moderate cold ($5 - 40^\circ\text{C}$) and warmth ($30 - 50^\circ\text{C}$) cause two different populations of neurones to fire, fig-3-9b.

Nociception (pain) All pain fibres are free nerve endings, but there are two distinct classes of pain in the peripheral nervous system - sharp pain and dull pain.

Sharp pain is rapid onset (0.1sec) caused when the skin is cut or subject to electric shock. It is not felt in most of the deeper tissues of the body.

Dull pain dull pain is associated with tissue destruction, and is slow onset. All pain fibres may respond to mechanical, thermal or chemical damage, but sub-populations show greater sensitivity to particular stimuli [60].

Proprioceptive sensory nerve endings

Mechanoreceptors in the musculoskeletal system are essential to proprioception.

Ruffini nerve endings as above, are slow adapting stretch receptors found in most connective tissues.

Pacinian corpuscles as above, are fast adapting change/vibration receptors found in most connective tissues.

Golgi tendon organs are special stretch receptors found in tendons that fire in response to the tension in the bundle of tendon fibres they are associated with.

Muscle spindles are stretch receptors in specialized muscle fibres that fire in response to changes of muscle length. They form a reflex arc with the gamma-motor neurones which control the contraction of the muscle.

Pain receptors as above are high threshold free nerve endings found in almost all tissues that respond to mechanical, chemical, or thermal tissue damage.

3.1.11 Structure and scale of somatosensory dendrites and nerve fibres

The cell bodies of peripheral somatosensory neurones lie in the dorsal root ganglion close to the entry of the nerves into the spinal cord. Therefore the part of the sensory neuron between the sensory receptor in the tissues, to the cell body in the ganglion is correctly termed the "dendrite" because it lies upstream of the cell body, as opposed to the axon downstream from the body in relation to the direction of travel of action potentials. However due to their functional equivalence it is common to refer to the peripheral parts of sensory nerves as 'axons'.

From studies of the human sural nerve [74], a purely sensory nerve in the lower leg, the average effective diameter for sensory nerve fibres including myelin sheath and surrounding connective tissue were found to have a bimodal distribution of 4 and 10.5 μm , corresponding to the modes for unmyelinated and myelinated nerves. As can be seen in figure-3-9a, the tactile and proprioceptive functions relevant to manipulation are carried by myelinated nerve fibres with axon diameters ranging from 5 to 20 μm .

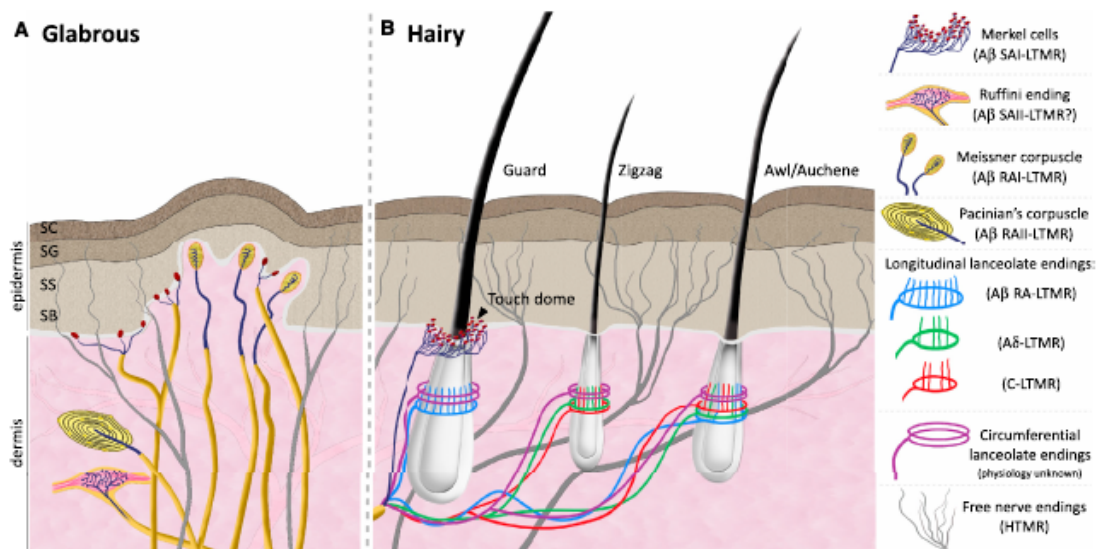


Figure 3-10: The Organization of Cutaneous Mechanoreceptors in Skin of the mouse. "Innocuous touch information is processed by both glabrous hairless (A) and hairy (B) skin. (A) In glabrous skin, innocuous touch is mediated by four types of mechanoreceptors. The Merkel cell-neurite complex is in the basal layer of the epidermis and it consists of clusters of Merkel cells making synapse-like associations with enlarged nerve terminals branching from a single Ab fibre. This complex and its associated SAI-LTMR responses help us in reconstructing acute spatial images of tactile stimuli. Meissner corpuscles are localized in the dermal papillae and consist of horizontal lamellar cells embedded in connective tissue. Their characteristic RAI-LTMR responses detect movement across the skin. Ruffini endings are localized deep in the dermis and are morphologically similar to the Golgi tendon organ, a large and thin spindle-shaped cylinder composed of layers of perineural tissue. Historically, Ruffini endings have been associated with SAII-LTMR responses, which respond best to skin stretch, though such correlations remain highly controversial. Lastly, Pacinian corpuscles are located in the dermis of glabrous skin where their characteristic onion-shaped lamellar cells encapsulate a single Ab ending. Their well-recognized RAI-LTMR responses detect high-frequency vibration. (B) In hairy skin, tactile stimuli are transduced through three types of hair follicles, defined in the mouse as guard, awl/auchene, and zigzag. The longest hair type, guard hairs, is associated with touch domes at the apex and Ab-LTMR longitudinal lanceolate endings at the base. Awl/auchene hairs are triply innervated by C-LTMR, Ad-LTMR, and Ab-LTMR longitudinal lanceolate endings. Zigzag hair follicles are the shortest and are innervated by both C- and Ad-LTMR longitudinal lanceolate endings. In addition, all three hair follicle types are innervated by circumferential lanceolate endings whose physiological properties remain unknown. Noxious touch is detected by free nerve endings found in the epidermis of both glabrous and hairy skin and are characterized by both Ad- and C-HTMR responses. Abbreviations: SA, slowly adapting; RA, rapidly adapting; LTMR, low-threshold mechanoreceptor; HTMR, high-threshold mechanoreceptor; SC, stratum corneum; SG, stratum granulosum; SS, stratum spinosum; SB, stratum basalis." Fig 1 from [72]



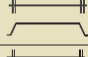
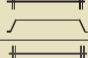



Physiological subtype	Associated fiber (conduction velocity ¹)	Skin type	End organ/ending type	Location	Optimal Stimulus ⁴	Response properties
SAI-LTMR	A β (16-96m/s)	Glabrous Hairy	Merkel cell Merkel cell (touch dome)	Basal Layer of epidermis Around Guard hair follicles	Indentation	
SAII-LTMR	A β (20-100m/s)	Glabrous Hairy	Ruffini ² unclear	Dermis ³ unclear	Stretch	
RAI-LTMR	A β (26-91m/s)	Glabrous Hairy	Meissner corpuscle Longitudinal lanceolate ending	Dermal papillae Guard/Awl-Auchene hair follicles	Skin movement Hair follicle deflection	
RAII-LTMR	A β (30-90m/s)	Glabrous	Pacinian corpuscle	Deep dermis	Vibration	
A δ -LTMR	A δ (5-30m/s)	Hairy	Longitudinal lanceolate ending	Awl-Auchene/ Zigzag hair follicles	Hair follicle deflection	
C-LTMR	C (0.2-2m/s)	Hairy	Longitudinal lanceolate ending	Awl-Auchene/ Zigzag hair follicles	Hair follicle deflection	
HTMR	A β /A δ /C (0.5-100m/s)	Glabrous Hairy	Free nerve ending	Epidermis/Dermis	Noxious mechanical	

Figure 3-11: "Skin is innervated by complex combinations of low- and high-threshold mechanoreceptors, each with unique physiological profiles and response properties elicited by distinct tactile stimuli. 1 Conduction velocities can vary across species; please see the following references for more detailed interspecies comparisons: Leem et al. (1993) (rat); Brown and Iggo (1967) and Burgess et al. (1968) (cat and rabbit); Perl (1968) (monkey); and Knibestol (1973) (human). 2 Though SAI-LTMR responses have been observed in both glabrous skin of humans and hairy skin of mice, they have only been postulated to arise from Ruffini endings, though direct evidence to support this idea is lacking (Chambers et al., 1972). 3 Although SAI-like responses are present in the mouse, Ruffini endings or Ruffini-like structures have not been identified in rodents. 4 The stimulus described is the optimal stimulus known to elicit the response properties depicted in the last column of this table. However, it is probable, and often times documented, that multiple physiological subtypes can be recruited with any one particular tactile stimulus. For example, indentation of hair skin is likely to activate not only SAI-LTMRs associated with guard hairs but also longitudinal lanceolate endings of the Ab-, Ad-, and C-LTMR type." Table 1 from [72]

3.2 Anatomical directions and terminology

This section provides an introduction to anatomical terms to facilitate the reader's understanding of the anatomy reviewed in this chapter.

There have historically been many different and not wholly compatible terminologies in the anatomical sciences. International standardisation of human anatomical terms was originally established under the "Nomina Anatomica" [75, 76]. This has since been superseded by the "Terminologia Anatomica" [77]. In the anatomy of non-human animals the current international standard is the "Nomina Anatomica Veterinaria" [78].

These standards define hierarchical lexicons of terms with the intention of minimising the number of synonyms in use. The semantic meaning of the terms, beyond their hierarchical relationship, is taken to be that in the wider anatomical literature. In human anatomy the long running textbook "Gray's Anatomy of the Human Body" [79] has quasi canonical standing as the definitive reference. It should be borne in mind that no general textbook can be wholly exhaustive in its coverage. Sections Ch.3.3,3.4,3.5 contain details of human hand anatomy not covered in Gray's Anatomy.

3.2.1 Directions:

proximal vs distal towards vs away from the trunk of the body

axial vs abaxial towards vs away from the long axis of a digit or limb

medial vs lateral towards vs away from the median plane of the body

dorsal vs ventral towards vs away from the surface of the back, when used in the trunk of the body.

posterior vs anterior human anatomy: towards vs away from the front or the rear of the body. Note due to different body orientation, in veterinary anatomy dorsal vs ventral are used.

cranial vs caudal towards vs away from the skull.

dorsal vs palmar, volar, plantar in hands, feet, paws and hooves; dorsal = away from the load bearing surface, palmar and volar are synonyms for the direction of the load bearing surface of the hand or foot of the front limb, plantar is the direction of the sole of the foot in humans or the hind foot of four legged animals.

3.2.2 Motions:

flexion vs extension the motions of joints associated with pulling/drawing towards the body versus pushing away from the body.

adduction vs abduction drawing together versus spreading apart of limbs or digits.

supination vs pronation rotating of the hand such that the thumb's side of the hand the passes dorsally then laterally versus medially then ventrally, or the equivalent motion of the foot.

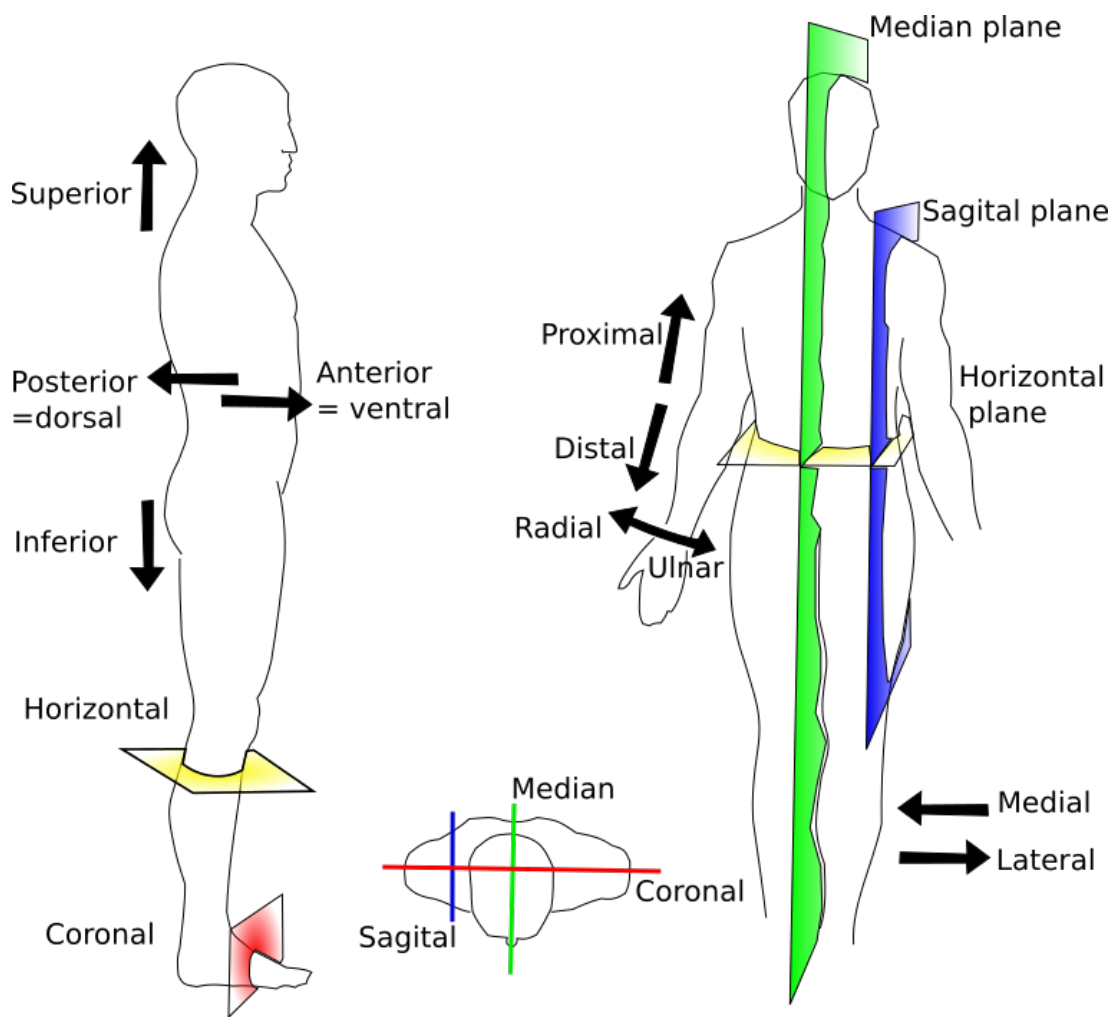


Figure 3-12: Anatomical planes and directions of the human body [75]

3.2.3 Locations:

lumen the interior of a cavity, eg of a tendon sheath, joint capsule or bursa.

'origin' of a muscle-tendon or ligament the proximal attachment, in bone, fascia or other load bearing structure from which the muscle-tendon or ligament arises.

'insertion' of a muscle, tendon or ligament the distal attachment, in bone, fascia, dermis or other load bearing structure into which the muscle-tendon or ligament inserts.

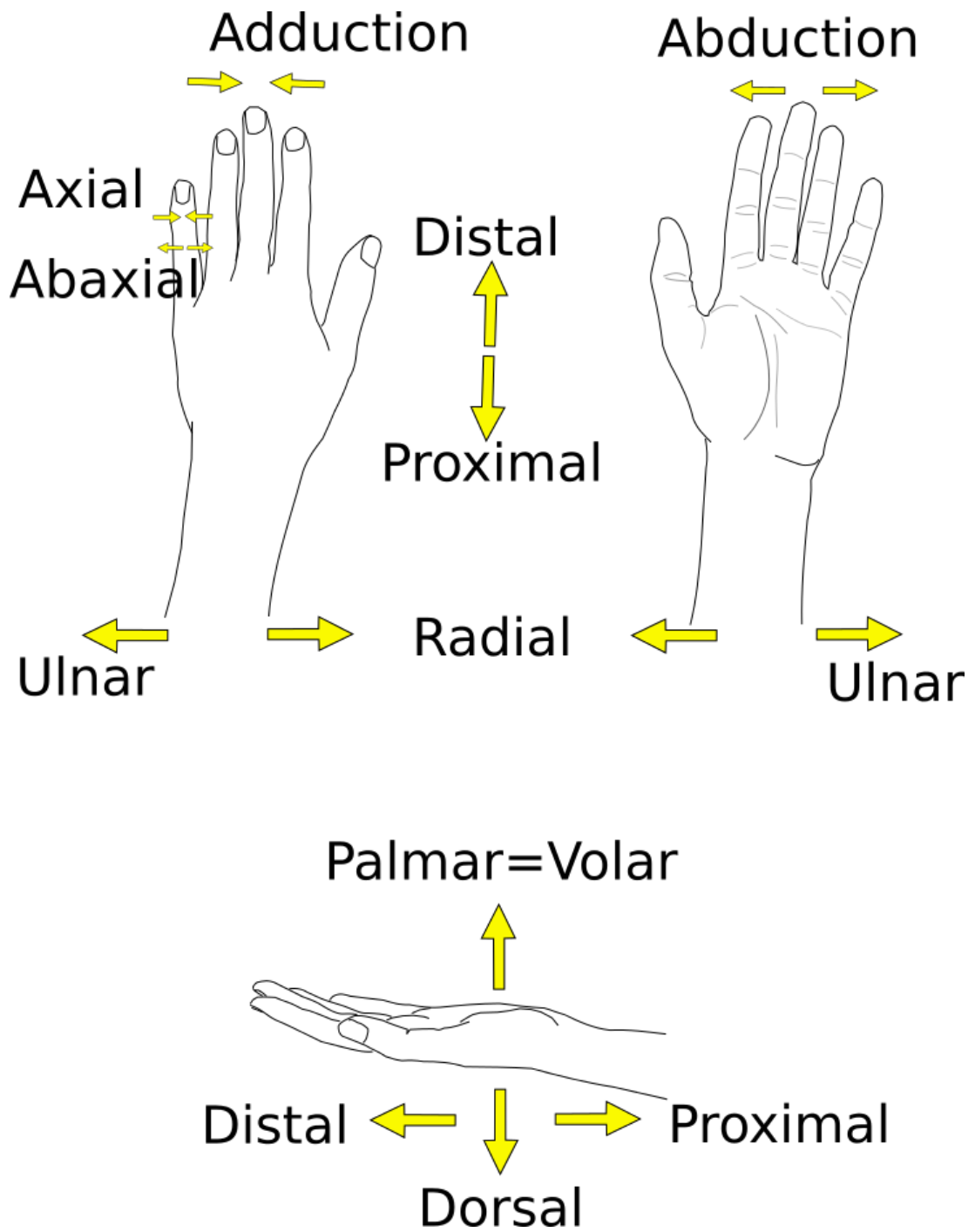


Figure 3-13: Anatomical directions of the human hand [75]

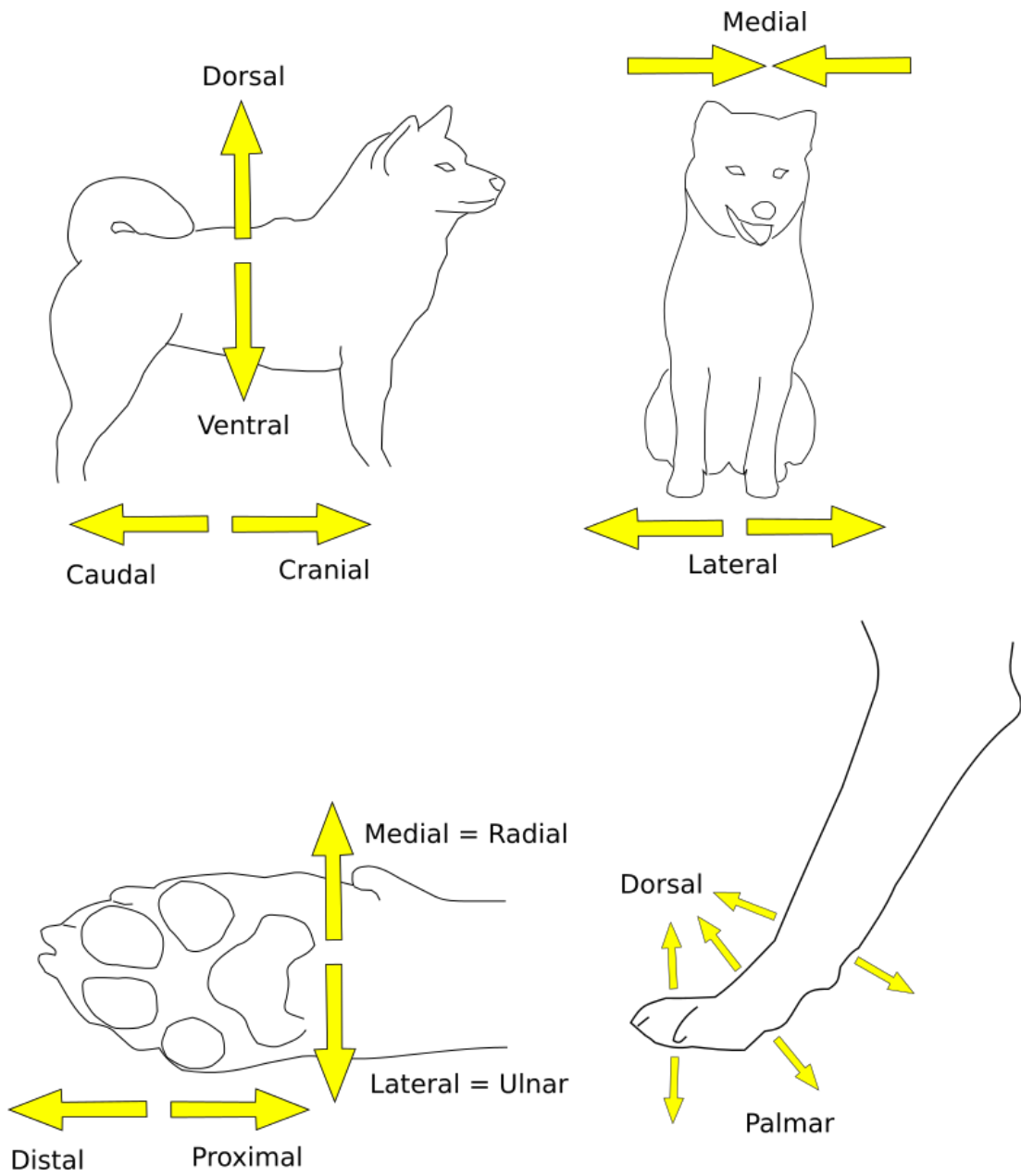


Figure 3-14: Anatomical directions of quadruped bodies [78]

3.3 Human hands: bones and joints

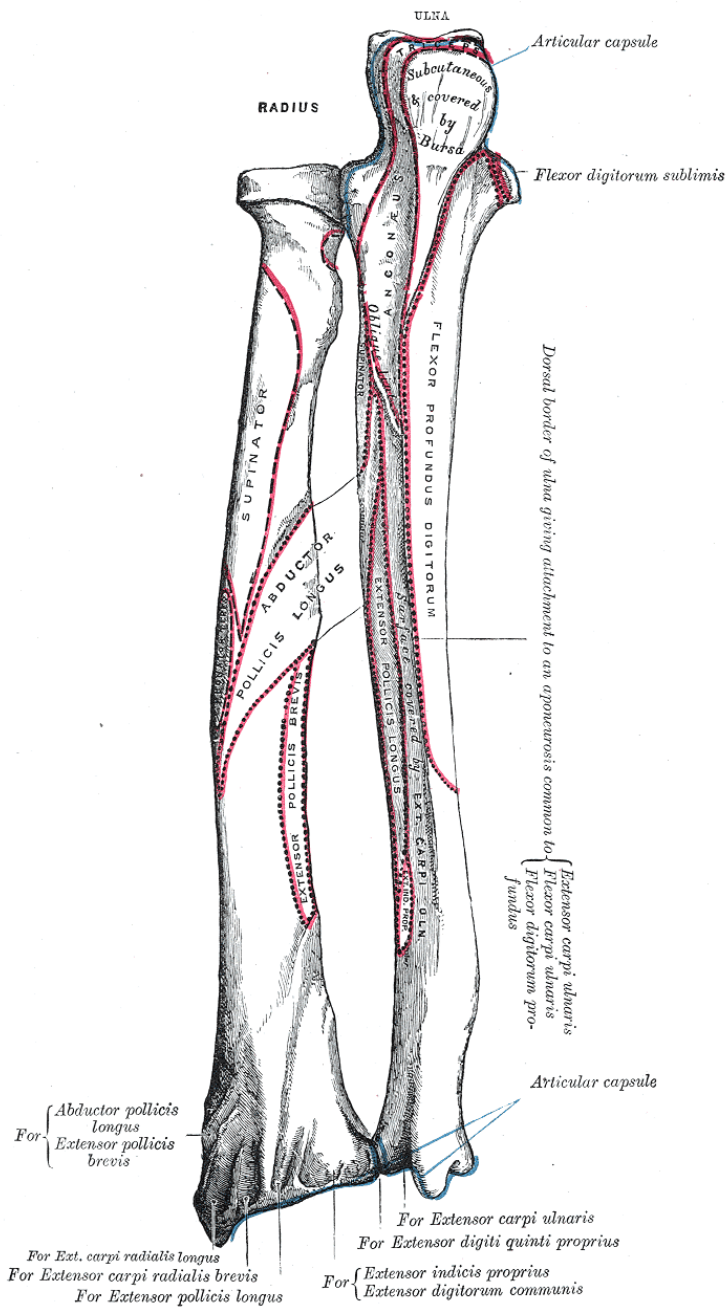


Figure 3-15: radius and ulna. The elbow would be at the top and wrist at the bottom of the diagram. Note the notches in the distal radius for various extensor tendons. Image214 from [62].

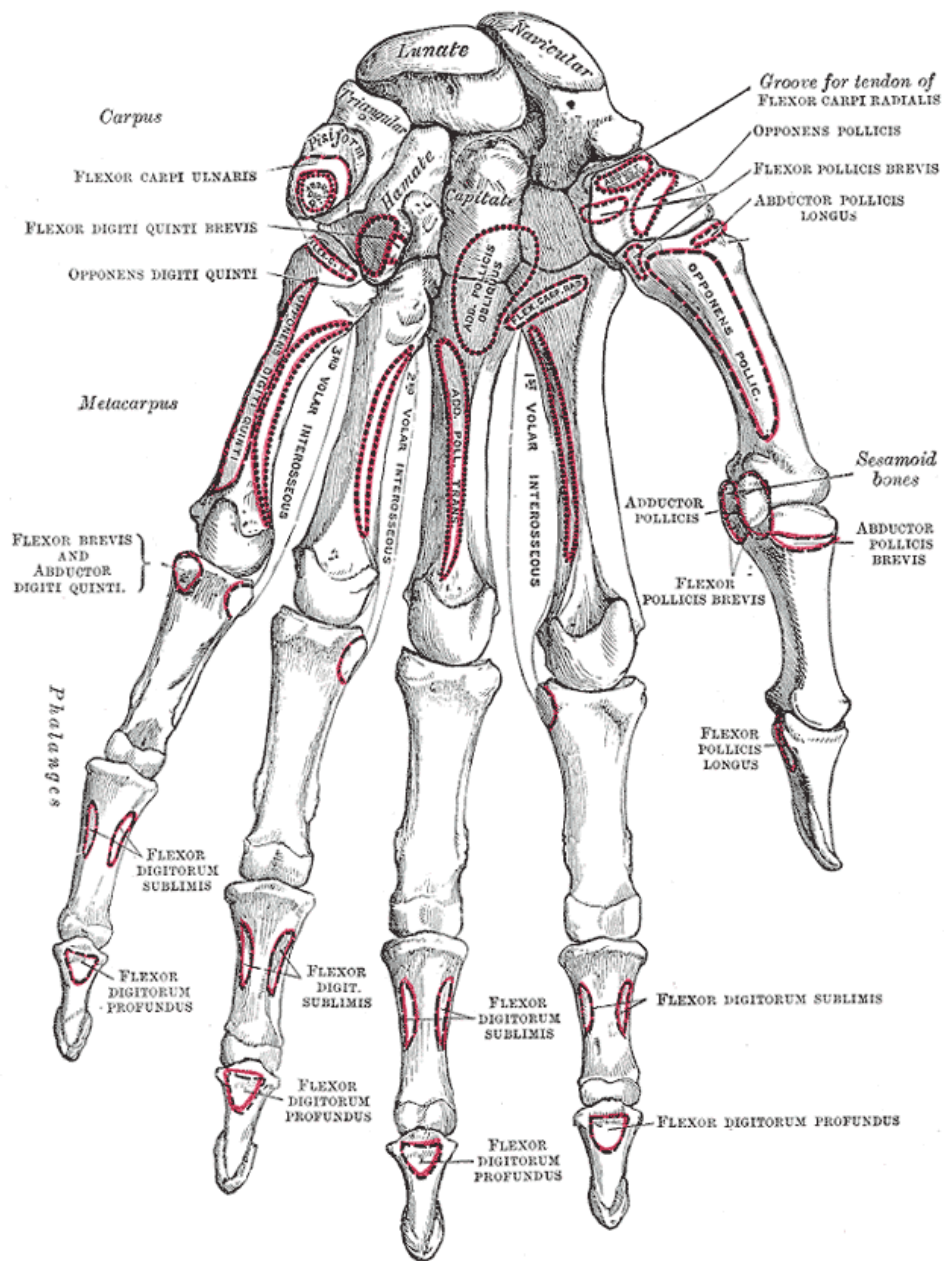


Figure 3-16: bones of hand palmar view, image219 from [62].

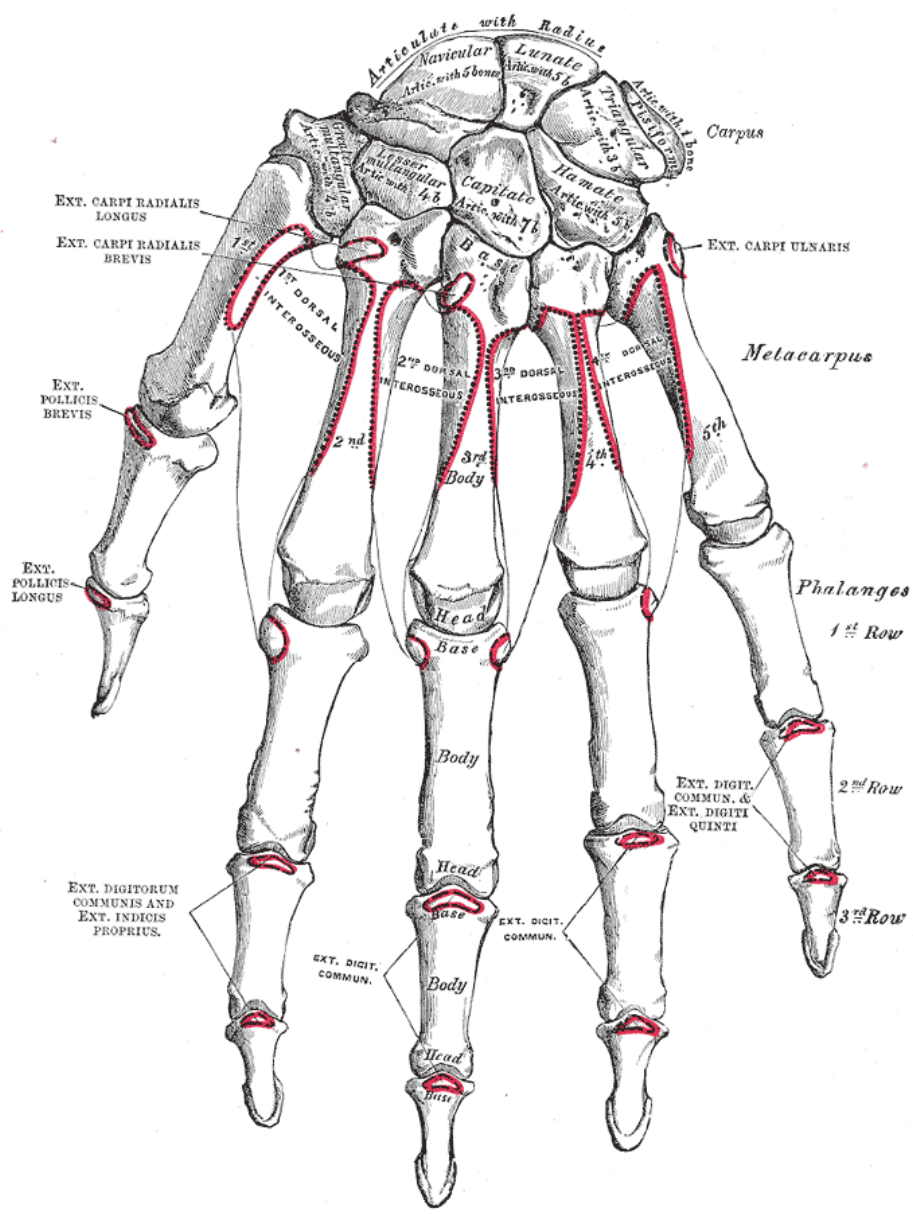
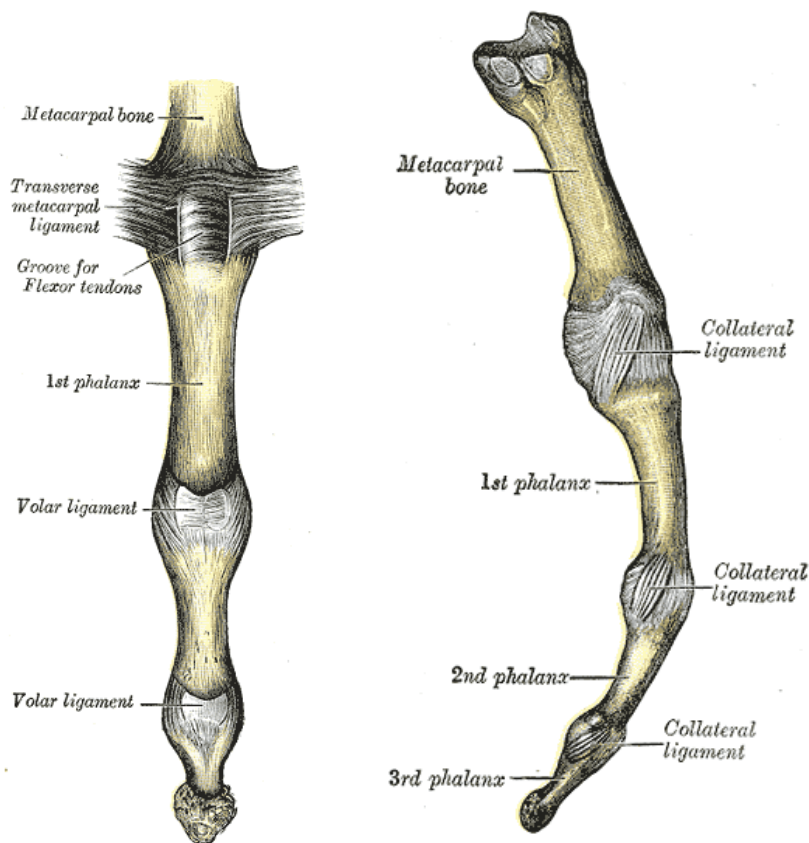


Figure 3-17: bones of hand dorsal view, image220 from [62].



(a) finger joints palmar view, image337 from [62].

(b) finger joints lateral view, image338 from [62].

Figure 3-18

3.3.1 Fingers

Bones of the fingers

The three phalanx bones of the fingers (plural phalanges) and two phalanges of the thumb are supported by the long metacarpal bones of the palm, figures 3-16, 3-17. Like all bones of the appendicular skeleton, they form by ossification of cartilaginous precursors. Like other long bones they are composed of an outer layer of dense lamellar bone, and an inner core of spongy bone. The central tubular region 'diaphysis' is non-circular in cross section and has the thickest lamellar bone, and the sparsest spongy bone. The diaphysis widens at either end to form the metaphysis. The physis is the cartilaginous 'growth plate' between the metaphysis and the epiphysis, where the bone grows in length. The epiphysis is the end of the bone which is filled with dense spongy bone tissue, covered on the sides with a thin layer of lamellar bone, and at the end by the hyaline cartilage of the joint surface, [80].

The distal phalanx has adaptations which are specifically human. These include the wide, flattened distal tuberosity that provides the attachment site of the nail bed, with its concave palmar side forming the 'ungula fossa', [81]. There is also bilaterally, a lateral ligament which connects between lateral

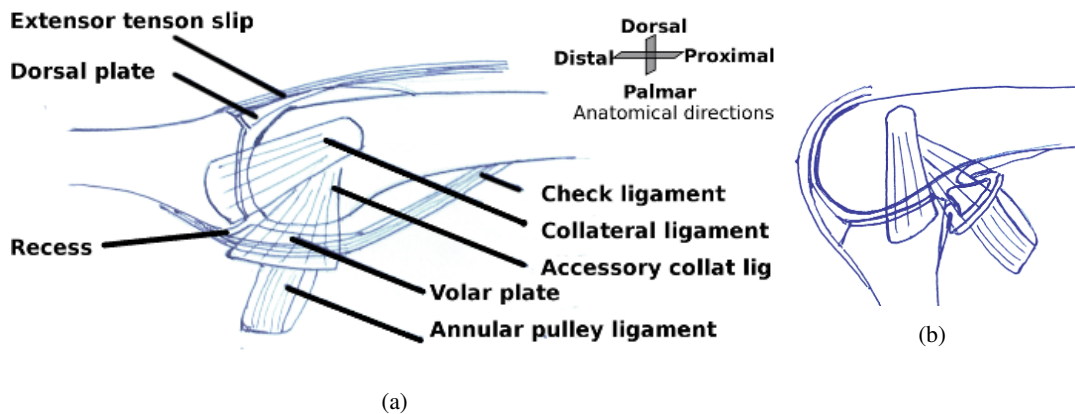


Figure 3-19: (a) Proximal interphalangeal joint extended (b) flexed, showing the movement of the ligaments, dorsal and volar plates. The flexor tendons pass through the annular pulley.

margins of the distal tuberosity and the lateral tubercle of the proximal end of the bone, bypassing the central shaft of the distal phalanx [82].

Interphalangeal joints

The joints of the finger - distal inter phalangeal (DIP) [82], proximal inter phalangeal (PIP) [83] and metacarpophalangeal (MCP) - are of very similar construction, see figure-3-19 They are synovial joints with a capsule, hyaline cartilage on the joint faces, and synovial fluid in the joint space. The distal joint surface is concave, matching the convex proximal surface. The shape of the joint surfaces is a surface of rotation about the axis of rotation of the joint, with a marked central groove, that would interfere in the event of other motions of the joint. The joint capsule extends proximally around the proximal bone, but is attached to the margins of the proximal end of the distal bone, forming a closed joint space.

The collateral ligaments are much thicker and stronger than the accessory collateral ligaments, and form the primary constraint on the motion of the joint. The collateral ligaments insert on the volar margin of the distal phalanx (DIP) or middle phalanx (PIP). For the PIP the site of origin of the collateral ligaments is an area centred on the axis of rotation of the joint [84]. The accessory collateral ligaments insert on the volar plate of the distal phalanx (DIP) or middle phalanx (PIP).

The interphalangeal joints are remarkably strong and tough for such slender joints. The lateral stability of the PIP was measured by [85] and found to vary from 6.7+/-2.8 degrees (middle finger) to 10.8+/-3.4 degrees (little finger) varus-valgus (inward/outward bowing of a joint) angulation under 0.1 Nm torque load, rising to 13.8+/-4.2 (middle finger) to 21.5+/-6.1 (little finger) under 0.5 Nm torque load. The constraint was found, by sequential cutting, to be almost entirely due to the lateral collateral ligament. The restraining moment to first sign of failure was found to vary from 2.38+/-0.87Nm and 15.3+/-2.4 degrees (middle finger) to 1.44+/-0.47Nm and 18.4+/-4.2 degrees (little finger).

Figure 3-19 shows the PIP. Note the fibrocartilaginous dorsal [86] and volar plates, and the buckling motion of the volar plate aided by the recess between its distal margin and the proximal phalanx [83]. The check ligament and the distal part of the accessory ligament limit the maximum extension of the joint.

The volar plate is a wedge shaped cartilaginous thickening of the volar check ligament of the DIP, PIP and MCP joints. The thick end of the wedge is distal and separated from the articular cartilage of the distal bone by a cleft that allows it to flex freely by its distal margin. When the joint is extended, the plate lies between the digital flexor tendons and the volar part of the articular surface of the proximal bone. It is subject to pressure and sliding on both faces when the fingers are flexed under load from the extended position.

Histologically the volar plate has three layers of fibres, [87]. The first layer has a proximal membranous region, and a distal cartilaginous region. The second layer contains ligament fibres that run from the volar aspect of proximal bone to the volar margin of the proximal end of the distal bone. The third layer comprises fibres orthogonal to the second, which connect to the accessory ligament dorsally, and the annular retinacular ligament of the flexor tendon sheath volarly. The middle layer is responsible for limiting the maximum extension of the joint,

Ultrasonographic studies of the movement of the volar plate, [88, 89] and magnetic resonance imaging [90] showed that in the climber's crimp grip position (PIP maximally flexed, MCP and DIP extended), that the PIP volar plate moves distally relative to the middle phalanx when the flexor tendons are under load, compared to its position in when the PIP is in the neutral position.

Metacarpo-phalangeal (MCP) joint

Though the MCP has topologically the same articular ligaments as the DIP and PIP, it differs in a number of important ways. Firstly the joint surface of the distal end of the metacarpal bone is hemispherical, while the proximal joint surface of the first phalanx is a matching shallow cup, see figures-3-16 & 3-17, as opposed to the condylar surfaces of the interphalangeal joints which are symmetrical about a single axis of rotation. Secondly the MCP motion has greater degrees of freedom. The MCP can be actively moved in adduction-abduction when extended. This motion is progressively curtailed to near zero at full flexion of the MCP. The MCP can also be passively rotated about the axis of the first phalanx. With tendons relaxed it can be passively distracted longitudinally by 2-3mm, and translated medio-laterally or dorso-palmarly.

In the MCP the extensor tendon slip is replaced by the extrinsic extensor tendon, which does not insert on the distal margin of the joint but joins the extensor hood instead, see figures-3-43a & 3-30a and section-3.4.3. In the MCP the collateral ligaments are attached dorsal to the centre of curvature of the metacarpal joint face, such that the collateral ligaments are slack if-and-only-if the joint is extended, allowing medio-lateral swinging of the joint.

Lateral translation of the MCP is limited by the attachment of the accessory collateral ligaments to the well developed volar plate. Dorsal translation of the MCP is counter acted by contraction of the flexor tendons, which pull volarly on the second annular retinacular ligament attached to the proximal phalanx, and produce compressive force in the bones of the finger. In vivo distraction and instability of the MCP are resisted by the elasticity of the joint capsule, and tension in the tendons surrounding the joint. In the extended position, abduction-adduction actuation by the interosseous tendons replaces stabilisation by the collateral ligaments.

While the ligaments are long enough to permit the motions described, the attachment of the liga-

ments and joint capsule around the margins of the concave joint surface of the first phalanx means that, they are sufficiently short to prevent dislocation of the MCP joint. Consequently contraction of any of the tendons brings the joint surfaces into congruence , [91], [92], [93], [94], [95], [96], [97]. Stabilisation of the MCP by the flexor and extensor tendon networks and their associated tendon retinacular ligaments is discussed further in section 3.4.

Sesamoid bones of the digits

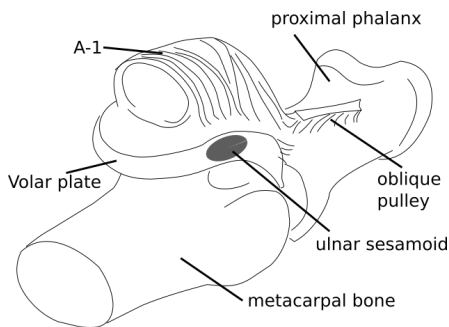


Figure 3-20: Thumb MCP joint showing the location of the sesamoid bones in the volar plate.

Sesamoid bones occur variably at the insertion of the accessory collateral ligaments in the lateral margins of the volar plate. They are well developed and consistently present at the thumb MCP, and usually present in the thumb IP, the index and little finger MCP joints and occasionally at other MCP, PIP and DIP joints, [98]. The incidence of sesamoid bones varies with population age, gender activity and ethnicity , [99], [100] , [101].

Metacarpal bones and joints

The metacarpal bones of the fingers form the bony part of the palm. The thumb web is formed by the the muscles and ligaments connecting the metacarpal bone of the thumb to the metacarpal bones of the fingers, see section-3.4.6.

The palm is a complex structure, that provides critical load bearing and balancing in both paws and hands.

Proximal and distal inter-metacarpal joints

Each metacarpal bone is connected to its neighbours by proximal and distal inter-metacarpal joints. There is no joint cavity or synovial articular surface at the distal inter-metacarpal joints. Other soft tissue structures separate the bones including the sagittal bands of the metacarpophalangeal joints and the tendons of the interosseous muscles. The metacarpals are held to each other by:

1. the inter-palmar-plate ligaments [102] that link the volar plates of the metacarpophalangeal joints to each other, collectively called the transverse metacarpal ligament,

2. the natatory ligament which connects the proximal margin of the second annular ligaments of the first phalanges,
3. the transverse fibres of the palmar aponeurosis [103] which are connected to the deep transverse metacarpal ligament by the septae of Legueu and Juvara [103] [102]. These structures are part of the flexor retinacular system and will be described in more detail in section 3.4.

The proximal inter-metacarpal joints have small articular facets, and three sets of ligaments - dorsal, palmar and interosseous - which allow minimal rotation of adjacent bones about each other [104].

Carpo-metacarpal joints

The carpo-metacarpal joints have short ligaments that allow very little movement. They do however have synovial capsules and hyaline cartilage joint surfaces. The movement is least in the metacarpal of the middle finger. In the ring-finger and little finger the motion of the carpo-metacarpal joint is essential to allowing the motion of these metacarpals in the flexing of the palm, see chapter-4.

3.3.2 Bones and joints of the thumb

The thumb normally has only two phalanges. Triphalangeal thumbs occur as a rare abnormality and are approximately 50% weaker in pinch grip strength than normal thumbs. Unlike the metacarpals of fingers, the thumb metacarpal does not have a distal inter-metacarpal joint binding it to its neighbours, but moves freely about its carpo-metacarpal joint relative to the other metacarpals.

Human thumbs are exceptionally large and strong relative to other primates. The thumb MCP is of similar structure to the other digits, but has less abduction-adduction range and tends to be coordinated with abduction-adduction of the carpo-metacarpal joint, [105], [106].

Trapezio-Metacarpal joint of the thumb

The 'Trapezium' is the name of the carpal bone to which the metacarpal of the thumb is attached. The thumb carpo-metacarpal joint is known as the trapezio-metacarpal joint. It is unusual in the body because it is a saddle joint, i.e. the curvatures of the joint surface are concave in opposite directions. This has important consequences, because it is impossible for the articular faces of a saddle joint to remain congruent over a wide range of actuation in both flexion-extension and abduction-adduction. Loss of congruence leads to small area of contact and consequent high pressure between the bones over part of the range. The trapezio-metacarpal joint suffers a significantly higher rate wear and degeneration than other metacarpal joints.

Note that:

1. The trapezio-metacarpal joint is also constrained by the (proximal) inter-metacarpal ligaments between the bases of the metacarpals of the thumb and index finger[107].
2. The trapezio-metacarpal joint acts together with the motion of the trapezium in the scapho-trapezio-trapezoidal joint[107].

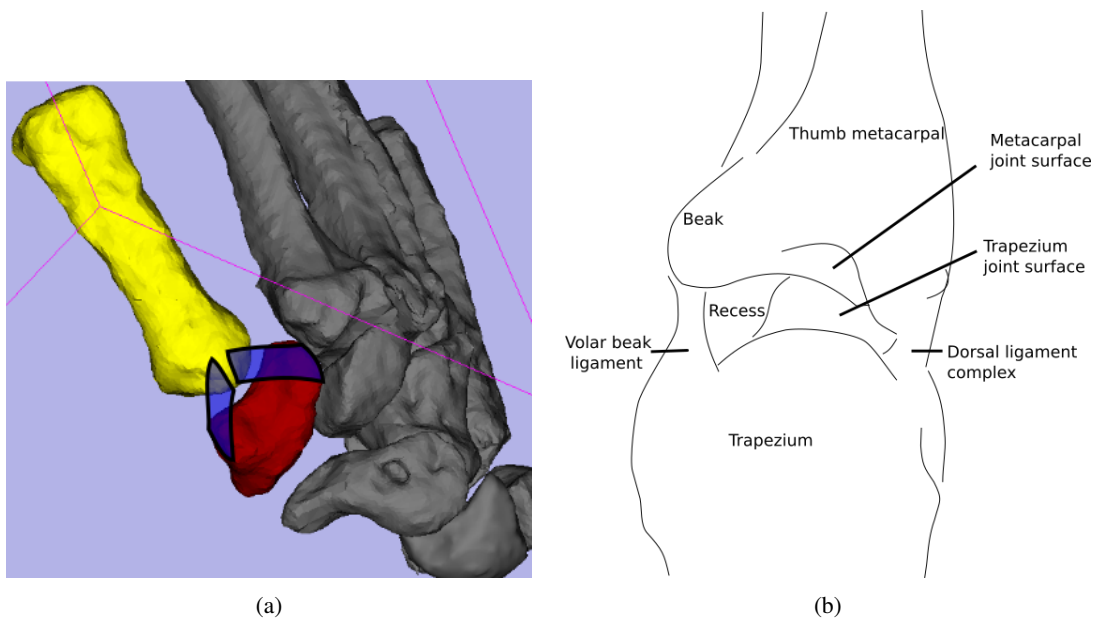


Figure 3-21: Ligaments of the trapezio-metacarpal joint. (a)Dorsal ligament complex. (b)Radial view of opened trapezio-metacarpal joint showing the volar beak ligament and dorsal ligament complex. Contraction of the muscles of the thumb closes the joint space, causing the saddle shaped joint surfaces to come into alignment. Drawn from figure-1 in [107]

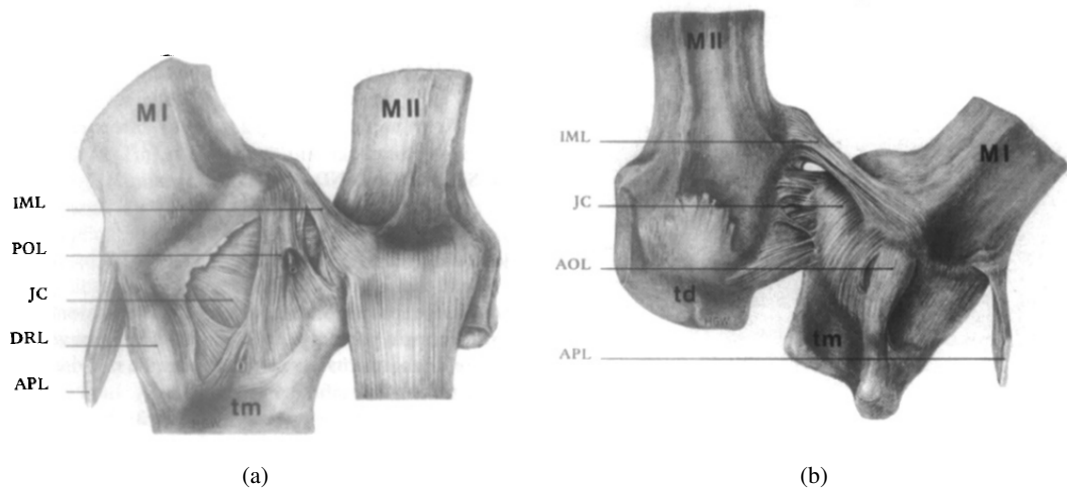


Figure 3-22: Drawings of the ligaments of the carpo-metacarpal joint of the thumb. (a) Volar (palmar) view of the right first carpo-metacarpal joint; (b) view from the posterior and distal side; MI=thumb metacarpal MII=index finger metacarpal, td=trapezoidal, tm=trapezium, IML=inter-metacarpal ligament, JC=joint capsule, AOL=anterior oblique ligament, APL=abductor pollicis longus tendon insertion, POL=posterior oblique ligament, DRL=dorsal radial ligament. Fig.III.10&.11 from [108] .

The combined motion results in rotation of the metacarpal of the thumb around the long axis of the metacarpal of the index finger - i.e. enabling opposition of the palmar surfaces of the thumb and fingers.

Measurements of the distances between the origin and insertion of the ligaments [109] show changes of $> 20\%$, and therefore that the collagen fibres of the ligaments would be slack through much of the range of motion of the trapezio-metacarpal joint. This is confirmed by the fact that relaxation of the muscles allows palpable distraction of the joint. The function of the ligaments is therefore to limit the extremes of motion of the joint faces, such that contraction of the muscles of the thumb will always bring the joint faces into congruence. In this regard the volar beak is responsible for "screw home" torque rotation of the thumb metacarpal [107].

The innervation of the ligaments of the trapezio-metacarpal joint was studied by immunofluorescence imaging, allowing the class of end receptors to be distinguished [110]. The mechanoreceptor endings found in the trapezio-metacarpal joint were predominantly Ruffini stretch receptors, while Pacinian corpuscles were found only rarely. This is in line with observations from carpal joints generally, indicating the importance of perception of joint position. This compares with studies of the joints of the foot and of the skin of the palm, where Pacinian corpuscles are common, indicating the importance of change detection. In some locations several Ruffini receptors were grouped forming a structure resembling a Golgi tendon organ. The posterior oblique, dorsal collateral, dorsal radial were consistently the most densely innervated ligaments, indicating the importance of the dorsal ligament complex for proprioception.

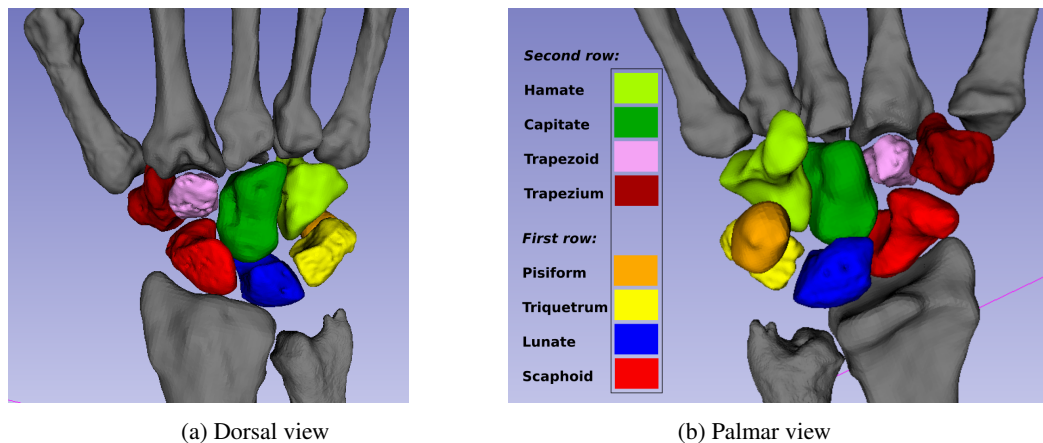


Figure 3-23: Terminologia Anatomica English names for the carpal bones. Note the gap between the ulna and the carpal bones is occupied by the triangular fibrocartilaginous complex” see 3.3.5.

3.3.3 Wrist

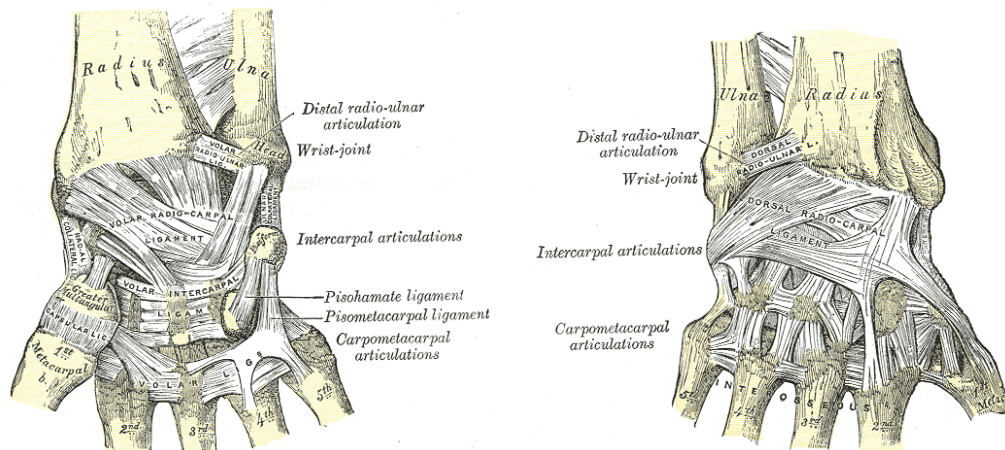
Bones of the wrist

The wrist is a complex joint composed of radius, ulna and eight small carpal bones. The various names have been used for the carpal bones. Figure-3-23 gives the current Terminologia Anatomica English names for human carpal bones, while the drawings in figure-3-24 use an older system that was current at the time of that reference [62]. Note that the Nomina Anatomica Veterinaria uses different naming system for the same bones.

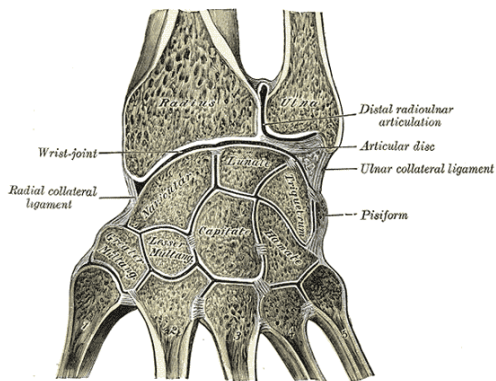
The contact surfaces of the bones form synovial joints allowing the bones to slide over each other. There are both short ligaments that connect adjacent bones, and long ligaments that connect bones that are not in contact with each other. Different ligaments become lax or taut in different relative positions of the bones, constraining the motion. There is considerable individual variation in the detailed geometry and topology of both bones and ligaments, that none the less produces healthy wrists with normal function e.g. [111].

It should be borne in mind that all active motions of the carpus, and loads borne by the carpus, occur under compression by the tendons of the wrist and of the extrinsic muscles of the hand. When these muscles are relaxed, there is sufficient slack in the ligaments that it is possible to visibly and palpably distract the radio-carpal and inter-carpal joints, and to translate the carpus dorso-palmarly and to a lesser extent radio-ulnarly and in axial torque.

The reader’s attention is drawn the large cross section area and radii of curvature that is maintained through the bony column, and the effect this has in (i)minimising peak compressive stresses, and (ii)largely eliminating shear stresses. Compare this to the stresses that would arise in a conventional gimbal system of the same external dimensions. This is discussed further in chapter-4.



(a) Wrist joint palmar view, image334 from [62]. (b) Wrist joint dorsal view, image335 from [62].



(c) Wrist joint cross section, image336 from [62].



(d) T2 weighted MRI, transverse section of the carpus.

Figure 3-24: Ligaments of the carpal bones.

3.3.4 Motions of the carpal bones

Motion of the trapezium in thumb opposition

As described in section 3.3.2, the trapezium (dark red bone in figure-3-23) can move palmar-dorsally with respect to the scaphoid (bright red) while rotating about the trapezoid (pink).

Motion of the hamate in palm folding

An important motion of the hand is the folding of the bony part of the palm. This involves the metacarpals of the ring and little fingers flexing forward with respect to the carpus, and rotating around the metacarpal of the middle finger at the distal inter-metacarpal joints. This motion is facilitated by:

1. the ring and little finger metacarpals sliding palmarly at the proximal inter-metacarpal joints, and at their carpo-metacarpal joints with the hamate bone (light green in figure-3-23).
2. the flexion of the hamate bone relative to the other carpal bones.

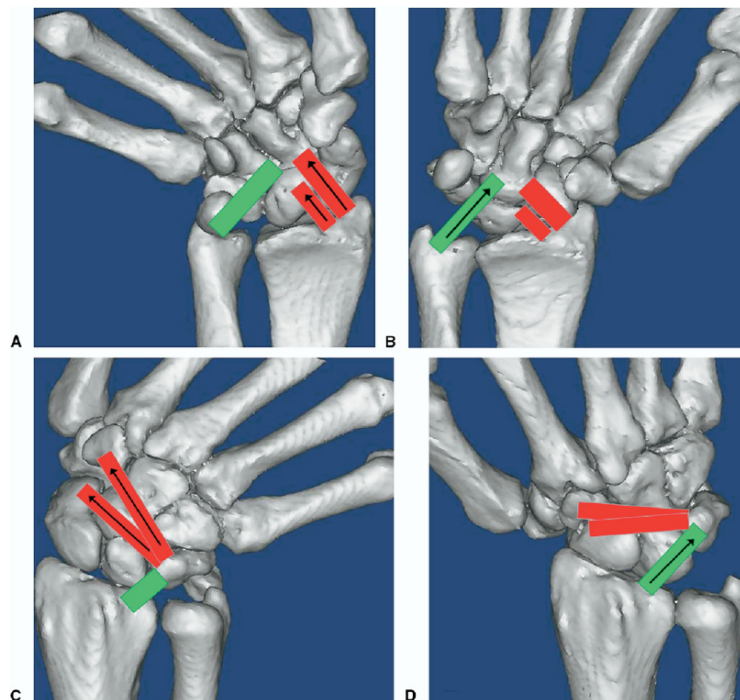


Figure 3-25: Length changes and potential tensional status of measured carpal ligaments during wrist radio-ulnar deviation. A, B Three palmar ligaments: RSC, LRL, and UC. The ligaments with the arrows are tensed. The sum of the lengths of the RSC and UC ligaments was consistent at 4 positions of radio-ulnar deviation. C, D Dorsal ligaments: DIC and DRC. The ligaments with arrows are tensed. The DIC and DRC ligaments have converse-length changes. A and C are at ulnar deviation; B and D are at radial deviation. Figure 5 from [112].

Radio-ulnar deviation of the wrist

Radio-ulnar deviation of the wrist - the 'hammering' motion - is essential to dexterity in grasping and many common manipulations. Figure-3-25 shows the motions of the carpal bones and how the long ligaments come into tension at different parts of the motion. Note how the second row of carpal bones rotates relative to the first row about a point in the proximal part of the capitate bone (dark green bone in figure-3-23). This is enabled by the flexion of the scaphoid (bright red bone in figure-3-23), providing space for the trapezoid (pink) during radial deviation. In ulnar deviation it is enabled by the flexion of the triquetrum (yellow), and triangular fibro-cartilagenous complex to make space for the hamate.

Carpal flexion-extension

The most dramatic motion of the wrist is its flexion-extension through $> 180^\circ$. This achieved by the radio-carpal and mid-carpal joints acting in series each providing approximately half of the motion, figure-3-26b. An elegant mechanism of ligaments and joint faces coordinates the motion of the second row of carpal bones relative to the first row, figure-3-26c.

The scaphoid (red), lunate (blue), triquetrum (yellow), capitate (green) each rotate about their own axis linked to each other by inter-carpal ligaments (black), such that their motions are coupled to each other. The distal row of carpal bones move with the capitate (green). The other bones of the second row, hamate, trapezoidal, and trapezium follow the motion of the capitate. The net effect is two consecutive axes of flexion-extension, enabling $> \pm 90^\circ$ of flexion and extension either side of the neutral point.

Note that the radio-carpal joint face is approximately toroidal centred on the capitate, with the ring of the minor axis passing through the first row carpal bones. If this were allowed to rotate about the minor axis to under flexion-extension it would become severely incongruent. The anatomical carpal joint maintains good congruence from 45° of flexion (pulling with hooked wrist), to $> 90^\circ$ extension (pushing with the palm).

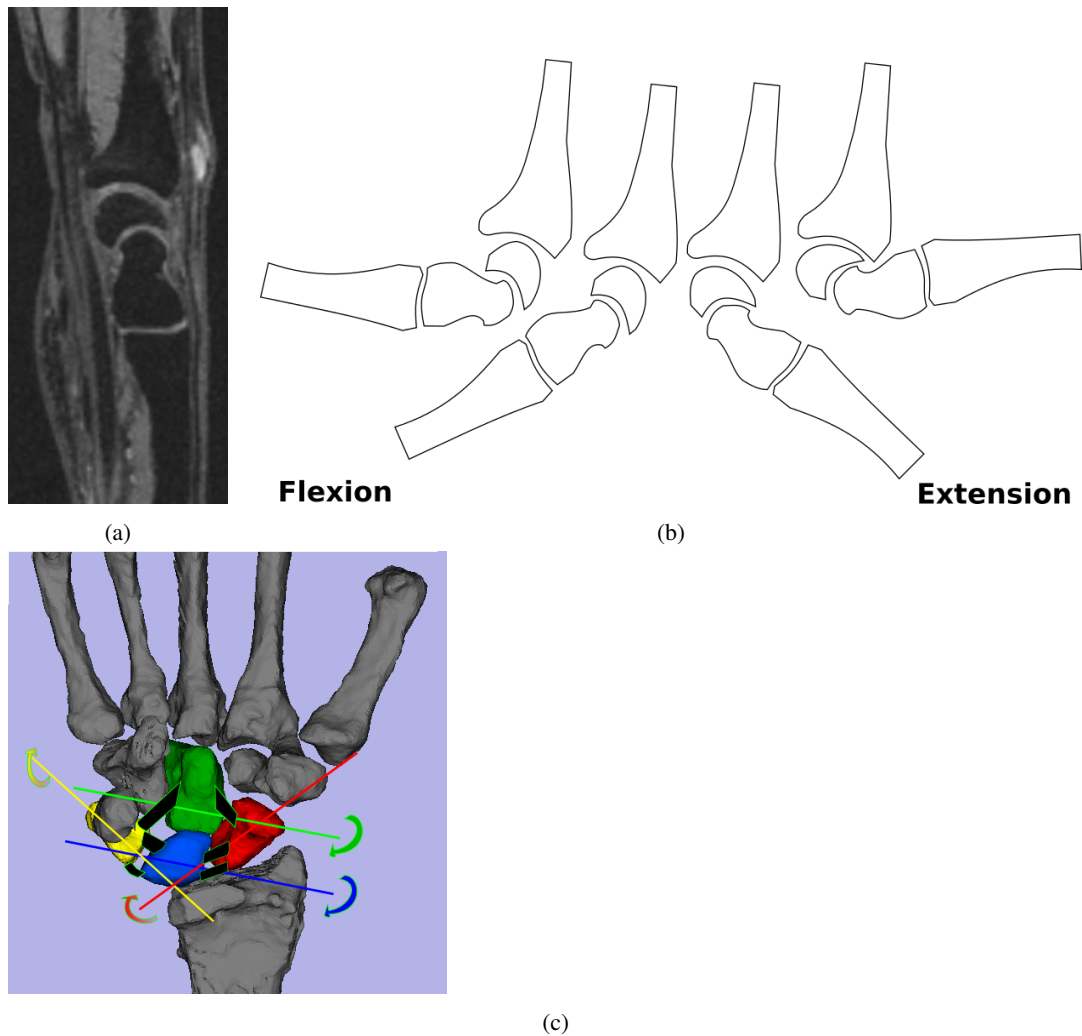


Figure 3-26: (a&b) Motion of the radio-carpal and inter-carpal joints in flexion and extension. (a) T2 weighted MRI scan, sagittal view at the level of the metacarpal of the middle finger, the capitate and lunate carpal bones, (b) diagram of motion of the joints. (c) Coordination of the motion of the individual carpal bones in flexion-extension. Each bone rotates about its own axis, linked by the ligaments (black).

3.3.5 Forearm

Muscle actuated rotation of the wrist (as opposed to torquing of the relaxed carpus) is provided by the radio-ulna joints, supported by the radio-ulna ligaments. The carpus and hand are fixed in rotation about the long axis of the radius (so long as they are in compression due to contraction of the extrinsic tendons of the hand). The ulna is fixed in axial rotation with respect to the humerus and upper arm, while the radius rotates about its own axis, causing the radius and everything distal to it to pronate-supinate with respect to the ulna. The muscles responsible for actuation are discussed in section-3.4.8.

There are two articulations, proximal and distal at either end of the radius, see figure-3-15.

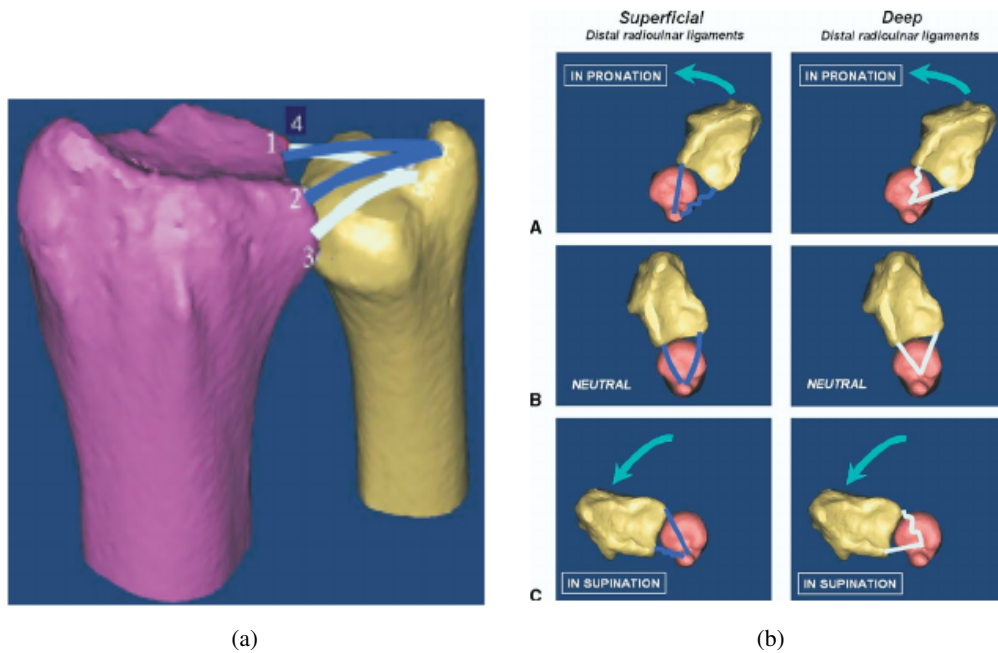


Figure 3-27: The ligaments of the distal radio-ulna joint, within the triangular fibrocartilaginous complex, at the distal margin of the joint. (a) The 4 ligaments studied: 1 and 2, palmar and dorsal superficial radio-ulnar ligaments (dark blue); 3 and 4, dorsal and palmar deep radio-ulnar ligaments (ligamentum subcruentum) (light blue), from figure-1 of [112]. (b) The tensional status in each component of the distal radio-ulnar ligaments at the positions of A forearm pronation, B neutral rotation, and C supination, from figure-2 of [112].

The distal radio-ulnar joint

Figure-3-27a shows the distal radio-ulnar joint, composed of the synovial articulation of the ulna head with the sigmoid notch of the radius. Note that while the ligaments of the triangular fibro-cartilaginous complex slide over each other and bear tension holding the distal radius and ulna together, they simultaneously bear compression from the triquetrum and lunate carpal bones in the ulna-carpal joint on the distal side of the triangular fibro-cartilaginous complex, see figure-3-23. Figure-3-27b shows how the tension load shifts between the ligaments through the motions of pronation-supination. CT studies showed that while the motion of the distal radio-ulna joint is dominated by sliding around the circum-

ference of the ulna head, there is also a significant movement of the centre of contact across the sigmoid notch of the radius, i.e. a rolling component to the motion, [113].

The triangular fibrocartilaginous complex

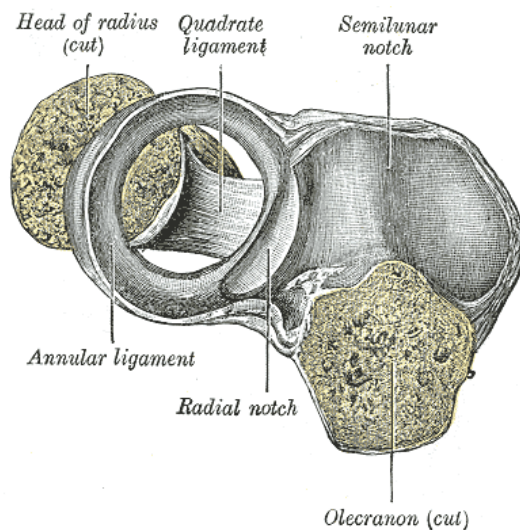
The triangular fibrocartilaginous complex is composed of the an articular disc part, the dorsal and volar radio-ulnar ligaments described above, an meniscus part, the ulnar collateral ligament of the carpus, and the sheath of the extensor carpi ulnaris tendon, [114]. These parts are fused together into a single fibro-elastic structure that cannot be dissected apart (i.e. the matrix is continuous without a low-modulus areolar loose connective tissue lamina separating the components).

The radio-ulnar ligaments

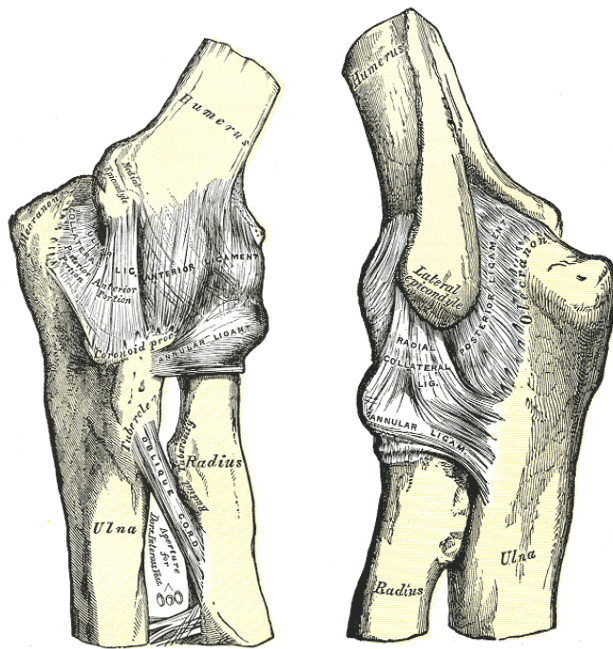
In addition to the dorsal and volar distal radio-ulnar ligaments described in the previous two sections, there is an radio-ulna interosseous band and an annular ligament at the proximal-radio ulnar joint, see figure-3-29e. The interosseous band has three parts proximal, central and distal which hold the radius and ulna to each other. The parts of the central band are arranged obliquely such that the central and distal parts draw the radius distally, while the proximal part opposes them, drawing the radius proximally, [115]. The annular radio-ulnar ligament forms part of the proximal radio-ulnar joint (see below).

The proximal radio-ulnar joint and the radio-humeral joint

The axial rotation of the radius is accommodated by the cartilaginous annular ligament which encircles the head of the radius, holding it to the ulna and forming a meniscus-like interface between the medial condyle of the humerus and the radius. The quadrate ligament limits the supination-pronation of the radius.

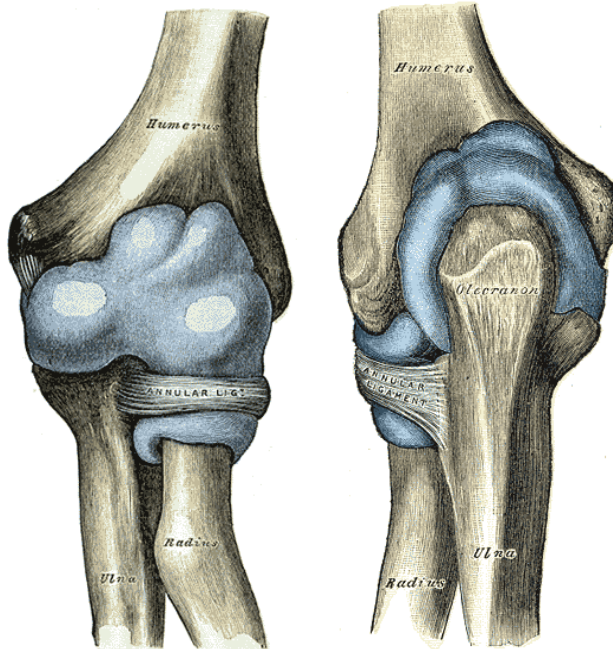


(a) elbow joint distal surface, image333 from [62]



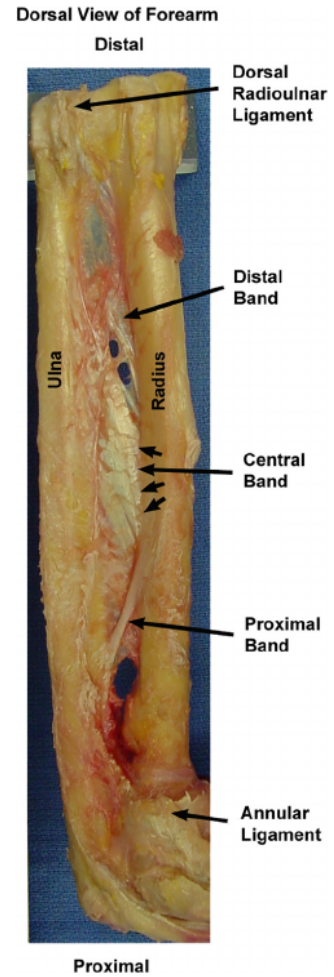
(a) elbow joint lateral view, image329 from [62]

(b) elbow joint medial view, image330 from [62]



(c) elbow bursa, image331 from [62]

(d) elbow joint bursa posterior view, image332 from [62]



(e) Dorsal view of the forearm, showing its primary stabilizers. Distally, the DRUL is shown; the PRUL is hidden. Three portions of the interosseous membrane are shown: the DB, CB, and PB. Multiple portions of the CB are denoted. The location of the AL is shown. Figure-1 from [115].

Figure 3-29

3.4 Human hands: muscle-tendon networks

Synovial joints necessitate tendon actuation, but the type of tendons are very different from the wires and strings conventionally used for tendons in robotics. The general structure of anatomical tendons is covered in section-3.1.8.

The basic layout of the hand is that there are flexor tendons on the palmar side, and extensor tendons on the dorsal side, figure-3-30 . The extrinsic flexor and extensor muscle bellies are located on the forearm, and their tendons under-actuate the wrist as well as the digits, figures-3-33 and 3-43 . The palm contains three sets of intrinsic muscles (1) the thenar muscles specific to the thumb, figure-3-30b&c , (2) the hypothenar muscles specific to the little finger, mirroring the thenar muscles, (3) the interosseous and lumbrical muscles which belong to the extensor hoods of each digit, figure-3-51 . There are no skeletal muscle bellies in the digits distal to the MCP joints.

Where tendons run in a curved path they exert a lateral force and have a synovial sheath or a synovial bursa extension from a joint capsule. Both the tendon and the sheath have a hyaline cartilage matrix and sliding surface where they bear pressure on each other. The digital flexor tendons have sheaths for most of their length from the wrist to the DIP joints, figure-3-30c . Tendons are held in their correct paths by retinacular ligaments.

3.4.1 The digital flexor apparatus

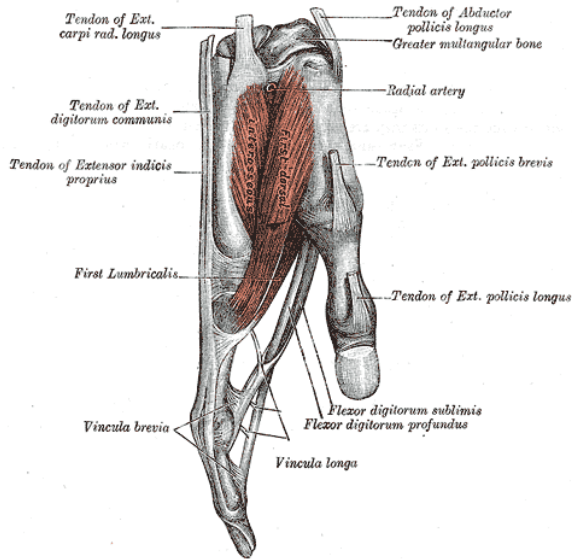
There is significant individual variation in the flexor apparatus. The extent and connectivity of sheaths, bursas and retinacular ligaments may differ between individuals. The account given below describes the canonical anatomy based on the normal findings in dissection reported in the literature.

Digital flexor tendons

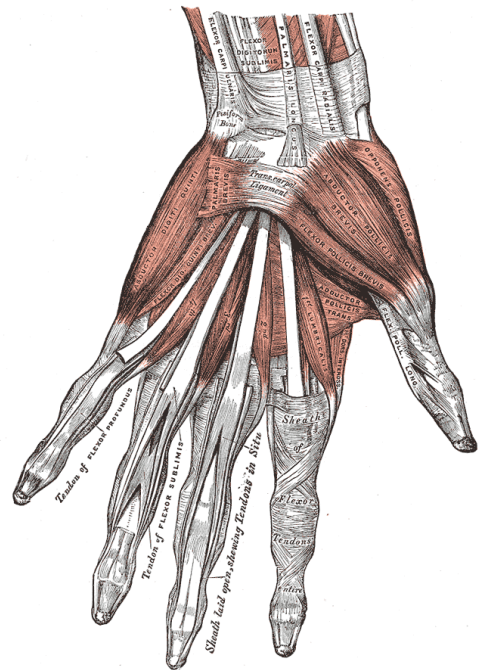
The digital flexors are the strongest tendons in the hand and are extrinsic muscles. Their muscle bellies on the forearm are highly pennate giving them an especially large physiologic cross-section area and contraction force. Each finger has a deep and a superficial digital flexor tendon which run together in a digital flexor sheath. The deep flexor tendons insert on the distal phalanx, run along the palmar surface of the bones, and flex every joint of the finger and wrist. The superficial digital flexor lies on the palmar side of the deep digital flexor (i.e. superficial to it with respect to the bones), and splits in to radial and ulnar branches at the level of the first phalanx. These branches then insert on the second phalanx. The deep digital flexor passes through the gap between these branches, called the "chiasma" of the superficial digital flexor tendon, figure-3-30a . The superficial tendon flexes all of the joints of the hand and wrist except the distal interphalangeal joint (DIP).

Digital flexor sheath

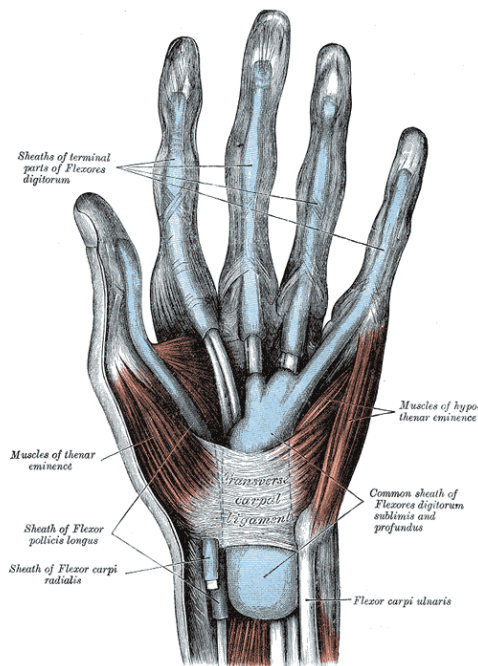
The tendon sheath of the flexor tendons is a thin membranous structure that encloses a potential space containing a small amount of synovial fluid around the flexor tendons. Topologically the sheath is a balloon and the tendons lie outside the cavity, but membrane wraps around the tendons from their superficial side such that geometrically they lie inside the sheath. The part of the sheath membrane



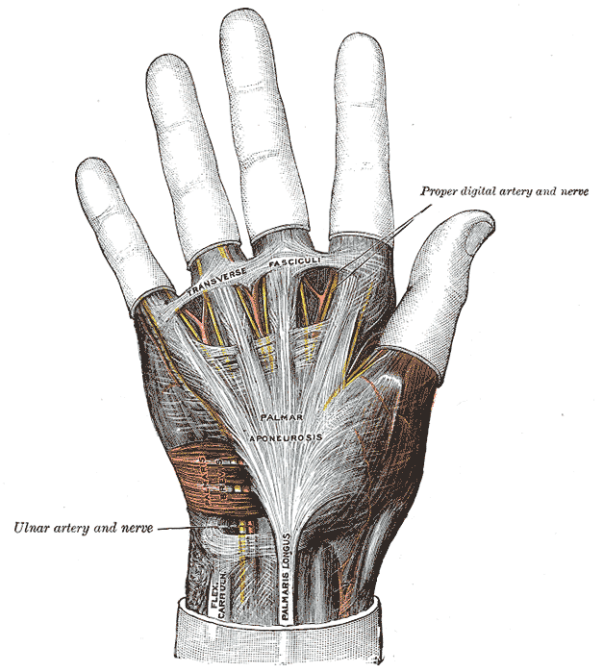
(a) image416 tendons of fingers medial view, from [62].



(b) image427 digital flexor tendons and superficial muscles of the palm, from [62].



(c) image423 hand flexor tendon sheaths, from [62].



(d) image425 superficial palmar fascia, from [62].

Figure 3-30

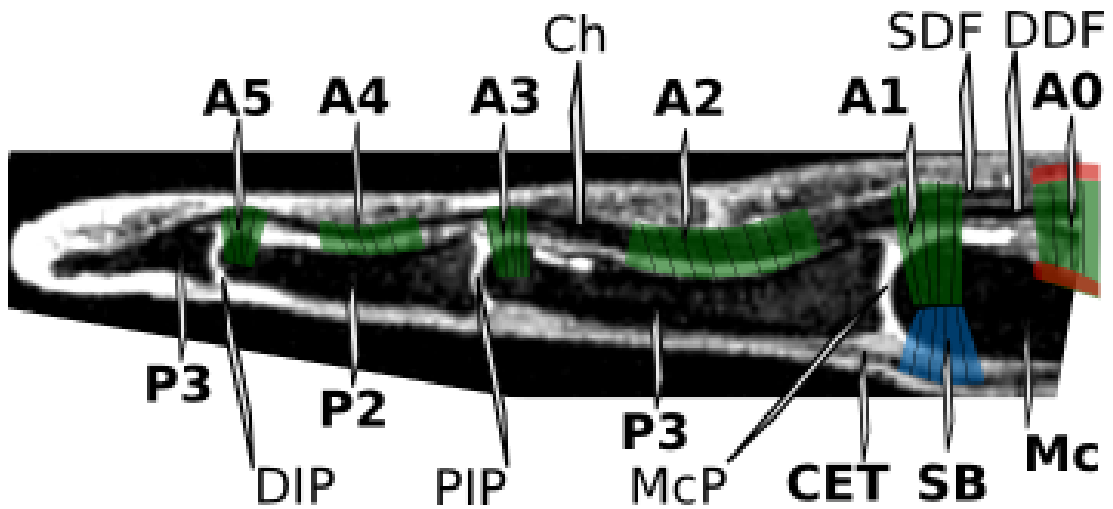


Figure 3-31: The undulating path of the flexor tendons of a finger in the extended position seen in an MRI scan, palm upwards in sagittal section. The location of the retinacular ligaments is superimposed on the scan. Labels: A0 'zeroth' annular ligament is formed by the transverse fibres of the superficial palmar fascia and the septae of Legueu and Juvara, A1-5 Annular retinacular ligaments, P1-3 phalanges, Mc meta-carpal bone, DIP distal inter-phalangeal joint, PIP proximal inter-phalangeal joint, McP metacarpo-phalangeal joint, CET common extensor tendon, SB sagittal bands, DDF deep digital flexor tendon, SDF superficial digital flexor tendon, Ch chiasma where DDF passes between the branches of the SDF. Note the DDF inserts on P3, while the branches of the SDF insert on P2.

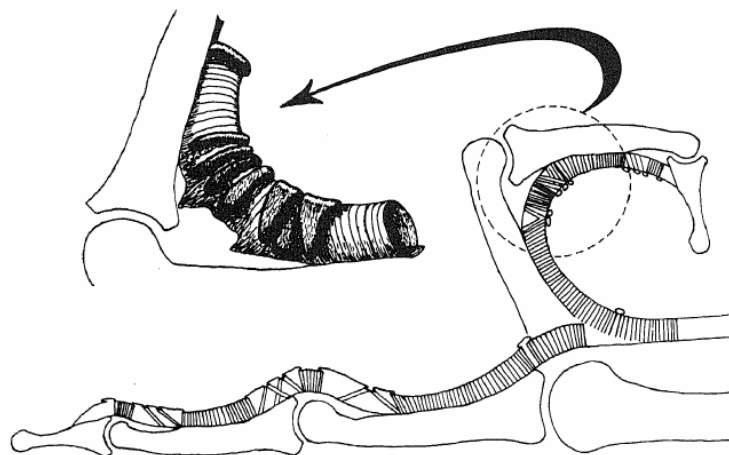
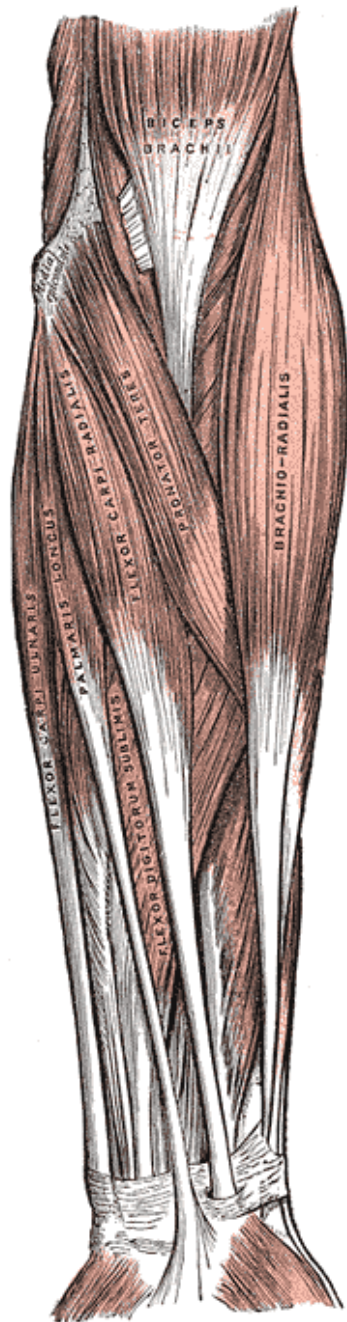
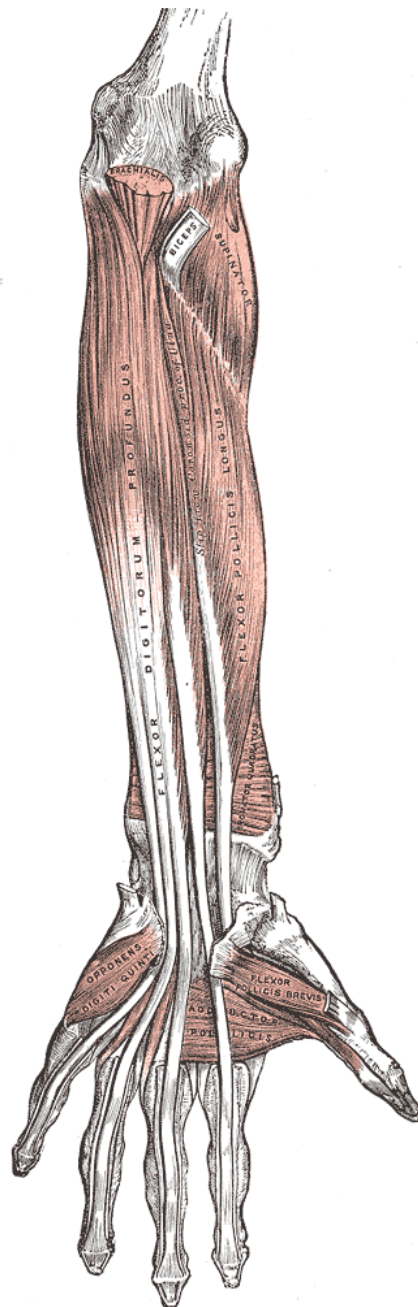


Figure 3-32: Interpretation of tenographic images: sheath bulging and flattening during flexion-extension. Insert: synovial pocket formation. Fig.3 from [116]. "Tenographic" = X-ray radiographs of finger with contrast medium injected into the flexor tendon sheath. Note: (1) the smooth curvature of the tendons at all stages of flexion-extension, (2) the cruciate retinacular ligaments between the annular ligaments and their role in producing a smoothly curved constraint on the tendons.



(a) image414 forearm superficial muscles palmar view with the carpal tunnel intact, from [62].



(b) image415 forearm deep muscles, palmar view with the carpal tunnel transected, from [62].

Figure 3-33

adhered to the surface of the tendons is termed 'visceral', while the part adhered to the tissues geometrically outside is termed 'parietal'. (Note, this visceral vs parietal terminology is used generally for

membrane lined cavities in the body.)

The sheath lies between the tendons and the retinacular ligaments (sections-3.4.1 & 3.4.1), and permits sliding contact under pressure between them. In the spaces between the ligaments the sheath balloons outward when the joints are flexed. This slack length of membrane is taken up when the joints are extended and the gap between the ligaments opens up.

Annular ligaments

The annular retinacular ligaments are by far the strongest ligaments of the digital flexor retinaculum. They are responsible for transmitting the load exerted by the flexor tendons on the digits, and retaining the tendons in their path relative to the bones. For this reason they are often called "the pulleys". Conventionally the annular ligaments are numbered "A1" to "A6" from proximal to distal. The odd numbered annular ligaments attach to the volar plates and accessory collateral ligaments of the MCP, PIP and DIP joints. The even numbered annular ligaments are attached to the diaphyses (mid-shafts) of the phalanges. The transverse fibres of the superficial palmar fascia, and the "septae of Legueu and Juvara" retain the flexor tendons close to the diaphyses of the metacarpal bones, in a manner equivalent to the the even numbered annular ligaments. For this reason they are sometimes described as the "A0" or "zeroth annular pulley". Figure-3-31 shows the location of the annular ligaments with respect to the tendons and phalanges. Note that there is a sixth annular ligament (not shown) on the distal phalanx that retains the deep flexor tendon where it runs along the palmar surface of P3 to insert along the length of the bone.

Cruciate ligaments

The cruciate (crossed) ligaments of the flexor retinaculum occur on the flexor sheath, between the annular ligaments. They do not play a significant role in transmitting force from the tendons. Their function is to stabilise the tendon sheath membrane in the gaps between the annular ligaments.

Natatory ligament

The natatory ligament lies in the finger webs and connects the proximal palmar margins of the second annular ligament of adjacent fingers. In figure-3-30d it is wrongly labelled "transverse fasciculi".

3.4.2 Palmar fascia

The flexible palm is crucial to the function of the hand and digits. It has a very specific structure which permits and constrains the relative movement of its many parts. Much of its subtlety lies in the network of fibrous ligaments that guide muscles and tendons, and bind the whole hand together.

It can be difficult to appreciate the relative position of structures especially in the palm where many muscles, tendons and ligaments run across each other. Figures-3-34 , 3-35 , 3-36 , 3-37 , 3-38 , provide axial sections through the palm in series from proximal to distal.

Superficial palmar fascia

The superficial palmar fascia (figure-3-30d) lies between the subcutis and the other musculoskeletal structures of the palm. It is composed of longitudinal and transverse fibres. The longitudinal fibres are the aponeurosis (flattened sheet tendon) continuation of the palmaris longus tendon, an extrinsic flexor of the carpus. The longitudinal fibres insert on the A1 and A2 annular ligaments, so also act as flexors of the MCP joints. The transverse fibres run from the ulnar margin of the little finger MCP joint to the radial margin of the index finger MCP joint. They are tightly fused to the longitudinal fibres where they cross and are also tied to the metacarpal diaphyses by the septa of Legueu and Juvara (section-3.4.2).

Deep palmar fascia - trans-metacarpal ligament

The deep palmar fascia consists of transverse ligaments linking the volar plates of adjacent MCP joints from the index finger to the little finger. It is visible in figure-3-36 , 3-39 and 3-40 where it forms the dorsal side of the lumbrical canals. The deep palmar fascia contributes along with the natatory ligament (section-3.4.1) to:

- limiting the phase difference between adjacent MCP joints, and
- limiting the abduction of the metacarpal bones.



Figure 3-34: Axial anatomic slice obtained at the dorsum of the hand show the extensor digitorum tendons (arrowheads) and extensor digiti minimi tendons (arrow), which are arranged on the same level. Note the difficulty of identifying the tendon for each finger owing to tendon multiplicity and variability. Fig.8a of [52] .

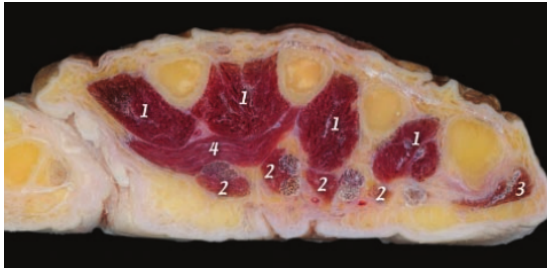


Figure 3-35: Axial anatomic slice obtained at a near level along the dorsum of the hand show the interosseous muscles (1), which are located in the inter-metacarpal spaces. The lumbrical muscles (2) are located on the radial sides of the flexor digitorum profundus tendons. 3 = abductor digiti minimi, 4 = adductor pollicis. Fig.16a of [52] .

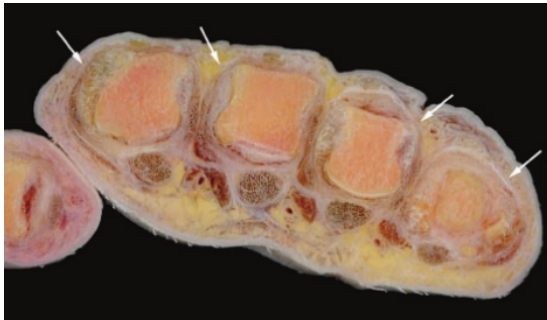


Figure 3-36: Axial anatomic slice obtained at the MCP joint show the sagittal bands (arrows), which extend from the extensor digitorum tendon to the palmar plate. Fig.13 of [52] .



Figure 3-37: Axial anatomic slice obtained at the MCP joint show the circumferential distribution of the dorsal apparatus over the dorsum of the fingers. Arrows = sagittal band. Fig.12 of [52] .

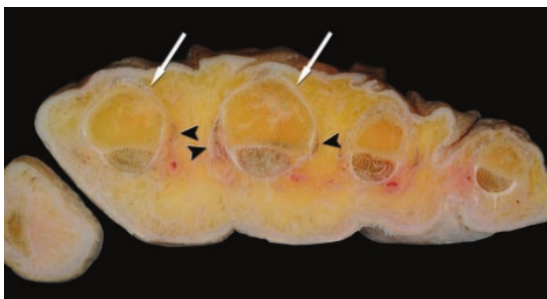


Figure 3-38: Axial anatomic slice obtained at the proximal phalanx show a dorsal condensation of fibres (arrows), which corresponds to the extensor digitorum tendon, and lateral and medial fibres (arrowheads), which correspond to the intrinsic contribution to the extensor apparatus by the interosseous and lumbrical tendons. Fig.17a of [52] .

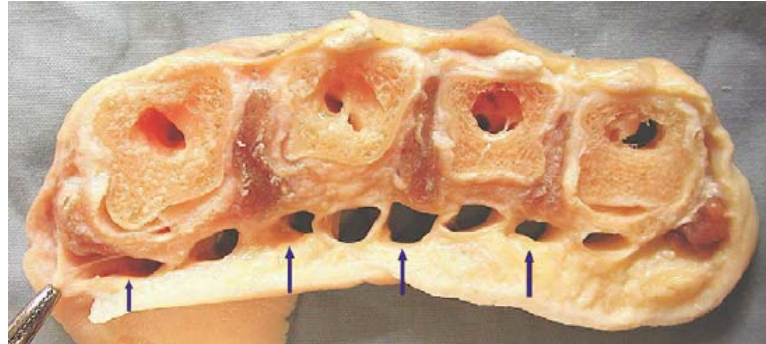


Figure 3-39: Cross-section of a hand at the level of septa of Legueu and Juvara, i.e. between the levels of fig-3-35 and fig-3-36 . Flexor tendons, lumbrical muscles, and neurovascular structures are removed. The hemostat is palmar and slightly radial to the first dorsal interosseous muscle. The arrows point to the 3 web space canals and a radial marginal canal. These are for hosting lumbrical muscles and common digital nerves and arteries, which are located radial to the flexor tendon canals. Eight well-defined septa can be seen clearly and a ninth thin membranous marginal septum is held by the hemostat. Fig.1 of [102] .

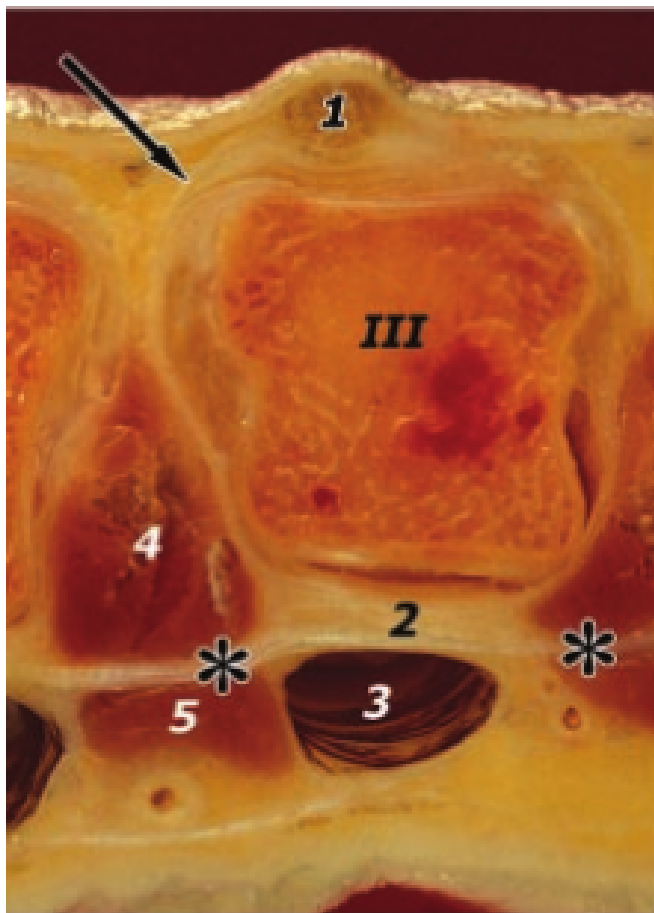


Figure 3-40: Axial anatomic slice (close-up view) show the sagittal band (arrow). 1 = extensor digitorum tendon, 2 = palmar plate, 3 = flexor tendon sheath, 3 = flexor tendon, 4 = interosseous muscle, 5 = lumbrical muscle, III = third metacarpal bone, * = deep transverse metacarpal ligament. Note that the interosseous muscle is dorsal to the deep transverse metacarpal ligament and the lumbrical muscle is palmar to the ligament. Fig.13c of [52] .

The septa of Legueu and Juvara

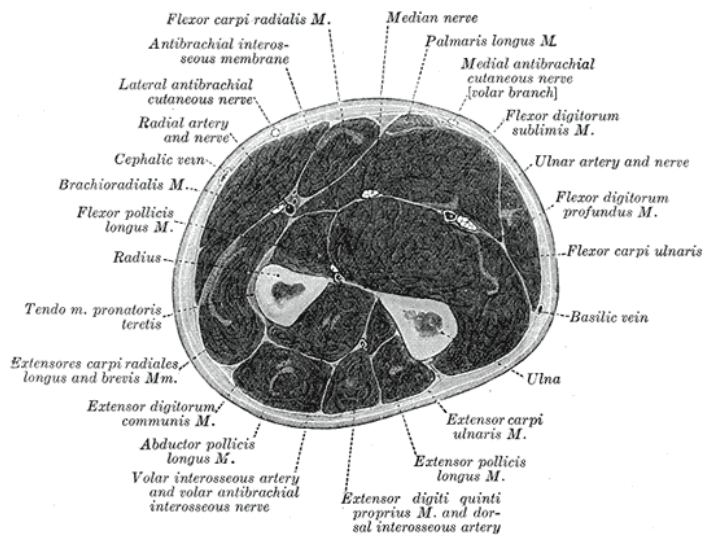
The septae of Legueu and Juvara originate on the radial and ulnar margins of the metacarpal diaphyses and insert in the transverse superficial palmar fascia, figure-3-36 , 3-39 and 3-40 . They lie proximal to the A1 first annular ligament figure-3-37, but distal to the thumb adductor muscles figure-3-35.

Carpal tunnel

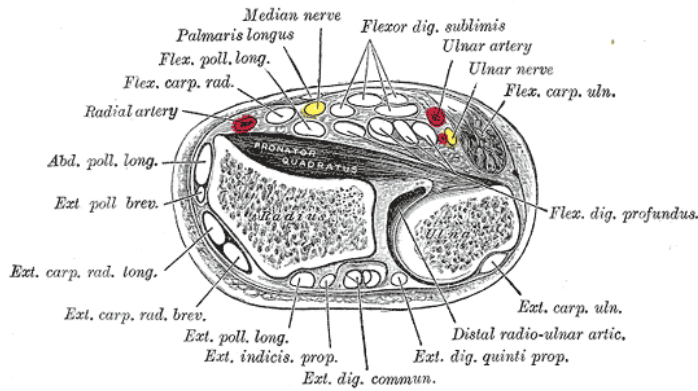
The carpal tunnel is formed by the trans-carpal ligament which functions as an annular flexor retinacular ligament at the carpus. For this reason the trans-carpal ligament is also referred to as the "flexor retinaculum" of the carpus. The trans-carpal ligament inserts over a broad area on the palmar surfaces of the hamate and pisiform carpal bones on the ulnar side and on the scaphoid and trapezium carpal bones on the radial side. All of the digital flexor tendons, including those of the little finger and thumb, pass through the carpal tunnel, figure-fig:image422-carpal-tunnel-cross-section.

Ulnar tunnel - Guyon's canal

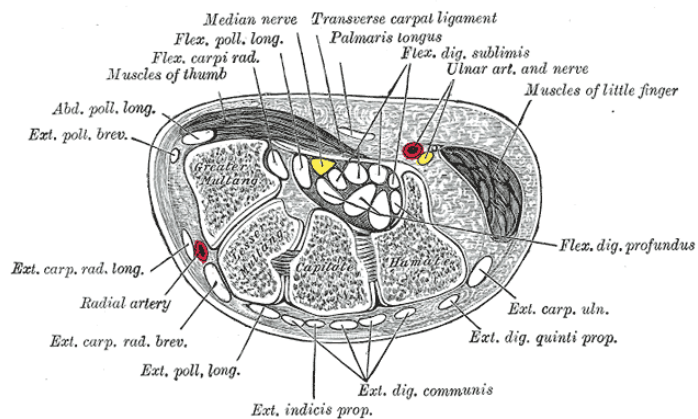
The ulnar tunnel contains no tendons, but does contain the ulnar nerve and artery. The ulnar tunnel lies superficial and ulnar to the carpal tunnel. It is formed by the palmar carpal ligament which originates on the pisiform carpal bone and inserts into the mid point of the trans carpal ligament.



(a) image417 forearm muscles cross section, from [62].



(b) image421 forearm distal cross section showing the tendons and nerves, from [62].



(c) image422 carpal tunnel cross section, from [62].

Figure 3-41

3.4.3 Digital extensor apparatus

The extensor apparatus of the fingers is composed of the extrinsic extensor muscles (below), the interosseous and lumbrical muscles (sections-3.4.3 and 3.4.3), and the extensor tendon hood (section-3.4.3).

Extrinsic digital extensor muscles

Common extensor - Extensor digitorum communis originates from the lateral epicondyle of the humerus and divides into multiple heads supplying multiple tendon slips. It is highly variable and may supply one or more tendon slips to each of the fingers where they join the digital extensor hood (section3.4.3). The slips are cross-linked by synechiaie (section-3.4.3).

Extensor of the index finger - Extensor indicis proprius originates from the dorsal aspect of the ulna and from the radio-ulnar interosseous membrane. It supplies a single tendon without connections synechiaie, to the extensor hood of the index finger. It provides independent extension of the index finger.

Extensor of the little finger - Extensor digiti quinti originates from a separate head of the common extensor, and inserts on the extensor hood of the little finger. It provides independent extension of the little finger.

Extensors of the thumb - Extensor pollicis longus and extensor pollicis brevis are covered in section-3.4.6 and 3.4.6.

Extensor tendon synechiaie - junctura tendinum - inter-tendinous connections

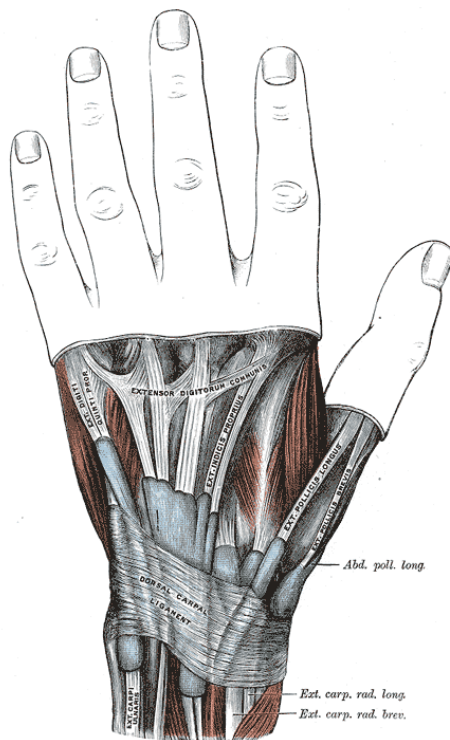
The synechiaie (inter-tendinous connections) of the tendons of the common digital extensor occur on the dorsal aspect of the hand between the levels of MCP joints and the dorsal carpal ligament. The synechiaie are indicated by arrow heads in the dissected extensor tendons in figure-3-46 . They are indicated by label "10" in figure-3-44a, and are visible in figures-3-42a and 3-43a.

The synechiaie show a high degree of individual variability, but have an important effect on the kinematics of the common extensor tendons. Their function is to transfer tension between the otherwise independently contracting branches of the common digital extensor. This limits the phase difference between different fingers, of extension of the finger joints due to the common extensor, and transfers work between tendon slips of the common digital extensor.

Dorsal carpal ligament and the extensor sheath of the carpus

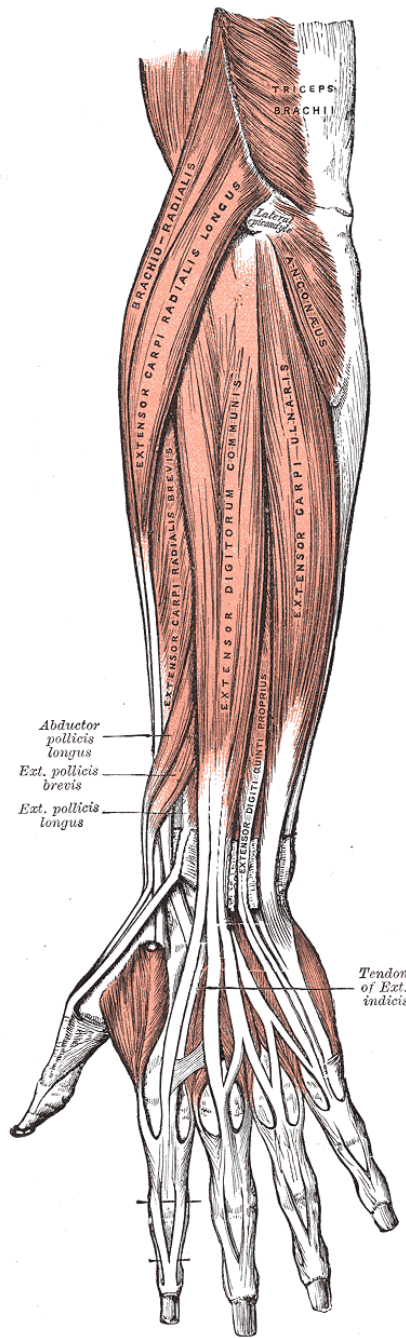
The digital extensors have a synovial bursa at the carpus [117] where they pass under the carpal extensor retinaculum, otherwise their movement is lubricated by hyperelastic peritendon tissue, figure-3-42a . The function of the ligament dorsal carpal ligament is:

1. to retain the extrinsic extensor tendons in their correct paths on the dorsal surface of the distal forearm, and
2. to prevent bowstringing of the tendons during hyper-extension of the wrist.

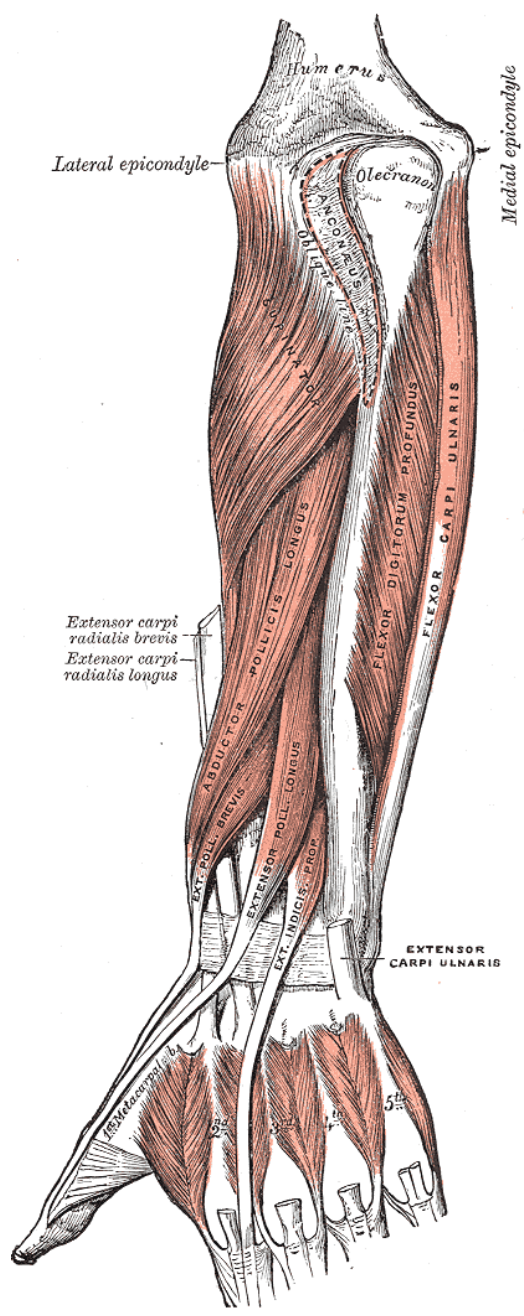


(a) image424 wrist extensor tendon sheaths, from [62].

Figure 3-42



(a) image418 forearm superficial muscles, dorsal view



(b) image419 forearm deep muscles, dorsal view, from [62].

Figure 3-43

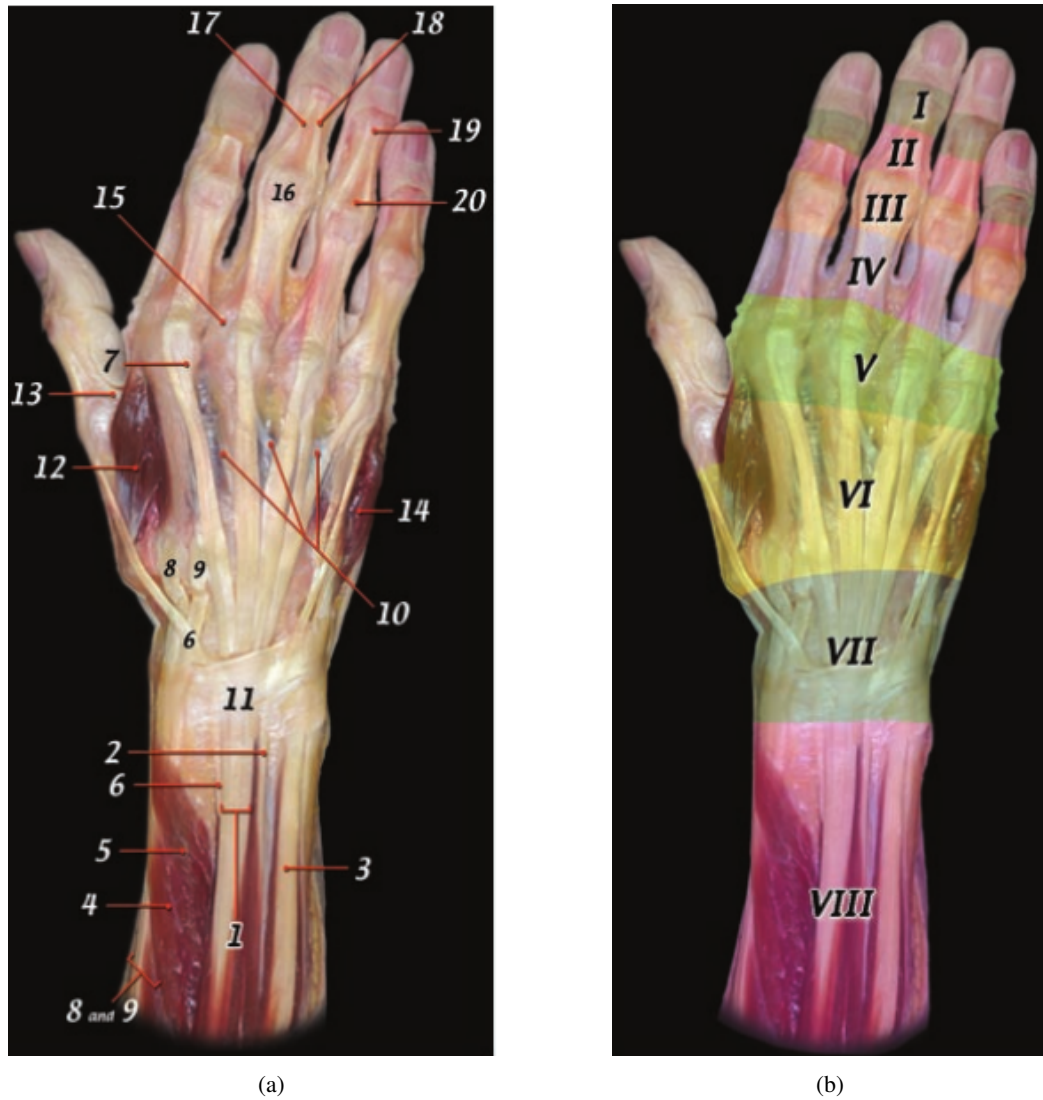


Figure 3-44: Anatomy of the extensor apparatus. (a) Drawing of the hand (dorsal view) shows the main anatomic structures. 1 = extensor digitorum muscle, 2 = extensor digiti minimi muscle, 3 = extensor carpi ulnaris muscle, 4 = abductor pollicis longus muscle, 5 = extensor pollicis brevis muscle, 6 = extensor pollicis longus tendon, 7 = extensor indicis tendon, 8 = extensor carpi radialis longus muscle, 9 = extensor carpi radialis brevis muscle, 10 = inter-tendinous connections, 11 = extensor retinaculum, 12 = first dorsal interosseous muscle, 13 = adductor pollicis tendon, 14 = abductor digiti minimi muscle, 15 = sagittal band, 16 = central slip, 17 = lateral conjoined tendon, 18 = medial conjoined tendon, 19 = terminal tendon, 20 = triangular ligament. (b) Drawing of the hand (dorsal view) shows the zones of the extensor system according to the Verdan classification (10). This classification was developed to categorize the lesion findings. I = DIP joint, II = middle phalanx, III = PIP joint, IV = proximal phalanx, V = MCP joint, VI = dorsum of hand, VII = wrist extensor compartment, VIII = extrinsic extensor muscles. Fig1. of [52].

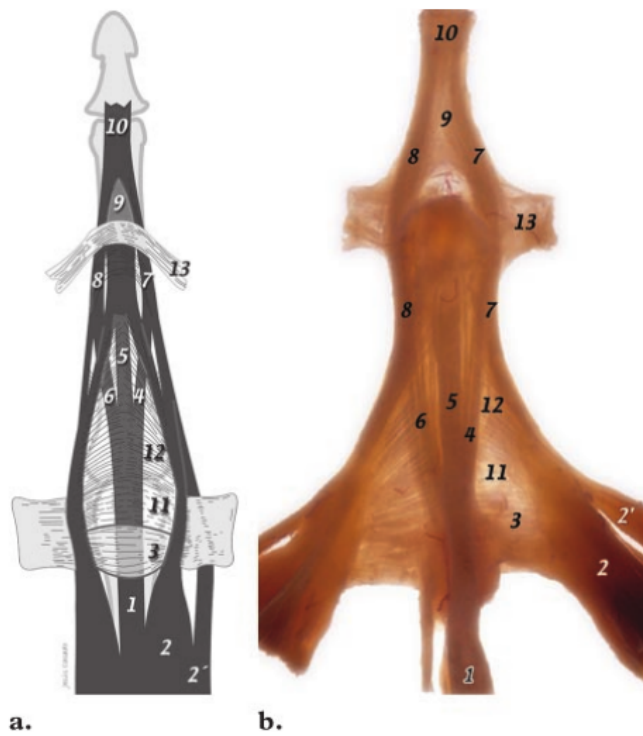


Figure 3-45: a) drawing b) trans-illuminated anatomic specimen (dorsal view) showing the extensor apparatus of the index finger (removed from its location). 1 = extensor digitorum tendon, 2 = interosseous muscle, 2' = lumbrical muscle, 3 = sagittal band, 4 = medial slip, 5 = central slip, 6 = lateral slip, 7 = medial conjoined tendon, 8 lateral conjoined tendon, 9 = triangular ligament, 10 = terminal tendon, 11 = transverse fibres, 12 = oblique fibres, 13 = retinacular ligament. Fig11a&b. of [52] .



Figure 3-46: Trans-illuminated anatomic specimen (dorsal view) shows the extensor tendons of the dorsum of the hand (removed from their location). Note the inter-tendinous connections (arrow-heads). 1 = extensor digitorum tendon for the index finger, 2 = extensor digitorum tendon for the middle finger, 3 = extensor digitorum tendon for the ring finger, 4 = extensor digiti minimi tendon. Fig.9b of [52] .

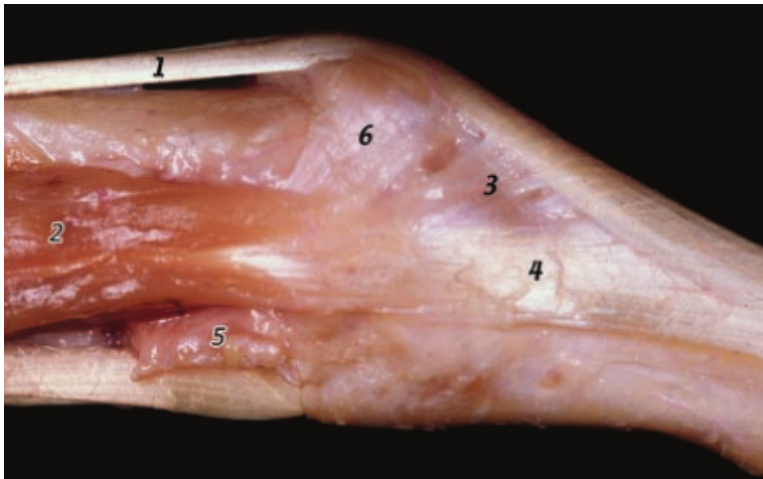


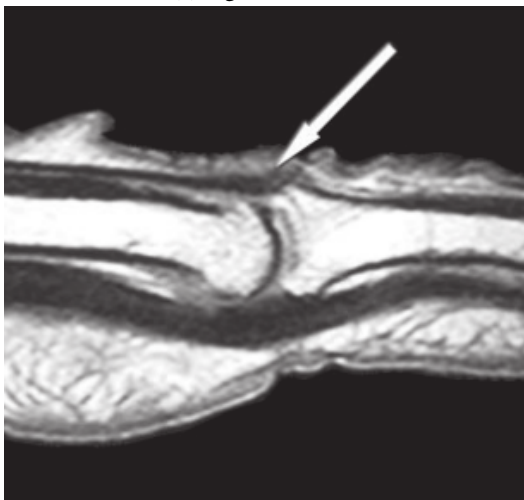
Figure 3-47: Anatomic photograph (medial view) shows the MCP joint level of the third finger. In this area, the extensor digitorum tendon (1) receives the intrinsic contribution of the interosseous muscle (2). This contribution consists of the transverse fibres (3) and oblique fibres (4). 5 = deep transverse metacarpal ligament, 6 = sagittal band. Fig.14 of [52] .



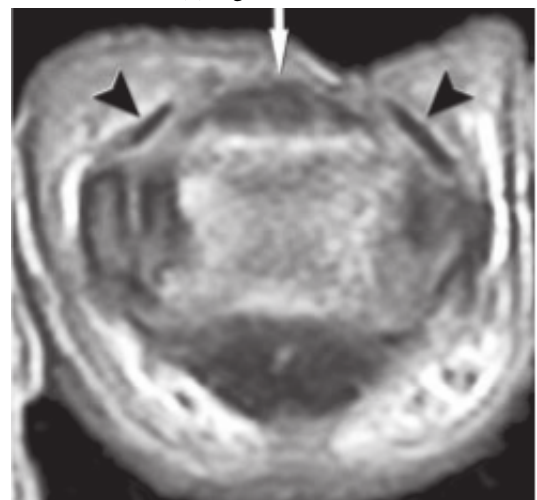
(a) Fig.18b of [52] .



(b) Fig.21a of [52] .



(c) Fig.18a of [52] .



(d) Fig.18c of [52] .

Figure 3-48: a)Sagittal anatomic slice obtained at the PIP joint show the insertion of the central slip (arrow) on the base of the middle phalanx. b) Sagittal anatomic slice obtained at the DIP joint show the insertion of the terminal tendon (arrow) on the base of the distal phalanx. c)T1-weighted MR image corresponding to (a). d)Axial T1-weighted MR image obtained at the head of the proximal phalanx shows the relationship between the central slip (arrow) and the medial and lateral slips (arrowheads).

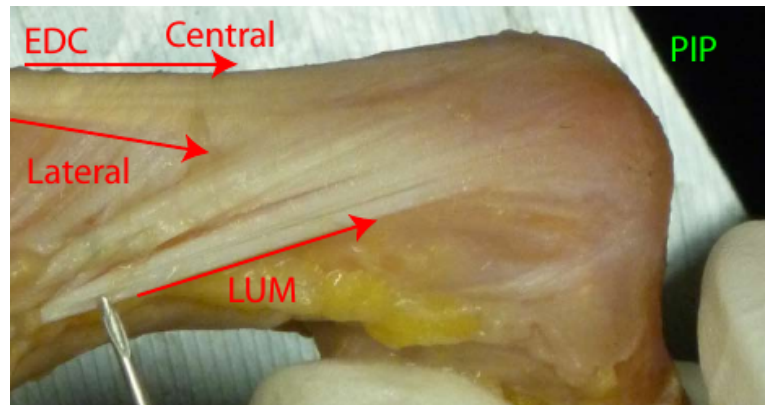


Figure 3-50: Radial view of the extensor hood. The central and extrinsic lateral bands of the EDC can be seen below the semi-transparent extensor hood. The lumbrical inserts into the bottom of the hood, near the needle point. Note that the lateral bands of the distal extensor pass dorsal to the axis of rotation of the PIP joint. The transverse retinacular ligament is visible immediately distal to the PIP. Fig.8.1 of [118].

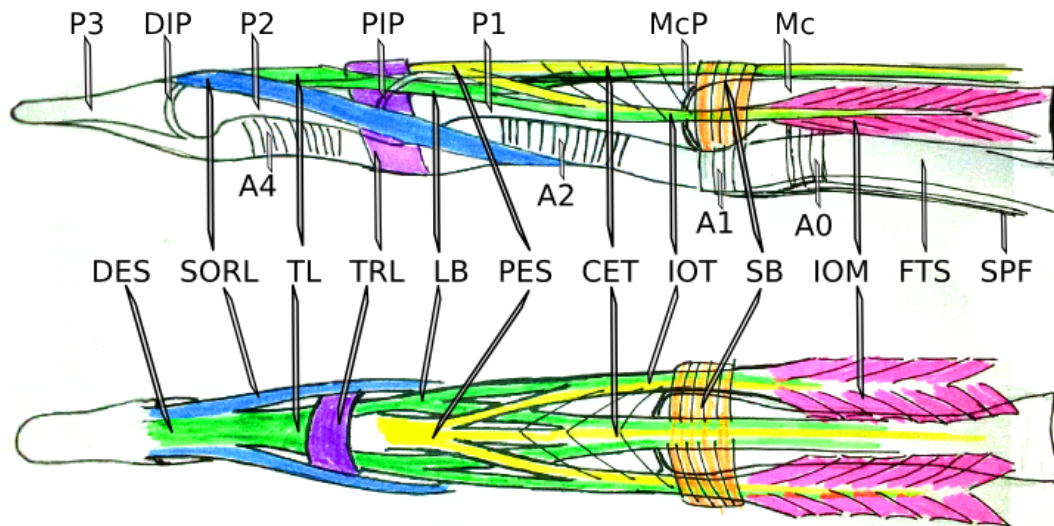


Figure 3-49: Topology of extensor tendon hood of the finger, lateral view palm downwards (top), dorsal view (bottom) : A0-5 Annular retinacular ligaments, P1-3 phalanges, Mc meta-carpal bone, DIP distal inter-phalangeal joint, PIP proximal inter-phalangeal joint, McP metacarpo-phalangeal joint, DES distal extensor slip, SORL spiral retinacular ligament, TL triangular ligament of DES, TRL transverse retinacular ligament, LB lateral band of DES, PES proximal extensor slip, CET common extensor tendon, IOT inter-osseous tendon, SB sagittal band, IOM inter-osseous muscle, FTS flexor tendon sheath, SPF longitudinal fibres of superficial palmar fascia.

Digital extensor hood

The extensor hood of the digit [119], (figures-3-49 , 3-46 , 3-50 and 3-47), is composed of fibres from the extrinsic extensor dorsally and interosseous tendons laterally, inserting onto the proximal and distal extensor slips of the middle and distal phalanges. At the MCP the interosseous tendons pass through short tendon sheaths. The sagittal bands arise from the first annular ligament, pass over the interosseous sheaths and bind to the extrinsic extensor tendon. A layer of hyper-elastic connective tissue beneath the sagittal bands allows the extrinsic extensor tendon to slide over the MCP, while the bands stabilise it laterally.

The extensor hood is stabilised over the dorsal surface of the digit by the triangular ligament of the distal extensor slip, the transverse retinacular ligament [120, 121] and the interosseous hood - composed of fibres connecting the interosseous tendons [119]. Collectively the mechanism has been described to perform 'anatomical computation' [122] "that non-linearly enables different torque production capabilities".

Distal extensor slip and triangular ligament

The DIP is actuated by the distal extensor slip, which is formed by the convergence of the lateral bands of the extensor hood, and the SORL (see next section).

The triangular ligament is a sheet of fibres orientated transversely to the paired SORL and lateral bands, and helps to draw them together on the dorsal aspect of the middle phalanx. Geometrically, its effect is greatest in ensuring that the SORL passes dorsally on the second phalanx to act as an extensor of the DIP even when the DIP is maximally flexed.

Spiral oblique retinacular ligament (SORL)

The SORL originates on the palmar aspect of the A2 flexor pulley, and passes palmar to the centre of rotation of the PIP, and helically around the second phalanx to joint the distal extensor slip. Therefore the SORL is both a flexor of the PIP, and an extensor of the DIP. It can go slack, but having no muscle belly it cannot contract. This arrangement has the important effects of:

- limiting the phase difference between the DIP and PIP
- transferring torque between the PIP and DIP, such that
 - extension of the PIP causes extension of the DIP, so that work done by the proximal extensor slip is transferred to the distal extensor slip
 - flexion of the DIP causes flexion of the PIP, so that buckling of the DIP under compression also causes buckling of the PIP, so protecting these small joints from excess force in impact.

The SORL permits 45 – 60° of motion of the DIP relative to the PIP, as compared to the 100° range of motion of the DIP and 120° range of motion of the PIP. This is important in excluding joint positions that are liable to cause excess stress on the extensor apparatus, which is much weaker than the flexor tendons.

Transverse retinacular ligament (TRL)

The TRL lies immediately distal to the PIP, where it is visible in figure-3-50, and is labelled in figures-3-49 and 3-46 . It wraps around the dorsal aspect of the middle phalanx and inserts symmetrically on either side on the palmar aspect of the proximal margin of the A4 flexor pulley. On the dorsal aspect of the middle phalanx it fuses with the lateral bands of the extensor apparatus.

The TRL functions in a manner similar to the sagittal bands of the extrinsic extensor at the MCP joint, stabilising the lateral bands on the dorsal aspect of the middle phalanx. It also prevents dorsal bowing of the extensor tendons in hyper extension, which causes "swan-neck deformity" when the TRL is ruptured [123].

Proximal extensor slip and PIP 'patella'

The proximal extensor slip is composed of the central branch of the extrinsic extensor tendon, and the medial branches of the interosseous tendons. It inserts on the dorsal proximal margin of the middle phalanx and extends the PIP joint. It is thickened with hyaline cartilage in the area that comes into contact with the articular surface of the first phalanx. This structure is sometimes referred to as the "PIP patella" or the "dorsal plate" and is considered to serve a similar function to a sesamoid bone, but at lower contact pressure.

Lateral bands

The lateral bands are formed from the convergence of the lateral branches of the extrinsic extensor and interosseous tendons and the lumbrical tendon. They pass either side of the proximal extensor slip dorsal to the centre of rotation of the PIP and are stabilized by the transverse retinacular ligament immediately distal to the PIP. The lateral bands continue distally to join the distal extensor slip.

Sagittal bands and extrinsic extensor tendon(s)

The extrinsic extensor tendon(s) are composed of the slips of the common digital extensor and the extensor digiti quinti in the little finger or the extensor indicis proprius in the index finger. The extrinsic extensor runs on the dorsal aspect of the metacarpal head and the first phalanx. The tendon is stabilised across the joint and on the metacarpal head by the sagittal bands. These are a thin lamina of fibres fused orthogonally across the tendon and inserting either side on the volar plate of the MCP, label (6) in figure-3-47 .

Interosseous muscles

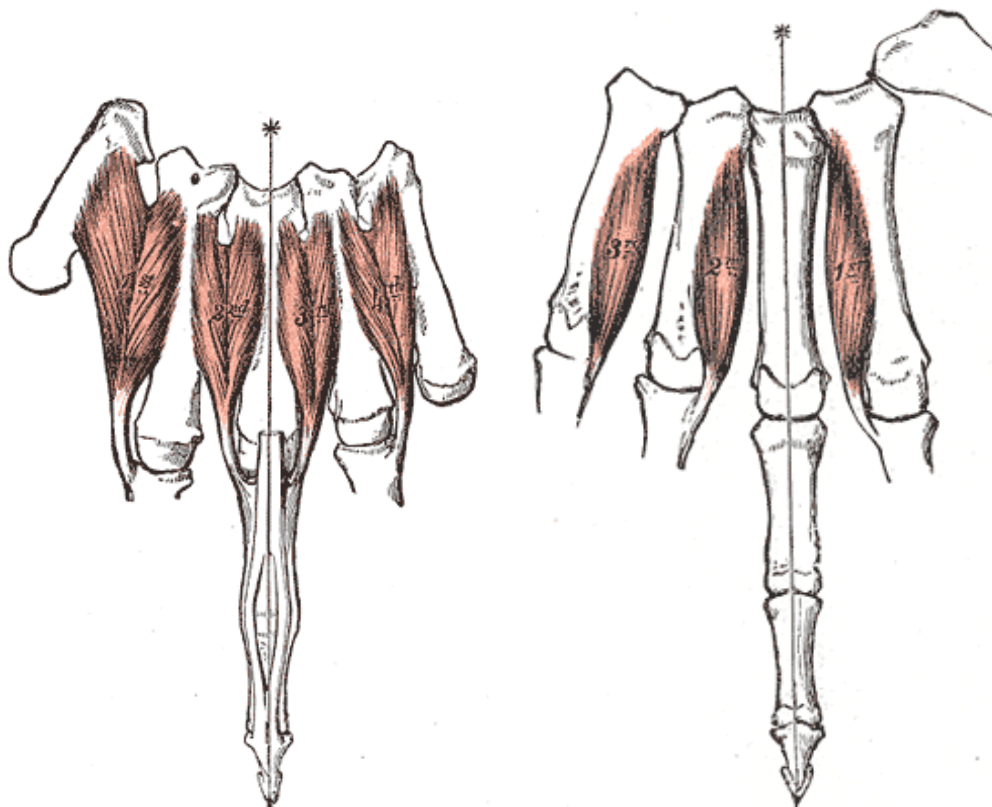
There are two sets of interosseous muscles (label "4") which lie between the metacarpal bones dorsal to the deep transverse metacarpal ligament (label "**"), in figure-3-40, and insert on the extensor hood:

dorsal interosseous muscles figure-3-51a , abduct the fingers at the MCP joints.

palmar interosseous muscles figure-3-51b , adduct the fingers at the MCP joints.

The fibres from the interosseous muscles insert in several places, figures-3-49 , 3-46 , 3-50 , 3-47 :

- directly on the proximal radial and ulnar margins of the first phalanges,
- some fan out dorsally over the first phalanx forming the superficial layer of the extensor hood, stabilising the extrinsic extensor tendon, and continuing symmetrically to the interosseous muscle on the opposite side of the digit,
- some join the central branch of the extrinsic extensor tendon to form the proximal extensor slip, inserting on the second phalanx,
- some join the lateral branches of the extrinsic extensor tendon to form the lateral bands, which continue past the PIP to form the distal extensor slip inserting on the third phalanx.



(a) image428-dorsal interosseous muscles, from [62].

(b) image429 palmar interosseous muscles, from [62].

Figure 3-51

Lumbrical muscles

The lumbrical muscles (label "5" in figure-3-40) are slender fusiform (i.e. non-pennate, with maximum contractile strain and minimum physiological cross-section area) that originate from the flexor tendons and insert on the palmar margin of the extensor hood. They run palmar to the deep transverse metacarpal ligament, with their own 'lumbrical canals' between the septae of Legueu and Juvara, figure-3-36 , and

3-39 . As a consequence they have a greater moment arm with respect to flexing the MCP joint than the interosseous muscles.

Contraction of the lumbricals has several effects:

1. if the digital flexors are contracting, lumbrical contraction alters the torque applied by the flexor tendon to the MCP, while decreasing the torque at the PIP and DIP,
2. if the flexors are relaxed, contraction of the lumbrical draws the flexor tendon distally so unloading the resistance to extension at the MCP, PIP and DIP joints,
3. sensation of the length of muscle spindles of the lumbricals provides proprioceptive information about the position of the finger joints.

Due to their very small physiologic cross-section area, the the effect of the lumbricals is minimal when other muscles are contracting at high force. However the lumbricals are important in controlling the movement of fingers before contact occurs i.e. 'preshaping' grasps, and in complex, precise, low force finger movements.

3.4.4 Carpal flexors

The following muscles act to flex the carpus:

Extrinsic digital flexors Under-actuate the carpus as they cross the radio-carpal joint and enter the carpal tunnel.

Palmaris longus Continues as the longitudinal fibres of the superficial palmar fascia.

Flexor carpi radialis Passes through the carpal tunnel and inserts on the palmar aspect of the proximal region of the metacarpal bone of the index finger.

Flexor carpi ulnaris Crosses the palmaro-lateral margin of the triangular fibrocartilaginous complex of the ulnar-carpal joint, and inserts on the pisiform carpal bone.

Flexor carpi ulnaris Crosses the palmaro-lateral margin of the triangular fibrocartilaginous complex of the ulnar-carpal joint, and inserts on the pisiform carpal bone.

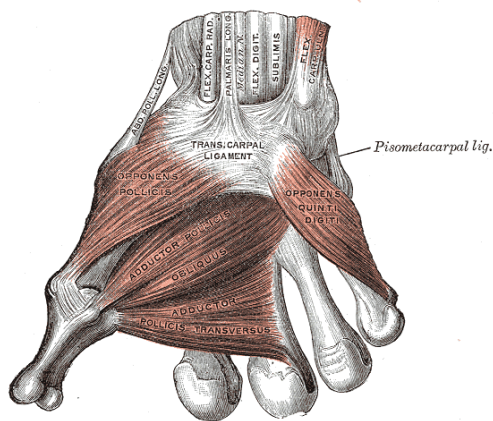
3.4.5 Carpal extensors

The following muscles act to extend the carpus:

Extrinsic digital extensors Including the extensor pollicis longus, under-actuate the carpus on the dorsal side of the radio-carpal joint.

Extensor carpi radialis Has brevis and longus bellies which give rise to parallel tendons that insert on the dorsal aspect of the metacarpal bones of the middle and index fingers respectively.

Extensor carpi ulnaris Inserts on the base of the metacarpal of the little finger.



(a) image426 deep intrinsic muscles of the thumb and little-finger, from [62].

Figure 3-52

3.4.6 Muscles and tendons of the thumb

Extrinsic muscles of the thumb

Extensor pollicis longus Crosses the radio-carpal joint on the dorsoradial aspect, then joins branches of the abductor pollicis brevis and the adductor pollicis at the level of the first phalanx, and inserts on the dorsal aspect of the base of the distal phalanx.

Extensor pollicis brevis Crosses the radio-carpal joint on the radial aspect, alongside the abductor pollicis longus, and inserts on the base of the first phalanx of the thumb.

Flexor pollicis longus Passes through the carpal tunnel and runs in the flexor sheath on the palmar aspect of the thumb, to insert on the base of the distal phalanx of the thumb.

Abductor pollicis longus crosses the radial aspect of the radio-carpal joint and inserts at two sites on the thumb. proximally on the trapezium and distally on the radial side of the base of the thumb metacarpal bone.

Sheaths and retinacular ligaments of the thumb

The flexor pollicis longus sheath is histologically and functionally similar to the flexor tendon sheaths of the other digits. It has two highly consistent annular retinacular ligaments, the A1 and A2 pulleys at the MCP and interphalangeal joints. It also has an oblique and associated variable annular retinacular ligament, the Av pulley. The oblique and Av pulleys occur on the proximal phalanx and are associated with the insertion of the adductor pollicis muscle.

Intrinsic muscles of the thumb

Adductor pollicis has bellies originating from the diaphysis of the middle finger metacarpal bone and from the trans-carpal ligament converging to insert on the ulnar aspect of

the proximal margin of the proximal phalangeal bone of the thumb.

First dorsal interosseous Originates in part from the ulnar side of the proximal region of the thumb metacarpal, and inserts on the extensor hood of the index finger. Consequently it acts as in part as an adductor of the thumb metacarpal.

Abductor pollicis brevis Originates from the transverse carpal ligament, the tubercle of the scaphoid carpal bone and variably the tubercle of the trapezium. It forms part of the thenar eminence, and inserts on the lateral aspect of the base of the proximal phalanx.

Flexor pollicis brevis Originates from the distal margin of the transverse carpal ligament and from the tubercle of the trapezium. It inserts on the radial side of the base of the proximal phalanx.

Opponens pollicis Originates from the transverse carpal ligament and the tubercle of the trapezium, and inserts on the radial side of the metacarpal bone of the thumb.

Thumb web

The thumb web is formed by the transverse head of the adductor pollicis, the first dorsal interosseous, the first lumbrical muscles, the proximal and distal commissural ligaments and the dermis overlying them.

These superficial ligaments provide passive elastic constraint to the motion of the thumb.

The distal commissural ligament of the distal margin of the thumbweb is the continuation of the natatory ligament connecting the A2 pulleys of adjacent digits, label (2) in figure-3-60 .

The proximal commissural ligament of the thumbweb is the continuation of the transverse fibres of the superficial palmar fascia, label (3).

The "fascial expansion" to the abductor pollicis brevis of the palmaris longus/longitudinal fibres of the superficial palmar fascia, label (7).

3.4.7 Little finger

The muscles of the little finger are similar in topology and function to those of the thumb.

Extrinsic muscles of the little finger

- flexor digitorum superficialis
- flexor digitorum profundus
- extensor digitorum communis
- extensor digitorum digiti quinti/minimi

Intrinsic muscles of the little finger

- Opponens digiti minimi
- Abductor minimi - 3rd palmar interosseous
- Flexor digiti minimi brevis
- 4th lumbrical

3.4.8 Rotators of the forearm

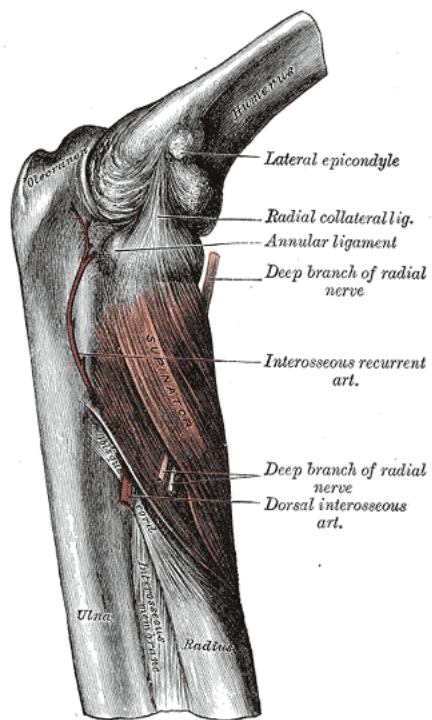


Figure 3-53: image420 elbow joint deep muscles and vessels, from [62].

3.5 Human hands: dermal structures

The general structure of skin and the two basic types of mammalian skin are introduced in section-3.1.9, and figure-3-10. The back of the hand and digits are covered by hairy skin, while the palmar surface of the digits and hand are covered by glabrous skin.

The fine detail of the ligaments of the skin is still an area of debate in the anatomical literature. Figures-3-54 (a,b), provide photographs of a sagittal section of a finger. Figures-3-54 (c-f), provide interpretations of the anatomical structure of the finger tip. Figure-3-55 shows an axial histological cross-section of the finger pad and fingernail of a macaque monkey, showing the fibrous septae within the digital fat pad. Figures 3-56 and 3-57 provide two dissections of the Grayson's and Cleland's ligaments, while figure 3-59 shows five different reported arrangements of these ligaments. Figure-3-58 provides a representation of the dermal ligaments of the finger in three dimensions. Figure-3-60 shows the ligaments of the superficial fascia and their relation to the thumb web and the skin creases of the palm.

3.5.1 Digital pads

Each of the phalanges of the human hand has a fatty pad on its palmar aspect. These are most developed on the distal phalanx where the deep flexor tendon and flexor sheath end. The finger tip pad makes up half the volume of the finger tip, figure-3-54b, and the distal phalanx is spatulated to support the pad. The fat (colourless) within the pads is divided into lobules by fine fibrous septae (stained blue) in figure-3-55. Pacinian corpuscles (fast adapting mechanoreceptors) are arranged between these septae producing a hierarchy of overlapping receptive fields [126].

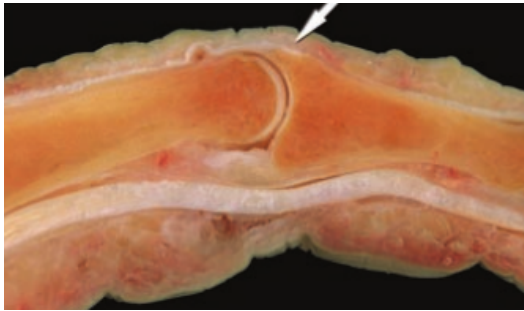
Cleland and Grayson's ligaments

Cleland's ligaments originate from the lateral midline of the phalangeal bones and form sheet septae that pass dorsal to the neurovascular bundle and insert in the dermis near margin between glabrous and hairy skin. Label "CL" in figure-3-58, and label "Cleland's ligaments" in figure3-57 .

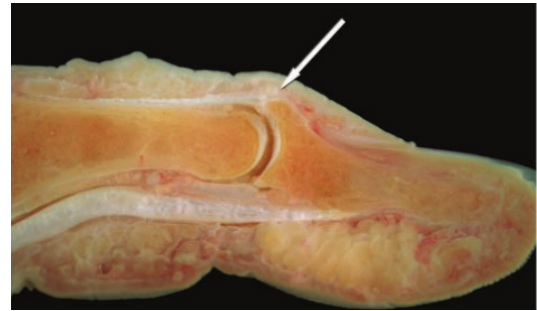
Grayson's ligaments Grayson's ligaments originate from the palmaro-lateral margins of the flexor tendon sheath and form sheet septae that pass palmar to the neurovascular bundle and insert in the dermis near to the insertions of Cleland's ligaments. Label "GL" in figure-3-58 , and label "Grayson's ligaments" in figure3-57 .

Together Cleland and Grayson's ligaments:

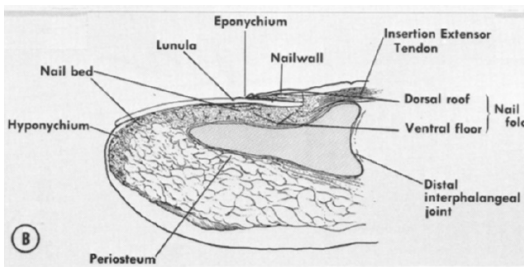
1. Stabilise the neurovascular bundle (containing the main nerves and blood vessels supplying the digit) in the protected routes bilaterally on the ventro-lateral margins of the fingers.
2. Retain the digital pads on the palmar aspect of the phalanges.
3. Provide one of the stronger ligamentous connections transferring shear forces between the dermis and musculoskeletal structures of the fingers, figure-3-58.



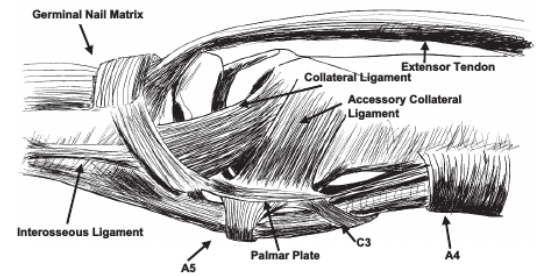
(a) Fig.18b of [52] .



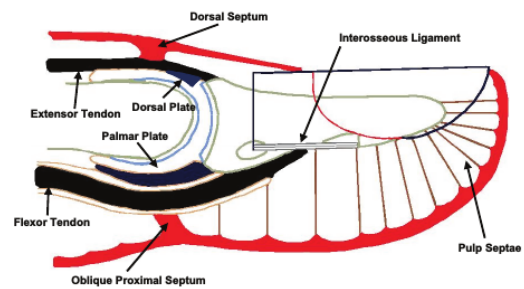
(b) Fig.21a of [52] .



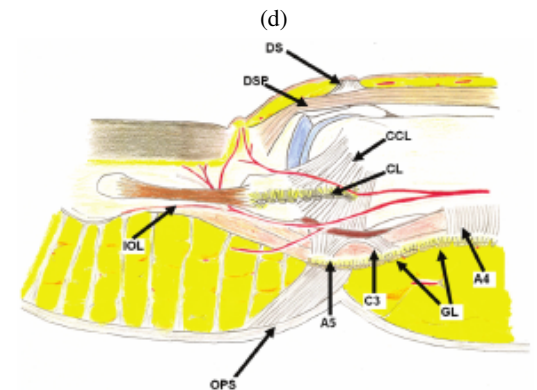
(c)



(d)



(e)



(f)

Figure 3-54: (a)&(b)Dermal anatomy of the distal finger. (a)&(b) Sagittal section of PIP and DIP repeated from fig-3-48a&3-48b , showing the dermal and skeletal structures. Note (i)the adhesion of the palmar creases to the A3 and A5 pulleys palmar to the volar plates, (ii)the relation of the fingernail to the distal phalanx, and distal finger pad. (c)Sagittal view of the perionychium and distal phalanx. Terminology for the anatomy Fig-1A from [124] . (d)Lateral ligaments of the DIPJ. Deep connective tissue structures of the DIPJ. A4, A5, and C3 represent pulleys of the flexor mechanism. Fig-1 from [125] . (e)Schematic sagittal section through the distal phalanx showing connective tissue structures in relation to the joint. Fig-2 from [125] . (f)DIP joint schematic representation. DS, dorsal septum; DSP, dorsal plate; CL, Clelands ligaments; GL, Graysons ligaments; OPS, oblique proximal septum; IOL, interosseous ligament; CCL, collateral ligament; VP, volar plate; PS, pulp septae; C3, A4, A5, flexor pulleys. Fig-8 from [125] .

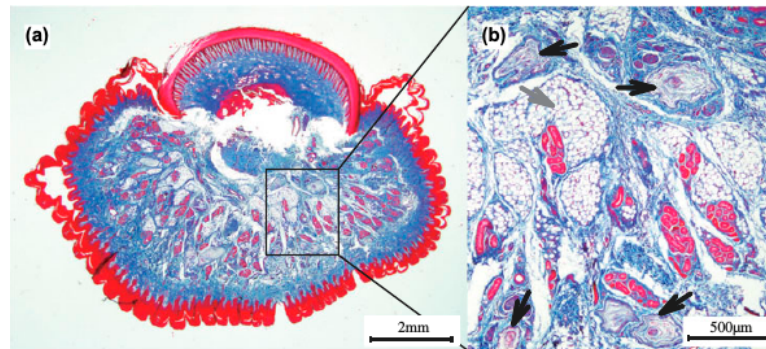


Figure 3-55: Transverse cross-sectional sample of the distal phalanx created from the thumb of a *Macaca fuscata*, with collagen fibres stained with Azan staining. The blue colour in the image indicates collagen fibres (a) Overall view. (b) Magnified view of a selected portion. Black arrows indicate Pacinian corpuscles and gray arrow indicates adipose tissue. Fig.1 from [126].

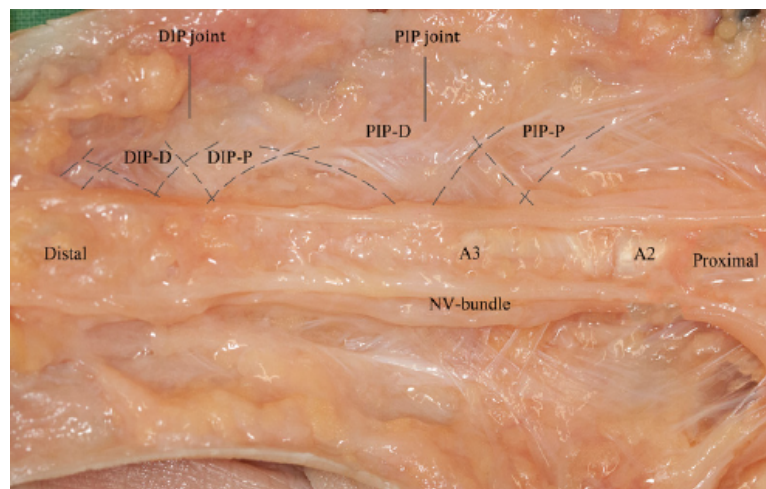


Figure 3-56: This picture shows the orientation of Cleland's ligaments; PIP-D and PIP-P originating mainly from the proximal phalanx and the DIP-D and DIP-P ligament arising from the distal part of the middle phalanx. The possible fifth ligament of Cleland is shown just distal to the DIP-D in a proximal direction. Fig-3 from [127].

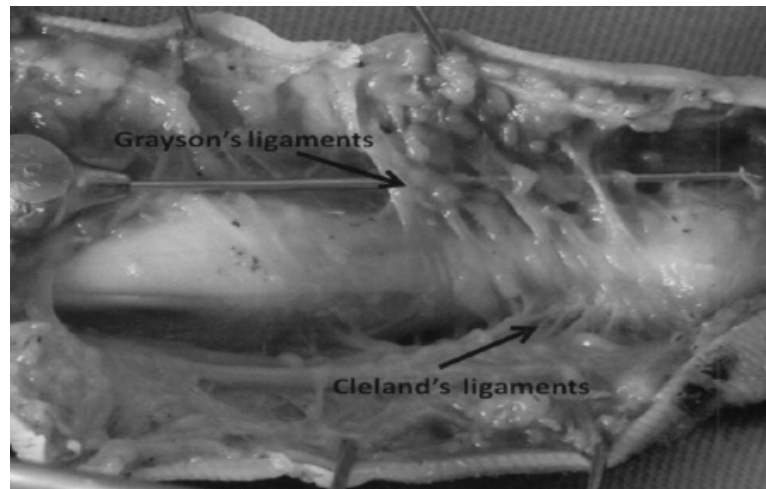


Figure 3-57: Dissection from the mid-ventral aspect via a palmar midline incision. The whole adipose tissue has been removed exposing the fibres. From the ventral aspect we first identified the Grayson ligaments overlying the neurovascular bundle. They were in the same level as the natatory ligaments. In the other side of the finger we observed the Clelands ligaments under the neurovascular bundle lying laterally to the skin in the dorsal part of the finger. Fig-3 from [128] .

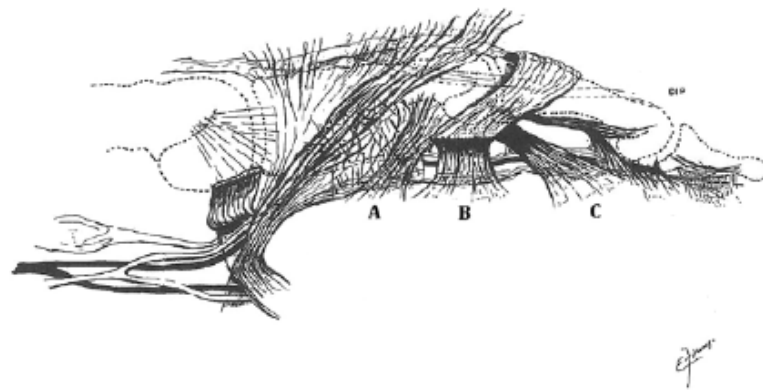


Figure 3-58: A detailed figure from Zancolli and Cozzis Atlas of Surgical Anatomy of the Hand [129]. (AC) show respectively the proximal fibres (A), middle fibres (B), and distal fibres (C) of Clelands ligaments. The middle fibres (B) are shown attached to Landsmeers transverse band. The distal ligaments of Cleland are not shown. Fig-6 from [127] .

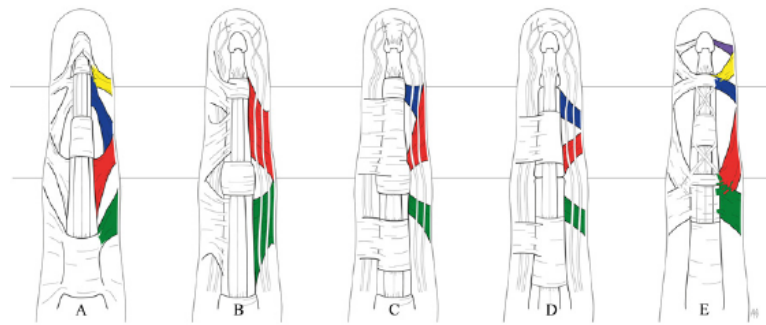


Figure 3-59: This illustration consists of redrawn copies of the most important historical drawings of Clelands ligaments. The differences between the authors are more visible in accordance with our findings (E). From left to right: Cleland (A), Grayson (B), Milford (C), McFarlane (D), and Zwanenburg (E). Each ligament is given a different colour; the same colour refers to the same ligament, in the authors opinion. Red: PIP-D; green: PIP-P; yellow: DIP-D; blue DIP-P; purple: a possible fifth ligament of Cleland (Cleland, 1878; Grayson, 1941; McFarlane, 1990; Milford, 1968). Fig-5 from [127] .

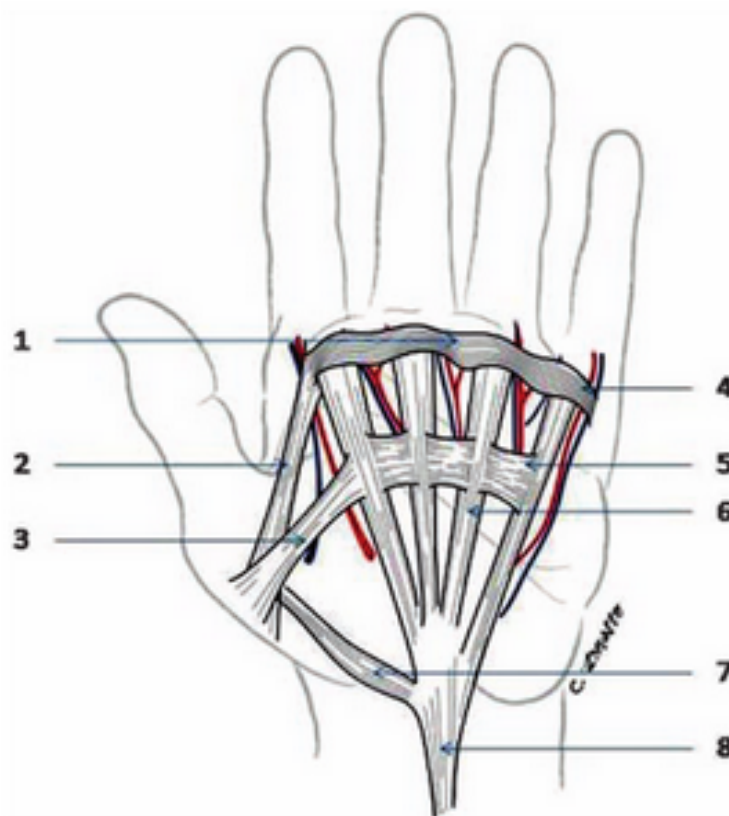


Figure 3-60: The main elements of the palmar facsia. (1)Natatory ligament. (2) Distal commissural ligament of the first web space. (4) Distal transverse palmar ligament. (5) Proximal transverse palmar ligament. (6) Pretendinous bands. (7) Palmar facial extension to abductor pollicis brevis. (8) Palmaris longus tendon. Fig.41.10 from [130] .

Interosseous ligament of the distal phalanx

The distal phalanx has a much narrower diaphysis than the other phalanges, set between a broad base at the DIP joint and spatulated tip. The paired interosseous ligaments of the distal phalanx run parallel to the diaphyseal shaft on either side, between the lateral margins of the base and tip of the bone, figure-3-54 (d,e,f). The interosseous ligament supports the proximal root of the nail bed, and the soft tissues of the lateral margins of the finger tip. Forces orthogonal to the fibres of the ligament cause bow-string stretching of the ligament and surrounding soft tissue, both of which contain stretch receptors.

3.5.2 Finger nail

Fingernails like hooves are modified claws that retain the same basic structure with different geometric proportions. The nail is an epidermal structure composed of the same keratin as the stratum corneum of the epidermis. The nailbed is a dermal structure tightly adhered to the underlying bone and interosseous ligaments of the distal phalanx. The interlocking dermal and epidermal papillae are replaced by longitudinal grooves that allow the nail to advance distally as it grows.

The mechanical effect of the fingernail is to provide rigid continuation of the bone outside the dermis. Forces are transmitted to nail through the finger tip pad causing strains in the and nailbed that are visible as colour changes due to the movement of blood into or out of their capillary beds. The nailbed, interosseous ligaments and marginal skin surrounding the nail are highly innervated with stretch, vibration, temperature and pain receptors.

3.5.3 Crease ligaments

The skin is creased on both dorsal and palmar sides of the joints of the digits, while the palm has characteristic transverse and oblique creases, and there creases on the wrist at the proximal margin of the palm. These creases depend on motion for their formation, but are also accompanied by thinning of the subcutaneous fat and ligamentous connections to the underlying musculoskeletal structures.

Palm creases

The transverse crease of the palm lies over the transverse fibres of the superficial palmar fascia, and marks the proximal limit of the metacarpal fat pad. The oblique palm crease running from the radial end of the transverse crease to to the base of the thumb lies over the radial margin on the longitudinal fibres of the superficial palmar fascia, and is the boundary of the fat pad covering the intrinsic muscles of the thumb (thenar eminence), figure-3-60 .

Palmar digital creases

The palmar creases of the fingers lie over the proximal margin of the A2 pulley, the A3 and A5 pulleys respectively. They are associated with ligamentous septae that connect the dermis to the fascia of the pulleys, label "Oblique Proximal Septum" in figure-3-54e and label "OPS" in figure-3-54f .

Dorsal digital creases

The dorsal creases of the digits are associated with fibrous septae connecting to the proximal and distal extensor slips, label "Dorsal Septum" in figure-3-54e and label "DS" in figure-3-54f .

3.5.4 Palmar pads

The pads of the palm are a combination of subcutaneous fat pads and the intrinsic muscles of the thumb and little finger. Note the minimal fat in the central palm region, compared to that covering the intrinsic muscles of the thumb and little finger at the sides of the palm in figure-3-36 .

The "thenar eminence" forms the radial side of the palm. It is composed of the abductor pollicis brevis, opponens pollicis and the proximal heads of the adductor pollicis muscles (section-3.4.6), covered by a subcutaneous fat pad.

The "hypothenar eminence" forms the ulnar side of the palm. It is composed of the opponens digiti minimi and flexor digiti minimi brevis muscles (section-3.4.7), covered by a subcutaneous fat pad.

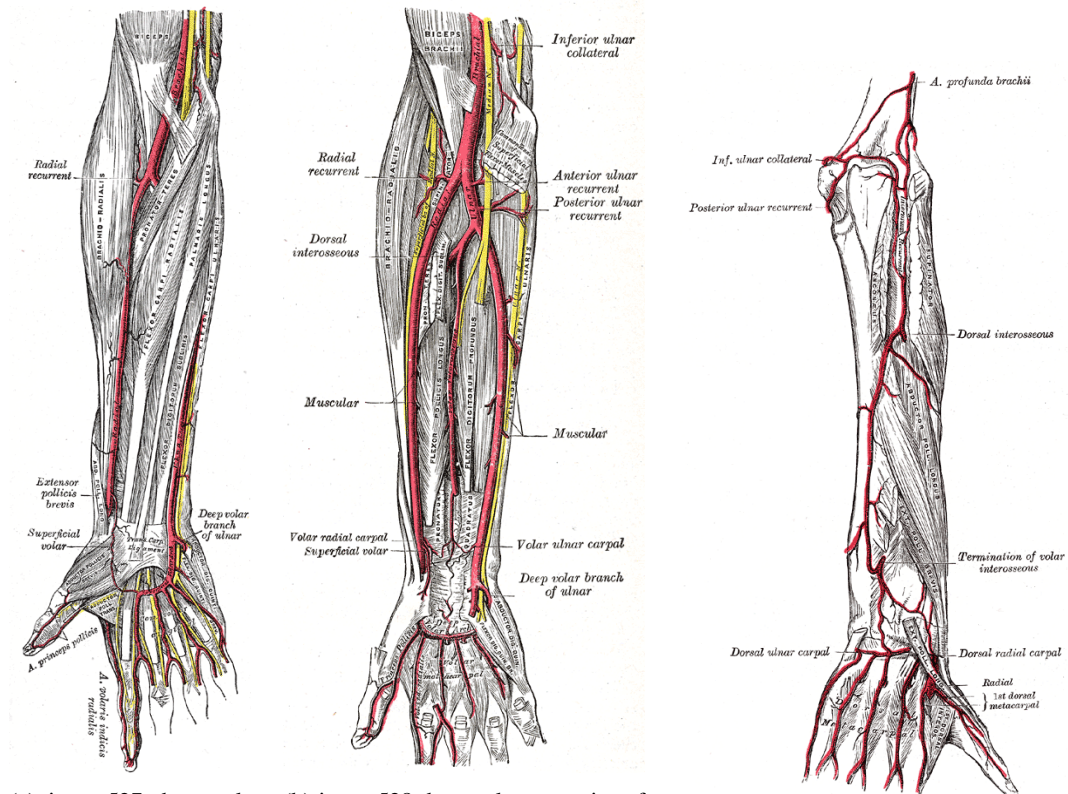
The heel of the palm forms the proximal margin of the palm. It is composed of the transcarpal ligament and overlying fat pad. Figures-3-34 and 3-35 show the fat pad in the 'heel' of the proximal palm.

The metacarpal pad forms the distal margin of the palm. It is composed of a subcutaneous fat pad lying over the MCP joints between the transverse palmar crease and the finger webs. Figures-3-37 and 3-38 show the thickness of the metacarpal pad distal to the transverse palmar crease.

3.6 Human hands: nerves and vessels

The nerves and blood vessels run in paths through the anatomy that protect them from risk of damage due to excess stretching or from impacts of the body with the external environment. They are therefore the obvious paths to lay both sensor signal fibres and electrical power cables.

Nerves and blood vessels are also elastic. The radial nerve requires 9.4 mm of excursion at the wrist to accommodate strain due to movements at the wrist, elbow and shoulder [131, 26] . The ulnar nerve requires 23.2 mm at the wrist and experiences nerve strain of 15% or greater at the elbow [132] .

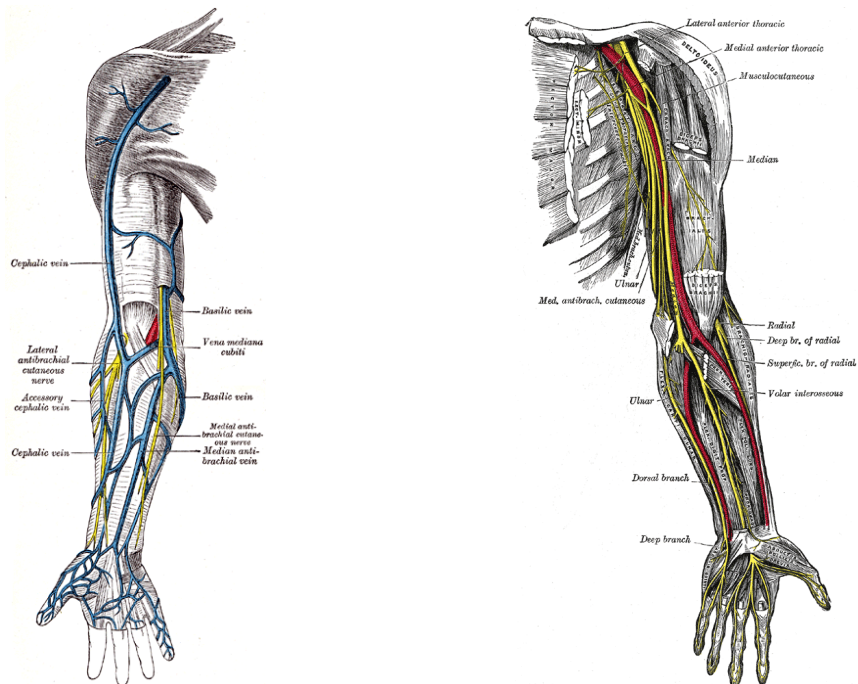


(a) image527 deep palmar arteries of the hand and forearm, from [62].

(b) image528 deep palmar arteries of hand and forearm uncovered, from [62].

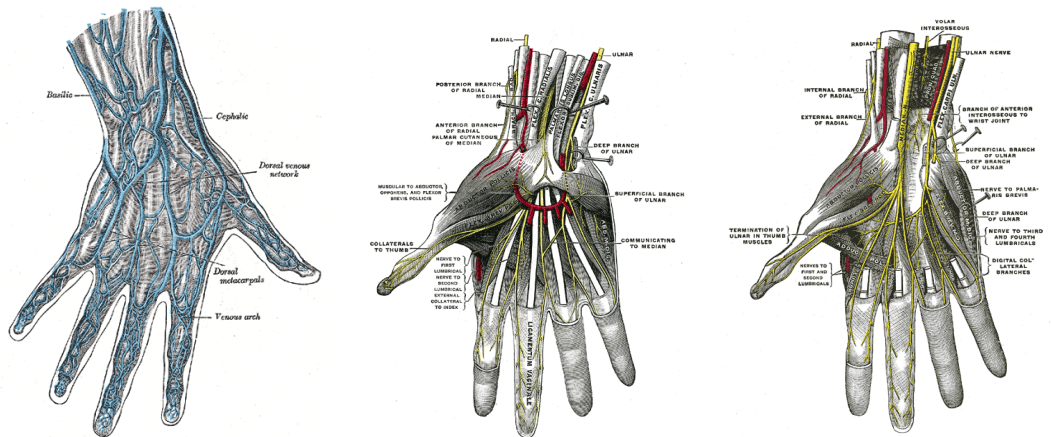
(c) image529 dorsal arteries of the hand and forearm, from [62].

Figure 3-61



(a) image574 palmar veins of hand and arm, from [62]. (b) image816 nerves of the palm and arm, from [62].

Figure 3-62

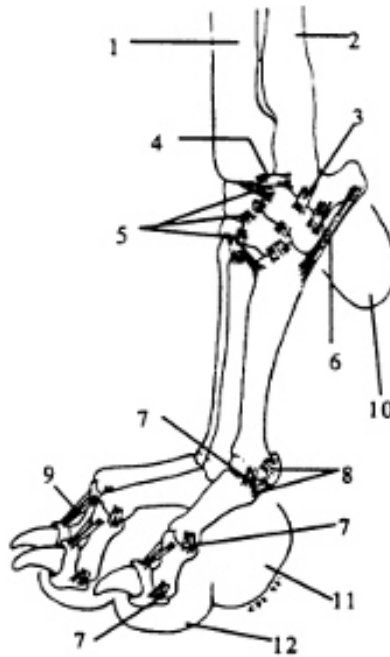


(a) image573 superficial veins of hand, from [62]. (b) image815-nn-of-palm, from [62]. (c) image817 nerves of the palm uncovered, from [62].

Figure 3-63

3.7 Comparative anatomy: canine lower forelimb

The hooves and paws of all mammals are derived from the same basic body plan, and retain the same topology with variation of geometric proportion and compositional proportion of the tissues. The canine paw was used for one prototype of ligament and tendon structures. The figures below present the bones and ligaments of the paw.



- | | |
|---|---|
| 1. <i>Radius</i> | 7. <i>Lig. collaterale laterale</i> |
| 2. <i>Ulna</i> | 8. <i>Lig. sesamoideum collaterale laterale</i> |
| 3. <i>Lig. collaterale carpi laterale</i> | 9. <i>Ligg. dorsalia</i> |
| 4. <i>Lig. radioulnare</i> | 10. <i>Torus carpeus</i> |
| 5. <i>Ligg. intercarpea dorsalia</i> | 11. <i>Torus metacarpeus</i> |
| 6. <i>Ligg. accessoriometacarpea</i> | 12. <i>Torus digitalis</i> |

Fig. 6.17 Ligaments of the *Manus* (lateral aspect)

Figure 3-64: From [133] .



1. *Radius*
2. *Ulna*
3. *Lig. collaterale carpi mediale*
4. *Lig. collaterale carpi laterale*
5. *Lig. radioulnare*
6. *Ligg. intercarpea dorsalia*
7. *Lig. collaterale mediale*
8. *Lig. collaterale laterale*
9. *Ligg. dorsalia*

**Fig. 6.15 Ligaments of the *Manus*
(dorsal aspect)**



1. *Radius*
2. *Ulna*
3. *Ligg. intercarpea palmaria*
4. *Ligg. accessoriometacarpea*
5. *Lig. collaterale lat. / med.*
6. *Lig. palmare*
7. *Lig. sesamoideum collaterale lat. / med.*
8. *Ligg. sesamoidea cruciata*

**Fig. 6.16 Ligaments of the *Manus*
(palmar aspect)**

Figure 3-65: From [133].

Chapter 4

Biomechanics

4.1 Biomechanics as the basis of sensorimotor ability

Tissue structure as sensor

For any sensor its location and physical connection to its surroundings are critical to the signal that it produces. The material properties of tissues and anatomical structure of the body determine what changes of mechanical strain occur at which locations and over what time scale.

Passive dynamics determine controllability

Active control of motion is limited by the latency inherent in the sense-compute-actuate of any control system. Passive dynamics determine both what happens during this delay and what energy is dissipated. Human nerve fibres take a significant amount of time to transmit information and nerve synapses also have significant processing delays. Together these result in a substantial minimal delay in active control, yet humans succeed in interacting with the uncontrolled external environment whose behaviour they can estimate with imperfect precision. Forward prediction and pre-emptive correction by the cerebellum helps to mitigate these delays, while the hierarchy of spinal reflexes helps to minimise the computational delays. However,

- **the key advantage of hand anatomy over existing robot designs is the many favourable kinematic and passive dynamic features that enable the hand to 'do the right thing' in response to disturbance within the timespan of the minimum reflex delay.**

The term 'preflex' was coined by [134] to denote *mechanical responses, which have zero delay and may be programmed by the nervous system over a wide range of magnitudes*. The 'program' may be set by the nervous system altering the activation states of the muscles, but it operates within the period of the sensori-motor delay. Preflexes are the product of the stiffness of the muscles, and the kinematics of the musculoskeletal system.

4.2 The role of dermal structures

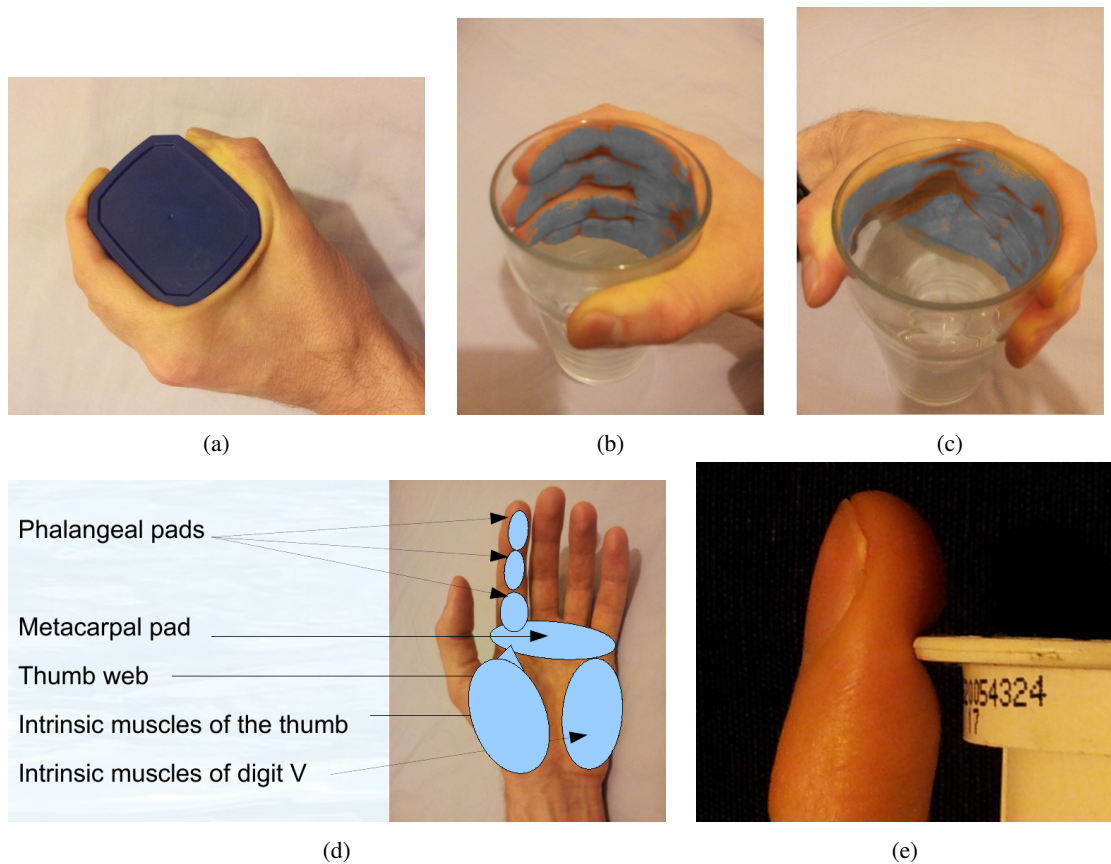


Figure 4-1: Soft contact surfaces: pads and thumb web

The dermal structures of the hand are described in section-3.5 , here their mechanical effects are discussed.

4.2.1 Soft pads

The first layers of compliance are the structures of the epidermis and dermis. The epidermis is keratinised, and far harder and stiffer than the underlying dermis, but except at the fingernails and calluses, it is thin enough to flex easily. On the palmar aspect of the hand the epidermis is thickened, formed into ridges, and secretes a mixture of oils, water and salts. The combined effect of texture and secretions create high friction with contact surfaces.

The pads allow compliance to arbitrary shapes, and provide large areas of contact with minimal pressure. Figure-4-1 shows the effects of the pads of the digits and palm. (a) Shows the compliance of the pads and the thumb web to the octagonal shape of a coffee jar lid. In (b)&(c) the area of the skin in contact with the glass has been coloured to make it more visible. The depth and compliance of the finger tip pad are demonstrated in (e).

Taken together the epidermal and dermal structures allow high friction with minimal compressive force, allowing both very smooth (e.g. glass) and highly irregular, even spiked objects (e.g. horse chestnuts) to be securely grasped.

4.2.2 Grip/slip

When the skin is under tangential load in contact with an object being grasped, a characteristic strain field is created in the dermis, dermal ligaments and subcutis. When stiction begins to fail, it does so progressively across the contact area creating a distinct region within the strain field. These strain fields and the changes in them are sensible by the slow (stretch) and fast (vibration) adapting mechanoreceptors in these tissues.

4.2.3 Vibration finger ridges

The ridges of the finger prints are particularly important for fine palpation and texture perception. They generate vibration when they are dragged over obstacles. This vibration enables spatial perception to a resolution significantly finer than the spatial distribution of tactile receptors. This enhanced acuity is why people stroke a surface to perceive its texture, rather than statically press the surface. It is also essential to reading Braille.

4.2.4 Structure of finger tip - spectrum of compliance

The finger tips are crucial to dexterity and tactile sensitivity. They have a highly specific structure described in more detail in section-3.5 and 3.3.1 . The distal part of the third phalanx is flattened providing attachment of the fingernail dorsally and support for the digital pad palmarly. The fingernail is an epidermal structure external to the dermis, so unlike the bone, it can support the dermis and epidermis to their most distal limit.

The nail is several orders of magnitude harder than the pad it supports, and the result is a spectrum of compliance from the palmar to distal aspects of the finger tip. This is used to sense and apply a wide range of forces in precision grips.

4.3 Hand movements

For a general reference on joint function see [135].

4.3.1 Kinematic support of movements

This section describes a number of commonly used hand actions and how their actuation and control are facilitated by the kinematics and passive dynamics of the hand.

Cupping of the palm

The flexible palm is crucial to enabling the hand to conform to the shapes of objects being grasped, and the ability to cup the palm to carry granular or liquid materials, figure-4-2 . The motion of the carpal bones that enables cupping of the palm is described in section-3.3.4. The muscles and tendons that actuate this motion are the opponens muscles of the thumb and of the little finger and the extrinsic digital flexors.



Figure 4-2: Flexion of the palm. (Top to bottom) The palm varies in concavity by opposition of the thumb web and of the metacarpals of the little and ring finger. (Left columns) digits flexed. (Right columns) digits extended.

Caging of the fingers

When the MCP joints are abducted and the palm cupped flexion of the digits causes the finger tips to converge towards the thumb tip and the digits form a cage around any object in the palm. This action is actuated simply by the extrinsic digital flexors, due to their convergence on the carpal tunnel they act

obliquely on the MCP joints, while they also under actuate the cupping of the palm at the inter-carpal and carpo-metacarpal joints.

Ball catching

If an object impacts on the palm of the hand it causes hyper-extension of the wrist (radio-carpal and inter-carpal joints). This takes up length and tension in the digital flexor tendons causing the digits to flex - producing the caging action described above. A while later when the spinal reflex arc has had time to act, contraction of the extrinsic digital flexors may tighten the grip and so ensure that the ball is not dropped. The kinematics of the hand and wrist provide the passive dynamics that enables the initial catch to occur without requiring active control in the first instant.

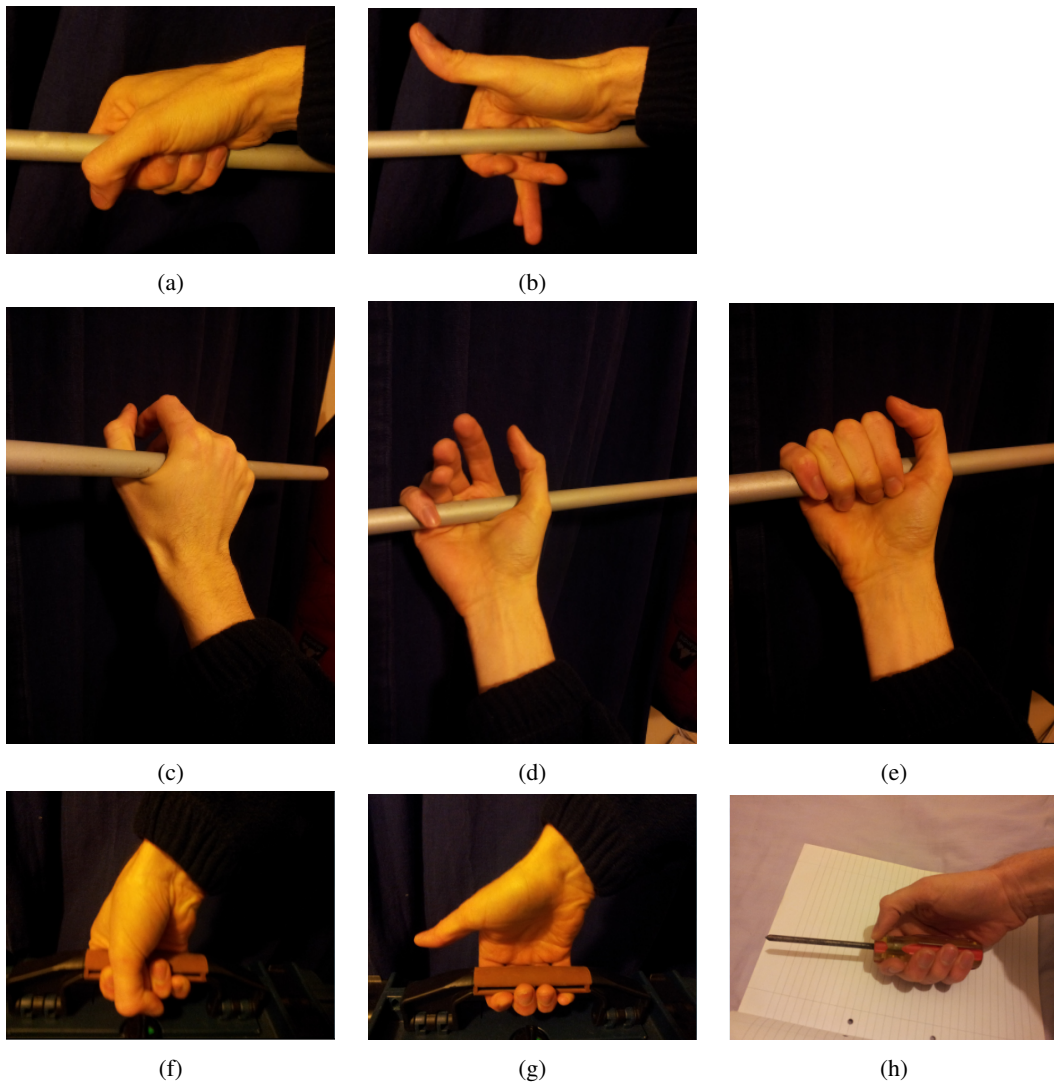


Figure 4-3: Power grips

Ball throwing

The most common grip used in throwing cricket/tennis/baseball sized objects, is a variant of the caged hand with the ring and little fingers fully flexed. This produces a cage with the opposed thumb on the proximo-radial side, the flexed ring finger on the proximo-ulnar side, and the abducted middle and index fingers wrapping distally around the object. The grip is held by contraction of the extrinsic flexor tendons. When the object is thrown, the wrist is initially hyper-extended during the acceleration phase of the arm motion. When the object is released the wrist is flexed, so slackening the extrinsic digital flexors. This releases the pressure between the thumb and ring finger, and allows the index and middle fingers to extend. The ball then rolls distally on the extended fingers. The kinematics of the hand do not require active control of the motions of the digits with respect to each other, only timing of the carpal flexors with respect to the arm motion.

Flexor under-actuation - hooking

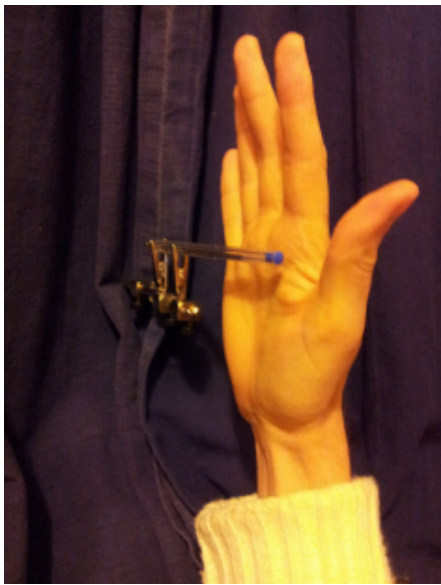
The flexor tendons are the strongest tendons of the hand and bear the principal tension in most high force actions of the fingers. Their under-actuation across all on the joints of the wrist and fingers produces a wrapping hook formation around any object that impacts on the palmar aspect of the hand or digits, figure-4-4 .

The deep and superficial digital flexor tendons run palmar to the axis of rotation of all the joints of the hand - so in fact provide under-actuated flexion of every joint from the inter-phalangeal joints to the radio-carpal joint. This under-actuation has a very useful effect in grip formation, in that force applied at any point on the palm, will cause extension of the joints proximal to it, and flexion of the joints distal to it - thus causing the hand to form a hook around any object that impacts on the palmar surface of the hand, regardless of where on the palm or fingers the object lands.

The digital flexor tendons also include a number of check ligaments or 'vinca' which limit the range of excursion. The check ligament of the distal inter-phalangeal joint is continuous with the main bulk of the superficial flexor tendon, where it is fused to the palmar surface of the middle phalanx. This arrangement is important because it allows high forces to be applied with the distal inter-phalangeal joint hyper-extended, with tension borne on both digital flexors such as in pinch grips and when lifting heavy objects.

All the digital flexor tendons run through the carpal tunnel, causing them to form a diverging fan across the palm. The carpo-metacarpal and distal inter-carpal joints of the 4th and 5th digits allow substantial flexion, increasing the reach of these digits in flexion, and causing the palm to flex laterally. Combined with the constraint of the collateral ligaments of the metacarpo-phalangeal joints, this arrangement causes the finger tips to converge when flexed, to a point near the base of the thumb. The net result is a kinematic mechanism that causes the hand to form cage around objects in the palm. This mechanism is exploited in many power grips.

The dorsal extensor tendon network of the digits has an elaborate mechanism that has been investigated in cadavers by [122], and in robotic models by [45, 43, 48].



(a)



(b)



(c)



(d)

Figure 4-4: Preflexes of the carpal tunnel, a force applied to the palmar surface of the hand causes the carpus to be extended, and flexor tendon length to be taken up at the carpal tunnel. This in turn causes the fingers to flex at the first joint distal to the pressure on the palm.

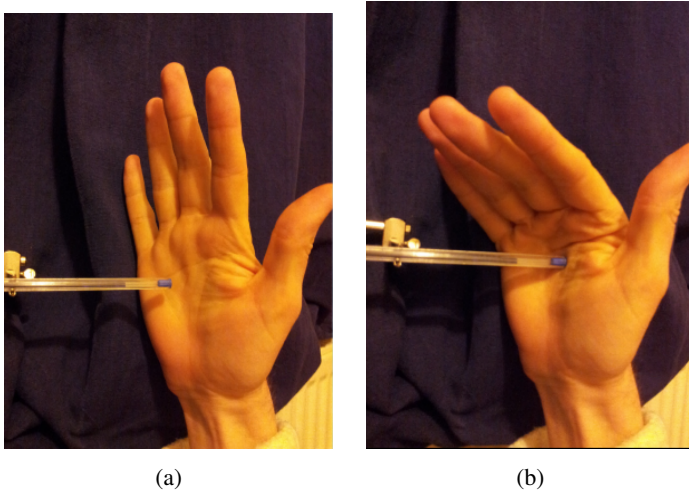


Figure 4-5: Preflexes of the superficial palmar fascia, when an object impacts the palm, the superficial palmar fascia, and the flexor tendons cause the MCP joints to the fingers to flex. This occurs even if tension in the carpal flexors prevents extension of the carpus, and the preflex of the carpal tunnel.

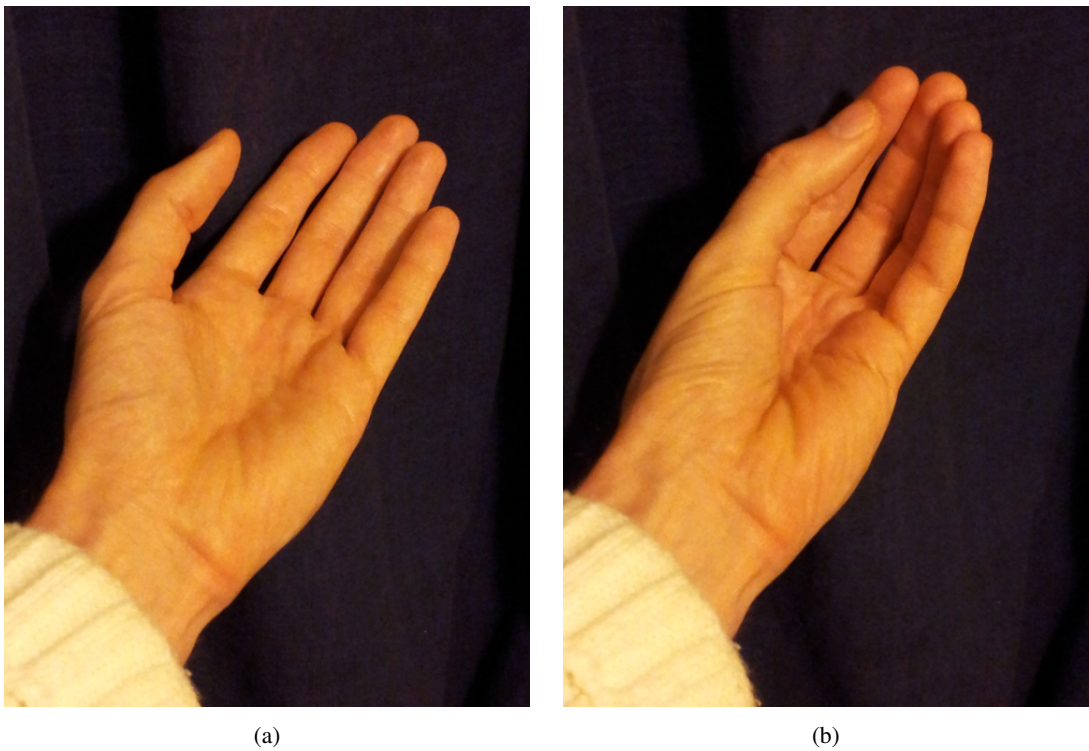


Figure 4-6: Folding motion of the palm: adduction and flexion of the carpo-metacarpal and inter-metacarpal joints of the thumb, ring and little fingers.

4.3.2 Thumb web

The structure of the thumb web is given in section-3.4.6 . Together with the flexor pollicis brevis, and the abductor pollicis brevis, the thumb web creates two useful reflexes.

1. If a large object impacts on the palm, the thumb may also be impacted, in which case the compliance of the flexor pollicis brevis, and the abductor pollicis brevis allow the thumb to be extended dorsally together with the palm of the hand. If however the thumb is not impacted then the elasticity of the adductors and abductors, causes the thumb to be brought to an adducted position behind the object. Together with the hook-forming action of the fingers described above, this action forms a grip around a bar - or a branch - when caught from palmar to the hand.
2. If an object impacts on the distal margin of the thumb web, then tension on the skin and the 1st dorsal interosseous causes the second metacarpo-phalangeal joint to flex. The interconnected joint capsules of the 2nd-5th metacarpo-phalangeal joints then cause the whole row of fingers to flex. The tension on the skin and the adductor pollicis transversus causes the thumb to adduct, rotate palmarly and flex at the metacarpo-phalangeal and inter-phalangeal joints. If the direction of the impact passes dorsal to the carpal joint then, the carpus will extend, so engaging the underactuated mechanism of the digital flexors. The net result is the hand forms a grip around a bar when caught from distal to the hand.

4.3.3 Precision Grips

For precision manipulation an object must be stabilized against unintended movements, and the finest resolution of control of its movement obtained over the required range. The potential resolution of control is determined by the number of independently innervated motor units - groups of muscle fibres supplied by the same alpha motor neuron.

Most precision grips involve bracing the fingers against each other in ways that reduce the kinematic freedom, and allow a smaller group of muscles to be used in opposition to each other. Precision grips generally are not instinctive, but are culturally distinct and have to be learned most often by imitation.

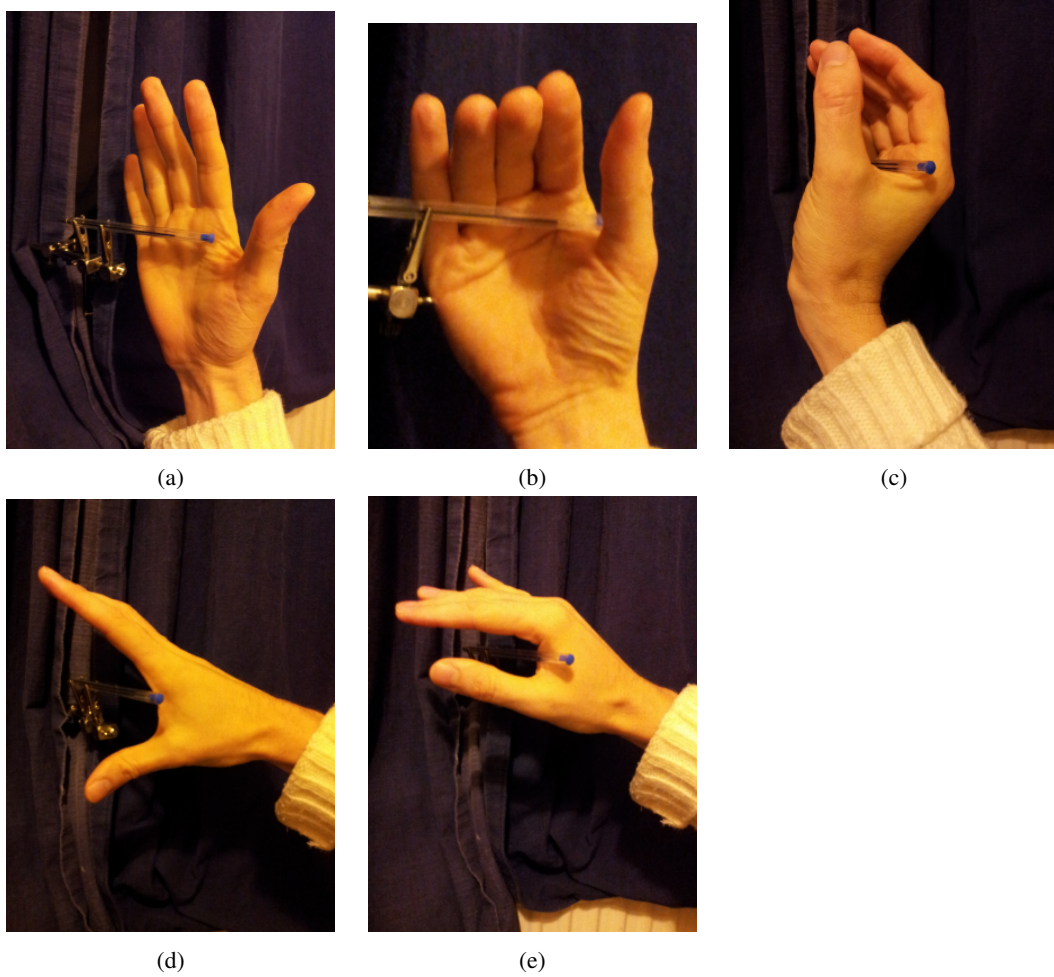


Figure 4-7: Preflexes of the thumb web, (a,b,c) when the carpus is extended by impact on the palmar surface of the fingers or distal palm, the thumb web elastically opposes the thumb behind the object - e.g. catching a branch. (d,e) when the thumb web is impacted distally by an object, the thumb web adducts the thumb and flexes the MCP joints of the fingers.

Chapter 5

Review of Materials

5.1 Flexible Materials

This section addresses the small amount of literature related to the materials which will be used to address some of the challenges of emulating the mechanics and function of histological structures.

5.1.1 Flexible composites

Flexible fibre reinforced composites are widely used for the casings of tyres, for conveyor/drive/timing belts. Structured flexible composites of rubbers and elastomeric foams are used for the soles of shoes. The uppers of training shoes present another type of structured flexible composite designed to transmit forces and to flex with particular kinematic effects. Studies of the computational simulation of such materials can be found in composite materials journals.

Despite their familiarity, the use of soft composite materials remains confined to particular niche applications. Most of the current soft composites are still far less flexible and hyper-elastic than the soft tissues that must be emulated for histomimetic robotics.

Carbon fibre reinforced hyper-elastic silicone composites are used in inflatable booms for satellites [136, 137]. The emulation of synovial joint meniscal tissue with composites made from polyvinyl alcohol reinforced by ultra high molecular weight polyethylene fibres, for orthopaedic implants [138], is directly transferable to histomimetic robotics. Likewise studies of the detailed material and structural properties of anatomical structures is transferable from orthopaedics [139] review of the tissue mechanics of inter-vertebral disks.

5.1.2 Elastic wires

The sensory system proposed in section 4.1 makes use of electrically conductive wires made of a hollow elastomeric polymer filled with a liquid metal amalgam as the conductor. Such wires have been made at a larger scale (1mm diameter) by and different process (gel-spinning) [140].

Part IV

Histomimetic Robot Construction - Experimental Section

Chapter 6

Equipment and Software

In order to provide techniques that may readily be taken up by others, all software used in the project was free and open source, and the hardware used was widely available low cost open design hardware.

6.1 Anatomical Imaging

The work in this thesis depended on being able to accurately reproduce the geometry of the many bones of human hands and wrists, and of dogs paws and carpal joints. This was done principally by segmenting MRI and CT scans to produce surface mesh files, followed by fused deposition 3D printing of models from those files.

The imaging also provided important evidence of the undulating path of the digital flexor tendons, and the geometric relationship of palmar fascia to adjacent structures, complementing the topological descriptions in the anatomical literature.

6.1.1 MRI scan of human hand

A set of scans of the author's right hand and wrist were provided by the University of Sussex Clinical imaging Research Centre. The scans were made using the centre's 1.2 Tesla MRI scanner with a voxel size of 0.8mm. T1 weighted scans, figure6-1b, in both transverse and coronal orientations, and a T2 weighted scan, figure6-1a, in coronal orientation were provided.

University of Sussex Clinical Imaging research centre

<https://www.bsms.ac.uk/research/cisc/index.aspx>

The Clinical Imaging Sciences Centre

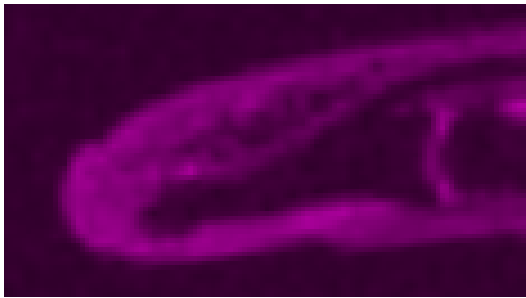
Brighton and Sussex Medical School

University of Sussex

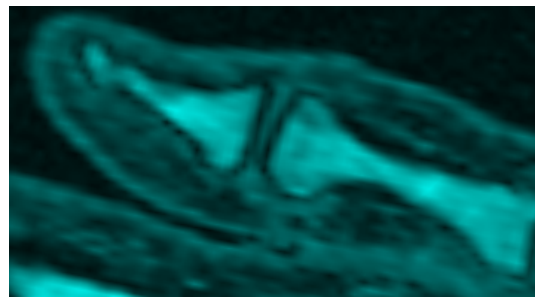
Falmer

BN1 9RR

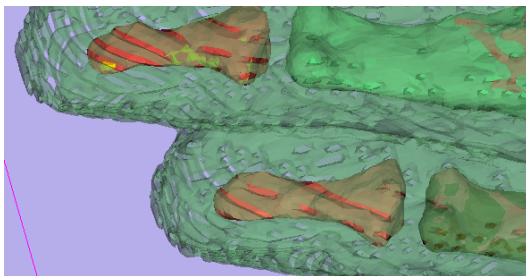
Email: cisc@bsms.ac.uk



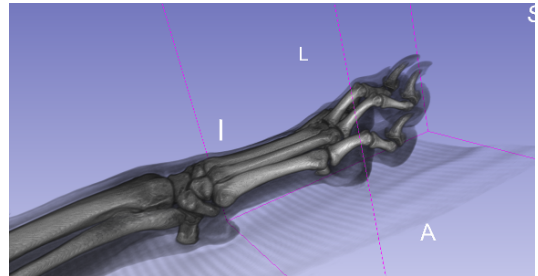
(a) Sagittal section of finger tip from T2 weighted MRI scan. Note that all bone and tendon are dark in this image.



(b) Sagittal section of thumb tip from T1 weighted MRI scan. Note the difference between the dark lamellar and light spongy bone.



(c) 3D models of skin surface and bones, segmented from MRI scan using Slicer3D software.



(d) 3D volume composite rendering of dog paw CT scan.

6.1.2 CT scan of dog's paw

An X-ray computed tomography (CT scan), figure6-1d, of a canine lower forelimb including the paw, carpus and elbow was provided by Fitzpatrick Referrals veterinary specialist neuro-orthopaedic clinic. The scan came from anonymised patient data from a medium sized domestic dog, and had a voxel size of 1mm.

Orthopaedics and Neurology

Fitzpatrick Referrals

<http://www.fitzpatrickreferrals.co.uk/contact-us/>

Halfway Lane

Eashing

Surrey

GU7 2QQ

6.2 Software

6.2.1 Clinical image segmentation

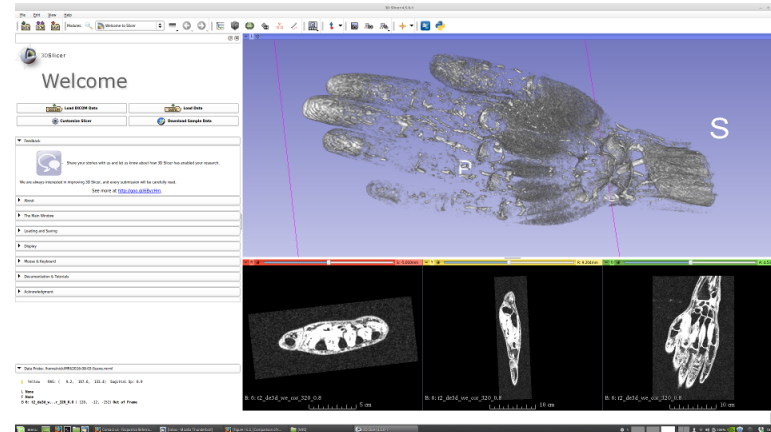


Figure 6-2: Slicer3D medical image processing and visualization system

Slicer

Segmentation of the MRI and CT scans was performed using the Slicer[141] medical imaging visualization and analysis software, figure6-2.

Slicer is available at <https://www.slicer.org/>.

6.2.2 3D printing software

MeshLab

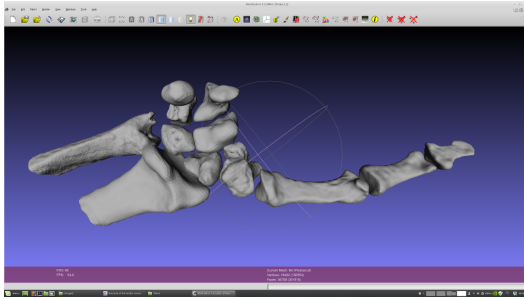
The surface meshes generated by Slicer were inspected and refined to eliminate meshing errors, and to smooth surface roughness using MeshLab, 6-3a. This reduced the size of the meshes by an order of magnitude while preserving relevant geometric detail, which greatly improved the speed and reliability of the subsequent preparation of 3D printing instruction 'G-code' files.

MeshLab is available at <http://meshlab.sourceforge.net/>.

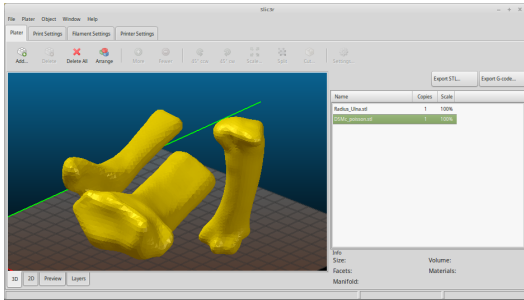
Slic3r

Prior to the preparation of G-code, it is necessary to position the .stl surface mesh file relative to the print bed to obtain the optimal orientation of the print layers in the structure to be printed. This was done using the Slic3r package, because its facilities for this task were superior to those available in the Pronterface 3D-print control software at that time, 6-3b.

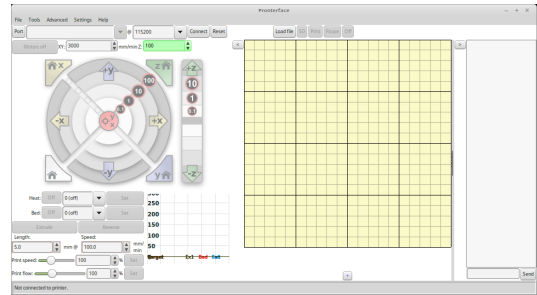
Slic3r is available at <http://slic3r.org/>.



(a) Meshlab 3D mesh editor



(b) Slic3r 3D G-code generator



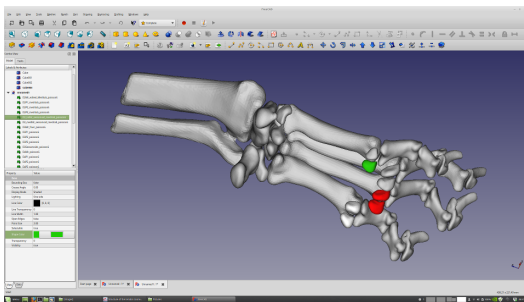
(c) Pronterface 3D print controller

Pronterface

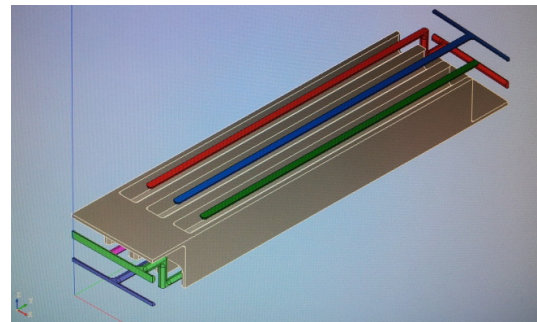
The control of the RepRap printer and the 'slicing' of .stl meshes to 'G-code' print instruction files was done using the Pronterface software, 6-3c.

Pronterface is available at <http://www.pronterface.com/>.

6.2.3 CAD software



(a) FreeCAD



(b) Salome-Meca

FreeCAD

The design of laser cut and 3D printed parts for the fibre drawing tower, fibre drawing nozzles, and moulds for dog paws was done using the FreeCAD CAD software, 6-4a.

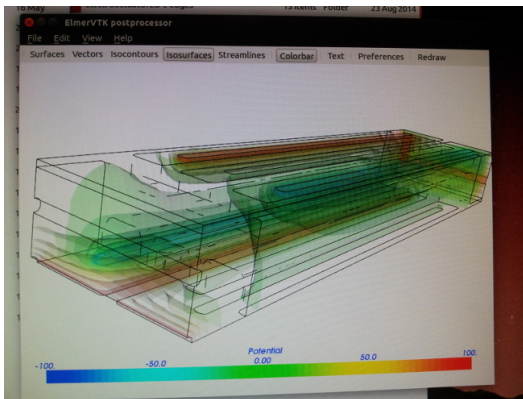
FreeCAD is available at <http://www.freecadweb.org/> , and <https://github.com/FreeCAD/FreeCAD>.

Salome Meca

The design of multi-partition finite element meshes for electrostatic analysis of the design for an iterative linear electrostatic actuator was done using Salome Meca, 6-4b.

Salome-Meca is available at <http://www.code-aster.org/V2/spip.php?article303> , and <http://www.code-aster.org/V2/spip.php?article146>

6.2.4 Finite element software



(a) Elmer

(b) Paraview

Elmer

Finite element modelling of the electrostatic field and electrostatic force of the iterative electrostatic actuator was done using the Elmer multi-physics finite element analysis software, figure6-5a.

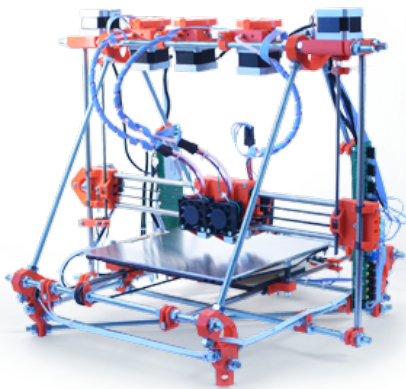
Elmer is available at <https://www.csc.fi/web/elmer/elmer> , and <https://github.com/ElmerCSC/elmerfem> .

Paraview

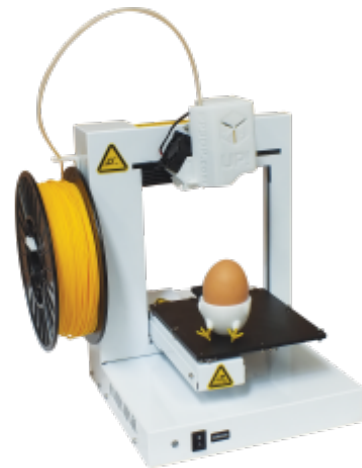
Post-processing and visualization of the finite element model was done using the Paraview software, figure6-5b.

Paraview is available at <http://www.paraview.org/> .

6.3 3D printers & materials



(a) RepRap Tricolour Mendel 3D printer, with three Bowden driven print heads installed.



(b) UP! Plus2 3D Printer

6.3.1 Up! Plus 2 3D-printer

The initial 3D printed bones used in the first joint and first finger prototypes were printed on an "Up! Plus 2" model printer, figure6-6b, using its standard ABS filament.

Specifications for the UP! Plus 2 are available at <http://up3dprinters.co.uk/up-plus-2-tech-specs/>. The printer used was purchased from <http://website.denford.ltd.uk/machines/141-3d-printers>.

6.3.2 RepRap Mendel 3D-printer

The 3D printed bones used in the later prototypes were printed on a RepRap Mendel printer, figure6-6a, with a single Bowden driven print head. The nozzle diameter was 0.3mm, and the filament used was 1.75mm PLA filament. The firmware used with this printer was the "Marlin" firmware.

Details of the RepRap Mendel printer design are available here <https://github.com/reprappro/Mendel>. Details of the Bowden driven print head are available here <https://github.com/reprappro/Extruder-drive>. The Marlin firmware is available here <https://github.com/MarlinFirmware/Marlin/tags>.

Chapter 7

Materials used in this thesis

Finding suitable base materials, capable of being combined into composites reproducing the mechanical properties of anatomical tissues has been central to the work of this thesis.

7.1 Notes on state transitions in polymers and amalgams

7.1.1 Polymers

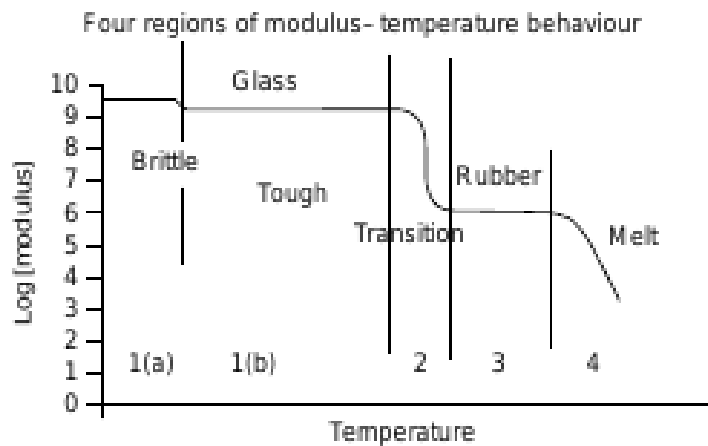


Figure 7-1: Modulus dependence on temperature for an ideal, linear, amorphous polymer. From fig 4.3 in [142].

In polymers the physical states are more complex than the solid/liquid/vapour phases of small molecules such as water. The length of polymer molecules prevents them from behaving as simple point masses. Polymer chains can become entangled with each other along their length. Movement of molecules relative to each other then requires snake-like movement known as 'reptation' of polymer chains along their length to escape entanglement.

Such motion is dependent on thermal flexion and rotation of covalent bonds of the molecule. The likelihood of such motion is dependent on the time period over which the polymer is observed, consequently the apparent stiffness of the material depends on the time period and the speed of extension. Loss of stress and increase in strain over time are known as 'creep', and are due to relative movement of polymer chains. The ability to recover the original shape depends on the existence of cross-links between polymer chains that preserve the topology of the polymer network.

The time required at a given temperature, for sufficient flexing to allow a given degree of slippage and stress relaxation, gives rise to a series of thermal transitions in the stiffness of a polymer. For amorphous polymers these are known as glass transitions. The largest of these is the 'glass-liquid transition', or if cross-links are present the 'glass-rubber transition' denoted T_g or T_α . The lesser transitions are denoted T_β , T_γ etc. with decreasing temperature and increasing embrittlement. T_g is always below T_m the melting point of the solid crystalline phase.

States of amorphous polymers

Melt When the temperature is high enough to allow reptation movement of polymer chains past their entanglements, the material is in the 'melt' state and behaves as a viscous fluid.

Rubber If and only if sparse cross-links exist in a linear polymeric material at a temperature at which there is enough energy to overcome entanglements, then the material will be in an elastomeric 'rubber' state. "The rubber state is unique to linear and lightly cross-linked polymeric materials. It is characterised by the ability to undergo very large reversible deformations, to recover its original shape, to absorb energy and to damp vibrations." [143]

Tough glass If there is sufficient thermal energy for minor mode flexion of the polymer chains to release a subset of entanglements, then the material will be in a 'tough glass' state.

Brittle glass When the material is cold enough that nearly all entanglements persist, then there will be no stress relaxation and the material will be in a 'brittle glass' state.

Cross-linking

Cross-links between polymer chain may be formed in a number of ways:

Covalent - vulcanization The most widely used form of cross linking is covalent sulphur bridge 'vulcanization' in thermoset rubbers.

Ionic Ionic side groups can form strong ionic bonds between polymers, but reversibly broken at lower temperatures than the covalent structure of the polymer. Ionomers are an important class of tough thermoplastics.

Co-block polymers A co-block polymer is composed of two or more monomers segregated into blocks along the length of the polymer chain. The blocks are commonly

immiscible with each other, and phase separate in the material. Where the dominant phase is in the melt state, but the minor phase is in a glassy or crystalline state and there are at least two minor phase blocks per polymer chain, then the minor phase acts a cross-link between polymer chains.

Thermoplastic vs thermoset polymers

If the covalent bonds of the polymer start to break at lower temperatures than either the glass-liquid transition or the cross links if present, then the polymer does not have a melt state, and is termed a 'thermoset' polymer. If the polymer has a melt state below the onset of thermal decomposition, then it is termed a 'thermoplastic'.

Crystalline and semi-crystalline polymers

Crystalline materials have highly ordered structure, with repeating patterns of molecular orientation. Many polymers are semi-crystalline with regions of crystalline order interspersed with disordered amorphous regions.

If a thermoplastic is crystalline then there will be a T_m crystalline melting point. This is a true phase change occurring at a fixed temperature, but is dependent on polymer chain length, and can be altered by the presence of small solvent molecules which may act as plasticizers.

Viscosity, elasticity and fracture in the melt state

The viscosity of polymer melts is dependent on entanglement and reptation. Short chains cannot entangle. Longer chains in dilute solution are separated into non-overlapping volumes so also fail to entangle. Such solutions have viscosity near to that of the solvent rising in proportion to the molar mass. If entanglement occurs then viscosity rises with a higher power of the molar mass (3 to 3.5).

If a melt is subject to rapid shear or elongation, then the polymer chains become elongated, as they do when stretched in the rubber state. This allows them to recoil elastically in the melt state, which causes rapidly extruded fibres to develop a roughened surface. If the strain rate applied exceeds the combined elastic and viscous accommodation then the melt will fracture.

7.1.2 Metal amalgams

Unlike pure metals, amalgams do not necessarily have a single melting and freezing point. When metal crystals form they do so with particular ratios of elements. An amalgam that does not have one of these ratios will change in relative concentration and freezing temperature during the process of freezing. Consequently there will be a range of temperatures between the fully frozen and the fully liquid states.

Liquidus - the temperature above which the amalgam is fully liquid.

Solidus - the temperature below which the amalgam is fully solid.

Eutectic - an alloy or amalgam for which the liquidus and solidus are equal.

7.2 Rigid matrix

For synthetic structures emulating anatomy, compression bearing materials are needed to replicate the mechanical function of the bones and hyaline cartilage. In the case of the bones the compressive stress and shear modulus may be quite high, but still substantially lower than common engineering materials such as aluminium alloys. While lamellar bone density approaches that of pure calcium phosphate apatite (specific gravity $3.143.21g/cm^3$, compared to $2.7g/cm^3$ for aluminium), this makes a small percentage of the total volume of bones, so a replacement material would need either to be patternable to similar detail as bone tissue, or be of lower specific gravity, in order to match the overall density and mass of anatomical bones.

In addition to density, compressive strength and modulus constraints, articular surface materials need to be able to reproduce the low sliding friction properties of hyaline cartilage. These depend on the ability to form a very smooth surface, as well as the retention of a lubricating fluid film between sliding surfaces, (Ch.3.1.6, and 3.1.2).

7.2.1 Thermoset polyurethane resin

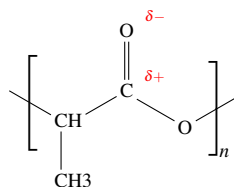
Polyurethane casting resins "Poly Optic 1410" and "Poly Optic 14-70" (flexible) (section-7.3.1) were bought from Mouldlife Ltd [144] Poly-Optic series 14 clear casting resins are low viscosity casting thermoset resins manufactured by Polytek Corp. [145] Low viscosity resins were selected for good penetration into fibres in lay up of composites. Poly-Optic 1410 rigid resin was used for casting finger bones. Poly-Optic 14-70 rubber was used to bond ligament fibres to the bones and form elastic joint capsules.

Resin	Shore hardness	Tensile strength	Elastic modulus	Flexural strength	Flexural modulus
Poly-Optic 1410	D-80	31.5MPa	667MPa	33.7MPa	994MPa
Poly-Optic 14-70	A-70	3.9	14.9	NA	NA

Table 7.1: Physical properties of Poly-Optic polyurethane casting resins [1]

7.2.2 Rigid thermoplastics

Poly(lactic acid) (PLA)



(a)



(b)

Figure 7-2: Poly(lactic acid) a) chemical structure of monomer, b) bulk material.

PLA is a widely used fused filament deposition 3D printing material. Naturally it is a transparent colourless material, but is commonly blended with pigments to make it opaque. PLA is the default material for the Rep-Rap series of 3D printers. It is also hydrolysable in vivo and used for both resorbable surgical sutures and as a tissue scaffold material in organ culture for regenerative medicine. Its intermolecular bonding is due primarily to its ketone side groups which form dipole attractions between the polymer chains.

Polycaprolactone (PCL)

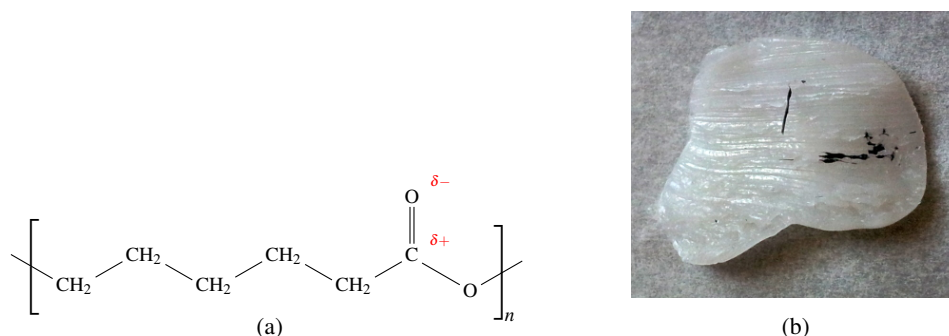


Figure 7-3: Polycaprolactone acid a) chemical structure of monomer, b) bulk material.

Polycaprolactone also known as 2-Oxepanone homopolymer or 6-Caprolactone polymer is sold at retail under the brands "Polymorph" and "Shapelock" among others. It is a member of the polyester group of polymers, and is normally glassy semi-crystalline translucent colourless solid at standard temperature.

The intermolecular bonding in PCL is due primarily to its ketone side groups which form dipole attractions between the polymer chains. Its melting point and molten viscosity depend on the polymer chain length. At around 60°C PCL melts to a very viscous clear colourless liquid with high surface tension in air. This is low melting point allows PCL to be handled and moulded by hand without protection in the molten state. The high surface tension has the very useful effect of producing very smooth surfaces. Once cooled and resolidified, these hard smooth surfaces have notably low friction.

Acrylonitrile butadiene styrene (ABS)

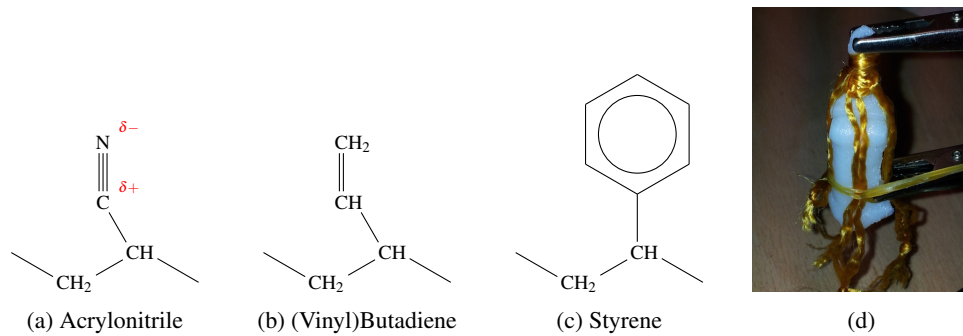


Figure 7-4: Acrylonitrile butadiene styrene acid a,b,c) chemical structure of monomers, d) bulk material (3D printed bone).

ABS is a widely used tri-polymer of the monomers acrylonitrile, butadiene and styrene. Its properties depend on the ratio of the monomers, whether they are arranged randomly or in contiguous blocks, and the length of the polymer chains. The styrene monomers produce significant van der Waals attractions to each other, as in the monopolymer polystyrene, while the acrylonitrile monomers provide a the polar $\text{—C}\equiv\text{N}$ group which can form dipole attractions or hydrogen bonds if a hydrogen donor group is present.

Note that there are three possible patterns of polymerisation for butadiene: cis, trans and vinyl depending on the location of the remaining $\text{C}=\text{C}$ double bond. This is determined by the catalyst and process used for polymerisation. The existence of this double bond means that polybutadiene and copolymers of it such as ABS can potentially be covalently cross-linked (vulcanized) to produce thermoset materials. In the absence of such covalent cross-linking, ABS is a thermoplastic.

In this thesis thermoplastic ABS fused deposition filament and pellets were used for 3D printing, thermoplastic welding and blending with other thermoplastics.

Polymer	melting temperature °C	Flexural Yield Strength MPa	Flexural Modulus GPa
PLA [146]	110 - 170	6.00 - 145	0.22 - 14
PCL [147]	58 - 60	84.1	2.8
ABS [148]	88 - 98 (heat deflection)	10.3 - 111	0.024 - 6.9

Table 7.2: Approximate ranges of properties of rigid thermoplastics. Note (1) ABS has no simple phase change. (2) All values are altered by chain length, monomer ratios, and compounding additives.

7.3 Flexible matrix

7.3.1 Thermoset elastomer resins

Polyoptic PU resin

Polyurethane casting resins "Poly Optic 14-70" (flexible) was bought from Mouldlife Ltd [144] Poly-Optic 14-70 rubber was used to bond ligament fibres to the bones and form elastic joint capsules.

Toms Viscolo silicone - Shore A 22

This is a platinum catalysed, addition cure, low modulus, silicone rubber. This type of poly-di-methyl-siloxane (PDMS) rubber comes as two equal parts that cure at room temperature after thorough mixing to form a solid rubber [149]. Platinum catalysed silicone rubbers are vulnerable to poisoning of the catalyst and tend to have low tear resistance relative to other rubbers.

7.3.2 ACC silicones

Silicone gel

E-3000 gel is a platinum cured silicone rubber and silicone oil based gel [150]. It has extremely low modulus, similar to the softest subcutaneous tissues.

Shore-A 6 Silicone rubber

ACC silicones MM906 is a tin catalysed condensation-cured silicone moulding rubber [151]. It has good tear resistance, Shore-A 6 hardness and can be blended with silicone oil to make silicone gels in the Shore-OO 'hardness' range. It requires a small quantity (5%) of tin catalyst [152]. This class of catalyst is much less prone to being 'poisoned' by other metals, but (ironically) requires some care in handling as it is moderately toxic.

Thixotropic agent

Thixotropic additive MMTA2[153] can be added to either tin or platinum cured silicones to make them thixotropic. This particularly useful when applying silicone to the exterior of a structure as it allows thicker layers to be set without requiring a mould.

Resin	Shore hardness	Tensile strength MPa	Elastic modulus MPa	Elongation at break
Poly-Optic 14-70 [1]	A-70	3.9	14.9	234%
Toms 22 [149]	22	41	NA	380%
ACC tin cure [151]	6	2.61	0.46	688%
ACC 3000 gel [150]	< 0	NA	NA	1000%

Table 7.3: Physical properties of thermoset elastomer resins

7.3.3 Thermoplastic elastomers

Poly-ethylene-vinyl-acetate (EVA) 'Elvax'TM,

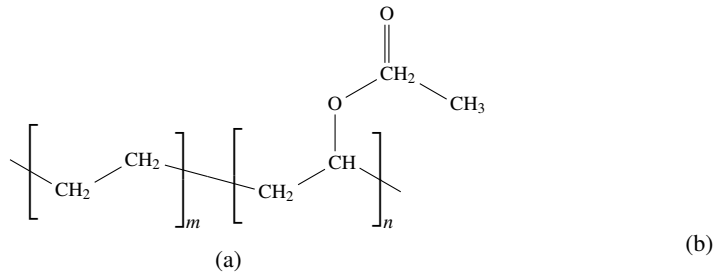


Figure 7-5: Ethylene Vinyl Acetate a) chemical structure, b) bulk material.

Ethylene vinyl acetate (EVA) is a random co-polymer of non-polar ethylene and polar vinyl acetate. In the pure form it has no cross-links so by the definition in [143] would be classed as an extreme example of a visco-elastic fluid not a rubber. As expected from the lack of cross links pure EVA does suffer higher creep over prolonged periods than other elastomers. The properties of EVA depend on the ratio of the monomers and the chain length. Polymers with > 50% vinyl-acetate are known as 'vinyl-acetate-ethylene' (VAE) and are water soluble. Polymers with nearly equal ratios of vinyl-acetate and ethylene exhibit the lowest modulus and melting temperatures, and the highest elasticity and creep. Polymers with a high proportion of ethylene become increasingly similar to polyethylene.

Samples of commercially available EVA polymers synthesized by DuPont were obtained from Disrupol. These are marketed under the 'Elvax' brand. The samples used in making prototype structures included [154]:

Elvax-40W has 40% by weight Vinyl Acetate, melt flow rate (190C/2.16kg) 52 g/10 min, melting point 47C, Shore-A 40

Elvax-40L-03 has 40% by weight Vinyl Acetate, high molecular weight 'long' chain, high melt viscosity, melt flow rate (190C/2.16kg) 3 g/10 min, melting point 58C

Elvax-150 has 32% by weight Vinyl Acetate, melt flow Rate (190C/2.16kg) 43 g/10 min, melting point 63C, hardness Shore-A 65

Poly(co-ethylene-co-acrylate) Sodium salt ionomer (PEAA-Na) 'Surlyn'TM 8320'

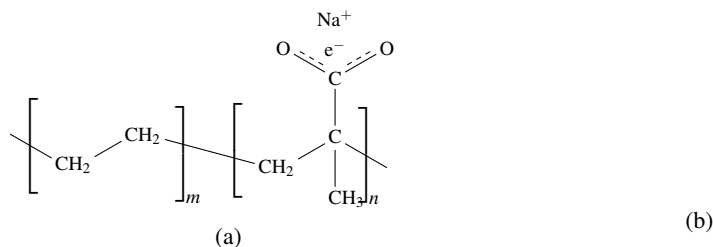


Figure 7-6: Poly(co-ethylene-co-acrylate) Sodium salt a) chemical structure, b) bulk material.

An ionomer is a polymer with some ionic bonding. The polymers sold by Du Pont under the brand 'Surlyn', are random co-polymers of ethylene and acrylic acid with a variety of metal ions (Mg^{+2} , Zn^{2+} , Li^+ , Na^+ , K^+) forming the ion-bridges between acrylic acid monomers. The degree of neutralization of the acrylic acid varies and some grades are corrosive, requiring chrome plated or high chrome stainless steel extrusion equipment. Surlyn is thermoplastic, bonds to metals, and forms hydrogen-bonds to hydrogen donor groups (eg alcohols, amides and carboxylic acid groups). It does not bond to non-hydrogen donor polar groups such as ketones. Consequently Surlyn bonds to polyamide ('Nylon') and ABS, but not PLA, PCL or SEBS. The intermolecular bonding and thermal properties of ionomers depend on the size, charge and polarity of the ions, the ratio of the monomers, the length and structure of the polymer chain.

Surlyn 8320[155] has sodium as its metal ion, and is the softest grade sold under this brand at Shore-D 36 hardness (approximately equivalent to Shore-A 85). This grade was used for articular surfaces and tendon sheaths both in its pure form, and softened by blending with paraffin oil. It is a hard to flexible plastic with modest elastic resilience, high hysteresis and high tensile elongation. Together these properties mean a lot of work must be done to break Surlyn, i.e. it is very tough. Surlyn has a high surface tension in air when molten. This causes it to produce a smooth low friction surface.

Styrene-ethylene-butylene-styrene (SEBS)

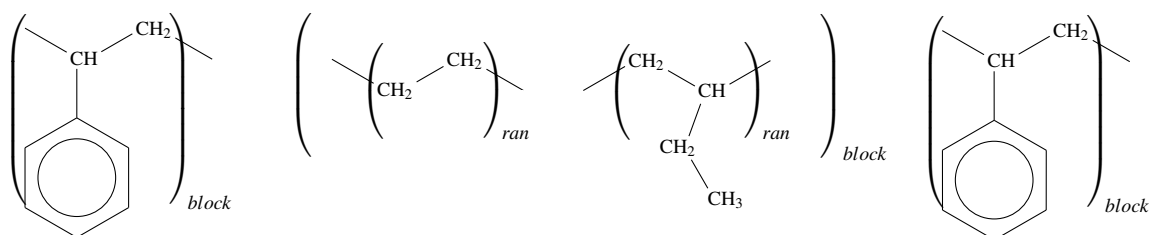


Figure 7-7: Polystyrene-co-block-poly(ran-ethylene-ran-butadiene)-co-block-polystyrene

SEBS is a co-block terpolymer (polymer of three monomers), of polystyrene end blocks and polyethylene-butylene mid-block. The two regions of the polymer form separate phases of ordered crystalline regions of polystyrene surrounded by amorphous polyethylene-butylene. This arrangement connects polymer molecules in a network where the polystyrene crystals form the 'knots' and polyethylene-butylene polymer chains form the connections between 'knots'. This arrangement allows the material to be deformed without breaking the structure, and hence to recoil elastically. SEBS and other co-block polymers with similar structure are hyper-elastic showing resilience to strains $\gg 100\%$.

The intermolecular bonding that maintains fixed topology of the network in SEBS in the solid state is principally van der Waals forces between the styrene groups of adjacent molecules. Consequently SEBS, like polystyrene, is thermoplastic.

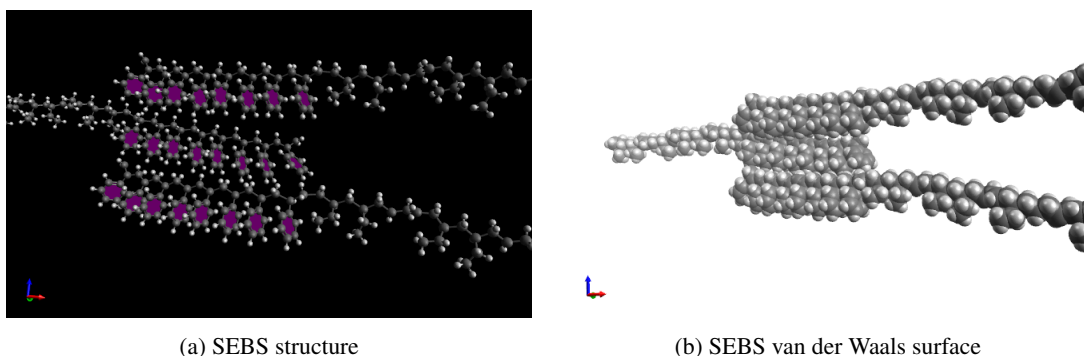


Figure 7-8: SEBS intermolecular behaviour, showing an ordered polystyrene domain linking polymer molecules by van der Waals forces between styrene rings, and surrounding disordered elastic polyethylene-ran-butylene domain. Models generated with Avogadro: an open-source molecular builder and visualization tool. Version 1.1.1. [156]

SEBS-paraffinic-oil-gel 'DryflexTM'

(a) SEBS rubber film

(b) SEBS rubber crumb

(c) SEBS-gel

Figure 7-9

The biphasic nature of co-block polymers such as SEBS enables a solvent to be added that dissolves only one phase. Where the solvent dissolves the mid-block the result is a gel. The lubrication of the movement of the mid-block polymer chains by the solvent, and the dilution effect dispersing the polymer in a larger volume, have the effect of reducing the modulus and strength of gel relative to the pure pure co-block polymer.

The poly(ethylene-ran-butylene) mid-block of SEBS can be dissolved in aliphatic oils, i.e. alkane hydrocarbons with no double bonds, and no cyclic structures, also known as paraffinic oils or 'paraffins'. The lack of cyclic structures and double bonds mean that such paraffins do not dissolve polystyrene. Consequently when paraffins are added to SEBS they are absorbed into the polymer, forming an SEBS-oil-gel, and swelling its volume.

Pure SEBS is commonly supplied as a white rubber crumb, with a high surface area granular structure similar to dried coffee (indicative of having been dried from a solution), and with elasticity similar to natural rubber. When this is gelled with paraffin it swells and softens, but remains a granular crumb. If the paraffin swelled SEBS is then heated to above the melting point of the polystyrene end blocks ($\approx 200^{\circ}\text{C}$), then the gel becomes a low viscosity fluid. When cooled this sets as a clear solid gel. Depending on the degree of dilution the modulus of the SEBS-paraffin-oil-gel can be extremely low (\approx Shore-OO 0).

If a solvent of polystyrene is added to the pure SEBS crumb, then it becomes a shear thinning thixotropic colloid, without any heating required. If the solvent is non-volatile (e.g. a 'yellow' motor oil or grease containing aromatic oils containing benzene rings) then the SEBS-oil colloid remains a slush. If the solvent is volatile (e.g. Xylene), and the SEBS solution is poured into a flat dish, then

evaporation of the solvent leaves a thin film of dense SEBS rubber. Rapid drying of this rubber may cause it to craze and revert to a material resembling the original SEBS crumb. Slower drying, possibly with the inclusion of a small fraction of non-volatile paraffin, produces a durable high clear colourless rubber of high modulus and elasticity. This demonstrates the potential for solution processing SEBS.

SEBS-gel was used as a hyperelastic matrix for soft tissues in the later prototypes. SEBS rubber, blends and laminates were used in a variety of joint and tendon structures.

Thermoplastic Elastomer	Melting point °C	Shore hardness	Tensile strength MPa	Elastic (100%) modulus MPa	Elongation at break
Surlyn 8320 [155]	70	D-36 (A-85)	18.6	n/a	555%
EVA Elvax 40W [157]	47	A-40	5.2-6.2	3.0	1,000–1,300%
EVA Elvax 40L [158]	58	A-48	10.3 (1500psi)	n/a	1270%
EVA Elvax 150 [159]	63	A-65	6.9-8.3	10.0	900–1,100%
SEBS-gels Elasto					
Dryflex 880101	150-200	A-40	5.0	1.0	> 600%
Dryflex 500000 [160]	150-200	OO-28 (\approx A-0)	1.0	0.100	1,000%
'180' crumb + paraffin	150-200	OO-0 to A-0	n/a	\ll 0.100	> 1,000%
'180' crumb + white spirit	solvent cast gel	\ll OO-0	n/a	$\ll\ll$ 0.100	> 1,000%

Table 7.4: Physical properties of thermoplastic elastomers and elastomer-gels.

7.4 Blending, laminating, plasticizing and cross-linking

7.4.1 PCL-SEBS blends and laminates

It is desirable to be able to produce materials with intermediate mechanical properties and to produce graduation in mechanical properties. SEBS and PCL do not adhere to each other but they can be mechanically blended to produce a range of elastic moduli, though the yield strain tends to be closer to PCL than SEBS.

A laminate was prepared from a stack of rolled sheets of blends graduated from pure PCL to pure SEBS-gel. The laminate was rolled into a thin sheet $< 0.5mm$ which could be laid on the surface of 3D printed PLA structures. When heated with a heat gun the PCL face of the laminate would bond to the PLA, producing a soft SEBS surface tightly adhered to the rigid 3D printed structure. SEBS structures could then be adhered to the SEBS face of the laminate.

This technique allowed specific areas of 3D printed bones to be made adhesive to SEBS, while other areas remained non-adhesive.

7.4.2 Polyacrylic acid polyacrylate plasticized with oil

Surlyn can be mechanically blended with paraffin (linear alkane) oils. The blended ionomer oil-gel is softer, more flexible and easier to shape than pure Surlyn. The blend also weeps oil, producing a lubricated surface. Surlyn oil-gel rolled film was used for tendon sheath and articular cartilage material in some of the later prototypes.

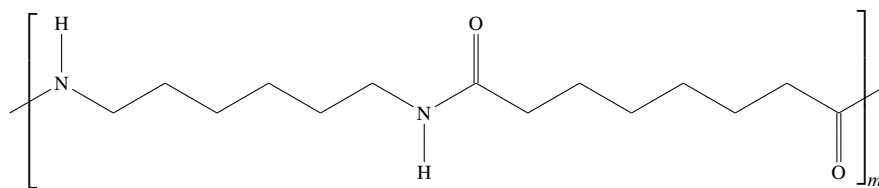
7.4.3 PCL plasticized with glycerol

Glycerol (propane-1,2,3-triol) is a short chain poly-alcohol which is miscible with PCL due to hydrogen bonding between the ketone groups of PCL and the alcohol groups of glycerol. Being a small unentangled molecule interposing between PCL polymer strands, glycerol facilitates movement so acts as a plasticizing agent. PCL softened with glycerol was used to make some joint faces more compliant.

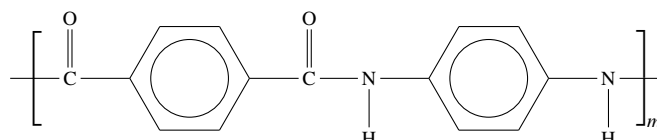
7.4.4 EVA cross linked with Sodium Borate

EVA can be vulcanized with covalent cross-links by peroxides, and a number of 'X-EVA' cross-linked EVA materials are available commercially. EVA can also be cross-linked by sodium borate ($Na_2B_4O_7 \cdot 10H_2O$) 'borax'. EVA cross-linked by blending with borax powder becomes much stiffer but remains thermoplastic. Several mechanisms may be involved in borax cross-linking of EVA. The borate ion ($B(OH)_4^-$) can form hydrogen bonds with the acetate groups. The acetate groups may be hydrolysed to alcohol groups and ethanoic acid in the alkaline environment. Covalent, but hydrolysable borate-esters may be formed.

7.5 Fibres



(a) Polyamide-6,6 (PA66) 'Nylon'



(b) Poly-paraphenylene terephthalamide (PAr) 'Kevlar'

Figure 7-10: Chemical structures of monomers.

(a)

(b)

Figure 7-11: Fibres of a) Nylon, b) Kevlar.

7.5.1 Polyamides

Polyamides (PA) including the subfamily polyaramides (PAr) have amide links between their monomers. These present both ketone groups and hydrogen bearing amide groups. The inter-molecular bonding in both PA and PAr is by hydrogen bonds between the ketone and amide side groups of adjacent polymers.

7.5.2 Polyamide-6,6 (Nylon)

Polyamide-6,6 (PA66) is widely known by the brand name 'Nylon' and is used in many consumer products. It is a semi-crystalline thermoplastic and commonly used as a fibre in fabric and ropes. PA66 exhibits significant elasticity and is used in climbing ropes to absorb the shock of falling without excess force. The PA66 fibres used in this thesis were obtained from a climbing rope. These are fine fibres approximately 20 microns in diameter, that are arranged as parallel tows with no twist or crimp. This arrangement helps to avoid weakening the fibres by tight radius bending and friction against each other.

7.5.3 Polyaramide (Kevlar)

Poly-paraphenylene terephthalamide 'Kevlar' para-aramid very crystalline Poly-paraphenylene terephthalamide (PAr) known by the brand name 'Kevlar' is a member of the para-aramid subfamily. It is very crystalline, resulting in a high degree of orientation of polymer molecules, conferring very high stiffness and strength. The highly crystalline nature also causes a very high T_m , above its thermal decomposition

temperature. Consequently Kevlar is a thermoset. The Kevlar used in this thesis was sources as dry loose weave reinforcing fabric for composites manufacture. This fabric consisted of tows of parallel fibres similar to the PA66 fibres above.

	melting point °C	elastic modulus MPa	tensile strength GPa	extension, %
Polyamide-6,6 (PA66)	255C	80	2.41	25
Polyaramide (PAr)	>500C	2,920	70.3	3.6

Table 7.5: Properties of 'Ensinger Tecamid 6/6 Nylon' [161] (PA66) and 'Kevlar-29' [162] (PAr).

7.6 Thermoplastic composites

7.6.1 Compatible thermoplastics

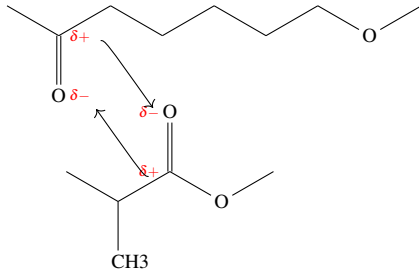


Figure 7-12: Ketone dipole attraction between polycaprolactone(top) and polylactic acid(bottom)

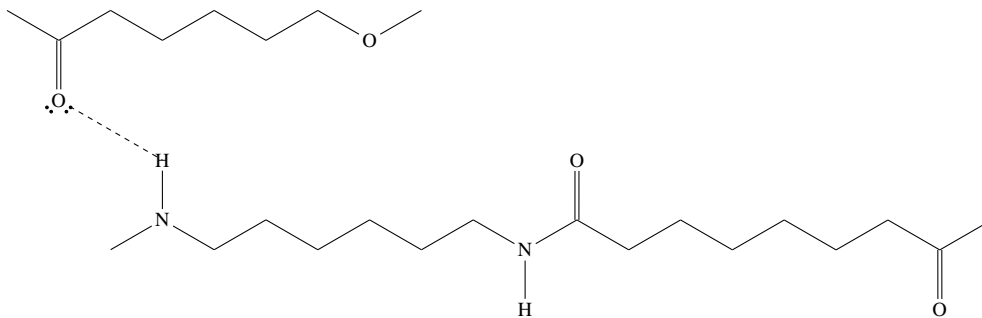


Figure 7-13: Hydrogen bonding between polycaprolactone and polyamide

Three different thermoplastics, polycaprolactone (PCL), polylactic acid (PLA), polyamide (PA) / polyaramide(PAr), were selected with different softening temperatures, table(7.5) and compatible intermolecular bonding. This combination of properties allows bonding by melting the lower temperature material while the higher temperature material retains its shape and structure.

PCL and PLA have the same intermolecular bonding based on ketone groups which form dipole attractions, figure 7-12 , consequently they are miscible when molten. Viscous molten PCL wets very well to solid PLA forming a high surface area of contact with 3D printed PLA parts. Figure 7-2b shows the surface of PCL forcefully peeled from 3D printed PLA. Note the pieces of (black) PLA still adhered to the (white) PCL, and the fine groove pattern mirrored from the print texture of the PLA. The ability to tear PLA by adhering PCL to it, indicates that the PCL-PLA adhesion approaches the strength of pure PLA.

Polyamides, and polyaramides present both ketone groups and hydrogen bearing amide groups. The ketone groups of PCL or PLA can form N-HO hydrogen bonds with the PA, which are stronger than the ketone dipole attractions within either PCL or PLA.

softening temperatures of plastics (deg C)		
Polycaprolactone (PCL)	60C [147]	glass transition
Polylactic acid (PLA)	150-160C [163]	melting point
Styrene-Ethylene-Butadiene-Styrene (SEBS)	170 210C [164]	melting point
Polyamide-6,6 (PA66)	135-254C [165]	melting point
Polyaramide (PAr)	>500C [166]	thermal decomposition

Table 7.6: Softening temperatures of plastics, temperatures will vary with polymer chain length and compounding additives.

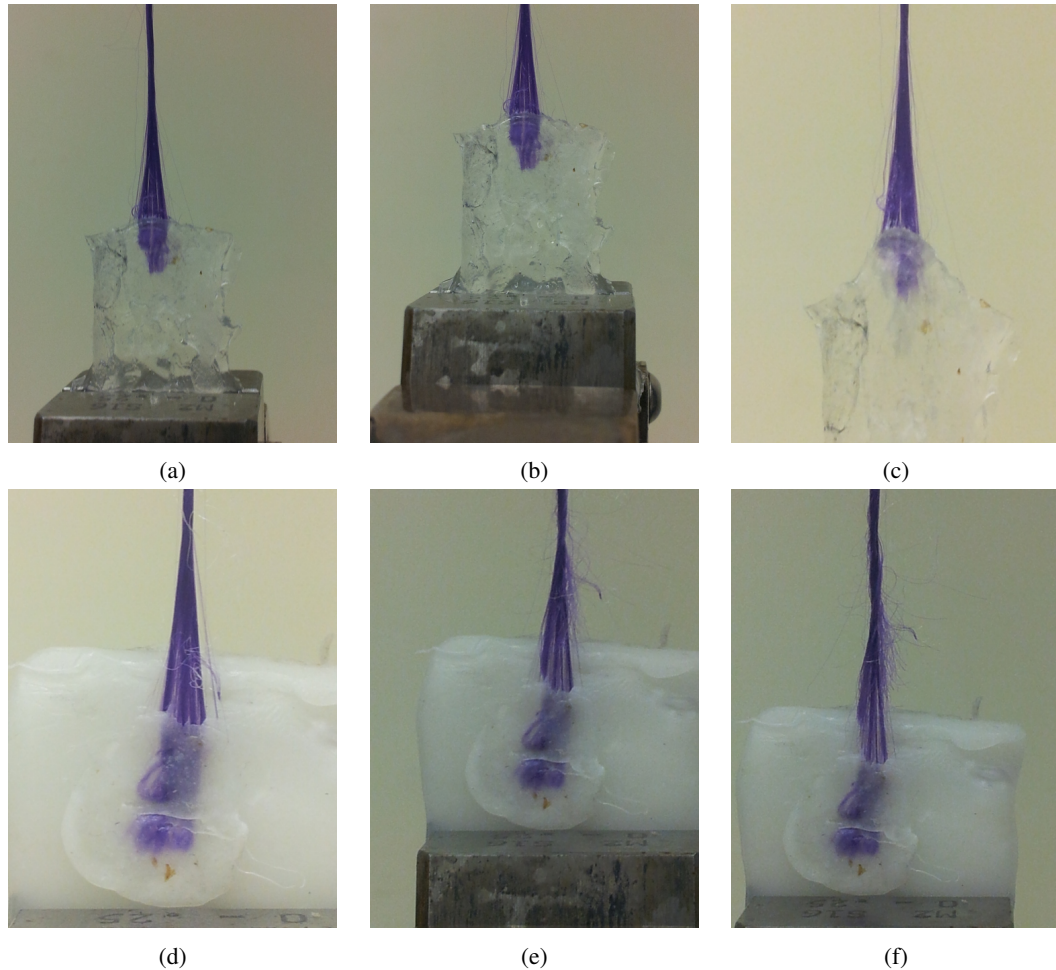


Figure 7-14: Fibre pull out testing. Top row, polyamide fibres in EVA (Elvax 40). Bottom row polyamide fibres in PCL (Polymorph).

7.6.2 Anchoring Polyamide and Polyaramide fibres in PCL

The hydrogen bonding between polyamides and polycaprolactone, combined with the lower melting point of PCL allows PA fibres to be welded into molten PCL. The strong bonding and high surface area to cross section area ratio of the fibres results in a very strong attachment. Figures 7-14d,7-14e,7-14f

show the result of pull out tests for PA66 fibres in PCL. Note that in figure 7-14f the fibres break without pulling out from the PCL. For comparison figures 7-14a,7-14b,7-14c show the results of pull out tests with the same PA66 fibres in EVA (Elvax 40), where the fibres pull out of the matrix. (Note EVA also has ketone groups as part of the vinyl-acetate group, but the lower modulus and creep behaviour of EVA probably contribute to the failure.)

The length of PA fibre embedded in the PCL in the test is approximately 10mm. This means that even short sections of PA embedded in PCL, such as the space available for the origins and insertions of ligaments, are sufficient to anchor the full strength of the ligament fibres.

7.6.3 Hyper-elastic composites

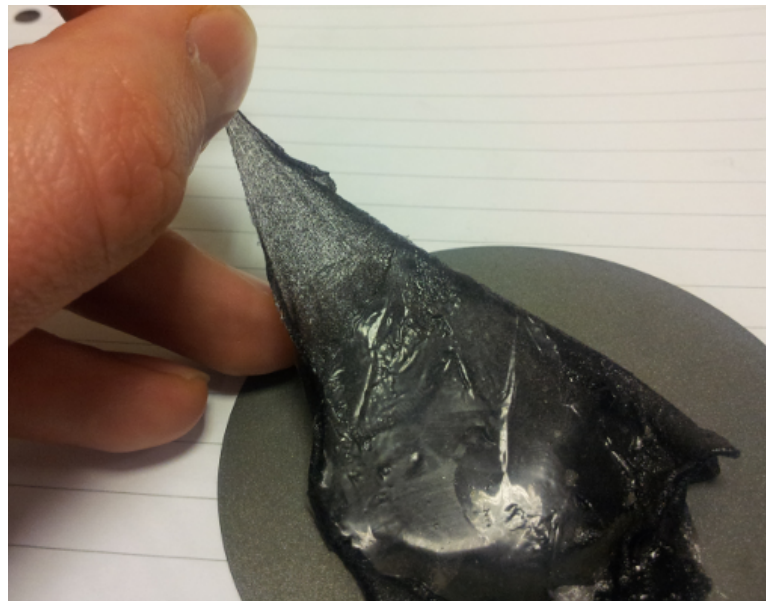


Figure 7-15: Hyperelastic composite of SEBS-gel matrix, polyamide knitted stocking fabric reinforcement and a thin surface lamina of dense SEBS rubber (cast from xylene solution).

As seen in Chapter 3, the anatomical soft tissues are hyper-elastic fibre-gel composites. To reproduce their mechanical properties it is necessary to create synthetic composites composed of base materials that have similar properties. The gel matrix of these tissues serves an important lubricating function, allowing relative movement of the fibres, while transmitting compressive forces and preventing other material from entering the space between the fibres.

Both thermoset (e.g. silicone) and thermoplastic (e.g. SEBS) gels can be used as the matrix of hyper-elastic composites. Parallel tows of polyamide or polyaramide fibres set in gel matrix were used to produce tendons and ligaments in many of the prototypes described in chapters 8 and 9.

Other tissues have different fibre arrangements. A dermal composite (figure7-15) was made by infusing SEBS-gel into knitted polyamide stocking material to form the dermis. A thin lamina of dense SEBS rubber was cast from solution in Xylene. This dense lamina was then adhered to the surface of the composite, by briefly heating with a heat gun. The dense lamina served the mechanical function of

the epidermis, eliminating the contact adhesive 'tack' behaviour of the gel, and providing an abrasion resistant surface.

The lamination of rubbers and gels, and laying of fibres and fabrics in particular layers and paths enables the emulation of a diversity of soft tissue structures. Both thermal and solvent bonding assist in achieving controlled local adhesion in the lay up process.

Hyperelastic solid lubrication

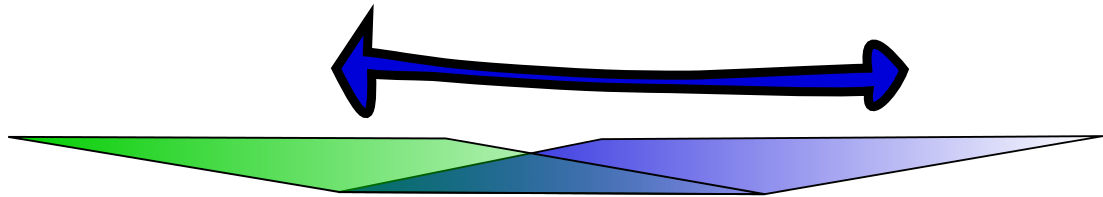


Figure 7-16: Elastic shear lubrication : a hyper-elastic lamina with elastic limit 1000% can permit shear 2x1000% times the thickness of the lamina. So a 0.5mm thick layer can lubricate 10mm of tendon excursion. This technique is essential for reproducing the movement of unsheathed anatomical tendons including the digital extensor hood.

Varying the ratio of oil to SEBS polymer results in different grades of gel. As the oil content increases the strength and stiffness decrease. Very soft high oil content gels can be used as solid hyper-elastic lubricant for motions of finite shear, figure 7-16.

A critical feature of anatomical tendon networks is the hyper-elastic peritendon tissue that allows the motion of tendons relative to surrounding tissues without any mechanical discontinuity such as a fluid lubricated tendon sheath or bursa. More generally the hyper-elastic areolar loose connective tissue allows the skin to move over muscles and bones, and allows muscles to move relative to each other. Silicone or SEBS gels allow the emulation of the areolar tissue and the replication of these structures in synthetic materials.

Hyperelastic mechanisms

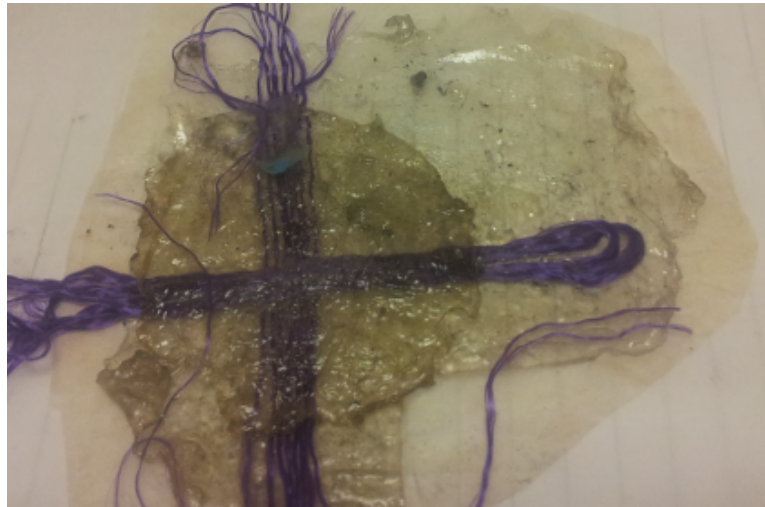


Figure 7-17

The use of gel layers as lubricants allows overlapping networks of tendons to be laid up over each other and wrapped around three dimensional surfaces that would otherwise cause them to fray and jam. Laminae of denser rubber can form a binding matrix that hold the fibres of tendons together or stably splay them to distribute force over a wider area. Dense rubber matrices can also be used to join branches of tendon networks to each other and to stabilizing 'retinacular' ligaments.

In this way the laying of gel and rubber laminae and fibres can allow complex mechanisms to be laid up in a few millimetres thickness over curved three dimensional surfaces. Figure 7-17 shows a prototype for the 'sagittal band' mechanism of the extrinsic extensor tendon of the digits. The fibres are impregnated with higher modulus SEBS and laminated onto each other. Above and below the fibres are laminae of low modulus SEBS gel. The transverse fibres serve as the sagittal bands preventing lateral movement of the longitudinal 'tendon' fibres. The gel lubrication allows the tendon and sagittal bands to move back and forth with the excursion of the tendon, while the ends of the sagittal bands remain fixed. This mechanism allows the tendon to be laid along the convex exterior surface of a joint without slipping off to the side of the joint under load.

A number of different mechanisms of this kind exist in anatomy of hands and other parts of the musculoskeletal system.

7.6.4 Controlled non-adhesion

There are places in the anatomy where fluid lubricate cavities exist - synovial joints, tendon sheaths and bursas - where it is important to preserve non-adhesion to allow movement. Generally these are areas where there is lateral pressure combined with shear, such that solid gel lubrication would tend to fail.

To replicate these it is useful to have materials that will not adhere to each other and tend to produce smooth low friction surfaces. This can be done by exploiting the side group interactions of polymers,

to produce surface material pairs that are immiscible due to incompatible intermolecular forces. In this way if these materials are heated to their molten state while in contact, they will not adhere but will instead produce a smooth minimum contact interface.

Pairs of materials which exhibit this behaviour include: SEBS to PCL, Surlyn to PCL, and Surlyn to SEBS.

7.6.5 Key concepts

- Viscoelastic behaviour in the melt state creates smooth surfaces
- Low temp thermoplastic welding allows precise fibre placement & adjustment
- Intermolecular forces allow controlled adhesion non-adhesion
- Hyper elasticity can take the place of lubrication
- Composite hyper-elastic structure creates mechanisms

7.7 Sensor fibre materials

7.7.1 Gallium-Indium amalgams

There are a variety of metal amalgams that are liquid at or below ambient temperatures habitable to humans. The most commonly used of these tend to be based on Gallium and Indium possibly with smaller concentrations of other metals. These have largely replaced mercury in modern usage due to the toxicity of mercury. Both Gallium and Indium are moderately high electrical conductivity metals and many of these amalgams have similarly high conductivities.

Eutectic Gallium-Indium 'eGaIn' 'Indalloy60'

[167] The most widely applied in recent robotics related publications is the simplest of these, 'eutectic Gallium-Indium' often referred to as 'eGaIn'. 'Eutectic' refers to the fact that this amalgam has a sharp melting/freezing point without separate liquidus and solidus temperatures. This occurs because this ratio of Gallium and Indium constitutes a thermodynamic minimum for melting point. Non-eutectic Gallium-Indium amalgams with ratios either side of eGaIn tend to form a paste of eGaIn and solid crystals of whichever metal is present in excess in the temperature range between the melting point of eGaIn and their own liquidus point. This mixed phase state accounts for their progressive melting over the temperature range between their liquidus and solidus points.

Thus eGaIn also represents a minimum in the melting point of Gallium-Indium amalgams, and an optimum for applications requiring low temperature liquid metals. It also makes eGaIn easy to prepare. Rubbing two pieces of solid pure Gallium and Indium together tends produce eGaIn at the contact face, which then flows away under gravity.

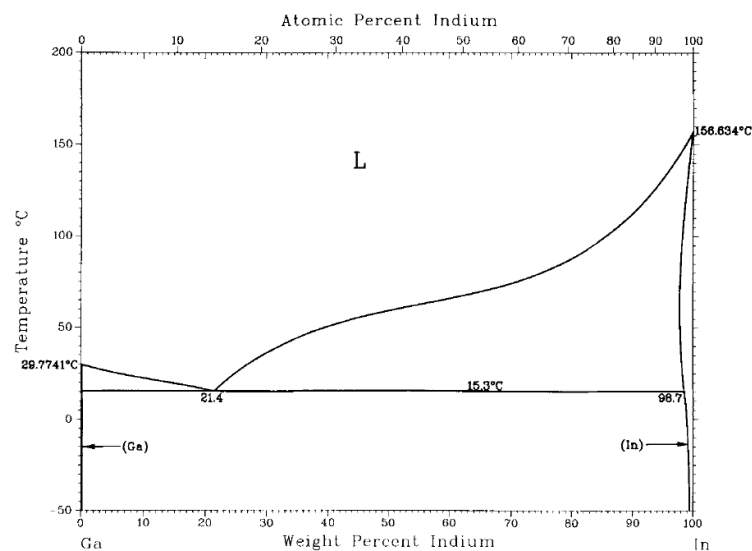


Figure 7-18: Assessed Ga-In phase diagram, from experimental data. Adapted from figure 1 in [168]

Complex Gallium-Indium alloys of published compositions

'Indalloy-46L' is a trademark of Indium Corporation, that is used to market a low melting point alloy for which the composition and properties are published. Indalloy-46L is specified as 61% Ga, 25% In, 13% Sn, 1%Zn by mass. It is non-eutectic with liquidus 7C solidus 6.5C, and electrical conductivity 33 ohm/meters. [169]

Indalloy number	Liquidus °C	Solidus °C	Composition	Electrical Resistivity $10^{-8}\Omega\text{m}$
Galinstan	-15	-19	68-69Ga/21-22In/9.5-10.5Sn/0-2Bi/0-2Sb	not provided
46L	7.6	6.5	61.0Ga/25.0In/13.0Sn/1.0Zn	33
51E	10.7	10.7	66.5Ga/20.5In/13.0Sn	28.9
60	15.7	15.7	75.5Ga/5In	29.4
14	29.78	29.78	100Ga	14.85
Copper			annealed copper	1.7
Steel			high carbon steel	17-30
Lead			pure lead	2064

Table 7.7: Composition, thermal and electrical properties of some low melting point metals, and comparison to common metals, [2]

Complex Gallium-Indium alloys with lower melting points

A number of low melting point alloys combining Gallium and Indium with other metals have been commercially marketed, e.g. [170]. The precise composition of these alloys is often not publicly available, but the likely range may be inferred from patents. Galinstan is a trademark of Geratherm AG [171] who hold US Patent US6019509 [172] which describes the invention:

"In this range of composition the liquid state of aggregation of the liquid extends from approx. -15 C. to more than +1800 C. under normal conditions. Gallium, indium and, if necessary, tin are preferential alloy elements because they lead to a particularly low eutectic point. Furthermore, this alloy is capable of conducting electricity ..."

"... In a further embodiment of the present invention the eutectic alloy may contain up to 2 wt.-% bismuth and up to 2 wt.-% antimony. Antimony raises the oxidation resistance while bismuth positively affects the fluidity of the alloy."

In this patent the following patent claims are made describing the composition range of the alloy:

" 4. A gallium, indium, and tin eutectic alloy, consisting of, in weight percent, 68-69% Ga, 21-22% In, 9.5-10.5% Sn, and optionally 0-2% Bi and 0-2% Sb, and inevitable impurities, wherein the melting point of said eutectic alloy is -15 C. or less."

"5. The eutectic alloy of claim 4 wherein the melting point is about -19.5 C."

The existence of such low melting point alloys indicates the range of temperatures to which the techniques developed in this chapter could be extended, without resorting to mercury which is considered hazardous due to its toxicity.

Corrosive behaviour with aluminium

Gallium is chemically very similar to aluminium. Both being in Group three of the periodic table of elements, have three unpaired electrons in their outer shell. Gallium is in period 4, one row below aluminium in period 3, consequently it has a larger atomic radius and lower electronegativity. Gallium and gallium amalgams are miscible with aluminium alloys, therefore gallium alloys dissolve aluminium alloys corroding away large quantities of material very quickly. Potentially more critically gallium also diffuses into solid aluminium alloys at a speed comparable to water being absorbed into tissue paper, with similarly catastrophic effects on the structural strength of aluminium. This behaviour can easily be demonstrated by applying a drop of liquid gallium amalgam to an aluminium can, causing the can to disintegrate.

Behaviour with copper

Gallium-indium alloys can dissolve copper when in cathodic contact [173], however rates of erosion are far lower than with aluminium alloys [174].

Surface oxide layer

Like aluminium, gallium alloys rapidly form an oxide layer in contact with air. This surface layer profoundly affects the apparent surface tension behaviour of such amalgams [175]. The oxide layer is solid and has a tensile strength that prevents free flowing of the amalgam at scales of a millimetre and below. This has profound effects in fine capillary channels with elastic walls (Ch.11.2.6)

7.7.2 Thermoplastic elastomers

The chemical structure and properties of these materials are given in Ch7.3. Here their properties relevant to their application in making sensor fibres are discussed.

Ethylene Vinyl Acetate (EVA)

EVA was the first material identified in this project as a potential sensor fibre material, due to (i) its elasticity in the solid state, making it extensible and robust, and (ii) its visco-elastic behaviour in the molten state giving it 'melt strength' making it very easy to draw into fine fibres. Molten EVA based 'soft' grades of 'hot glues' can readily be pulled by hand into ultra fine fibres of approximately 10 microns diameter. Such fine fibres require cross lighting on a dark background to make them visible, and tend to float on convection currents indoors. This simple experiment demonstrates the potential ease with which nerve axon scale fibres can be manufactured.

Annealing contraction after drawing

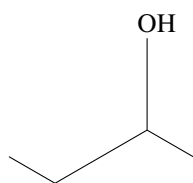
Styrene Ethylene Butylene Styrene (SEBS) and SEBS-oil gels

SEBS has substantially lower elastic modulus and greater breaking strain than EVA. This is potentially beneficial because it could create a sensor fibre with breaking strain as great or greater than that of the surrounding tissue, which would prevent damage to the sensor fibres by forces less than that sufficient to destroy the surrounding structure. The major disadvantage of SEBS, and especially SEBS-oil gels is their extremely low melt strength.

Sucrose glass

Molten sucrose can be drawn into fine fibres (e.g. 'candy floss' or 'cotton candy') and is used as teaching material for fibre drawing [176], [177]. As a potential support cladding for fibres of low melt strength sucrose glass has two potential advantages (i) good fibre drawing melt strength, (ii) high solubility in water, allowing easy removal from the drawn fibre. The key constraint of sucrose is its susceptibility to thermal decomposition (caramelisation) which starts above 120°C and occurs faster at higher temperatures [178].

Polyvinyl Alcohol (PV-OH) 'Monopol'



(a)



Figure 7-19: Acrylonitrile butadiene styrene acid a) chemical structure of monomers, b) bulk material (thick part of the fibre to the left).

PV-OH is a water soluble thermoplastic. These have higher melt strength, lower water solubility and higher heat tolerance than sucrose glass. MonoSol, the water soluble films division of polymer firm Kuraray [179], sell a range of water soluble polyvinyl alcohol thermoplastics under the brand MonoPol. These have hydrogen bonding between their $-OH$ alcohol side groups and their principle intermolecular bonding. A sample of Monopol "PC106" (production code 46/D052/5/01 and X1164) was provided by the Monosol's UK office.

Poly(ethylene-co-methacrylate) ionomer, (PEMA) 'Surlyn'

PEMA is an insoluble thermoplastic, with good drawing properties, modest elasticity and high toughness. As a potential sensor fibre material it has the advantage of adhering well to most metals due to its ionomer bonding.

7.7.3 Modifying additives

Plasticizing and cross-linking agents to modify the mechanical properties of polymers were covered in Ch7.4. The materials covered here are wetting agents to improve the wetting of polymers by Gallium-Indium amalgams. Non-wetting can otherwise cause a lower limit to the size of channel that can be filled with amalgam, Ch.11.2.6.

Indium Tin Oxide $In_2O_3 : SnO_2$ (ITO) powder, micron and nano grades

Indium Tin Oxide $In_2O_3 : SnO_2$ (ITO) is widely used as a transparent conductor in consumer electronics displays. In that application it is usually patterned by physical vapour deposition in a film 0.1-0.3 microns thick. It is also used in conductive inks for printed electronics, as an anti-static coating and as an infra-red reflective coating in glazing. It has a niche application as a wetting agent for Gallium amalgams[180]. ITO is available commercially as powder of micron [181] or nano [182].

Sodium Stearate (soap)

Sodium stearate is the most widely used detergent, being the principal ingredient of soap. It belongs to the class of anionic surfactants, being the metal salt of a fatty acid. In non-polar solution the ionic head is attracted to metals, ionic and polar compounds, so acts as a wetting agent for metals when blended into a polymer. Unlike ITO, it can dissolve in molten polymers, so is not limited by particle size. It has the additional advantage of being very cheap.

7.7.4 Piezoresistive composite sensor materials

Piezoresistive composite materials were investigated as a potential simple micron-scale sensor device for embedded mechanosensory arrays. These materials consist of conductive powder filled elastomers that have been known since at least the 1940's [183] and used as strain sensors since the 1960's [184]. Fill level needs to be at a level where the particles are not quite in contact with each other in the relaxed material, in order that distortion of the material can close the gap and so alter the conductivity. Inevitably for approximately spherical particles, this is also close to the mechanical jamming fill level, hence it reduces the compliance and elastic limit relative to the unfilled elastomer.

Silicone micron nickel

Nickel powder[185] filled silicone rubber is an established method for making piezoresistive materials, Silicone rubber has a very high resistivity while nickel has good metallic conductivity, hence the composite has a very wide range of conductivities. The low modulus of silicone rubber allows large strains and relative movement of the nickel particles for small stresses. The spiky shape of the vapour precipitated nickel particles avoids trapping silicone between nickel particles as they are pushed towards each other. Together these produce a very high gauge factor.

A batch of piezoresistive composite was prepared by blending Toms Shore-A 22 silicone with approximately 50% by volume micron nickel powder. A number of difficulties were encountered with applying the material as a sensor.

- The silicone did not adhere reliably to the thermoplastic elastomers (EVA and SEBS) from which sensor fibres were being drawn.
- It was difficult to maintain good electrical contact with the surface of the material, especially in a fully flexible setting as needed for somatosensation.
- The scale of the powder particles (50 microns) was too large for the composite to be used at the scale of sensory nerve endings (100 micron diameter).
- Being a thermoset formulation it takes a long time to cure and new batches have to be made every time it is applied because it cannot be reworked later.

Silicone nano nickel

To solve the problem of scale, sub-micron nickel powder [186] was purchased. Being a 'nano-powder' alters the behaviour of Nickel, due to the very high surface area to volume ratio. Nickel is normally inert in air at STP, but Nickel nano-powder has to be protected from air to prevent rapid exothermic oxidation.

A new batch (0.5g) was prepared using the same Toms silicone. This batch failed to cure and remained liquid. Discussion with ACC Silicones concluded that the likely cause of the problem was poisoning of the platinum catalyst, due to the greater reactivity of nickel nano-powder. A sample of tin catalysed condensation cure silicone rubber was obtained, and a new batch made. The new rubber successfully cured and formed a working piezoresistive composite. Nickel nano-powder was observed to diffuse through silicone rubber over a period of days, in a manner akin to a solvent rather than a solid powder. This behaviour calls into question its reliability as a sensor material, and possibly its safety in the long term.

SEBS-gel nickel

To create a thermoplastic sensor material, a set of batches were prepared using SEBS-gel (Elasto 5000) 7.3.3. It was found that fill levels that retained elasticity were non-conductive. Fill levels that achieved some conduction became friable pastes. It is thought that this is due to the different composition of a gel versus a rubber. Specifically the solvent in the gel allows particles to move more freely, preventing them from being brought into contact, so failing to change the conductivity.

Silicone-gel nickel

To create a lower modulus sensor, suitable for embedding into gel structures, a set of batches were prepared using micron nickel and ACC silicones E-gel 7.3.2. Like the SEBS, this failed to produce conductivity while remaining a low modulus gel.

EVA nickel

A second attempt to make a thermoplastic sensor material using EVA elastomer (Elvax 40) 7.3.3 and micron nickel powder. Here it was found that fill rates required to make a working sensor resulted in

a very much stiffer material than pure EVA, and that hysteresis and creep of the shape of the material were severe.

Shortcomings of piezoresistive composites as sensors

While the possible solutions for thermoplastic piezoresistive composite have not been exhaustively searched, the results were not promising. Given the high price and challenging handling of nickel nano-powders that would be required to make adequately small sensors, it was concluded that MEMS sensors would be a better solution. There are many such designs already published. The remainder of this thesis was spent on challenges that do not yet have satisfactory solutions.

Chapter 8

Synthetic ligamentous Joints

The anatomy of human hands and dogs paws were used as the template for the demonstration specimens. Despite their differences of proportion, they are composed of the same tissues and share most of their basic topology of bones and ligaments.

The variation in anatomy of healthy individuals shows that the material properties may vary by an order of magnitude without altering the function. Developmental anatomy shows that ligamentous joints are formed by progressive differentiation of tissues, and are fully functional whilst entirely soft prior to calcification of the bones. What is critical is sufficient strain tolerance and the ratio of stiffness between the different materials.

Ligaments do not generally provide the stiffness of constraint provided by engineering joints in rigid materials. For example for any given ligament it is generally possible to manipulate the joint to a position where the ligament is slack enough to pass a probe under it.

The stability of ligamentous joints is also dependent on direction of the load and the action of the tendons/muscles around the joint. By itself the joint capsule, including ligaments, prevents dislocation of the compression bearing articular surfaces, but commonly does allow some separation of the joint surfaces if tension is not opposed by muscle contraction. Ligaments are generally much less substantial than the principal tendons of the joint and usually have less leverage. Further, the series arrangement and under-actuation of joints is such that a load not supported by a tendon will commonly cause rotation of other joints that either transfers the load onto a tendon, or releases the load altogether. The exception to this being the function of suspensory and check ligaments which act in parallel with muscles in “passive stay” mechanisms.

8.1 Nature of fibrous mechanisms

This chapter investigates methods to build emulations of anatomical ligamentous joints. The detailed influences of fibre-based mechanisms to the overall behaviours of the system is provided in the following sections:

- Chapter 1 Section 1.3 details the principles used to produce functional emulations anatomical

tissues and structures.

- The mechanism of these structures is covered in chapter 3 sections 3.3 to 3.5. In particular chapter 3 section 3.4 and Figure 3-1 illustrate the why *”Fibrous transmission of tension is very important because it saves weight and bulk, while making the joints tougher and more robust”* and *”also allows larger cross section area for transmission of compression, and larger radius of curvature where compressive force transmission occurs across a discontinuity,”* when compared to joints made of rigid materials.
- The specific mechanisms of each joint are detailed in section 3.3. The details of the mechanisms of the tendon networks and dermal structures are given in chapter 3 sections 3.4 & 3.5.
- Chapter 4 covers the combined effect of all the anatomical structures described in producing the sensorimotor function of the hand. In particular it shows how the structure creates favourable kinematics and passive dynamics for useful sensory perception and control.

It must be emphasised that the author does not claim the invention or discovery of any new mechanism. All of the information in chapters 1, 3 & 4 is well documented in the anatomical sciences, and references are provided.

8.2 Layup iterations

8.2.1 First prototype ligamentous joint

The first prototype ligamentous joint was a distal interphalangeal (DIP) joint. The bones were 3D printed in ABS on a Denford 3D (Ch.6.3.1) printer using the .stl files (Ch.6.2.1) produced from the MRI scan of the author’s right hand 6.1.1.

Polyaramide tows were attached by ‘clove-hitch’ knots around the distal phalangeal bone and laid across the joint to form the ligaments, figure8-1a. A temporary non-anatomical ‘dorsal’ ligament was included to stabilize the joint in the extend position during manufacture. The tows were held proximally with an elastic band while they were adjusted. Once the tows were tensioned, a thin polyamide tow was tightly wrapped over the tows, several times around the middle phalanx bone and tied to hold them at the correct lengths and paths. The entire structure was then painted with polyurethane rubber resin (Poly Optic 14-70, Ch.7.3.1), and impregnated into the fibres of the ligaments. The rubber formed the matrix of the ligaments and joint capsule, and their permanent attachment to the bones. Once the resin was cured, the dorsal ligament and dorsal aspect of the ‘joint capsule’ were cut to allow the joint to be flexed, figure 8-1b.

Assessment of result

The spatial resolution of printer and quality of the .stl surface mesh limited the accuracy of shape of the printed ABS bone. The size of the .stl file generated from the segmentation of the MRI scan could be quite large, and this caused problems of tractability for the software of the Denford 3D printer. The bones had a strongly lamellar texture from the print layers, which had to be aligned with the axis of

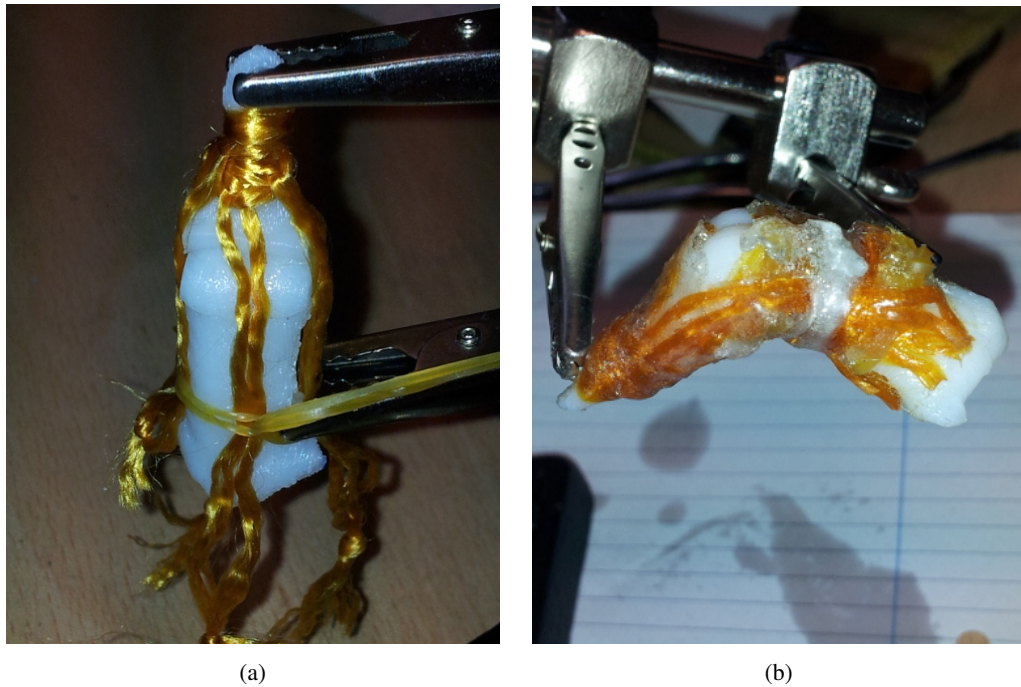


Figure 8-1: First prototype ligamentous joint, using ABS 3D printed bones on Denford (Ch.6.3.1) from MRI scan (Ch.6.1.1), Kevlar (Ch.7.5.3) polyaramide fibres and Poly-Optic 14-70 (Ch.7.3.1) polyurethane elastomer resin.

rotation of the joint to avoid friction. To achieve adequate strength in the ABS it was necessary to thick, three layer 'skin' and nearly solid 'fill' in the 3D print. The polyurethane rubber was not as easily stretched as had been hoped, hence the need to cut the dorsal joint capsule to permit flexion.

Despite these reservations, the joint flexed in the correct axis and was constrained against other motions. It demonstrated the feasibility of making ligamentous joints, and was deemed a satisfactory first iteration.

8.2.2 First multi-jointed finger

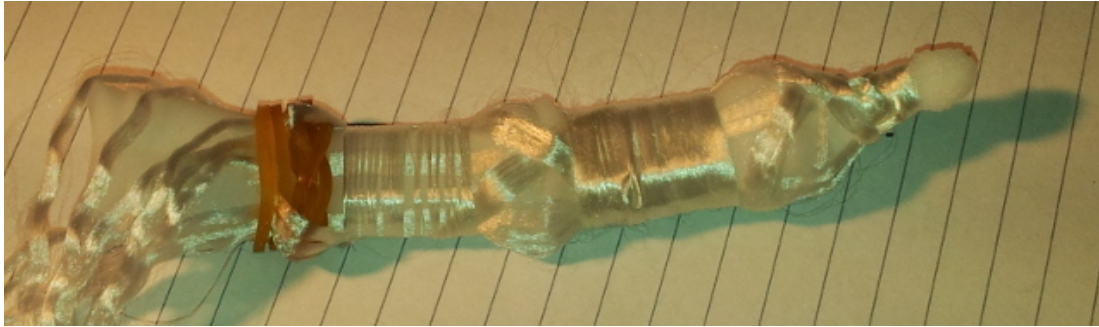
The first multi-jointed finger prototype used simplified CAD models of the phalangeal and metacarpal bones. Polyamide tows were laid along the medial and lateral aspects of the finger to replicate the effect of the collateral ligaments and wrapped helically, crossing on the palmar aspect of the joints to replicate the accessory collateral ligaments and volar plate, figure-8-2a. These fibres were then bound in place by polyamide fibres wound circumferentially around the bones, figure-8-2b. The bones were then coated in flexible polyurethane forming the joint capsule and the matrix of the ligaments, figure-8-2c.

Assessment of result

The use of simplified CAD models reduced the size of the .stl files and solved the tractability problem, however the geometry was clearly inferior to that of natural bones. Specifically the CAD model had



(a)



(b)



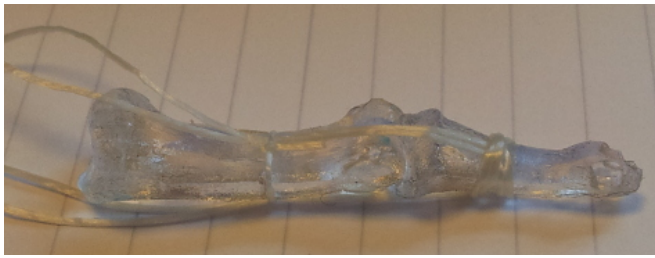
(c)

Figure 8-2: First multi-jointed finger, using ABS 3D printed bones from simplified CAD model, polyamide fibres and Poly-Optic 14-70 polyurethane elastomer resin.

angular vertices and edges at the joint margins that were liable to protrude. Refinement of the model to eliminate the shortcomings would bring it close to the geometry of natural bones, but would be labour intensive to achieve. For these reasons starting from natural bones would be more efficient, if the tractability problem could be solved.

The joints of the finger prototype worked reasonably well, though the stiffness of the polyurethane elastomer joint capsule was not ideal. The ligaments in conjunction with the joint surfaces were effective at resisting axial torsion and lateral flexion of the proximal and distal interphalangeal joints.

8.2.3 Polyurethane bones moulded from anatomy skeleton



(a)



(b)



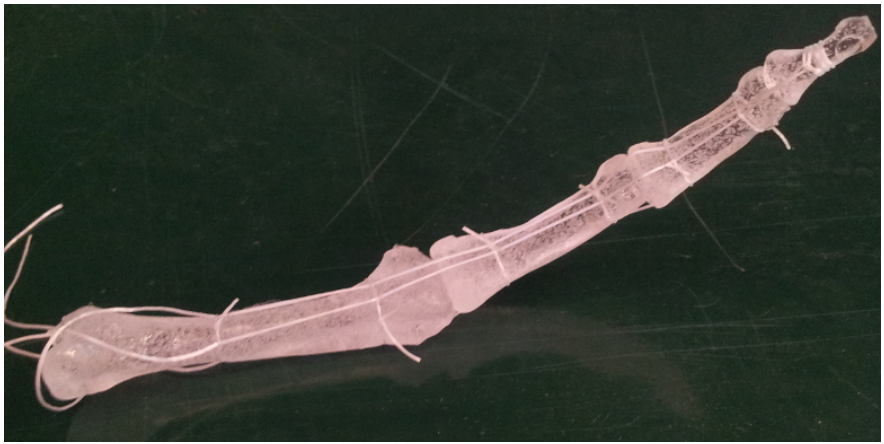
(c)

Figure 8-3: Layup of ligamentous joint using Poly-Optic 1410 rigid polyurethane bones cast from anatomy skeleton.

First polyurethane boned finger

Rigid polyurethane resin (Ch.7.2.1), was used for the next set of finger bones to provide smooth joint surfaces and correct anatomical geometry. Polyurethane moulds, figure-8-7a were taken from a human anatomy skeleton, itself derived from casts of a human skeleton. These moulds were then used to cast new bones in rigid polyurethane. The moulds were coated with petroleum jelly to prevent adhesion between the mould and the resin being cast in it. The result was much improved geometry and surface finish, figure-8-3a.

Elastane (commercial polyurethane-polyurea elastomer) thread was used as the initial stabilisation of the bones while laying up the ligaments. This had the advantage of allowing flexion and dislocation on any axis, but always returning the joints to the extended position, figure-8-3a. This allowed testing of the constraints of ligaments and flexion of joints during the layup process. Two separate sets of polyamide tows were used to simulate the accessory collateral ligaments (purple) figure-8-3b, and volar plate (blue) figure-8-3c. The joint surfaces were greased with petroleum jelly to prevent accidental bonding of the joint, prior to applying the polyurethane elastomer resin to the ligaments.



(a)



(b)



(c)



(d)



(e)

Figure 8-4: Polyurethane rubber matrix ligaments on rigid polyurethane bones

Second polyurethane boned finger

A second version of the polyurethane boned finger was made, with thicker tows of polyamide for the ligaments. Figures-8-4b-d show how the parallel fibres of the tows are laid flat on the surface of the bones.

High density polyethylene joint capsule



(a)



(b)

Figure 8-5: High density polyethylene joint capsule - to keep polyurethane rubber matrix of ligaments separate from rigid polyurethane of bones.

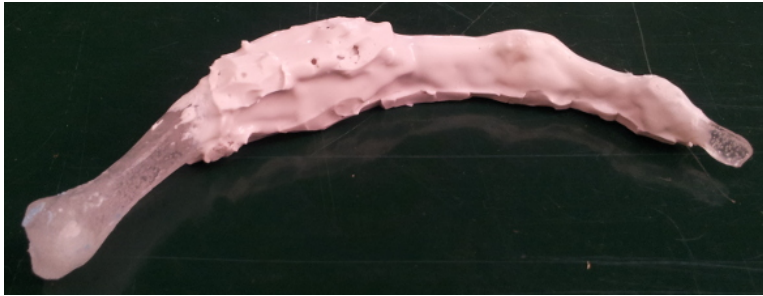
High density polyethylene (HD-PE) was used as joint capsule material, figure-8-5, to test if it could provide freer movement than the polyurethane rubber capsule. The HD-PE film is approximately 20 microns thick, reused from a supermarket shopping bag.

Assessment of result PU boned fingers

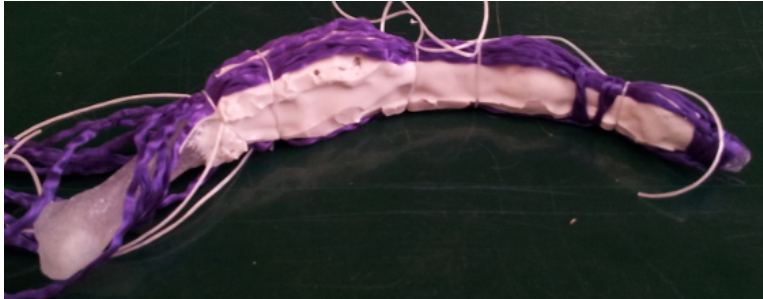
Polyurethane rubber on rigid polyurethane gave good adhesion and good infusion of the tows, providing secure anchoring of the ligaments. However Poly Optic 14-70 rubber was too stiff to allow low resistance flexion of the joints. PU bones needed lubrication between the joint faces to prevent excessive friction.

A critical limiting factor in the technique is the control of fibre placement, due to the difficulty of stabilising the tows until the PU rubber sets. The slow curing process with a recommended 'de-mould time' of 24-48hrs is also a problem with this technique. The most serious problem however was the creep under load of the Poly Optic 1410 rigid PU resin used for the bones.

8.2.4 Ultra soft silicone joint capsule and ligament matrix



(a)



(b)



(c)



(d)

Figure 8-6: Silicone joint capsule on polyurethane finger with polyamide ligaments.

To produce a finger with less stiffness in the joints, the third polyurethane boned finger used soft (Shore-A 6) silicone rubber (Ch.7.3.2) for the joint capsules and matrix of the ligaments. The bones

were first coated with silicone mixed with a thixotropic additive (Ch.7.3.2) to form a capsule around the joints, figure-8-6a. The silicone was then trimmed and the collateral and accessory collateral ligaments laid up, figure-8-6b-d. The ligaments were then infused with silicone, figure-8-6d.

Assessment of result silicone matrix on PU fingers

While the softer silicone matrix substantially reduced the resistance to flexion of the joints, it had weak adhesion to the PU bones. Consequently the joints were significantly less stable than with PU rubber matrix.

8.2.5 Moulded polycaprolactone bones



Figure 8-7: Polyurethane mould from anatomy skeleton bones to make polycaprolactone bones

To produce creep free, durable bones the low temperature thermoplastic polycaprolactone (PCL) (Ch.7.2.2) was press moulded in the same rigid polyurethane moulds that had been used for casting polyurethane bones, figure-8-7b. The resulting bones were less detailed than the polyurethane bones, but stiffer and free from creep under load. Due to the surface tension and viscosity of molten PCL the surface could be made locally very smooth. The hard semi-crystalline solid PCL presents a low friction surface in contact with most other materials, including itself.

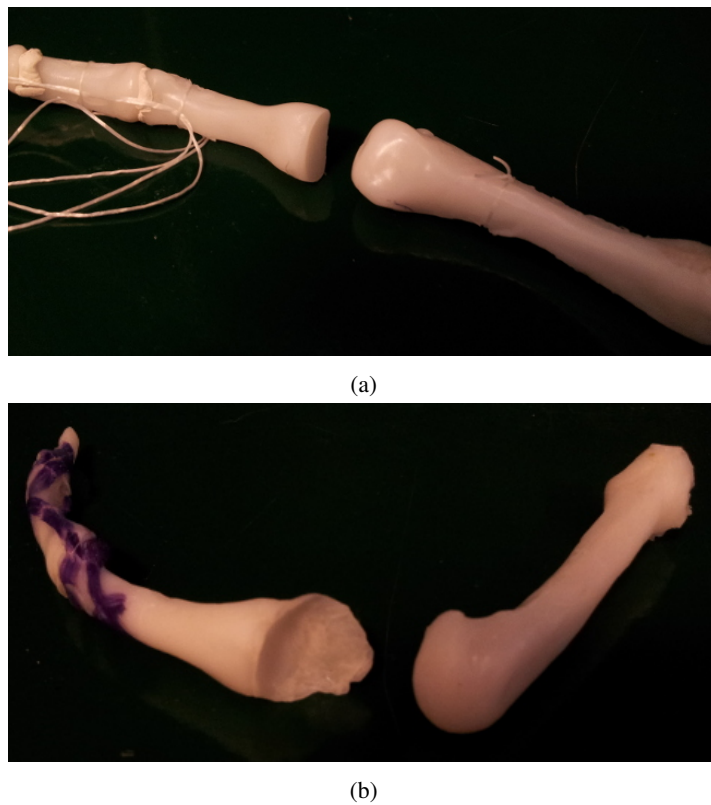


Figure 8-8: Polycaprolactone bone joint surfaces forged against each other.

Forging polycaprolactone joint surfaces

PCL melts at 60°C to a clear highly visco-elastic liquid which can be handled and worked by hand. This allows a special type of forming - hot against cold forging - to be applied to fit the joint faces to each other. One bone is kept cold, and therefore rigid, while the articular surface of the opposite bone is warmed with a heat gun until the surface melts. The joint is lubricated with paraffin oil to prevent direct contact. The bones are then pressed together and worked through their range of motion, taking care to keep the articular surfaces constantly moving to prevent fusion. The bones are then separated and cooled. The process is then repeated with the hot and cold bones reversed. The result is very smooth, matching joint surfaces that exhibit close fit and very low friction, figure-8-8a.

The working of molten PCL can also include drawing the material under tension. This was done for the MCP joint in figure-8-8b where the proximal margin of the proximal phalanx was drawn to increase the cupping around the condyle of the metacarpal bone.

Assessment of result of PCL bones

The hand press moulding technique was very quick, but imprecise and requires a mould which still needs to be shaped somehow. The bones are much stiffer than the polyurethane bones, but not as stiff as the 3D printed ABS bones. The surface finish is clearly superior to both PU and printed ABS, and this provides well fitting, low friction joint faces. As a joint surface material PCL is significantly harder than the hyaline cartilage of anatomical synovial joints. A key weakness of PCL as a bone material is its vulnerability to softening and deforming the whole bone when heated. This became an issue when heating it locally to weld other structures to it.

8.2.6 Thermoplastically welded ligaments



(a)



(b)



(c)

Figure 8-9: Polycaprolactone bones with thermoplastically welded polyamide ligaments and tendons, with silicone joint capsule

Connecting ligament fibres to PCL bones demands a different approach. The smooth surface of PCL does not provide strong attachment for polyurethane or silicone resins, but the low melting point of PCL allows polyamide fibres to be welded into the PCL matrix (Ch.7.2.2). This is possible despite the fact that polyamide is also a thermoplastic because the melting point of PCL 60°C is below $200^{\circ}\text{C}@0.45\text{MPa}$ [187] the heat deflection temperature of polyamide (Ch.7.5.2). (Note there are a variety of ways to draw polyamide-6,6 fibres, producing different levels of crystallinity leading to different softening and melting points, but all are well above that of PCL.)

A thermostat controlled soldering iron was found to be the most useful tool for welding fibres into PCL. The temperature setting being well above the melting point of PCL, but not so high as to cause rapid thermal decomposition of molten PCL, or damage to the polyamide fibres. The optimal

temperature setting depended on the particular soldering iron, as the actual temperature of the outer surface of the iron depends on the distance to the heat sensor. It should be noted that the tip becomes coated in molten plastic which needs to be cleaned off periodically as it degrades thermally above 220°C[188]. Not all soldering irons are mechanically suitable, because large lateral forces are applied to the tip when working the viscous molten PCL.

Good adhesion of fibres to PCL requires infiltrating the PCL into the tow and wetting of the surface of the fibres by the molten PCL to achieve a high surface area of contact between the two materials. Three techniques may be used to achieve this:

1. melting of the surface of the bone, followed by pressing the fibres into the molten PCL
2. adding more PCL on to the exterior of the attachment and working it into the underlying fibres
3. pre-impregnating PCL into the section of the tow to be welded, forcing out excess PCL, then pressing the impregnated tow onto the PCL bone

It was found that a combination of last and first techniques above produced the strongest attachment, with the least alteration of the shape and bulk of the bone. It was also best to work the PCL into the tow by stroking it towards the free end of the tow, while pulling the tow in the opposite direction. The attachment of polyamide to PCL in this way was found to be very strong. Approximately 10mm fibre length of weld was sufficient to exceed the strength of the fibres themselves, (Ch.7.6.2). This meant that even on the smallest bones, e.g. the distal phalanx, there was ample space to secure ligaments and tendons, without bulky knots or extra binding fibres.

Positioning and adjusting attachment of ligaments and tendons

When welding a tow of fibres to a bone, best positioning was achieved if the tow was initially attached only at the points of origin and insertion of the ligament, and the ends of the tow left free. This allowed the motion and constraint of the joint to be checked and if necessary the attachment could be rewarmed with the soldering iron and repositioned. A variant of this technique was to set the length of a ligament by keeping one of its attachment points soft, and allowing the action of the joint to pull through sufficient length of fibre to permit the desired motion.

Assessment of result of PCL bones with welded ligaments

Figure-8-9 shows the first PCL finger, with minimal polyamide ligaments. In figure-8-9c soft silicone rubber has been used to form the joint capsules. This was found to have too few fibres in the ligaments to provide adequate strength. The silicone depended on enmeshing the ligament fibres for its attachment, and did not adhere to the PCL bone matrix.

Figure-8-10 shows the second PCL finger, with greatly increased ligament fibres. This finger was comparable in strength, flexibility and robustness to a human index finger.

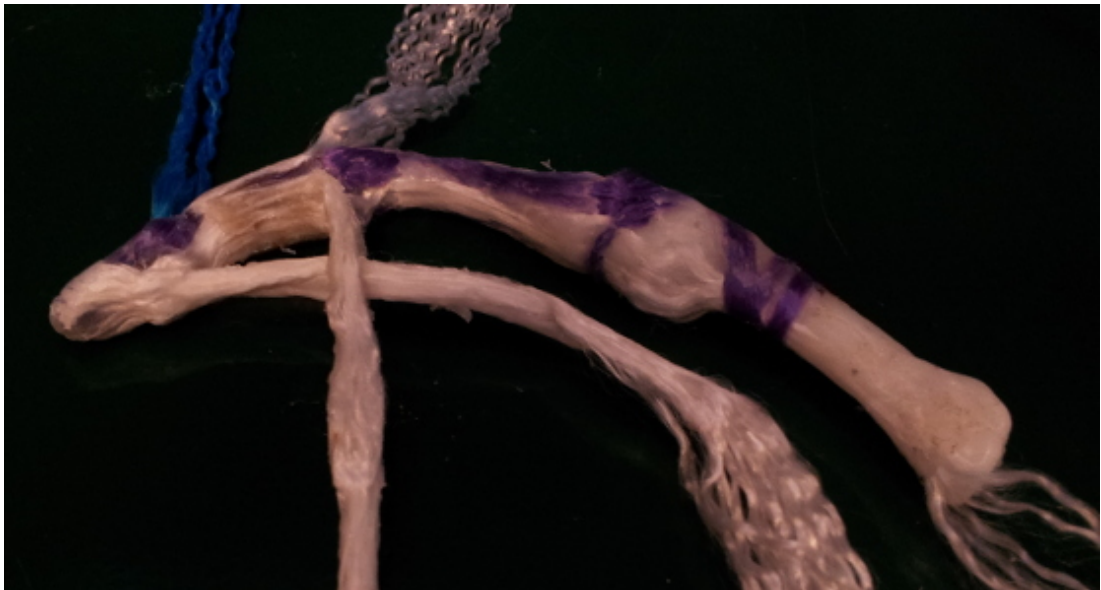


Figure 8-10: Polyamide ligaments welded into polycaprolactone bones

8.2.7 Polylactic Acid (PLA) Printed bones



(a)



(b)



(c)

Figure 8-11: 3D printing PLA bones on RepRap from MRI scans

Segmenting and printing

To escape the need for moulded bones, fused deposition 3D printing was examined again with a different printer, RepRap Mendel (Ch.6.3.2), and printing material, polylactic acid (PLA) (Ch.7.2.2). The primary advantage of the RepRap is that it is an open hardware design intended to be adapted and modified to print diverse materials. PLA is the default material for fused filament deposition printing on the RepRap. Depending on the formulation, PLA can have greater stiffness and strength than ABS, (table 7.2). The default printing nozzle however has a larger diameter (0.3mm) than that of the Denford (0.15mm) resulting in thicker layers and coarser print resolution, but also quicker printing.

There is a diversity of both free-and-open source and proprietary software available for both the RepRap firmware and for the preparation of files for printing. To facilitate reproduction and use of techniques from this thesis by others, only freely available free-and-open software was used.

The bones of a dog's front forelimb from the elbow down were segmented from a CT scan provided by [189]. The segmentation was performed using the 3DSlicer software (Ch.6.2.1). The .stl surface mesh files were inspected, smoothed and refined using MeshLab (Ch.6.2.2). The Slic3r printing software (Ch.6.2.2) was used to position the bone models relative to the print-bed such that the print layers were arranged along the length of the bones and parallel with the motion at the joint surfaces. The printing process was controlled using the PronterFace software (Ch.6.2.2), and the Marlin firmware (Ch.6.3.2).

Assessment of PLA print and segmentation

The bones were all printed with the 0.3mm nozzle, triple layer outer wall, dense honey comb fill, raft and support material. The resulting bones were hard, textured with ridges from the print layers, watertight, hollow, and less dense than water. The bones were very difficult to break by hand, though they could be crushed with pliers or shattered with a hammer.

The first test bone printed on the RepRap was the ulnar of a dog, figure-8-11a. The thicker nozzle of the RepRap resulted in heavier support material, figure-8-11b, which left a rough surface after removal, figure-8-11c. This problem was usually more significant with larger bones, which involved longer, heavier overhangs, and spent longer time on the hot printer bed.

The refinement of .stl meshes on MeshLab produced smooth surfaces that were better suited for 3D printing, and eliminated errors in the .stl files such as inverted facets. Refinement also reduced the file size by an order of magnitude and eliminated the tractability problems of the .stl files produced directly from the segmentation on Slicer. This meant that bone models segmented from clinical imaging were a practical option, which allows anatomical geometry to be exploited, keeping the design close to the working biological example being emulated. It would be possible to modify these models by scaling and warping if desired.

Coating PLA bones with PCL

To overcome the rough joint surfaces of the PLA printed bones PCL was rolled into thin sheets and fused to the surface of the PLA bones by melting with a heat gun and smoothing by hand. The finished

bones were translucent white in colour, showing the black pigmented PLA under the surface, once the PCL had fully cooled and returned to its semi-crystalline solid phase.

PLA has melting point $180^{\circ}\text{C} - 220^{\circ}\text{C}$, and heat deflection temperature $60^{\circ}\text{C}@0.55\text{MPa}$, (Ch.7.2.2). This means that molten sheets of PCL can be applied to cool PLA structures without deforming them, so long as excess force and heating are avoided. PCL and PLA share intermolecular bonding, are miscible with each other and form strong adhesion 7-12, as demonstrated in Ch.7.6.1.

Assessment of PCL-coated PLA bones

3D printing allows nearly free-form manufacture. PLA bones have good strength and rigidity, while the PCL coating produces the same advantages of smooth surface (concealing the rough PLA print surface, figure 8-12b) and weldability as solid PCL bones. The PCL coating on a PLA bone can be used to weld polyamide ligaments, with the same strength as PCL bones, but with less risk of heat softening the PLA bone, figure-7-14. PCL-on-PLA composite structure also has a beneficial toughening effect relative to pure PLA.

8.2.8 Dog's paw - complete carpus and digits

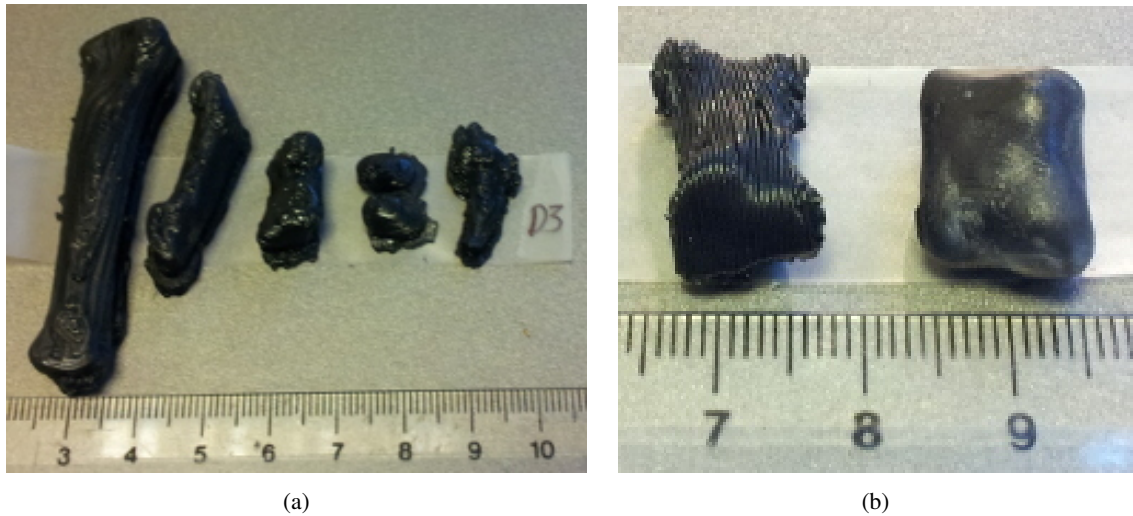


Figure 8-12: Paw bones printed in PLA then coated with PLC. a)Bones of the third digit from left to right: metacarpal, proximal phalanx, middle phalanx, paired sesamoid bones of the metacarpophalangeal joint, distal phalanx. b)Two middle phalanx bones, left - PLA bone with support material removed, right - coated in PCL, still molten and transparent.

The full set of canine phalanges, metacarpals, carpals, radius and ulna were printed. Once cleaned of support material they were then coated with a layer of PCL. Figure-8-12a shows the bones of the third digit (equivalent to the human middle finger) freshly printed with support material still attached. Figure-8-12b shows two middle phalanx bones before and after coating with PCL.

Layup of digits

The structure of the canine digits is described in Ch.3.7

After coating with PCL, strips of PCL rolled sheet were added to the articular surface such that the free ends of the strips extended palmar and dorsal to the joint surface to form the volar and dorsal plates of the joint. The articular surfaces of the digits were then forged against each other as in Ch.8.2.5. Polyamide collateral ligaments were welded to the PCL coating by the method described in Ch.8.2.6. The PCL volar plates were fused with the polyamide palmar check ligaments. The dorsal plates were fused with the extensor tendon slips. Polyamide transverse fibres were fused into the volar plates and continued either side to form the accessory collateral ligaments. At the MCP joints the sesamoid bones were fused with the PCL volar plate of the proximal phalanx.

Layup of palm

Despite the difference in geometric proportions, the structure of the canine palm is topologically very similar to that of the human palm described in Ch.3.3 and Ch.3.4. Because the articular ligaments of the inter-metacarpal joints are intimately connected with the retinacular ligaments of the flexor tendons,

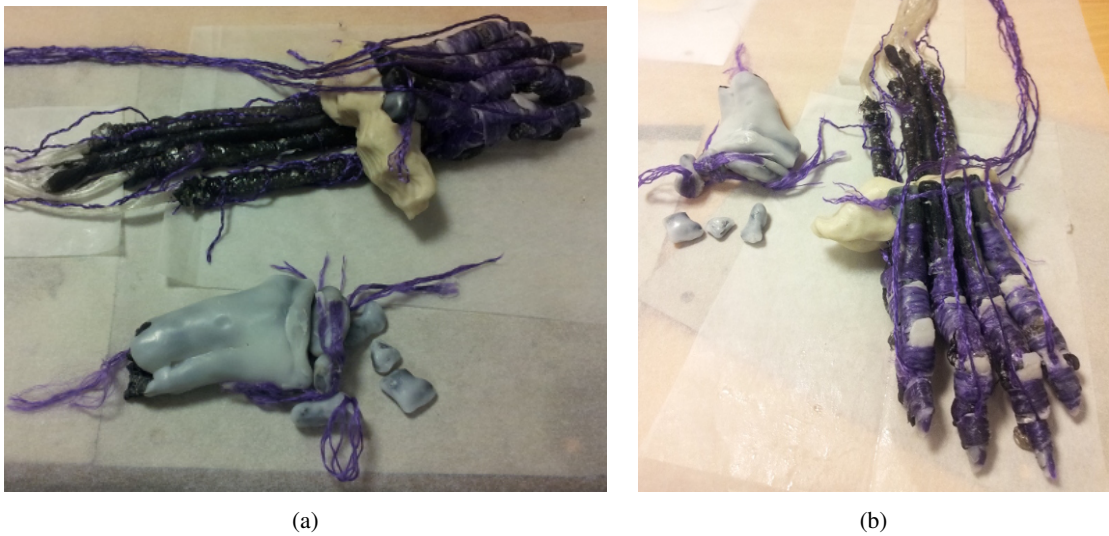


Figure 8-13: Paw digits and carpal bones

the flexor tendons and tendon sheaths had to be constructed before assembling the palm. The details of the how the flexor system was constructed are given in Ch.9.1.7.

The completed digits, including metacarpal bones and flexor tendon sheaths, were assembled into the palm by constructing:

1. The dorsal, palmar, and cruciate ligaments of the proximal inter-metacarpal joints.
2. The deep transverse palmar ligament connecting the palmar plates of the MCP joints, proximal to accessory collateral ligaments and first annular pulley ligament.
3. The natatory ligament (blue band of polyamide fibres connecting the palmar aspects of the first annular retinacular ligament, figure-8-14b).
4. The septae of Legueu and Juvara and transverse fibres of the superficial palmar fascia (purple transverse band proximal to the natatory ligament in figure-8-14b).

Layup of carpus

The structure of the canine carpus is described in Ch.3.7



(a)



(b)



(c)



(d)



(e)



(f)



(g)

Figure 8-14: Paw palm and carpus

Assessment of the paw



Figure 8-15: Paw : flexibility of the palm

The paw as constructed was robust, flexible, and reproduced the range of motion of anatomical canine paws. Figure-8-14e shows the range of flexion achieved by the carpal joint. Figure-8-15 shows the flexibility of the paw palm and digits in distributing load on an uneven surface.

This is an important advance because it is the first time that the complex fibrous structure of the palm with multiple bone-rays has been built. This allows the kind of constrained compliance seen in the anatomy of human palms, chapter-4, as opposed to the hinged plate palms of existing robotic hands section-2.1, [18, 24, 23]. It also demonstrates the feasibility of building an anatomical wrist mechanism, because while the kinematics of this carpus are different from the human carpus, the anatomical tissues are the same, therefore the construction techniques can be transferred.

A key problem that was encountered in constructing the paw was that several of the interphalangeal joints were accidentally fused due to their PCL joint faces becoming too warm. Also this paw still lacks an elastomeric soft tissue joint capsule, and neither the SEBS nor the silicone elastomers adhere well to either PCL or PLA.

8.2.9 First finger with PCL-SEBS matrix soft tissues

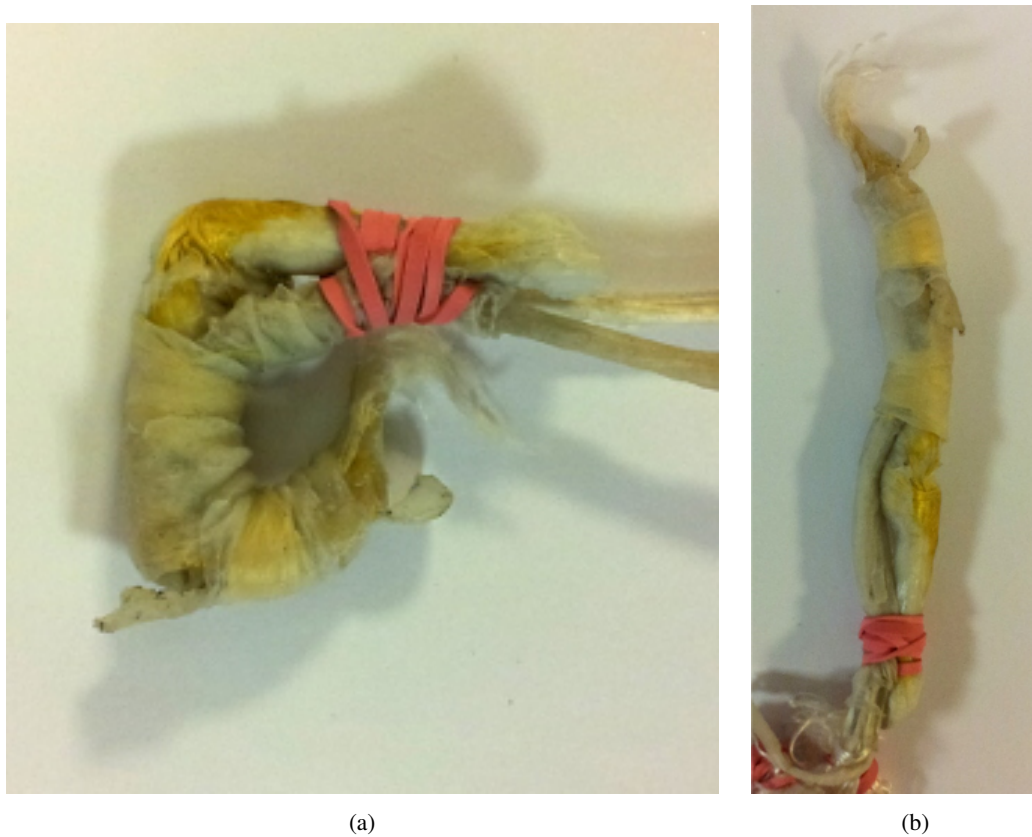


Figure 8-16: The first finger with blended SEBS-PCL soft tissue matrix. (Note: The digital flexor sheath and tendons are included in these images. The red elastic band serves as the palmer fascia that would be built if this finger were integrated into a hand.)

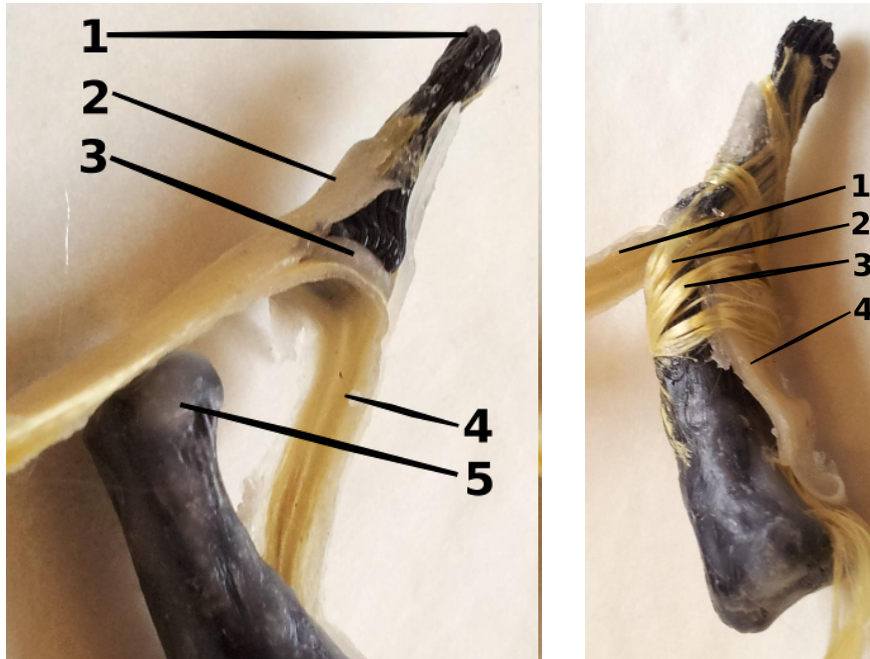
To create a soft matrix for the joint capsules and ligaments, PCL was mechanically blended with SEBS and rolled into thin sheets, (Ch.7.4.1). The resulting material was soft, rubbery and resilient to strains of around 40%, while being able to bond to PCL. To maximise the ability of ligament fibres to adhere to the SEBS-PCL blend and to resist the higher melting point of the SEBS, polyaramide (Kevlar, Ch.7.5.3) fibres were used. The blended SEBS-PCL sheet was applied by wrapping the joints then fusing it into the ligaments by heating with a heat gun.

Assessment finger

Figure-8-16 shows the assembled finger including its flexor tendon sheath. The SEBS-PCL blend lacked the degree of resilience, abrasion and tear resistance of SEBS-gel or SEBS rubber. It did however make the finger slimmer and more supple than previous iterations. A critical shortcoming with this iteration was that the blended SEBS-PCL rolled sheet used for the joint capsule matrix was not as elastic as the matrix of anatomical joint capsules. This tended to clash with the rigidity of the PCL lamina in the dorsal plate.

8.2.10 Second finger with SEBS matrix soft tissues

laminated joint structures



(a) 1)distal phalanx, 2)insertion of distal extensor tendon slip, 3)pad of SEBS-PCL, 4)volar plate - SEBS surface of laminated strip, 5)condyle of middle phalanx - PCL coated.

(b) 1)dorsal plate of extensor tendon slip, 2)co-lateral ligament directly connects the bones, 3)accessory co-lateral ligament stabilizes the volar plate, 4)volar plate of the check ligament.

Figure 8-17: Laminated joint surface layout: PCL and SEBS do not adhere to each other when molten, preventing fusion of the joint during layup. Laminated graduated blends of SEBS and PCL used for the distal joint surface present PCL face to distal phalanx, and SEBS face to the proximal joint surface.

To create opposing joint faces that would not fuse if they become overheated during manufacture, a new technique was developed to present SEBS as the opposing distal joint surface, facing PCL on the proximal joint surface. SEBS is immiscible with both PCL and PLA due to differences of intermolecular bonding (Ch.7.6.4). In order to be able to bond SEBS-gel (Ch.7.3.3), to the PCL coated bones the two thermoplastics were mechanically blended and rolled into thin sheets. A stack of sheets with progressively changing ratios from pure SEBS to pure PCL on opposite faces was laminated into a single thin sheet.

A ribbon of composite SEBS-gel-PCL film, section(7.6.1), was laminated with polyaramide fibres on the PCL side. One ribbon was placed running palmar-dorsal on the concave articular surface of the distal bone, with the SEBS side facing the proximal bone. Additional ribbons were placed on the dorsal and palmar surfaces of the distal bone and laminated to the first ribbon to form the check ligament of the volar plate and extensor tendon slip, (fig.8-17a). Pads of blended PCL-SEBS-gel were added to the portions of the volar plate and extensor slip adjacent to the distal bone, to emulate the fibrocartilaginous

pads of the anatomical structures (fig.3-19a&8-17b).

Assessment of laminated joint structures

The pad of SEBS-PCL on the distal joint face was too thick, making this structure softer than ideal, so reducing the stability of the joint a little. The ribbons of laminated SEBS-PCL, ('3' in figure-8-17a) were stiffer than ideal due to the rigidity of the PCL face of the laminate. Without lubrication the SEBS-gel face produced high friction in the joint, though with paraffin oil the friction was greatly reduced.

The SEBS-PCL laminate technique was successful in producing joint faces that could not adhere to each other, graduated stiffness in the dorsal and volar plates which helped the stability of the joint, and in presenting an SEBS adherable surface on the bones to facilitate attachment of SEBS-matrix soft tissues. The joint was stronger and closer to the anatomical joint in its graduated stiffness and cohesion of materials than the previous iteration, resulting in an equally slender and more robust joint.

Construction of second finger with SEBS soft tissues

A set of fingers for a hand were printed and laid up using the laminated SEBS-PCL method for the joint surfaces, following the pattern of the anatomy, (Ch.3.3.1 and 3.3.1). Polyaramide(PAr) was used for the ligaments, in order to provide a wide temperature tolerance for infusing SEBS-gel matrix. Polyamide deep and superficial flexor tendons and associated polyaramide flexor retinacular ligaments were fitted to the finger to assess the range of motion. Details of the tendon system are provided in Ch 9.1.9.

At this stage thermoplastic welding allowed sufficiently precise fibre placement and adjustment to improve the emulation of the fibre paths of anatomical ligaments.

Paths of ligaments of inter-phalangeal joints

Figures 3-18 and 3-19 show the structure of the anatomical proximal and distal phalangeal joints. This iteration of the finger reproduced the following structures:

Volar plate is a three layered structure comprising from palmar to dorsal:

transverse fibres continuous dorsally with the accessory collateral ligaments and palmarly annular retinacular ligament of the flexor tendon sheath.

longitudinal fibres forming the palmar check ligament, originating from the middle of the palmar aspect of the proximal bone, and inserting on the palmar aspect of the distal bone 2-3 millimetres distal the proximal margin of the distal bone.

cartilaginous pad forming the contact surface between the volar plate and the condyles of the proximal bone, over the distal end of the plate.

membranous region forming the thinner, flexible proximal half of the plate, containing only the longitudinal fibres and their SEBS matrix

Collateral ligaments fibres originate from the sides of the condyles of the proximal bone, at the centre of curvature of the condyles, and insert on the ventro-lateral aspect of the proximal margin of the distal bone.



(a)



(b)

Figure 8-18: Second SEBS finger

Accessory collateral ligaments fibres originate from the dorso-lateral aspect of the condyles, and insert into the volar plate of the palmar check ligament. The fibres connect across the volar plate, forming the transverse fibres of the plate.

Camming action of the metacarpo-phalangeal joints

Precise positioning and adjustment of fibre length allowed emulation of the camming action of the metacarpo-phalangeal (MCP) joints, (Ch.3.3.1). The origin of the collateral ligaments on the metacarpal bone is dorsal to the centre of curvature of the joint surface of the metacarpal condyle. This means that the collateral ligaments are slack when the MCP joint is extended, but come into tension as the joint is flexed. This has the effect of allowing yaw of the MCP joint for abduction/adduction of the fingers while the joint is extended, and progressively constraining abduction as joint is flexed.

Assessment of the finger

The resulting fingers match the dimensions of the musculo-skeletal components of the hand in the MRI image, leaving the normal anatomical space for dermal and sub-dermal structures to be added. This is important because robot fingers are usually thicker than human fingers of the same length and lack the soft pads and other dermal structures.

The joints (MCP, PIP and DIP) allow the normal anatomical range of flexion-extension, while providing constraint against yaw and axial rotation. As with the previous iteration, oil lubrication of the joint surfaces was required to reduce friction. Unfortunately the collateral ligaments of the proximal and distal inter phalangeal joints were not set tight enough, resulting in unwanted laxity and yaw at these joints. Having the articular ligaments dry (without matrix) in the interior of the joint was a cause of friction that was not eliminated by paraffin lubrication.

8.2.11 Final iteration



(a)



(b)



(c)

Figure 8-19: Final finger, return to simple joint surfaces and soft joint capsule, a) unpigmented transparent PLA bones, proximal and middle phalanges already coated in PCL, b) densely laid polyaramide ligament fibres, c) joint capsules formed of a thin layer of SEBS rubber wrapped and fused into ligaments.

The final iteration changed the way that the SEBS-PCL laminate was used. Here it was applied specifically to rigid bone surfaces to facilitate the adhesion of high and low modulus SEBS-gels, (table 7.4). Laminate was used to form the distal joint face, but not the dorsal and volar plates. Once the articular ligaments had been welded into the PCL coating of the bones, (figure 8-19b), the laminate was applied to the bones over the origins and insertions of the ligaments, but not to the flexible region of the

ligament. The matrix of the ligaments and joint capsules was then formed by wrapping the joints with high modulus SEBS-gel sheet (Elasto 880101) and fusing it into the fibres by briefly heating with a heat gun (figure 8-19c). Paraffin oil lubrication was sealed into the joint by the joint capsule to maintain low friction between SEBS and PCL joint faces.

Assessment of the finger

The SEBS joint capsule adhered securely to the bone where the SEBS-PCL laminate had been laid, and not in the joint cavity where the PCL surface of the bone remained. This produced a sealed joint capsule that retained the lubricating paraffin oil. (Note that it is essential that any oil in contact with SEBS not contain cyclic or double bonded hydrocarbons as these would weaken or dissolve the SEBS)

Eliminating PCL from the dorsal and volar plates eliminated the 'lumpiness' due to excess rigidity that it gave these structures. The high modulus SEBS-gel joint capsule and ligament matrix was substantially more resilient than the SEBS-PCL blend, and an adequate approximation of the anatomical joint capsule. With an all SEBS matrix for the volar plate (and tendon slips/dorsal plate later) the joint was supple and slender with low friction, good constraint and good range of movement.

8.3 Discussion

8.3.1 Key features of technique

1. the use of multiple matrix materials of stiffness ranging from rigid to low modulus hyper-elastic,
2. exploiting intermolecular forces of different polymers to control adhesion/non-adhesion of materials,
3. use of thermoplastic welding of the matrix of the composite to achieve accurate fibre placement,
4. higher modulus reinforcing fibres in soft (hyper-elastic) matrices creating extreme anisotropies,
5. fibres fine enough to
 - provide high surface area to cross-section area ratio for strong adhesion to the matrix
 - be easily flexible without suffering fatigue,
 - not cause compressive or flexural stiffening,
6. fibres not spun or braided (i.e. avoid small radius bending),
7. fibres not in abrasive contact with anything,
8. fibres cross matrix boundaries creating topological connections in a deformable structure,
9. ligament fibre paths matched to the motion due to joint surface shape - producing either constant or joint angle dependent constraint as needed.

Together these features integrate material composition with mechanical structure to produce a functional machine as a single piece deformable mechanism.

Benefits of thermoplastic welding

The central component of the technique is the use of thermoplastic welding of the matrix of the composite to achieve accurate fibre placement. This allows tows to be individually laid, immediately fixed and adjusted during the layup. It also points to how the process could be automated to achieve precise and repeatable construction by laying fibre tows and thermoplastic tapes.

The strength of the weld between a fine fibre and a compatible thermoplastic matrix makes it possible to have compact attachment regions for ligaments that match the anatomy being emulated. It also makes it straightforward to estimate the quantity of ligament fibre needed to impart a given strength to a joint.

Scale of emulation

To reproduce the function of anatomical fingers and paws at 1:1 scale it was necessary to emulate the tissue structure at a scale between 300-100 microns. Human finger anatomy involves many layers of ligamentous and tendinous tissues, hence it is important that these are kept thin to achieve slender dextrous fingers.

8.3.2 Comparison to other joint types

Joints of rigid materials

It is well understood that for a cable and a chain made of the same material and having the same tensile strength, the chain has to be heavier and bulkier than the cable. The chain is approximately three times the diameter of the cable, because of the need for the rigid links to loop around each other to transmit tension as compression between the contact faces of the links.

Relative to joints made only of rigid materials, ligamentous joints enjoy a similar advantage to that of a cable over a chain, the difference is that joints also transmit compression as well as tension to form a truss. Ligamentous joints provide a simpler path for compressive and tensile forces carried by the column of bones and the tendons respectively. Transmission of tension by continuous fibres in ligaments provides the same advantage as in a cable. In transmission of compression ligamentous joints benefit from a larger radius of curvature at the compression bearing surface for the same external dimensions of the joint, because the concave face does not need to encircle the convex face. The larger radius of curvature provides a greater area for transmitting compression, so for the same joint surface pressure greater force can be transmitted.

These advantages in geometry mean that for materials of similar performance a ligamentous joint can be made more compact than a rigid joint of the same strength. This is a critical advantage for the fingers of a hand. A second advantage is toughness, in that fibrous structures are generally more resilient to impacts than rigid structures. A third advantage is in complex joints such as the carpus, which allow very large range of motion, combined with large forces.

Flexural joints

The major difference between flexural and ligamentous joints is that flexural joints lack a rigid compression bearing structure. Consequently ligamentous joints have a greater capacity to bear compressive loads due to the large area of direct contact between the bones. This translates to the ability to support greater actuation force by tendons, for a given size of joint. Flexural and ligamentous joints share the ability to deflect to off axis loads, which is beneficial both for complying to unknown surfaces in grasping, and to avoid breaking in collisions.

8.3.3 Conclusions

Contrary to previous expectations [24][18] direct emulation of the mechanical properties of histological tissues and anatomical structures is feasible. The key distinction is to emulate the mechanical, but not necessarily the chemical or biological properties of the materials.

The ability to produce tough ligamentous joints opens the possibility of exploiting known anatomical mechanisms whose function is hard to match with conventional mechatronic techniques.

Chapter 9

Tendon Networks

Tendon actuation is found extensively in vertebrate anatomy. It offers a way to produce lighter more compact lower limbs and digits by keeping muscle mass closer to the body core. The under-actuation of joints by tendons creates important reflexes by linking joint torques along the kinematic chain. Tendon actuation requires stabilization of tendon paths.

Tendons are used in many robots in legged locomotion, flexible spines and humanoid hands. However, artificial tendons and tendon stabilisation systems have very different material properties and structure from anatomical tendon systems. Artificial tendons used in robots suffer rates of fatigue failure and friction much higher than anatomical tendon systems.

Artificial ligamentous joints, as described in Ch.8 require compatible tendon networks and reticular ligaments to hold the tendons in their correct paths. This chapter presents the development of a method for making tendons modelled on the mechanical properties of the materials and the mechanism of anatomical tendon networks.

9.1 Layup iterations

9.1.1 First flexor sheath

The first prototype for the digital flexor tendons and sheath (figure 9-1) was built on the ligamentous joint prototype, (figure 8-1). The deep digital flexor tendon was a tow of parallel polyamide fibres attached to the distal phalanx by a clove hitch knot and impregnated with silicone gel[150] matrix. The sheath was formed of high density polyethylene film thickness approximately 20 microns, wrapped around the tendon and lubricated with silicone oil[190]. The Sheath was held in place by the annular ligaments of the distal and middle phalanx. These were formed by wrapping polyamide tow around the phalanx and tendon sheath and infusing it with polyurethane rubber[1] to form the matrix of the annular ligament and bond the annular ligaments to the phalanges.



Figure 9-1: First test flexor tendon sheath - polyamide tendon with silicone gel matrix and silicone oil tendon fluid, high density polyethylene sheath, polyamide annular ligaments with silicone gel matrix

Assessment of result

The tendon in sheath with annular ligaments had moderate friction, and was improved by the addition of lubrication oil to the sheath. It approximated the anatomical proportions and allowed a functional range of flexion of the joint.

9.1.2 First tendon actuated finger

First flexor sheath on whole finger

The second tendon prototype was built by the same method on the first whole finger prototype (8-2), but had both deep and superficial flexor tendons and extensor hood. Annular ligaments A0, A2, A4, A6 (Ch.3.4.1) were implemented holding the flexor tendons in their sheath to the meta carpal, proximal middle and distal phalangeal bones respectively, figures 9-2c and 9-2d.

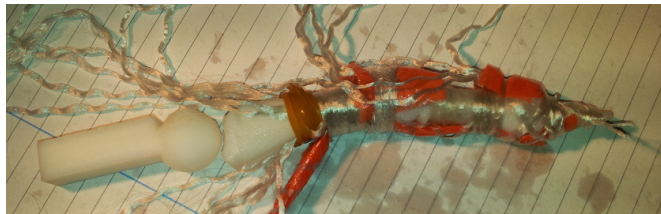
Once the polyurethane matrix of the annular ligaments had cured, silicone rubber Toms Shore-A 22 (Ch.7.3.1), was painted on with thixotropic agent (Ch.7.3.2). This formed the joint capsules and fascia surrounding the flexor sheath, figure 9-2e.



(a)



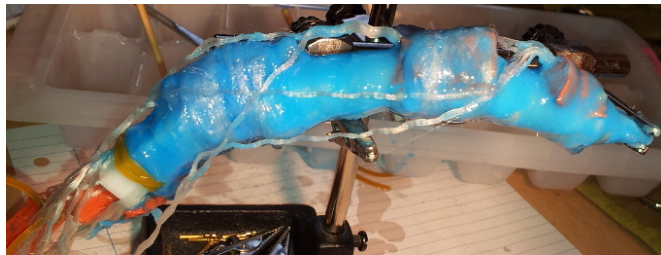
(b)



(c)



(d)



(e)

Figure 9-2: Layup of flexor tendon sheath

First extensor hood

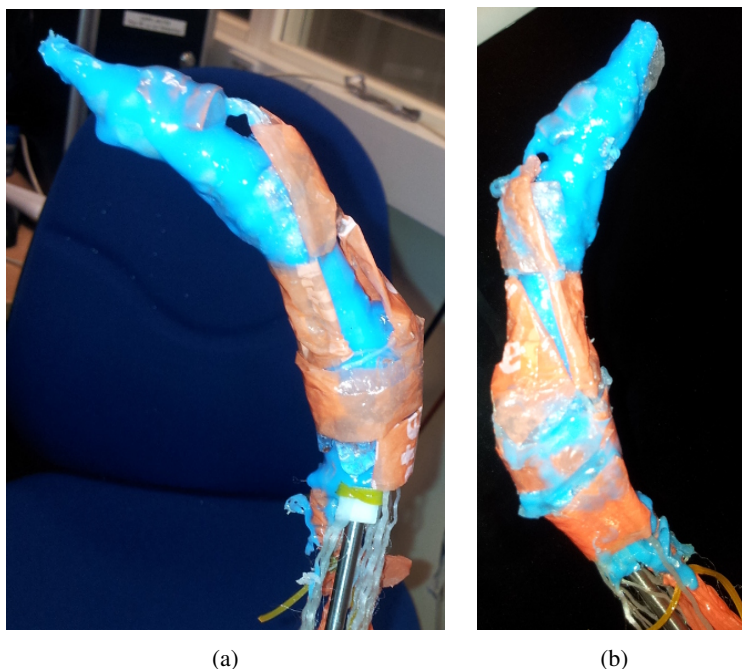


Figure 9-3: Layup of extensor hood with high density polyethylene film and silicone gel.

The extensor tendons (figure 9-2e), were lighter than the flexor tendons, each branch being a single polyamide (PA-66) tow. Soft silicone gel (Ch.7.3.2) was infused into the tows to form the matrix of the tendons and bind the fibres together. A system of hood aponeuroses (figure 9-3), were made from HD-PE film to reproduce the topology and approximate geometry of the anatomical extensor tendon hood 3.4.3. The HD-PE film was folded around the PA-66 tows, and bonded with a minimal coat of silicone gel. Pads of silicone gel were placed under the hoods to lubricate their motion over the denser silicone rubber.

Assessment of first tendon actuated finger

The flexor tendons with their sheath and annular ligaments were effective in actuating the finger, and capable of delivering an appropriate level of force. Under-actuation of the flexor tendons successfully reproduced the hooking motion of the finger around objects striking the palmar surface of the finger, figure 9-4c. However, friction between the tendons and sheath was clearly higher than in anatomical fingers. The Tomps silicone rubber joint capsules and deep fascia prove too stiff in their resilience, contributing to friction in flexing.

The extensor apparatus was functional, being able to extend and abduct/adduct the finger. The silicone gel pads were notably effective in eliminating friction between the extensor tendon network and the underlying structures. A shortcoming of the silicone gel is that it adhered primarily by extreme mechanical softness producing 'tack', and could be rolled or peeled off. The HD-PE film was too

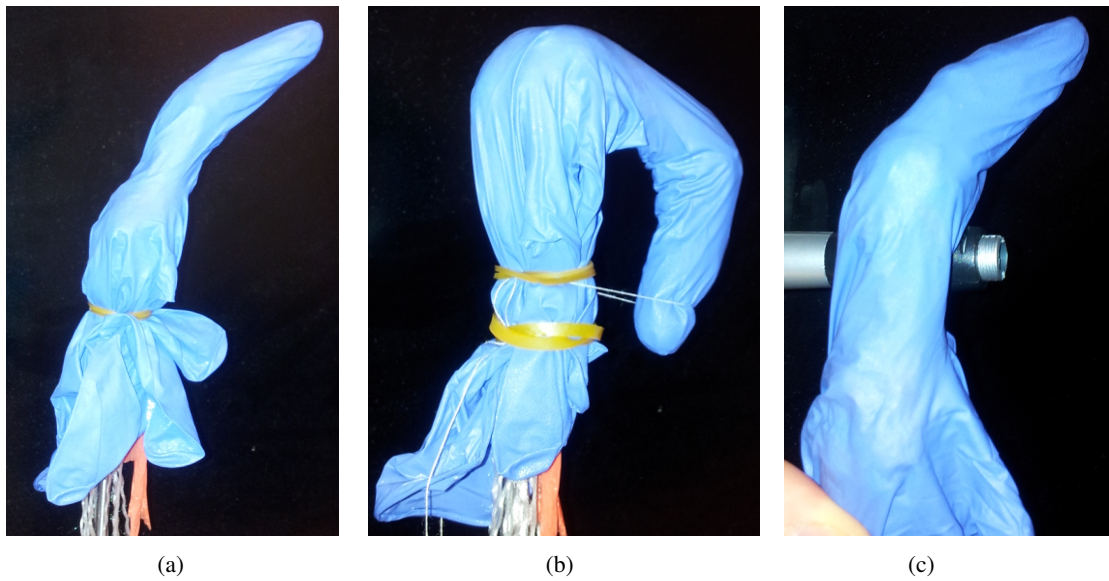


Figure 9-4: Flexion of finger.

inelastic and behaved as a semi-rigid film. This meant that it did not comply well to the shape of the surface over which it moved. A material with more fibro-elastic and surface conforming behaviour is needed for better load balancing across the network, and smoother movement. Transverse retinacular ligaments are essential for stabilisation of the extensor hood.

9.1.3 Second tendon actuated finger - polyurethane rubber matrix retinacular ligaments

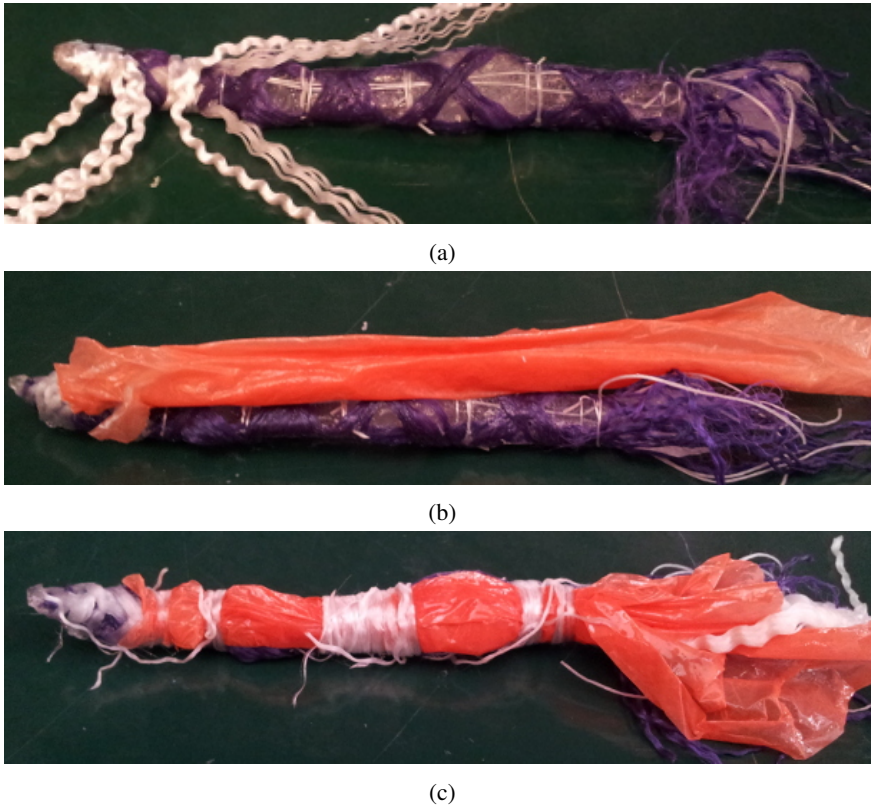


Figure 9-5: High density polyethylene flexor tendon sheath

The second set of tendons were built on a cast polyurethane ligamentous finger, Ch.8.2.3. The same flexor sheath construction as the first finger was used. PU rubber (Poly Optic 14-70) was used as the matrix of the annular ligaments, figure 9-5c. The extensor tendons were not implemented on this finger.

Assessment of result

This finger was found to be too stiff, partly due to the PU rubber matrix in the articular ligaments. There was a need to improve the technique to reduce the bulk of the tendons and sheath to keep finger slender. There was also a need to reduce friction to allow passive flexion/extension and ensure low wear.

9.1.4 PCL matrix tendons, silicone gel lubrication pad and EVA flexor sheath



(a)



(b)



(c)



(d)

Figure 9-6: PCL matrix tendons, silicone gel lubrication pad and EVA flexor sheath, built on the first PCL boned finger.

The next flexor and extensor tendon system was built on the first moulded PCL bone finger, (Ch.8.2.5).

The PA-66 tendons were attached by welding them into the PCL with a soldering iron (Ch.7.6.2), in the same way that the articular ligaments had been.

A small amount of PCL was worked into the length of the tendons to serve as a sparse matrix. This allowed the tendons to be hot pressed to a thick ribbon-like form, and to bond to each other. This facilitated the formation of the chiasma of the superficial digital flexor (Ch.3.4.1), where it splits into two branches that attach to the middle phalanx either side of the deep digital flexor. It also enabled the extensor tendon network to be created by bonding the branches of the tendons to each other to form the proximal and distal slips, the inter osseous and extrinsic extensor tendons. The triangular ligament (Ch.3.4.3) of the distal extensor slip was formed by fusing a thin sheet of PCL between the distal branches of the interosseous and extensor tendons. Pads of silicone gel were placed under the extensor tendons on the dorsal aspect of the condyles of the proximal and middle phalanx, and metacarpal bones.

The flexor tendon sheath was formed by rolling a tube of rolled EVA (Elvax 150) film around the flexor tendons, cutting and sealing the margin with a soldering iron. The flexor sheath was lubricated with paraffin oil and bound in place with annular ligaments.

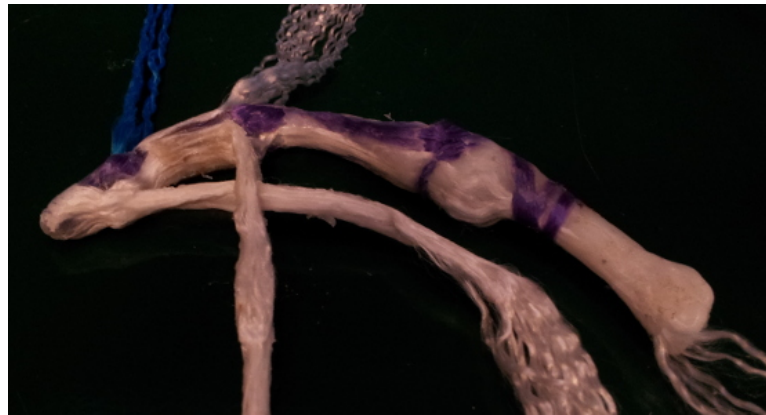
Assessment of result

The EVA tendon sheath was not tough enough, and tended to abrade and tear. This was partly due to the weld along its margin being weak. The tendons and annular ligaments were well attached, strong & compact. The silicone gel lubricant works, but needs better attachment. The soft silicone rubber joint capsules were frayed by extensor tendons.

9.1.5 Dry PCL finger - individual extensor tendons

The next iteration was built on second PCL boned finger (Ch.8.2.6). This iteration was built 'dry', i.e. no soft matrix material or elastic gel layers were used. The tendons were much more substantial than the previous iteration, figure9-7. As in the previous iteration, sufficient PCL was applied to the flexor tendons to bind the fibres together, while leaving the tendons flexible.

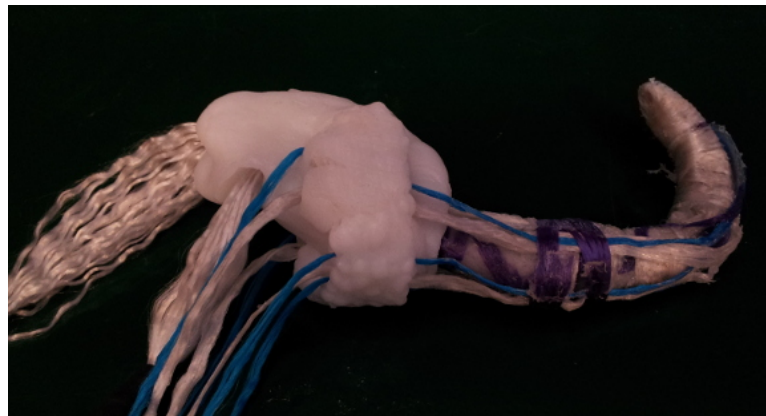
Each branch of the extensor tendon network was routed through a separate channel in a block of PCL attached to the head of the metacarpal bone. This allowed testing of the effect of each branch independently and in combination. Knowing the potential effect of each branch aided adjustment of lengths and routes of the branches in later iterations.



(a)



(b)



(c)

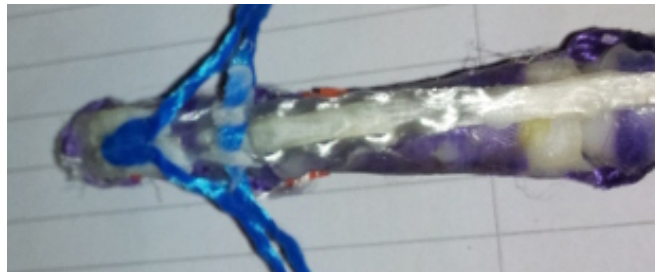
Figure 9-7: Dry PCL finger with individual extensor tendons, for investigation of individual tendon effects.

9.1.6 Second dry PCL finger

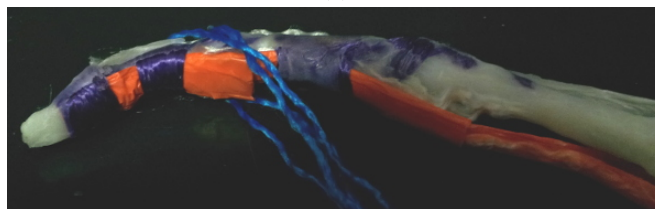
A second dry PCL finger (figure 9-8) was made with tendon and ligament bulk intermediate between the previous two iterations.



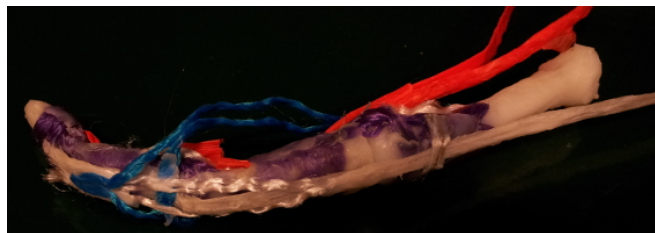
(a)



(b)



(c)



(d)

Figure 9-8: 'Dry' finger with no matrix in flexible regions of articular ligaments, polycaprolactone matrix in extensor tendon slips and flexor retinaculum annular ligaments, fused high density polyethylene matrix and sheath for flexor tendons.

Fused HD-PE flexor sheath

The design of the tendon sheath was changed, (figure 9-8a). The new tendons were formed by folding HD-PE film tightly around PA-66 tows, wrapping in foil and pressing with a hot iron to fuse the film to the tows. The sheath was formed by wrapping several layers of HD-PE film, outside the foil then fusing the sheath to itself by pressing with a hot iron. The foil layer was removed, leaving a semi-rigid flattened ribbon tendon inside a similarly flattened tube of HD-PE sheath. The tendons in their sheath were then fixed in place with PA-66 annular ligaments as before. Both water and paraffin oil were trialed as lubricants for the new flexor sheath.

Extensor network

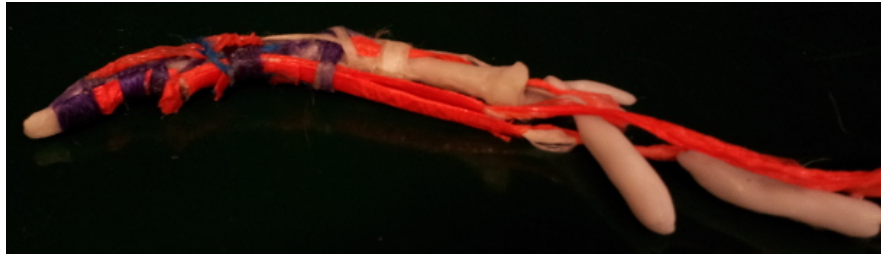
The triangular ligament of the distal extensor slip, the transverse and spiral oblique retinacular ligaments (blue tows, figure 9-8, Ch.3.4.3), of the extensor apparatus were implemented, but not the dorsal hood connecting the interosseous tendons. The sagittal bands were implemented as a fixed channel through which the extrinsic extensor tendon ran, as opposed to the anatomical sagittal bands which adhere to the tendon and slide with it over the dorsal aspect of the metacarpal condyles. The use of polyamide tendon slips with PCL matrix allowed repeated adjustment of the relative lengths of the extensor tendon network, until a functional network was achieved. Notably the branches of the extrinsic extensor tendon to the distal extensor slip were located more dorsally at the proximal interphalangeal joint than they are often portrayed in anatomy texts, and stabilized in that position by the transverse retinacular ligament. No lumbrical tendons were implemented.

Assessment of result

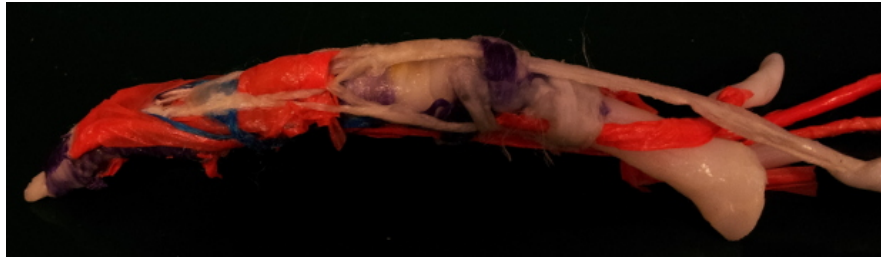
The resulting finger was very strong, robust and slender, with a good approximation of the anatomical range of movement. With paraffin lubrication of the joints and tendon sheath friction was acceptable, though higher than in anatomical fingers.

Importantly it was able to demonstrate the mechanism of the extensor network. Specifically that tension on both the interosseous tendons and the extrinsic extensor are required to extend the finger. The interosseous bilaterally without the extrinsic extensor, extend the interphalangeal joints but flex the metacarpophalangeal joint (MCP). Conversely the extrinsic extensor alone starting from fully flexed would extend only the MCP. Guidance of the interosseous tendons at the MCP is critical for the mechanism to function. Abduction/adduction of the finger required the combination of unilateral tension on one interosseous tendon combined with the extrinsic extensor.

The spiral oblique retinacular ligament assisted in extending the distal interphalangeal joint (DIP) when the proximal interphalangeal joint (PIP) is extended, and also flexing the PIP when the DIP is flexed. The SORL limits the phase difference between the DIP and PIP, and preventing the finger from arriving at positions where the joints could not be actuated. The triangular ligament of the distal extensor slip and the transverse ligament keep the tendon branches leading to the distal extensor slip stabilized on the dorsal aspect of the finger.



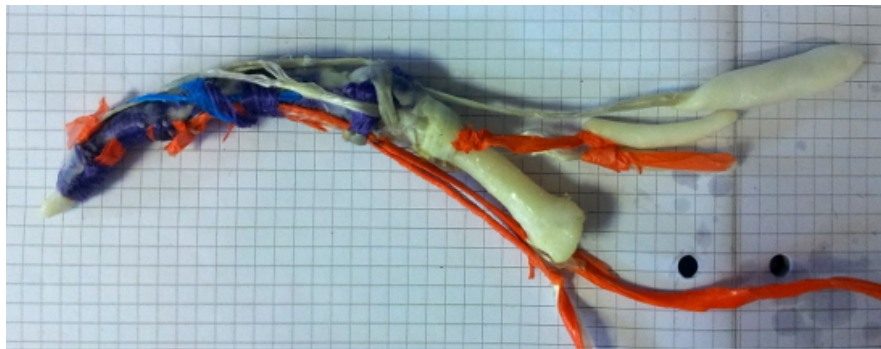
(a)



(b)



(c)



(d)

Figure 9-9: 'Dry' finger - complete

9.1.7 Canine paw and carpus - flexor and extensor tendon networks

An emulation of a dog's paw and carpus (Ch.3.7) with ligamentous joints described in [191] and Ch.8.2.8, was fitted with flexor and extensor tendons including palmar fascia and carpal tunnel. The lumbrical and interosseous tendons were omitted as were the dew claws (1st digit, remnant of the thumb).

Flexor sheaths and annular ligaments of the digits

The tendons were attached by clove hitches to the middle (superficial flexor) and distal (deep flexor) phalanges. The polyamide fibres of the flexor tendons were then infused with a matrix of soft SEBS-paraffin gel on a hot plate. The matrix of the two branches of the superficial flexor were fused together to form the chiasma through which the deep flexor tendon runs, immediately proximal to the insertion of the superficial flexor on the middle phalanx.

The flexor tendons were then wrapped into a tube of SEBS-gel-stocking fabric composite (Ch.7.6.3). This was sealed along its length with a soldering iron to form the flexor tendon sheath (figure.9-10). Paraffin oil was then infiltrated down the inside of the sheath to lubricate the excursion of the tendons.

The sheathed flexor tendons of all four digits of the paw were then laid along the palmar aspect of the bones, (Fig 9-11). Annular ligaments of polyamide tows in a PCL matrix were wrapped around the flexor sheaths at the proximal and middle phalanges.

Flexor retinaculum of the palm

The flexor retinaculum of the palm is part of both the tendon network and the ligamentous constraint of the joints, hence it is also discussed in Ch.8.2.8. The sheathed tendons were laid across the palm and carpus. The natatory ligament (Ch.3.4.1) was formed by a band of polyamide tows (blue fibres, figure-9-12) connecting the proximal margins of palmar side of the second annular ligament, palmar to the first phalanx.

The septae of Legueu and Juvara (Ch.3.4.2) and transverse fibres of the superficial palmar fascia (Ch.3.4.2, and purple fibres proximal to the blue natatory ligament in figure-9-11) were formed by wrapping polyamide-PCL tows around the metacarpals. Short pieces of PCL rolled sheet were placed between the flexor sheath and the transverse fibres to produce more gradual margin to the constraint on the flexor sheath.

Carpal tunnel

The carpal tunnel (Ch.3.4.2) was formed by laying the flexor tendons in their individual sheaths across the carpus between the malleolus of the hamate bone and the accessory carpal bone, (figure.9-11). The transverse carpal ligament was then formed by laying a broad band of polyamide tows across the tendons, connecting the accessory carpal bone to the hamate bone (figure.9-12c).

Carpal flexor tendons

The radial and ulnar carpal flexors (white tows, figure.9-11) were attached to the malleolus of the hamate bone and the accessory carpal bone and continued to the metacarpal bones as ligaments.

Superficial palmar fascia (longitudinal fibres)

The longitudinal fibres of the superficial palmar fascia (white tows, figure.10-2) were fixed at their origin to the transverse carpal ligament, and inserted on the natatory ligament on the palmar aspect of the 1st annular retinacular ligament, and finally on the proximal phalanges.

Extensor tendons

A layer of SEBS-paraffin gel was laid on the dorsal surface of the paw from the digits to the radius, (figure-9-13). The extensor tendons were tied to the distal phalanges, and laid on the gel layer. A series of polyamide tows were then laid orthogonally over the extensor tendons and welded to the annular ligaments on the palmar side of the paw. Lightweight (10 Denier) stocking material was then drawn over the paw. The extensor tendons, orthogonal tows and stocking material were then fused with the gel layer by heating them with a fifty watt halogen lamp until the surface of the gel began to melt, (figure-9-15).

Assessment of canine paw and carpus - flexor and extensor tendon networks

Both the extensor and flexor tendons provided robust actuation of the carpal, metacarpal, and interphalangeal joints. The major problem with the technique was that several of the joints of the digits were accidentally fused during the attachment of the annular ligaments of the flexor tendons. The PCL matrix used in the flexor retinacular ligaments made them significantly stiffer than the anatomical flexor retinacular ligaments.

The stabilising orthogonal tows and the gel layer under the extensor tendons, were thicker than necessary. The stocking material was essential to present a tack-free surface. While it was constructed as it was to allow the underlying structures to be seen, a paw for use on a robot would need a dermal covering. A variant of the gel-stockings composite (Ch.7.6.3) using a single sided pile fleece fabric would provide an emulation of furred skin.



(a)



(b)

Figure 9-10: Paw digits and metacarpals assembled with tendons, radius and carpal bones partly assembled.

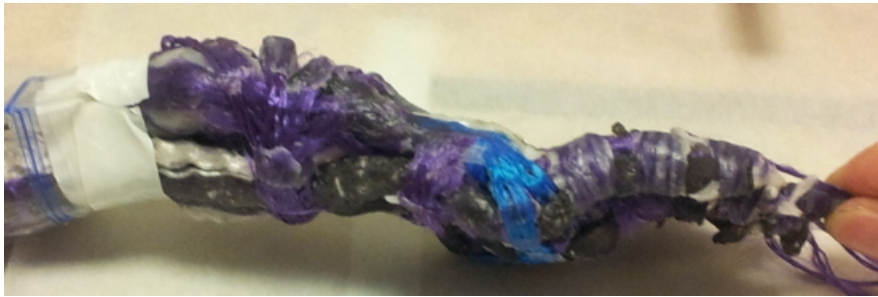


(a)



(b)

Figure 9-11: Paw, palmar fascia. Blue fibres - natatory ligament.



(a)



(b)



(c)

Figure 9-12



(a)



(b)

Figure 9-13: Hyper-elastic SEBS-paraffin gel layer laid under the extrinsic extensor tendons.



Figure 9-14: Paw extensor retinaculum - lateral view



Figure 9-15: Paw extensor retinaculum - dorsal view



Figure 9-16: Paw superficial palmar fascia longitudinal fibres - white tows

9.1.8 First SEBS-PCL flexor sheath



(a)



(b)

Figure 9-17: The first SEBS-PCL flexor sheath, built on the first finger with SEBS-PCL matrix soft tissues. Figure-8-16 repeated.

A new finger flexor tendon iteration was built using soft blended SEBS-PCL matrix materials, on the first finger with SEBS matrix soft tissues for the ligamentous joints (Ch.8.2.9). The flexor tendons

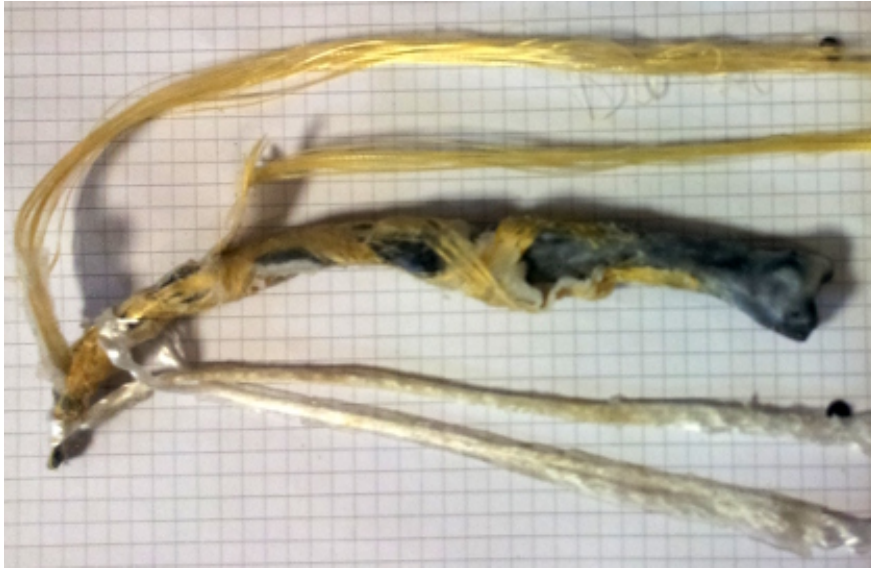
were filled with an SEBS-PCL matrix by working them with a soldering iron. The chiasma of the superficial flexor was formed by fusing together the matrix of the branches of the tendon. A rolled film of SEBS-PCL was wrapped around the tendons and welded closed along its length to form the flexor sheath. The second and fourth annular ligaments were wound around the sheath and the proximal and middle phalanges using polyaramide (PAr) tows. A sheet of SEBS-PCL was then wrapped around the annular ligaments and fused to them by heating briefly with a heat gun. Paraffin oil was infiltrated down the flexor sheath to lubricate it.

Assessment of result

The SEBS-PCL sheath requires lubrication with paraffin. With repeated use blended SEBS-PCL film is vulnerable to abrasion and tearing. The articular ligaments lost some of their constraint after repeated use of the heat gun to fuse layers to SEBS-PCL film into joint capsules and retinacular ligaments.

Because of these shortcomings no extensor tendon network was built in this iteration.

9.1.9 Structured flexor sheath



(a) Tendons prior to assembling the sheath



(b) Assembled flexor sheath and annular ligaments

Figure 9-18: The second finger with SEBS matrix soft tissues (Duplicated from Fig8-18)

After a revision of the ligamentous joint structure (Ch.8.2.10), a new finger was built (Ch.8.2.10), and flexor and extensor tendon networks built on it. The new iteration of tendon networks experimented with the high tack (contact adhesion) of SEBS films wrapped onto surfaces, especially other SEBS layers, as a way to reduce the use of heat to adhere layers.

The flexor tendons were polyamide (PA-66), and were infused with an SEBS-paraffin gel matrix. A lining was made on the interior surface of the tendon sheath using film from a freezer bag. This film provisionally identified as medium density polyethylene MD-PE blown film approximately 10-20 microns thick, on the basis of its tangible properties relative to the HD-PE and LD-PE films used



Figure 9-19: Structure of flexor sheath - (1)PA-66 tendons with SEBS-paraffin gel matrix, (2)MD-PE lining, (3)Elasto-5000 layers around sheath and as (4)matrix to annular ligaments, (5)polyaramide (PAr) tows of annular ligament, (6)PCL coated PLA bone.

previously. This lining was the wrapped with a covering of Elasto 5000 SEBS gel.

The structure relied substantially on the contact adhesion (tack) of SEBS gels layers to each other. Additional SEBS-gel was melted into the annular ligaments at the palmar aspect of the flexor sheath, using a soldering iron. The space around the flexor tendons, inside the lining of the sheath was lubricated with paraffin.

Assessment of result

The largely dry (matrix free) annular ligaments were not as compact or secure as hoped. The SEBS film wrapped around the PCL coated PLA bones did not have adequate attachment by friction alone, a bondable interface layer is needed. It would be better to fuse the SEBS matrix into tows before laying them, to minimize the heating required to fuse together annular ligaments, and to minimise the total thickness of the flexor retinaculum. It is essential to keep each layer as thin as possible to prevent the finger becoming bulkier than anatomical fingers. SEBS matrix in the flexor tendons did not produce the very smooth and slippery surface of anatomical sheathed tendons, though paraffin lubrication the contact with the MD-PE lining of the sheath was effective. Adhesion between the MD-PE lining and the SEBS-gel of the sheath was strong where they were welded.

9.1.10 First SEBS-gel film lubricated extensor hood



(a)



(b)



(c)

Figure 9-20: Laying extensor tendons between lubricating hyper-elastic gel laminae.

A first prototype of hyper-elastic gel lubricated extensor tendon mechanism was built over the flexor apparatus (previous section, above). The finger was wrapped with a film of SEBS-paraffin gel. Pol-yaramide was used for the extensor tendons, and laid 'dry' (without a matrix) on the surface of the gel layer (figure-9-20a). Tows were wrapped around the finger to form the transverse retinacular ligament and the sagittal bands ('TRL' & 'SB' in figure-3-49). A second layer of SEBS-paraffin gel was wrapped on top of the tows. Finally a layer of Elasto-5000 SEBS-gel was wrapped over this to form the outer

non-tacky epidermal layer.

Assessment of result

The low modulus gel layers did allow excursion of the extensor tendons, but the overall resistance was too high due to the splinting effect of the stiffer outer layer, and friction associated with the flexor apparatus. The stabilisation of the extensor tendons was ineffective. The lack of matrix in the extensor tendons caused their fibres to splay too far. If a higher modulus tendon matrix had been present it would have provided secure attachment between tendon branches and to the extensor retinacular ligaments. Embedding in low modulus matrix was insufficient to provide these.

9.1.11 Final finger

Ionomer flexor sheath

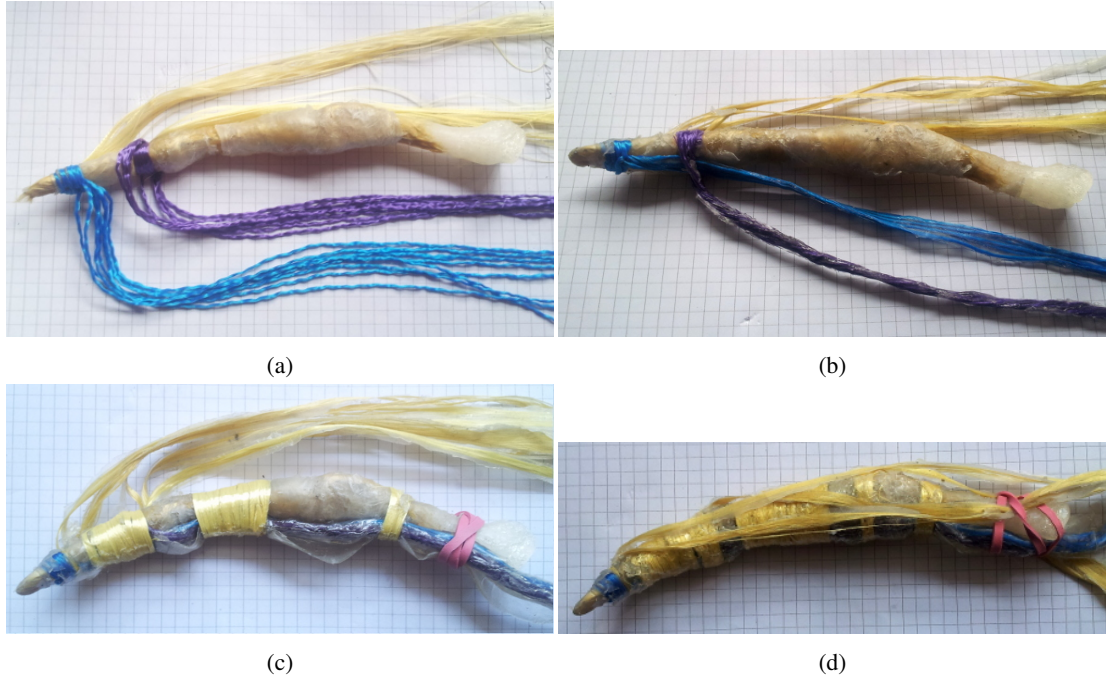


Figure 9-21

The final iteration of the tendon networks was built on the final ligamentous finger (Ch.8.2.11) with SEBS joint capsules and SEBS-PCL laminate as a bonding layer on the bones, (figure-9-21a).

The polyamide tows of the deep (blue) and superficial (purple) flexor tendons were fused into flat ribbons with Elasto-5000 SEBS matrix (figure-9-21b). Smooth surfaces were created by folding sheets of baking paper around them and pressing the tendons with a hot iron.

To provide a smooth contact surface and reduced bulk elastomeric tendon sheath, Surllyn (Ch.7.3.3) plasticised with paraffin was used to construct the flexor sheath. A broad seam was pressed with a hot iron and folded onto the palmar surface to create a thicker layer to the sheath on interior palmar surface of the annular ligaments, where the main pressure is exerted by the flexor tendons. Polyaramide tows were used for the annular ligaments as in the previous iteration, but with no SEBS wrapping around the sheath or phalanges, (though the SEBS of the joint capsules was present).

Assessment of result

The flexor sheath was much more compact than the previous iteration. However it was necessary to cut away the welded seam in the gaps between the annular ligaments to allow the sheath to flex freely. This caused the sheath to rupture along its side, exposing the tendon fibres and causing significant friction.

After a number of months the SEBS-gel matrix of the tendons began to peel away. This revealed that the SEBS-gel had not wet into the interior of the tows and was not strongly adhered to the fibres.



Figure 9-22

Fraying of the SEBS caused substantial friction in the aged prototype. When first made the SEBS-gel had provided a smooth envelope around the tendons. This had high friction when dry, by very low friction when lubricated with paraffin.

Modifying SEBS to alter its inter-molecular interactions would be one way to improve matrix adhesion. A number of graft polymerisations allow side groups to be added to either the styrene or ethylene-butylene blocks. For example, malate side groups can be added to the rubber mid-block, and produce hydrogen bonding with polyamides which improves adhesion between SEBS and polyamides. Malate grafted SEBS polymers are available commercially [192] or custom polymers can be ordered from laboratory suppliers [193].

SEBS rubber fused tow extensor network

The final iteration of the extensor hood used polyaramide tows fused into flattened ribbons with Elasto-5000 SEBS-gel matrix. This matrix allowed the branches to be fused to each other to form the tendon network. An hyper-elastic lubricant layer of SEBS-paraffin gel was wrapped around the digit beneath the extensor tendons, adhering to the SEBS-PCL laminate coating on the bones and the Elasto-5000 SEBS gel of the joint capsules, (figure-9-21).

Short tendon sheaths for the interosseous tendons at the MCP joints were made with Surlyn-paraffin blend as for the flexor tendon sheath. The sagittal bands were then wrapped around the MCP joint and welded to the first annular ligament, the interosseous sheaths, and the extrinsic extensor tendon, thus stabilising both the interosseous sheaths and the extrinsic extensor.

The transverse retinacular ligament was laid under the branches of the distal extensor slip, and over the proximal extensor slip at the level of the PIP. The ends of the transverse retinacular ligament were welded to the palmar side of the second annular ligament. The relative lengths of the branches of the interosseous and extrinsic extensor tendons to the proximal and distal extensor slips were then adjusted, before welding the branches to each other and the transverse retinacular ligament to fix their lengths.



(a) Flexion of MCP, PIP, and DIP due to contraction of the deep digital flexor tendon.



(b) Flexion of the MCP and PIP but not the DIP due to contraction of the superficial digital flexor tendon.



(c) Flexion at MCP, extension at PIP and DIP due to contraction of interosseous tendons.



(d) Extension of the MCP, PIP and DIP by contraction of the extrinsic extensor and both interosseous tendons.



(e) Passive hyper extension of the finger at the MCP.

Figure 9-23: Flexion-extension of the finger, shown with first prototype skin and subcutis fitted.

Testing finger motion and force

The joints allowed anatomical range of motion, and it was possible to actuate the finger via the tendons, figure-9-25. The flexor tendons allowed substantial force to be exerted 9-24.



Figure 9-24: Demonstration of the strength of the finger as initially built. The flexor tendons were able to actuate the finger with force comparable to a human finger. Shown here lifting a fire extinguisher, approximately 5kg.

Correction to extensor hood

Testing the extensor mechanism then showed that the tendon slips were falling too far palmarly on the sides of the flexed finger and failing to extend it. The interosseous hood and triangular ligament of the distal extensor slip were then constructed to correct this. A membrane of SEBS-paraffin gel was laid over the branches of the extrinsic extensor, and a second membrane of Dryflex 880101 was laid over this such that the branches of the interosseous tendons to the distal extensor slip lay along the margins of the Dryflex membrane.

Polyamide pseudo-monofilament thread was then repeatedly looped around the interosseous slips and dorsally over and through the margins of the Dryflex membrane. This formed an interosseous hood with a smooth stiff Dryflex 880101 face sliding over the underlying extrinsic extensor slips. The triangular ligament of the distal extensor slip was formed in a similar way supporting branches of the distal extensor slip from its insertion to the transverse retinacular ligament.



Figure 9-25: Adduction-abduction of MCP by action of the interosseous tendons

Assessment of extensor tendon network

The this iteration encountered several issues which indicate improvements to be made:

Constraint The correction to the extensor network was crude but served to demonstrate the necessity of the hood membrane at the proximal phalanx, and triangular ligament at the middle phalanx, as well as the transverse retinacular ligament. The problem of the branches of the distal extensor slip falling down the sides of the phalanges is the key challenge of the extensor tendon network. If the tendon slips pass to the palmar side of the axis of rotation of the proximal interphalangeal joint, they become flexors of that joint, making extension very difficult.

Bulk The thickness of joint capsule material under the annular ligaments and of the lubricant gel layer was too great and reduced the stability of the structure. It is critical to keep each layer as thin as possible to minimise bulk.

Friction The extensor tendons have a severe mechanical disadvantage and consequently are very sensitive to any friction in the flexor tendon system or joints. It would be very useful to have a shear thinning lubricant fluid and an elastomeric gel which exudes

that fluid under pressure, to emulate the behaviour of synovial joint fluid and hyaline cartilage (Ch.3.1.6). Polymer and oligomer 'synthetic' additives to refined mineral oils can potentially be used in this way.

Solvent diffusion One of the problems encountered with the prototypes after months of storage was that the gels became stiffer apparently due to loss of solvent volume. It would also be useful to replace the paraffin solvent used in the present work with a higher molecular weight paraffin that would not evaporate over time. It would also be useful to have co-block polymers of a variety of rubber mid-block lengths. The mid-block length determines the extensibility of the polymer network, and therefore the modulus of the rubber and the maximum swelling of the gel. This would allow high and low modulus laminae to be in equilibrium with each other with respect to diffusion of the solvent, so preventing deterioration due to solvent migration between structures. An alternative solution would be the use of so called 'bottle brush' polymers which exhibit gel-like behaviour without any solvent fraction.

Adhesion to fibres Over the long term the adhesion of SEBS to polyaramide (PAr) is better than to polyamide (PA-66) but is still poor relative to the adhesion of both PA-66 and PAr to PCL. It would be very useful to have an elastomer capable of hydrogen bonds or other strong bonds with the fibres.

9.2 Discussion

The technique so far is tantalizing but not yet adequate. The paw and the second dry PCL finger were the most successful prototypes. For each of the issues there are a number of possible avenues to solving them.

9.2.1 Control of fusion

It is clear that precision placement of fibres, supported by checking and adjusting during manufacture, are critical. In this regard control of heat and fusion is critical to prevent accidental fusion that affected several joints on the paw.

Further techniques that may help in this regard include:

Ultrasonic spot welding hand held spot welders are available [194]. These would minimize the amount of heat used, and help keep the affected volume focused only where fusion is desired.

Cooling of the work piece to remove heat, e.g. quenching in (faster but gets wet) or between slush bags of crushed ice.

Higher temperature thermoplastics for deep structures e.g. the harder grades of Surlyn

Barrier material interposed between surfaces either temporary or permanent to prevent fusion, e.g. HD-PE film, Parafilm (soluble in short chain paraffins) or cling film (PVC, LD-PE, linear-LD-PE, very thin 8-15 microns).

9.2.2 Control of friction

Control of friction in the flexor tendon sheath and in ligamentous joints is critical for free and supple movement, and especially for the operation of the extensor tendon hood. Human synovial joints, and by extension tendon sheaths and bursas, function with an extremely low friction coefficient ($\mu = 0.04 - 0.001$) [195]. Unlike hydrodynamic bearings in common engineering applications, the movement is oscillatory rather than continuous rotation and often static or low shear rate. Pressures in the human hip joint for example, can reach $3MPa$ in walking. The literature on hypothesised mechanisms of lubrication in synovial joints is discussed in detail in [196].

There are several complementary ways that the existing technique might be developed to improve the control of friction.

Surlyn-PCL-SEBS joint surface and capsule

SEBS is problematic as a joint surface material due to its high friction when dry. Paraffin-plasticised Surlyn could be used instead of SEBS facing PCL at the joint face. This produces a smooth slippery surface and weeps oil, similar to the weeping lubrication theory of hyaline cartilage. Surlyn would need a polyamide interface lamina to adhere to PLA bones. If Surlyn were used on the convex face (i.e. on the condyle) it would also present an oil-weeping non-adhering surface to the (SEBS) joint capsule.

Shear thinning and boundary lubricants

Shear thinning greases are made by emulsifying oils and surfactants. The mixture exhibits high viscosity at low stress, but tends to the viscosity of the base oil when subject to shear due to fracturing of droplets. A similar effect is seen with polymers in dilute solution due to disentangling and balling of polymer molecules.

Amphiphilic molecules with hydrophilic (polar or ionic) and hydrophobic regions act as surfactants for liquids and small particles, and as boundary lubricants for solid surfaces. A boundary lubricant binds to the surface interposing itself between the contact surfaces, and produces pressure resistant thin film.

In the case of fatty acids, hydrogen bonds form with the ketone groups of PCL, and ionic bonds form with the metal ions of Surlyn. This produces a covering of short-chain alkyl groups on the surface. This adhered lipophilic surface maintains the film separating the surfaces under pressure.

“Bottle brush” polymers can be used to form a more sophisticated form of boundary lubricant. [197] demonstrated cartilage-like values of $\mu = 0.01 - 0.0001$ at very low shear rates, with concentrated polystyrene polymer brushes in solvents. The mechanism hypothesized was entropic non-interpenetration of brushes from opposite surfaces. This would imply a form of super-lubricity produced elastomeric smoothing of the surface at the molecular level.

Float-casting and vulcanising SEBS

A key factor in surface friction is micro/nano scale surface roughness causing localised high pressure solid-solid contact. This is referred to as ‘asperity’, and the surface protrusions causing the contact are ‘asperities’. A potential way to minimise the asperity of SEBS rubber for joint capsule and flexor sheath linings, would be to cast it in a film on a polar melt bed (e.g. PCL). This would produce a very smooth, minimum surface area interface, due to non-wetting between two immiscible fluids. The smooth surface would be preserved in the solid film, similar to the smooth surface of float glass. The smoothness would help to maintain a fluid boundary layer when lubricant is subsequently added.

It would also be beneficial if the surface membrane of the joint capsule or tendon sheath were higher modulus than the material behind it, and thermoset so that it is not damaged when further SEBS layers are added to it. This could be achieved by casting the SEBS from solution (e.g. in xylene) and evaporating the solvent to form a thin dense rubber film, then cross-linking the rubber. A number of cross-linking agents are available for polyethylene-butylene[198] or for polystyrene including[199].

Surlyn-oil matrix flexor tendons

Rearrangement of materials could benefit the flexor tendon system. If the flexor tendon matrix is Surlyn-oil blend, the bearing surface of the annular ligaments PCL, and the matrix of the retinacular ligaments and sheath membrane are SEBS then the system would have the same advantages as the proposed new joint structure. Using a thin dense SEBS sheath membrane would minimise the flexural stiffness of the free portions of the sheath between the ligaments.

Due to the high melt stiffness of Surlyn, the blend would need to be rolled into a thin film. The fibres of the tendon could then be splayed across the film and rolled up together to form the tendon.

The assembled tendon could then be rolled between two rigid plates to form a smooth constant diameter tendon.

PCL annular ligament bearing surface

A PCL bearing surface to the lining of the annular ligaments, possibly softened by blending with glycerol, would provide a non-sticking surface for the Surlyn tendons. It can also be used to aid construction of the optimal geometry of the annular ligaments, which should form a smooth spiral in the fully flexed finger. This geometry ensures maximum radius of curvature, and prevents kinking of the tendons, which helps to minimise friction.

This can be done by starting with a continuous strip of PCL, then laying up the annular ligaments around the tendons and PCL strip with the finger in the flexed position. Once the ligaments are complete then the strip can be cut between the ligaments to allow the finger to extend again. Note that if the matrix of the ligaments is to be SEBS, then the PCL strip would need to be laminated with ABS to provide a surface that will bond to SEBS.

Compensation of friction

The work against friction required to return the flexor tendons to their relaxed position, can be done by an SEBS-gel 'return spring' on the dorsal surface of the deep flexor tendon, and the dorso-lateral margins of the superficial flexor tendon. This would emulate part of the function of the lumbrical muscles. This is important because of the 'capstan friction' effect. This is where the friction of a rope against a capstan depends on the tension applied to the free end of the rope. When extending the joints of the finger, the flexor tendons act as the 'free end'. Tension in the flexor tendons causes pressure and friction at the joint surface, adding to the friction in the flexor tendons themselves. This more significant in extending than flexing the fingers because the extensor tendons have much less leverage and are much thinner and lighter than the flexors.

9.2.3 SEBS matrix wetting and adhesion of fibres

The non-wetting and non-adhesion of SEBS-gel to PA-66 and PAr fibres was a significant problem in the later iterations. This is important for the extensor tendons, and for all ligaments. Wetting of fibres could be achieved by adding a surfactant (e.g sodium stearate, soap) to the SEBS-oil gel.

Positive adhesion between the SEBS polymer and the PA-66/PAr fibres would require chemical bond or attraction. There are a number of ways to graft polymerise different groups onto either styrene or ethylene-butylene. The Kraton "FG" family [192] of polymers are commercially available SEBS with maleic anhydride graft polymerised to the ethylene-butylene mid-block. The maleic anhydride group provides hydrogen bonding to the amide group of polyamides, and ketone dipole attractions to PLA and PCL.

Where polar polymers need to be embedded in unmodified SEBS matrix, surface treatments may be beneficial. Washing polyamide fibres with e.g magnesium phenyl acetate, may provide a way of creating a styrene-philic surface, ionically bonded to the polyamide.

9.2.4 Precision of manufacture

It is easier to attach fibres precisely and securely to harder thermoplastics, and when using pre-impregnated tows. This presents a challenge for ligaments where matrix must change twice in the space of about 10mm. Special tools, and prepared thermoplastic tapes could help here.

Using pre-shaped semi-rigid elements could help. printed bones is one example, using PCL strip to form the spiral shape of the annular ligaments would be another.

9.2.5 The problem of measurement & possibility of automation

The major challenge underlying this thesis and soft tissue anatomy more generally is the difficulty of precision measurement. In chapter 13 the outline of a computer visual-tactile fusion algorithm is given that would provide a solution to the problem of measurement. Given a real-time, automatic system for building models of soft tissue structures from video and tactile data, several things would become possible. Models could be acquired from anatomical dissection. These models could then be edited as CAD models to create modified designs. The models could be used to plan automated layup of structures. Crucially the ability to constantly generate new models of what has been built, would allow visual-tactile closed loop control of automatic layup, with re-planning in response to actual rather than expected outcomes.

9.2.6 Conclusion

The demonstration pieces were hand built without special tools, consequently the quality control was poor and the build process variable. However they serve their purpose in that they demonstrate a suite of base materials, composites and layup techniques that allow emulation of the mechanical composition and behaviour of vertebrate soft tissue tendon networks and dermal structures. The demonstration pieces have also shown the critical role of hyper-elastic tissues, and precise geometry of ligaments and tendon networks. SEBS-paraffin oil-gels were shown to meet and exceed the softness and hyper-elasticity required to emulate loose connective tissues.

Much better quality control could be achieved with mechanical mixers and rollers for blending thermoplastics and producing thin membranes. Special tools for laying, pressing, fusing membranes would potentially improve build quality and provide the possibility of automating the layup. Automated layup would provide CNC control and repeatability. This however would require a CAD-CAM system capable of modelling very soft hyper-elastic and highly anisotropic materials, and some means of monitoring the build process.

Further development of the materials might include custom block-polymers and bottlebrush polymers to facilitate controlled elasticity and adhesion or immiscibility.

Chapter 10

Dermal Structures

10.1 Importance of dermal structures

Dermal structures comprise haired and hairless skin, dermal pads and ligaments, nails, claws, and hooves (Ch.3.5). Together these are responsible for the body's contact with the external world. They protect the rest of the body and provide:

Friction for traction and manipulation,

Abrasion resistance at the contact surfaces,

Impact protection for the musculoskeletal system,

Graded compliance for control of contact force and pressure,

Tactile sensation for perception of grip, slip, contact and surface characteristics.

10.2 Canine paw pad and epidermis

The anatomical canine paw pad is a highly fibro-elastic structure composed of adipose tissue dominated by many fibrous septa radiating from the underlying musculoskeletal fascia to the dermis. The dermis forms an elastic capsule with a thickened keratinised epidermis on the ground contact surface of the pad. Together these provide impact absorption, abrasion resistance and friction on a wide range of surfaces, and tactile perception of traction and slip.

To explore possible materials and layup methods for making paw pads, a female mould of the (radiographic) outer surface of the dogs paw was printed in PLA from the same CT scan as the bones of the paw, figure-10-1. The rough printed surface of the mould was then coated in soft modelling wax as a releasing agent.



Figure 10-1: Paw pad mould, 3D printed PLA, lined with modelling wax as a releasing layer.

10.2.1 Canine paw dermal pads

The mould was partially filled with Toms Shore-A 22 silicone rubber. Then a section of deep pile soft fleece material pushed into the mould and pressed against the walls with a probe. Additional silicone was added to fill the mould and bubbles were worked out of the material. Once cured the fleece-silicone-rubber composite was removed, figure-10-2a.

10.2.2 Canine paw epidermis

To create a tough epidermis for the paw, Poly Optic 14-70 polyurethane rubber was poured into the mould and rotated until partially cured. A section of deep pile fleece was impregnated with more of the PU rubber, then pushed into the mould and pressed against the existing layer of PU rubber. The interior space of the mould was then packed with polyethylene bags to press the fleece against the walls of the mould, figure-10-2b.

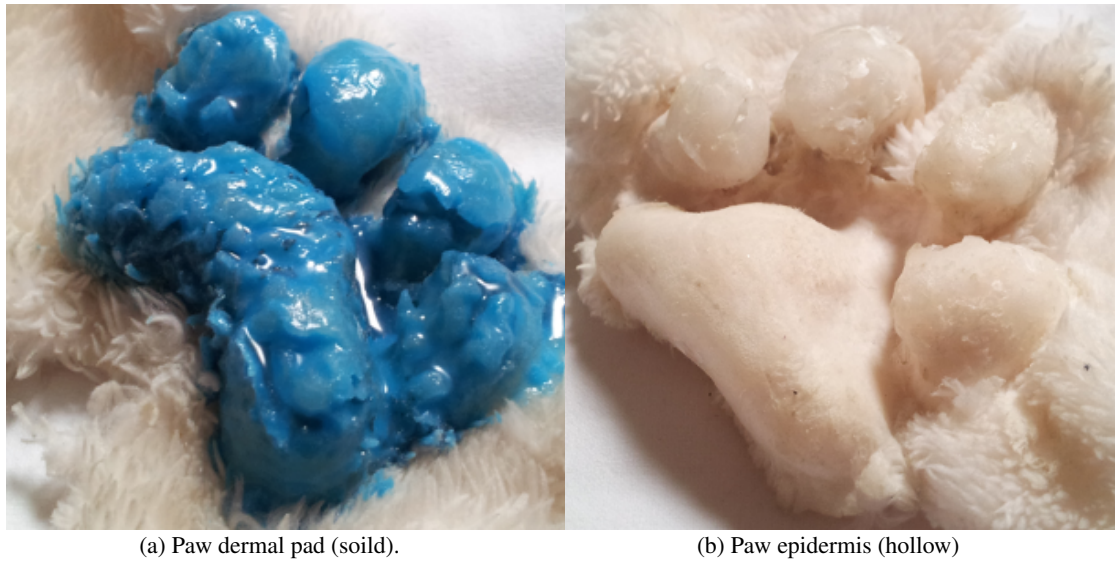


Figure 10-2

10.2.3 Assessment of canine paw pads

The PU-rubber used for the epidermis produced a surface with inadequate friction, but demonstrated the effectiveness of making a shaped and layered elastomer-fibre composite in this way. The moulding of the digital pads was problematic due to their bulbous nature, being narrower at their attachment than at their contact surface. A split mould would help to solve this, while other rubbers used for tyre treads would provide good friction. The dermal pads provided a credible emulation of the material visco-elasticity of anatomical paw pads. A pad for fitting to a robot would be cast as one piece with the pad inside the dermis/epidermis. To conclude, no major obstacles were found to emulating paw pad structures, therefore no further time was spent on this topic.

10.3 First finger prototype - subcutis-epidermis

To provide a first approximation of the ultra soft subcutis and tough cutis (dermis and epidermis), silicone gel digital pads (figure 9-3b), and subcutis were laid on the finger and covered with a nitrile rubber glove (figure 9-4).

Assessment of subcutis-epidermis

Silicone gel digital pads provided a credible first approximation of finger pad mechanics inside glove. The nitrile-rubber glove gives adequate epidermal stiffness, but lacks dermis and attachment to underlying skeleton. A fibre-gel dermal layer and dermal ligaments are needed.

10.4 Fingernail prototype

The fingernail is an epidermal structure that provides a relatively high modulus force transmission between the bone of the distal phalanx to external environment. The nail bed is a highly innervated structure that makes a substantial contribution to tactile sensation of both the finger nail and the finger pad (Ch.3.5.2, 4.2.4).

A prototype finger tip with nail, nailbed, digital pad and bone were made to explore materials for these structures. The bone was 3D printed in ABS. The nail was a sheet of rigid polyurethane resin (Poly Optic 1410). The nail bed was a thin layer of silicone rubber (Toms Shore-A22). The epidermis was formed by the fingertip of a nitrile rubber examination glove, while the subcutis was formed by filling the remaining space within the glove fingertip with ultra soft silicone gel (ACC Silicones E-Gel, Ch.7.3.2). A hole was cut in the glove around the nail, and the margins if the glove were bonded to the silicone rubber under the nail - reproducing the relationship of the skin of the finger tip with the fingernail.

Assessment of fingernail

Mechanically the fingernail was an acceptable first approximation of the human fingernail. It provided a hard edge to the soft finger pad, and had modest compliance between the nail and bone from the silicone rubber nail bed. The adhesion between the nitrile rubber and the silicone rubber was weak causing the margin of the glove under the nail to become detached. The rigid polyurethane resin suffered the same creep plasticity encountered when it was used for bones (Ch.8.2.3).

The major shortcoming of this initial prototype however was its aesthetics. The appearance of an approximately human structure and materials, with crude shape and finish, and partial failure of adhesion of the glove - found a low point of the 'uncanny valley'.

Mechanically and aesthetically better nails are readily available in the form of cosmetic nail extensions. The adhesion problem of nitrile rubber to silicone rubber would be solved by using two rubbers of compatible bonding (e.g. SEBS based rubbers and gels) or by appropriate surface treatment (e.g. silane treatment for bonding to silicones). No major obstacles were found to emulating fingernail structures, therefore no further time was spent on this topic.

10.5 Final finger prototype - subcutis-epidermis

The ability to securely attach a structured fibre-gel skin and subcutis to the musculoskeletal core of the finger would be essential for producing a functional emulation of a human finger. A prototype subcutis and epidermis were built on the final prototype finger (Ch.8.2.11 and 9.1.11) using SEBS based thermoplastic elastomers.

Simplified digital pads were constructed on the palmar side of the finger, (Fig 10-3). The pads were cut from a solid block of SEBS-paraffin gel and positioned on the palmar face of the flexor apparatus over each of the phalanges, and the MCP joint. These were then covered with a membrane of Dryflex 5000 (Shore A 0 hardness). This membrane was then welded to the sides of the finger immediately palmar to the extensor apparatus. The palmar creases were then formed by laying strips of Dryflex

5000 membrane over the palmar faces of the joints, so as to separate the digital pads, and welding these 'crease ligaments' to the lateral faces of the joints.



(a) Finger with tendons wrapped in film of SEBS-paraffin gel forming the subcutis.



(b) Blocks of SEBS-paraffin gel forming the digital pads



(c) Dense SEBS film epidermis covering the subcutis, and welded at the crease ligaments to the underlying musculoskeletal fascia.

Figure 10-3

Assessment of Final finger - subcutis-epidermis

The thermoplastic welding of SEBS gels of different elastic moduli to each other and the underlying tissue (with SEBS matrix) provides good adhesion and allows complex structures to be created. These soft elastic gels provide the right mechanical properties, particularly visco-elasticity, resilience, and variation of elastic modulus. The dense Dryflex 5000 SEBS-gel provides a tact-free high friction surface to the ultra-soft SEBS-paraffin gel.

The gel blocks used for the pads were too thick, resulting in a 'swollen' finger. The gel pads will need to be cast to provide correct shape. There needs to be a fibrous dermal layer to convey sufficient strength, and septae in the pads.

10.6 Conclusions

The SEBS gels, rubbers and polyamide composites of them, are sufficient to reproduce the mechanical properties and potentially the structure of the epidermis, dermis, subcutis and dermal ligaments of the skin of the hand. The missing critical function is somatosensation. This will require both embedded sensors and signal conducting fibres to play the role of nerve axons. These need not only to work in place, but to have a practical way to build them into the structure. MEMS sensors already exist, the next chapter addresses how suitable fibres might be made.

The placement of the signal fibres is likely to be closely linked to constructing the fibrous septae of the digital pads, as both require the same topological connection to the dermis. Options include casting the subcutis in the interior of the dermis, then inserting the fibres and septae, or constructing the septae and axons first then casting the gel of the subcutis. The later option makes access easier and ensures the correct final volume of the structure, but would require a thermoset gel in order not to damage the septae axons. If silicone gel is used treatment of the SEBS surface e.g. with silane, would allow improved attachment of thermoset gel.

The epidermis should ideally have a finger print, both for friction and generate vibration for tactile sensation. This could most easily be provided by taking a mould from a human hand, or alternately using the texture of fused deposition 3D printing, though a nozzle finer than 0.3mm diameter would be required to approximate the texture of a human finger print. The epidermis should also be readily resurfaced to repair wear and tear, and repairable in the event of cuts/grazes. SEBS offers the possibility of doing these things, by rotomoulding thin textured films, and being bondable by either thermoplastic or solvent welding.

Chapter 11

Sensor signal fibres

If a robot is to have somatosensation in soft tissues approximating that of humans, then it is necessary to have sensors implanted in the different layers of tissues to sample the strain, pressure, vibration and temperature, that are of approximately the same size and number as sensory nerve endings. Given that the anatomical sensory nerve endings are of the order of 100 microns in external dimensions, there are a diversity of MEMS sensors that could fill these roles. The unsolved key challenge is to find a way to connect large numbers of such implanted sensors, robustly and without detrimentally altering the material properties of the soft structures into which they are implanted.

11.1 Concept & structure

The axons of tactile and proprioceptive sensory nerves are of the range 5 – 20 microns in external diameter including their myelin sheaths. Nerve axons are soft and tolerate at least as much flexing and stretching as the tissues surrounding them. Assuming that robot fingers do not require fluid circulation it would be possible to use the space and paths through the anatomy of the arteries and veins as well as that of the nerves. This means that we could afford thicker 'axons' of perhaps 50 microns external diameter. However electrical signalling requires at least two, possibly more wires per sensor. For this reason the work in this chapter has focused on parallel pair wires, and is adaptable to wires with multiple parallel channels.

For such thin parallel pair wires to transmit sensor signals at low voltages with reasonable signal to noise ratio, would require metallic levels of conductivity and high resistivity insulation. Hypothetically one might use a helically coiled copper wire set in an elastomeric insulator. Flat meandering gold wires on polyimide embedded in silicone substrate have been published [200]. The expected disadvantage of solid metal wires is that after repeated bending and crushing, the wires would suffer fatigue failure. This would cause short service life for any robot soft tissue somatosensory system.

To eliminate fatigue failure Gallium-Indium (GaIn) liquid metal amalgam was used as the conductor, chapter 7.7.1. These amalgams typically have conductivities around 1/10 that of copper, table 7.7. Given that they are liquid they do not need to be coiled or undulated to allow longitudinal strain. The greater conductive cross-section and shorter conductive length mean that GaIn 'wires' can be of equal

effective conductivity and smaller diameter compared to helical copper wires.

The techniques developed in this chapter focus on melt drawing of structured thermoplastic elastomer fibres with GaIn conductor channels. Section 7.7 discusses the materials used, section 11.2 describes drawing from a preform, section 11.3 describes melt spinning from a fine nozzle.

11.2 Drawing from preform

11.2.1 Background - optical fibres

The concept of drawing fibres thermoplastically from a preform came from optical fibre drawing, metal-in-glass [201], and Indium in polymethyl-methacrylate polymer electro-optical fibres [202]. Prior to the start of this thesis, unpublished work by the author had investigated the potential of polymer optic fibres for tactile arrays. The conclusion of that work was that permanent light loss due to kinking of polymer fibres under tight radius bending made them unsuitable, but that given a liquid or gel electrical conductor immune to fatigue cracking, polymer electrical fibres could potentially serve as surrogate nerve axons.

Maximum robustness in service of the electrical fibre would be achieved if the polymer of the fibre had greater yield strain than the surrounding 'tissue' into which it would be implanted, hence the polymer should be a thermoplastic elastomer with high yield strain, i.e hyper-elastic. The elastomer would need a degree of adhesion to the other materials into which the fibre would be implanted, and to the potential MEMS sensors to be attached to it. Given the expected length and small separation of the electrical conductor channels within the fibre, the elastomer would also need high electrical resistance to prevent leakage of current and a low permittivity to minimise capacitance and maximise signal transmission. Finally the liquid conductor would need sufficiently high electrical conductivity to transmit the signal.

11.2.2 Preform

The preform provides the cross section shape of the fibre, which can be scaled almost arbitrarily fine by varying the relative speeds of the fibre winding and preform advancement. Figure 11-1a shows a pair of preforms cast from the same mould with Surlyn and PCL respectively. The Surlyn preform has been drawn from, showing how plastic flow under tension produces dimension reduction while preserving cross section shape.

Alloy moulds

A number of alloy moulds were milled to allow shaped preforms to be pressed or cast.

(i) figure of eight mould This was the first mould, figure-11-2a & 11-2b . It consisted of a two part split block and a lid, all aligned with steel dowels. The block held a cavity of two parallel intersecting 20mm diameter cylinders, forming a prism with figure-of-eight cross-section. The lid held two 5mm diameter steel rods, positioned at the centres of the two cylinders of the cavity. The cavity formed the shape of the elastomer, while the rods formed the channels for the amalgam.

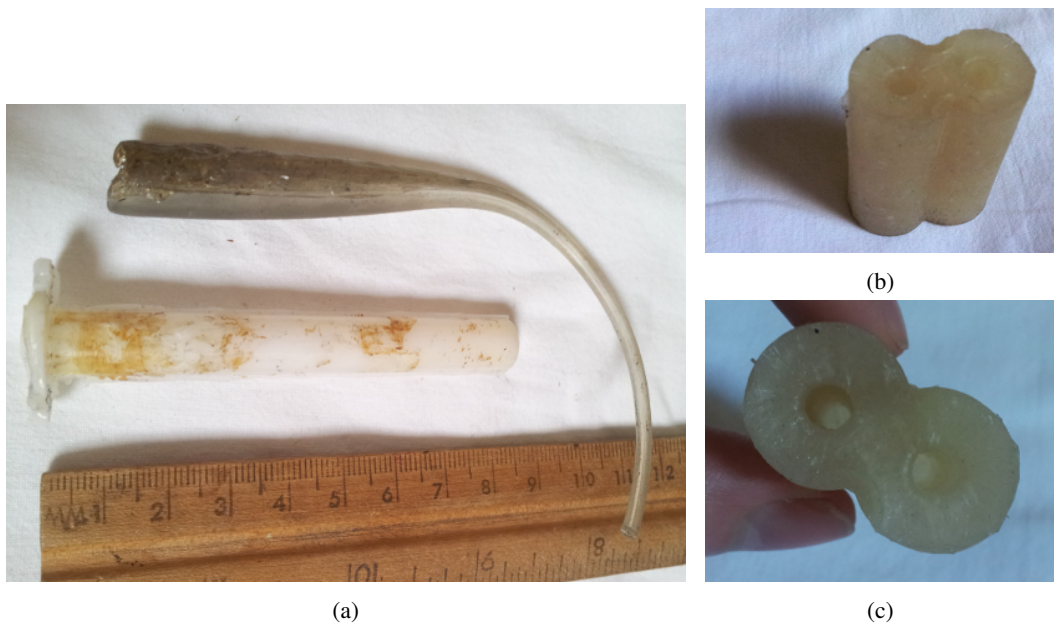
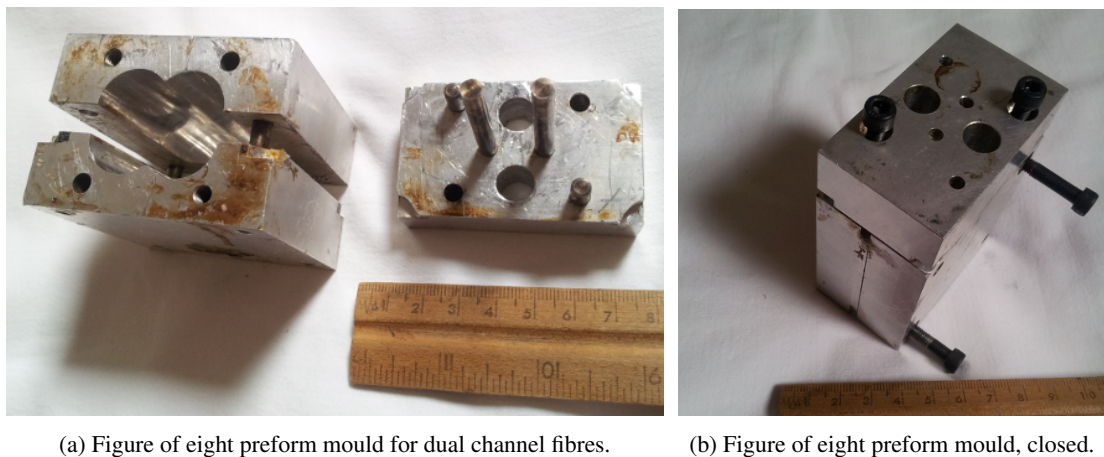


Figure 11-1: (a) Simple preforms. Top, a Surlyn preform after drawing a fibre. Bottom, a PCL preform as cast in the mould. (b) 'Figure of eight' dual channel preform. (c) Dual channel preform, end view.



(a) Figure of eight preform mould for dual channel fibres.

(b) Figure of eight preform mould, closed.

Figure 11-2

This preform was relatively large, and contained sufficient volume of material make fibre for a large array of sensors, e.g. for a whole hand. A preform made from this mould is shown in figure-11-1b & 11-2b . This shows the two channels formed by the rods, which are subsequently filled with amalgam to form the conductors.

(ii) double layer mould A smaller single channel mould was made to create double layered preforms with support material surrounding the elastomer, figure-11-3. This had two sets of split plates with different 10mm and 15mm radius single cylinder cavities.

EVA preforms

The first preform made used Elvax 150 EVA elastomer (Ch.7.3.3). This highly visco-elastic in the molten state. Beads of EVA were packed into the figure-of-eight mould with the top open. Both the assembled split-block and the lid were heated in a closed chamber until the EVA was molten. The hot lid was then pressed onto the hot mould, forcing the rods of the lid into the EVA. Correct positioning was guaranteed by the steel dowel aligning the lid to the split-block. The mould was then allowed to cool before opening and removing the formed EVA. One catch with this design was the tendency of the elastomer to form a vacuum seal, making it hard to open the mould and remove the preform.

Once the preform was removed from the mould, the channels were filled with GaIn and sealed to prevent spillage.

SEBS preforms

The process of making SEBS preforms was very similar, except the material behaviour of SEBS was substantially different. The grade used was very soft Elasto Dryflex 5000, and Elasto crumb with paraffin oil (Ch.7.3.3). The melting point of SEBS is higher, but the phase change more marked. The SEBS-oil gel first becomes friable, then a low viscosity liquid. The low viscosity means that no force is required placing the lid on the mould, and there is little risk of air cavities. However SEBS shows marked thermal expansion between standard temperature and its melting point. Consequently there was a tendency to form large bubbles in the SEBS on cooling. This was prevented by drilling a pair of 10mm diameter openings in the lid. This allowed extra SEBS to be added to the closed mould, which was drawn down into the preform during cooling.

Double layer preforms

Double layer preforms were made where two thermoplastics were to be drawn together, (figure-11-3). This was done for two different reasons :-

1. To provide a wettable surface to the interior of the channel a preform was made with EVA blended with ITO powder on the interior and plain EVA on the exterior.
2. To provide a removable support material to assist in drawing amalgam filled SEBS fibres, a number of preforms were made with other materials around the SEBS preform, including polyethylene, Surlyn and 'Monosol' polyvinyl alcohol (PV-OH).

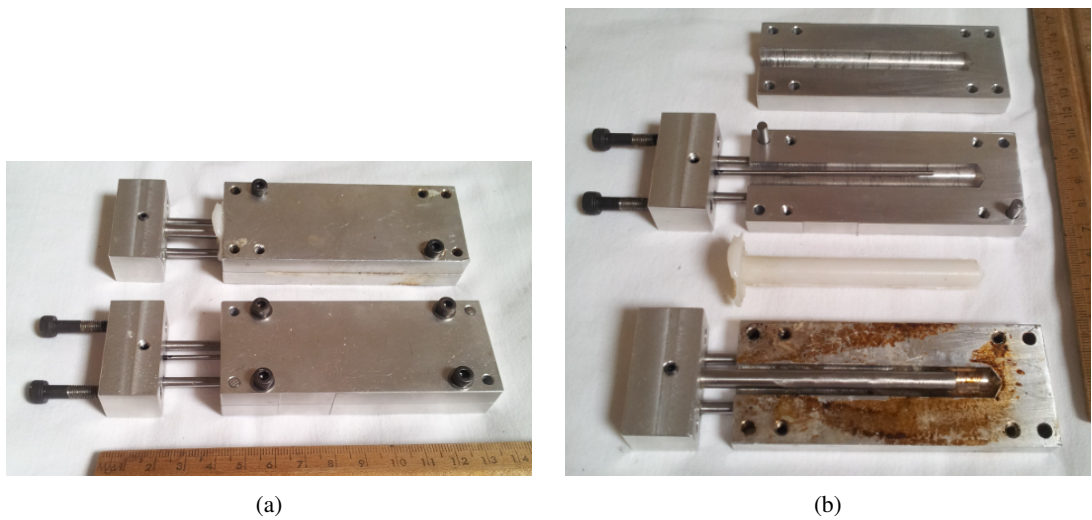


Figure 11-3: Mould set for concentric preforms. (a) moulds open showing different sizes of core rod, and a PCL preform. (b) Moulds closed, with rods partially inserted.

11.2.3 Fibre drawing tower

The tower was built in three sections from laser cut 6mm acrylic sheet,

Base The lower two thirds of the structure. This included the fibre winding reel and geared encoder motor at the bottom, and the fibre cooling space between the furnace and the reel.

Furnace The furnace where the tip of the preform is heated, and the fibre drawn from it. Three versions were made, described below, Ch.11.2.4.

Preform advance This consisted of a clamp, mounted on a slider and a stepper motor with a worm drive to very slowly advance the preform into the furnace.

The tower ran on 12V d.c. power, and was controlled by a set of power FETs and an Arduino Mega microcontroller [203]. In the first version the PID control was used for heating, winding and preform advance together with a GUI implemented in Java with the 'Processing' library [204]. The GUI ran on a laptop connected to the Arduino via USB, and allowed the control parameters, set points and inputs to be observed. Unfortunately the 'mega' model of Arduino has markedly slow USB data rate for two way communication, and substantial lags between the GUI and the controller resulted. Consequently the control software was re-written with hardware POT dials for input of set points, and output of text to the Arduino serial monitor on the host computer for monitoring temperature, winding speed and heat input.

The temperature of the preform in the draw down zone was monitored using a narrow angle non-contact infra red thermometer [205]. This provided measurements precise to 0.1°C, and included correction for the temperature of the device itself. This allowed drawing conditions to be repeated. (Note that calibration for the infra-red emissivity of each preform material would be required for accuracy of absolute temperature measurement, but was not needed for repeatability with the same material.)

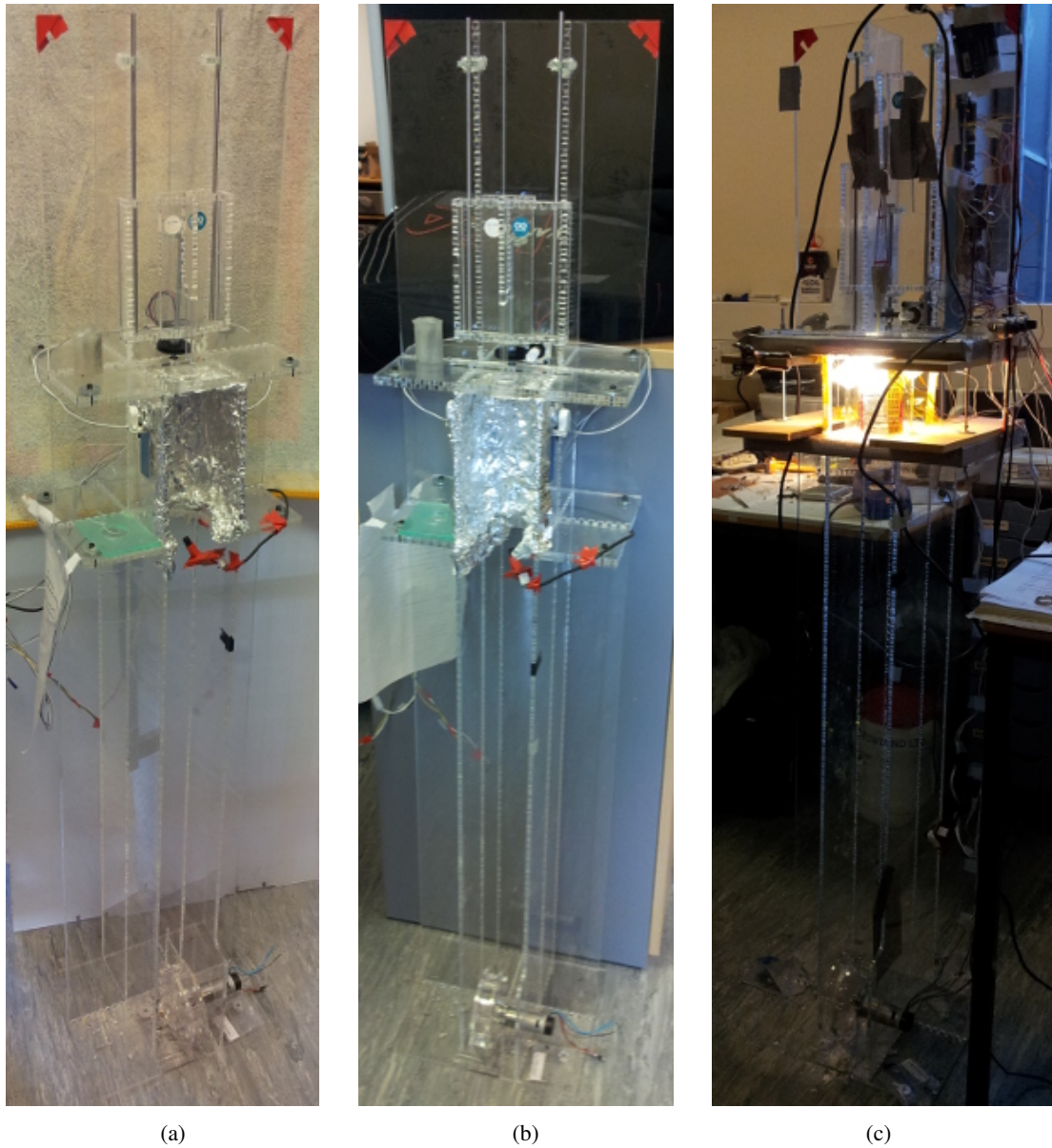
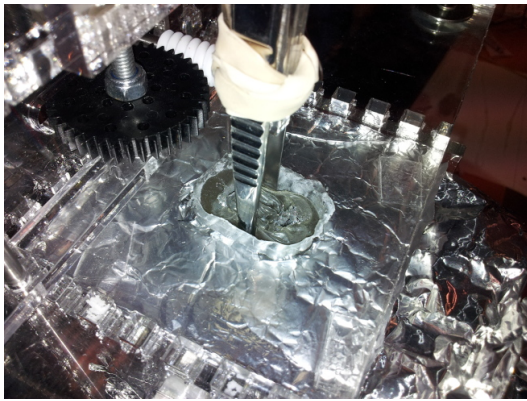
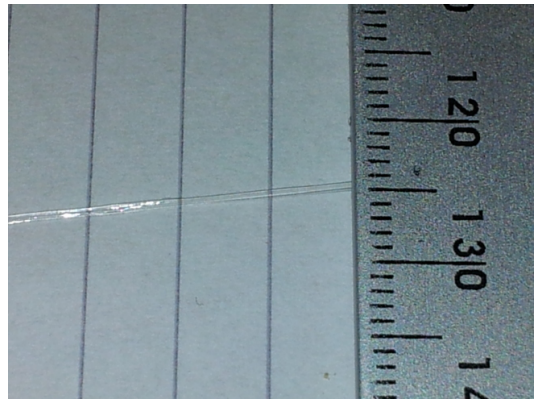


Figure 11-4: Fibre drawing tower, a)&b) original form with 2x 50watt reflector bulbs for the 'furnace', c) later form with double cylindrical glass furnace, nichrome heater wire and 4x 40watt bulbs.

Figure-11-5e shows the IR thermometer in its CAN package, but without the black anodized tubular alloy housing that provides a narrow angle of view for the thermometer. The thermometer was connected to the arduino using the "I2C McMaster" library [206] following the guide at [207].



(a) Preform drive on the top of the drawing tower



(b) First demonstration of EVA fibre drawing



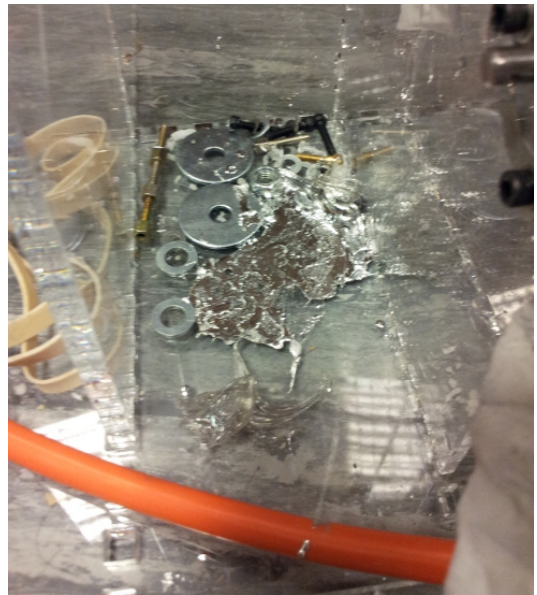
(c) Preform in furnace



(d) GaIn filled preform in furnace



(e) Infra-red thermometer



(f) GaIn spilt after preform rupture

Figure 11-5

11.2.4 Furnace

Version 1 - lamps

The first version of the furnace used a pair of 12volt 50watt reflector halogen reflector bulbs, with their infra red filters removed, as its heat source. The acrylic structure was shielded by aluminium foil and an air gap to protect it from the heat. An aperture plate at the top entrance of the furnace prevented convection of hot air up the sides of the preform.

A number of shortcomings were found with the first furnace

- Heat containment was not adequate and the lamp fittings were gradually damaged,
- The visible component of light from the lamps was so bright that observation of the preform during drawing was difficult,
- The temperature reached was not reliably high enough for drawing SEBS fibres

Version 2 - nichrome cylindrical furnace

To overcome the shortcomings of the first furnace a new design was made, using Nichrome heater wire wrapped around an inner cylinder of silica glass, and shielded by an outer cylinder of borosilicate glass, figure-11-6. The new furnace was thermally isolated from the tower sections above and below it by a double layer of fireproof silica fibre insulation board.

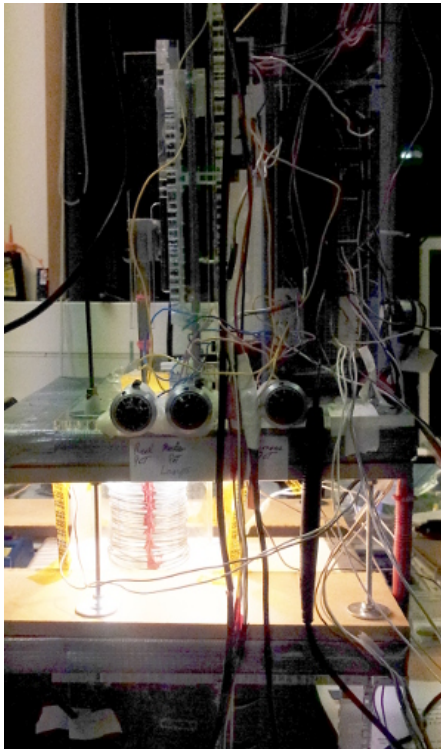
While this version solved the visibility and heat containment problems, it was slow to heat up and was not able to reach sufficient temperature for drawing SEBS fibres.



Figure 11-6: Cylindrical furnace, inner silica glass tube with nichrome resistor wire and high temperature silicone. The outer borosilicate glass tube is not shown.

Version 3 - nichrome plus lamp array

Additional heating power was added in the form of a ring of four 12volt40watt bulbs, and a second power supply, figures11-4c & 11-7a.



(a) Close up of double cylindrical furnace and control POT dials.



(b) Hollow SEBS fibre drawn in the tower.

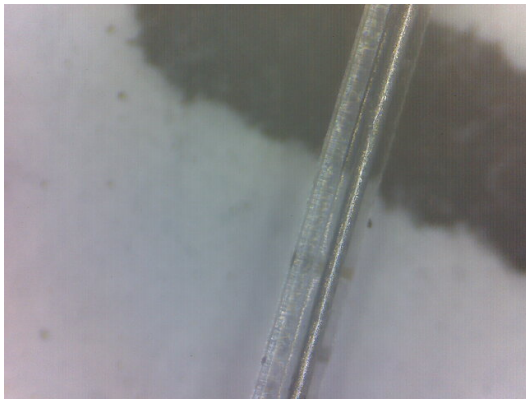
Figure 11-7

11.2.5 EVA

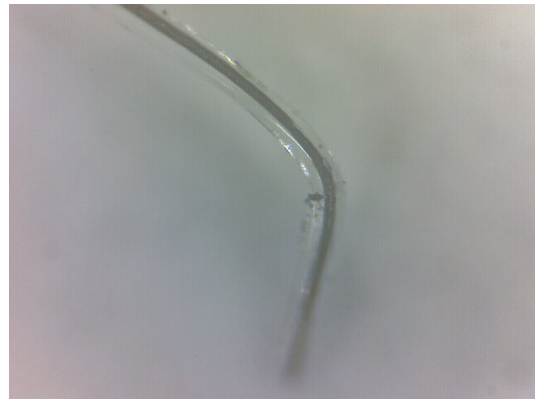
EVA was the first material used to make preforms and to draw structured fibres. Several grades were obtained and tested. The grade with the lowest modulus, and highest resilience, Elvax 40 (Ch.7.3.3), was selected.

Hollow

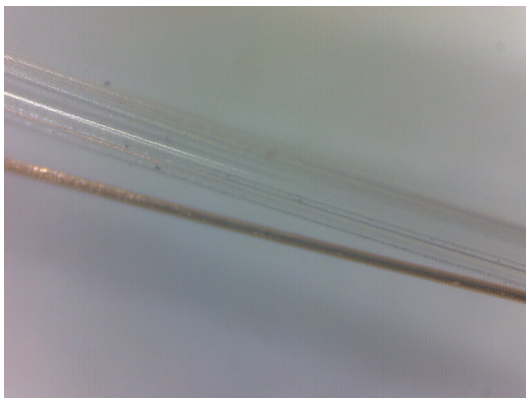
The first test fibre was drawn using pure EVA formed using the figure-of-eight cross section mould and the first version of the drawing tower furnace. First hollow fibre was drawn with only air in the conductor channels. This established that heating and reel speed parameters for stable fibre drawing were readily found and that fibres down to < 100 microns external diameter could be drawn. Figure-11-8c shows an EVA dual channel hollow fibre alongside a 30 micron copper wire.



(a) Dual channel fibre with one channel filled with GaIn, lying on 10pt laser printed text.



(b) Single channel fibre filled with GaIn

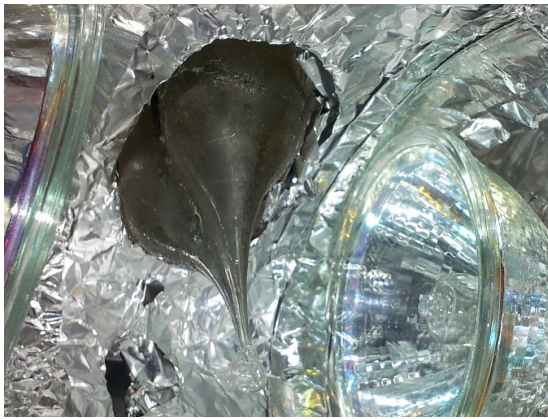


(c) Dual channel hollow fibre alongside a $30\mu\text{m}$ copper wire.

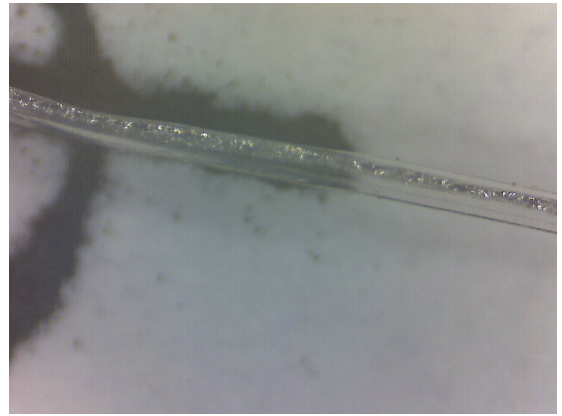
Figure 11-8

GaIn filled

Following success in drawing hollow fibres, the conductor channels of the preform were filled with GaIn amalgam. The first finding was that, significantly more power was required to heat the preform to drawing temperature. This is expected to be due to thermal conductivity of the amalgam being much greater than that of EVA, hence heat being conducted away from the drawing region to the higher part of the preform. New settings were found that enabled drawing of amalgam filled EVA fibres.



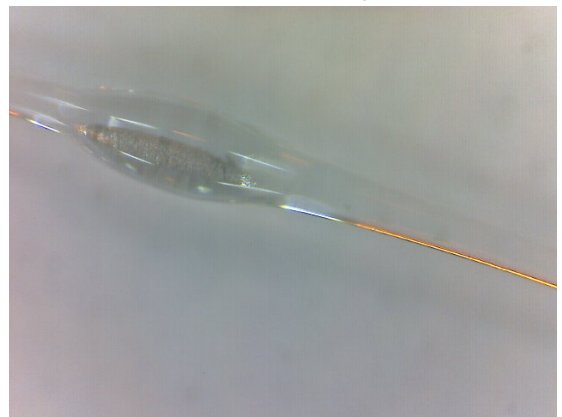
(a) Fibre SEBS preform drawing



(b) Fibre EVA non-wetting of GaIn



(c) Fibre EVA with micron-ITO (green) wetting agent



(d) Fibre SEBS 'aneurysm' preventing filling with GaIn



(e) Double channel fibre with GaIn in righthand channel

Figure 11-9

Non-wetting problem

Testing of the EVA-GaIn fibre revealed a compatibility problem between the two materials. GaIn tended to leak out of the fibres if they were not sealed at both ends. GaIn would leak past needles inserted into the wire to make electrical contact. Most critically the wires would cease conducting after being stretched and relaxed repeatedly. Examination along the length of the fibre by microscope revealed that discontinuities in the amalgam column appeared, hence creating a break in the 'wire', figure 11-9b.

Further testing of the interaction between EVA and GaIn showed that the amalgam had a heightened surface tension and tendency to un-wet areas of EVA that it had been in contact with. **This was demonstrated most clearly when a small well a few mm wide and deep was made in a block of EVA. If a drop of GaIn was placed in the bottom of this well, it would eject itself from the well against the force of gravity.** It was concluded that in fine capillary tubes a few microns in diameter, such as the conductor channels of the EVA fibres, the repulsion between EVA and GaIn could be sufficient to maintain a vacuum bubble once initiated by stretching of the fibre.

Indium-Tin-Oxide (ITO) filled EVA

After discussion with technical advisers from Indium Corp[180] a sample of indium tin oxide powder was provided as a way to improve the wettability of surfaces to GaIn. The particle size of the sample was approximately 50 microns. A blend of EVA and ITO was produced with the highest ITO content that still allowed drawing of filaments from the molten material. The resulting blend was opaque pale green due to the ITO powder.

The material was tested initially in an open ribbon preform with a track of GaIn laid on a thin strip of ITO-EVA blend on a thicker strip of pure EVA. Fibre was successfully drawn from the open preform on a hot plate, figure-11-9c. This allowed the interaction of GaIn with the ITO-EVA blend to be observed, and the lack of constraint would allow the GaIn to form into beads if non-wetting occurred. Examination of the open ribbon fibre produced showed that the GaIn formed a continuous liquid 'wire' on top of the green track of ITO-EVA on the fibre.

A new figure-or-eight cross-section dual channel preform was made with ITO-EVA lining the conductor channels. Pure EVA separated the linings of the two channels and formed the exterior of the preform. An initial difficulty was encountered in that the ITO-EVA used in the first version had too high an ITO content, which caused the preform to fracture rather than draw into a fibre. A second preform was made with slightly reduced ITO ratio. This allowed fine GaIn filled fibres to be drawn. The limit in how fine these fibres could be drawn was caused by the particle size of the ITO powder. Below 100microns external diameter the particles caused lumps in the fibre, preventing further drawing.

Enquires were made about the availability of sub-micron powders of ITO, but these were found to be prohibitively expensive.

Sodium Stearate (soap) blended EVA

Common soap (sodium stearate) was trialled as a wetting agent, on grounds that (i) as an anionic surfactant it could potentially bond to a metal matrix and (ii) as a lipophilic thermoplastic material it was potentially miscible in molten EVA. Liquid phase miscibility would allow complete dispersion of

sodium stearate in EVA to a molecular level, and hence arbitrarily fine drawing of a GaIn wettable Na-stearate-EVA fibre.

A new double channel preform was made with sodium stearate-EVA blend, and fibres drawn. The new material was cloudy in bulk, and wettable to GaIn. The fibres had much reduced leakage, and did not suffer discontinuities of the amalgam after stretching.

Elasticity and annealing behaviour

While the elasticity of the Elvax 40 EVA fibres was significantly greater than that of the original EVA based hot-glue fibres, the elasticity of the drawn fibres was noticeably less than that of the solid EVA before drawing. It is expected that this is due to longitudinal orientation of the polymer molecules by the drawing process. Heating the drawn fibre to near its melting point caused it to contract, becoming shorter and thicker. Post annealing the fibre was substantially more elastic with reduced modulus, increased resilience and yield strain.

Despite the increased elasticity of the annealed fibre, it was not near enough to the yield strain of the SEBS gel being used as the matrix of soft tissues in the dermal structures, or the SEBS rubber being used in the joint capsules and ligaments.

11.2.6 SEBS

In order to create sensor fibres of modulus and yield strain matching the soft tissues into which they would be implanted, preforms were made from the same grade of ultra soft (hardness Shore-A 0) Elasto Dryflex 5000 SEBS-oil gel (Ch.7.3.3).

Hollow

The first SEBS fibre was drawn from a figure-of-eight cross section dual channel preform, using the first version of the drawing tower furnace. The fibre was drawn vertically with only air in the conductor channels. The drawing temperature was higher, registering around 200°C on the IR thermometer at the drawing zone of the preform. This temperature required almost constant full power from the lamps of the furnace.

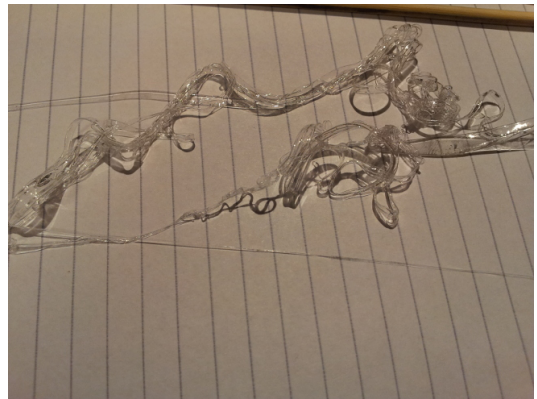
The melt strength was much less than the EVA fibre, but fine fibre could be drawn steadily so long as the winding speed was not changed too suddenly. The fibre was hollow with two channels as designed and of consistent cross section. The fibre displayed hyper-elasticity typical of SEBS-oil gel with low modulus and yield strain around 1,000%.

Filling problem

Filling the fibre conductor channels with GaIn revealed an unexpected problem. A section of hollow SEBS fibre from the first drawing was used that tapered from macro size with fibre diameter of a few millimetres, reducing over a length of about a metre to a fibre diameter of less than 100 microns. The fibre was filled with GaIn by injecting slowly from an insulin syringe into the thick end of the fibre, with the fibre clamped behind the syringe, to prevent amalgam escaping from the large end on the fibre.



(a) Preform torn by hydrostatic pressure of GaIn during drawing of SEBS fibre



(b) Hollow SEBS fibre initial drawing with empty channels



(c) Horizontal drawing over water - an experiment to draw SEBS fibres with GaIn filled channels



(d) GaIn 'aneurysm' preventing post drawing filling of hollow channelled SEBS fibre.

Figure 11-10

The amalgam initially flowed along the fibre filling one conductor channel into the region of the fibre substantially less than one millimetre in diameter. The fibre then started to balloon at one point mid way along the column of amalgam, figure-11-10d. The conductor channel appeared blocked at the end of the column of amalgam, although no blockage was visible. It is now thought that the 'blockage' is a scale effect of the fibre and the surface oxide film of the amalgam. When the conductor channel diameter falls low enough, the pressure required to push the amalgam along the channel exceeds the

pressure required to stretch the elastomeric tube - akin to inflating a party balloon.

GaIn filled SEBS preform - hydrostatic problem

To avoid the fibre filling problem, and to produce a more efficient continuous manufacturing process, an attempt was made to draw the SEBS fibre with the conductor channels filled with GaIn. This failed when the preform ruptured, spilling the GaIn, figure-11-5f & 11-10a. The cause of the failure was that the hydrostatic pressure of a few millimetres of liquid GaIn in the preform exceeded the melt strength of SEBS in the drawing region.

Horizontal drawing

To minimize the effects of hydrostatic pressure the drawing tower was rearranged for horizontal drawing, with a water trough to prevent the fibre from sticking if it touched the floor of the rig while initiating fibre drawing, figure-11-10c. This approach however failed due to sagging of the preform under lateral loading and the tendency to produce asymmetrical fibres vulnerable to rupture of the conductor channel.

Horizontal drawing was used successfully with smaller test samples drawn from the hotplate in all sections. Two factors appear critical, providing mechanical support for the hot preform, and keeping the scale of the preform smaller than the 20x40mm cross-section figure-or-eight preforms. This was further supported by the results of vertical and horizontal nozzle drawing in section 11.3.4.

Sucrose glass support material

To overcome the problems of low melt strength of SEBS, a second material was sought that would act as a mechanical support during the drawing process. In order to facilitate separation of the SEBS fibre from the support material after drawing, materials were sought that had good drawing properties and were soluble in a solvent for which SEBS was insoluble.

The first support material tested was sucrose-glass. This is used in confectionery and commonly known as 'boiled sugar' or 'candy glass'. It is also used as a demonstration material for teaching fibre drawing, (Ch.7.7.2). Sucrose is highly soluble in water, whereas SEBS is wholly insoluble in water.

Experiments on a hotplate showed that strips of sugar glass carrying a section of thick SEBS fibre could be drawn into fibres, producing proportionally finer SEBS fibres. However the temperature required to draw the SEBS fibre caused rapid thermal degradation of the sucrose. Hence while the method was feasible, sucrose was not suitable for any sustained process.

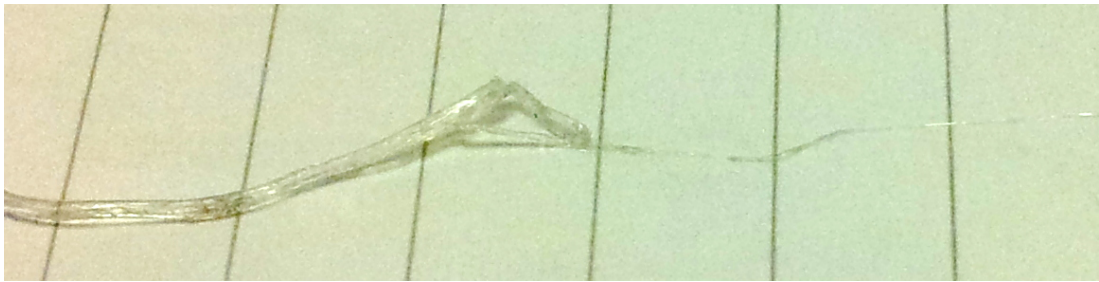


Figure 11-11: PV-OH supported drawing of SEBS. Fine SEBS fibre partially separated from thicker PV-OH support material

PV-OH support material

A sample of the water soluble thermoplastic polyvinyl-alcohol, trade name "Monopol" (Ch.7.7.2), was obtained from the manufacturer. The sample provided was specified to have a melting point of 200C, i.e. above the specified melting point of SEBS. This grade of PV-OH is in the Shore-D hardness range similar to Surlyn, and much harder than either SEBS or EVA. In order to make a preform with an outer layer of PV-OH surrounding SEBS, with a hollow channel for GaIn, a new mould was made (Ch11.2.2)

Glycerol plasticiser & new furnace

To soften the PV-OH and reduce the temperature and tension required to draw it into a fibre, the PV-OH was blended with glycerol. Glycerol is a short chain (three carbon atoms) tri-alcohol, hence it is miscible with PV-OH, but unlike water has a boiling point above the melting point of PV-OH.

The higher melting point of PV-OH meant that the original furnace of the drawing tower was ineffective. Two further iterations of the furnace were needed to produce a furnace hot enough, and to overcome the other shortcomings of the first furnace (Ch11.2.4).

A test fibre was drawn from the two layer PV-OH-SEBS preform without GaIn, figure-11-11. The fibre was placed in warm water to dissolve the PV-OH. After several hours the PV-OH was soft enough that the SEBS fibre could be peeled from it.

11.2.7 Ionomer fibres

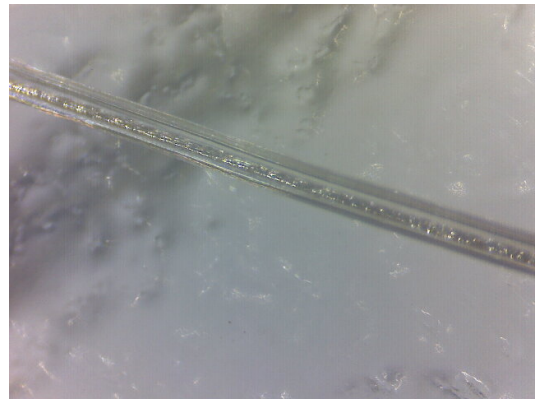
Surlyn being an ionomer has good adhesion to most solid metals, and wets well with Ga-In amalgams. It also has very good melt strength for fibre drawing. A small single channel Surlyn preform was made and GaIn filled fibre was drawn with it. The major difficulties were separating Surlyn from a metal preform, and the high temperature required. The fibre produced was high modulus and relatively inelastic. Surlyn does have a high breaking strain, so excess stretching tends to cause plastic deformation rather than breakage. This would imply laying Surlyn signal fibres such that they are slack below the breaking strain of the surrounding tissues. The hardness of Surlyn is potentially beneficial in that it would ensure relatively constant diameter and length of the fibre, making its resistance more stable.

As a material for long, very fine conductive fibres the relatively modest resistivity of Surlyn would be expected to cause signal degradation more rapidly than SEBS. Surlyn also has poor adhesion to the

SEBS-based soft tissues. These might be remedied by using Surlyn as the wetting layer around the amalgam channels, and ABS for the outer layer of the fibre. The grade of ABS should be chosen for high breaking strain and lower modulus to ensure flexural toughness.



(a)



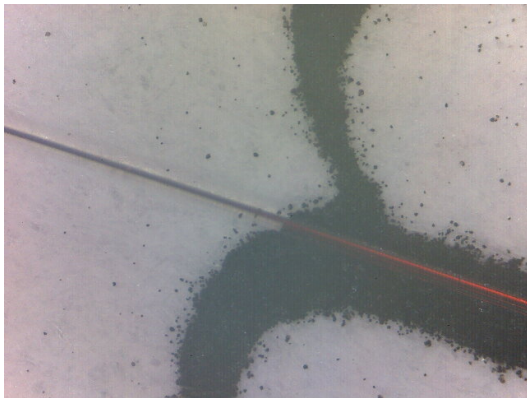
(b)



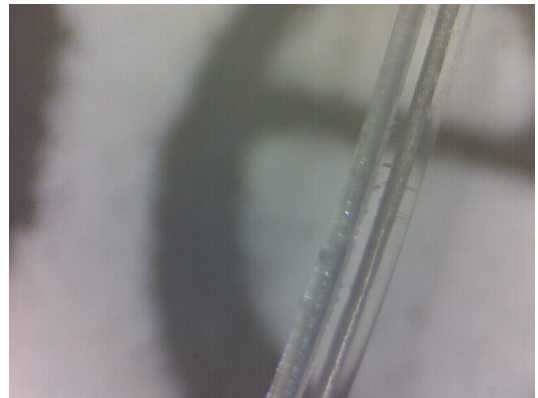
(c)



(d)



(e)



(f)

Figure 11-12: The problem of illuminating and visualising GaIn filled fibres – the smooth surface of the polymer presents dielectric specular reflection and refraction, while the amalgam presents metallic reflection. With very little matt reflection it is difficult to tell whether a fine fibre is or is not filled with GaIn. The colour in (c) and (e) are due to the LED illumination. Finer fibres (not shown) may be $< 10\mu m$ in diameter, given visible light $\lambda = 400 - 700nm$, the specular highlights which form the visible part of the fibres may approach a single wavelength in width.

11.3 Drawing from nozzle

11.3.1 Background - melt spinning

Melt spinning of fibres is a well established technique in both textile and optical fibre production. It belongs to the wider family of polymer fibre spinning techniques including wet spinning, dry spinning, gel spinning, and electrospinning. All involve a liquid precursor emerging from a fine nozzle and solidifying to form the fibre. In the case of melt spinning the fibre precursor is simply the molten polymer, which cools on leaving the nozzle to form the fibre. [208]. Variants of melt spinning are sometimes used to produce step gradient optical fibres in either glass or polymer materials. Textile fibres melt-spun with liquid cores have recently been reported [209]. Note that the liquid was of similar mass density and thermal conductivity to the polymer, unlike the liquid metal amalgam filled fibres described in this thesis.

The work in this section seeks to find a low cost, bench top method of melt spinning elastomeric fibres containing electrically conductive liquid metal amalgam cores. The motivation for exploring melt spinning was to facilitate the use of low melt strength thermoplastic elastomers such as SEBS.

11.3.2 Nozzles

Several techniques were explored to produce a nozzle capable of producing parallel pair wires with two conductive cores, suitable for signal transmission.

Glass nozzle

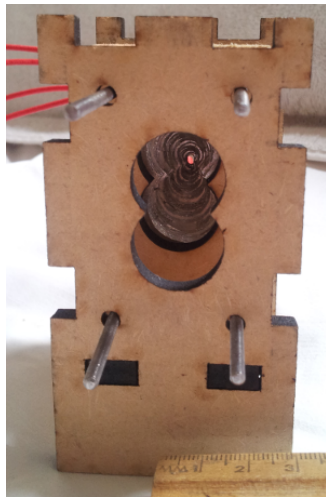
The first nozzle was a glass conical funnel made made elliptical and without a spout, prepared by the University's artisan glass blower in the department of Chemistry. It was made such that the tips of two glass dropping pipettes could fit in the outflow with about a millimetre of clearance around them.

The major difficulties encountered with this nozzle were how (i) to heat it adequately to melt the SEBS (ii) lack of pressure control of the SEBS. The latter problem meant that the nozzle could only be used in the vertical position, which meant that the problem of hydrostatic pressure in the amalgam was not addressed.

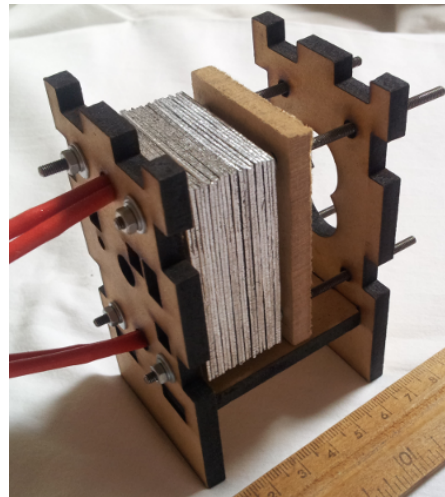
Laminated alloy sheet nozzle

To solve the problems of heating and pressure in the SEBS to allow horizontal drawing, a new nozzle was made from a stack of alloy sheets, figure-11-13. These were drilled with progressively smaller figure-of-eight hole to accept a double channel fibre preform as used in Ch.11.2.6 . Additional holes were made for heater cartridges and thermistors, and the whole nozzle housed in a laser cut fibre board casing for thermal insulation. The preform was pressed into the rear of the nozzle. The temperature was controlled by Arduino, to a set point given by text command via the console.

The method was not successful. Pushing the preform into the nozzle to make thermal contact, caused pressure in the SEBS to collapse the amalgam channel at the front, pushing the amalgam to the back of the preform. The fibre drawn from the nozzle contained no amalgam.



(a) Laminated nozzle, interior.

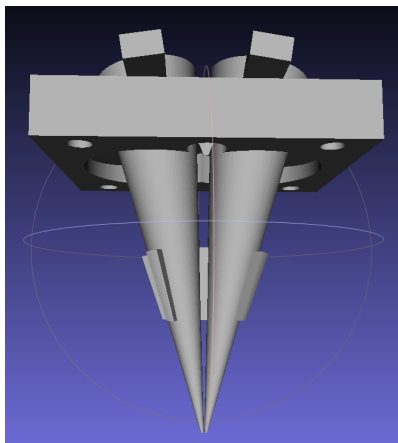


(b) Laminated nozzle, side view.

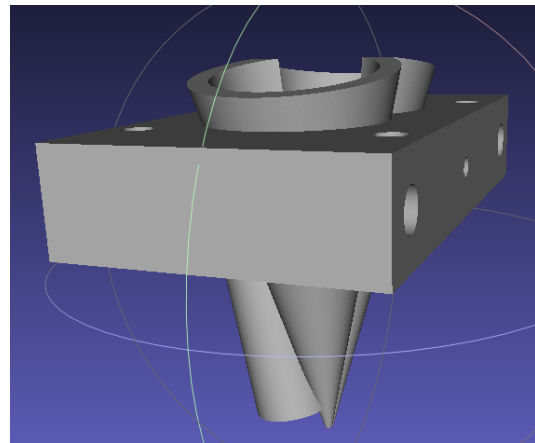
Figure 11-13

3D printed nickel nozzle

The opportunity arose to have a nozzle made from Nickel powder by "Selective laser melting" - a form of metal 3D printing[26]. The key advantage of this technique was the ability to make complex geometry from a CAD model, without the constraints of feasible tool paths for a milled part. This nozzle was provided by 3D Metal Printing, Innovation Centre, University of Bath [210] as a demonstration of the fine resolution feasible with current commercial equipment.



(a)



(b)

Figure 11-14: CAD model of dual nozzle a)inner nozzle, b)outer nozzle

CAD design & concept

The nozzle, (figure-11-14) was designed to fit onto the existing nozzle of the low cost bench top extruder 'Filastuder' [26]. The extruder provided volume/pressure control of the SEBS supply. Two interior nozzles (figure-11-14a) provided independent control of amalgam pressure, while a heater cartridge port in the outer nozzle (figure-11-14b) provided controlled heating of the nozzle tip.

Finishing the printed nozzle

The nozzle was intentionally printed to the limit of resolution at the tip, providing the finest nozzle feasible with the technique. This left a ragged tip figure-11-15 and figure-11-16. The nozzle tips were sawn with a scalpel blade to produce a cleaner finish, figure-11-19 & 11-20.

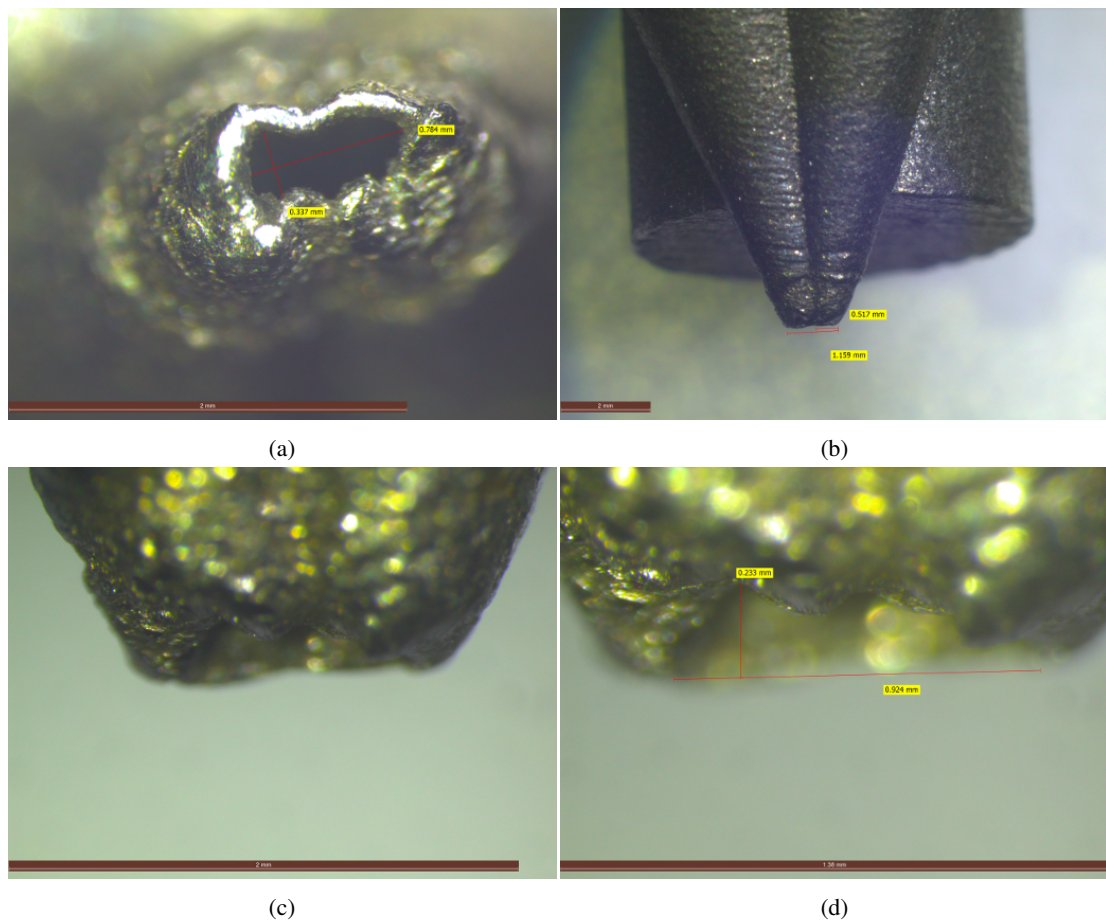


Figure 11-15: Outer nozzle tip as printed. Zoom in to see measurements. (a) Shows the distortion of the opening of the nozzle caused by the limit of resolution of the print. The figure of eight channel is $337\mu\text{m}$ by $827\mu\text{m}$. (b) The exterior of the tip is 1.159mm wide. (c) One side of the tip was not level. (d) The deficit was $233\mu\text{m}$ deep. Note that the walls at the tip are approximately $100\mu\text{m}$ thick.

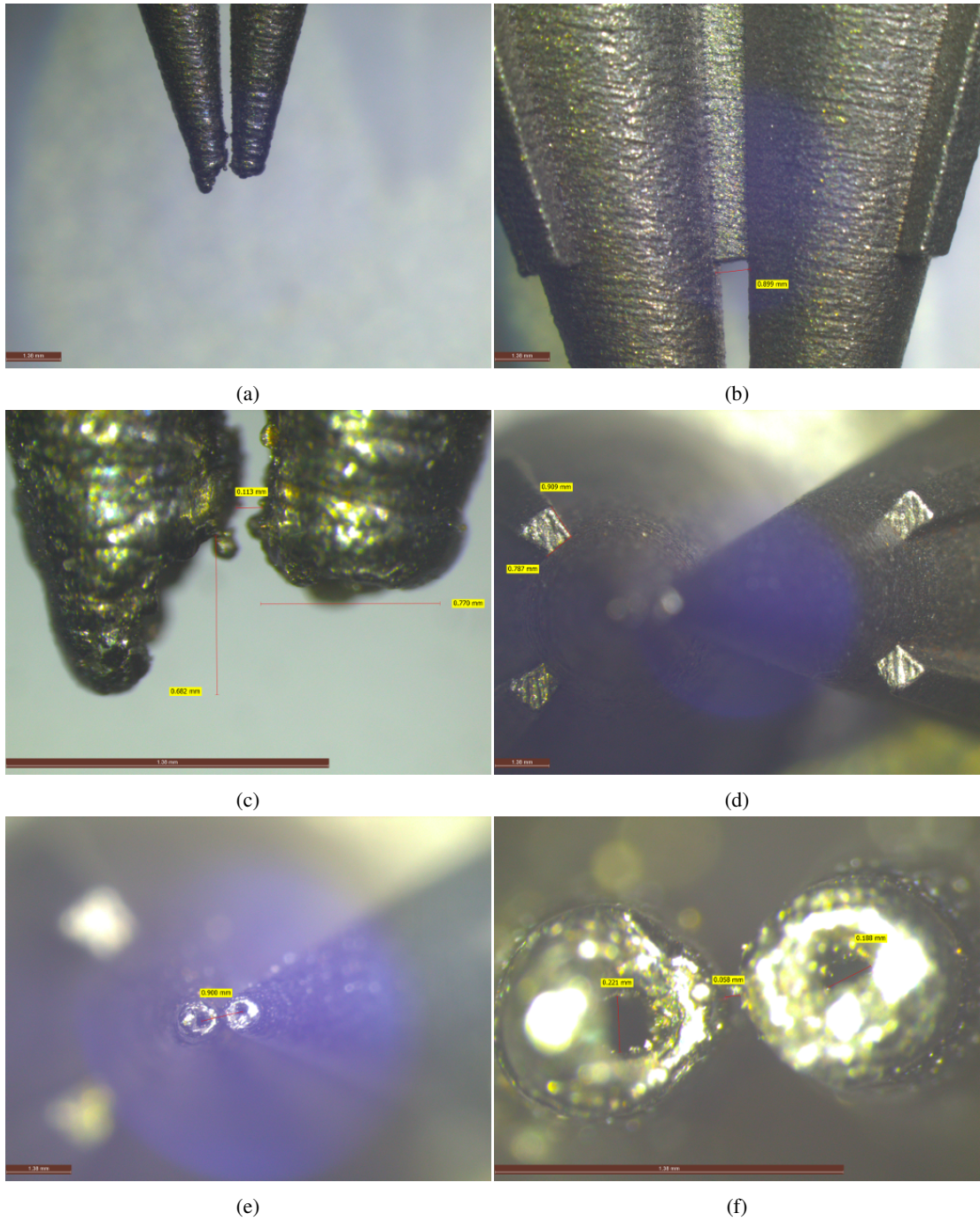


Figure 11-16: Paired inner nozzle as printed. Zoom in to see measurements. (a) Showing asymmetry at the tips. (b) Showing the connecting bridge and spacers at the mid point of the nozzles, that fix the inner nozzles to each other and hold them in position relative to the outer nozzle. (c) Detail of the tip asymmetry. The inner nozzle tips are separated by $113\mu\text{m}$, and $770\mu\text{m}$ wide each. The deficit in the left tip was $682\mu\text{m}$. (d) Showing the nozzles end on with the spacers in the plane of focus, and (e) with tips in focus. The Nozzle apertures are $900\mu\text{m}$ apart. (f) Close up of the inner nozzle tips end on, showing their apertures. Their interior diameters are $221\mu\text{m}$ and $188\mu\text{m}$. The clear space between the nozzle tips is $56\mu\text{m}$.

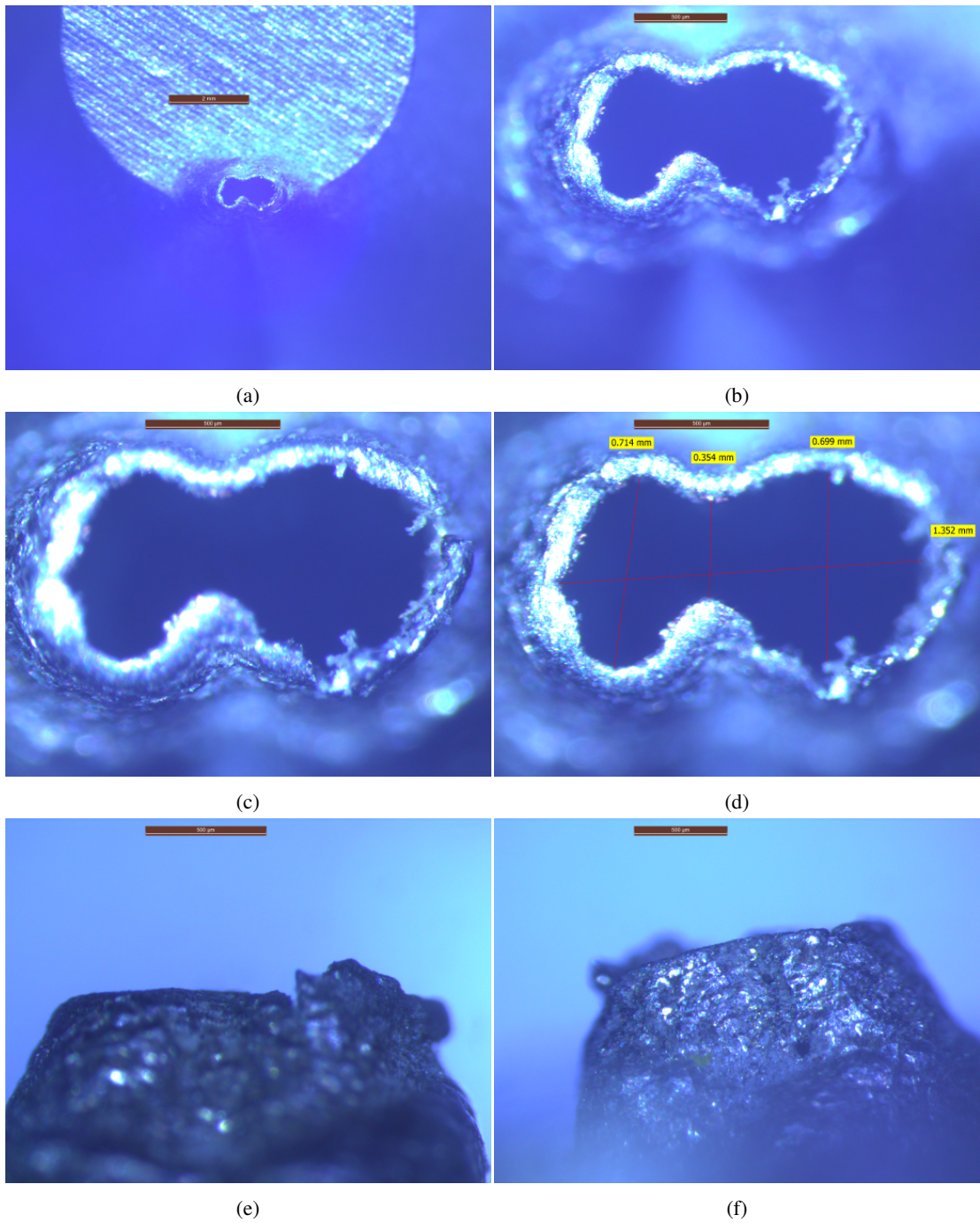


Figure 11-17: The outer nozzle after conservative cutting and grinding. The aim was to improve the geometry with minimal cutting back of the tip, in order to achieve the smallest possible functioning aperture, and to align the end points of the inner and outer nozzles. (d) Shows the new dimensions of the aperture 1.352mm on the long axis, 714μm and 699μm for each lobe, and 354μm for the narrow point of the figure-of-eight.

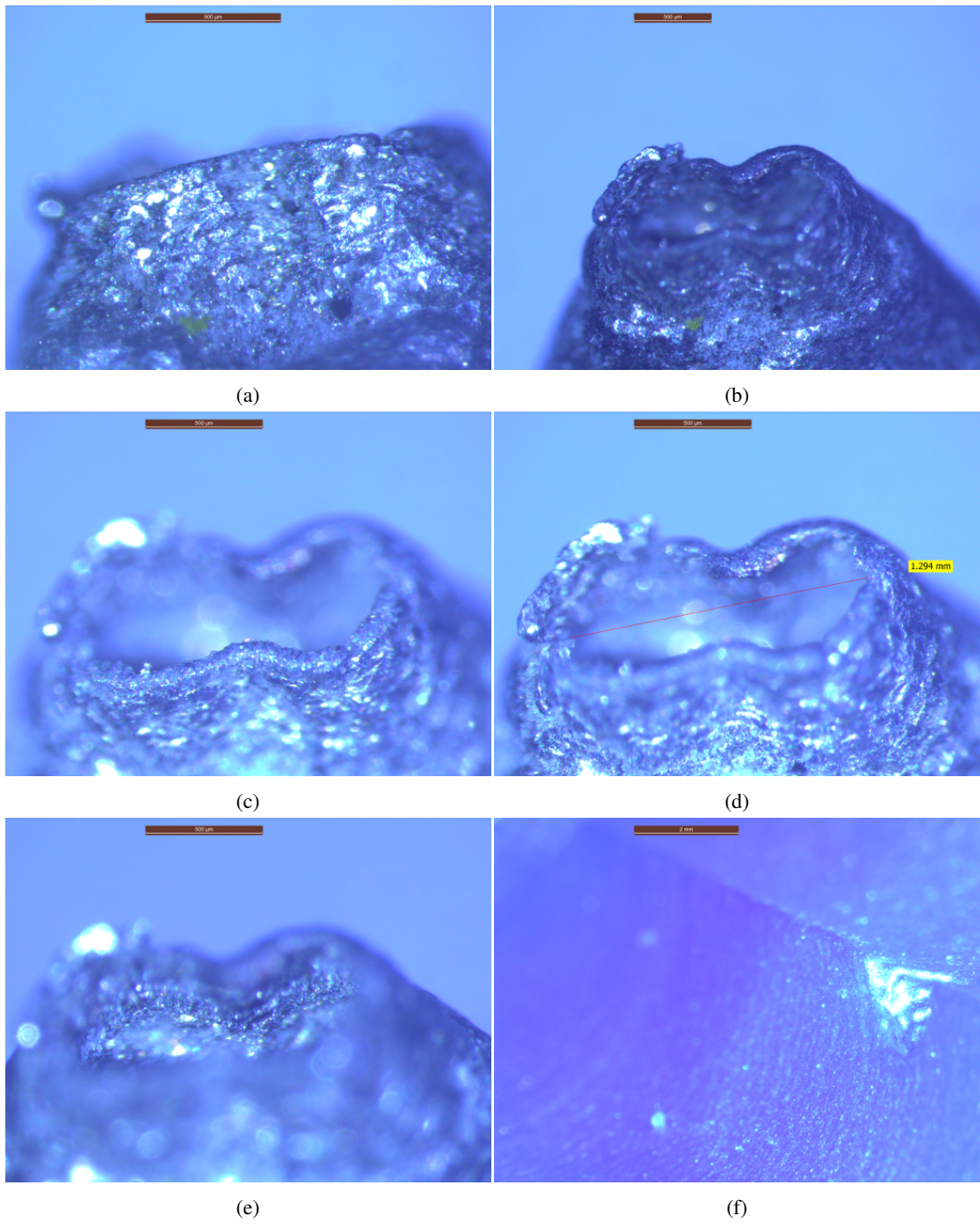
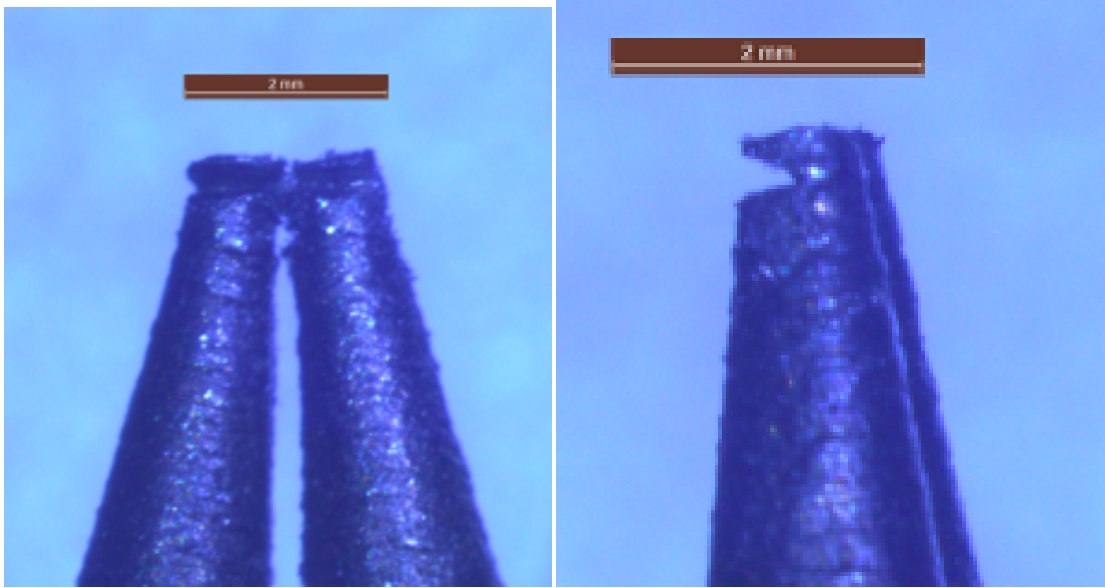
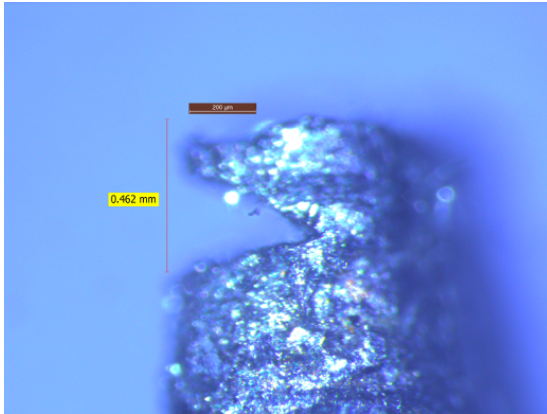


Figure 11-18: (a-e)Close up oblique views of the outer nozzle, showing the 3d shape of the nozzle, and the texture of the material. (f) View of the SEBS port outlet into the interior of the outer nozzle. The other end of the channel aligns with the outlet of the Filastruder.

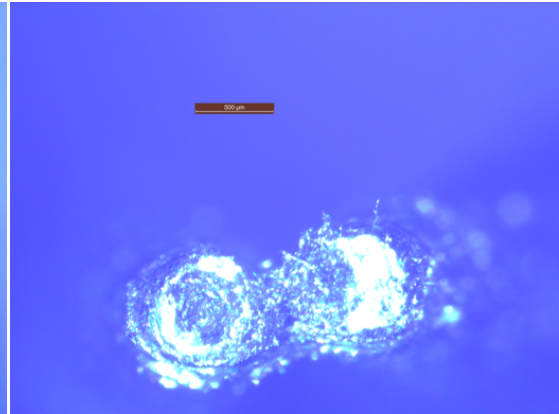


(a)

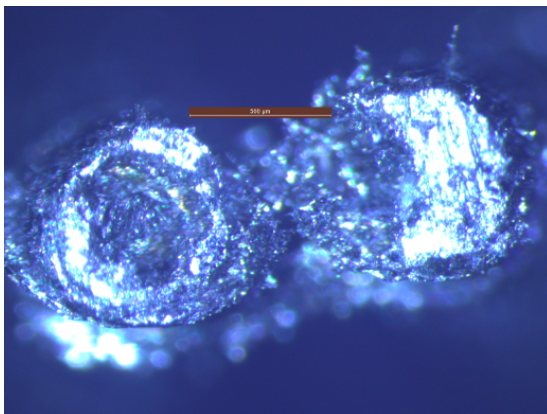
(b)



(c)



(d)



(e)

Figure 11-19: (a-c)The inner nozzle tips were sawn with a steel scalpel blade to produce a clean end level with the tips of the outer nozzle. (d-e) End on view of the sawn inner nozzle tips, showing blocked apertures after cutting. These were cleared by probing with $30\mu m$ copper wire and backward flushing to remove debris.

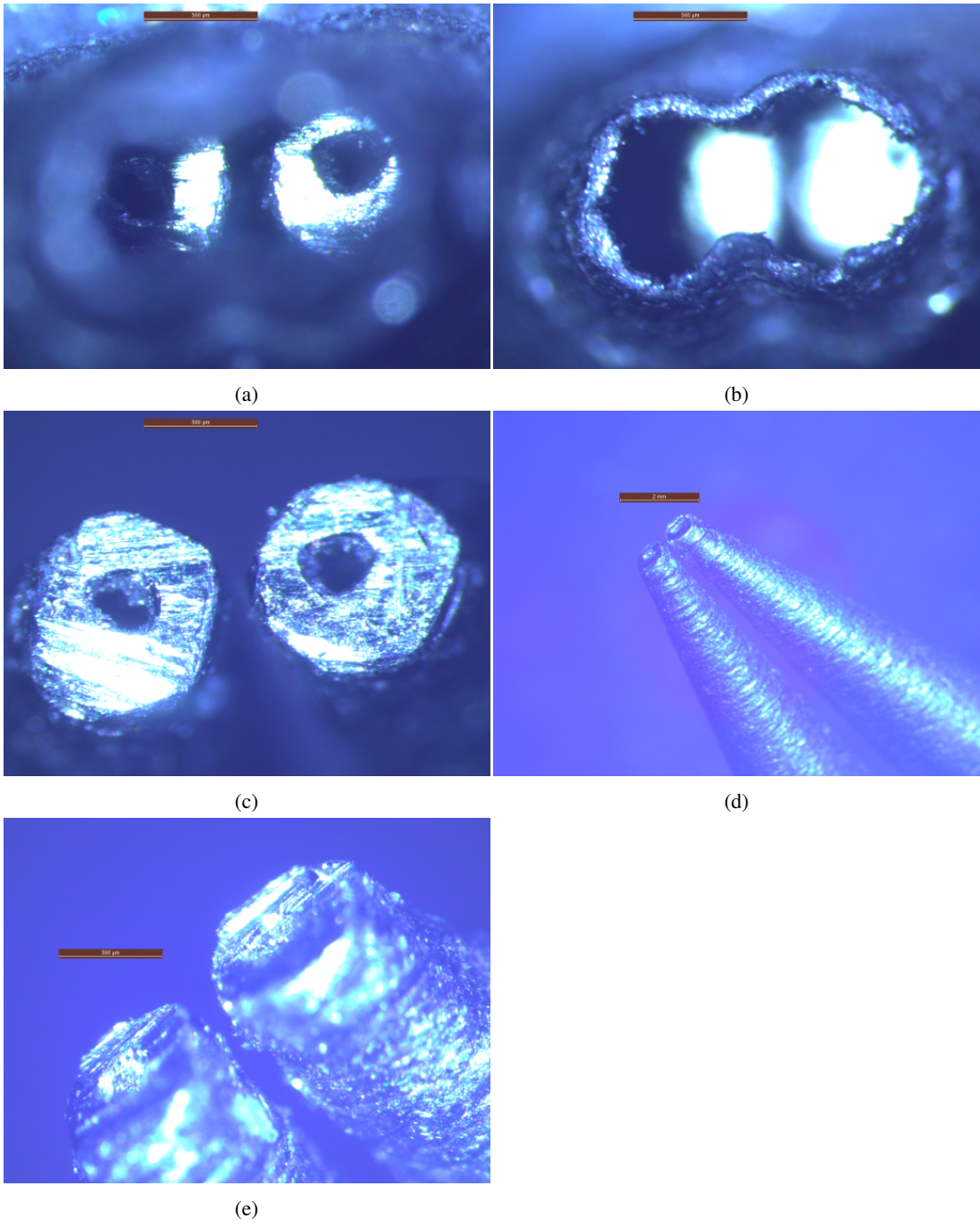


Figure 11-20: (a-b) Tip of the assembled inner and outer nozzles. (c-e) Tips of the inner nozzles after cleaning.)

11.3.3 Setup

The Filastruder is designed to extrude 1.75mm diameter filaments for use in fused deposition printers such as the RepRap. The fibre drawing nozzle was bolted to the filament extrusion nozzle of the Filastuder, such that the Filastuder pumped pressurized SEBS into the fibre drawing nozzle. Thermistors were used to monitor the temperature of the hot end of the filastruder and the tip of the nozzle. The hot end of the apparatus was shielded with aluminium foil to reduce radiation and convection heat losses. The rear openings of the inner nozzles were plugged with silicone, pierced with a needle and connected to a syringe. The amalgam pressure was controlled by PID from the Arduino by a syringe driver and stepper motor. The drive speed of the filastruder, and syringe driver were controlled by POT dials via the Arduino. The filastruder was used to pump molten SEBS-gel-soap blend into the hot nozzle.

11.3.4 Operation

Vertical drawing

The initial set up was for vertical drawing, with the winding reel below the nozzle. This allowed hollow fibres to be drawn, but adding amalgam to the inner nozzles for gravity feed, tended to cause breakage. It was however possible to fill these fibres with amalgam after drawing.

Horizontal drawing & hot plate

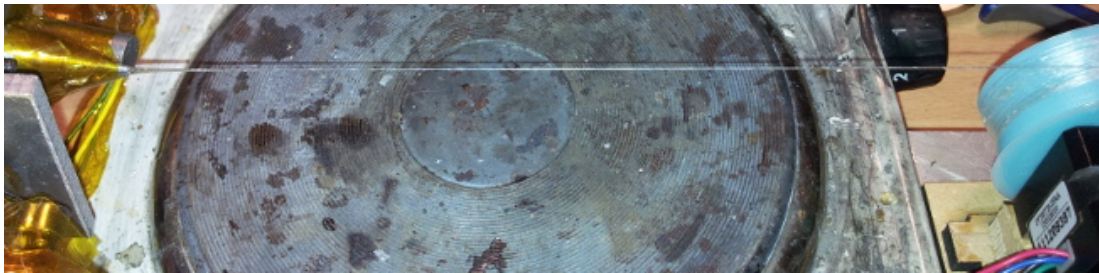
The set up was changed to horizontal drawing, figure-11-21 . A hotplate was placed under the fibre between the nozzle and the winding reel to reduce the cooling rate and thereby allow finer fibres to be drawn. Horizontal orientation of the nozzle necessitated sealing the inner nozzles and adding the syringe driver. Horizontal drawing with syringe driven amalgam allowed SEBS-gel-soap blend fibres to be drawn with amalgam in the conductor channels, figure-11-21b .

11.3.5 Fibre quality

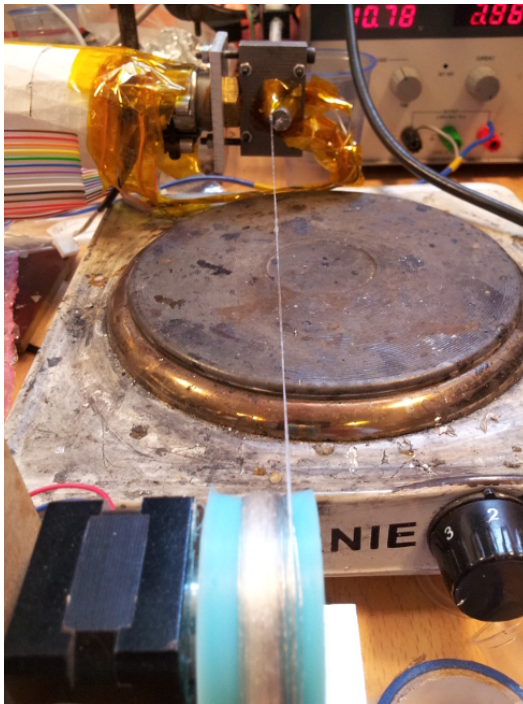
Poor cross-section geometry and rough finish

Compared to the fibres drawn from preforms, the nozzle drawn fibres have a very rough finish, figure 11-22b and could not be drawn as fine. Two reasons for the rough finish are apparent. Firstly the aperture of the nozzle is visibly rough in the micrographs figure 11-20b, due to the grain of the nickel powder from which they were made. This produces longitudinal grooving on the fibres. Secondly excess shear rate will cause turbulence in a fluid, which in fibre spinning results in an irregular rough finish to the fibres. Both types of fault were present in the nozzle-drawn fibres.

Given the dominance of longitudinal ridges, and the distortion of the cross-section, the surface roughness of the nozzle is due to the limit of manufacturing resolution is the dominant effect in the fibres drawn. Correcting this would involve subtractive manufacture finishing of the nozzle tip. This would need to be applied to both the interior of the outer nozzle and the exterior of the inner nozzle. In practice this would probably mean changing back to conventional subtractive manufacture and assembly of parts.



(a) Drawing over a hotplate allowed greater draw down of fibre diameter.



(b) Horizontal drawing, note the change in fibre colour on the reel where amalgam injection starts.



(c) The tip of the drawing nozzle in operation

Figure 11-21: Horizontal nozzle drawing with amalgam

Limited draw down of fibre diameter

The horizontal drawing of SEBS did not allow as fine fibres to be drawn as preform drawing did. A number of factors are likely to contribute. Firstly the nozzle drawn fibre may have had less strength to weight ratio in the melt state, either due to the sharp cut off of support at the nozzle, or the rough surface and distorted cross-section of the fibres. Secondly drawing temperatures of both the SEBS emerging from the nozzle and the air in contact with the fibre in the drawing region may have been different.

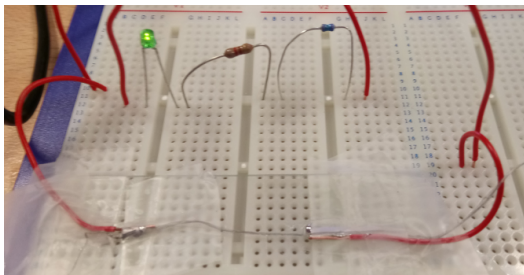
11.3.6 The fibre conducts

Despite the limitations, the fibres conducted electricity both when relaxed and when stretched. Conductivity was at the level expected for GaIn given the length and diameter of the conducting channels.

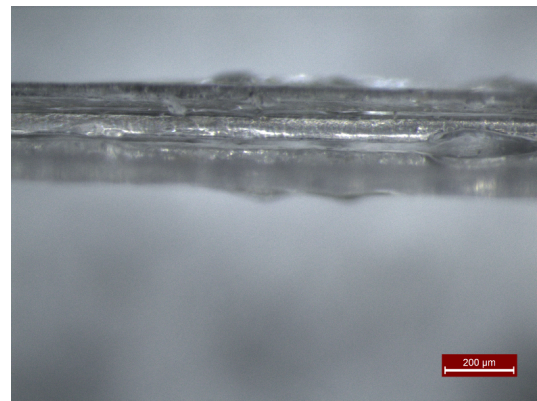
Figure 11-22a shows the initial demonstration of conduction, with a LED being lit and the fibre carrying a current of $1.74mA$. The micrograph in figure 11-22b shows the roughened shape of the nozzle drawn fibre. The conductive amalgam channel is approximately $100\mu m$ in diameter, though refractive distortion by the fibre makes precise diameter uncertain.

Figure 11-22c shows the variation of resistance per unit length with strain. Given an estimated channel and amalgam column diameter of $100\mu m$, the cross section area would be approximately $15.7 \times 10^{-9} m^2$. With a resistance per unit length of $0.26 \Omega m^{-1}$ at zero strain, this would give a resistivity of the column of $40.9 \times 10^{-8} \Omega m$. This compares to $33 \times 10^{-8} \Omega m$ for the Indalloy 46L amalgam. The difference is likely to be due to the uncertainty in the estimate of the channel diameter.

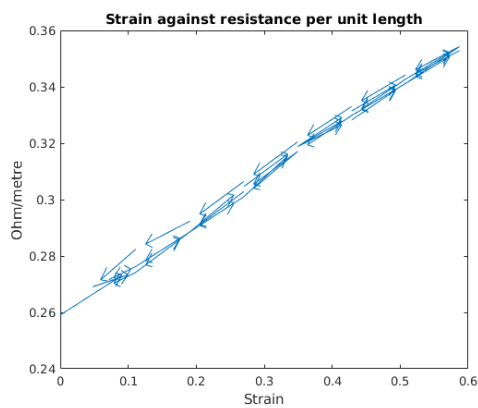
Figure 11-22d shows the stress:strain hysteresis curve for the fibre. The fibre shows marked time dependent hysteresis, as expected for an elastomer-gel. The drawn fibre is stiffer than the cast SEBS gel and has lower breaking strain, however it is still a low modulus hyper-elastic material. The strain of 60% demonstrated in the test exceeds that injury-free strain of peripheral nerve fibres, so would be more than sufficient for connecting sensors embedded in soft structures of a histomimetic robot.



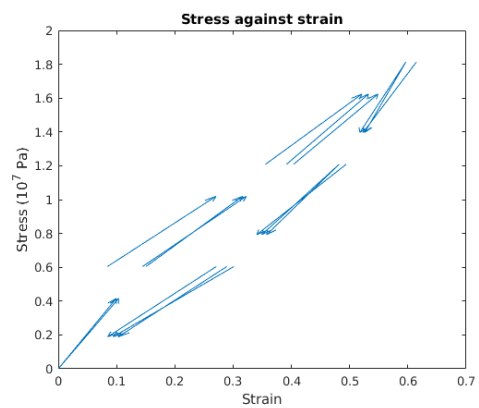
(a) Nozzle drawn fibre (in foreground) demonstrating conduction.



(b) Nozzle drawn fibre showing conductive amalgam channel.



(c) Resistance against strain.



(d) Stress-strain hysteresis curve

Figure 11-22: Testing of nozzle drawn fibre

11.4 Discussion

11.4.1 Conclusions on preform drawing

There is clearly potential for fine ($\ll 100\mu\text{m}$), elastic electrical wires drawn from amalgam-filled thermoplastic-elastomer preforms. A fibre with external diameter $20\mu\text{m}$ could contain a parallel pair of amalgam columns of diameter $5\mu\text{m}$ each. A 1.5m fibre would give a circuit length of 3m , with a resistance of $6.3\text{k}\Omega$ for the amalgam column. This would be acceptable for a sensor circuit supplying the gate of a field effect transistor. Common CMOS video sensors provide arrays of millions of transistors, that could be used to read the signal from the tens of thousands of fibres. This would allow human scale somatosensory sensation in a histomimetic robot.

Critical factors include:

- wetting of amalgam
- drawing behaviour
- electrical resistivity
- elasticity/yield strain
- adhesion to soft tissues
- adhesion to MEMS sensors.

Horizontal drawing

Contrary to the usual method for vertical drawing glass or polymer optical fibres, horizontal drawing is preferred for drawing amalgam filled low modulus elastomer fibres such as SEBS. The reason in both cases is the effect of gravity on the drawing process. Vertical drawing best preserves preform geometry in the fibre when the materials are nearly homogeneous density. GaIn amalgam however is much denser than polymer, and being a low viscosity liquid, exerts substantial hydrostatic pressure. EVA has much higher melt strength, so does not suffer from these problems.

Co-block polymer rheology

The friable stage of SEBS melting may correspond to the emulsion-gel state reported for Styrene-Butadiene-Styrene block copolymers [211] cited in [212]. This is a temperature range at which both the styrene and rubber blocks are in the liquid state, but remain phase separated. At higher temperatures the phase separation breaks down and the melt becomes free flowing. In the case of SEBS-oil gels the high oil fraction results in low viscosity. The melt flow behaviour of styrene block polymers has been studied extensively in polymer science and engineering. The information from that field should be included in future iterations of SEBS fibre drawing.

Control of temperature

The furnace was not particularly successful in all its iterations. The major disadvantage of halogen lamps is that they are so bright that it is difficult to see the preform. Non-contact heating makes accurate absolute temperature measurement uncertain. Heat loss and consequent power requirements were a challenge for lab power supplies.

Future iterations will use direct contact heating and mains power. Two variants, high and low heat capacity, will be investigated: heater cartridges in metal preform heater blocks, and polyimide foil heater tubes. Both methods will allow thermometers to be mounted adjacent to the drawing zone.

Scale of rigs and preforms

Perhaps surprisingly the 20x40mm cross section preforms and tower with 1m drawing space were larger than necessary, and consequently slower and more expensive to work with. Bench top drawing rigs are much easier to work with, and the smaller size makes them much more responsive. It is quite practical to make structured preforms of 10mm external diameter, and draw hundreds of metres of fibre.

Tools for preparing preforms

What is needed for making preform moulds and other parts is access to a bench top model engineering mill, and appropriate cutting bits. Surlyn and PV-OH are best handled with high chromium stainless steel tooling when molten due to their adhesion to aluminium and Surlyn's potential for acidic corrosion. Silicone grease can be used as a releasing agent and lubricant for polymers in metal moulds and drawing tubes.

Blending and preparing polymers in this thesis was done by hand on a hot plate (with a lot of elbow grease). This is far from ideal. A 'Fliastruder' bench top extruder was used in section-11.3, but was generally too large for the quantities needed for making preforms. Its design is rather crude, and problematic to purge and clean. Industrial laboratory bench-top polymer blenders and extruders are available but very expensive.

An adequate mini-extruder could be made using a high chromium stainless steel plate with heater cartridges, a small high torque motor (electric screwdriver) and a small (5mm) stainless steel drill bit as an auger. If the polymer is melted at the entrance to the auger, then the diameter of the bit can be smaller than the polymer pellets. A split-plate design with a recirculation circuit for blending, and interchangeable nozzles would be ideal. This would allow reactive blending techniques such as maleic anhydride grafting of SEBS.

High melt viscosity polymers such as Surlyn can be added to preforms (and other structures) by winding films around a mandrel. It is important to be able to roll thin polymer films of consistent thickness. In this thesis, this had to be done by hand on a hot plate with an alloy roller, which allowed only minimal quality control. A small heated, thermostat controlled calendaring machine could be made to allow precise thicknesses of films to be prepared.

Preform design

A number of preform designs are suggested from this work. SEBS-gels require a support material which has good drawing properties and may either be (i)soluble or (ii)mechanically separable. (i)The former would have a cladding of PH-OV or similar material. This would allow the preform to be rotated during drawing to cancel the effect of gravity, than may cause the amalgam to sink within the molten SEBS. Note that smaller preforms are also less affected by gravity. (ii)Mechanically separable cladding would be open at the top, forming a tough around the SEBS of material, that draws well at the same temperature, e.g. HD-PE or Surlyn. The fibre would be split by drawing it over a tight radius bar, causing the 'trough' of support material to splay open, while the SEBS fibre was wound on to a separate reel.

SEBS-oil-soap blends have reduced electrical resistivity, so should be used to line the amalgam channel, and insulated by soap-free SEBS-gel. Such preforms could be constructed by wrapping SEBS film around a mandrel. Parallel pair preforms could be created by wrapping two SEBS preforms with another layer of SEBS film, then pressing this into a mould formed support channel.

The third type of preform is the Surlyn-ABS preform, which does not need support material. The Surlyn inner layer would be wrapped or dipped in ABS, then removed from the mandrel, and filled with amalgam.

Polymer selection

An important area of further work is to investigate more grades of the polymers used, and other candidate polymers that were not available during this project. There are softer lower melting temperature and faster dissolving grades of PV-OH available commercially that would be expected to perform better as soluble cladding. There are many grades of SEBS that vary in chain length, block ratio and the number of blocks per molecule. These can be expected to have significant impact on drawing behaviour and modulus of the finished fibre.

Two major new categories of thermoplastic elastomers that may be useful are thermoplastic olefin elastomers (TPO-E) and brush polymers. TPO-E are semi-crystalline olefin polymers having blocks of highly ordered monomers which form crystalline phases, alternating with randomly arranged monomers which form the rubber phase. TPO-E are sometimes referred to as 'metallocene olefins' for the class of catalyst used to synthesize them [213].

Brush polymers are molecules which have a long polymer backbone nearly saturated with long chain side groups. These side groups can behave like the solvent phase of a gel, but they cannot evaporate or diffuse away. Cross-linked Brush polymers can form hyper-elastic gels without solvents, and crucially have the potential to retain high viscosity in the molten state. This means that they could provide a very low modulus elastomer that unlike solvent gels, has good fibre drawing behaviour.

Thermoplastic GaIn Amalgam-gel

Finally there is also the possibility of synthesizing a variety of co-block polymers with desirable combinations of blocks via controlled radical polymerisation (also used to synthesize some brush polymers). It may be possible to form a polymer with amalgam wettable mid-blocks, that would form a gel with

GaIn as the solvent. This would allow GaIn-gel to be a thermoplastic elastomeric metallic conductor, which would help to retain GaIn in place in open-ended fibres and other channels.

11.4.2 Preform drawing is preferred over nozzle drawing

Where possible preform drawing produces better fibre finish, being free of both turbulent and grooving defects that are caused by flowing from an narrow aperture. Preforms avoid the need for micro scale manufacturing of tools, so are simpler and cheaper to make.

Improvements for nozzle drawing

Blender – Having a proper blending machine would improve the homogeneity of the polymer blend.

Extruder – Having a smaller and better quality extruder would allow fine control of a smaller nozzle.

Nozzle finish – Smooth finish to the flow surfaces of the nozzle and especially the final extrusion aperture would substantially improve the geometry of the fibre. This could be achieved by subtractive manufacture (drilling) or by using a drawn metal or glass tube for the nozzle. Drawn nozzle components would themselves need to be made from preforms, but would allow very fine apertures if desired.

Rotating spinner – Simple single conductor fibres could be twisted together during the drawing process. This would allow a rotating horizontal two nozzle melt-spinner to cancel the effects of gravity and produce a twisted pair wire.

Control of fibre cooling – The cooling rate of the fibre during melt-spinning is critical, therefore control of conductive, convective and radiant cooling would be expected to improve the consistency of the drawing, and facilitate stable drawing of finer fibres.

Grade of SEBS – Changing the molecular weight, using multi-block grades of SEBS and including viscosity modifiers in the solvent fraction of SEBS-oil gels could potentially improve the drawing behaviour.

Thermoplastic olefins and brush polymers – As with preform drawing, using solvent-less thermoplastic elastomers would potentially improve the melt strength and drawing behaviour, facilitating the drawing of finer fibres.

Part V

**Histomimetic Robot Construction -
Theoretical Section**

Chapter 12

Actuators

This chapter examines theoretical bounds for two plausible classes of muscle-like electrostatic actuator, how they might be manufactured, and how they could be integrated with the techniques developed in Section IV. In this the concepts laid out in the first chapter are followed on emulating the mechanical properties and function of anatomy laid out in Ch. 1.3 as applicable to muscle, Ch. 1.3.3

The first section considers what performance would be needed from an actuator to perform the function of skeletal muscles. The second section examines the conventional rolled dielectric elastomer actuator (R-DEA), optimal materials and how fibre drawing might be applied in manufacturing this class of actuator. The third section considers a proposed bulk-MEMS version of the "Dual Excitation Multiphase Electrostatic Drive" (DEMED), and a novel way to manufacture it in a cost effective way.

12.1 Requirements

12.1.1 Specific power & work per stroke

Theoretical maximum

According to [214], the maximum single contraction specific power per unit muscle mass recorded for skeletal muscle is 371 Wkg^{-1} for the semimembranosus muscle of *Rana pipiens* (northern leopard frog) recorded by [215]. [214] calculates a theoretical maximum of 380 Wkg for typical fast glycolytic muscle fibres based on data from [216]. Higher effective transient specific power can be achieved in muscle-tendon units through the simultaneous release of energy stored elastically by the tendons [214]. [217] report an effective maximum specific work per stroke of skeletal muscle-tendon units of approximately 80 J/kg , and maximum specific power of 800 Watts/kg for jumping gibbons.

The above values represent maximum single actuation performance, and hence actin-myosin fibre density. Human muscle is optimised for longer duration activities, and its peak specific power is much less than the muscles of monkeys. Lower levels of performance are found at the 'phosphate limit' (store of ATP and creatinine phosphate in the muscle fibre), the 'lactate limit' (store of glucose/glycogen in the muscle), 'myoglobin limit' of oxygen stored in the muscles, 'aerobic limit' (the maximum cardiovascular rate of oxygen delivery) and 'fat burning limit' (the maximum rate of fat mobilisation, after

glycogen reserves and food have been exhausted).

Measured instantaneous peak power during contraction in humans

Ferretti (1994)[3] measured instantaneous peak power during a single contraction by performing maximal vertical jumps starting from squatting position. Measurements were taken for children, three age groups of sedentary adults and adult volleyball athletes. This is a combined muscle plus tendon recoil power, rather than instantaneous muscle output alone.

Age years	20-35	35-50	>50	8-13	athletes
Watts per kg body mass	43.1	39.5	34.8	31.6	55.3

Table 12.1: Maximum power per unit body mass for a single jump, for sedentary adults, children and athletes[3].

Measured anaerobic work and power

Anaerobic power fatigues exponentially, figure-12-1, leading to different power measurements for different duration of exercise. A standard way of measuring anaerobic output is the 'Wingate' cycle-ergometer test which measures power produced by the legs pedalling against a resistance. A sample of the literature on power output of different groups of young sports players demonstrates the range of performance.

Davies (1989) [4] calculated the instantaneous pedalling power of students, sprint cyclists and pursuit cyclists, by measuring the decay of their power output over time, then finding the regression to zero duration of exertion. Inbar (1986) measured 5 and 30 second anaerobic pedalling power of male children and adolescents. Bencke(2002)[218] measured the anaerobic pedalling power output of elite and non-elite child sports players.

Subjects	Age years	Weight Kg	Maximum instantaneous power watts	Speed Hz
Sprint cyclists	18.7 ± 2.7	72.5 ± 9.8	1241 ± 266	2.2
Pursuit cyclists	18.5 ± 2.5	68.0 ± 9.9	962 ± 206	2.03
Student cyclists	23.9 ± 4.7	74.8 ± 10.1	1019 ± 183	1.97

Table 12.2: Maximum instantaneous pedalling leg power, calculated by regression of fatigue curve. (Data read from graphs in figure 1 of [4] .)

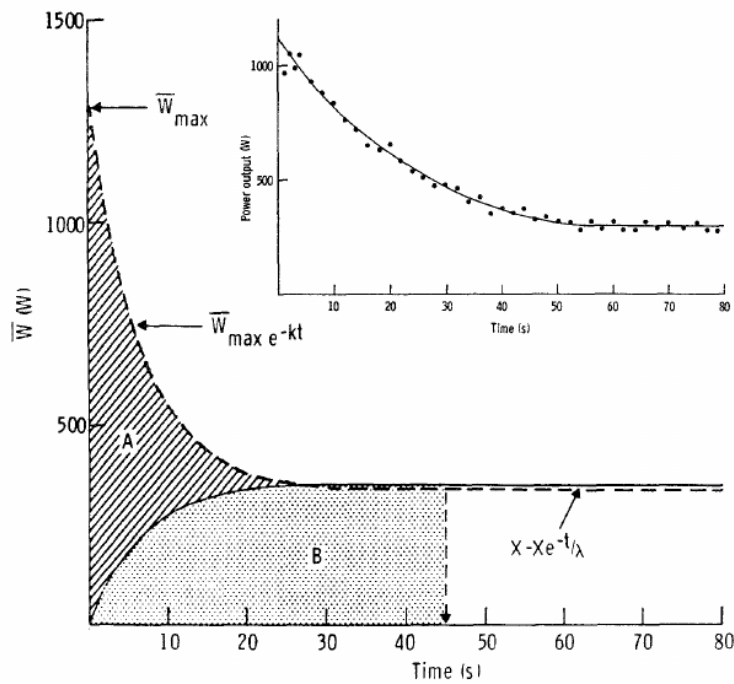


Figure 12-1: Figure 1 from [4], showing how the maximum power out put was calculated from the measured output fatiguing over duration of exertion. "The relationship between average mechanical power production (\bar{W}) and duration of effort(t) showing the method of analysis and derivation of the theoretical oxidative ($W_{o_2} - AreaB$) and anaerobic ($W_{cap} - AreaA$) of the total maximal mechanical work ($\bar{W}_{tot} - AreasA + B$) produced during an 80s all-out test on an isokinetic bicycle ergometer. The exponential decline of mechanical work with time is represented by the equation $\bar{W}_{max}e^{-kt}$, where \bar{W}_{max} is the mechanical work at zero time, t equals time (s) and k is a constant. The theoretical rise in mechanical work production which can be attributed to the muscle oxidation is represented by the equation $X - Xe^{-t/\lambda}$, where X is equal to average mechanical work performed during the last 20s of exercise, t is time and λ (the theoretical half time of the oxidative processes) is taken to be 6s. The analysis was performed to a constant duration of 45s. Inset shows original data taken from a pursuit cyclist."

Subjects	Age years	Weight Kg	Power (5 sec) watts	Power (30 sec) watts	Specific Power (5 sec) watts/Kg body mass	Specific Power (30sec) watts/Kg body mass	Source
Boys	10-11.9	37.5(SD 7.8)	220	180	6.5	6	[219]
Boys	14-15.9	53.4(SD 11.1)	400	330	8.1	7	[219]
Men	18-24.9	67.7(SD 11.9)	570	470	8.1	7	[219]
Men	35-44	76.1(SD 7.1)	650	500	8.5	6.2	[219]
Boys elite handball players	12.5(11.7-12.7)	42.7(33.0-52.5)	380(298-537)	310(268-477)	9.0(6.1-10.2)	8.0(5.6-9.3)	[218]
Girls elite handball players	12.3(11.1-12.9)	47.2(38.7-53.3)	411(330-502)	350(283-395)	8.7(6.9-9.8)	7.2(6.1-8.1)	[218]
Boys non-elite swimmers	11.4(10.0-12.9)	40.0(30.0-52.2)	316(248-477)	254(220-370)	8.0(5.2-9.1)	6.6(4.6-7.9)	[218]
Girls non-elite swimmers	10.7(10.2-11.5)	33.9(25.1-51.8)	276(180-332)	238(160-301)	7.8(7.2-9.1)	6.8(5.6-8.2)	[218]

Table 12.3: Anaerobic leg power over 5 and 30 seconds, measured by pedalling. The data demonstrate the range of performance due to maturation, fitness level and focus of training.

Aerobic work and power

Hawley (1992)[5] measured the sustained power output of adult male and female, cyclists and triathletes competing in races over 40km to 100km. The participants ranged from amateur to Olympic athletes.

Subjects	Age years	Weight Kg	Power watts	Specific Power watts/Kg body mass
Women	32.2(SD 6.8)	56.2 (SD 8.8)	209.8(140.0-300.0)watts(peak)	3.73
Men	29.4(SD 5.6)	72.3 (SD 12.2)	312.8(209.0-515.0)watts(peak)	4.32

Table 12.4: Aerobic maximum pedalling power of adult long distance cyclists, from [5]. Subjects remained seated and cycled at a rate of 80-90 rpm (1.33-1.5Hz).

Skeletal muscle mass, distribution and % of body weight

Poortmans (2005)[6] measured the total body skeletal muscle mass by anthropometry in children, adolescents and young adults and found

	age years	body mass kg	skeletal muscle mass kg	muscle mass %
boys	10.4	33.4±2.4	12.5±0.5	37.4
boys	15.2	61.6±2.9	25.8±1.1	41.8
men	23.4	69.5±2.1	29.4±0.9	42.3
girls	10.3	33.3±1.3	11.6±0.4	34.8
girls	14.8	54.0±2.9	19.2±1.0	35.5
women	22.7	59.7±2.4	22.4±0.8	37.5

Table 12.5: Whole body skeletal muscle mass, measured by anthropometry [6] .

Jansen (2000)[7] measured the skeletal muscle mass distribution in 468 men and women aged 18 to 88 years.

subjects	age years	body mass kg	skeletal muscle kg	muscle mass % of body	lower body kg	upper body kg
Women	18-29	65	21.8	34	12.5	8.7
	40-49	75	21.4	29	12.7	8.4
	70+	61	18.0	30	9.7	7.7
Men	18-29	80	33.7	42	18.5	14.3
	40-49	90	33.5	37	18.3	14.1
	70+	79	27.8	36	13.8	13.5

Table 12.6: Muscle mass, proportion and distribution for different age groups of adults. Data from table 1 of [7] .

Estimating specific power and work of muscle tissue

Taking the power and muscle mass data from the previous sections, the specific power of muscle tissue can be estimated for different durations of exertion. These estimates depend on the assumption that the subjects of the various studies are approximately similar for similar categories.

The estimates of specific work per contraction use the pedalling frequency. This would be the speed of contraction at which the greatest power is generated. The maximum pedalling speed with zero resistance was fastest for sprint cyclist at $262 \pm 8rpm(4.4Hz)$ [4].

Note that 'explosive' jumping relates to the highest instantaneous force and speed during the jumping motion, hence it is not representative of the work done over the duration of the contraction. As previously noted instantaneous peak power output during contraction is a "muscle plus tendon recoil" combined power. This is distinct from the instantaneous anaerobic power which is for a complete contraction cycle, where net tendon recoil would be zero.

No pedalling speeds were provided in [26] so the 'students' speed of 1.9 Hz from [26] was used for the '5 second' anaerobic work per stroke. For the '30 second' anaerobic work per stroke the mid point between the students and the aerobic cyclists pedalling rates was used, 1.66Hz.

subjects	lower body muscle (kg)	power watts	frequency Hz	specific power watts/kg (muscle)	specific work J/Kg (muscle)	duration energy(kJ)
Men 20-35yrs (table12.1)	18.5	3448	n/a	186	n/a	jumping
Sprint cyclist (table12.2)	18.5	1241	2.2	67.1	30.5	'instantaneous'
Men 35-44yrs (table12.3)	18.3	650	1.9	35.5	18.7	5 second 3.2
Men 35-44yrs (table12.3)	18.3	500	1.66	27.3	16.4	30 second 15
Women (table12.4)	12.7	209.8	1.42	16.5	11.6	aerobic 2-5hrs 1510-3775
Men (table12.4)	18.5	312.8	1.42	16.9	11.9	aerobic 2-5hrs 2246-5615

Table 12.7: Estimates of specific power of muscle tissue for different durations and subjects, based on tables listed and muscle mass data from table 12.6.

Maximum isometric tension

Figures of $350kNm^2$ have been cited for skeletal muscle tension in comparison with artificial actuators [220], however the reference Huxley (1980) [221] is hard to obtain, but the other papers published by the same author on muscle tension around that time relate to frogs not humans [222].

[223] measured the in vivo tension during maximum voluntary contraction in the soleus and tibialis muscles of men, taking account of pennation angles and fascicular lengths. The results showed tensions of $150kN/m^2$ for the soleus and $155kN/m^2$ for the tibialis, which is in agreement with in vitro results for muscles predominately composed of type 1 fibres, as these are.

[224] measured in vivo specific tension of $30.3Ncm^{-2} = 300kNm^{-2}$ in the quadriceps femoris. This is composed of predominantly type 2 muscle fibres, and expected to be stronger. These are isometric contractions representing the stalling tension. From them a quasi-static work per stroke can be calculated. This is an upper bound because the maximum isometric tension declines substantially away from mid range of contraction. Taking the $300kN/m^2$ value of tension and a 50% strain, this gives quasi-static work per stroke:

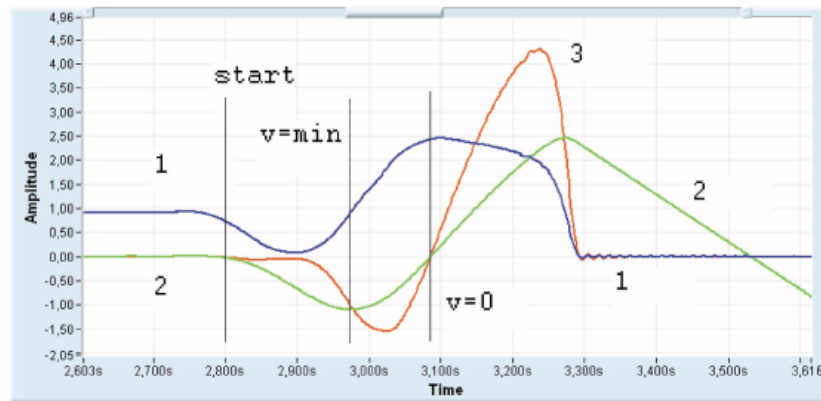
$$specific\ WD_{quasi-static} \ll \frac{tension \times strain}{density} = \frac{300kNm^{-2} \times 0.5}{1000kgm^3} = 150Jkg^{-1}$$

12.1.2 Required muscle performance for safe operation

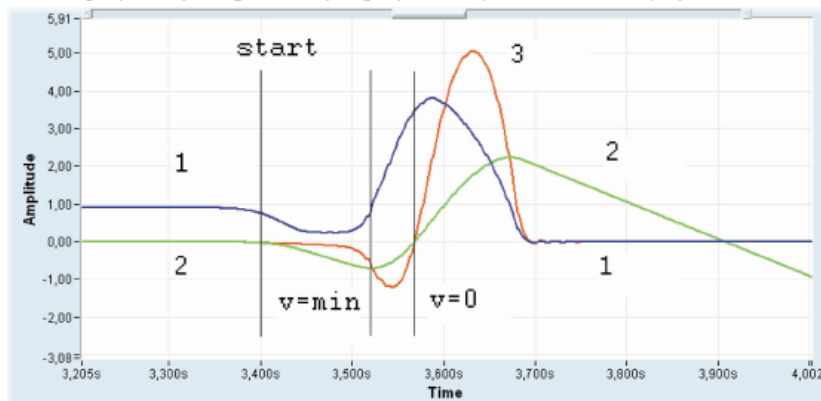
Frailty in humans

The athletic performance reported above far exceeds the minimum required for daily tasks and mobility. A robot hand or whole humanoid/animat would still be useful for many applications without necessarily matching human athletic limits. It is useful therefore to consider the minimum muscle performance required for normal human activity.

Reid (2012) [65] found that peak muscle power was an important predictor of functional limitations in older adults. The decline in muscle performance in old age is a common cause of frailty leading to disability in humans. Often sufficient strength remains for undisturbed locomotion, but vulnerability comes due to lack of power and speed to respond to disturbance - if you haven't the power to recover your balance when you stumble then you are not safe to walk. Similar requirements apply to manipulation, hence the limited ability of many robots to catch object that slip or fall.



(a) Jumping as high as possible=jumping with highest final velocity (get the banana)



(b) Jumping with high stiffness=high force, i.e., moving as quickly as possible from the spot=jumping with maximal force (get away from the snake)

Figure 12-2: Figures a,b represent two different kinds of 2-legged jump. Male subject M.R., 93.4 kg, age 56. Line 1 (blue) represents the force, line 2 (green) the vertical velocity of the centre of mass, line 3 (red) the power. x-axis=amplitude of the parameters, y-axis = time course (ms). Figure 1 from [225].

Kinetic parameters of the 2 jumps

Parameter	Fig12-2a "as high as possible" get the banana	Fig12-2b "as quick and hard as possible" get away from the snake
height [m]	0.40	0.34
maximal force [N]	2450	3800
maximal velocity [m/s]	2.45	2.23
maximal Watt/ kg BW	46.07	54.01

"The time between the first and third vertical marker (start to $v=0$) is the countermovement, i.e., going down to a squatting position. Deceleration and energy storing begins at the second vertical marker ($v=\min$). Decisive for the final height and velocity is the amount of energy which is generated during the movement. Energy during jumping can be calculated as the product of force x velocity x time. Please pay attention to the duration of the counter-movement (different scale!)." [225].

Runge (2006) [225] reviewed the 'determinants of musculoskeletal frailty' in old age and highlighted the importance of sudden high force avoidance reactions for physical safety. Figure 12-2 shows how self protective reactions differ from non-urgent utility actions in a 56 year old 94kg male subject. Note that for both actions there is a 0.2 second reaction delay between stimulus and the onset of movement, but in the case of avoidance reaction the onset of force is sooner, steeper and reaches a higher peak. It takes only 0.10 seconds for force to rise from near zero to four times the force when standing at rest. Peak power is reached at 0.13 seconds and peak velocity at 0.17 seconds after the onset of positive contraction, and 0.46 seconds from the stimulus. These parameters indicate the response times required of a muscle-like actuator.

Bassey (1992) [226] examined leg extensor power and functional performance in a group of frail men and women in their eighties residents in a chronic care hospital. It was found that with respect to mean power per bodyweight for the group and abilities in stair climbing, walking and rising from seated in a chair, that:

"In those who used their arms to rise from a chair, **leg extensor power** was 1.1 versus 1.9 W/kg and in those who needed a walking frame it was 0.86 versus 1.87 W/kg."

Muscular causes of frailty in old age

Lexel (1995) [227] reported the change in composition of muscles with age. The total number and mean cross-section area of fast-twitch (type II) fibres decline with increasing rapidity in old. Numbers of aerobic slow twitch (type-I) fibres remain approximately constant with age. Eighty year olds have on average 2/3rds the mean area per type-II muscle fibre, and half the number of muscle fibres of twenty year olds. Consequently the percentage of muscle cross-section area composed of type-II fibres declines from 55% in twenty year olds to 35% in ninety year olds. Concurrently as reported in [7] there is a decline in percentage muscle mass in the body from 42% in 20 year old men to 36% in men over seventy.

Given the relative contraction speed and power of human type-I, type-IIA (figure 12-3) reported in [228], the changes reported by [227] would be expected to disproportionately affect peak power, force and speed, while leaving endurance and postural strength relatively less affected. (Note that Ranatunga (1987) [229] reported a 30% drop in voluntary force at 12°C as used for the measurements in [228] relative to the more physiological 35 – 25°C temperature range.)

Trappe (2003) [8] measured knee extension muscle power and body weight in young (25yrs) and old (78-80yrs) men and women. This data reveals a decline of fifty percent in power to weight ratio of the body from peak strength in young adulthood to old age. The sample excluded diseases likely to impair performance, so this decline is representative of ageing otherwise in good health.

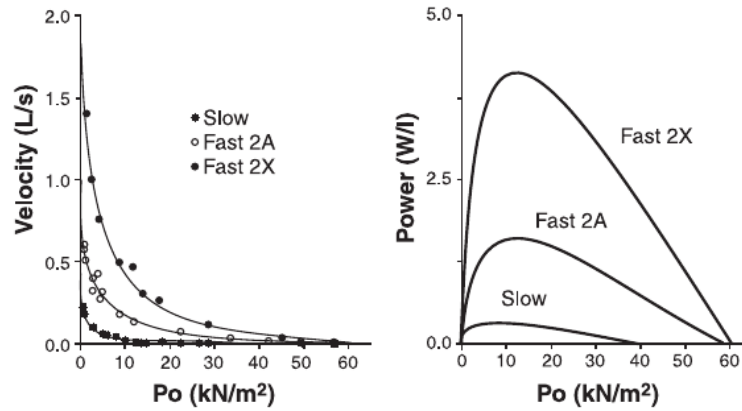


Figure 12-3: Contraction kinetics of slow and fast fibres. A: representative force-velocity (left panel) and force-power (right panel) curves of three single human muscle fibres (slow, fast 2A, and fast 2X) permeabilized and maximally activated at 12°C. From figure 10A in [228]

Group	Age years	Weight kg	Whole muscle Watts	Power:weight Watts/Kg	Old/Young power:weight %
Young men	25	79	604 ± 35	7.6	
Young women	25	58	312 ± 15	5.3	
Old men	80	83	326 ± 57	3.9	51
Old women	78	62	162 ± 6	2.6	49

Table 12.8: The decline in power to weight ratio of the body with age. Data on whole body muscle power and body weight from Table 1 of [8]. Note that the **power here is for knee extension only** on an isokinetic dynamometer for single repetition maximum force.

12.1.3 Performance trade-offs in muscles

While the contraction speed of a single sarcomere depends on the biochemistry of the specific myosin subtypes, the speed and force of contraction of a given muscle also depends on the length of the sarcomeres, and degree of pennation of the muscle. Longer sarcomeres provide greater force at the cost of slower strain rate of contraction, while increased pennation provides greater force but reduced fibre length hence reduced tendon excursion.

Specific muscles are adapted to the work per stroke, tendon excursion, speed of contraction and endurance required of them by varying the proportions of fibre types, sarcomere length, pennation and muscle mass.

Muscle types in the hand

[230, 231, 232, 233] provide a detailed review of the varying structure of the intrinsic and extrinsic muscles of the hand and wrist, summarised in Ch-3.4. While the dimensions of intrinsic muscles of the hand were largely determined by the available space in the palm, the mass, and effective cross section area varied widely between the different muscles.

12.1.4 Minimum specifications for a muscle-like actuator

Structure and speed

Firstly to fit in the available spaces a muscle like actuator must be fibrous in structure to at least the sub millimetre scale. Fibrous actuator structure also implicitly permits the physiological solution to control of actuation force, by selective recruitment of fibres within a muscle belly.

As seen from Runge (2006) [225] and Ranatunga (1987) [229] the actuator must reach full force within 0.1 seconds ideally within 0.06 seconds, and show similarly quick relaxation times. Notably in the relaxed state it should be slack and flexible such as to provide negligible resistance to joint motion. From the pedalling speeds of cyclists in Davies (1989) [4] a muscle-like actuator should be capable of completing an contraction-extension cycle at peak power at 2Hz, and 4.4Hz with no load. For at least some muscles the actuator must be capable of actuations of at least 40% strain. Note that these speeds are required for safe coordination and are related to the size of the human or robot by their toppling period as an inverted pendulum.

Specific power

From Reid (2012) [65] and Bassey (1992) [226] the critical role of peak power and force per unit body weight would need to be met. For the able bodied elderly in table 12.8 this was approximately half the whole body specific power of young adults. Table 12.7 showed that for the muscle tissue of athletic adults the '*instantaneous*' specific power and work of muscle tissues was 67.1watts/kg , 30.5J/kg and the '*5second*' duration specific power was 35.5watts/kg , 18.7J/kg .

Allowing that low performance of an actuator could be compensated by increasing actuator mass as a proportion of robot body weight, a '**muscle bound weakling**' robot concept would have actuator mass at the high end of the human range, and whole body specific power above the threshold of frailty.

Spent (1993)[234] reports percentage muscle mass as high as 65% in body builders, compared to the 42% for young adult males in table 12.6 this provides 150% of 'normal' muscle mass.

Combining the previous two paragraphs would make actuator performance 1/3 of human muscle specific power and specific work per stroke the acceptable. This would set as the **lower bounds of acceptable performance:**

instantaneous specific work and power $\geq 10.2J/kg, 22.3watts/kg$

'5 second' duration specific work and power $\geq 6.6J/kg, 11.6watts/kg$

Burst power supply and sustained power energy store requirements

Human-like performance also requires endurance and gradual reduction of maximum power with increasing duration. The peak single jump, and 5 second maximum power in table 12.7 both come to approximately 3.2kJ for an 80kg man. The 30 second anaerobic output of 500 watts produces 15kJ of work. This must be multiplied by the efficiency of the actuator to find the required input energy. Human's achieve 24% efficiency in oxidising carbohydrate and fat to do muscular work pedalling an ergometer. This can be considered a combined 'fuel cell, actuator and body mechanics' efficiency. By comparison dielectric elastomer actuators can operate at 90% mechanical efficiency [235]. If we allow 70% efficiency after hysteresis in the robot's body, the 30 second 500watt 'anaerobic' output would require 22kJ input of electrical power.

Aerobic exercise is long endurance, hence large amounts of energy are consumed. An 80kg man cycling at 312 watts for five hours produces 5.6MJ of work. At 70% efficiency this would require 8.0MJ electrical power input.

Battery and fuel cell performance

High burst power for robots has been demonstrated with an electric double layer 'super' capacitor. [236] used a 100volt 13.5 Farad capacitor weighting 8.9kg with a theoretical energy store of 67.5KJ, and 7.6kJ/kg specific energy, to supplement battery power in a 46kg bipedal lower body humanoid robot. Given the low specific energy of capacitors it would be preferable to use this only for a few seconds of power, equivalent to the physiological creatinine phosphate energy store. A 0.6kg capacitor would hold 4.5KJ of energy.

Commercially available lithium polymer (Li-Po) batteries have specific energies up to 250Wh/kg (900kJ/kg) [237]. Conventionally a 250Wh Li-Po battery would be designed to allow 2C (i.e. 500 watts) continuous power draw, and should be charged at or below 1C (250 watts). Depending on the design burst power draw up to 70C (16kW) might be permissible. At 70% efficiency 500watts output would require 715watts of electrical power. If this is supplied by the battery in parallel with 200watt 'aerobic' power supply, this would amount to a 515watt draw on the Li-Po battery marginally above 2C.

Without resorting to internal combustion engines, the highest specific energy electrical power comes from aviation fuel cells. A commercially available example is the HES AeroPack solid fuel cell is designed to power small UAVs[238]. Configured for 10 hours operation, at 200watts output it weighs

2.3kg including the hydrogen generator. (The same fuel cell configured with a compressed H₂ gas tank instead weights 4.3kg.) This is an energy store of 7.2MJ, specific energy of 3.1MJ/kg, and specific power of 86watts/kg.

Combining these three electrical power sources, an 80kg humanoid robot might use a 0.6kg capacitor, a 1kg Li-Po battery, and two 2.3kg fuel cells giving a 6.1kg power pack for an 'able senior robot', or double that at 12.2 kg (15.3% of body weight) for an 'able bodied robot'.

12.2 Rolled dielectric elastomer actuator

12.2.1 Concept

The rolled dielectric elastomer actuator (r-DEA) has been studied [244]. In this section the effects of materials, scale, and manufacturing by fibre drawing are discussed theoretically. Subsequently the potential and limitations of this class of actuator for integration in histomimetic robots are assessed.

Structure and actuation

Dielectric elastomer actuators are capacitors constructed of elastomeric materials such that they deform under electrostatic force to provide actuation. r-DEAs are rolled thin film capacitors that extend longitudinally when charged, figure-12-4.

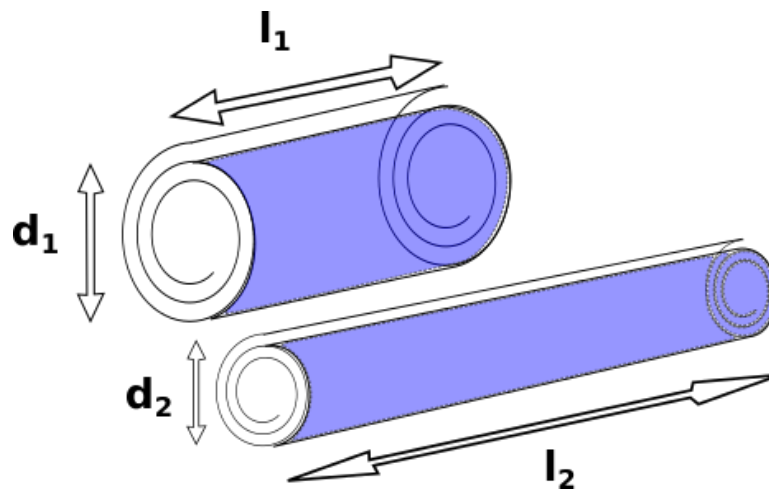


Figure 12-4: Actuation of the rolled dielectric elastomer actuator. Applying voltage causes the plates to attract each other, squeezing the dielectric, resulting in extension of the fibre. Thus the actuator contracts elastically when it is discharged, and is charged to relax it. d_1 , d_2 , l_1 , l_2 are the diameters and lengths before and after charging.

The materials of the actuator are rubber or gel elastomers, which are effectively incompressible, so the volume is constant. When charge is applied, the plates attract reducing the diameter of the roll. Conservation of volume causes the actuator to extend in length.

If $l_2 = 2l_1$, representing 50% actuation, then by conservation of volume of the cylinder

$$\begin{aligned} vol &= 2\pi r^2 h = 2\pi \left(\frac{d_1}{2}\right)^2 l_1 = 2\pi \left(\frac{d_2}{2}\right)^2 2l_1 \\ d_1^2 &= 2d_2^2 \\ d_1 &= \sqrt{2d_2^2} \\ d_1 &= d_2\sqrt{2} \end{aligned}$$

The capacitance changes due to both change of separation distance and increase in area of the plates. Given that plate area A is equal to the length of the actuator times the length of the rolled edge, and the length of the rolled edge is proportional to the circumference, and therefore to the diameter of the actuator:

$$\begin{aligned} A_1 &\propto d_1 l_1 \\ \frac{A_1}{A_2} &= \frac{d_1 l_1}{d_2 l_2} = \frac{d_1}{d_2} \times \frac{l_1}{l_2} = \frac{1}{\sqrt{2}} \times 2 \\ A_2 &= A_1 \sqrt{2} \end{aligned}$$

Capacitance C of the plates is given by $C = \frac{\epsilon A}{S}$, where ϵ is the permittivity of the dielectric, A is the area of the plates, and separation of the plates $S \propto d$ the diameter of the actuator, hence:

$$\begin{aligned} \frac{C_2}{C_1} &= \frac{\frac{\epsilon A_2}{S_2}}{\frac{\epsilon A_1}{S_1}} = \frac{A_2 d_1}{A_1 d_2} = \sqrt{2} \times \sqrt{2} \\ C_2 &= 2C_1 \end{aligned}$$

The electrical energy stored in a capacitor is given by $Energy = CU^2$ where U is the potential difference across the plates. So as the actuator doubles in length, the capacitance and the electrical energy stored also double. The electrostatic force between the plates does work against elastic resistance, thereby storing elastic energy.

12.2.2 Optimising performance of the actuator

The energy stored is proportional to the capacitance, and therefore to both the permittivity of the dielectric and to the inverse of the separation of the plates, but it is proportional to the square of the potential difference. This implies that increasing both the relative dielectric constant and especially the dielectric strength are desirable to maximise the specific energy stored and therefore specific work of the actuator.

Relative dielectric constant can be increased by including mobile polar groups, such as ketone dipoles, in the chemical structure of the dielectric elastomer. However ionizable groups such as carboxylic acids must be avoided because they provide mobile charge carriers that dramatically reduce the dielectric strength.

Dielectric strength is not a fixed parameter, but depends on temperature, shape and the work function of the electrode material. (Note that the work function for removing an electron from a solid is always lower than the first ionization energy of the corresponding monomer gas, [239].) Heat, kinetic energy of atoms and molecules, may contribute energy to dislodge an electron, hence the heating of cathodes controls thermionic emission in vacuum tubes. The shape of the electrode determines the local electric field strength. The locally flat and parallel geometry of capacitor plates minimises local electric field intensity and hence the risk of dielectric breakdown.

The two properties of the dielectric itself that most contribute to measured dielectric strength are the work function of the dielectric and the absolute distance across the dielectric.

Thin film dielectric strength

Thin films have much higher dielectric strength than thicker layers of the same material. e.g. Polyethylene bulk material has dielectric strength in the range $18.9 - 21.7 \text{ MVm}^{-1}$ [240], but a $40 \mu\text{m}$ film of polyethylene has a dielectric strength of 300 MVm^{-1} [241]. Figure-12-5 shows the measured and predicted dielectric strength of three short chain aliphatic hydrocarbons. Note the hyperbolic rise in dielectric strength in the theoretical line below one micron separation, confirmed by measurement of heptane (C_7H_{16}) at $3 \mu\text{m}$ giving a value of 300 MVm^{-1} [242].

While the details of the mechanisms are the subject of ongoing research [243], thick layers suffer a cascade effect once mobile electrons or ions are released, whereby these are accelerated by the electric field to an energy above that required to ionise other molecules that they collide with. If the dielectric film separating the plates is made sufficiently thin, then at the same electric field strength, the potential difference across the dielectric falls below the work function of the dielectric. In this circumstance the cascade mechanism is not available, though heating will occur and contribute to a more gradual breakdown process if local temperature rises.

Hence an optimal dielectric elastomer actuator would have dielectric layers thin enough that the potential difference across the plates would be less than the work function of both the dielectric and the electrodes. Typical rolled dielectric elastomer actuators published in the robotics literature [244, 245] are made by wrapping films around a core where the film thickness is in the range $250 - 90 \mu\text{m}$. This results in potential differences that are well above the first ionisation energy, and hence the full benefit of the higher dielectric strength of thin films is not obtained. It also means that special insulation is required for safety of high voltages around the actuator. Reducing the thickness of the wrapped

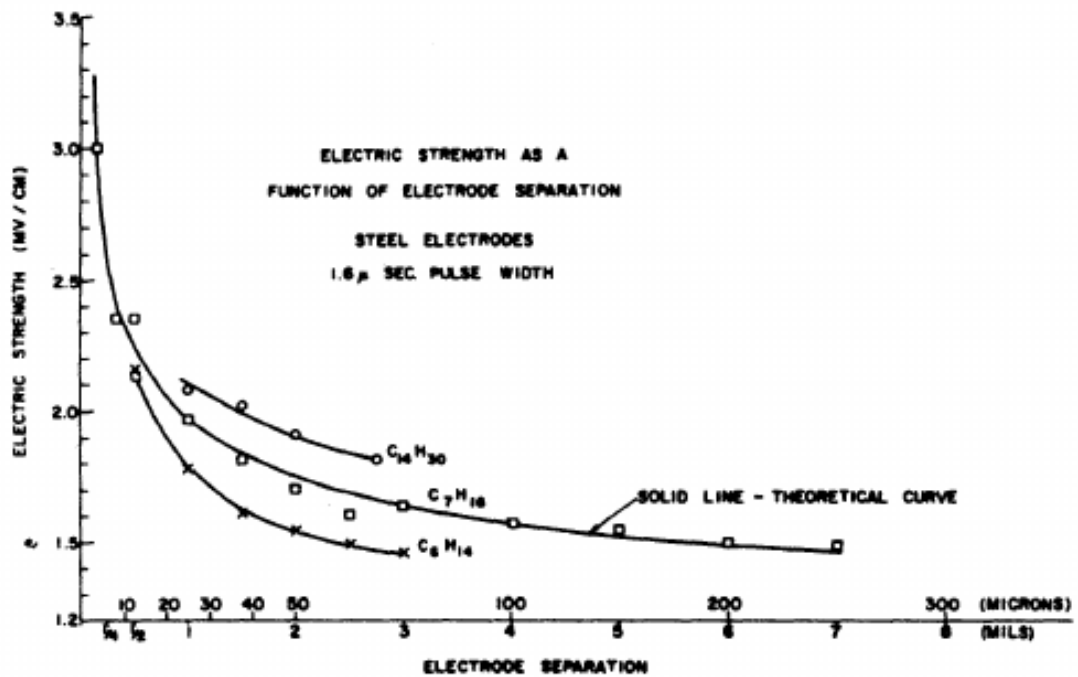


Figure 12-5: Electric strength as a function of electrode separation. Fig 1 from [242]

film would substantially increase the labour of manufacture and present quality control challenges for maintaining constant thickness. A different way of manufacturing rolled dielectric elastomer actuators is needed to enable optimal geometry for maximum specific work and low voltage operation.

Manufacture by drawing from a preform

Thermoplastic elastomer fibre drawing as used in the production of signal fibres in chapter 11.2 would allow geometry reduction from an actuator preform. A preform of 10mm diameter constructed by wrapping 100 μ m film capacitor, composed of four 25 μ m dielectric and electrode layers around a 5mm diameter elastomer core, could be drawn down to a fibre 100 μ m in diameter. This would produce dielectric layers 250nm thick.

Materials

SEBS rubbers would provide very good elasticity and dielectric strength, but as seen in chapter 11.2.6 they have poor melt strength and can be problematic for drawing. One option would be to blend SEBS with non-cross-linked poly-ethylene-propylene rubber to increase the melt viscosity. The dielectric constant of the dielectric layer can be increased by using SEBS with maleic anhydride grafted to the mid-block though this requires at a gel with polymer content < 30% to allow free orientation of the malate group [246]. Cyclopentanone can be used as a high dielectric constant extender, because it does not dissolve polystyrene, but has relative dielectric constant of 13.8 at 20°C [247], and a first ionization energy of 9.26eV comparable to alkanes [248].

In order to be drawn in a fibre the electrodes would also need to be thermoplastic elastomers. To adhere well to the SEBS/EPR dielectric, a styrene co-block hydrogel could be used such as the styrene-propylacrylamide-styrene amphiphilic triblock copolymers synthesised in [249]. If needed polyvinyl alcohol could be used to increase the melt viscosity of the electrodes, and glycerol could be used as a plasticiser with a boiling point above the drawing temperature.

Given the phase structure of SEBS contains styrene micelles with a hard sphere radius of 16nm (depending on the styrene block length) and phase structure repetition of 36nm (greater for higher proportions of ethylene-butylene/EPR phase), the proposed 250nm thick electrode and dielectric laminae would be near the limiting scale for this class of polymer.

Specific work attainable

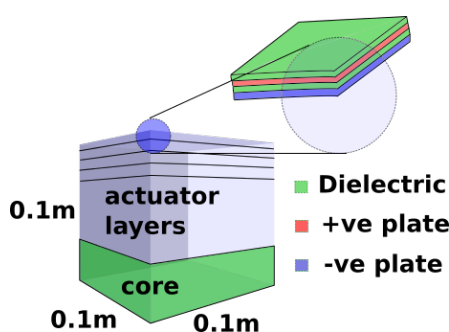


Figure 12-6: An equivalent cube of actuator for calculating the electrical energy density and therefore the maximum work density of a rolled dielectric elastomer actuator.

We may calculate the maximum work density by volume of this actuator, assuming elastomer modulus matched to the electrostatic energy stored (by selecting the material of the elastomer core) by considering a cube $0.1m \times 0.1m \times 0.1m$ of actuator. The plate area per unit volume can be found by multiplying the height of the cube by the proportion by volume of the fibre of the actuator layers, then finding the number of layers.

$$\text{Proportion of actuator layers} = \frac{r_{preform}^2 - r_{core}^2}{r_{preform}^2} = \frac{10^2 - 5^2}{10^2} = 0.75$$

$$\text{Number of layers } n = \frac{0.1m \times 0.75}{10^{-6}m} = 7.5 \times 10^5 \text{ layers}$$

Plate area must be counted above and below, so

$$\text{effective plate area } A = 0.1m \times 0.1m \times 7.5 \times 10^5 \times 2 = 1.4 \times 10^4 m^2$$

At $250nm$ we can expect that the dielectric strength will be substantially greater than the $300V\mu m^{-1}$ given for polyethylene at $1\mu m$. For SEBS with no added dipoles would have a relative dielectric constant of 2.2. If we take an electric field strength of $200V\mu m^{-1}$ there will be a good margin of safety below the break down voltage. This gives a potential difference between the plates of $50V$. The energy stored

in the capacitor is given by

$$\begin{aligned}
 \text{Energy} &= CU^2 = U^2 \frac{\epsilon A}{S} \\
 &\approx 50^2 V^2 \frac{2.2 \times 8.85 \times 10^{-12} Fm^{-1} \times 10^4 m^2}{250 \times 10^{-9} m} \\
 &\approx 1950 Jkg^{-1}
 \end{aligned}$$

This estimate of the theoretical upper bound is more than ten times times the specific energy required to match the quasi-static specific work in section 12.1.1, more than sixty times the 30.5J/kg instantaneous specific work of able bodied adults, and two hundred times the 10.2J/kg minimum required for useable humanoid robot section 12.1.4. It follows that there is grounds to expect that an effective muscle-like actuator can be made by fibre drawing rolled dielectric elastomer actuators. There will be many details of the polymer chemistry, and drawing technique to be investigated in order to achieve that. Perhaps the most important feature of fibre drawn rolled-DEAs is that they would provide a practical way to achieve the very thin layers needed to bring the actuation voltage down to safe levels.

12.2.3 Fibrous rolled dielectric elastomer sensor (FR-DES)

It has long been known that variable capacitors, of which DEAs are a sub-class, can be used as sensors. DEAs have been applied in this role as high sensitivity tactile sensors e.g. [250]. Fibrous rolled-DEAs with low elastic modulus have potential as the sensor element of mechanoreceptors of the same scale as sensory nerve endings. Being drawn from a preform allows fibrous rolled DEAs to have many more layers and therefore greater capacitance and gauge factor than micro-DEAs made by conventional MEMS layering and patterning techniques. Simple MEMS structures could be used to provide the connection between an FR-DES and sensor signal fibres in chapter 11.

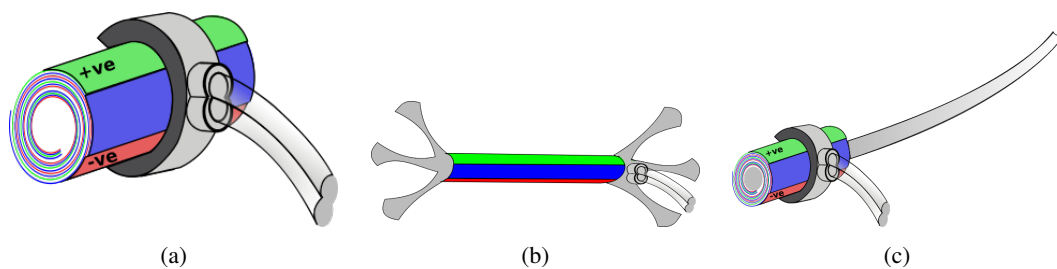


Figure 12-7: Proposed MEMS mechanoreceptors using fibre drawn rolled dielectric elastomer sensors. Simple MEMS components would be used to connect the sensor to the signal fibre and anchor the sensor to the tissues. a)Pressure/vibration sensor (equivalent to Paccinian or Merkel sensory endings) b)Stretch receptor (equivalent to Ruffini ending, muscle spindle or Golgi tendon organ) c)Hair follicle, with hair fibre co-drawn then stripped.

12.3 Dual excitation multiphase electrostatic drive

There is another class of electrostatic actuator with potential to form muscle-like fibrous actuators. The 'dual excitation multiphase electrostatic drive' (DEMED) is a class of linear electrostatic actuator first published by Niino et al (1995) [251]. In minimal form this consists of two plates of at least three phases of parallel electrodes. The plates slide over each other orthogonally to the electrodes when an alternating current is applied.



Figure 12-8: a) Schematic of Dual Excitation Multiphase Electrostatic Drive (DEMED). The electrodes are connected into three phases, fig-1 from [251]. b) Schematic cross sectional view of basic DEMED. Two potential distribution around electrodes are indicated by bold lines, fig-2 from [251].

This class of actuator has three key advantages with respect to dielectric elastomer actuators. Firstly it is relaxed in the discharged state and only requires electrical potential in proportion to the square root of force to be generated. This reduces magnitude and duration of exposure of the materials to high electrical potentials, so reduces the risk of dielectric break down. Secondly it is an iterative actuator that cycles through many phases in one contraction stroke. This allows it to extract the energy from the electric field many times in one contraction. Thirdly contraction and the force-extension relationship are not principally dependent on elastic recoil, therefore there is greater flexibility for control.

The versions of the actuator described in [251] already achieve high specific work ($11J/Kg$), power ($228W/kg$) and force ($628N/kg$) for the first example in their paper. These values already exceed the minimum requirements of $\geq 10.2J/kg, 22.3watts/kg$ instantaneous specific work and power in section 12.1.4. However they are macro scale actuators made of rigid polyimide (Kapton) foil, and operate at high voltages (up to $2.5kV$). To be usable as a muscle in a histomimetic robot the DEMED design would need to be adjusted to a quasi-fibrous form. For practical use the operation voltage would need to be reduced by at least tenfold, an ideally the specific work per stroke should be increased at least threefold.

In their paper Niino et al state that the force per unit area of the actuator is independent of the pitch of the electrodes and therefore the scale of the design. However as scale is reduced the layers become thinner, hence the specific force per unit mass and force density per unit volume are inversely proportional to the scale.

It should also be taken into account that the dielectric strength of films increases approximately hyperbolically with decreasing scale, table 12.9, and the force produced is proportional to the square of the potential difference. It should be borne in mind that the increasing dielectric strength would be partly off set by the reduced radius of curvature of the electrodes at smaller scale which increases risk of dielectric breakdown. Consequently the achievable specific force, would be expected to increase with the $> scale^{-1}$ but $< scale^{-3}$. The achievable dielectric strength, actuation force and actuator life span

Film thickness μm	125	75	50	25
Dielectric strength $V\mu m^{-1}$	154	205	240	303

Table 12.9: Increasing dielectric strength with decreasing film thickness for DuPont Kapton-HRTM (poly-oxydiphenylene-pyromellitimide), from [9]. Test condition 60 Hz, 1/4 in electrodes, 500 V/sec rise.

would depend on the precise geometry, the curing of the polyimide, the absence contaminants and the manner in which the actuator was operated.

12.3.1 Proposed quasi-fibrous DEMED

A scale reduction of the DEMED by a factor of twenty would bring the specific work to above that required to match the quasi-static work of maximal isometric contraction. It would also reduce the electrode width from 135 to $6.75\mu m$ and the vertical separation from 100 to $5\mu m$. At this scale the peak actuation voltage would be reduced from $2.5kV$ to $125V$.

To form a useful muscle, fibre actuators of up to $600mm$ long [252] need to be made, and in sufficient quantity to produce the $\approx 32kg$ of muscle in an adult male body. This rules out the one sheet at a time flexible circuit-board photolithographic method used by Niino et al. A roll to roll printing technique would be desirable, and it is essential to have 3D interconnects to connect three or more phases of electrodes. It would also be beneficial to have rounded edges to the electrodes to reduce the local field intensity and to minimise the proportion of metal used to save weight.

Roll-to-roll hot embossed polyimide microfluidic manufacturing

The precursor of polyimide is polyamic acid, which is thermally cured to polyimide. Partially cured polyimide is plastic and can be embossed with a stamp or roller that have been patterned photolithographically. When a pair of patterned embossing rollers are used together, both channels in the plane of the film and vertical perforations through it can be formed. When patterned films are laminated together complex fluidic channel systems can be formed. When the part-cured polyimide is heated to annealing temperature, the channels become rounded in cross section. The cured polyimide is thermally stable to above $400^{\circ}C$.

If the microfluidic system is first evacuated under a vacuum, then heated to above the melting point of a low viscosity (e.g. Indium based) solder, then the solder can be driven into the microfluidic channels. If the vacuum is not too high, gas bubbles will remain in the blind ending electrodes. If each phase is charged individually, while the others remain grounded and the solder remains molten, then electrostatic force will distribute the solder on the interior surface of the electrode channels. The system is then cooled to solidify the solder. In this way hollow cylindrical electrodes with rounded ends can be formed. Since the electrodes themselves form most of the volume of the channel system, this allows the quantity of metal and mass density of the actuator to be reduced.

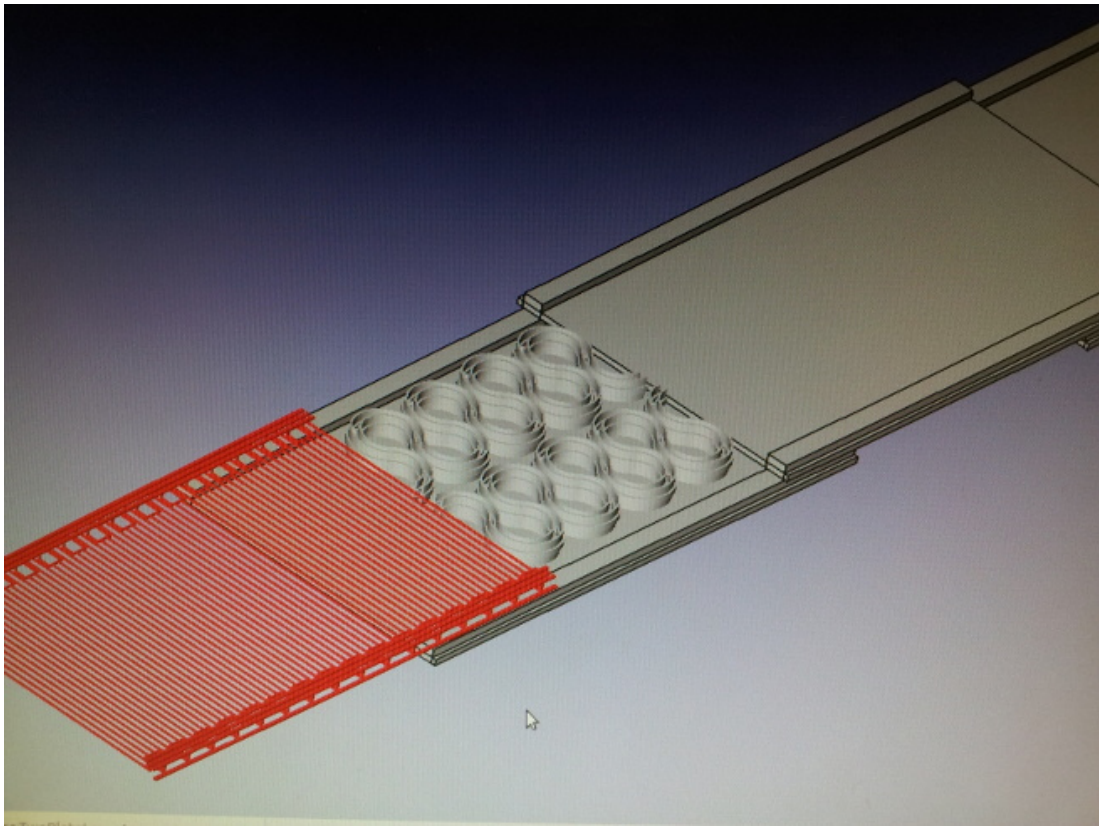


Figure 12-9: CAD model of microfluidic DEMED actuator, showing MEMS springs connecting consecutive plates electrically and mechanically. There are four phases of electrodes with power rails at the margins (red), which would be set inside polyimide dielectric plates. Geometry is constrained by the need to maintain minimum distances between phases at all points to avoid dielectric breakdown. The vertical electrical interconnects to the plates above and below would be at the mid point of the springs.

Electro-mechanical design

The basic structure of the fibrous DEMED would be electrode plates arranged like bricks in a wall, with gaps between consecutive plates to allow actuation. The 'wall' would have many layers, making it approximately as tall as the plates were wide. The number of electrodes per plate would depend on the balance of contraction speed and specific work per stroke.

Electrically the plates would have four phases, with one in-plane and one raised power rail on either side of the plate. Consecutive plates would be electrically connected by wires carried in MEMS springs (figure 12-9). Plates would be connected vertically at the midpoint of the springs to the midpoint of the plates above and below. The springs are made of polyimide and are part of the laminae of the plates in their row. They serve multiple mechanical roles, maintaining the separation between the plates and connecting wires, acting as a return spring, and managing the flow of fluid into the gap opened between consecutive plates when the fibre extends.

The fibre would be enveloped in SEBS-paraffin gel. The SEBS cladding of the fibre-DEMED forms the matrix of the muscle, and helps to protect the actuators from lateral pressure by allowing them to

splay relative to each other. To maximise the dielectric constant the fibre would be filled with cyclopentanone (relative dielectric constant $\epsilon_r = 13.8$ [247]). Cyclopentanone can also be used as a solvent in processing polyamic acid to make polyimide structures. Allowing cyclopentanone retention in the polyimide would increase its dielectric constant, but would also need to be controlled to limit the effect of swelling on the designed geometry.

It would be important to minimize friction between the plates where they are pulled together in the working overlap region. The glass beads used in Niino et al (1995) would not be an option in a fibrous actuator to be used in all orientations with respect to gravity. Viscosity must also be kept to a minimum, so a boundary lubricant similar to that proposed for joints and tendons in chapter 9.2.2 would be suitable. However fatty acids would not be suitable, due to being ionizable so reducing the dielectric strength. Polyimide presents ketone dipoles as its intermolecular bonding group. A potential family of boundary lubricants would be long chain di-amines. These have a single hydrogen and two alkane chains on the nitrogen atom. Each ketone group presents two pairs electrons available for hydrogen bonding. This would allow at least four alkane chains to be attached to each exposed ketone group by two hydrogen bonds. To completely eliminate the possibility of ion formation, 'olefination' treatments such as the 'Wittig' reaction could be considered.

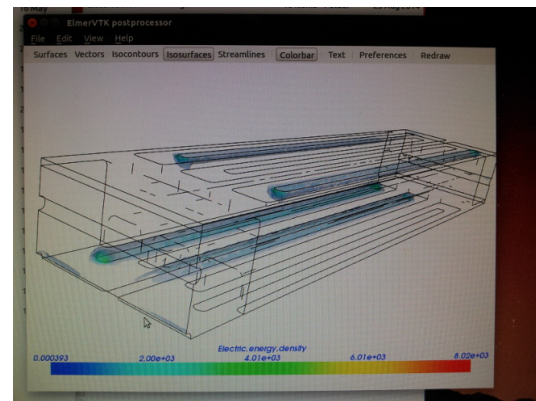
Electrostatic FEM Models to verify design

In preparation to produce an initial prototype, CAD models were made on FreeCAD (chapter-6.2.3), (figure- 12-9) were created to verify geometry for the actuator in operation, the masks for the embossing pattern, and lamination process. Electrostatic finite-element models were made on Salome-Meca chapter6.2.3 (figure 12-10d) and computed on Elmer (chapter-6.2.4) for electric field (figure 12-10b), electrical potential (figure 12-10c), and electrostatic force (figure 12-10b). Mechanical stress analysis was also planned.

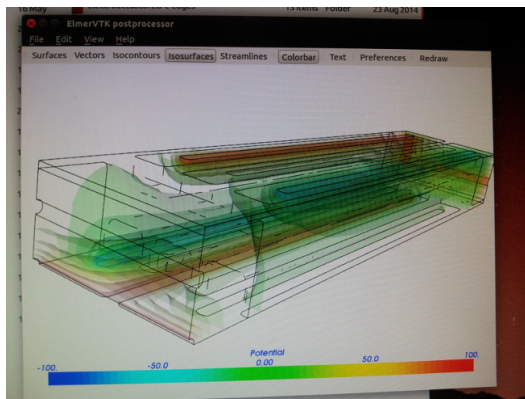
Unfortunately these models were destroyed in a hard drive failure, and there has not yet been time to recreate them.



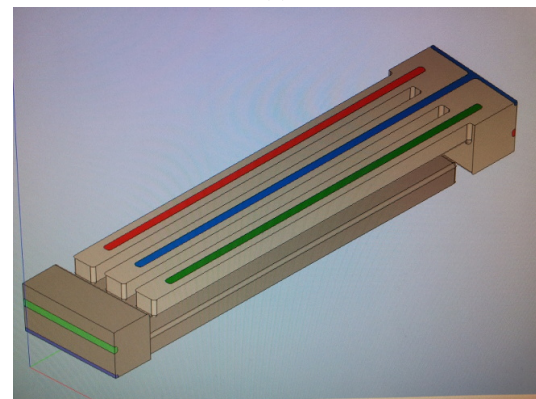
(a)



(b)



(c)



(d)

Figure 12-10: Elmer electrostatic finite element analysis of a unit cell of a microfluidic DEMED actuator. Note this is a different layout of the DEMED with three phases and central power rails. (a) Electric force density. (b) Electric energy density. (c) Electric potential contour surfaces. (d) Salome-Meca model from which the multi-partition mesh was made.

Chapter 13

Perception

The difficulty of quantitative measurement and modelling of soft matter has been a recurrent issue in this thesis. It is central the obstacle to the general application of quantitative methods to the science of anatomy. It would be central to a perception system able to fuse the mechanosensory data from a histomimetic robot hand (alone or with other senses) to make inference about the shape and material properties of objects and the environment. It would also be essential to automation of the design and layout of complex soft composite structures such as those of histomimetic robots.

To provide a viable solution to these problems the Smoothed Particle Machine Perception (SPMP) algorithm was developed [253]. Time did not allow for an executable software code to be written, but funding was secured to do so, section-15.1. An early version of the theory was published as a poster, section 16.1.4. What follows is an overview of the theory and its application for histomimetic robotics.

13.1 Visual tactile fusion challenges

13.1.1 Representation and modelling

The conventional approach to anatomical modelling uses finite element models for tissue deformation, linked to separate boundary meshes and bounding boxes for contact modelling and collision detection, e.g. the SOFA surgical simulation framework [17]. This has been effective for developing surgical simulations but has a number of shortcomings. Finite element models need additional processes to handle material flow and collision. Hyper-elastic deformation can be particularly problematic because the computation is liable to become unstable when the elements are highly distorted. The system of separate surface rendering, contact modelling, collision detection and material deformation meshes for each object, is effective for designed simulations but becomes brittle in complex scenes with many objects.

13.1.2 Inference from sensor data

Inferring the structure and physical properties of the world from sensor data poses particular challenges.

The specific scene is not known *a priori*, and new objects, materials and phenomena may be encountered. It is necessary to have a system that allows the perceived model of the scene to be progressively fitted and updated to sensory data as it becomes available. Ideally this should be adaptable to integrate multiple sensors of any sensor modality - e.g. force/displacement tactile/proprioceptive sensors, vision, sound.

Generally problems of sensory perception are strictly under defined. That is there are multiple possible arrangements of the world that could give rise to any given combination of sensor signals. In order to justify one group of possible solutions over others additional constraints are needed.

Real world scenes are constantly changing. Things move and deform. Illumination changes alter the appearance of scenes. Both the the representation and the sensory inference of a perception system must allow the changes that can and do occur in the world.

13.2 Terminology in machine perception

SLAM/SFM "Simultaneous location and mapping" (SLAM) or "structure from motion" (SFM) is the joint estimation problem of inferring 3D shape from a series of images from different relative camera poses (e.g. consecutive video frames), without being given the camera poses *a priori*.

dense SLAM SLAM algorithms that generate a 3D depth estimate for every pixel in an image are called "dense SLAM" or "dense SFM" algorithms.

Rigid world hypothesis The rigid world hypothesis is the assumption that everything in the scene remains stationary and only the camera moves. This reduces the possible solutions, making the solution easier to find, but causing an algorithm the uses it to fail when there are independently moving or deforming objects in the scene.

Dynamic SLAM/NR-SFM dynamic SLAM algorithms, also referred to as as 'non-rigid structure from motion' (NR-SFM) generate 3D models of scenes where the rigid world hypothesis does not hold.

active an active depth sensor emits a signal to enable it to estimate 3D depth, e.g. LIDAR, and structured light rgb-d cameras such as MS Kinect.

passive a passive camera is an ordinary camera with no active depth sensing

stereo a stereo pair of cameras has a pre-calibrated pose transform between the two cameras.

monocular a monocular camera is a single camera, parallax motion in the image is generated by moving the camera.

rgb red, green, blue - i.e. a normal three colour camera, as opposed to rgb-d with active depth sensing included.

tactile SLAM perception of the shape of the world from touch sensation, as opposed to vision, sonar, LIDAR, radar or other sensor modalities.

13.3 Recent publications that are close to SPMP

”Dense Tracking and Mapping” ’DTAM’ [254] <https://www.youtube.com/watch?v=Df9WhgibCQA> was the first algorithm to provide real-time dense 3D reconstruction from passive monocular video. DTAM generates a depth map by optimisation of a photometric cost volume using anisotropic total-variational smoothing and exhaustive search over a restricted range of depths. The optimisation is accelerated by using an auxiliary variable and primal-dual optimisation to define the range of exhaustive search [255, 256]. Frame to frame camera pose tracking is done in parallel with mapping, using the dense depth map. Combined with forward prediction of the pose transform of the next frame, this provides a fast, accurate estimate of pose transform which in turn improves the quality of the depth map. DTAM assumes a ’rigid world’ i.e. that only the camera moves, and segments out any pixels that do not fit this assumption.

”Shape Illumination and Reflectance from Shading” ’SIRFS’ [257] <https://www.youtube.com/watch?v=NnePYprvFvA> is a single image reconstruction algorithm that, produces a spherical illumination model and maps of depth, surface normal, and Lambertian reflectance, see figure-13-1. It uses a set of prior expectations about smoothness, convexity, and parsimony of materials, jointly optimised for photometric fit on a Gaussian pyramid. This is an important concept because while the problem is strictly under constrained, the likely real world solutions are tightly clustered. The cost functions express natural scene statistics which make the task of finding the most probable solution well constrained. Note that the use of cost functions in a cost volume make the techniques in DTAM and SIRFS compatible. This is exploited in SPMP see section-13.4.2.



Figure 13-1: Analysis of a single static image by SIRFS [257]. From left to right: original image, shape, surface normals, reflectance, shading, illumination.

”Better Together” [258] <https://www.youtube.com/watch?v=gT25sLQw1IA> is a an algorithm for passive monocular rgb video, non-rigid 3D reconstruction including specular reflection and shading. It uses a prior template captured while the object (human faces in their demonstration) is stationary and not deforming. Once the template is captured it tracks the deformation of the face during facial expressions and changing light conditions.

”Dynamic Fusion” [259] https://www.youtube.com/watch?v=i1eZekcc_1M uses monocular active rgb-d sensor as its input and does not require a prior template. It tracks moving, deforming (human upper body, arms, hands and fingers in their demonstration) using energy minimisation in a network of deformation nodes underlying a dense surface mesh.

13.4 Smoothed Particle Machine Perception (SPMP)

SPMP is a passive dynamic visual-tactile fusion algorithm that builds soft matter physics models from sensor data. The SPMP algorithm uses a smoothed particle hydrodynamics (SPH) physics model as its representation of the scene. Techniques from DTAM and SIRFS are combined and extended to fit the model to the sensor data. It provides a reciprocal interaction with recognition as grounding for higher cognition able to generate physical simulations from semantic descriptions.

13.4.1 Smoothed particle hydrodynamics (SPH) as the basis of a physical perception system

'Hydrodynamics' is a misnomer due to the earlier application of SPH to open surface fluid flow modelling. SPH is a 'mesh-less Lagrangian' i.e. particle based discretisation. Matter is represented as a collection of point masses and the effect of physical forces between particles is computed by finite basis smoothing kernels that provide a tractable approximation of the true physical forces.

SPH has several important properties:

- Its parameters can be adjusted to simulate all classes of matter especially fluid, plastic, elastic, fibrous and granular materials that are common in real world scenes [260, 261, 262].
- The system intrinsically handles collision and permanent deformations e.g. cutting.
- The spatial resolution of a model can be varied locally in a running simulation by particle splitting/combining [263, 264, 265, 266]. This allows detail and computational load to be concentrated in the area of interest i.e. perceptual foveation.
- As a physics simulation it can predict the signal of any class of sensor, so provides a basis for multi-modal sensor fusion.
- It provides physical conservation laws so allows perception of the flow of mass, momentum, energy, detection of sources and sinks, e.g. detection of powered machines/animals/people versus passive objects.
- SPH codes written for graphics processing units (GPUs) can run simulations of millions of particles in real time, e.g. Fluids v3 [267] and OpenCL-SPH [268]. (Note OpenCL-SPH was written by the PhD student funded to implement SPMP for anatomical modelling, see the chapter on further work, section-15.1).

13.4.2 How SPMP works

Dynamic SLAM with reflectance

We start by combining the techniques of DTAM and SIRFS to get a rigid-world dense passive monocular SLAM that is invariant to illumination changes. We then achieve dynamic SLAM by treating camera pose as a pixel-wise property with strong edge preserving regularisation e.g. anisotropic total variational smoothing on a pose-transform map. This allows us to track a moving deforming surface. The

combination of parallax data greatly accelerates the estimation of shape, and therefore the deconvolution of reflectance and illumination.

Specular reflection and translucency/transparency cause additional optima in the depth map, which for convex surfaces are always further away than the true surface. Including these is important for robust perception in real-world scenes.

Foveation allows the periphery to be tracked for awareness and localization, while concentrating computational effort on the area of interest. This allows the system to provide a balance of detail and robustness in a real-time system. It also means we must direct attention from a combination of bottom up saliency and top down interest. (More on this later.)

Fitting the smoothed particle physics model

The dynamic surface map becomes the surface of a smoothed particle model. Typically half of the particles in a model will be the visible surface and other places directly responsible for sensor data e.g. the contact with a tactile sensor. The remainder of the particles form the structure behind the surface. The smoothed particle model provides forward prediction of the sensor data that is used to accelerate the optimisation of the perception of the surface in the steps above.

The fitting of the parameters of the particles, as in SIRFS is constrained by cost functions expressing scene statistics to constrain the problem to find the most probable real-world solution. These are closely related to the prior expectations in SIRFS, but expressed in 3D, i.e. parsimony of materials, smoothness, convexity, and a cost for the number of particles required in the model. Typical models would be about 1/100th the size of the maximum forward simulation on the hardware, i.e. tens of thousands of particles, to allow multiple models in parallel for fitting of the parameters.

Motion planning and control

The ability to simplify models by combining particles allows minimal, very fast models of objects and mechanisms of interest to be generated. The expansion of kernel radii of these small models provides a quick way to generate attractor-repeller fields to guide avoidance and grasping. Particle inflation also allows representation of probabilistic future states e.g. risk and consequence of an object falling.

Reciprocal physical and semantic perception

Perceiving physical properties provides a much more robust basis for recognition than raw sensor data. Recognition can also be applied as an additional cost function in fitting the physical model i.e. the properties of the particles can be adjusted to better fit the recognised object within what is compatible with the sensor data. This provides a mechanism for object completion, that corrects itself if it is contradicted by new sensor data, e.g. you discover there is a hole in the cup.

Episodic memory, imagination

Recording the state of the recognition system (the matrix of activation values of any semantic segmentation system e.g. deformable part models, fully convolutional neural networks etc.) provides a semantic

description of the scene. This approximates the scene graph of a conventional top down simulation, because it holds the same information. The SPH simulation can be regenerated, by setting the record as the target state for the recognition system, then adjusting the number, location, and parameters of particles.

The form of the compressed record would be a sparse tensor holding the most significant outputs over time. In this way it can be recursively compressed by dropping the least significant remaining outputs. This resembles the way human episodic memory fades over time. The decision about how significant an element is will take account of its relevance to on going concerns, i.e. "you don't forget the things you worry about".

Novel scenes can be simulated by editing the semantic description, or synthesising one from a few high-level abstract descriptions.

Recognition of actions and learning procedures

The transformation of an object over time, plus perception of the forces acting on the object allows perception of causal relations and therefore subject-object relations in actions. Having episodic semantic memory of chains of actions allows the learning of procedures. Being able to generate and vary simulations from observed procedures allows a robot to investigate which factors are critical to the success of the procedure. This supports one-shot learning. Zero-shot learning would be where only the start and desired end are known, and a sequence of feasible intermediate steps is sought.

13.4.3 Interpretations of smoothed particle models for higher perception

Smoothed particle models can be viewed as

- Gaussian mixture model partition of 3D space,
- Topological network,
- Markov random field predicting the propagation of forces.

They also provide the constraints of conservation of mass, momentum and energy. Consequently causal relations and energy sources are evident. This allows the distinction of powered machines and agents from passively moved objects in a scene. Theory of mind can then be grounded as a hidden Markov random field of intentions, drives and knowledge of an agent whose causal mechanisms are not completely known.

The process of graph sparsification [269, 270] can help to identify crucial factors for predicting future events of interest. This is in some ways similar to credit assignment in back-propagation, and involves considering counterfactuals at least at the level of the effect of different values at a node. These crucial factors provide top-down cognitive saliency, and can guide attention, and the choice of percepts to monitor for control of a given action.

The topological network view of SPH models can be useful in guiding saccading to find the parts of an object for deformable part based recognition. This would enable recognition of even highly distorted perspective or artistic images, or an object after flexion of joints.

13.5 Applications of SPMP for histomimetic robotics

13.5.1 Digital Anatomy

SPMP can be applied to the capture of anatomical models from dissection. These models would then provide a starting point for the design of histomimetic structures for anatomy. Capture would involve fitting strain gauges to dissection instruments and calibrating them against a load cell to obtain force measurements of the process of dissection. Eye tracking cameras would be worn by the anatomist to capture their field of view in stereo and their saccades. The anatomist's eye movement would be used to guide the fovea of the perception system, so that detail is added to the model in the areas of interest. The instruments would be tracked and the forces they apply would be propagated through the model to learn the structure of the specimen being dissected.

13.5.2 CADEM for histomimetic robots

Having a semantically segmented smoothed particle model of an anatomical structure, this can be edited to adjust geometric proportions and material properties, or to add or remove structures as a CAD for complex soft composite structures. This could be done either by editing the SPH model directly or by editing the semantic model and adjusting the SPH model to fit. Running the SPH model as a simulation would provide CAE analysis to predict the behaviour of the design under load.

Once a design is ready for prototyping, the tool paths and layup sequence for fibre and matrix deposition, and sensor implanting can be computed from the SPH model.

13.5.3 Closed loop control of CNC lay up

The robotic layup of dry tows of fibres and soft thermoplastic matrix materials on the free-form 3D surface of complex composite structures would be too unpredictable for reliable for open-loop control as used in common 3D printers. Visual-tactile tracking of the layup process with SPMP would allow the result of each action to be perceived and subsequent tool paths to be re-planned. In this way errors can be incrementally corrected as they occur to keep the layup process as close as possible to the design.

13.5.4 Visual-tactile perception and motion planning by histomimetic robots

SPMP would allow a histomimetic robot to learn the structure of its own body and surroundings in relation to its tactile and proprioceptive sensors, and to fuse vision, hearing or other senses into a single model of its surroundings. Episodic memory and procedural learning would allow the robot to learn the effects of its actuators, and how to coordinate them to perform effective actions.

Part VI

Conclusions

Chapter 14

Conclusions

The principal conclusion of the thesis is that histomimetic robotics is a viable avenue of inquiry. That is, that the functional emulation of anatomic structures is feasible by engineering synthetic composites and mechanisms that reproduce the physical properties of anatomical tissues.

This conclusion is important because it is widely believed in the robotics community that it is either much too difficult [11] [18] or that suitable materials will not be available for a long time [24], both views leading to the assertion that detailed emulation of biological materials and mechanisms is not a viable approach. The evidence of this thesis supports a more optimistic view.

The necessary information and materials to build direct mechanical emulations of anatomical tissues, structures and mechanisms are available, but widely dispersed across different disciplines. Expensive hard to obtain materials are not required, commercially available commodity materials are sufficient to build such emulations of musculoskeletal and dermal structures. This thesis collates some of that information to identify a viable palette of materials and techniques. It also provides an entry point into the anatomical literature and other disciplines of use to those who may wish to investigate this approach to building robots.

Perhaps the most important lesson from this project has been a methodological one of (i) the importance of asking the right questions to support the goal and (ii) not restricting the search for answers to a comfort zone of familiar disciplines. The first step has been to use the information from anatomy/histology/pathology/surgery to determine what is necessary and sufficient for the useful functions that are to be reproduced. In this the critical role of low modulus hyper-elastic matrix materials and complex topologies of fibres must be appreciated. These structures cannot be functionally approximated by rigid materials or quasi rigid-body simulations. The second step has been to ask not whether, but how the necessary material properties can be provided by synthetic materials. This involved stepping down in scale far enough, but not further, to find a level at which simple synthetic materials could match the relevant properties of anatomical tissues, then reconstructing anatomical structures upwards from that scale.

For those accustomed to numerical disciplines, the anatomy of soft tissues is the most alien discipline required for the techniques in this thesis, because it remains a principally descriptive non-numerical science. Accessing and understanding the information in the anatomical sciences also re-

quires direct experience of dissection to provide tangible grounding for that understanding. However machine perception is on the verge of being able to change the non-numerical nature of anatomy, by providing computational physical perception and semantic recognition of complex soft matter structures. The algorithm outlined in chapter-13 is one candidate for providing this. The same advance in machine perception will also provide solutions both to automate the manufacture of histomimetic robots and to interpret the somatosensory data that such robots will provide.

14.1 Synergies, reflexes and biomechanics

The joint actuation synergies observed in human hand motions for grasping and manipulation, and more broadly in vertebrate movement generally are substantially due to 'reflexes'. These are the mechanical effect of the kinematics and dynamics arising from tendon networks and the state of contraction of their associated muscles. These provide favourable mechanical behaviour, which reduces the demands on sensing, control and actuation latency.

14.2 Complex composites

The key passive mechanical structures of the musculoskeletal system and skin can be emulated by composites in which fibres cross boundaries between hard and soft matrices, and in which material structure and mechanism are merged. Several points are important:

Elastomers Ultra low modulus, hyper-elastic matrices are critical to emulating soft tissue material properties. Co-block polymer thermoplastic elastomers are particularly suitable for this due to the advantages during layup of rapid setting and remelting for bonding and adjustment. SEBS oil-gels provide very low modulus but suffer migration and evaporation of the oil over the longer term. Brush polymers potentially offer solvent-less low modulus thermoplastic elastomers.

Thermoplastic welding The precise topology and geometry of fibre paths is critical to reproducing soft tissue mechanisms of ligaments, tendon networks and fascia structures. Thermoplastic welding of fibre tows into matrix materials with lower melting points enables the necessary control of fibre placement.

Fine parallel fibres It is essential that tension bearing the fibres used are sufficiently fine diameter, both for surface area to bond with the matrix, and to ensure flexibility. It is also essential to avoid spun or braided fibres because these cause tight radius bending and abrasion.

Compatible polymers For both bonding of fibres to matrices and also for non-adhesion and smooth interface formation, the chemical side groups of polymers are critical to their intermolecular interaction.

Surface treatments The adhesion or conversely the boundary lubrication of surfaces can be modified by chemical reagents that bond to the available side groups.

14.3 Bulk MEMS

Critical active functions of sensing and actuation can be achieved by bulk volumes of micro-patterned materials.

14.3.1 Fibre drawing

Thermoplastic drawing of complex fibres from preforms provides a way to make fine elastic electrical signal fibres for connecting mechanosensors embedded in soft structures. It potentially also provides a way to make large quantities of very fine scale rolled dielectric elastomer capacitors that may be used as either actuators or sensors.

14.3.2 Muscle-like actuators

Fibre drawn rolled dielectric elastomer actuators would provide one route to producing a fibrous muscle like actuator. Roll-to-roll micro-embossing and laminating potentially provides a means to manufacture "DEMED" electrostatic actuators at a micro-scale. The theoretical upper bound of performance of these actuators is well above that of human skeletal muscle, indicating that it is likely to be feasible to match muscle specific work per stroke and specific power.

Chapter 15

Future Work

15.1 Soft matter perception

Implementing SPMP as an executable code would solve the soft matter measurement problem of anatomy, support the building of histomimetic robots (section-15.2) and provide further benefits in robotics and commercial applications. Funding has been obtained for work on sections-15.1.1 , 15.1.2 and 15.1.3 .

15.1.1 Smoothed particle modelling of anatomical soft tissues

The first step would be developing smoothed particle modelling of anatomical tissues. This includes writing a GPU accelerated smoothed particle code capable of real-time incompressible fluid simulations of $> 1\text{million}$ particles. The code should include elastic, fibrous (anisotropic) solids and particle splitting for locally adaptive resolution.

15.1.2 Capture of anatomical models from dissection

Using the smoothed particle code above, visual-tactile fusion would be implemented for perception of the material properties of everyday soft matter, and its integration with recognition and forward simulation. This will enable canonical anatomy to be captured objectively from video and force sensor data of dissection and integrated with clinical imaging. These models would then be used to generate patient specific models from clinical images, for surgical simulation and robotic surgery.

15.1.3 Application of SPMP to robotic manipulation

Perception of soft material properties and structure is widely applicable in robotic manipulation, not only robotic surgery.

15.1.4 Commercial applications of Smoothed Particle Machine Perception

Capture of computer graphic models from video, will allow editing of live action as computer graphics for film television and video game production.

15.2 Complex composites

The author is currently discussing potential collaboration with a number of partner universities in the UK and EU.

15.2.1 Automatic laying heads, path planning

Automation of the manufacturing of complex composite structures such as those used to emulate ligamentous joints, tendon networks and dermal structures requires tool heads for laying fibre and thermo-plastic matrix on free-form 3D surfaces. Automating the layup also requires path planning that takes account of the layering, topology and tensioning of fibres and matrix material.

15.2.2 CADEM

The critical precursors to automated layup are:

1. effective CAD for specifying the design,
2. CAE simulation of the mechanical properties of designs to test and refine them in simulation,
3. visual tracking and mapping of the build process to enable closed loop replanning of tool paths,
4. design rules and example structures as a starting point for new robot designs.

Each of these components can be provided through application of smoothed particle machine perception.

15.2.3 Materials

There is considerable scope for development of new materials with better control of bonding, elasticity and melt-flow to support the manufacture and final performance of histomimetic structures.

Blending and Calendaring

Affordable bench top blending and laminating tools will help speed up investigations of materials and composites while cutting costs. The experience gained in this thesis points to a number of small machines that could be made for much less than the cost of industrial polymer lab equipment.

Polymer chemistry

There are a number of avenues of investigation that would yield useful improvements and increase the palette of materials:

Graft polymerisation to chemically modify polymers that will enable commodity polymers to be adapted to improve their adhesion of other properties for use in histomimetic structures.

Brush polymers as solvent-free gel elastomers.

Boundary lubricants for sheathed tendons and synovial joints.

Cross-linking agents to eliminate long-term creep in rubbers and gels

Controlled radical polymerisation to make custom co-block-polymers, e.g. long chain poly-block co-polymers with high melt strength for fibre drawing.

15.3 Bulk MEMS

The author is preparing a number of projects with colleagues and PhD students at the University of Birmingham to further develop techniques initiated in this thesis.

15.3.1 Elastic electrical wires

Drawing equipment

A new iteration of preform drawing equipment is planned (see section 11.4).

Materials

In conjunction with blending and polymer chemistry (above) further materials will be tested to improve the drawing behaviour and elasticity of amalgam filled fibres.

Drawn, rolled DEA sensor

The fibre-drawn rolled dielectric elastomer sensor proposed in chapter-12.2.3 will be made and tested for use in sensor arrays.

15.3.2 Somatosensory arrays

MEMS assembly

Given MEMS mechanosensors and amalgam filled sensor fibres an efficient and reliable means of assembling them in large numbers is required. To approach human-level somatosensory spatial resolution this would require of the order of ten thousand sensors embedded in the skin and musculoskeletal system.

Integration into structures

Tools and layup procedure need to be developed to efficiently implant the sensors and lay the fibres during the building of histomimetic robots. Manual tools should be precursors to full automation of layup.

Reading large arrays of sensors

Large arrays of somatosensors also require a system for reading them that is compact and efficient to assemble, and provides sufficient resolution in time and degree to extract the necessary stretch and vibration information. It would also need to provide multiplexing down to a manageable number of channels for interfacing with a computer. Given the size and number of the fibres printed microelectronic circuits such as thin-film-transistor (TFT) technology as used in computer screens would be a suitable candidate. (By comparison a 1920x1080 HD screen on a mobile phone has 2,073,600 pixels each containing three LED or LCD colour channels and associated control circuits.)

Once the raw sensory data is read into a computer, the obvious candidate for reconstruction of the somatotopic map would be to use the Kohonen Self-Organized Map[271]. If the neurons of the self-organized map are abstracted to the 3D space of particles in a smoothed particle model, then the somatotopic self-organizing map can be induced to fit itself to a model of the 3D anatomy of the robot. In this way the somatosensory input can be fed in to the smoothed particle machine perception model of the sensory space, facilitating fusion with vision and other senses.

15.3.3 Muscle-like actuators

FEA design optimisation

The design optimisation by finite element analysis of electric field densities, electrostatic force and elastic stresses on the structure should be completed so that prototyping starts with a well justified design that is expected to have the best geometry for generating useful work and avoiding dielectric breakdown.

Initial Prototype

Initial prototyping and testing of both the proposed manufacturing process and the performance of the actuator can be done using pad printing on a micro-positioning stage using embossing plates photolithographically etched with a direct laser writer. If initial prototypes use a feature size of $10\mu m$ then widely available $1\mu m$ resolution direct laser writers could be used.

Roll to roll embossing and laminating

Once the initial prototype is demonstrated, and any modifications included, then transferring the system to a roll-to-roll embossing and laminating system will allow manufacturing volume to be gradually scaled up to produce useful bulk-MEMS muscles.

Building and actuating muscles

Further steps would include (i) integration of actuators into muscle-tendon units, (ii) integration of power delivery, (iii) sensing of muscle behaviour (stress and strain sensation equivalent to Golgi tendon organs and muscle spindles) and, (iv) control of individual muscle tendon units.

Integration into robots

Given the ability to make muscle tendon units of the correct size, shape, power and work-per-stroke, these assemblies must be integrated into the layup of a robot. The initial development of sensorimotor control could be done in simulation. Once a robot hands or other parts become available a period of cross-calibration would be required to learn the unique somatosensory array and actuators of a given histomimetic robot body.

Part VII

Appendices

Chapter 16

Supplementary material

16.1 Publications

16.1.1 IEEE Humanoids paper : Artificial ligamentous joints

Artificial ligamentous joints : methods, materials and characteristics

Nick Hockings, Pejman Iravani and Chris R. Bowen

Abstract—This paper presents a novel method for making ligamentous articulations for robots. Ligamentous joints are widely found in animals, but they have been of limited application in robotics due to lack of analogous synthetic materials. The method presented combines 3D printing, tow laying and thermoplastic welding which enables manufacturing of this type of structure.

I. INTRODUCTION

Locomotion and manipulation require interaction with an uncertain physical world. Consequently robotic limbs and hands need robust joints, with good range of motion. Vertebrate anatomy provides evidence of one physical solution - ligamentous synovial joints - that remains superior to other methods. This is highlighted by the work of Melchorri et al (2013) who stated,

“The replication of the human hand’s functionality and appearance is one of the main reasons for the development of robot hands. Despite 40 years of research in the field, the reproduction of human capabilities, in terms of dexterous manipulation, still seems unachievable by the state-of-the-art technologies.” [16]

and of Grebenstein (2014),

“The gap between the basic principles and solutions of bio-mechanical systems and the capabilities of technical systems is too wide to develop a proper hand design by simply copying the human hand using methods and solutions of the current robotics state of the art. It is currently still not possible to construct an exact copy of the human hand.” [12]

The challenge is how to reproduce the material properties of the soft tissues involved, and how to layup those materials to reproduce the mechanism of anatomical joints. This is commonly considered a difficult task, e.g.

“many joints are held together ... by ligaments or tough soft tissues which are almost impossible to duplicate” [4]

This paper presents a method for making ligamentous articulations for robots, using 3D printing, tow laying and thermoplastic welding.

The approach applied here is to examine the established anatomical and histological knowledge of the structures being emulated and ask - *what properties of these materials and structures are sufficient to predict the useful behaviour that we wish to reproduce?*

Specifically, histology reveals that anatomical tissues are fibrous composites. Most of these tissues are hyperelastic and anisotropic, as such they cannot be approximated in a simple way by rigid body models. The behaviour of such

materials is determined by the arrangement and properties of their constituent materials : the diameter and stiffness of the fibres, the elasticity and hysteresis of the matrix, and the adhesion between the fibres and matrix. The kinematics are largely dependent on the topology and length of the fibres. The structure of anatomical tissues is known through all scales down to molecular structure. The choice of scale at which to emulate the materials determines the design.

A. Review of quasi-ligamentous joints in robots, machines and orthopaedics

In robotics flexural joints have been used in 3D printed structures, notably the iRobot-Harvard-Yale hand [18]. These allow buckling and axial twisting of the joint, and can be built into a shape deposition cast skeleton. The flexible mechanism is robust to collisions, but this flexibility limits the ability to stably transmit force along the column of bones.

Another example of fibrous joints are the ribbon joints of the “Kilck-Klack” or “Jacobs Ladder” falling blocks illusion toy, [1] [19]. The mechanism is close to that of a four bar linkage, and to the cruciate ligaments of knees. The fibrous constraint is very stable, but the contact area between the blocks is minimal for all but one point in the range of motion. Consequently the motion is well constrained, but any compressive force would produce high pressure loadings at the contact surfaces.

Etoundi et al [8] [7] produced a condylar knee mechanism that used nylon cord ligaments in a four bar linkage, emulating the cruciate ligament mechanism of knees. Cords were also used as ligaments in ECCE Robot [15] to prevent dislocation of the shoulder joint. These were composed of stiff cords of ultra high molecular weight polyethylene (UHMWPE), or series combination of elastic and stiff cords. While these cord-ligaments reproduce some of the topology of anatomical ligaments, they lack the broad attachment and integration with the bones that make anatomical joints robust.

Van den Broek et al [22] [21] developed a prototype artificial inter-vertebral disk (AID) emulating the structure of anatomical inter-vertebral disks. The AID was composed of an ionized hydrogel core, wrapped in a hydrophobic membrane, enveloped by five layers of UHMWPE fibre, reproducing the nucleus pulposus constrained by the annulus fibrosus. Loading and fatigue testing showed that the prototype could withstand the maximum biological loading and fatigue, while providing stiffness and hysteresis close to that of healthy anatomical inter-vertebral disks.

The closest approximation of a ligamentous joint in a robot may be the silicone rubber joint capsule tested on the Anatomically Correct Testbed (ACT) hand [27]. This

*This work was supported by UK EPSRC DTA

¹ Department of Mechanical Engineering, University of Bath, BA2 7AY, The United Kingdom. N.C.Hockings@bath.ac.uk

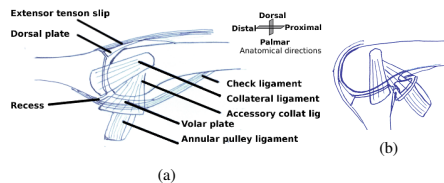


Fig. 1: (a) Proximal interphalangeal joint extended (b) flexed, showing the movement of the ligaments, dorsal and volar plates. The flexor tendons pass through the annular pulley.

lacks the stiff fibrous constraint of articular ligaments, but does preserve the large radius, compression bearing articular faces.

II. TECHNIQUE

A. Anatomical structures

This section describes the scale level at which the anatomical structures were emulated, and provides the keywords for roboticists to access the relevant anatomical literature.

The anatomy of human hands and dogs paws were used as the template for the demonstration specimens. Despite their differences of proportion, these are composed of the same tissues and share the same basic topology of bones and ligaments.

The variation in anatomy of healthy individuals shows that the material properties may vary by an order of magnitude without altering the function. Developmental anatomy shows that ligamentous joints are formed by progressive differentiation of tissues, and are fully functional whilst entirely soft prior to calcification of the bones. What is critical is sufficient strain tolerance and the ratio of stiffness between the different materials.

Ligaments do not generally provide the stiffness of constraint provided by engineering joints in rigid materials. For example for any given ligament it is generally possible to manipulate the joint to a position where the ligament is slack enough to pass a probe under it.

The stability of ligamentous joints is also dependent on direction of the load and the action of the tendons/muscles around the joint. By itself the joint capsule, including ligaments, prevents dislocation of the compression bearing articular surfaces, but commonly does allow some separation of the joint surfaces if tension is not opposed by muscle contraction. Ligaments are generally much less substantial than the principal tendons of the joint and usually have less leverage. Further, the series arrangement and under-actuation of joints is such that a load not supported by a tendon will commonly cause rotation of other joints that either transfers the load onto a tendon, or releases the load altogether. The exception to this being the function of suspensory and check ligaments which act on tendons in parallel with muscles in "passive stay" mechanisms.

1) *Tissues of synovial joints:* Articular cartilage is a thin layer of tough hyaline hydrogel with collagen fibre reinforcement in the plane. Synovial fluid is a viscous shear thinning fluid that acts as a boundary lubricant between the articular surfaces, and between the joint capsule and articular convex surface [9].

The joint capsule is continuous with the articular cartilage of the concave side of the joint. The hyaline content of the matrix is progressively replaced by hyper-elastic elastin. The capsule is reinforced with dense orientated collagen fibres. The matrix allows the capsule to stretch orthogonal to the collagen, and lubricates relative movement of the fibres in shear motions. The articular ligaments are dense bundles of collagen fibres in the joint capsule.

2) *Structure of finger joints:* The joints of the finger - distal inter phalangeal (DIP) [11], proximal inter phalangeal (PIP) [3] and metacarpophalangeal (MCP) - are of very similar construction. In the MCP the extensor tendon slip is replaced by the extrinsic extensor tendon, which does not insert on the distal margin of the joint but joins the extensor hood instead.

Figure 1 shows the PIP. Note the fibrocartilaginous dorsal [20] and volar plates, and the buckling motion of the volar plate aided by the recess between its distal margin and the proximal phalanx [3]. The check ligament and the distal part of the accessory ligament limit the maximum extension of the joint.

The collateral ligaments are much thicker and stronger than the accessory collateral ligaments, and form the primary constraint on the motion of the joint. In the MCP the collateral ligaments are attached and the joint faces shaped, such that the collateral ligaments are slack if and only if the joint is extended, allowing medio-lateral swinging of the joint. [17]

3) *Structure of the palm:* The palm is a complex structure, that provides critical load bearing and balancing in both paws and hands. Reproducing these functions by rigid mechatronic parts has been particularly difficult.

Figure.2 shows the ligamentous tissues of the palm. There is no synovial articular surface at the distal inter-metacarpal joints. Other soft tissue structures separate the bones including the sagittal bands of the metacarpophalangeal joints and the tendons of the interosseous muscles. The metacarpals are held to each other by (i) the inter-palmar-plate ligaments [2] that link the volar plates of the metacarpophalangeal joints to each other, collectively called the transverse metacarpal ligament, (ii) the natatory ligament which connects the proximal margin of the second annular ligaments of the first phalanges, (iii) the transverse fibres of the palmar aponeurosis [5] which are connected to the deep transverse metacarpal ligament by the septae of Legueu and Juvara [5] [2].

The proximal inter-metacarpal joints have small articular facets, and three sets of ligaments - dorsal, palmar and interosseous - which allow minimal rotation of adjacent bones about each other [6]. The carpometacarpal joints have short ligaments that allow very little movement.

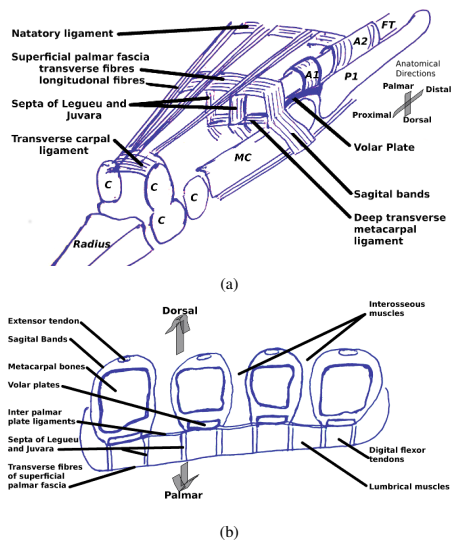


Fig. 2: (a) Palmar-oblique view of the ligamentous structures of the palm : A1-1st annular lig, A2-2nd annular lig, C-carpal bones, FT-digital flexor tendons, Mc-metacarpal bone, P1-1st phalanx bone. (b) Transverse section of the palm at the level of the deep transverse metacarpal ligament (DTML). Note the DTML is composed of the volar (palmar) plates and the inter palmar plate ligaments.

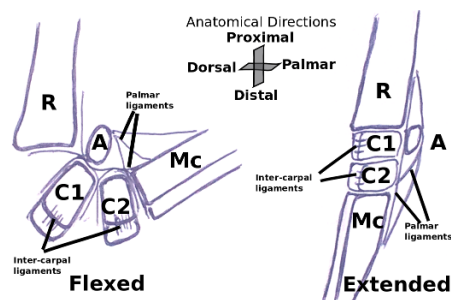


Fig. 3: Simplified diagram of ungulate-like carpal mechanism implemented - Flexed left, extended right. Ligaments stabilise relative dorsal-palmar movement between the bones, while allowing flexion about the palmar margin of the carpal bones. R-radius, C1 & C2-1st & 2nd row carpal bones, A-accessory carpal bone, Mc-metacarpal bones.

4) *Structure of carpus*: The carpal mechanism of ungulates (mammals with hoof feet) (fig. 3) was used rather than that of dogs because it has a simpler motion and was easier to construct. The carpal bones are arranged in two horizontal rows and flex by hinge motion about their palmar ligaments. As such it is close to a flexural joint when flexing, but bears compression on a continuous column of bones when extended. On the dorsal side the intercarpal ligaments connect only between bones on the same row. On the palmar side long ligaments from proximal row accessory carpal and radial carpal bones to the metacarpals limit the maximum extension of the intercarpal joint.

B. Materials

1) *Compatible thermoplastics*: Three different thermoplastics, polycaprolactone (PCL), polylactic acid (PLA), polyamide (PA), were selected with different softening temperatures, table(1) and compatible inter-molecular bonding. PCL and PLA have the same intermolecular bonding based on ketone groups which form dipole attractions, consequently they are miscible when molten. Softened PCL wets very well to solid PLA forming a high surface area of contact with 3D printed PLA parts, (fig.4c). PCL-PLA adhesion approaches the strength of pure PCL or PLA.

Polyamides(PA) including polyaramide(PAr) have amide links between their monomers. These present both ketone groups and hydrogen bearing amide groups. The ketone groups of PCL or PLA can form N-H⁺O hydrogen bonds with the PA, which are stronger than the ketone dipole attractions within either PCL or PLA. This strong intermolecular bonding allows the PA ligaments to be firmly attached to the bones.

Glycerol (propane-1,2,3-triol) is a short chain polyalcohol which is miscible with PCL and can be used as a plasticising agent. PCL softened with glycerol was used to make some joint faces more compliant.

Styrene-ethylene-butadiene-styrene (SEBS) is a block copolymer that forms very soft (0 Shore-A [23]) hyperelastic oil-gels (SEBS-gel) with alkane oils. SEBS-gel is used as a hyperelastic matrix for soft tissues. SEBS-gel does not adhere to polar polymers but can be mechanically blended with PCL, or infused between PA fibres as a matrix. Varying the ratio of SEBS-gel:PCL produces blends of intermediate stiffness and elastic limit. A stack of rolled films of blends of SEBS and PCL of progressively varied ratios can be rolled together on a hotplate to produce a composite film with pure PCL on one face and pure SEBS-gel on the opposite face. These composite films were used both to adhere SEBS to PCL and to prevent adhesion between PCL surfaces in contact.

2) *Low temperature thermoplastic welding*: PCL undergoes transition from opaque rigid semicrystalline state to transparent amorphous glassy plastic state at around 60C. In this state it is viscoelastic with substantial surface tension. This allows PCL to be molded by hand and causes it to form a smooth surface if allowed to relax in the plastic state. Small spots in PCL material a few millimetres in diameter can be

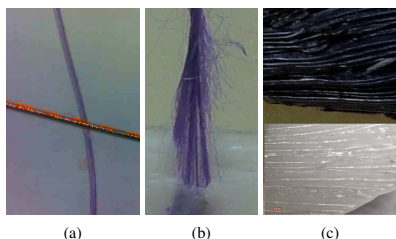


Fig. 4: (a) Thickness of polyamide (PA) fibre (purple) compared to 30micron motor wire. Fine fibres confer flexibility to ligaments and provide high surface area for adhesion to the matrix. (b) PA fibres failing under tension, before a 10mm long weld into a polycaprolactone (PCL) matrix, in a pull out test (c) PCL (white) forms close key with 3D printed poly(lactic acid) (PLA, black), reproducing the 0.3mm ridge pattern of the surface. PCL-PLA adhesion approaches the strength of pure PCL or PLA

softening temperatures of plastics (deg C)		
Polycaprolactone (PCL)	60C [26]	glass transition
Poly(lactic acid) (PLA)	150-160C [24]	melting point
Styrene-Ethylene-Butadiene-Styrene (SEBS)	170 210C [23]	melting point
Polyamide-6,6 (PA66)	135-254C [25]	melting point
Polyamide (PAr)	>500C [28]	thermal decomposition

TABLE I: Softening temperatures of plastics, temperatures will vary with polymer chain length and compounding additives.

heated above the phase change with a soldering iron. This allows spot welding of PCL to itself and other compatible materials without softening adjacent structures, and for such welds to be resoftened and their position adjusted. Spot welding is used to precisely position ligament attachment points.

Tows of parallel non-spun polyamide (PA) fibres, either polyamide-6,6 (PA66) or polyamide (PAr), approximately 25 microns in diameter, (fig.4a), were used for the tendons and ligaments. The combination of high surface area of the fine fibres, with good wetting of PCL to PA and strength of hydrogen bonding produced strong welds between PCL and PA. In pull-out tension testing PA fibres fail before their connection to PCL (fig.4b), hence the strength of PA ligaments is limited by the strength of the fibres not the attachment to PCL.

C. Layup process

1) *Bone geometry from volume imaging:* The bones were 3D printed in PLA using a RepRap fused filament deposition printer [14]. The models of the bones were segmented from MRI and CT scans using Slicer3D software [10]. These bones as printed in PLA approximate geometry of the calcified tissues (cortical bone, cancellous bone, and calcified cartilage) which are distinct from noncalcified tissues in

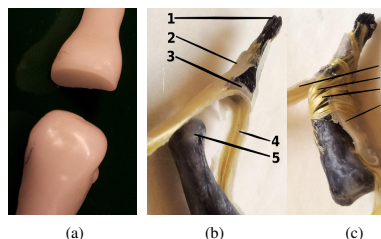


Fig. 5: Making articular surfaces (a) Method One forging polycaprolactone (PCL) articular surfaces against each other (b) Method Two laminated joint surfaces. Materials: 1.Poly(lactic acid) (PLA) bone, 2.PCL-SEBS graded laminate, with PCL face bonded to PLA bone, 3.PCL-Glycerol blend, forms a compliant socket, 4.Polyamide (PAr) fibres between PCL faces of laminate, form the palmar plate and dorsal extensor slip continuous with the socket, 5.PCL coating on poly(lactic acid) (PLA) bones. PCL of articular surface faces SEBS of laminate hence faces cannot adhere, but do require oil lubrication, (c) DIP joint Method Two with ligaments: 1.Extensor slip, 2.Collateral ligament, 3.Accessory collateral ligament, 4.Volar plate

clinical imaging. This does not however include the articular cartilage which is a critical compression bearing tissue in synovial joints, but much more difficult to accurately segment from medical volume imaging.

The PLA printed bones were then overlaid with PCL. This provided a layer of low temperature thermoplastic firmly adhered to the PLA, that could be formed and welded without deforming the printed structure. In the region of the articular surfaces PCL softened with glycerol was used to better approximate the compliance of articular cartilage.

2) *Articular surfaces - method 1:* The articular surfaces were formed by forging opposing surfaces against each other with one bone chilled and the other heated above the phase transition of PCL. The cartilaginous part of the joint capsule was formed by drawing the warm PCL by hand from the concave side of the joint over the chilled convex side of the joint, (fig.5a). During the forging process the opposing faces were lubricated with a film of oil and kept continuously in relative motion to prevent fusing between them. The flexing of the joint during forging helps to ensure that the shape formed permits the range of motion required and that the articular surfaces are congruent throughout the motion.

3) *Articular surfaces - method 2:* A ribbon of composite SEBS-gel-PCL film, section(II-B.1), was laminated with polyamid fibres on the PCL side. One ribbon was placed running palmar-dorsal on the concave articular surface of the distal bone, with the SEBS side facing the proximal bone. Additional ribbons were placed on the dorsal and palmar surfaces of the distal bone and laminated to the first ribbon to form the check ligament of the volar plate and extensor tendon slip, (fig.5b). Pads of blended PCL-SEBS-gel were

added to the portions of the volar plate and extensor slip adjacent to the distal bone, to emulate the fibrocartilaginous pads of the anatomical structures (fig.1a&5c).

4) *Articular ligaments and joint capsule:* Ligaments are attached by working warm PCL into a point near the end of a tow of PA66 with a soldering iron, then pressing this to the prewarmed insertion point in the PCL covering the PLA bone. This method allows good wetting of the PA66 by the PCL. The insertion point can then be adjusted by pulling on the tow either side of the attachment point. The PCL can then be cooled to solidify it and fix the attachment point.

The PA66 tow is then laid across the joint to locate the correct point for its 'origin' attachment. The fibres of the tow are worked into the attachment site and more PCL added as needed to ensure good adhesion of the fibres. The tension of the ligament can then be adjusted by pulling on the free end of the tow while flexing the joint while the attachment site is soft.

The joint capsule and the elastic matrix of the ligaments outside of the bone is applied by wrapping the joint in PCL-SEBS-gel film, then briefly melting the film with hot air from a heat gun.

III. DEMONSTRATION

A. Finger

A set of fingers for a hand were printed and laid up using method 2, section(II-C.3), for the joints, following the pattern of the anatomy, section(II-A.2). Polyaramide(PAR) was used for the ligaments, in order to provide a wide temperature tolerance for infusing PCL-SEBS-gel matrix. Polyamide deep and superficial flexor tendons and associated polyaramide flexor retinacular ligaments were fitted to the finger to assess the range of motion. Details of the tendon system are provided in [13].

The resulting fingers match the dimensions of the musculo-skeletal components of the hand in the MRI image, leaving the normal anatomical space for dermal and subdermal structures to be added. This is important because robot fingers are usually thicker than human fingers of the same length and lack the soft pads and other dermal structures. The joints (MCP, PIP and DIP) allow the normal anatomical range of flexion-extension, (fig.6a&6b).

Lateral stability of the DIP and PIP was slightly slacker (7 versus 5 degrees of yaw) than that of the human hand in the MRI image. Strength of lateral stabilization was tested by loading the PIP to 0.6Nm static torque without damage, (fig.6d). This corresponds to a lateral load of 3kg weight supported by a single finger at two centimetres distal to the joint, which exceeds the maximum loads normally exerted in this way by adult humans in a domestic setting. Note that heavy loads would normally be lifted on the palmar surface of the finger with tension borne by the digital flexor tendons, which are many times stronger than the collateral ligaments.

The MCP reproduced the cam tensioning action of the collateral ligaments, allowing wide yaw (25 degrees) in the extended position, and much reduced yaw (10 degrees) in

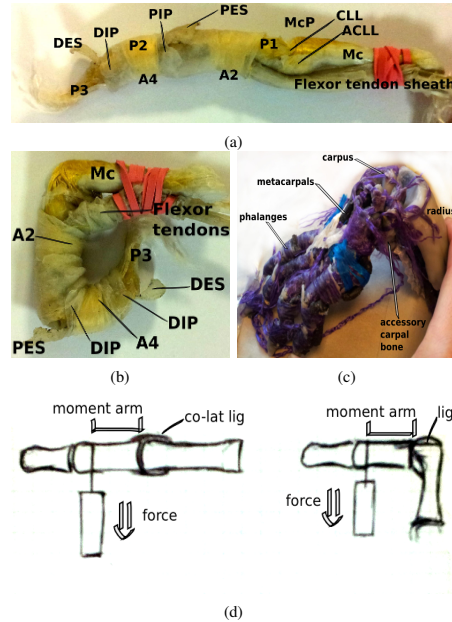


Fig. 6: Joint motions (a) finger extended : Mc metacarpus, ACLL accessory co-lat lig, CLL co-lat lig, MCP metacarpophalangeal joint, P1 first phalanx, A2 second annular lig, PES proximal extensor slip, PIP proximal inter-phalangeal joint, A4 fourth annular lig, P2 second phalanx, DIP distal inter-phalangeal joint, DES distal extensor slip, P3 third phalanx, (b) finger flexed, (c) paw carpus flexed, (d) torque testing of PIP, extended and 90 flexed.

the flexed position. This action helps to close the fingers in a cage around an object in the palm in humans.

In the extended position the MCP, PIP and DIP in series permitted a total axial roll of 45 degrees. This motion is important in allowing the finger tips to comply to the orientation of the contact surface.

Friction with the joints dry was high, as expected given the contact between soft SEBS-gel and hard PCL. When lubricated with paraffin (alkane) oil friction was very low and comparable to synovial joints. This reflects that paraffin is the solvent component of the SEBS-gel, so wets very well to that surface, while the PCL surface is very smooth having been shaped by surface tension in the glassy phase.

The joint capsule was less satisfactory. The PCL-SEBS-gel film was not well fused into the ligaments. This was partly due to the heat gun being oversized and lacking fine temperature control, which made it difficult to deliver the right amount of heat without damage by excess heating.

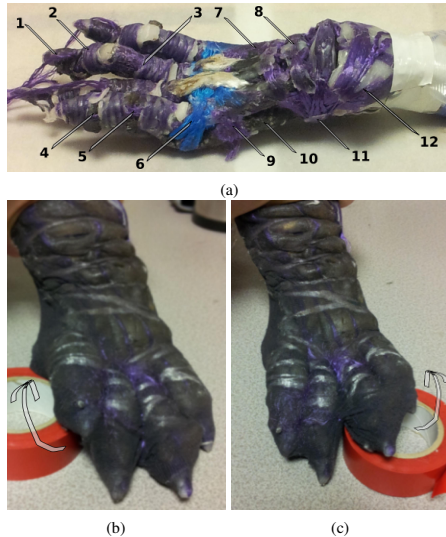


Fig. 7: Joint motions (a) paw carpus extended, 1.third phalanx, 2.second phalanx, 3.first phalanx, 4.DIP, 5.PIP, 6.MCP, 7.metacarpal bones, 8.carpal bones & inter-carpal lig, 9.septa of Legueu and Juvara, 10.flexor tendon sheaths, 11.accessory carpal bone, 12.radius, (b)&(c) passive supination/pronation of the paw demonstrates load balancing function of palm.

B. Paw

The paw was printed and laid up using method 1, section II-C.2, for the joints, following the pattern of the anatomy described in section II-A. Polyamide-6,6 (PA66) was used for all ligaments and tendons.

The flexion of the carpus is approximately 120 degrees shown in (fig.6c,7a) matching that of dogs. The passive supination/pronation of the paw by differential extension of the carpo-metacarpal and inter-metacarpal joints is shown in (fig.6c,7a). This motion is important to comply with the shape of the terrain and distribute load across the paw.

The paw was based a CT scan of the front paw of a dog weighing 200N, and tolerates repeated static loads greater than 120N without flexor tendon actuation. In use the flexor tendons would bear part of the tension resisting hyperextension of the joints.

An important shortcoming of the paw is that method-1 for making the joints resulted in some of the MCP and PIP joints being unintentionally fused during the layup.

IV. DISCUSSION

The key features of the materials produced are (i) the use of multiple matrix materials of stiffness ranging from rigid to low modulus hyper-elastic (ii) stiff reinforcing fibres in

soft matrices creating extreme anisotropies (iii) that fibres cross matrix boundaries creating topological connections in a deformable structure, and (iv) specific fibre paths matched to the geometric shape of the rigid matrix regions. Together these features integrate material composition with mechanical structure to produce a functional machine as a single piece deformable mechanism.

The central component of the technique is the use of thermoplastic welding of the matrix of the composite to achieve accurate fibre placement. This allows tows to be individually laid, immediately fixed and adjusted during the layup. It also points to how the process could be automated to achieve precise and repeatable construction by laying tows and thermoplastic tapes.

The strength of the weld between a fine fibre and a compatible thermoplastic matrix makes it possible to have compact attachment regions for ligaments that match the anatomy being emulated. It also makes it straightforward to estimate the quantity of ligament fibre needed to impart a given strength to a joint.

To reproduce the function of anatomical fingers and paws at 1:1 scale it was necessary to emulate the tissue structure at a scale between 300-100 microns. Human finger anatomy involves many layers of ligamentous and tendinous tissues, hence it is important that these are kept thin to achieve slender dextrous fingers.

A. Comparison to other joint types

Relative to pin-hinge joints, ligamentous joints provide a simpler path for compressive and tensile forces carried by the column of bones and the tendons respectively. In joints composed purely of rigid materials, such as pin-hinge joints there has to be a discontinuity in the tension bearing structure, and a conversion the tension to a compressive force that can be transmitted by contact between rigid parts. This requires that the force doubles back on itself around the pin or other retaining part, which requires more material and more space than a ligamentous joint made of materials of similar strength.

Compared to flexural joints, ligamentous joints have a greater capacity to bear compressive loads due to the large area of direct contact between the bones. This translates to the ability to support greater actuation force by tendons, for a given size of joint. Flexural and ligamentous joints share the ability to deflect to off axis loads, which is beneficial both for complying to unknown surfaces in grasping, and to avoid breaking in collisions.

B. Actuation

In animals both actuation and additional stabilisation are provided by tendons. Tendons in animals are held in their correct paths by a second set of ligaments known as 'retinacular ligaments'. Animal tendons are proportionally much thicker than those commonly used in robots. The load bearing fibres of tendons are parallel, held together by an elastic matrix. Bowden tubes and rotating pulleys are not found in animals. Friction of tendons is lubricated

by fluid filled sheaths and hyalinized load bearing surfaces resembling synovial joints. Where lateral pressure is low, tendons are lubricated by solid hyperelastic tissue.

The methods and materials described in this paper lend themselves to emulating anatomical tendon networks. The techniques for this will be addressed in another paper.

C. Further work

Further work will involve creep and fatigue cycle testing to assess durability and reparability of structures built in this way. Materials development may include new thermoplastic blends, custom co-block polymers, and custom 3D printer G-code for emulation of gross bone structure. Thermoplastic tape and tow laying tools could improve build consistency. Given suitable CAD-CAM modelling and process monitoring it would be possible to automate the lay up process.

Further components that are needed are dermal structures (pads, dermis, nails, claws and hooves), actuators, and embedded sensors for tactile and proprioceptive sensation.

V. CONCLUSIONS

Contrary to previous expectations [12] [4] direct emulation of the mechanical properties of histological tissues and anatomical structures is feasible. The key distinction is to emulate the mechanical, but not necessarily the chemical or biological properties of the materials.

The ability to produce tough ligamentous joints opens the possibility of exploiting known anatomical mechanisms whose function is hard to match with conventional mechatronic techniques.

REFERENCES

- [1] anon. Jacob's ladder. *Scientific American*, 61(15):227, 1889. Available at <http://archive.org/stream/scientific-american-1889-10-12/scientific-american-v61-n15-1889-10-12#page/n3/mode/2up> Accessed: 2014-09-16.
- [2] Karl K Bilderback and Ghazi M Rayan. The septa of legueu and juvara: an anatomic study. *The Journal of hand surgery*, 29(3):494–499, 2004.
- [3] William H Bowers, John W Wolf Jr, John L Nehil, and Shellye Bittinger. The proximal interphalangeal joint volar plate. i. an anatomical and biomechanical study. *The Journal of hand surgery*, 5(1):79–88, 1980.
- [4] Alan Diamond, Rob Knight, David Devereux, and Owen Holland. Anthropomorphic robots: concept, construction and modelling. *Int J Adv Robotic Sy*, 9(209), 2012.
- [5] James R Doyle. Anatomy and function of the palmar aponeurosis pulley. *The Journal of hand surgery*, 15(1):78–82, 1990.
- [6] William W Dzwierzynski, Hani S Matloub, Ji-Geng Yan, Shiliang Deng, James R Sanger, and N John Younis. Anatomy of the intermetacarpal ligaments of the carpo-metacarpal joints of the fingers. *The Journal of hand surgery*, 22(5):931–934, 1997.
- [7] Appolinaire C Etouadi, Stuart C Burgess, and Ravi Vaidyanathan. A bio-inspired condylar hinge for robotic limbs. *Journal of Mechanisms and Robotics*, 5(3):031011, 2013.
- [8] Appolinaire C Etouadi, Ravi Vaidyanathan, and Stuart C Burgess. A bio-inspired condylar hinge joint for mobile robots. In *Intelligent Robots and Systems (IROS)*, 2011 IEEE/RSJ International Conference on, pages 4042–4047. IEEE, 2011.
- [9] H Fam, JT Bryant, and M Kontopoulou. Rheological properties of synovial fluids. *Biorheology*, 44(2):59–74, 2007.
- [10] Andriy Fedorov, Reinhard Beichel, Jayashree Kalpathy-Cramer, Julien Finet, Jean-Christophe Fillion-Robin, Sonia Pujol, Christian Bauer, Dominique Jennings, Fiona Fennessy, Milan Sonka, et al. 3d slicer as an image computing platform for the quantitative imaging network. *Magnetic resonance imaging*, 30(9):1323–1341, 2012.
- [11] Panayotis Ioannis Gligis and Kazimierz Kuczyński. The distal interphalangeal joints of human fingers. *The Journal of hand surgery*, 7(2):176–182, 1982.
- [12] Markus Grebenstein. Methodology. In *Approaching Human Performance: The Functionality-Driven Awiwi Robot Hand*, volume 98 of *Springer Tracts in Advanced Robotics*, chapter 1.6, page 9. Springer Publishing Company, Incorporated, 2014.
- [13] Nick Hockings, Pejman Irvani, and Chris R Bowen. Tendon networks for artificial ligamentous joints : methods, materials and characteristics. submitted to: *Humanoid Robots (Humanoids)*, 2014 14th IEEE-RAS International Conference on, 2014.
- [14] Rhys Jones, Patrick Haufe, Edward Sells, Pejman Irvani, Vik Olliver, Chris Palmer, and Adrian Bowyer. Reprap—the replicating rapid prototyper. *Robotica*, 29(01):177–191, 2011.
- [15] Hugo Gravato Marques, Michael Jantsch, Steffen Wittmeier, Owen Holland, Cristiano Alessandro, Alan Diamond, Max Lungarella, and Rob Knight. Ecce1: the first of a series of anthropomorphic musculoskeletal upper torsos. In *Humanoid Robots (Humanoids)*, 2010 10th IEEE-RAS International Conference on, pages 391–396. IEEE, 2010.
- [16] Claudio Melchiorri, Gianluca Palli, Giovanni Berselli, and Gabriele Vassura. On the development of the ub-hand iv: an overview of design solutions and enabling technologies. *Robotics & Automation Magazine*, 20(3), September 2013.
- [17] Akio Minami, Kai-Nan An, William P Cooney III, Ronald L Linscheid, and Edmund Chao. Ligament stability of the metacarpophalangeal joint: a biomechanical study. *The Journal of hand surgery*, 10(2):255–260, 1985.
- [18] Lael U Odhner, Leif P Jentoft, Mark R Claffee, Nicholas Corson, Yaroslav Tenzer, Raymond R Ma, Martin Buehler, Robert Kohout, Robert D Howe, and Aaron M Dollar. A compliant, underactuated hand for robust manipulation. *The International Journal of Robotics Research*, 33(5):736–752, 2014.
- [19] Donald Simanek. Toys, tricks and teasers. <http://www.lhup.edu/dsimanek/TTT-rings/rings.htm>. Accessed: 2014-06-23.
- [20] PG Slattery. The dorsal plate of the proximal interphalangeal joint. *The Journal of Hand Surgery: British & European Volume*, 15(1):68–73, 1990.
- [21] Peter R van den Broek, Jacques M Huyghe, and Keita Ito. Biomechanical behavior of a biomimetic artificial intervertebral disc. *spine*, 37(6):E367–E373, 2012.
- [22] Peter R Van den Broek, Jacques M Huyghe, Wouter Wilson, and Keita Ito. Design of next generation total disk replacements. *Journal of biomechanics*, 45(1):134–140, 2012.
- [23] www.hexpolte.com. mediprene-s.htm. <http://www.hexpolte.com/en/mediprene-s.htm>. Accessed: 2014-06-23.
- [24] www.matbase.com. material-properties-of-poly(lactic-acid)-monomere-pla-m.html. [http://www.matbase.com/material-categories/natural-and-synthetic-polymers/agro-based-polymers/material-properties-of-poly\(lactic-acid\)-monomere-pla-m.html#thermal-properties](http://www.matbase.com/material-categories/natural-and-synthetic-polymers/agro-based-polymers/material-properties-of-poly(lactic-acid)-monomere-pla-m.html#thermal-properties). Accessed: 2014-06-23.
- [25] www.matweb.com. Overview of materials for nylon 66 fiber. <http://www.matweb.com/search/DataSheet.aspx?MatGUID=af1029dd5d724a718a1740642b5ed3a8>. Accessed: 2014-06-23.
- [26] www.perstorp.com. Product data sheet capa 6800 eng-6139.pdf. <https://www.perstorp.com/en/Products/Capa.6800#>. Accessed: 2014-06-23.
- [27] Zhe Xu, Emanuel Todorov, Brian Dellon, and Yoky Matsuoka. Design and analysis of an artificial finger joint for anthropomorphic robotic hands. In *Robotics and Automation (ICRA)*, 2011 IEEE International Conference on, pages 5096–5102. IEEE, 2011.
- [28] Hong-Ting Zhang. Comparison and analysis of thermal degradation process of aramid fibers (kevlar 49 and nomex). *J Fiber Bioeng Inform*, 3(3):163–167, 2010.

16.1.2 Technical report: tendon networks for artificial ligamentous joints

Tendon networks for artificial ligamentous joints : methods, materials and characteristics

Nick Hockings, Pejman Irvani and Chris R. Bowen

Abstract—This paper presents a novel method for making tendon networks for robots with ligamentous joints. Unlike tendons commonly used in robots, this technique emulates the material properties and mechanisms of vertebrate tendon networks.

Hyperelastic gels are used as solid lubricants for finite shear, and as matrices for highly anisotropic fibrous soft composites. Flexible composite structures are used to create compact robust compliant mechanisms. Differential miscibility and adhesion of thermoplastics is exploited to control the formation of cavities which facilitate flexion of the mechanisms.

Emulations of the flexor and extensor tendon networks of a human finger and of the paw of a dog were used to demonstrate the technique.

This approach is expected to be useful for building service robots and for evaluating biomechanics.

I. INTRODUCTION

Tendon actuation is found extensively in vertebrate anatomy. It offers a way to produce compact lower limbs and digits with beneficial underactuation, but requires stabilisation of tendon paths. Tendons are used in many robots in legged locomotion, flexible spines and humanoid hands, however artificial tendons suffer problems of fatigue failure and friction.

Artificial ligamentous joints, as described in [10] require compatible tendon networks and retinacular ligaments to hold the tendons in their correct paths.

This paper presents a method for making tendons that closely match the mechanical properties of the materials and the mechanism of anatomical tendon networks.

A. A brief review of tendon actuation in robots

Tendon actuation is widely used in robotic hands, primarily because it allows the actuators to be situated outside the hand, thereby avoiding the space constraints of intrinsic actuators. However the tendon materials and networks used in robot hands differ substantially from anatomical tendon networks.

The Anatomically Correct Testbed (ACT) hand [4] is the exception in that it sets out to reproduce the topology of human digital extensor tendons. The tendons are braided SpectraTM ultra high molecular weight polyethylene (UHMW-PE) strings. The extensor hood is implemented by a crocheted nylon structure which aims to reproduce the tension distribution of the anatomical extensor hood. The retinacular constraints are partly implemented by rigid eyelet tendon guides.

*This work was supported by UK EPSRC DTA

¹ Department of Mechanical Engineering, University of Bath, BA2 7AY, The United Kingdom. N.C.Hockings@bath.ac.uk

The DLR Hand Arm System [9] has a full dexterous hand-wrist system with all actuators located in the forearm. The tendons are braided UHMW-PE. An elaborate system of rolling tendon guides maintains low friction, while incidentally minimising under-actuation at the wrist. Thirty eight tendons are used to actuate the DLR IV hand, as compared to approximately 34 intrinsic and extrinsic muscles of human hands (depending on individual variation and choice of nomenclature).

The IIT/Pisa Soft Hand [3] is a highly under-actuated hand capable of forming strong power grasps on a wide range of objects. It uses a single flexor tendon acting in series through all its fingers, opposed by elastic extensors on each joint. Except for its pulley wheels it is a largely 3D printed structure, that uses low friction Hill-Berry rolling contact joints.

The 'Highly Adaptive SDM hand' [6] uses an under-actuated flexor tendon in each finger, opposed by the viscoelasticity of the flexural joints. The mechanism exploits 'Shape Deposition Manufacturing' (SMD) to produce a multi-material composite, with additional insert components embedded in the structure. This is a multi-step thermoset casting process.

The MIT Cheetah [1] uses tendons to actuate its joints while minimising bending loads on the compression bearing bones. This emulates the function and geometry of the tendon-bone relationship in vertebrate locomotor apparatus. The tendons of the MIT Cheetah are made from Kevlar(TM) polyaramide braided webbing, and attached by implanting into the bone during the resin transfer moulding manufacture of the bones. The bones are made from thermoset polyurethane resin with a foam core and solid shell akin to the spongy core and lamellar cortex of vertebrae bones.

1) Difference between robot and anatomical tendons:

Stabilization and control of friction are critical in tendon networks. All of the robot tendons described above use rigid constraints and minimise sliding contact to avoid friction. These tendons are made of spun, braided cord or webbing. This differs markedly from anatomical tendons, which are composed of parallel fibres held together in a hierarchy of bundles by endotendon matrix and epitendon fibrous membrane. Anatomical tendons are in continuous contact with surrounding tissues along their length. They are enveloped in soft tissue either hyperelastic peritendon loose connective tissue, or fluid lubricated synovial tendon sheaths and bursas formed by extension of the capsule of synovial joints. Unlike Bowden cables, tendon sheaths do not bear compression along their length.

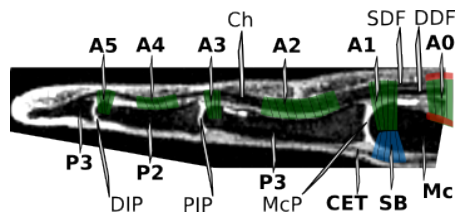


Fig. 1: The undulating path of the flexor tendons of a finger in the extended position seen in an MRI scan, palm upwards in sagittal section. The location of the retinacular ligaments is superimposed on the scan. Labels: A0 'zeroth' annular ligament is formed by the transverse fibres of the superficial palmar fascia and the septae of Legueu and Javara, A1-5 Annular retinacular ligaments, P1-3 phalanges, Mc metacarpal bone, DIP distal inter-phalangeal joint, PIP proximal inter-phalangeal joint, McP metacarpo-phalangeal joint, CET common extensor tendon, SB sagittal bands, DDF deep digital flexor tendon, SDF superficial digital flexor tendon, Ch chiasma where DDF passes between the branches of the SDF. Note the DDF inserts on P3, while the branches of the SDF insert on P2.

B. Anatomical structures

It has been believed that the materials are not available to allow direct emulation of musculoskeletal fibrous soft tissue structures [5]. It is the purpose of this paper to demonstrate a set of materials that can be used to reproduce the mechanical properties and structures of sheathed and unsheathed tendon networks. The material and mechanical structure of the bodies of vertebrates have been extensively studied in the anatomical sciences. Developing equivalent synthetic materials allows this knowledge to be exploited for robotics.

It is important to appreciate the dominant role of fibre topology and elastic matrices in musculoskeletal tissues. Normal variation in healthy bodies shows the strength and stiffness of tissues can vary by an order of magnitude without disrupting the function of anatomical structures, e.g. hands are fully functional before calcification of the bones of the wrist in late childhood. The critical material factors of joint and tendon mechanisms are strain tolerance and relative stiffness differing by several orders of magnitude between different tissues or directions within fibrous structures.

The anatomy of human hands and dogs paws were used as the template for the demonstration specimens in this paper. Despite their differences of proportion, these share the same topology of bones, ligaments and tendons. This section describes the structures that were emulated.

1) *The digital flexor apparatus:* The digital flexor tendons are by far the strongest tension bearing structure in the hands, being several times greater in cross section area than any of the other tendons or ligaments. They connect

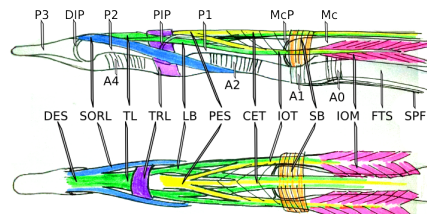


Fig. 2: Topology of extensor tendon hood of the finger, lateral view palm downwards (top), dorsal view (bottom) : A0-5 Annular retinacular ligaments, P1-3 phalanges, Mc metacarpal bone, DIP distal inter-phalangeal joint, PIP proximal inter-phalangeal joint, McP metacarpo-phalangeal joint, DES distal extensor slip, SORL spiral retinacular ligament, TL triangular ligament of DES, TRL transverse retinacular ligament, LB lateral band of DES, PES proximal extensor slip, CET common extensor tendon, IOT inter-osseous tendon, SB sagittal band, IOM inter-osseous muscle, FTS flexor tendon sheath, SPF longitudinal fibres of superficial palmar fascia.

the extrinsic digital flexor muscles in the forearm to the distal phalanges (deep digital flexor tendon) and the middle phalanges (superficial digital flexor tendon). Consequently they underactuate flexion of all the joints of the fingers, palm and wrist.

This underactuated tendon topology gives rise to important reflexes [12] - passive dynamic behaviours due to kinematics.

- Pressure at any point on the palmar surface of the hand extends the carpus, and flexes the joints distal to the point of contact, causing the hand to hook around the object,
- The flexor tendons fan out from the carpal tunnel to the metacarpo-phalangeal (MCP) joints, causing the finger tips to converge when flexed, forming a cage around any object on the palm,
- Flexion of the small and ring fingers also flexes their carpo-metacarpal joints, making the palm concave.

The flexor tendons are lubricated by a synovial tendon sheath [8] in the fingers and a bursa at the carpus. The sheath is composed of a thin fibrous membrane that is closely adhered to the annular ligaments. Between the annular ligaments the sheath is stabilized by a second lighter set of cruciate ligaments.

The digital flexor tendons are held in their correct path by a series of annular ligaments known as "the pulleys of the digits" [7], the palmar fascia (septae of Legueu and Javara, and transverse fibres of the superficial palmar fascia) [2], the transcarpal ligament, and the antebrachial fascia of the distal forearm [15]. Of these the strongest and most critical are the transcarpal ligament, the second and fourth annular ligaments of the fingers.

The annular ligaments are shaped longitudinally such that

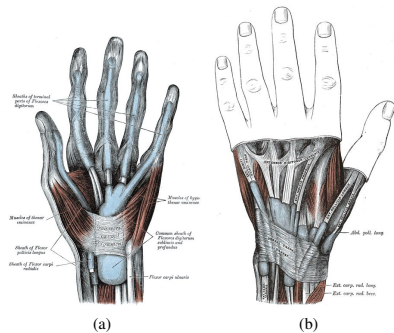


Fig. 3: From Gray(1918) [11] figs 423 & 424. Tendon sheaths of the hand (a) palmar, (b) dorsal. The tendons are unsheathed in the forearm, mid palm, and distal to the wrist (carpus) dorsally. Note the how the carpal tunnel collects the flexor tendons on the palmar surface of the wrist, causing the fingers to converge when flexed.

when the fingers are maximally flexed, the tendons form a smooth helix - thereby maximising the radius of bending of the tendon at all points along its length. The first, third and fifth annular ligaments are located on the palmar plates of the metacarpophalangeal (MCP), proximal interphalangeal (PIP) and distal interphalangeal (DIP) joints respectively. When these joints are extended the volar plates push the flexor tendons palmar relative to the second and fourth annular ligaments so that the tendons lie in an undulating path. This arrangement helps to ensure that the tendons apply torque to the joints throughout their range of motion.

The annular ligaments also serve as the attachment point for other structures. The spiral oblique retinacular ligament [17] originates from the palmar side of the second annular ligament on the proximal phalanx. It passes palmar to the proximal inter-phalangeal joint (PIP) and dorsal to the distal inter-phalangeal joint (DIP), before inserting in the distal extensor slip. The mechanical effect being to limit the phase difference between the flexion of the PIP and DIP. The transverse retinacular ligament [14], originates at the level of the third annular ligament on the PIP, and passes dorsally over the finger, stabilising the lateral and medial branches of the distal extensor slip, close to the axis of rotation of the PIP. The ligaments of the skin of the fingers attach to the fascia of the flexor apparatus including : the septae of the digital pads (Grayson's ligaments), palmar crease ligaments, the ligament of the finger webs (natatory ligament), and Cleland's ligaments [19](constraining the lateral margins of the digital pads).

2) *Digital extensor tendons:* The digital extensors have a synovial bursa at the carpus [16] where they pass under the carpal extensor retinaculum, otherwise their movement is lubricated by hyperelastic peritendon tissue.

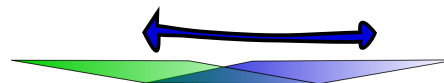


Fig. 4: Elastic shear lubrication : a hyper-elastic lamina with elastic limit 1000% can permit shear 2x1000% times the thickness of the lamina. So a 0.5mm thick layer can lubricate 10mm of tendon excursion. This technique is essential for reproducing the movement of unsheathed anatomical tendons including the digital extensor hood.

The extensor hood of the digit [13] is composed of fibres from the extrinsic extensor dorsally and interosseous tendons laterally, inserting onto the proximal and distal extensor slips of the middle and distal phalanges. At the MCP the interosseous tendons pass through short tendon sheaths. The sagittal bands arise from the first annular ligament, pass over the interosseous sheaths and bind to the extrinsic extensor tendon. A layer of hyper-elastic connective tissue beneath the sagittal bands allows the extrinsic extensor tendon to slide over the MCP, while the bands stabilise it laterally.

The extensor hood is stabilised over the dorsal surface of the digit by the triangular ligament of the distal extensor slip, the transverse retinacular ligament [14] and the interosseous hood - composed of fibres connecting the interosseous tendons [13]. Collectively the mechanism has been described to perform 'anatomical computation' [18] "that nonlinearly enables different torque production capabilities".

II. MATERIALS

A. *Fibres and rigid thermoplastics*

The tendons and associated retinacular structures were laid up over ligamentous joints, composed of polylactic acid (PLA) 3D printed bones coated in polycaprolactone (PCL) and connected with polyamide fibre ligaments, described in [10]. Tows of parallel non-spun polyamide fibres approximately 25 microns in diameter were used for the tendons and ligaments (polyaramide Kevlar, and polyamide-6,6).

B. *Hyperelastic Gels*

The technique developed here exploits a thermoplastic hyper-elastic gel in homogeneous layers as a solid elastic lubricant and as a matrix for anisotropic composites. The gel used is based on partial solution of Styrene-Ethylene-Butene-Styrene (SEBS) co-block polymer rubber [Elasto 180] in paraffinic oil [WD-40 Co Ltd, 3-IN-ONE 'multi purpose drip oil']. The resulting gel permits strains in excess of 1000% extension and shear.

Two stiffer preformulated SEBS oil-gels were also used, Elasto Dryflex 5000 (Shore A 0 hardness) and Dryflex 880101 (approximately Shore A 40 hardness).

1) *Hyper-elastic solid lubricant:* Varying the ratio of oil to SEBS polymer results in different grades of gel. As the oil content increases the strength and stiffness decrease. Very soft high oil content gels can be used as solid hyper-elastic lubricant for motions of finite shear, Fig.4.

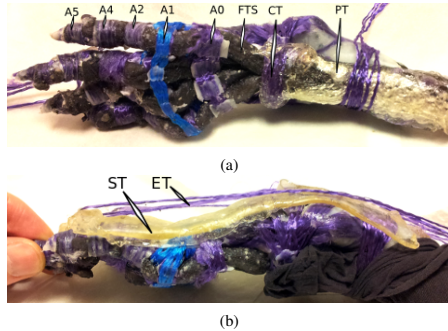


Fig. 5: (a) Paw palmar aspect showing: FTS flexor tendon sheaths, A0-5 annular retinacular ligaments, CT carpal tunnel, and PT peritendon tissue (SEBS-gel) in the forearm. (b) Paw lateral aspect during manufacture, showing: ST soft tissue layer (SEBS-gel) separating ET extensor tendons from underlying skeleton.

2) *Elastomeric composites*: A fibre reinforced composite material was produced by infiltrating the gel into polyester stocking material. The resulting composite remained hyper-elastic but was easier to handle and less prone to tearing than the homogeneous gel. 4

C. Ionomer thermoplastic elastomers

Poly(ethylene, acrylic acid, acrylate, zinc) ionomer was used when a thermoplastic elastomer immiscible with SEBS was required. Du Pont Surlyn 9320 was blended with paraffin to make tendon sheath membranes, Surlyn 1706 was used to form articular surfaces on condyles.

III. DESIGN OF TENDON NETWORKS

A. Paw

An emulation of a dog's paw and carpus with ligamentous joints described in [10], was fitted with flexor and extensor tendons including palmar fascia and carpal tunnel.

1) *Flexor tendons*: The tendons were attached by clove hitches to the middle (superficial flexor) and distal (deep flexor) phalanges. The polyamide fibres were then infused with a matrix of SEBS-paraffin gel on a hot plate. The matrix of two branches of the superficial flexor were fused together to form the chiasma through which the deep flexor tendon runs, immediately proximal to the insertion of the superficial flexor on the middle phalanx.

The flexor tendons were then wrapped into a tube of SEBS-gel-stockin fabric composite. This was sealed along its length with a soldering iron to form the flexor tendon sheath. Paraffin oil was then infiltrated down the inside of the sheath to lubricate the excursion of the tendons.

The sheathed flexor tendons of all four digits of the paw were then laid along the palmar aspect of the bones, (Fig

5a). Annular ligaments of polyamide tows in a PCL matrix were wrapped around the flexor sheaths at the proximal and middle phalanges. Likewise the septae of Legueu and Javara and transverse palmar fascia were formed by wrapping polyamide-PCL tows around the metacarpals. The natatory ligament was formed by a band of polyamide tows connecting the proximal margins of palmar side of the second annular ligament, palmar to the first phalanx.

The carpal tunnel was formed by laying the flexor tendons in their individual sheaths across the carpus between the maleolus of the hamate bone and the accessory carpal bone. The transverse carpal ligament was then formed by laying a broad band of polyamide tows across the tendons, connecting the accessory carpal to the hamate.

2) *Extensor tendons*: A layer of SEBS-paraffin gel was laid on the dorsal surface of the paw from the digits to the radius, (Fig 5b). The extensor tendons were tied to the distal phalanges, and laid on the gel layer. A series of polyamide tows were then laid orthogonally over the extensor tendons and welded to the annular ligaments on the palmar side of the paw. Lightweight (10 Denier) stocking material was then drawn over the paw. The extensor tendons, orthogonal tows and stocking material were then fused with the gel layer by heating them with a fifty watt halogen lamp until the surface of the gel began to melt.

3) *Performance of tendons of the paw*: Both the extensor and flexor tendons provided robust actuation of the carpal, metacarpal, and interphalangeal joints. The major problem with the technique was that several of the joints of the digits were accidentally fused during the attachment of the annular ligaments of the flexor tendons.

B. Finger without soft tissue

An initial emulation of a human finger was made without soft tissues, to test the layout of the tendon apparatus, (Fig 6a). The phalangeal and metacarpal bones were moulded in PCL and connected with polyamide ligaments as described in [10]. The tendons and retinacular ligaments were made from tows of polyamide, with PCL matrix.

1) *Flexor tendons*: The flexor tendons were made from polyamide tows wrapped in high density polyethylene (HD-PE) film and hot pressed to bond them. This gave a smooth hard surface on semi-flexible thick ribbon-like tendon. These were wrapped in a second layer of HD-PE to form tendon sheaths for each of the annular ligaments.

2) *Extensor tendons*: The triangular ligament of the distal extensor slip, the transverse and oblique retinacular ligaments of the extensor apparatus were implemented, but not the dorsal hood connecting the interosseous tendons. The sagittal bands were implemented as a fixed channel through which the extrinsic extensor tendon ran, as opposed to the anatomical sagittal bands which adhere to the tendon and slide with it over the dorsal aspect of the metacarpal condyles. The use of polyamide tendon slips with PCL matrix allowed repeated adjustment of the relative lengths of the extensor tendon network, until a functional network was achieved. Notably the branches of the extrinsic extensor tendon to

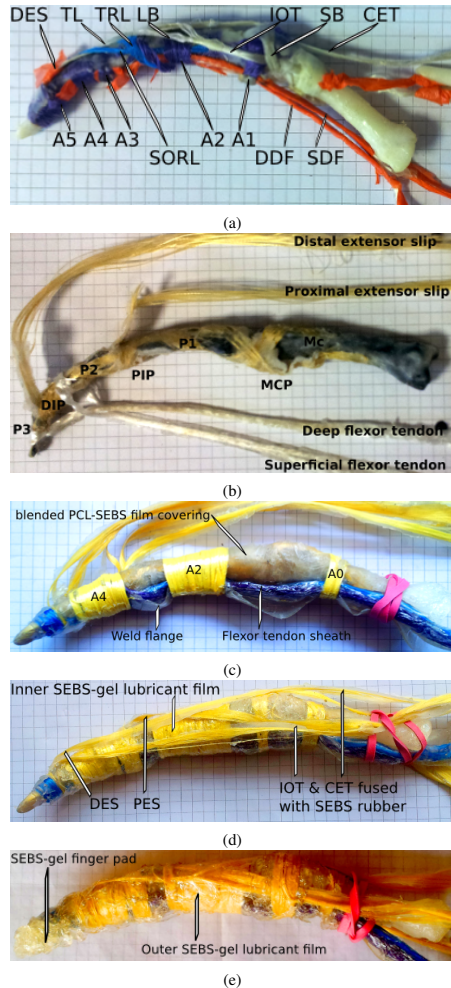


Fig. 6: Layup tendons (a) dry demo, (b) tendons attached & named, (c) flexor sheath, palmar pulley, 2nd and 4th annular ligaments, (d) inner lubricant gel layer under extensor network, (e) outer lubricant gel layer over extensor network. Squares are 5mm for scale. Labels: DES distal extensor slip, TL triangular ligament, TRL transverse reinacular ligament, LB lateral band, IOT interosseous tendon, SB sagittal bands, CET common extensor tendon, SORL spiral oblique reinacular ligament, DDF deep digital flexor, SDF superficial digital flexor, A0-5 annular reinacular ligaments, P-3 phalanges, DIP distal interphalangeal joint, PIP phalangeal interphalangeal joint, McP metacarpo phlangeal joint.

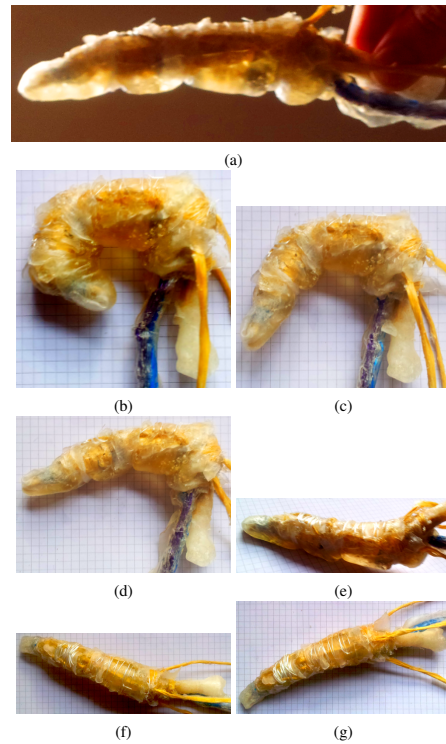


Fig. 7: Flexion of finger (a) Extrinsic extensor and both interosseous tendons contracted, showing gel fingerpads, (b) Deep digital flexor fully flexed, (c) Superficial flexor flexion, (d) Interosseous bilateral contraction, (e) MCP hyper-extension, (f) MCP lateral flexion, unilateral interosseous contraction (g) MCP medial flexion, opposite unilateral interosseous contraction

the distal extensor slip were located more dorsally at the proximal interphalangeal joint than they are often portrayed in anatomy texts, and stabilized in that position by the transverse retinacular ligament.

3) *Performance of finger without soft tissue:* The completed finger skeleton and tendon network was compact, being nearly as slender as the musculoskeletal system of the human finger on which it was based. Despite the low friction of PCL and HD-PE surfaces, the finger required lubricating with paraffin oil in the joints and tendon apparatus to achieve smooth actuation.

The range of motion and of the finger joints and excursion of the tendons matched the normal human range. The mech-

anism demonstrated that both interosseous muscles and the extrinsic extensor are required to fully extend all the joints of the finger.

C. Finger with soft tissue

A finger tendon network including soft tissues was laid up on bones and ligamentous joints described in [10], (Fig 6b). These joints differed from those in the paw, in that they used immiscible thermoplastics to prevent fusion of the joints during the layup of the tendon network. A membrane of SEBS-paraffin gel blended with PCL was wrapped over the ligaments and bones and thermally bonded to them, making the surface adhesive to SEBS.

1) *Flexor apparatus*: Polyamide tows were tied with clove-hitches to the distal and middle phalanges, then infused with SEBS-paraffin gel matrix. The radial and ulnar branches of the superficial flexor tendon were fused together above the deep flexor tendon as before.

The sheath for the flexor tendons was made from Surlyn 9320 (random copolymer ionomer of poly-ethylene-acrylic-acid-acrylate-Zinc) blended with paraffin to soften it. This produced a soft tough elastomeric thermoplastic membrane that could bond to polyamides, but not to SEBS. This membrane was then wrapped around the flexor tendons and welded closed. The distal end of the sheath was tied to the distal phalanx by the insertion of the distal extensor slip, and welded to it. Paraffin was infused down the sheath to lubricate the tendons.

The annular ligaments were formed by wrapping Kevlar polyaramide tows around the phalanges the flexor sheath, (Fig 6c). The weld flange of the sheath was folded to the palmar face of the sheath and used to weld the sheath to the annular ligaments. Between annular ligaments the weld flange was trimmed away to facilitate flexion. The palmar pulley and digital annular ligaments were made in this way.

2) *Extensor apparatus*: The extensor tendons and associated retinacular ligaments were made from Kevlar tows. The Distal extensor slip was tied with a clove hitch to the distal phalanx and welded to the flexor tendon sheath (see above). The proximal and distal extensor slips were welded to the patellae of the DIP and PIP. The tendon slips were infused with a Dryflex 5000 SEBS oil-gel matrix and pressed flat into ribbons. The bones, joints and flexor apparatus were then wrapped in a membrane of SEBS-paraffin gel, excluding the extensor tendons, to serve as the lubricant layer under the extensor apparatus. This arrangement provided the tendons with a flexible matrix that bound their fibres to each other while allowing them to slide over the underlying bones and joints, (Fig 6d).

Tendon sheaths for the interosseous tendons at the MCP joints were made with Surlyn-paraffin blend as for the flexor tendon sheath. The sagittal bands were then wrapped around the MCP joint and welded to the first annular ligament, the interosseous sheaths, and the extrinsic extensor tendon, thus stabilising both the interosseous sheaths and the extrinsic extensor, (Fig 6e).

The transverse retinacular ligament was laid under the branches of the distal extensor slip, and over the proximal extensor slip at the level of the PIP. The ends of the transverse retinacular ligament were welded to the palmar side of the second annular ligament. The relative lengths of the branches of the interosseous and extrinsic extensor tendons to the proximal and distal extensor slips were then adjusted, before welding the branches to each other and the transverse retinacular ligament to fix their lengths.

Testing the extensor mechanism then showed that the tendon slips were falling too far palmarly on the sides of the flexed finger and failing to extend it. The interosseous hood and triangular ligament of the distal extensor slip were then constructed to correct this. A membrane of SEBS-paraffin gel was laid over the branches of the extrinsic extensor, and a second membrane of Dryflex 880101 was laid over this such that the branches of the interosseous tendons to the distal extensor slip lay along the margins of the Dryflex membrane. Polyamide pseudo-monofilament thread was then repeatedly looped around the interosseous slips and dorsally over and through the margins of the Dryflex membrane. This formed an interosseous hood with a smooth stiff Dryflex 880101 face sliding over the underlying extrinsic extensor slips. The triangular ligament of the distal extensor slip was formed in a similar way supporting branches of the distal extensor slip from its insertion to the transverse retinacular ligament.

3) *Dermal structures attached to the flexor apparatus*:

The ability to securely attach a structured fibre-gel dermis to the musculoskeletal core of the finger would be essential for producing a functional emulation of a human finger. An initial demonstration of materials was made by constructing simplified digital pads on the palmar side of the finger, (Fig 7a).

The pads were cut from a solid block of SEBS-paraffin gel and positioned on the palmar face of the flexor apparatus over each of the phalanges, and the MCP joint. These were then covered with a membrane of Dryflex 5000 (Shore A 0 hardness). This membrane was then welded to the sides of the finger immediately palmar to the extensor apparatus. The palmar creases were then formed by laying strips of Dryflex 5000 membrane over the palmar faces of the joints, so as to separate the digital pads, and welding these 'crease ligaments' to the lateral faces of the joints.

4) *Performance of soft tissue finger*: The range of motion of the finger for each tendon's actuation is shown by Fig.7.

The finger as built is nearly twice the thickness of the human finger on which it was based. Several faults contribute to this. The gel blocks used for the pads are twice the thickness of the anatomical pads, too soft and lack fibrous septae (Grayson's ligaments). The retrofitted interosseous hood and triangular ligament of the extensor apparatus are too thick, and need to be constructed with thinner membranes and welding instead of sewing. The flexor tendons have too many tows and are twice the diameter of the anatomical tendons. The flexor sheath is thicker than ideal and the weld flange adds to its bulk. The lubricant gel layers of the extensor apparatus were thicker than they need to be.

The finger does not flex as tightly as it should. This is mostly due to errors manufacturing the joints of the finger used for the last iteration of soft tissue tendons.

IV. DISCUSSION

The demonstration pieces were hand built without special tools, consequently the quality control was poor and the build process variable. However they serve their purpose in that they demonstrate a suite of base materials, composites and layup techniques that allow emulation of the mechanical composition and behaviour of vertebrate soft tissue tendon networks and dermal structures. The demonstration pieces have also shown the critical role of hyper-elastic tissues, and precise geometry of ligaments and tendon networks. SEBS-paraffin oil-gels were shown to meet and exceed the softness and hyper-elasticity required to emulate loose connective tissues.

Much better quality control could be achieved with mechanical mixers and rollers for blending thermoplastics and producing thin membranes. Special tools for laying, pressing, fusing membranes would potentially improve build quality and provide the possibility of automating the layup. Automated layup would provide CNC control and repeatability. This however would require a CAD-CAM system capable of modelling very soft hyper-elastic and highly anisotropic materials, and some means of monitoring the build process.

Further development of the materials might include custom block-polymers to facilitate controlled elasticity and adhesion or immiscibility.

V. CONCLUSIONS AND FURTHER WORK

The method described provides a way to build known anatomical tendon mechanisms on ligamentous joints.

The technique is likely to be most competitive versus other robot architectures for complex compact structures such as hands and feet. Here the reproduction of joint and tendon path geometry allows advantageous anatomical kinematics to be exploited, such as the reflexes of the hand. It would also be applicable for building humanoid faces and vocal tracts.

To be useful robot hands built in this way require actuators that would fit into the muscle spaces, and provide substantially similar actuation. This would imply a soft linear actuator, with a fast clutch-release behaviour and low modulus in the relaxed (floppy) state. Alternatively new tendon routes would need to be designed that allowed all the actuators to be extrinsic. For pawed and hoofed feet this is not a problem because the anatomical tendons are extrinsic.

Hands and feet also require tactile sensitivity. The reproduction of soft tissues provides the possibility of sampling mechanical strain as somatosensory mechanoreceptors do.

This would require sub-millimetre sized strain sensors, connected by soft wires that can tolerate the strain of the tissues through which they must pass.

REFERENCES

- [1] Arvind Ananthanarayanan, Mojtaba Azadi, and Sangbae Kim. Towards a bio-inspired leg design for high-speed running. *Bioinspiration & Biomimetics*, 7(4):046005, 2012.
- [2] Karl K Bilderback and Ghazi M Rayan. The septa of legueu and juvara: an anatomic study. *The Journal of hand surgery*, 29(3):494–499, 2004.
- [3] MANUEL GIUSEPPE CATALANO. *Soft Robotics: Design for Simplicity, Performance, and Robustness of Robots for Interaction with Humans*. PhD thesis, Universit degli Studi di Pisa, Italy, 2013.
- [4] A.D. Deshpande, Zhe Xu, M.J.V. Weghe, B.H. Brown, J. Ko, D.D. Chang, L.Y.; Wilkinson, S.M. Bidic, and Y. Matsuoka. Mechanisms of the anatomically correct testbed hand. *Mechatronics, IEEE/ASME Transactions on*, pages 238–250, Feb 2013.
- [5] Alan Diamond, Rob Knight, David Devereux, and Owen Holland. Anthropomorphic robots: concept, construction and modelling. *Int J Adv Robotic Sy*, 9(209), 2012.
- [6] Aaron M Dollar and Robert D Howe. The highly adaptive sdm hand: Design and performance evaluation. *The international journal of robotics research*, 29(5):585–597, 2010.
- [7] James R Doyle. Palmar and digital flexor tendon pulleys. *Clinical orthopaedics and related research*, 383:84–96, 2001.
- [8] Jonathan Mark Fussey, KF Chin, N Gogi, S Gella, and SC Deshmukh. An anatomic study of flexor tendon sheaths: a cadaveric study. *Journal of Hand Surgery (European Volume)*, 34(6):762–765, 2009.
- [9] Markus Grebenstein, Maxime Chalon, Werner Friedl, Sami Haddadin, Thomas Wimbck, Gerd Hirzinger, and Roland Siegwart. The hand of the dlr hand arm system: Designed for interaction. *Int J Robotics Research*, 31(13):15311555, 2012.
- [10] Nick Hockings, Pejman Iravani, and Chris R. Bowen. Artificial ligamentous joints : methods, materials and characteristics. Accepted to IEEE Humanoids 2014, preprint available at <http://people.bath.ac.uk/nch28/pdfs/Artificial%20Ligamentous%20Joints%20-%20Methods%20Materials%20and%20Characteristics.pdf>, 2014.
- [11] WARREN H. LEWIS, editor. *Grays Anatomy of the Human Body*. LEA & FEBIGER : BARTLEBY.COM, 2000, 20 edition, 1918.
- [12] GE Loeb. Control implications of musculoskeletal mechanics. In *Engineering in Medicine and Biology Society*. 1995. IEEE 17th Annual Conference, volume 2, pages 1393–1394. IEEE, 1995.
- [13] Robert J Schultz, James Furlong II, and Anthony Storage. Detailed anatomy of the extensor mechanism at the proximal aspect of the finger. *The Journal of hand surgery*, 6(5):493–498, 1981.
- [14] Timothy P Schweitzer and Ghazi M Rayan. The terminal tendon of the digital extensor mechanism: Part i, anatomic study. *The Journal of hand surgery*, 29(5):898–902, 2004.
- [15] Carla Stecco, Veronica Maccchi, Luca Lancerotto, Cesare Tiengo, Andrea Porzionato, and Raffaele De Caro. Comparison of transverse carpal ligament and flexor retinaculum terminology for the wrist. *The Journal of hand surgery*, 35(5):746–753, 2010.
- [16] Julio Taleisnik, Richard H Gelberman, Brent W Miller, and Robert M Szabo. The extensor retinaculum of the wrist. *The Journal of hand surgery*, 9(4):495–501, 1984.
- [17] James S Thompson, J William Littler, and Joseph Upton. The spiral oblique retinacular ligament (sorl). *The Journal of hand surgery*, 3(5):482–487, 1978.
- [18] Francisco J Valero-Cuevas, Jae-Woong Yi, Daniel Brown, Robert V McNamara, Chandana Paul, and Hod Lipson. The tendon network of the fingers performs anatomical computation at a macroscopic scale. *Biomedical Engineering, IEEE Transactions on*, 54(6):1161–1166, 2007.
- [19] RL Zwanenburg, PMN Werker, and DA McGroutner. The anatomy and function of clelands ligaments. *Journal of Hand Surgery (European Volume)*, 39(5):482–490, 2014.

**16.1.3 Visual Image Interpretation in Humans and Machines (ViiHM) 2014 poster:
Smoothed-Particle-Machine-Perception**

Smoothed Particle Machine Perception

Nick Hockings, Pejman Irvani, Chris Bowen
Robotics Lab, Dept Mechanical Engineering, University of Bath
n.c.hockings@bath.ac.uk

Work started this year, looking for collaborators and potential users.

Abstract

A sensor fusion and spacial perception algorithm is proposed that generates a lagrangian meshless multiphysics model of the sensory space around a robot. Its advantage lies in modelling solids and liquids with a single model. This allows it to handle everyday phenomena including multibody movement, collisions, open surface fluid flow, elastic and plastic deformation. Particle splitting/combining allows foveation of the model for tractability.

Because the model is based on forces between particles, tactile/proprioceptive forces from palpation and manipulation can be incorporated. These can then be used to learn the mechanical properties and structure of the objects being handled.

The model provides a space in which to perform the recognition of tangible objects and events. The recognition of nouns and verbs produces episodic memory of a scene as a semantic network. Fitting the smoothed particle model to canonical and episodic memories produces top down perception and imagination.

Physical-spacial perception

Smoothed Particle Multiphysics (Meshless Lagrangian)

Model

- 1) Mass divided into point particles,
- 2) Properties interpolated by compact kernel,
- 3) Anisotropic (fibrous) solids by particle pair specific elasticity.

Simulation loop

- 1) At each particle find neighbours, density, pressure,
- 2) Calculate accelerations due to: pressure gradient, viscosity, elasticity, surface tension, gravity,
- 3) Calculate new velocities, and positions at next time step.

Acceleration of particle a

$$\frac{d^2x_a}{dt^2} = \sum_b m_b \left(\frac{(S_a - P_a) + (S_b - P_b)}{\rho_a \rho_b} + \Pi_{ab} + R_{ab} \right) \nabla_a W_{ab}$$

where

- b are the particles within range of the smoothing kernel of a
- m_b is the mass of particle b
- S_a is the elastic force due to the density of a at b
- P is the pressure force
- ρ is the density
- Π is the viscosity force
- ∇_a is the gradient in coordinates of particle a
- W_{ab} is the angular momentum term

Adapted from Monaghan (2012).

Rather than specifying all these terms apriori, learning the terms, not just their parameters, would provide a more general and extensible solution.

Particles

For each scene there is a palate of particles, akin to the colours of a group of pictures in video compression. Each particle has mass, position and velocity. Each class of particles has reflectance (Lambertian & specular), elasticity, viscosity and density.

Sensor prediction

The parameters of the model allow simulation of elastic and plastic solids, and common fluids moving, colliding and deforming. Because the model is based on the forces between masses, the outcome of physical interactions can be predicted, which is useful for manipulation tasks. The physics model can be extended to allow prediction of the signal from any type of sensor.

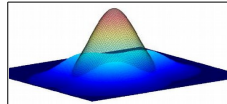


Fig 1. The approximation and replacement of three small kernels by one larger kernel. Particle splitting and combining is a technique used to vary the spacial resolution of smoothed particle models, to provide detail only where needed.

Tractability in real-time can be increased by foveation of the model, scaled by inverse distance from centre of attention. This is achieved by the smoothed particle modelling technique of splitting and combining particles in the running model. This allows the total number of particles being simulated to be kept constant. Details learnt can be stored, and reinserted into the model when needed.

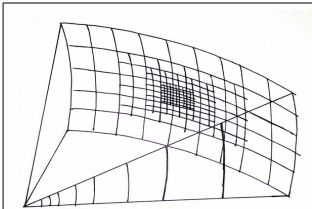


Fig 2 View space ordering and foveation: particles in the larger peripheral voxels are combined into fewer larger particles, large particles entering finer voxels are split into smaller particles. Sorting the particles by view ray and inverse distance accelerates sensor prediction.

Passive rgb camera prediction

Viewspace ordering of the particles, and partitioning of the model by the dominant sensor of each region, allows the predicted visible surface to be constructed quickly. Given the surface normals, and the reflectance of the surface particles, plus the dominant light sources, the image can be predicted.

Illumination can be modelled as locally smooth light fields, blending a small number of illumination spectra in the first instance. These can be further structured by estimating the location and shape of the light source. For most real world scenes the first three light sources account for most of the appearance of any given pixel (ie discotheque lighting is rare). This is partly a matter of selective attention - it can be computed when it is simple/useful/salient and time allows. Computing illumination provides shape from shading in low detail regions.

Tactile force prediction

The model is based on forces between masses, and the detection of proximity between particles - sorting by spacial location - is step 1 of the simulation loop. Thus prediction of contact and force at the sensors is 'free'.

Energy functional, as per DTAM (Newcombe et al 2011)

$$E_{\xi, \alpha} = \int_{\Omega} \left\{ g(u) \|\nabla \xi(u)\|_H + \frac{1}{2g} (\xi(u) - \alpha(u))^2 + \lambda C(u, \alpha(u)) \right\} du$$

where

- Ω is the image domain
- $g(u)$ is the per pixel weight
- $\|\nabla \xi(u)\|_H$ is the Huber norm of the gradient of the model*
- $\frac{1}{2g} (\xi(u) - \alpha(u))^2$ coupling term
- $\lambda C(u, \alpha(u))$ cost volume of the sensor error

* the model is different.

Model building/fitting

The data gathered from the sensors is compared to the predictions. From this a cost volume of the sensor-space is generated. We then follow the approach of Newcombe et al (2011) using total variational regularisation on the model parameters to render the problem solvable, and a coupling term between the cost volume and the smoothing term to provide an energy functional amenable to fast primal-dual optimisation.

Regularisation

Where Newcombe et al used the inverse depth map, and the texture to provide a rigid world model, we have the Smoothed particle multi-physics model. Specifically we propose to fit the parameters in the following way:

The position and velocity of particles are regularised with total variation.

The reflectance, elasticity, viscosity and density parameters are regularised with a combination of weak total variation and membership of a palate of particle classes.

The illumination field is composed of a small number of classes defining spectrum, while intensity, direction and solid angle are subject to strong total variational smoothing. The illumination source requires the direction and solid angles of an illumination class to converge on the location of the source.

The strength of regularisation, number of classes of particles and number of illumination sources can be relaxed to extract more detail about the scene if time allows.

Tracking

Foveation allows the position, velocity and acceleration of camera pose to be tracked against the wide angle background, which is likely to capture a largely stable scene. It also obliges a saccading and tracking strategy to fix the object of interest at the fovea.

Frequent, high resolution and low latency updating of the model at the focus of attention is the purpose of fixing the fovea on it. Foveation reduces the total complexity of the model, by several orders of magnitude relative to a uniform high resolution model. This makes whole scene tracking much more tractable, but also requires a 'the world as its own best model' perceptual strategy.

Applications:

Learning structure from manipulation

Tactile-proprioceptive interaction provides calibration of forces between the particles, while the deformation of the visible surface provides information about the propagation of force through the object. Together these lead to the accumulation of detail in the model about the internal structure of the object.

Robot self-identification

The first object that a robot manipulates is itself. This leads to modelling of its own body and calibration of its actuators and sensors with respect to each other.

Robot motion planning & control

Small, fast models can be created by reducing resolution and pruning details that do not affect the answers sought. Because these models are based on sensory perception, they allow rapid adaptation to factors such as using tools that extend the robot.

The models generated can be applied to planning by adding attractor and repeller fields that guide the motion. These fields can be created by combining the particles of the target and hazard objects and inflating their smoothing kernel width.

This provides robust online re-planning in response to disturbance of the trajectory, or movement of the objects. The force-distance curve of the attractor can be adjusted to control the time and velocity of convergence.

Control of execution can be achieved by optimising actuator force to approximate the planned trajectory. Forward modelling of the expected visual and proprioceptive sensory consequence allows the applied force to be pre-emptively corrected.

Machine tool control & calibration

Live photogrammetry of workpiece and tracking of tool for detection and correction of deviations from design.

Video production - editing focus & lighting

The 3D model generated would permit bokeh to be applied retrospectively to deep depth of field video. This would allow shallow depth of field video of unpredictable ad lib action. The reflectance and illumination model would allow recolouring and relighting of scenes.

Digital anatomy & surgery

Anatomical structure can be learnt objectively from sensor data (without subjective opinion) by recording video plus the forces on anatomist's instruments during dissection.

The model learnt can be morphed to fit MRI/CT/Ultrasound scans to create patient specific anatomical models. These models would facilitate haptic virtual dissection, surgical rehearsal and pathophysiological modelling of disease processes.

Smoothed Particle Machine Perception

Nick Hockings, Pejman Irvani, Chris Bowen
Robotics Lab, Dept Mechanical Engineering, University of Bath
n.c.hockings@bath.ac.uk

Cognitive perception

Given a robust multi-physics model of the perceptual space, canonical memory and top-down perception can be developed by reciprocal interactions between the model and machine learning based semantic recognition.

A semantic recognition system grounded in this way can give rise to syntax in a semantic network, which in turn permits higher cognitive functions including episodic memory, imagination, procedural and one-shot learning.

Semantic recognition

Feature recognition in smoothed particles
The smoothed particle model provides many features by which to recognise and segment objects, including spatial arrangement, properties and classes of particles.

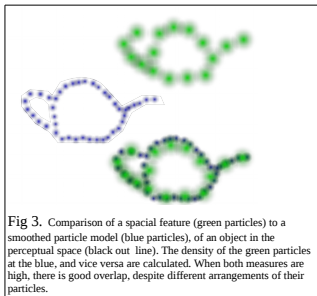


Fig 3. Comparison of a spatial feature (green particles) to a smoothed particle model (blue particles), of an object in the perceptual space (black outline). The density of the green particles at the blue, and vice versa are calculated. When both measures are high, there is good overlap, despite different arrangements of their particles.

Force, energy & mass flows

The smoothed particle model conserves energy, mass and momentum. Consequently the flow of these quantities through the model can be traced.

Excess kinetic energy is dissipated by hysteresis in collisions, and matter is removed where it leaves the perceptual space.

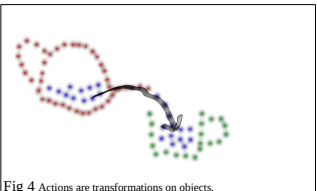


Fig 4 Actions are transformations on objects.

Action features ground verbs and syntax

Actions are apparent in the model as transformations on objects. The availability of both forces and energy flows in the model allows causal relations to be traced. The flow of energy allows the passive (grammatical object) and active (subject) parties of an action to be identified.

Actions ground verbs, and the implied relation between two objects grounds syntax.

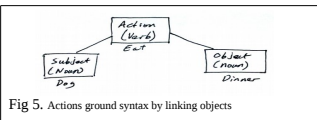


Fig 5. Actions ground syntax by linking objects

Perception of machines and agents

Where a machine, or animal is active in the perceptual space, the energy, impulse or new matter they release into the scene is added to the model in the tracking process. These sources are evident as centres of expansion in the energy flow field.

Depending on the behaviour of an energy source, it may be modelled as part of a state machine, or as the effect of a willful agent with purposeful action selection.

Top down perception

Recognition of an object or action in the scene allows the insertion of prior expectations associated with it. This can be done by giving the fit of the model to the recognized object or action a modest positive value in the optimisation of the model.

This allows particles with low sensory information to be rearranged. E.g. the unseen sides of an object are shaped to match prior experience of objects of that class.

Higher cognitive perception

Semantic network of scene

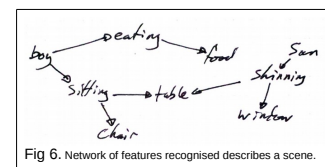


Fig 6. Network of features recognised describes a scene.

The collection of actions (verbs), objects (nouns) and modifiers (adverbs & adjectives) and relations (prepositions) that are recognised in a scene form a semantic network which describes the scene.

Episodic memory, forgetting & imagination

Because actions extend over time, and contain hierarchies of shorter actions, the semantic network links a series of scenes. This continuous graph over time provides a form of highly compressed episodic memory.

The subsidiary networks of scenes recorded in this way can be progressively archived or pruned by their current saliency and significance. Regions of the network can be indexed by the combinations of features they contain, weighted by their significance in the scene. If those features reoccur in perception the scene can then be retrieved. This provides a form of lossy compression by forgetting, and a means of recall.

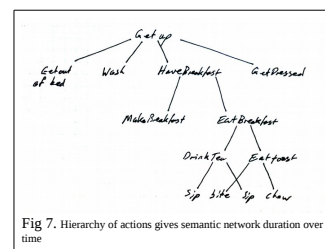


Fig 7. Hierarchy of actions gives semantic network duration over time

Past scenes can be re-visualized by using the recognition of their components as the fitting criteria for a smoothed particle model. This allows the physical simulation of the scene to be replayed at any given resolution, and to be varied by modifying the parameters or adding new components to the scene. This visualisation can be extended to entirely novel scenes and the physical consequences simulated. This provides a system for both physical and semantic imagination.

Dreaming & one shot learning

Replay 'memories'

to make inferences from temporally separated events
lossy re-compression of episodic memory - pruning the semantic network => graceful decay over time
learn canonical & procedural knowledge => generalize for future predictions

Procedural learning

Rehearse sequence of actions
Mirror - imitation and empathy
Estimate equivalent state of self to that seen from other agent's actions - simplified

Recursive/recurrent feature recognition

-> open ended, depends on consistent clustering in data.
Need to direct both sensory and cognitive attention
=> need autonomous system? to select actions on basis of goals.

Applications:

Video production - tracking & animation

Track centre(s) of attention in video - guide focus, lighting etc
Map facial anatomy to actors - recognise & manipulate (animate) facial expression and gesture.

Digital anatomy & surgery -

Name & know significance - link histology & physiology to anatomy

Semantic recognition of anatomical tissues and structures allows macro-scale knowledge to be linked to histology, cytology, physiology, pathology.

Know the significance of alterations of anatomy can be understood by the system, which allows it to examine, diagnose, medicate and perform surgery.

Machine tool control & calibration

Safe operation, procedural learning & refinement

Recognition, understanding and correction of disturbances in the workspace.

One shot learning from demonstration, followed by improvement of technique from rehearsal in simulation (imagination) and from experience.

Adaptation of technique to new tasks.

References

- Monaghan, J. J. "Smoothed particle hydrodynamics and its diverse applications." *Annual Review of Fluid Mechanics* 44 (2012): 323-346.
- Newcombe, Richard A., Steven J. Lovegrove, and Andrew J. Davison. "DTAM: Dense tracking and mapping in real-time." *Computer Vision (ICCV), 2011 IEEE International Conference on*. IEEE, 2011.

16.1.4 Building Bridges to Building Brains (BBtBB) 2013 poster: Simulation of somatosensory input

Work from my MSc thesis at The University of Sussex using simulation to demonstrate the role of the mechanical properties of soft tissues in tactile perception associated with the human finger-pad, fingernail and nailbed complex.

The experience of soft tissue modelling using the INRIA SOFA surgical simulation framework, led to the selection of smoothed particle modelling as the modelling system for anatomical soft tissues and soft matter generally. This led to the development of the Smoothed Particle Machine Perception algorithm.

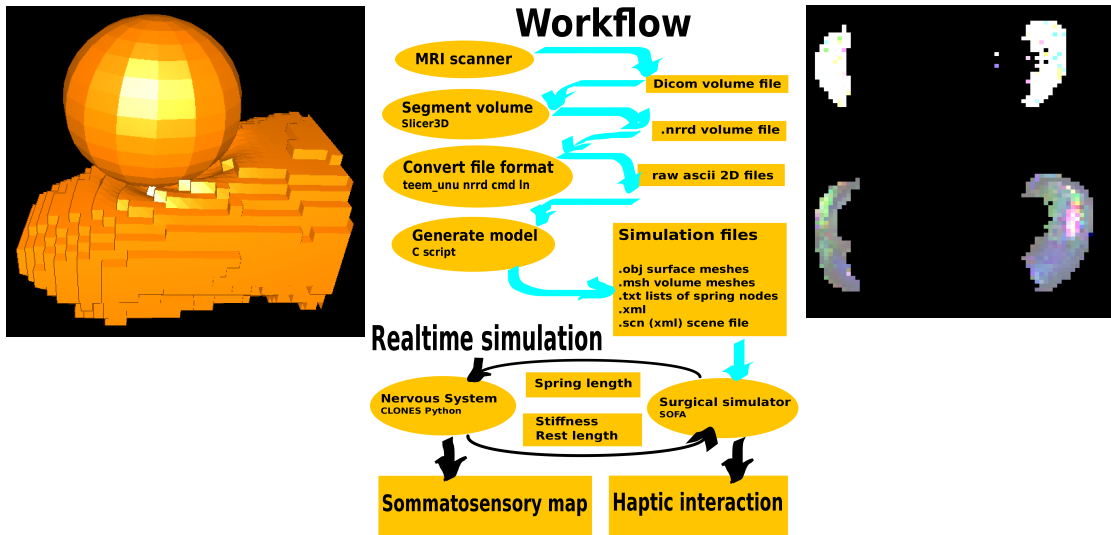
Simulation of somatosensory input

Nick Hockings nch28@bath.ac.uk

The SOFA real-time surgical simulation software from INRIA was used to simulate the deformation of dermal structures in the finger tip as a result of contact with an object. The CLONES plugin to SOFA allowed the deformations to be output to another program via shared memory.

This allows a simulation of the somatosensory input to be generated and displayed as a live somatosensory map, which could be used as the input to a simulation of the somatosensory nervous system. CLONES also permits the rest length and stiffness of 'muscles' to be altered by input via shared memo.

This methodology allows (i) investigation of the dependence of somatosensation on tissue structure and compliance, and (ii) the creation of environmental-sensorimotor interactions for simulated nervous systems.



[Faure F. et al](#)

SOFA: A Multi-Model Framework for Interactive Physical Simulation
Soft Tissue Biomechanical Modeling for Computer Assisted Surgery
Springer (Ed.) (2012) DOI : [10.1007/978-1-4419-9999-9_125](https://doi.org/10.1007/978-1-4419-9999-9_125)

[Allard J. et al](#)

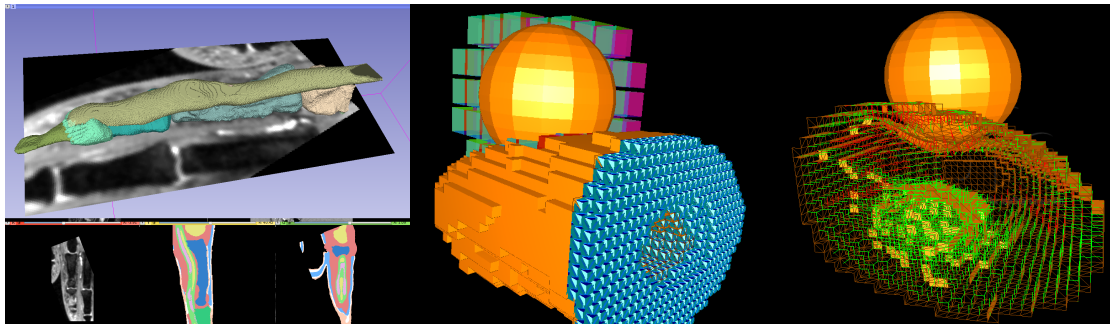
Volume Contact Constraints at Arbitrary Resolution. ACM Transactions on Graphics (Proceedings of SIGGRAPH 2010) 29, 3, Aug. 2010

[Voegtlin T.](#)

CLONES : A Closed-Loop Simulation Framework for Body, Muscles and Neurons Twentieth Annual Computational Neuroscience Meeting - CNS 2011 (2011) <http://hal.inria.fr/hal-00643270>

[Pieper S., Halle M., Kikinis R.](#)

3D SLICER. Proceedings of the 1st IEEE International Symposium on Biomedical Imaging: From Nano to Macro 2004; 1:632-635.
<http://www.slicer.org>



List of Figures

1-1	21
2-1	The articulation of the biomimetic joint. Fig.7 from [44]	35
2-4	The fully assembled biomimetic robotic hand. Left: The palmar aspect of the biomimetic robotic hand system. Top right: The dorsal view of the robotic hand. Bottom right: The laser-cut extensor hood integrated with intrinsic muscles. Note: The total weight of our biomimetic robotic hand is less than 1 kg (942 grams) including the actuation system. Fig.1 from [54]	37
2-5	The skeleton of the 3D-printed finger connected by crocheted ligaments and laser-cut joint soft tissues. Note: All the crocheted ligaments are anchored by 1 mm screws at their biological insertion sites. Fig.5 from [54]	38
2-6	Snapshots of an assembled finger showing both the gliding mechanism of the extensor hood and the bulging effect of the tendon sheaths during finger flexion. Fig.7 from [54] .	38
2-7	Fabrication stages of the index finger. The capsule ligament covers the joint cavity by attaching to end parts of bones with hot melt adhesives (a)(c). Collateral ligaments whose geometry is highlighted in (e) are placed on the side for torsional stability of joints (d)(e). Remaining joints are covered with ligaments with the same method (f). Low friction short tube pieces are placed on anatomically inspired pulley positions (g). Pulleys are fixed with additional hot melt adhesives and nitrile rubber to withstand torques (h). Tendon cables are routed through pulleys and longer tubes on non-moving bones (i). Fig.3 from [55]	40
2-8	A picture of the built soft robotic hand. Fig.1 from [56]	40
3-1	Force paths through ligamentous versus pin-hinge joints. (Blue) tensile force, (Pink) compressive force. Note how the force has to be transmitted as compression across the discontinuity of rigid materials, and consequently the has to double back on itself making the pin-hinge joint much bulkier than the ligamentous joint for the same strength. This also causes a lateral dog-leg in the compressive force path and, reduced radius and increased pressure at the contact surfaces.	44

3-2	Organisation of Skeletal muscle, from the gross to the molecular level. F,G,H, and I are cross sections at the levels indicated.(Drawing by Sylvia Colard Keene. Modified from Fawcett: Bloom and Fawcett: A Textbook of Histology. Philadelphia, W.B.Sunders Company, 1986.) Adapted from fig.6-1 [60]	49
3-5	Contraction kinetics of slow and fast fibres. A: representative force-velocity (left panel) and force-power (right panel) curves of three single human muscle fibres (slow, fast 2A, and fast 2X) permeabilized and maximally activated at 12C. B: comparison of unloaded shortening velocity values (V_o) of mouse and human muscle fibres classified according to myosin heavy chain composition. Each column represents the average of V_o values obtained with the slack test protocol on 6 25 single fibres, permeabilized and maximally activated at 12C. C: correlation between sliding filament velocity of purified myosins (V_f) determined by in vitro motility assay at 25C and unloaded shortening velocity of corresponding isolated single fibres (V_o) permeabilized and maximally activated at 12C. Fibres were obtained from four different species. [Modified from Pellegrino et al. (594).] D: correlation between unloaded shortening velocity of isolated single muscle fibres (V_o) and ADP affinity (K_{AD}) of corresponding myosins from different muscles and different species. [Modified from Nyitrai et al. (570), with permission from Elsevier. Adapted from fig.10 [61]	52
3-6	A, fusiform; B, unipennate; C, bipennate; P.C.S., physiological cross-section, from fig.365 of [62].	53
3-7	The organization of tendon structure from collagen fibrils to the entire tendon. From Fig.1 [66]	55
3-8	57
3-9	58

3-10 The Organization of Cutaneous Mechanoreceptors in Skin of the mouse. "Innocuous touch information is processed by both glabrous hairless (A) and hairy (B) skin. (A) In glabrous skin, innocuous touch is mediated by four types of mechanoreceptors. The Merkel cell-neurite complex is in the basal layer of the epidermis and it consists of clusters of Merkel cells making synapse-like associations with enlarged nerve terminals branching from a single Ab fibre. This complex and its associated SAI-LTMR responses help us in reconstructing acute spatial images of tactile stimuli. Meissner corpuscles are localized in the dermal papillae and consist of horizontal lamellar cells embedded in connective tissue. Their characteristic RAI-LTMR responses detect movement across the skin. Ruffini endings are localized deep in the dermis and are morphologically similar to the Golgi tendon organ, a large and thin spindle-shaped cylinder composed of layers of perineural tissue. Historically, Ruffini endings have been associated with SAII-LTMR responses, which respond best to skin stretch, though such correlations remain highly controversial. Lastly, Pacinian corpuscles are located in the dermis of glabrous skin where their characteristic onion-shaped lamellar cells encapsulate a single Ab ending. Their well-recognized RAI-LTMR responses detect high-frequency vibration. (B) In hairy skin, tactile stimuli are transduced through three types of hair follicles, defined in the mouse as guard, awl/auchene, and zigzag. The longest hair type, guard hairs, is associated with touch domes at the apex and Ab-LTMR longitudinal lanceolate endings at the base. Awl/auchene hairs are triply innervated by C-LTMR, Ad-LTMR, and Ab-LTMR longitudinal lanceolate endings. Zigzag hair follicles are the shortest and are innervated by both C- and Ad-LTMR longitudinal lanceolate endings. In addition, all three hair follicle types are innervated by circumferential lanceolate endings whose physiological properties remain unknown. Noxious touch is detected by free nerve endings found in the epidermis of both glabrous and hairy skin and are characterized by both Ad- and C-HTMR responses. Abbreviations: SA, slowly adapting; RA, rapidly adapting; LTMR, low-threshold mechanoreceptor; HTMR, high-threshold mechanoreceptor; SC, stratum corneum; SG, stratum granulosum; SS, stratum spinosum; SB, stratum basalis." Fig 1 from [72]

60

3-11	”Skin is innervated by complex combinations of low- and high-threshold mechanoreceptors, each with unique physiological profiles and response properties elicited by distinct tactile stimuli. 1 Conduction velocities can vary across species; please see the following references for more detailed interspecies comparisons: Leem et al. (1993) (rat); Brown and Iggo (1967) and Burgess et al. (1968) (cat and rabbit); Perl (1968) (monkey); and Knibestol (1973) (human). 2 Though SAI-LTMR responses have been observed in both glabrous skin of humans and hairy skin of mice, they have only been postulated to arise from Ruffini endings, though direct evidence to support this idea is lacking (Chambers et al., 1972). 3 Although SAI-like responses are present in the mouse, Ruffini endings or Ruffini-like structures have not been identified in rodents. 4 The stimulus described is the optimal stimulus known to elicit the response properties depicted in the last column of this table. However, it is probable, and often times documented, that multiple physiological subtypes can be recruited with any one particular tactile stimulus. For example, indentation of hair skin is likely to activate not only SAI-LTMRs associated with guard hairs but also longitudinal lanceolate endings of the Ab-, Ad-, and C-LTMR type.” Table 1 from [72]	61
3-12	Anatomical planes and directions of the human body [75]	63
3-13	Anatomical directions of the human hand [75]	64
3-14	Anatomical directions of quadruped bodies [78]	65
3-15	radius and ulna. The elbow would be at the top and wrist at the bottom of the diagram. Note the notches in the distal radius for various extensor tendons. Image214 from [62].	66
3-16	bones of hand palmar view, image219 from [62].	67
3-17	bones of hand dorsal view, image220 from [62].	68
3-18		69
3-19	(a) Proximal interphalangeal joint extended (b) flexed, showing the movement of the ligaments, dorsal and volar plates. The flexor tendons pass through the annular pulley.	70
3-20	Thumb MCP joint showing the location of the sesamoid bones in the volar plate.	72
3-21	Ligaments of the trapezio-metacarpal joint. (a)Dorsal ligament complex. (b)Radial view of opened trapezio-metacarpal joint showing the volar beak ligament and dorsal ligament complex. Contraction of the muscles of the thumb closes the joint space, causing the saddle shaped joint surfaces to come into alignment. Drawn from figure-1 in [107]	74
3-22	Drawings of the ligaments of the carpo-metacarpal joint of the thumb. (a) Volar (palmar) view of the right first carpo-metacarpal joint; (b) view from the posterior and distal side; MI=thumb metacarpal MII=index finger metacarpal, td=trapezoidal, tm=trapezium, IML=inter-metacarpal ligament, JC=joint capsule, AOL=anterior oblique ligament, APL=abductor pollicis longus tendon insertion, POL=posterior oblique ligament, DRL=dorsal radial ligament. Fig.III.10&.11 from [108].	74
3-23	Terminologia Anatomica English names for the carpal bones. Note the gap between the ulna and the carpal bones is occupied by the triangular fibrocartilaginous complex” see 3.3.5.	76

3-24	Ligaments of the carpal bones.	77
3-25	Length changes and potential tensional status of measured carpal ligaments during wrist radio-ulnar deviation. A, B Three palmar ligaments: RSC, LRL, and UC. The ligaments with the arrows are tensed. The sum of the lengths of the RSC and UC ligaments was consistent at 4 positions of radio-ulnar deviation. C, D Dorsal ligaments: DIC and DRC. The ligaments with arrows are tensed. The DIC and DRC ligaments have converse-length changes. A and C are at ulnar deviation; B and D are at radial deviation. Figure 5 from [112].	78
3-26	(a&b) Motion of the radio-carpal and inter-carpal joints in flexion and extension. (a) T2 weighted MRI scan, sagittal view at the level of the metacarpal of the middle finger, the capitate and lunate carpal bones, (b) diagram of motion of the joints. (c) Coordination of the motion of the individual carpal bones in flexion-extension. Each bone rotates about its own axis, linked by the ligaments (black).	79
3-27	The ligaments of the distal radio-ulna joint, within the triangular fibrocartilaginous complex, at the distal margin of the joint. (a) The 4 ligaments studied: 1 and 2, palmar and dorsal superficial radio-ulnar ligaments (dark blue); 3 and 4, dorsal and palmar deep radio-ulnar ligaments (ligamentum subcruentum) (light blue), from figure-1 of [112]. (b) The tensional status in each component of the distal radio-ulnar ligaments at the positions of A forearm pronation, B neutral rotation, and C supination, from figure-2 of [112].	80
3-29	82
3-30	84
3-31	The undulating path of the flexor tendons of a finger in the extended position seen in an MRI scan, palm upwards in sagittal section. The location of the retinacular ligaments is superimposed on the scan. Labels: A0 'zeroth' annular ligament is formed by the transverse fibres of the superficial palmar fascia and the septae of Legueu and Juvara, A1-5 Annular retinacular ligaments, P1-3 phalanges, Mc meta-carpal bone, DIP distal inter-phalangeal joint, PIP proximal inter-phalangeal joint, McP metacarpo-phalangeal joint, CET common extensor tendon, SB sagittal bands, DDF deep digital flexor tendon, SDF superficial digital flexor tendon, Ch chiasma where DDF passes between the branches of the SDF. Note the DDF inserts on P3, while the branches of the SDF insert on P2.	85
3-32	Interpretation of tenographic images: sheath bulging and flattening during flexion-extension. Insert: synovial pocket formation. Fig.3 from [116] . "Tenographic" = X-ray radiographs of finger with contrast medium injected into the flexor tendon sheath. Note: (1) the smooth curvature of the tendons at all stages of flexion-extension, (2) the cruciate retinacular ligaments between the annular ligaments and their role in producing a smoothly curved constraint on the tendons.	85
3-33	86

3-34	Axial anatomic slice obtained at the dorsum of the hand show the extensor digitorum tendons (arrowheads) and extensor digiti minimi tendons (arrow), which are arranged on the same level. Note the difficulty of identifying the tendon for each finger owing to tendon multiplicity and variability. Fig.8a of [52]	89
3-35	Axial anatomic slice obtained at a near level along the dorsum of the hand show the interosseous muscles (1), which are located in the inter-metacarpal spaces. The lumbrical muscles (2) are located on the radial sides of the flexor digitorum profundus tendons. 3 = abductor digiti minimi, 4 = adductor pollicis. Fig.16a of [52]	89
3-36	Axial anatomic slice obtained at the MCP joint show the sagittal bands (arrows), which extend from the extensor digitorum tendon to the palmar plate. Fig.13 of [52]	89
3-37	Axial anatomic slice obtained at the MCP joint show the circumferential distribution of the dorsal apparatus over the dorsum of the fingers. Arrows = sagittal band. Fig.12 of [52]	89
3-38	Axial anatomic slice obtained at the proximal phalanx show a dorsal condensation of fibres (arrows), which corresponds to the extensor digitorum tendon, and lateral and medial fibres (arrowheads), which correspond to the intrinsic contribution to the extensor apparatus by the interosseous and lumbrical tendons. Fig.17a of [52]	89
3-39	Cross-section of a hand at the level of septa of Legueu and Juvara, i.e. between the levels of fig-3-35 and fig-3-36 . Flexor tendons, lumbrical muscles, and neurovascular structures are removed. The hemostat is palmar and slightly radial to the first dorsal interosseous muscle. The arrows point to the 3 web space canals and a radial marginal canal. These are for hosting lumbrical muscles and common digital nerves and arteries, which are located radial to the flexor tendon canals. Eight well-defined septa can be seen clearly and a ninth thin membranous marginal septum is held by the hemostat. Fig.1 of [102]	90
3-40	Axial anatomic slice (close-up view) show the sagittal band (arrow). 1 = extensor digitorum tendon, 2 = palmar plate, 3 = flexor tendon sheath, 3 = flexor tendon, 4 = interosseous muscle, 5 = lumbrical muscle, III = third metacarpal bone, * = deep transverse metacarpal ligament. Note that the interosseous muscle is dorsal to the deep transverse metacarpal ligament and the lumbrical muscle is palmar to the ligament. Fig.13c of [52]	90
3-41	92
3-42	94
3-43	95

3-44	Anatomy of the extensor apparatus. (a) Drawing of the hand (dorsal view) shows the main anatomic structures. 1 = extensor digitorum muscle, 2 = extensor digiti minimi muscle, 3 = extensor carpi ulnaris muscle, 4 = abductor pollicis longus muscle, 5 = extensor pollicis brevis muscle, 6 = extensor pollicis longus tendon, 7 = extensor indicis tendon, 8 = extensor carpi radialis longus muscle, 9 = extensor carpi radialis brevis muscle, 10 = inter-tendinous connections, 11 = extensor retinaculum, 12 = first dorsal interosseous muscle, 13 = adductor pollicis tendon, 14 = abductor digiti minimi muscle, 15 = sagittal band, 16 = central slip, 17 = lateral conjoined tendon, 18 = medial conjoined tendon, 19 = terminal tendon, 20 = triangular ligament. (b) Drawing of the hand (dorsal view) shows the zones of the extensor system according to the Verdan classification (10). This classification was developed to categorize the lesion findings. I = DIP joint, II = middle phalanx, III = PIP joint, IV = proximal phalanx, V = MCP joint, VI = dorsum of hand, VII = wrist extensor compartment, VIII = extrinsic extensor muscles. Fig1. of [52]	96
3-45	a) drawing b) trans-illuminated anatomic specimen (dorsal view) showing the extensor apparatus of the index finger (removed from its location). 1 = extensor digitorum tendon, 2 = interosseous muscle, 2 = lumbrical muscle, 3 = sagittal band, 4 = medial slip, 5 = central slip, 6 = lateral slip, 7 = medial conjoined tendon, 8 lateral conjoined tendon, 9 = triangular ligament, 10 = terminal tendon, 11 = transverse fibres, 12 = oblique fibres, 13 = retinacular ligament. Fig11a&b. of [52]	97
3-46	Trans-illuminated anatomic specimen (dorsal view) shows the extensor tendons of the dorsum of the hand (removed from their location). Note the inter-tendinous connections (arrow-heads). 1 = extensor digitorum tendon for the index finger, 2 = extensor digitorum tendon for the middle finger, 3 = extensor digitorum tendon for the ring finger, 4 = extensor digiti minimi tendon. Fig.9b of [52]	97
3-47	Anatomic photograph (medial view) shows the MCP joint level of the third finger. In this area, the extensor digitorum tendon (1) receives the intrinsic contribution of the interosseous muscle (2). This contribution consists of the transverse fibres (3) and oblique fibres (4). 5 = deep transverse metacarpal ligament, 6 = sagittal band. Fig.14 of [52]	98
3-48	a) Sagittal anatomic slice obtained at the PIP joint show the insertion of the central slip (arrow) on the base of the middle phalanx. b) Sagittal anatomic slice obtained at the DIP joint show the insertion of the terminal tendon (arrow) on the base of the distal phalanx. c) T1-weighted MR image corresponding to (a). d) Axial T1-weighted MR image obtained at the head of the proximal phalanx shows the relationship between the central slip (arrow) and the medial and lateral slips (arrowheads).	98
3-50	Radial view of the extensor hood. The central and extrinsic lateral bands of the EDC can be seen below the semi-transparent extensor hood. The lumbrical inserts into the bottom of the hood, near the needle point. Note that the lateral bands of the distal extensor pass dorsal to the axis of rotation of the PIP joint. The transverse retinacular ligament is visible immediately distal to the PIP. Fig.8.1 of [118]	99

3-49	Topology of extensor tendon hood of the finger, lateral view palm downwards (top), dorsal view (bottom) : A0-5 Annular retinacular ligaments, P1-3 phalanges, Mc metacarpal bone, DIP distal inter-phalangeal joint, PIP proximal inter-phalangeal joint, McP metacarpo-phalangeal joint, DES distal extensor slip, SORL spiral retinacular ligament, TL triangular ligament of DES, TRL transverse retinacular ligament, LB lateral band of DES, PES proximal extensor slip , CET common extensor tendon, IOT inter-osseous tendon, SB sagittal band, IOM inter-osseous muscle, FTS flexor tendon sheath, SPF longitudinal fibres of superficial palmar fascia.	99
3-51	102
3-52	104
3-53	image420 elbow joint deep muscles and vessels, from [62].	106
3-54	(a)&(b)Dermal anatomy of the distal finger. (a)&(b) Sagittal section of PIP and DIP repeated from fig-3-48a&3-48b , showing the dermal and skeletal structures. Note (i)the adhesion of the palmar creases to the A3 and A5 pulleys palmar to the volar plates, (ii)the relation of the fingernail to the distal phalanx, and distal finger pad. (c)Sagittal view of the perionychium and distal phalanx. Terminology for the anatomy Fig-1A from [124] . (d)Lateral ligaments of the DIPJ. Deep connective tissue structures of the DIPJ. A4, A5, and C3 represent pulleys of the flexor mechanism. Fig-1 from [125] . (e)Schematic sagittal section through the distal phalanx showing connective tissue structures in relation to the joint. Fig-2 from [125] . (f)DIP joint schematic representation. DS, dorsal septum; DSP, dorsal plate; CL, Clelands ligaments; GL, Graysons ligaments; OPS, oblique proximal septum; IOL, interosseous ligament; CCL, collateral ligament; VP, volar plate; PS, pulp septae; C3, A4, A5, flexor pulleys. Fig-8 from [125]	108
3-55	Transverse cross-sectional sample of the distal phalanx created from the thumb of a <i>Macaca fuscata</i> , with collagen fibres stained with Azan staining. The blue colour in the image indicates collagen fibres (a) Overall view. (b) Magnified view of a selected portion. Black arrows indicate Pacinian corpuscles and gray arrow indicates adipose tissue. Fig.1 from [126]	109
3-56	This picture shows the orientation of Clelands ligaments; PIP-D and PIP-P originating mainly from the proximal phalanx and the DIP-D and DIP-P ligament arising from the distal part of the middle phalanx. The possible fifth ligament of Cleland is shown just distal to the DIP-D in a proximal direction. Fig-3 from [127]	109
3-57	Dissection from the mid-ventral aspect via a palmar midline incision. The whole adipose tissue has been removed exposing the fibres. From the ventral aspect we first identified the Grayson ligaments overlying the neurovascular bundle. They were in the same level as the natatory ligaments. In the other side of the finger we observed the Clelands ligaments under the neurovascular bundle lying laterally to the skin in the dorsal part of the finger. Fig-3 from [128]	110

3-58	A detailed figure from Zancolli and Cozzis Atlas of Surgical Anatomy of the Hand [129]. (AC) show respectively the proximal fibres (A), middle fibres (B), and distal fibres (C) of Clelands ligaments. The middle fibres (B) are shown attached to Landsmeers transverse band. The distal ligaments of Cleland are not shown. Fig-6 from [127].	110
3-59	This illustration consists of redrawn copies of the most important historical drawings of Clelands ligaments. The differences between the authors are more visible in accordance with our findings (E). From left to right: Cleland (A), Grayson (B), Milford (C), McFarlane (D), and Zwanenburg (E). Each ligament is given a different colour; the same colour refers to the same ligament, in the authors opinion. Red: PIP-D; green: PIP-P; yellow: DIP-D; blue DIP-P; purple: a possible fifth ligament of Cleland (Cleland, 1878; Grayson, 1941; McFarlane, 1990; Milford, 1968). Fig-5 from [127].	111
3-60	The main elements of the palmar fascia. (1) Natatory ligament. (2) Distal commissural ligament of the first web space. (4) Distal transverse palmar ligament. (5) Proximal transverse palmar ligament. (6) Pretendinous bands. (7) Palmar facial extension to abductor pollicis brevis. (8) Palmaris longus tendon. Fig.41.10 from [130].	111
3-61	114
3-62	115
3-63	115
3-64	From [133].	116
3-65	From [133].	117
4-1	Soft contact surfaces: pads and thumb web	119
4-2	Flexion of the palm. (Top to bottom) The palm varies in concavity by opposition of the thumb web and of the metacarpals of the little and ring finger. (Left columns) digits flexed. (Right columns) digits extended.	121
4-3	Power grips	122
4-4	Preflexes of the carpal tunnel, a force applied to the palmar surface of the hand causes the carpus to be extended, and flexor tendon length to be taken up at the carpal tunnel. This in turn causes the fingers to flex at the first joint distal to the pressure on the palm.	124
4-5	Preflexes of the superficial palmar fascia, when an object impacts the palm, the superficial palmar fascia, and the flexor tendons cause the MCP joints to the fingers to flex. This occurs even if tension in the carpal flexors prevents extension of the carpus, and the preflex of the carpal tunnel.	125
4-6	Folding motion of the palm: adduction and flexion of the carpo-metacarpal and inter-metacarpal joints of the thumb, ring and little fingers.	125
4-7	Preflexes of the thumb web, (a,b,c) when the carpus is extended by impact on the palmar surface of the fingers or distal palm, the thumb web elastically opposes the thumb behind the object - e.g. catching a branch. (d,e) when the thumb web is impacted distally by an object, the thumb web adducts the thumb and flexes the MCP joints of the fingers.	127
6-2	Slicer3D medical image processing and visualization system	132

7-1	Modulus dependence on temperature for an ideal, linear, amorphous polymer. From fig 4.3 in [142].	136
7-2	Poly(lactic acid) a) chemical structure of monomer, b) bulk material.	139
7-3	Polycaprolactone acid a) chemical structure of monomer, b) bulk material.	140
7-4	Acrylonitrile butadiene styrene acid a,b,c) chemical structure of monomers, d) bulk material (3D printed bone).	141
7-5	Ethylene Vinyl Acetate a) chemical structure, b) bulk material.	143
7-6	Poly(co-ethylene-co-acrylate) Sodium salt a) chemical structure, b) bulk material.	143
7-7	Polystyrene-co-block-poly(ran-ethylene-ran-butadiene)-co-block-polystyrene	144
7-8	SEBS intermolecular behaviour, showing an ordered polystyrene domain linking polymer molecules by van der Waals forces between styrene rings, and surrounding disordered elastic poly-ethylene-ran-butylene domain. Models generated with Avogadro: an open-source molecular builder and visualization tool. Version 1.1.1. [156]	145
7-9	145
7-10	Chemical structures of monomers.	148
7-11	Fibres of a) Nylon, b) Kevlar.	148
7-12	Ketone dipole attraction between polycaprolactone(top) and poly(lactic acid)(bottom)	150
7-13	Hydrogen bonding between polycaprolactone and polyamide	150
7-14	Fibre pull out testing. Top row, polyamide fibres in EVA (Elvax 40). Bottom row polyamide fibres in PCL (Polymorph).	151
7-15	Hyperelastic composite of SEBS-gel matrix, polyamide knitted stocking fabric reinforcement and a thin surface lamina of dense SEBS rubber (cast from xylene solution).	152
7-16	Elastic shear lubrication : a hyper-elastic lamina with elastic limit 1000% can permit shear 2x1000% times the thickness of the lamina. So a 0.5mm thick layer can lubricate 10mm of tendon excursion. This technique is essential for reproducing the movement of unsheathed anatomical tendons including the digital extensor hood.	153
7-17	154
7-18	Assessed Ga-In phase diagram, from experimental data. Adapted from figure 1 in [168]	156
7-19	Acrylonitrile butadiene styrene acid a) chemical structure of monomers, b) bulk material (thick part of the fibre to the left).	159
8-1	First prototype ligamentous joint, using ABS 3D printed bones on Denford (Ch.6.3.1) from MRI scan (Ch.6.1.1), Kevlar (Ch.7.5.3) polyamide fibres and Poly-Optic 14-70 (Ch.7.3.1) polyurethane elastomer resin.	165
8-2	First multi-jointed finger, using ABS 3D printed bones from simplified CAD model, polyamide fibres and Poly-Optic 14-70 polyurethane elastomer resin.	166
8-3	Layup of ligamentous joint using Poly-Optic 1410 rigid polyurethane bones cast from anatomy skeleton.	167
8-4	Polyurethane rubber matrix ligaments on rigid polyurethane bones	168
8-5	High density polyethylene joint capsule - to keep polyurethane rubber matrix of ligaments separate from rigid polyurethane of bones.	169

8-6	Silicone joint capsule on polyurethane finger with polyamide ligaments.	170
8-7	Polyurethane mould from anatomy skeleton bones to make polycaprolactone bones . .	172
8-8	Polycaprolactone bone joint surfaces forged against each other.	172
8-9	Polycaprolactone bones with thermoplastically welded polyamide ligaments and tendons, with silicone joint capsule	174
8-10	Polyamide ligaments welded into polycaprolactone bones	176
8-11	3D printing PLA bones on RepRap from MRI scans	177
8-12	Paw bones printed in PLA then coated with PLC. a)Bones of the third digit from left to right: metacarpal, proximal phalanx, middle phalanx, paired sesamoid bones of the metacarpo-phalangeal joint, distal phalanx. b)Two middle phalanx bones, left - PLA bone with support material removed, right - coated in PCL, still molten and transparent.	180
8-13	Paw digits and carpal bones	181
8-14	Paw palm and carpus	182
8-15	Paw : flexibility of the palm	183
8-16	The first finger with blended SEBS-PCL soft tissue matrix. (Note: The digital flexor sheath and tendons are included in these images. The red elastic band serves as the palmer fascia that would be built if this finger were integrated into a hand.)	184
8-17	Laminated joint surface layup: PCL and SEBS do not adhere to each other when molten, preventing fusion of the joint during layup. Laminated graduated blends of SEBS and PCL used for the distal joint surface present PCL face to distal phalanx, and SEBS face to the proximal joint surface.	185
8-18	Second SEBS finger	187
8-19	Final finger, return to simple joint surfaces and soft joint capsule, a) unpigmented transparent PLA bones, proximal and middle phalanges already coated in PCL, b) densely laid polyaramide ligament fibres, c) joint capsules formed of a thin layer of SEBS rubber wrapped and fused into ligaments.	189
9-1	First test flexor tendon sheath - polyamide tendon with silicone gel matrix and silicone oil tendon fluid, high density polyethylene sheath, polyamide annular ligaments with silicone gel matrix	194
9-2	Layup of flexor tendon sheath	195
9-3	Layup of extensor hood with high density polyethylene film and silicone gel.	196
9-4	Flexion of finger.	197
9-5	High density polyethylene flexor tendon sheath	198
9-6	PCL matrix tendons, silicone gel lubrication pad and EVA flexor sheath, built on the first PCL boned finger.	199
9-7	Dry PCL finger with individual extensor tendons, for investigation of individual tendon effects.	201
9-8	'Dry' finger with no matrix in flexible regions of articular ligaments, polycaprolactone matrix in extensor tendon slips and flexor retinaculum annular ligaments, fused high density polyethylene matrix and sheath for flexor tendons.	202

9-9	'Dry' finger - complete	204
9-10	Paw digits and metacarpals assembled with tendons, radius and carpal bones partly assembled.	207
9-11	Paw, palmar fascia. Blue fibres - natatory ligament.	208
9-12	209
9-13	Hyper-elastic SEBS-paraffin gel layer laid under the extrinsic extensor tendons.	210
9-14	Paw extensor retinaculum - lateral view	210
9-15	Paw extensor retinaculum - dorsal view	211
9-16	Paw superficial palmar fascia longitudinal fibres - white tows	211
9-17	The first SEBS-PCL flexor sheath, built on the first finger with SEBS-PCL matrix soft tissues. Figure-8-16 repeated.	212
9-18	The second finger with SEBS matrix soft tissues (Duplicated from Fig8-18)	214
9-19	Structure of flexor sheath - (1)PA-66 tendons with SEBS-paraffin gel matrix, (2)MD-PE lining, (3)Elasto-5000 layers around sheath and as (4)matrix to annular ligaments, (5)polyaramide (PAr) tows of annular ligament, (6)PCL coated PLA bone.	215
9-20	Laying extensor tendons between lubricating hyper-elastic gel laminae.	216
9-21	218
9-22	219
9-23	Flexion-extension of the finger, shown with first prototype skin and subcutis fitted.	220
9-24	Demonstration of the strength of the finger as initially built. The flexor tendons were able to actuate the finger with force comparable to a human finger. Shown here lifting a fire extinguisher, approximately 5kg.	221
9-25	Adduction-abduction of MCP by action of the interosseous tendons	222
10-1	Paw pad mould, 3D printed PLA, lined with modelling wax as a releasing layer.	229
10-2	230
10-3	232
11-1	(a) Simple preforms. Top, a Surlyn preform after drawing a fibre. Bottom, a PCL preform as cast in the mould. (b) 'Figure of eight' dual channel preform. (c) Dual channel preform, end view.	236
11-2	236
11-3	Mould set for concentric preforms. (a) moulds open showing different sizes of core rod, and a PCL preform. (b)Moulds closed, with rods partially inserted.	238
11-4	Fibre drawing tower, a)&b) original form with 2x 50watt reflector bulbs for the 'furnace', c) later form with double cylindrical glass furnace, nichrome heater wire and 4x 40watt bulbs.	239
11-5	240
11-6	Cylindrical furnace, inner silica glass tube with nichrome resistor wire and high temperature silicone. The outer borosilicate glass tube is not shown.	241
11-7	242

11-8	243
11-9	244
11-10	247
11-11 PV-OH supported drawing of SEBS. Fine SEBS fibre partially separated from thicker PV-OH support material	249
11-12 The problem of illuminating and visualising GaIn filled fibres – the smooth surface of the polymer presents dielectric specular reflection and refraction, while the amalgam presents metallic reflection. With very little matt reflection it is difficult to tell whether a fine fibre is or is not filled with GaIn. The colour in (c) and (e) are due to the LED illumination. Finer fibres (not shown) may be $< 10\mu m$ in diameter, given visible light $\lambda = 400 - 700nm$, the specular highlights which form the visible part of the fibres may approach a single wavelength in width.	251
11-13	253
11-14 CAD model of dual nozzle a) inner nozzle, b) outer nozzle	253
11-15 Outer nozzle tip as printed. Zoom in to see measurements. (a) Shows the distortion of the opening of the nozzle caused by the limit of resolution of the print. The figure of eight channel is $337\mu m$ by $827\mu m$. (b) The exterior of the tip is $1.159mm$ wide. (c) One side of the tip was not level. (d) The deficit was $233\mu m$ deep. Note that the walls at the tip are approximately $100\mu m$ thick.	254
11-16 Paired inner nozzle as printed. Zoom in to see measurements. (a) Showing asymmetry at the tips. (b) Showing the connecting bridge and spacers at the mid point of the nozzles, that fix the inner nozzles to each other and hold them in position relative to the outer nozzle. (c) Detail of the tip asymmetry. The inner nozzle tips are separated by $113\mu m$, and $770\mu m$ wide each. The deficit in the left tip was $682\mu m$. (d) Showing the nozzles end on with the spacers in the plane of focus, and (e) with tips in focus. The Nozzle apertures are $900\mu m$ apart. (f) Close up of the inner nozzle tips end on, showing their apertures. Their interior diameters are $221\mu m$ and $188\mu m$. The clear space between the nozzle tips is $56\mu m$.	255
11-17 The outer nozzle after conservative cutting and grinding. The aim was to improve the geometry with minimal cutting back of the tip, in order to achieve the smallest possible functioning aperture, and to align the end points of the inner and outer nozzles. (d) Shows the new dimensions of the aperture $1.352mm$ on the long axis, $714\mu m$ and $699\mu m$ for each lobe, and $354\mu m$ for the narrow point of the figure-of-eight.	256
11-18 (a-e) Close up oblique views of the outer nozzle, showing the 3d shape of the nozzle, and the texture of the material. (f) View of the SEBS port outlet into the interior of the outer nozzle. The other end of the channel aligns with the outlet of the Filastruder.	257
11-19 (a-c) The inner nozzle tips were sawn with a steel scalpel blade to produce a clean end level with the tips of the outer nozzle. (d-e) End on view of the sawn inner nozzle tips, showing blocked apertures after cutting. These were cleared by probing with $30\mu m$ copper wire and backward flushing to remove debris.	258

11-20(a-b) Tip of the assembled inner and outer nozzles. (c-e) Tips of the inner nozzles after cleaning.)	259
11-21Horizontal nozzle drawing with amalgam	261
11-22Testing of nozzle drawn fibre	262
12-1 Figure 1 from [4], showing how the maximum power out put was calculated from the measured output fatiguing over duration of exertion. "The relationship between average mechanical power production (\tilde{W}) and duration of effort(t) showing the method of analysis and derivation of the theoretical oxidative ($W_{o2} - AreaB$) and anaerobic ($W_{cap} - AreaA$) of the total maximal mechanical work ($\tilde{W}_{tot} - AreasA + B$) produced during an 80s all-out test on an isokinetic bicycle ergometer. The exponential decline of mechanical work with time is represented by the equation $W_{max}e^{-kt}$, where \tilde{W}_{max} is the mechanical work at zero time, t equals time (s) and k is a constant. The theoretical rise in mechanical work production which can be attributed to the muscle oxidation is represented by the equation $X - Xe^{-t/\lambda}$, where X is equal to average mechanical work performed during the last 20s of exercise, t is time and λ (the theoretical half time of the oxidative processes) is taken to be 6s. The analysis was performed to a constant duration of 45s. Inset shows original data taken from a pursuit cyclist."	270
12-2 Figures a,b represent two different kinds of 2-legged jump. Male subject M.R., 93.4 kg, age 56. Line 1 (blue) represents the force, line 2 (green) the vertical velocity of the centre of mass, line 3 (red) the power. x-axis=amplitude of the parameters, y-axis = time course (ms). Figure 1 from [225].	275
12-3 Contraction kinetics of slow and fast fibres. A: representative force-velocity (left panel) and force-power (right panel) curves of three single human muscle fibres (slow, fast 2A, and fast 2X) permeabilized and maximally activated at 12°C. From figure 10A in [228]	277
12-4 Actuation of the rolled dielectric elastomer actuator. Applying voltage causes the plates to attract each other, squeezing the dielectric, resulting in extension of the fibre. Thus the actuator contracts elastically when it is discharged, and is charged to relax it. d_1, d_2, l_1, l_2 are the diameters and lengths before and after charging.	281
12-5 Electric strength as a function of electrode separation. Fig 1 from [242]	284
12-6 An equivalent cube of actuator for calculating the electrical energy density and therefore the maximum work density of a rolled dielectric elastomer actuator.	285
12-7 Proposed MEMS mechanoreceptors using fibre drawn rolled dielectric elastomer sensors. Simple MEMS components would be used to connect the sensor to the signal fibre and anchor the sensor to the tissues. a)Pressure/vibration sensor (equivalent to Paccinian or Merkel sensory endings) b)Stretch receptor (equivalent to Ruffini ending, muscle spindle or Golgi tendon organ) c)Hair follicle, with hair fibre co-drawn then stripped.	286

12-8	a) Schematic of Dual Excitation Multiphase Electrostatic Drive (DEMED). The electrodes are connected into three phases, fig-1 from [251]. b) Schematic cross sectional view of basic DEMED. Two potential distribution around electrodes are indicated by bold lines, fig-2 from [251].	287
12-9	CAD model of microfluidic DEMED actuator, showing MEMS springs connecting consecutive plates electrically and mechanically. There are four phases of electrodes with power rails at the margins (red), which would be set inside polyimide dielectric plates. Geometry is constrained by the need to maintain minimum distances between phases at all points to avoid dielectric breakdown. The vertical electrical interconnects to the plates above and below would be at the mid point of the springs.	289
12-10	Elmer electrostatic finite element analysis of a unit cell of a microfluidic DEMED actuator. Note this is a different layout of the DEMED with three phases and central power rails. (a) Electric force density. (b) Electric energy density. (c) Electric potential contour surfaces. (d) Salome-Meca model from which the multi-partition mesh was made. . . .	291
13-1	Analysis of a single static image by SIRFS [257]. From left to right: original image, shape, surface normals, reflectance, shading, illumination.	294

Chapter 17

References

- [1] Polytek Development Corp. Physical properties of polytek poly-optic 14 series liquid plastics. https://www.polytek.com/wp-content/uploads/14Series_PhysicalProperties_Polytek.pdf, 2010. accessed September 22nd, 2016.
- [2] www.matweb.com. IndalloyTM alloys liquid at room temperature, product data sheet. <http://www.indium.com/technical-documents/product-data-sheets/download.php?docid=622>. accessed September 22nd, 2016.
- [3] Guido Ferretti, MV Narici, Tiziano Binzoni, L Gariod, JF Le Bas, H Reutenauer, and P Cerretelli. Determinants of peak muscle power: effects of age and physical conditioning. European journal of applied physiology and occupational physiology, 68(2):111–115, 1994.
- [4] CTM Davies and ER Sandstrom. Maximal mechanical power output and capacity of cyclists and young adults. European journal of applied physiology and occupational physiology, 58(8):838–844, 1989.
- [5] John A Hawley and Timothy D Noakes. Peak power output predicts maximal oxygen uptake and performance time in trained cyclists. European journal of applied physiology and occupational physiology, 65(1):79–83, 1992.
- [6] Jacques R Poortmans, Nathalie Boisseau, Jean-Jacques Moraine, Rodrigo Moreno-Reyes, and Serge Goldman. Estimation of total-body skeletal muscle mass in children and adolescents. Med Sci Sports Exerc, 37(2):316–322, 2005.
- [7] Ian Janssen, Steven B Heymsfield, ZiMian Wang, and Robert Ross. Skeletal muscle mass and distribution in 468 men and women aged 18–88 yr. Journal of applied physiology, 89(1):81–88, 2000.
- [8] Scott Trappe, Philip Gallagher, Matthew Harber, John Carrithers, James Fluckey, and Todd Trappe. Single muscle fibre contractile properties in young and old men and women. The Journal of physiology, 552(1):47–58, 2003.

- [9] www.dupont.com. DupontTM kaptonTMhn polyimide film, technical data sheet. <http://www.dupont.com/content/dam/dupont/products-and-services/membranes-and-films/polyimide-films/documents/DEC-Kapton-HN-datasheet.pdf>. accessed September 22nd, 2016.
- [10] Iain MacLaren. A brief history of the royal college of surgeons of edinburgh. *Res Medica*, 268(2), 2005.
- [11] Gary Taubes. Better than nature made it. *Science*, 288(5463):81–81, 2000.
- [12] Barbara Webb. Can robots make good models of biological behaviour? *Behavioral and brain sciences*, 24(06):1033–1050, 2001.
- [13] Ramesh Balasubramaniam, Anatol G Feldman, Jean-Paul Banquet, Philippe Gaussier, Mathias Quoy, Arnaud Revel, Catherine Belzunga, Catherine Chevalley, Carolina Chang, Robert I. Damper, Fred Delcomyn, Carlo De Lillo, Judith A. Effken, Robert E. Shaw, Donald R. Franceschetti, Stan Franklin, Ronald N. Giere, Jrn Hoklanda, Beatrix Vereijken, Kristen N. Jaax, Peter R. Killeen, Rolf Ktter, Mark A. Krause, Susanne Lohmann, Malcolm A. MacIver, Ludovic Marina, Olivier Oullier, Giorgio Metta, Giulio Sandini, Peter E. Midford, Ralph R. Miller, Francisco Arcediano, Titus R. Neumann, Susanne Huberb, Heinrich H. Blthoff, Ernst Niebur, Mounya Elhilali, Iyad Obeid, Justin Werfel, Mark Blanchard, Mattia Frasca, Kaushik Ghose, Constanze Hofstoetter, Giovanni Indiverih, Mark W. Tildeni, Irene M. Pepperberg, John Pickering, George N. Reeke, Jeffrey C. Schank, Matthias Scheutz, Allen I. Selverston, Luc Steels, Thomas Sugara, Michael McBeath, Daniel L. Younga, and Chi-Sang Poomb. Commentaries on: Can robots make good models of biological behaviour? *Behavioral and brain sciences*, 24(06):1050–1081, 2001.
- [14] Robert J Full and Daniel E Koditschek. Templates and anchors: neuromechanical hypotheses of legged locomotion on land. *Journal of experimental biology*, 202(23):3325–3332, 1999.
- [15] W.T.B. Kelvin. *Electrical Units of Measurement. Being One of the Series of Lectures Delivered at the Institution of Civil Engineers, Session 1882-83*. Institution of Civil Engineers, 1883. <https://books.google.co.uk/books?id=xZxsHAAACAAJ>.
- [16] Charlie Cooper and Lucy Anna Gray. Lack of anatomy training could lead to shortage of surgeons. <http://www.independent.co.uk/life-style/health-and-families/health-news/lack-of-anatomy-training-could-lead-to-shortage-of-surgeons-9570684.html>, 2014. accessed September 22nd, 2016.
- [17] François Faure, Christian Duriez, Hervé Delingette, Jérémie Allard, Benjamin Gilles, Stéphanie Marchesseau, Hugo Talbot, Hadrien Courtecuisse, Guillaume Bousquet, Igor Peterlik, et al. Sofa: A multi-model framework for interactive physical simulation. In *Soft Tissue Biomechanical Modeling for Computer Assisted Surgery*, pages 283–321. Springer, 2012.

- [18] Alan Diamond, Rob Knight, David Devereux, and Owen Holland. Anthropomorphic robots: concept, construction and modelling. Int J Adv Robotic Sy, 9(209), 2012.
- [19] Richard L Lieber. Skeletal muscle is a biological example of a linear electroactive actuator. In 1999 Symposium on Smart Structures and Materials, pages 19–25. International Society for Optics and Photonics, 1999.
- [20] RS Johansson and JR Flanagan. 6.05 tactile sensory control of object manipulation in humans. The Senses: A Comprehensive Reference, Academic Press, New York, NY, pages 67–86, 2008.
- [21] Marco Controzzi, Christian Cipriani, and Maria Chiara Carrozza. Design of artificial hands: A review. In The Human Hand as an Inspiration for Robot Hand Development, pages 219–246. Springer, 2014.
- [22] Markus Grebenstein. Analysis of the current state of robot hands. In Approaching Human Performance, pages 11–37. Springer, 2014.
- [23] Claudio Melchiorri, Gianluca Palli, Giovanni Berselli, and Gabriele Vassura. On the development of the ub-hand iv: an overview of design solutions and enabling technologies. Robotics & Automation Magazine, 20(3), September 2013.
- [24] Markus Grebenstein. Methodology. In Approaching Human Performance: The Functionality-Driven Awiwi Robot Hand, volume 98 of Springer Tracts in Advanced Robotics, chapter 1.6, page 9. Springer Publishing Company, Incorporated, 2014.
- [25] Heinrich A Ernst. Mh-1, a computer-operated mechanical hand. In Proceedings of the May 1-3, 1962, spring joint computer conference, pages 39–51. ACM, 1962.
- [26] accessed September 22nd, 2016.
- [27] Shouhei Shirafuji, Shuhei Ikemoto, and Koh Hosoda. Design of an anthropomorphic tendon-driven robotic finger. In Robotics and Biomimetics (ROBIO), 2012 IEEE International Conference on, pages 372–377. IEEE, 2012.
- [28] MANUEL GIUSEPPE CATALANO. Soft Robotics: Design for Simplicity, Performance, and Robustness of Robots for Interaction with Humans. PhD thesis, Universit degli Studi di Pisa, Italy, 2013.
- [29] Aaron M Dollar and Robert D Howe. The highly adaptive sdm hand: Design and performance evaluation. The international journal of robotics research, 29(5):585–597, 2010.
- [30] Tapio VJ Tarvainen, Wenwei Yu, and Jose Gonzalez. Development of morphhand: design of an underactuated anthropomorphic rubber finger for a prosthetic hand using compliant joints. In Robotics and Biomimetics (ROBIO), 2012 IEEE International Conference on, pages 142–147. IEEE, 2012.

- [31] Matei Ciocarlie and Peter Allen. Data-driven optimization for underactuated robotic hands. In Robotics and Automation (ICRA), 2010 IEEE International Conference on, pages 1292–1299. IEEE, 2010.
- [32] Markus Grebenstein, Maxime Chalon, Werner Friedl, Sami Haddadin, Thomas Wimbck, Gerd Hirzinger, and Roland Siegwart. The hand of the dlr hand arm system: Designed for interaction. Int J Robotics Research, 31(13):15311555, 2012.
- [33] Shadow Robot. Shadow dexterous hand technical specification. Available at http://www.shadowrobot.com/wp-content/uploads/shadow_dexterous_hand_technical_specification_E1_20130101.pdf, 2013. accessed September 22nd, 2016.
- [34] Lael U Odhner, Leif P Jentoft, Mark R Claffee, Nicholas Corson, Yaroslav Tenzer, Raymond R Ma, Martin Buehler, Robert Kohout, Robert D Howe, and Aaron M Dollar. A compliant, underactuated hand for robust manipulation. The International Journal of Robotics Research, 33(5):736–752, 2014.
- [35] Rob BN Scharff, Eugeni L Dubrovski, Wim A Poelman, Pieter P Jonker, Charlie CL Wang, and Jo MP Geraedts. Towards behavior design of a 3d-printed soft robotic hand. In Soft Robotics: Trends, Applications and Challenges, pages 23–29. Springer, 2017.
- [36] anon. Jacob’s ladder. Scientific American, 61(15):227, 1889. Available at <http://archive.org/stream/scientific-american-1889-10-12/scientific-american-v61-n15-1889-10-12#page/n3/mode/2up> Accessed: 2014-09-16.
- [37] Donald Simanek. Toys, tricks and teasers. <http://www.lhup.edu/~dsimanek/TTT-rings/rings.htm>. Accessed: 2014-06-23.
- [38] Appolinaire C Etoundi, Ravi Vaidyanathan, and Stuart C Burgess. A bio-inspired condylar hinge joint for mobile robots. In Intelligent Robots and Systems (IROS), 2011 IEEE/RSJ International Conference on, pages 4042–4047. IEEE, 2011.
- [39] Appolinaire C Etoundi, Stuart C Burgess, and Ravi Vaidyanathan. A bio-inspired condylar hinge for robotic limbs. Journal of Mechanisms and Robotics, 5(3):031011, 2013.
- [40] Hugo Gravato Marques, Michael Jantsch, Steffen Wittmeier, Owen Holland, Cristiano Alessandro, Alan Diamond, Max Lungarella, and Rob Knight. Ecce1: the first of a series of anthropomorphic musculoskeletal upper torsos. In Humanoid Robots (Humanoids), 2010 10th IEEE-RAS International Conference on, pages 391–396. IEEE, 2010.
- [41] Peter R Van den Broek, Jacques M Huyghe, Wouter Wilson, and Keita Ito. Design of next generation total disk replacements. Journal of biomechanics, 45(1):134–140, 2012.
- [42] Peter R van den Broek, Jacques M Huyghe, and Keita Ito. Biomechanical behavior of a biomimetic artificial intervertebral disc. spine, 37(6):E367–E373, 2012.

- [43] Zhe Xu, Emanuel Todorov, Brian Dellon, and Yoky Matsuoka. Design and analysis of an artificial finger joint for anthropomorphic robotic hands. In Robotics and Automation (ICRA), 2011 IEEE International Conference on, pages 5096–5102. IEEE, 2011.
- [44] Norbert Sárkány, György Cserey, and Péter Szolgay. An introduction of the biomimetic hand testbed: Skeletal structure and actuation. In Robotic and Sensors Environments (ROSE), 2013 IEEE International Symposium on, pages 43–48. IEEE, 2013.
- [45] David D Wilkinson, Michael Vande Weghe, and Yoky Matsuoka. An extensor mechanism for an anatomical robotic hand. In Robotics and Automation, 2003. Proceedings. ICRA'03. IEEE International Conference on, volume 1, pages 238–243. IEEE, 2003.
- [46] M Vande Weghe, Matthew Rogers, Michael Weissert, and Yoky Matsuoka. The act hand: design of the skeletal structure. In Robotics and Automation, 2004. Proceedings. ICRA'04. 2004 IEEE International Conference on, volume 4, pages 3375–3379. IEEE, 2004.
- [47] Ashish D Deshpande, Jonathan Ko, Dieter Fox, and Yoky Matsuoka. Anatomically correct testbed hand control: muscle and joint control strategies. In Robotics and Automation, 2009. ICRA'09. IEEE International Conference on, pages 4416–4422. IEEE, 2009.
- [48] A.D. Deshpande, Zhe Xu, M.J.V. Weghe, B.H. Brown, J. Ko, D.D. Chang, L.Y.; Wilkinson, S.M. Bidic, and Y. Matsuoka. Mechanisms of the anatomically correct testbed hand. Mechatronics, IEEE/ASME Transactions on, pages 238–250, Feb 2013.
- [49] Mark Malhotra, Eric Rombokas, Evangelos Theodorou, Emanuel Todorov, and Yoky Matsuoka. Reduced dimensionality control for the act hand. In Robotics and Automation (ICRA), 2012 IEEE International Conference on, pages 5117–5122. IEEE, 2012.
- [50] Eric Rombokas, Mark Malhotra, and Yoky Matsuoka. Task-specific demonstration and practiced synergies for writing with the act hand. In Robotics and Automation (ICRA), 2011 IEEE International Conference on, pages 5363–5368. IEEE, 2011.
- [51] Zhe Xu, Vikash Kumar, Yoky Matsuoka, and Emanuel Todorov. Design of an anthropomorphic robotic finger system with biomimetic artificial joints. In 2012 4th IEEE RAS & EMBS International Conference on Biomedical Robotics and Biomechatronics (BioRob), pages 568–574. IEEE, 2012.
- [52] Juan A Clavero, Pau Golanó, Oscar Fariñas, Xavier Alomar, Josep M Monill, and Mireia Espluga. Extensor mechanism of the fingers: Mr imaging–anatomic correlation 1. Radiographics, 23(3):593–611, 2003.
- [53] Zhe Xu. Design and control of an anthropomorphic robotic hand: Learning advantages from the human body & brain. PhD thesis, University of Washington, USA, 2015.
- [54] Zhe VXu and Emanuel Todorov. Design of a highly biomimetic anthropomorphic robotic hand towards artificial limb regeneration. In Robotics and Automation, 2016. Proceedings. ICRA'16. IEEE International Conference on, pages 3485–3492. IEEE, 2016.

- [55] Utku Çulha and Fumiya Iida. Enhancement of finger motion range with compliant anthropomorphic joint design. *Bioinspiration & biomimetics*, 11(2):026001, 2016.
- [56] Mariya Chepishcheva, Utku Culha, and Fumiya Iida. A biologically inspired soft robotic hand using chopsticks for grasping tasks. In *International Conference on Simulation of Adaptive Behavior*, pages 195–206. Springer, 2016.
- [57] Johan Matthijs Frederik Landsmeer. *Atlas of anatomy of the hand*. Churchill Livingstone, 1976.
- [58] H Fam, JT Bryant, and M Kontopoulou. Rheological properties of synovial fluids. *Biorheology*, 44(2):59–74, 2007.
- [59] Harvey Lodish, Arnold Berk, S Lawrence Zipursky, Paul Matsudaira, David Baltimore, and James Darnell. *Molecular Cell Biology: An Integrated View of Cells at Work*, chapter 18.3. WH Freeman, New York, 4 edition, 2000. An optional Available from: <http://www.ncbi.nlm.nih.gov/books/NBK21724/>.
- [60] AC Guyton and JE Hall. *Human physiology and mechanisms of disease saunders*. Philadelphia, PA, 1992.
- [61] Stefano Schiaffino and Carlo Reggiani. Fiber types in mammalian skeletal muscles. *Physiological Reviews*, 91(4):1447–1531, 2011.
- [62] Henry Gray. *Anatomy of the human body*. Lea & Febiger, 1918. Available at <http://www.bartleby.com/107/>.
- [63] Anthony J. Channon, James R. Usherwood, Robin H. Crompton, Michael M. Günther, and Evie E. Vereecke. The extraordinary athletic performance of leaping gibbons. *Biology Letters*, 8(1):46–49, 2012.
- [64] JL Ivy, DL Costill, and BD Maxwell. Skeletal muscle determinants of maximum aerobic power in man. *European journal of applied physiology and occupational physiology*, 44(1):1–8, 1980.
- [65] Kieran F Reid and Roger A Fielding. Skeletal muscle power: a critical determinant of physical functioning in older adults. *Exercise and sport sciences reviews*, 40(1):4, 2012.
- [66] P Kannus. Structure of the tendon connective tissue. *Scandinavian journal of medicine & science in sports*, 10(6):312–320, 2000.
- [67] J Dargahi and S Najarian. Human tactile perception as a standard for artificial tactile sensing a review. *The International Journal of Medical Robotics and Computer Assisted Surgery*, 1(1):23–35, 2004.
- [68] Ravinder S Dahiya, Giorgio Metta, Maurizio Valle, and Giulio Sandini. Tactile sensing from humans to humanoid. *IEEE Transactions on Robotics*, 26(1):1–20, 2010.
- [69] Chiara Lucarotti, Calogero Maria Oddo, Nicola Vitiello, and Maria Chiara Carrozza. Synthetic and bio-artificial tactile sensing: A review. *Sensors*, 13(2):1435–1466, 2013.

- [70] JA McGrath and J Uitto. Anatomy and organization of human skin. Rook's Textbook of Dermatology, Eighth Edition, pages 1–53, 2010.
- [71] F Rice and P Albrecht. The senses: A comprehensive reference. vol. 6, somatosensation. 2008.
- [72] Victoria E Abaira and David D Ginty. The sensory neurons of touch. Neuron, 79(4):618–639, 2013.
- [73] Radhika Palkar, Erika K Lippoldt, and David D McKemy. The molecular and cellular basis of thermosensation in mammals. Current opinion in neurobiology, 34:14–19, 2015.
- [74] JM Jacobs and S Love. Qualitative and quantitative morphology of human sural nerve at different ages. Brain, 108(4):897–924, 1985.
- [75] International Anatomical Nomenclature Committee. Nomina anatomica : authorised by the Twelfth International Congress of Anatomists in London, 1985. Churchill Livingstone, Edinburgh, 6 edition, 1989. ISBN 0443040850.
- [76] David Kachlik, Vaclav Baca, Ivana Bozdechova, Pavel Cech, and Vladimir Musil. Anatomical terminology and nomenclature: past, present and highlights. Surgical and Radiologic Anatomy, 30(6):459–466, 2008.
- [77] Federative Committee on Anatomical Terminology. Terminologia anatomica. Georg Thieme Verlag, 1998. Available at <https://www.unifr.ch/ifaa/Public/EntryPage/ViewSource.html>.
- [78] International Committee on Veterinary Gross Anatomical Nomenclature (I.C.V.G.A.N.). Nomina anatomica veterinaria. http://www.wava-amav.org/Downloads/nav_2012.pdf, 2003. accessed September 22nd, 2016.
- [79] Susan Standring. Gray's anatomy: the anatomical basis of clinical practice. Elsevier Health Sciences, 2015.
- [80] Frances P Schuller-Ellis and George T Lazar. Internal morphology of human phalanges. The Journal of hand surgery, 9(4):490–495, 1984.
- [81] Marvin M Shrewsbury and Richard K Johnson. Form, function, and evolution of the distal phalanx. The Journal of hand surgery, 8(4):475–479, 1983.
- [82] Panayotis Ioannis Gigis and Kazimierz Kuczynski. The distal interphalangeal joints of human fingers. The Journal of hand surgery, 7(2):176–182, 1982.
- [83] William H Bowers, John W Wolf, John L Nehil, and Shellye Bittinger. The proximal interphalangeal joint volar plate. i. an anatomical and biomechanical study. The Journal of hand surgery, 5(1):79–88, 1980.
- [84] Peter V Loubert, Thomas J Masterson, Matthew S Schroeder, and Aaron M Mazza. Proximity of collateral ligament origin to the axis of rotation of the proximal interphalangeal joint of the finger. journal of orthopaedic & sports physical therapy, 37(12):179–185, 2007.

- [85] Thomas R Kiefhaber, Peter J Stern, and Edward S Grood. Lateral stability of the proximal interphalangeal joint. The Journal of hand surgery, 11(5):661–669, 1986.
- [86] PG Slattery. The dorsal plate of the proximal interphalangeal joint. The Journal of Hand Surgery: British & European Volume, 15(1):68–73, 1990.
- [87] Hiroyoshi Watanabe, Hiroyuki Hashizume, Hajime Inoue, and Takashi Ogura. Collagen framework of the volar plate of human proximal interphalangeal joint. Acta medica Okayama, 48(2):101–108, 1994.
- [88] Susumu Saito, Shigehiko Suzuki, and Yoshihisa Suzuki. Biomechanical differences of the proximal interphalangeal joint volar plate during active and passive motion: a dynamic ultrasonographic study. The Journal of hand surgery, 37(7):1335–1341, 2012.
- [89] Susumu Saito and Yoshihisa Suzuki. Biomechanics of the volar plate of the proximal interphalangeal joint: a dynamic ultrasonographic study. The Journal of hand surgery, 36(2):265–271, 2011.
- [90] Thomas Bayer, Andreas Schweizer, Magdalena Müller-Gerbl, and Georg Bongartz. Proximal interphalangeal joint volar plate configuration in the crimp grip position. The Journal of hand surgery, 37(5):899–905, 2012.
- [91] S Pagowski and K Piekarski. Biomechanics of metacarpophalangeal joint. Journal of biomechanics, 10(3):205–209, 1977.
- [92] N Berme, JP Paul, and WK Purves. A biomechanical analysis of the metacarpo-phalangeal joint. Journal of Biomechanics, 10(7):409–412, 1977.
- [93] C Fontaine. Anatomie des articulations métacarpo-phalangiennes des doigts longs. Chirurgie de la Main, 31(6):432–433, 2012.
- [94] Toshiyuki Kataoka, Hisao Moritomo, Tsuyoshi Murase, Junichi Miyake, and Kazuomi Sugamoto. Changes in lengths of the collateral ligament and the accessory collateral ligament during flexion of the metacarpophalangeal joint: Not a clinical study. The Journal of Hand Surgery, 35(10):56, 2010.
- [95] Akio Minami, Kai-Nan An, William P Cooney, Ronald L Linscheid, and Edmund YS Chao. Ligament stability of the metacarpophalangeal joint: a biomechanical study. The Journal of hand surgery, 10(2):255–260, 1985.
- [96] Pei-Hsin Kuo and Ashish D Deshpande. Muscle-tendon units provide limited contributions to the passive stiffness of the index finger metacarpophalangeal joint. Journal of biomechanics, 45(15):2531–2538, 2012.
- [97] Christopher J Dy, Scott M Tucker, Peter L Kok, Krystle A Hearn, and Michelle Gerwin Carlson. Anatomy of the radial collateral ligament of the index metacarpophalangeal joint. The Journal of hand surgery, 38(1):124–128, 2013.

- [98] Kaissar Yammine. The prevalence of the sesamoid bones of the hand: A systematic review and meta-analysis. *Clinical Anatomy*, 27(8):1291–1303, 2014.
- [99] Yasuhiro Seki, Yuko Hoshino, and Hiroshi Kuroda. Prevalence of sesamoid bones in the interphalangeal joint of the thumb and fingers: a radiographic study. *Clinical Anatomy*, 26(7), 2013.
- [100] Ozkan Kose, Ferhat Guler, Adil Turan, K Ecanbora, and Serdar Akalin. Prevalence and distribution of sesamoid bones of the hand. a radiographic study in turkish subjects. *Int. J. Morphol*, 30(3):1094–9, 2012.
- [101] AS Dharap, H Al-Hashimi, S Kassab, and MF Abu-Hijleh. Incidence and ossification of sesamoid bones in the hands and feet: a radiographic study in an arab population. *Clinical Anatomy*, 20(4):416–423, 2007.
- [102] Karl K Bilderback and Ghazi M Rayan. The septa of legueu and juvara: an anatomic study. *The Journal of hand surgery*, 29(3):494–499, 2004.
- [103] James R Doyle. Anatomy and function of the palmar aponeurosis pulley. *The Journal of hand surgery*, 15(1):78–82, 1990.
- [104] William W Dzwierzynski, Hani S Matloub, Ji-Geng Yan, Shiliang Deng, James R Sanger, and N John Yousif. Anatomy of the intermetacarpal ligaments of the carpometacarpal joints of the fingers. *The Journal of hand surgery*, 22(5):931–934, 1997.
- [105] Barbara Jemec, Liaquat Suleman Verjee, Abhilash Jain, and Fiona Sandford. Rotation in the interphalangeal thumb joint in vivo. *The Journal of hand surgery*, 35(3):425–429, 2010.
- [106] Michelle Gerwin Carlson, Kristin K Warner, Kathleen N Meyers, Krystle A Hearn, and Peter L Kok. Anatomy of the thumb metacarpophalangeal ulnar and radial collateral ligaments. *The Journal of hand surgery*, 37(10):2021–2026, 2012.
- [107] J Ollie Edmunds. Current concepts of the anatomy of the thumb trapeziometacarpal joint. *The Journal of hand surgery*, 36(1):170–182, 2011.
- [108] Arnold Paul Pieron. The mechanism of the first carpometacarpal (cmc) joint: an anatomical and mechanical analysis. *Acta Orthopaedica Scandinavica*, 44(sup148):1–104, 1973.
- [109] Jun Tan, Jing Xu, Ren Guo Xie, Ai Dong Deng, and Jin Bo Tang. In vivo length and changes of ligaments stabilizing the thumb carpometacarpal joint. *The Journal of hand surgery*, 36(3):420–427, 2011.
- [110] Elisabet Hagert, Julia Lee, and Amy L Ladd. Innervation patterns of thumb trapeziometacarpal joint ligaments. *The Journal of hand surgery*, 37(4):706–714, 2012.
- [111] Daniel M Sirkett. *Investigating the influence of contact area on carpal bone motion*. PhD thesis, UNIVERSITY OF BATH (UNITED KINGDOM), 2004.

- [112] Jing Xu and Jin Bo Tang. In vivo length changes of selected carpal ligaments during wrist radioulnar deviation. The Journal of hand surgery, 34(3):401–408, 2009.
- [113] Yan Rong Chen and Jin Bo Tang. In vivo gliding and contact characteristics of the sigmoid notch and the ulna in forearm rotation. The Journal of hand surgery, 38(8):1513–1519, 2013.
- [114] Andrew K Palmer and Frederick W Werner. The triangular fibrocartilage complex of the wrist— anatomy and function. The Journal of hand surgery, 6(2):153–162, 1981.
- [115] Frederick W Werner, Jennifer L Taormina, Levi G Sutton, and Brian J Harley. Structural properties of 6 forearm ligaments. The Journal of hand surgery, 36(12):1981–1987, 2011.
- [116] S Mester, B Schmidt, K Derczy, J Nyarady, and V Biro. Biomechanics of the human flexor tendon sheath investigated by tenography. Journal of Hand Surgery (British and European Volume), 20(4):500–504, 1995.
- [117] Julio Taleisnik, Richard H Gelberman, Brent W Miller, and Robert M Szabo. The extensor retinaculum of the wrist. The Journal of hand surgery, 9(4):495–501, 1984.
- [118] Shinjiro Sueda. Strand-based Musculotendon Simulation of the Hand. PhD thesis, University of British Columbia, Canada, 2010.
- [119] Robert J Schultz, James Furlong, and Anthony Storace. Detailed anatomy of the extensor mechanism at the proximal aspect of the finger. The Journal of hand surgery, 6(5):493–498, 1981.
- [120] Timothy P Schweitzer and Ghazi M Rayan. The terminal tendon of the digital extensor mechanism: Part i, anatomic study. The Journal of hand surgery, 29(5):898–902, 2004.
- [121] Timothy P Schweitzer and Ghazi M Rayan. The terminal tendon of the digital extensor mechanism: Part ii, kinematic study. The Journal of hand surgery, 29(5):903–908, 2004.
- [122] Francisco J Valero-Cuevas, Jae-Woong Yi, Daniel Brown, Robert V McNamara, Chandana Paul, and Hod Lipson. The tendon network of the fingers performs anatomical computation at a macroscopic scale. Biomedical Engineering, IEEE Transactions on, 54(6):1161–1166, 2007.
- [123] JNAL Leijnse and CW Spoor. Reverse engineering finger extensor apparatus morphology from measured coupled interphalangeal joint angle trajectories a generic 2d kinematic model. Journal of biomechanics, 45(3):569–578, 2012.
- [124] Elvin G Zook, Allen L Van Beek, Robert C Russell, and Michael E Beatty. Anatomy and physiology of the perionychium: a review of the literature and anatomic study. The Journal of hand surgery, 5(6):528–536, 1980.
- [125] D Slattery, C Aland, G Durbridge, and G Cowin. The connective tissue and ligaments of the distal interphalangeal joint: a review and investigation using ultra-high field 16.4 tesla magnetic resonance imaging. Journal of Hand Surgery (European Volume), page 1753193413496949, 2013.

- [126] Y Tanaka, T Ito, M Hashimoto, M Fukasawa, N Usuda, and A Sano. Collagen fibers induce expansion of receptive field of pacinian corpuscles. Advanced Robotics, 29(11):735–741, 2015.
- [127] RL Zwanenburg, PMN Werker, and DA McGrouther. The anatomy and function of clelands ligaments. Journal of Hand Surgery (European Volume), 39(5):482–490, 2014.
- [128] Muzaffer SİNDEL, Ramazan Yavuz ARICAN, Haluk ÖZCANLI, Menekşe CENGİZ, Semih GÜR, and Nigar KELEŞ. Clelands and graysons ligaments: an anatomic study. Fizyoterapi Rehabilitasyon, page 245.
- [129] Eduardo A Zancolli and Elbio P Cozzi. Atlas of surgical anatomy of the hand. Churchill Livingstone, 1992.
- [130] Marita Eisenmann-Klein and Maria Z Siemionow. Plastic and reconstructive surgery, with 476 illustrations., 2010.
- [131] Thomas W Wright, Frank Glowczewskie, David Cowin, and Donna L Wheeler. Radial nerve excursion and strain at the elbow and wrist associated with upper-extremity motion. The Journal of hand surgery, 30(5):990–996, 2005.
- [132] Thomas W Wright, Frank Glowczewskie, David Cowin, and Donna L Wheeler. Ulnar nerve excursion and strain at the elbow and wrist associated with upper extremity motion. The Journal of hand surgery, 26(4):655–662, 2001.
- [133] Odendal et al. Canine anatomy. Lecture Notes, Faculty of Veterinary Science, University of Pretoria, South Africa., 1996.
- [134] GE Loeb. Control implications of musculoskeletal mechanics. In Engineering in Medicine and Biology Society, 1995., IEEE 17th Annual Conference, volume 2, pages 1393–1394. IEEE, 1995.
- [135] IA Kapandji and LH Honoré. The physiology of the joints: The upper limb, vol. 1. churchill livingstone, 2007.
- [136] Francisco López Jiménez and Sergio Pellegrino. Constitutive modeling of fiber composites with a soft hyperelastic matrix. International Journal of Solids and Structures, 49(3):635–647, 2012.
- [137] Francisco López Jiménez and Sergio Pellegrino. Folding of fiber composites with a hyperelastic matrix. International Journal of Solids and Structures, 49(3):395–407, 2012.
- [138] Julianne L Holloway, Anthony M Lowman, and Giuseppe R Palmese. Mechanical evaluation of poly (vinyl alcohol)-based fibrous composites as biomaterials for meniscal tissue replacement. Acta biomaterialia, 6(12):4716–4724, 2010.
- [139] Nandan L Nerurkar, Dawn M Elliott, and Robert L Mauck. Mechanical design criteria for intervertebral disc tissue engineering. Journal of biomechanics, 43(6):1017–1030, 2010.
- [140] Shu Zhu, Ju-Hee So, Robin Mays, Sharvil Desai, William R Barnes, Behnam Pourdeyhimi, and Michael D Dickey. Ultrastretchable fibers with metallic conductivity using a liquid metal alloy core. Advanced Functional Materials, 23(18):2308–2314, 2013.

- [141] Andriy Fedorov, Reinhard Beichel, Jayashree Kalpathy-Cramer, Julien Finet, Jean-CristopheC. Fillion-Robin, Sonia Pujol, Christian Bauer, Dominique Jennings, FionaM Fennessy, Milan Sonka, John Buatti, StephenR Aylward, JamesV Miller, Steve Pieper, and Ron Kikinis. 3d slicer as an image computing platform for the quantitative imaging network. Magnetic Resonance Imaging, 30(9):1323–41, 11 2012.
- [142] Richard Arthur Pethrick, Taweechai Amornsakchai, and Alastair M North. Introduction to molecular motion in polymers. Whittles Publishing, 2011. Electronic Isbn 978-1-62870-078-7.
- [143] Richard Arthur Pethrick, Taweechai Amornsakchai, and Alastair M North. Introduction to molecular motion in polymers, page 85. Whittles Publishing, 2011. Electronic Isbn 978-1-62870-078-7.
- [144] Mouldlife Ltd. Mouldlife ltd, miro house, western way, bury st edmunds, suffolk, ip33 3sp, england. www.mouldlife.net. accessed September 22nd, 2016.
- [145] Polytek Development Corp. Polytek development corp. 55 hilton street, easton, pa 18042, usa. www.polytek.com. accessed September 22nd, 2016.
- [146] www.matweb.com. Overview of materials for polylactic acid (pla) biopolymer. <http://www.matweb.com/search/DataSheet.aspx?MatGUID=ab96a4c0655c4018a8785ac4031b9278&ckck=1>. accessed September 22nd, 2016.
- [147] www.perstorp.com. Product data sheet capa 6800 eng-6139.pdf. https://www.perstorp.com/en/Products/Capa_6800#. Accessed: 2014-06-23.
- [148] www.matweb.com. Overview of materials for acrylonitrile butadiene styrene (abs), molded. <http://www.matweb.com/search/datasheet.aspx?MatGUID=eb7a78f5948d481c9493a67f0d089646>. accessed September 22nd, 2016.
- [149] www.tomps.com. Addition cure rtv silicone rubber 22 shore a. <http://www.tomps.com/addition-cure-rtv-silicone-rubber-22-shore-a-500g-to-10kg-kits-addition-rtv-silicone/>. accessed September 22nd, 2016.
- [150] www.acc-silicones.com. Egel3000 2 part silicone gel low viscosity. <https://www.acc-silicones.com/content/featured-products/silicone-gels/egel3000.ashx>. accessed September 22nd, 2016.
- [151] www.acc-silicones.com. Mm906 condensation cure silicone moulding rubber base high tear. <https://www.acc-silicones.com/content/products/mould-making/mm906.ashx>. accessed September 22nd, 2016.
- [152] www.acc-silicones.com. Mm cat r5 nt tin catalyst fast cure speed, red. <https://www.acc-silicones.com/content/products/mould-making/mm-cat-r5-nt.ashx>. accessed September 22nd, 2016.

- [153] www.acc-silicones.com. Mmta2 thixotroping additive for condensation cure moulding rubber. <https://www.acc-silicones.com/content/products/mould-making/mmta2.ashx>. accessed September 22nd, 2016.
- [154] www.dupont.com/. Dupont elvax eva reains for adhesives, sealants and wax blends. http://www.dupont.com/content/dam/dupont/products-and-services/packaging-materials-and-solutions/packaging-materials-and-solutions-landing/documents/elvax_adhesives_wax_blends.pdf. accessed September 22nd, 2016.
- [155] www.dupont.co.uk. Dupont surlyn 8320 product data sheet. http://www.dupont.co.uk/content/dam/dupont/products-and-services/packaging-materials-and-solutions/packaging-materials-and-solutions-landing/documents/surlyn_8320.pdf. accessed September 22nd, 2016.
- [156] Marcus D Hanwell, Donald E Curtis, David C Lonie, Tim Vandermeersch, Eva Zurek, and Geoffrey R Hutchison. Avogadro: an advanced semantic chemical editor, visualization, and analysis platform. *Journal of cheminformatics*, 4(1):1, 2012.
- [157] www.ulprospector.com. Elvax40w ethylene vinyl acetate. <http://catalog.ides.com/Datasheet.aspx?I=9837&U=0&CULTURE=en-US&E=5658>. accessed September 22nd, 2016.
- [158] www.ulprospector.com. Elvax40l ethylene vinyl acetate. <http://catalog.ides.com/Datasheet.aspx?I=9837&U=0&CULTURE=en-US&E=39784>. accessed September 22nd, 2016.
- [159] www.ulprospector.com. Elvax150 ethylene vinyl acetate. <http://catalog.ides.com/Datasheet.aspx?I=9837&U=0&CULTURE=en-US&E=11759>. accessed September 22nd, 2016.
- [160] www.ulprospector.com. Elasto dryflex 500000 (shore oo hardness 28). <http://catalog.ides.com/Datasheet.aspx?I=9837&U=0&CULTURE=en-US&E=277435>. accessed September 22nd, 2016.
- [161] www.matweb.com. Ensinger tecamid 6/6 nylon. <http://www.matweb.com/search/datasheet.aspx?matguid=e95795afec4f46539c51269e453cba2b>. accessed September 22nd, 2016.
- [162] www.matweb.com. Kevlar-29. <http://www.matweb.com/search/DataSheet.aspx?MatGUID=7323d8a43cce4fe795d772b67207eac8>. accessed September 22nd, 2016.
- [163] www.matbase.com. material-properties-of-poly(lactic-acid)-monomere-pla-m.html. [http://www.matbase.com/material-categories/natural-and-synthetic-polymers/agro-based-polymers/material-properties-of-poly\(lactic-acid\)-monomere-pla-m.html#thermal-properties](http://www.matbase.com/material-categories/natural-and-synthetic-polymers/agro-based-polymers/material-properties-of-poly(lactic-acid)-monomere-pla-m.html#thermal-properties). Accessed: 2014-06-23.

- [164] www.hexpoltpc.com. mediprene-s.htm. <http://www.hexpoltpc.com/en/mediprene-s.htm>. Accessed: 2014-06-23.
- [165] www.matweb.com. Overview of materials for nylon 66 fiber. <http://www.matweb.com/search/DataSheet.aspx?MatGUID=af1029dd5d724a718a1740642b5ed3a8>. Accessed: 2014-06-23.
- [166] Hong-Ting Zhang. Comparison and analysis of thermal degradation process of aramid fibers (kevlar 49 and nomex). *J Fiber Bioeng Inform*, 3(3):163–167, 2010.
- [167] www.matweb.com. IndalloyTM 60 ga-in eutectic alloy. <http://www.matweb.com/search/datasheet.aspx?MatGUID=149bdf42822f44a2a7d46983b2ff3c72>. accessed September 22nd, 2016.
- [168] TJ Anderson and I Ansara. The ga-in(gallium–indium) system. *Journal of phase equilibria*, 12(1):64–72, 1991.
- [169] www.matweb.com. IndalloyTM 46 ga-in alloy. <http://www.matweb.com/search/datasheet.aspx?matguid=e7b61ba887f948fc87f55d0220e6282e&ckck=1>. accessed September 22nd, 2016.
- [170] www.chemicalonline.com. Nontoxic liquid metal alloy could substitute for mercury. <http://www.chemicalonline.com/doc/nontoxic-liquid-metal-alloy-could-substitute-0001>. accessed September 22nd, 2016.
- [171] Geratherm Medical AG. Geratherm medical ag. <http://geratherm.de/en/geratherm-2/company/>. accessed September 22nd, 2016.
- [172] G. Speckbrock, S. Kamitz, M. Alt, and H. Schmitt. Low melting gallium, indium, and tin eutectic alloys, and thermometers employing same. US Patent US6019509A, 1997. Assignee: Geraberger Thermometerwerk GmbH (DE). Accessed September 22nd, 2016.
- [173] R. A. Burton and R. G. Burton. Control of surface attack by gallium alloys in electrical contacts. *NASA STI/Recon Technical Report N*, 87, March 1986.
- [174] Yue-Guang Deng and Jing Liu. Corrosion development between liquid gallium and four typical metal substrates used in chip cooling device. *Applied Physics A*, 95(3):907–915, 2009.
- [175] Qin Xu, Nikolai Oudalov, Qiti Guo, Heinrich M Jaeger, and Eric Brown. Effect of oxidation on the mechanical properties of liquid gallium and eutectic gallium-indium. *Physics of Fluids (1994-present)*, 24(6):063101, 2012.
- [176] Lehigh University International Materials Institute. Glass education for students, teachers & general public: Glass education & videos. <http://www.lehigh.edu/imi/scied/libraryglassedu.html>. accessed September 22nd, 2016.

- [177] William R Heffner and Himanshu Jain. Building a low cost, hands-on learning curriculum on glass science and engineering using candy glass. In MRS Proceedings, volume 1233, pages 1233–PP03. Cambridge Univ Press, 2009.
- [178] Lothar W Kroh. Caramelisation in food and beverages. Food Chemistry, 51(4):373–379, 1994.
- [179] Kuraray WS Film Division. Monosol water soluble polymers. www.monosol.com. accessed September 22nd, 2016.
- [180] www.indium.com. Private communication indium corp. <http://www.indium.com>. accessed September 22nd, 2016.
- [181] www.indium.com. Indium tin oxide (ito) (in₂o₃):(sno₂). <http://www.indium.com/inorganic-compounds/indium-compounds/indium-tin-oxide/#products>. accessed September 22nd, 2016.
- [182] www.sigmaaldrich.com. Indium tin oxide nanopowder, 50 nm particle size. <http://www.sigmaaldrich.com/catalog/product/aldrich/544876?lang=en®ion=GB>. accessed September 22nd, 2016.
- [183] D Bulgin. Electrically conductive rubber. Rubber Chemistry and Technology, 19(3):667–695, 1946.
- [184] CRH Wildevuur, GL Mrava, MJ Crosby, JI Wright, HL Hladky, GJ Andreson, RM Pierson, T Kon, and Y Nosé. An artificial heart sensitive to atrial volume. ASAIO Journal, 14(1):276–283, 1968.
- [185] www.sigmaaldrich.com. Nickel powder, <50 μ m, 99.7% trace metals basis. <http://www.sigmaaldrich.com/catalog/product/aldrich/266981?lang=en®ion=GB>. accessed September 22nd, 2016.
- [186] www.sigmaaldrich.com. Nickel powder, <1 μ m, 99.8% trace metals basis. <http://www.sigmaaldrich.com/catalog/product/aldrich/268283?lang=en®ion=GB>. accessed September 22nd, 2016.
- [187] www.goodfellow.com. Polyamide - nylon 6,6 (pa 6,6). <http://www.goodfellow.com/E/Polyamide-Nylon-6-6.html>. accessed September 22nd, 2016.
- [188] Olivier Persenaire, Michael Alexandre, Philippe Degée, and Philippe Dubois. Mechanisms and kinetics of thermal degradation of poly (ϵ -caprolactone). Biomacromolecules, 2(1):288–294, 2001.
- [189] N Fitzpatrick. Annonomized clinical ct scan of canine forelimb and pes. Private communication. Noel Fitzpatrick, MVB, CertSAO, CertVR, Fitzpatrick Referrals, Halfway Lane, Eashing, Surrey GU7 2QQ, UK. E-mail: noelF@fitzpatrickreferrals.co.uk.

- [190] www.acc silicones.com. F111/100 pdms fluid technical data sheet. <https://www.acc-silicones.com/content/products/lubrication/f111.ashx>. accessed September 22nd, 2016.
- [191] Nick Hockings, Pejman Iravani, and Chris Bowen. Artificial ligamentous joints: methods, materials and characteristics. In IEEE-RAS International Conference on Humanoid Robots. University of Bath, 2014.
- [192] www.kraton.com. Product families kratonTM-fg. http://www.kraton.com/products/kraton_fg.php. accessed September 22nd, 2016.
- [193] www.sigmaaldrich.com. Polystyrene-block-poly(ethylene-ran-butylene)-block-polystyrene-graft-maleic anhydride. <http://www.sigmaaldrich.com/catalog/product/aldrich/432431?lang=en®ion=GB>. accessed September 22nd, 2016.
- [194] www.sonics.com. Plastics assembly hand welders compact and portable ultrasonics. <http://www.sonics.com/pa-ultra-handheld.htm>. accessed September 22nd, 2016.
- [195] H Forster and J Fisher. The influence of loading time and lubricant on the friction of articular cartilage. Proceedings of the Institution of Mechanical Engineers, Part H: Journal of Engineering in Medicine, 210(2):109–119, 1996.
- [196] Jing Liang. Investigation of Synthetic and Natural Lubricants. PhD thesis, North Carolina State University, Raleigh, NC 27695, USA, 8 2008. ISBN 0549822542, 9780549822547, <https://repository.lib.ncsu.edu/handle/1840.16/5805>.
- [197] Akihiro Nomura, Kenji Okayasu, Kohji Ohno, Takeshi Fukuda, and Yoshinobu Tsujii. Lubrication mechanism of concentrated polymer brushes in solvents: effect of solvent quality and thereby swelling state. Macromolecules, 44(12):5013–5019, 2011.
- [198] SM Tamboli, ST Mhaske, DD Kale, et al. Crosslinked polyethylene. Indian journal of chemical technology, 11(6):853–864, 2004.
- [199] GEO Specialty Chemicals. Di-cupTM and vul-cupTM peroxide fundamentals of crosslinking. <http://www.quimisor.com.mx/catalogo/hojastecnicas/infotecnica/ORC101.pdf>. accessed September 22nd, 2016.
- [200] Rik Verplancke, Frederick Bossuyt, Dieter Cuypers, and Jan Vanfleteren. Thin-film stretchable electronics technology based on meandering interconnections: fabrication and mechanical performance. Journal of Micromechanics and Microengineering, 22(1):015002, 2011.
- [201] Guangming Tao, Ayman F Abouraddy, Alexander M Stolyarov, and Yoel Fink. Multimaterial fibers. In Lab-on-Fiber Technology, pages 1–26. Springer, 2015.
- [202] David J Welker, Jeff Tostenrude, Dennis W Garvey, Brian K Canfield, and Mark G Kuzyk. Fabrication and characterization of single-mode electro-optic polymer optical fiber. Optics letters, 23(23):1826–1828, 1998.

- [203] www.arduino.cc. Arduino mega 2560 & genuino mega 2560. <https://www.arduino.cc/en/Main/ArduinoBoardMega2560>. accessed September 22nd, 2016.
- [204] processing.org. Processing. <https://processing.org/>. accessed September 22nd, 2016.
- [205] www.digikey.co.uk. Melexis technologies nv mlx90614esf-acf-000-tu. <http://www.digikey.co.uk/product-detail/en/melexis-technologies-nv/MLX90614ESF-ACF-000-TU/MLX90614ESF-ACF-000-TU-ND/2652200>. accessed September 22nd, 2016.
- [206] Eero Heurlin af. Is it hot? arduino + mlx90614 ir thermometer. <https://github.com/rambo/I2C>. See source code for full list of contributors. Accessed September 22nd, 2016.
- [207] bildr.org. Is it hot? arduino + mlx90614 ir thermometer. <http://bildr.org/2011/02/mlx90614-arduino/>. accessed September 22nd, 2016.
- [208] Markus Beckers, Tobias Schlüter, Thomas Vad, Thomas Gries, and Christian-Alexander Bunge. An overview on fabrication methods for polymer optical fibers. *Polymer International*, 64(1):25–36, 2015.
- [209] Mohammadreza Naeimirad, Ali Zadhoush, Afshin Abrishamkar, Ahmadreza Pishavar, and Andres Leal. Melt-spun liquid core fibers: physical and morphological characteristics. *Iranian Polymer Journal*, 25(5):397–403, 2016.
- [210] Broad Quay Bath Somerset BA1 1UD 3D Metal Printing Innovation Centre, University of Bath. 3d metal sintering. <http://3dmetalprinting.co.uk/>. accessed September 22nd, 2016.
- [211] KR Arnold and DJ Meier. A rheological characterization of sbs block copolymers. *Journal of Applied Polymer Science*, 14(2):427–440, 1970.
- [212] Qiumei Zeng. Characterizing the ultimate properties of triblock styrene-diene thermoplastic elastomers. PhD thesis, Texas Tech University, 2005.
- [213] George Benedikt. Metallocene technology in commercial applications. William Andrew, 1999.
- [214] Peter Aerts. Vertical jumping in galago senegalensis: the quest for an obligate mechanical power amplifier. *Philosophical Transactions of the Royal Society B: Biological Sciences*, 353(1375):1607–1620, 1998.
- [215] GJ Lutz and LC Rome. Built for jumping: the design of the frog muscular system. *Science (New York, NY)*, 263(5145):370, 1994.
- [216] W. Herzog. Muscle, chapter 2.7, pages 154–190. John Wiley & Sons, 1994. ISBN 0 471 94444.
- [217] Anthony J Channon, James R Usherwood, Robin H Crompton, Michael M Günther, and Evie E Vereecke. The extraordinary athletic performance of leaping gibbons. *Biology letters*, 8(1):46–49, 2012.

- [218] Jesper Bencke, R Damsgaard, Anders Saekmose, P Jørgensen, Kurt Jørgensen, and K Klausen. Anaerobic power and muscle strength characteristics of 11 years old elite and non-elite boys and girls from gymnastics, team handball, tennis and swimming. Scandinavian journal of medicine & science in sports, 12(3):171–178, 2002.
- [219] OMRI Inbar and ODED Bar-Or. Anaerobic characteristics in male children and adolescents. Med Sci Sports Exerc, 18(3):264–9, 1986.
- [220] Ian W Hunter and Serge Lafontaine. A comparison of muscle with artificial actuators. In Solid-State Sensor and Actuator Workshop, 1992. 5th Technical Digest., IEEE, pages 178–185. IEEE, 1992.
- [221] Andrew (Sir) Huxley. Reflections on muscle. In Volume 14 of The Sherrington lectures ; 14. Liverpool University Press, 1980.
- [222] LE Ford, AF Huxley, and RM Simmons. Tension responses to sudden length change in stimulated frog muscle fibres near slack length. The Journal of physiology, 269(2):441–515, 1977.
- [223] Constantinos N Maganaris, Vasilios Baltzopoulos, Derek Ball, and Anthony J Sargeant. In vivo specific tension of human skeletal muscle. Journal of applied physiology, 90(3):865–872, 2001.
- [224] Robert M Erskine, David A Jones, Constantinos N Maganaris, and Hans Degens. In vivo specific tension of the human quadriceps femoris muscle. European journal of applied physiology, 106(6):827–838, 2009.
- [225] M Runge and G Hunter. Determinants of musculoskeletal frailty and the risk of falls in old age. Journal of musculoskeletal and neuronal interactions, 6(2):167, 2006.
- [226] E Joan Bassey, Maria A Fiatarone, Evelyn F O’neill, Margaret Kelly, William J Evans, and Lewis A Lipsitz. Leg extensor power and functional performance in very old men and women. Clinical science, 82(3):321–327, 1992.
- [227] William J Evans and Jan Lexell. Human aging, muscle mass, and fiber type composition. The Journals of Gerontology Series A: Biological Sciences and Medical Sciences, 50(Special Issue):11–16, 1995.
- [228] Stefano Schiaffino and Carlo Reggiani. Fiber types in mammalian skeletal muscles. Physiological reviews, 91(4):1447–1531, 2011.
- [229] KW Ranatunga, BARBARA Sharpe, and B Turnbull. Contractions of a human skeletal muscle at different temperatures. The Journal of physiology, 390:383, 1987.
- [230] Mark D Jacobson, Rajnik Raab, Babak M Fazeli, Reid A Abrams, Michael J Botte, and Richard L Lieber. Architectural design of the human intrinsic hand muscles. The Journal of hand surgery, 17(5):804–809, 1992.

- [231] Richard L Lieber, Mark D Jacobson, Babak M Fazeli, Reid A Abrams, and Michael J Botte. Architecture of selected muscles of the arm and forearm: anatomy and implications for tendon transfer. The Journal of hand surgery, 17(5):787–798, 1992.
- [232] Richard L Lieber, Babak M Fazeli, and Michael J Botte. Architecture of selected wrist flexor and extensor muscles. The Journal of hand surgery, 15(2):244–250, 1990.
- [233] Roger V Gonzalez, Thomas S Buchanan, and Scott L Delp. How muscle architecture and moment arms affect wrist flexion-extension moments. Journal of biomechanics, 30(7):705–712, 1997.
- [234] Linda F Spenst, Alan D Martin, and Donald T Drinkwater. Muscle mass of competitive male athletes. Journal of sports sciences, 11(1):3–8, 1993.
- [235] Patrick Lochmatter, Gabor Kovacs, and Michael Wissler. Characterization of dielectric elastomer actuators based on a visco-hyperelastic film model. Smart Materials and Structures, 16(2):477, 2007.
- [236] Junichi Urata, Yuto Nakanishi, Kei Okada, and Masayuki Inaba. Design of high torque and high speed leg module for high power humanoid. In Intelligent Robots and Systems (IROS), 2010 IEEE/RSJ International Conference on, pages 4497–4502. IEEE, 2010.
- [237] www.amicell.co.il. Extreme high energy density lithium polymer series. <http://www.amicell.co.il/batteries/rechargeable-batteries/our-extreme-high-energy-density-lithium-polymer-series/>. accessed September 22nd, 2016.
- [238] HES Energy Systems <http://www.hes.sg/>. Aeropack worls’s longest endurance power solutions for electric uavs. http://media.wix.com/ugd/047f54_18f6b9d95c7c40c8859787879c130417.pdf. accessed September 22nd, 2016.
- [239] CF Gallo and WL Lama. Classical electrostatic description of the work function and ionization energy of insulators. IEEE Transactions on Industry Applications, IA-12(1):7–11, 1976.
- [240] LI Berger. Dielectric strength of insulating materials, chapter 15-46. CRC press, Boca Raton, Florida, 2014. in "CRC Handbook of Chemistry and Physics", 95th Edition.
- [241] Hidenori Suzuki, Shigeo Mukai, Yoshimichi Ohki, Yoshinobu Nakamichi, and Kohji Ajiki. Dielectric breakdown of low-density polyethylene under simulated inverter voltages. IEEE transactions on dielectrics and electrical insulation, 4(2):238–240, 1997.
- [242] AH Sharbaugh, JK Bragg, and RW Crowe. The dependence of the measured electric strengths of liquids on electrode spacing. In 1953 Conference on Electrical Insulation, pages 16–18. IEEE, 1953.
- [243] VA Zakrevskii et al. Electrical breakdown of thin polymer films. Physics of the Solid State, 47(5):961–967, 2005.

- [244] LJ Romasanta, MA Lopez-Manchado, and R Verdejo. Increasing the performance of dielectric elastomer actuators: A review from the materials perspective. Progress in Polymer Science, 51:188–211, 2015.
- [245] Gih-Keong Lau, Hoong-Ta Lim, Jing-Ying Teo, and Yao-Wei Chin. Lightweight mechanical amplifiers for rolled dielectric elastomer actuators and their integration with bio-inspired wing flappers. Smart Materials and Structures, 23(2):025021, 2014.
- [246] Chong Min Koo. Electroactive thermoplastic dielectric elastomers as a new generation polymer actuators. INTECH Open Access Publisher, 2012.
- [247] EL Grove and GE Walden. Variation of dielectric constant with temperature for some five- and six-carbon ketones. Journal of Chemical and Engineering Data, 10(2):98–100, 1965.
- [248] A Streitwieser. Ionization potentials in organic chemistry. In Progress in Physical Organic Chemistry, volume 1, page 1. Interscience New York, 1963.
- [249] Achille M. Bivigou-Koumba, Eckhard Görnitz, André Laschewsky, Peter Müller-Buschbaum, and Christine M. Papadakis. Thermoresponsive amphiphilic symmetrical triblock copolymers with a hydrophilic middle block made of poly(n-isopropylacrylamide): synthesis, self-organization, and hydrogel formation. Colloid and Polymer Science, 288(5):499–517, 2010.
- [250] Stefan CB Mannsfeld, Benjamin CK Tee, Randall M Stoltenberg, Christopher V HH Chen, Soumendra Barman, Beinn VO Muir, Anatoliy N Sokolov, Colin Reese, and Zhenan Bao. Highly sensitive flexible pressure sensors with microstructured rubber dielectric layers. Nature materials, 9(10):859–864, 2010.
- [251] Toshiro Niino, Toshiro Higuchi, and Saku Egawa. Dual excitation multiphase electrostatic drive. In Industry Applications Conference, 1995. Thirtieth IAS Annual Meeting, IAS'95., Conference Record of the 1995 IEEE, volume 2, pages 1318–1325. IEEE, 1995.
- [252] A John Harris, Marilyn J Duxson, Jane E Butler, Paul W Hodges, Janet L Taylor, and Simon C Gandevia. Muscle fiber and motor unit behavior in the longest human skeletal muscle. The Journal of neuroscience, 25(37):8528–8533, 2005.
- [253] NC Hockings, P Iravani, and CR Bowen. Smoothed particle machine perception. Poster, Visual Image Interpretation in Humans and Machines, 2014.
- [254] Richard A Newcombe, Steven J Lovegrove, and Andrew J Davison. Dtam: Dense tracking and mapping in real-time. In 2011 international conference on computer vision, pages 2320–2327. IEEE, 2011.
- [255] Ankur Handa, Richard A Newcombe, Adrien Angeli, and Andrew J Davison. Applications of legendre-fenchel transformation to computer vision problems. Department of Computing at Imperial College London. DTR11-7, 45, 2011.

- [256] Nikos Komodakis and Jean-Christophe Pesquet. Playing with duality: An overview of recent primal? dual approaches for solving large-scale optimization problems. IEEE Signal Processing Magazine, 32(6):31–54, 2015.
- [257] Jonathan T Barron and Jitendra Malik. Shape, illumination, and reflectance from shading. IEEE transactions on pattern analysis and machine intelligence, 37(8):1670–1687, 2015.
- [258] Qi Liu-Yin, Rui Yu, Andrew Fitzgibbon, Lourdes Agapito, and Chris Russell. Better together: Joint reasoning for non-rigid 3d reconstruction with specularities and shading. In Proceedings of the British Machine Vision Conference 2016. BMVA Press, September 2016.
- [259] Richard A Newcombe, Dieter Fox, and Steven M Seitz. Dynamicfusion: Reconstruction and tracking of non-rigid scenes in real-time. In Proceedings of the IEEE conference on computer vision and pattern recognition, pages 343–352, 2015.
- [260] JJ Monaghan. Smoothed particle hydrodynamics and its diverse applications. Annual Review of Fluid Mechanics, 44:323–346, 2012.
- [261] Joe J Monaghan. Smoothed particle hydrodynamics. Reports on progress in physics, 68(8):1703, 2005.
- [262] Xiao Yan, Yun-Tao Jiang, Chen-Feng Li, Ralph R Martin, and Shi-Min Hu. Multiphase sph simulation for interactive fluids and solids. ACM Transactions on Graphics (TOG), 35(4):79, 2016.
- [263] Fabian Spreng, Dirk Schnabel, Alexandra Mueller, and Peter Eberhard. A local adaptive discretization algorithm for smoothed particle hydrodynamics. Computational Particle Mechanics, 1(2):131–145, 2014.
- [264] Bart Adams, Mark Pauly, Richard Keiser, and Leonidas J Guibas. Adaptively sampled particle fluids. In ACM Transactions on Graphics (TOG), volume 26, page 48. ACM, 2007.
- [265] R Vacondio, BD Rogers, PK Stansby, P Mignosa, and J Feldman. Variable resolution for sph: a dynamic particle coalescing and splitting scheme. Computer Methods in Applied Mechanics and Engineering, 256:132–148, 2013.
- [266] Qingang Xiong, Bo Li, and Ji Xu. Gpu-accelerated adaptive particle splitting and merging in sph. Computer Physics Communications, 184(7):1701–1707, 2013.
- [267] Rama C. Hoetzlein. Fast fixed-radius nearest neighbors: Interactive million-particle fluids. GPU Technology Conference, 2014. San Jose, CA. Online at <http://fluids3.com>, 2014. accessed September 22nd, 2016.
- [268] Adam Jacobs, Pejman Iravani, and Katherine Fraser. Opencl-sph. <https://github.com/tauroid/openc1-sph>, 2016. accessed September 22nd, 2016.

- [269] Wai Shing Fung, Ramesh Hariharan, Nicholas JA Harvey, and Debmalya Panigrahi. A general framework for graph sparsification. In Proceedings of the forty-third annual ACM symposium on Theory of computing, pages 71–80. ACM, 2011.
- [270] Nicholas Carlevaris-Bianco and Ryan M Eustice. Conservative edge sparsification for graph slam node removal. In 2014 IEEE International Conference on Robotics and Automation (ICRA), pages 854–860. IEEE, 2014.
- [271] Teuvo Kohonen. Self-organized formation of topologically correct feature maps. Biological cybernetics, 43(1):59–69, 1982.